CONDENSATION OF HYDROCARBONS AND ZEOTROPIC HYDROCARBON/REFRIGERANT MIXTURES IN HORIZONTAL TUBES

A Dissertation
Presented to
The Academic Faculty

By

Jeffrey A. Milkie

In Partial Fulfillment
Of the Requirements for the Degree
Doctor of Philosophy in Mechanical Engineering

Georgia Institute of Technology

May 2014

CONDENSATION OF HYDROCARBONS AND ZEOTROPIC HYDROCARBON/REFRIGERANT MIXTURES IN HORIZONTAL TUBES

Approved by:

Dr. Srinivas Garimella, Advisor
G.W. Woodruff School of Mechanical Engineering
Georgia Institute of Technology

Dr. Thomas Fuller
School of Chemical & Biomolecular Engineering
Georgia Institute of Technology

Dr. S. Mostafa Ghiaasiaan
G.W. Woodruff School of Mechanical Engineering
Georgia Institute of Technology

Dr. William Koros
School of Chemical & Biomolecular Engineering
Georgia Institute of Technology

Dr. Satish Kumar
G.W. Woodruff School of Mechanical Engineering
Georgia Institute of Technology

Date Approved: [March 3, 2014]

To my wife, Angela

ACKNOWLEDGMENTS

TABLE OF CONTENTS

LIST OF TABLES

viii

LIST OF FIGURES

xvii

NOMENCLATURE
Symbols

a	Empirical coefficient, [-]
A	Area, [m^2]
AD	Average deviation, [-]
AAD	Absolute average deviation, [-]
b	Empirical coefficient, [-]
Bo	Bond number $\equiv \rho g L^2 \sigma^{-1}$, [-]
c	Empirical coefficient, [-]
C_0	Distribution parameter, [-]
C_p	Specific heat, [kJ kg^{-1} K^{-1}]
C_T	Molar concentration, [kmol m^{-3}]
D	Diameter, [mm]
D_{12}	Binary diffusion coefficient, [m^2 s^{-1}]
e	Surface roughness, [m]
f	Friction factor, [-]
f(,)	Function of, [-]
f_i	Interfacial friction factor, [-]
F	Stress ratio $\equiv \tau_\text{wall}/\rho_\text{l} g \delta$, [-]
Fr	Froude number $\equiv U/\sqrt{gD}$, [-]
G	Mass flux, [kg m^{-2} s^{-1}]
g	Gravitational constant, 9.81 [m s^{-2}]
Ga	Galileo number $\equiv \left(gD^3 \rho^2\right)/\mu^2$, [-]

h	Heat transfer coefficient, [kW m^{-2} K^{-1}]
h_L	Liquid height, [mm]
h_G	Gas/Vapor-phase height, [mm]
i	Enthalpy,[kJ kg^{-1}]
i_{fg}	Latent heat, [kJ kg^{-1}]
j	Superficial velocity, [m s^{-1}]
Ja	Jacob Number $\equiv \rho_l C_{pl} \Delta T / \rho_v i_{fg}$, [-]
J_G	Dimensionless gas velocity $\equiv Gq / \sqrt{Dg\rho_v (\rho_l - \rho_v)}$, [-]
J_G^{T}	Transitional dimensionless gas velocity, [-]
k	Thermal conductivity,[kW m^{-1} s^{-1}]
L	Length, [mm]
Le	Lewis number $\equiv \alpha / D_{12}$, [-]
$LMTD$	Log-mean temperature difference, [K]
$\dot{m}$	Mass flow rate, [kg s^{-1}]
MW	Molecular weight, [kg kmol^{-1}]
$\tilde{N}$	Net molar condensation rate, [kmol s^{-1}]
Nu	Nusselt number $\equiv hD/k$, [-]
P	Pressure, [kPa]
Px	Pixel, [-]
P_r	Reduced pressure, [-]
Pr	Prandtl number $\equiv C_p \mu / k$, [-]
Q	Energy, [kJ]

$\dot{Q}$ — Heat duty, [W]

q — Mass based quality $\equiv \dot{m}_v / \dot{m}_T$, [-]

q'' — Heat flux, [kW m^{-2}]

R — Thermal resistance, [K W^{-1}]

$r*$ — Radii ratio $\equiv r_{outer} / r_{inner}$, [-]

R_u — Universal gas constant $\equiv 8.314$ [kJ kmol^{-1}K^{-1}]

Ra — Rayleigh number $\equiv \left(g\beta(\Delta T)L^3 \right) / (\nu\alpha)$, [-]

Ra^* — Modified Rayleigh number, [-]

Re — Reynolds number, [-]

S — Slip Ratio, [-]

Sc — Schmidt number $\equiv \mu / (D_{12} \cdot \rho)$, [-]

Sh — Sherwood number $\equiv Nu \cdot (Sc/Pr)$, [-]

T — Temperature, [°C]

UA — Overall conductance, [W K^{-1}]

U — Velocity, [m s^{-1}]

$\dot{V}$ — Volumetric flow rate, [L min^{-1}]

$\dot{W}$ — Work, [W]

We — Weber number $\equiv DG^2 / \rho\sigma$, [-]

x — Bulk mass based concentration, [kg kg^{-1}]

X_{LM} — Lockhart-Martinelli parameter $\equiv \left(\left.\frac{dP}{dL}\right|_{VO} \middle/ \left.\frac{dP}{dL}\right|_{LO} \right)$, [-]

X_{tt} *Turbulent-turbulent* Lockhart-Martinelli parameter, [-]

$\hat{x}$ Liquid phase mass concentration, [kg kg^{-1}]

$\tilde{x}$ Liquid phase mole concentration, [kmol kmol^{-1}]

$\hat{y}$ Vapor phase mass concentration, [kg kg^{-1}]

$\tilde{y}$ Vapor phase mole concentration, [kmol kmol^{-1}]

$\tilde{z}$ Mole flux ratio $\equiv \tilde{N}_1 \Big/ \left(\tilde{N}_1 + \tilde{N}_2 \right)$, [-]

Greek Symbols

α Void fraction $\equiv A_v / A$, [-]

OR Thermal diffusivity, [m^2 s^{-1}]

Volumetric expansion coefficient, [K^{-1}]

β OR Mass transfer coefficient, [m s^{-1}]

OR Homogeneous void fraction,[-]

Δ Difference between or change in, [-]

δ Film thickness, [mm]

Γ Pressure drop ratio $\equiv \left(\dfrac{dP}{dL}\bigg|_{VO} \Big/ \dfrac{dP}{dL}\bigg|_{LO} \right)$, [-]

ε Emissivity, [-]

θ Internal angle, [radians]

ϕ Two-phase multiplier, [-]

γ Slip factor, [-]

μ Dynamic viscosity, [kg m^{-1} s^{-1}]

v	Kinematic viscosity, $[\text{m}^2\,\text{s}^{-1}]$
ρ	Density, $[\text{kg m}^{-3}]$
σ_{SB}	Stephan-Boltzmann constant $\equiv 5.67 \times 10^{-8}$, $[\text{Wm}^{-2}\text{K}^{-4}]$
σ	Surface tension, $[\text{N m}^{-1}]$
τ	Torque, $[\text{N m}]$
τ_{wall}	Wall shear stress, $[\text{Pa}]$
ω	Angular velocity, $[\text{radians min}^{-1}]$
	OR Frequency, $[\text{s}^{-1}]$
ξ	Wetted perimeter ratio, $[\text{-}]$
∇	Gradient, change per unit length, $[\text{-}]$
Ψ	Lee and Lee (2001) correction factor, $[\text{-}]$

Subscripts and Superscripts

Actual	Actual work
Air	Ambient air
Amb	Ambient
Annulus	Annulus between inner and outer test section tubes
Avg	Average
B	Bottom
Bub	Bubble point
c	Cross sectional
	OR Characteristic
conv	Convection

Core	Vapor core
crit	Critical
CU	Critical upper
D	ΔT-dependent
Dew	Dew point
Decel	Deceleration pressure drop
eq	Equivalent
Effective	Effective
Evap	Evaporator
f	Condensing fluid or mixture
fr	frictional
film	Film
Glide	Temperature glide
h	Hydraulic
HT	Heat transfer
I	ΔT-independent
i	inner
in	inlet
int	interface
ins	Insulation
l	liquid
L	Lower
LO	Liquid-only

loop	Entire experimental loop
loss	Ambient loss
m	Mixture
Measured	Measured Value
nat,conv	Natural convection
o	outer
OT	Outer tube
out	outlet
PB	Price and Bell (1974)
Pre	Pre-condenser
Pri	Primary loop
Pool	Liquid Pool
Post	Post-Condenser
Pump	Primary loop pump
rad	Radiation
sat	Saturation
Sec	Secondary loop
shaft	Shaft work
ST	Stratified
So	Soliman(1982) modified Froude or Weber number
Source	Source
Sub	Subcool
Sup	Superheat

T	Total
	OR Top
Tee	Tee connected to test section
Test	Test section
Tube	Tube
U	Upper
v	Vapor
tp	Two-phase
w	Coolant water
wall	wall

SUMMARY

An experimental investigation of condensation of hydrocarbons and hydrocarbon/refrigerant mixtures in horizontal tubes was conducted. Heat transfer coefficients and frictional pressure drops during condensation of a zeotropic binary mixture of R245fa and *n*-pentane in a 7.75 mm internal diameter round tube were measured across the entire vapor-liquid dome, for mass fluxes ranging from 150 to 600 kg m^{-2} s^{-1}, and reduced pressures ranging from 0.06 to 0.23. Condensation experiments were conducted for the mixture, as well as its pure constituents over a similar range of conditions. In addition, condensing flow of the hydrocarbon propane was documented visually using high-speed video recordings. Results from these experiments were used to establish the two-phase flow regimes, void fractions, and liquid film thicknesses during condensation of propane flowing through horizontal tubes with internal diameters of 7 and 15 mm. These measurements were made over mass fluxes ranging from 75 to 450 kg m^{-2} s^{-1}, operating pressures ranging from 952 to 1218 kPa, and vapor qualities ranging from 0.05 to 0.95. Liquid film thickness and void fraction data were subsequently be used to assist the development of heat transfer and pressure drop models. In particular, the heat transfer coefficients and pressure drops observed in the mixture were compared with the corresponding values for the pure constituents. Models for heat transfer and pressure drop in the pure components as well as the mixtures were developed based on the data from the present study. This work extends the available literature on two-phase flow regimes for air-water mixtures, steam, and refrigerants to include hydrocarbons. Additionally, the limited information on condensation in multi-constituent hydrocarbon-hydrocarbon and refrigerant-refrigerant mixtures was extended to include hydrocarbon-

refrigerant mixtures. The findings of this study are expected to benefit applications such as refrigeration, low-grade heat-driven power generation, and the development of heat exchangers for the chemical and process industries.

CHAPTER 1.INTRODUCTION

As the rate of fossil fuel usage and concerns regarding the subsequent environmental effects increase, there has been renewed interest in the development and utilization of geothermal energy sources. Geothermal systems use low-grade thermal energy to generate electric power. Efficient and economic recovery of such energy for power generation poses significant challenges, such as the use of working fluids for power cycles. The constant phase-change temperature of the typically used pure fluids results in temperature pinches that cause exergy losses in the heat exchangers coupling geothermal heat sources to the power cycles, resulting in a notable drop in overall system efficiency. This is particularly important in geothermal cycles because the low source temperatures at which such energy is available, compared to fossil fuel combustion, already limits power generation efficiencies. One way to reduce these losses is to develop new working fluids that avoid temperature pinches.

The desire for new working fluids is amplified by the need for increased energy efficiency across many applications: for power generation, HVAC&R, water heating, and chemical processing. Furthermore, with respect to environmental concerns, it is necessary to find high-efficiency fluids with low Global Warming Potentials (GWP). Zeotropic mixtures have been proposed as working fluids to increase the thermodynamic efficiency of binary power generation cycles coupled to low-grade ($T < 150°C$) geothermal reservoirs DiPippo (2005) and other low-temperature sources such as solar thermal and industrial process waste heat (Wu, 1985; Wang and Zhao, 2009; Chys *et al.*, 2012; Ho *et al.*, 2012) and Zhao, 2009; Chys *et al.*, 2012; Ho *et al.*, 2012). Zeotropic mixtures are classified as mixtures of two or more fluids where the concentrations of the liquid ($\hat{x}$)

and vapor ($\hat{y}$) phases differ at equilibrium. The result is a change in the equilibrium temperature through the phase-change region, referred to as a temperature glide. A *T-x-y* diagram with the mass fraction of R245fa on the abscissa and the equilibrium temperature on the ordinate is shown in Figure 1.1. For a mixture of 45% R245fa/55% *n*-pentane (by mass), the mixture begins to condense at (B' – B) at 71.2°C and the last vapor is condensed at (D' – D) at 55.0°C, resulting in a temperature glide of 16.2°C. Mixtures of two components can form a zeortropic mixture or an azeotropic mixture, depending on the concentration of each fluid. At an approximate concentration of 83% R245fa/17% *n*-pentane (by mass) as shown in Figure 1.1, the mixture exhibits an azeotropic point, where the bubble point and dew point lines converge. Here, this mixture behaves as a pure fluid in the phase-change region, while at other concentrations, it would be considered a zeotropic mixture.
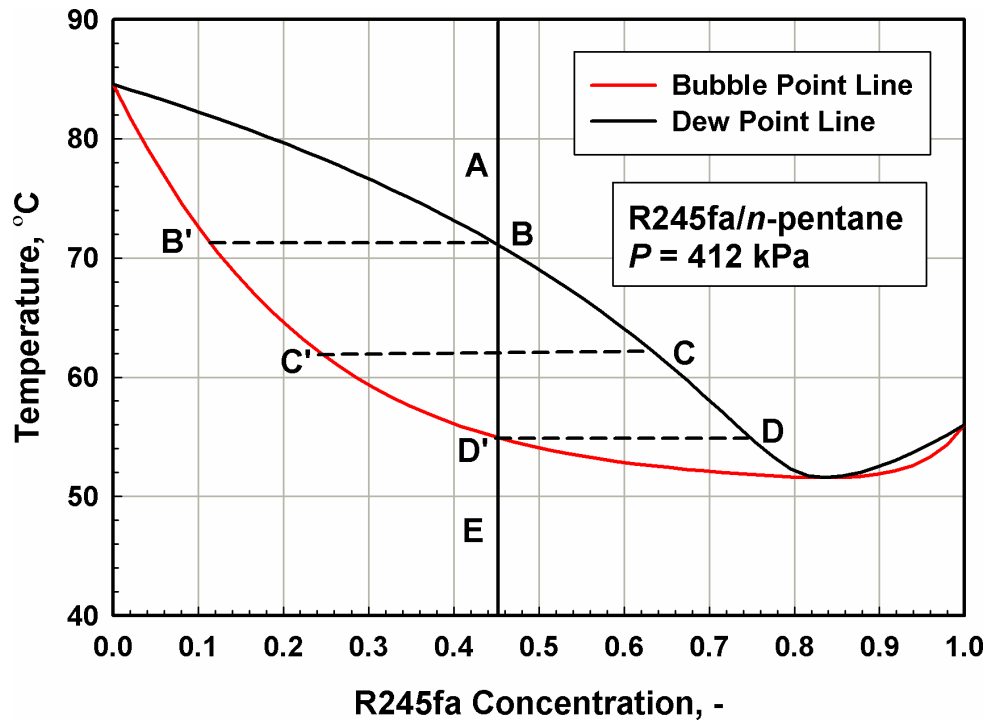
Figure 1.1. Zeotropic mixture *T-x-y* diagram for R245fa/*n*-pentane (mass concentration basis)

Two representative power cycles with representative source and sink temperature profiles overlaid are shown in Figure 1.2, the cycle on the left shows a zeotropic mixture (R245fa/*n*-pentane), while the cycle on the right shows a pure fluid (steam) for comparision. The zeotropic mixture exhibits a temperature glide though the phase-change regions. By tailoring the concentration of the zeotropic mixture to a specific souce, the temperature differences in the boiler and condenser are smaller for the zeotropic mixture, resulting in lower irreversibilities in the heat transfer process. Furthermore, the zeotropic mixtures decrease the potential for temperature pinchpoints.
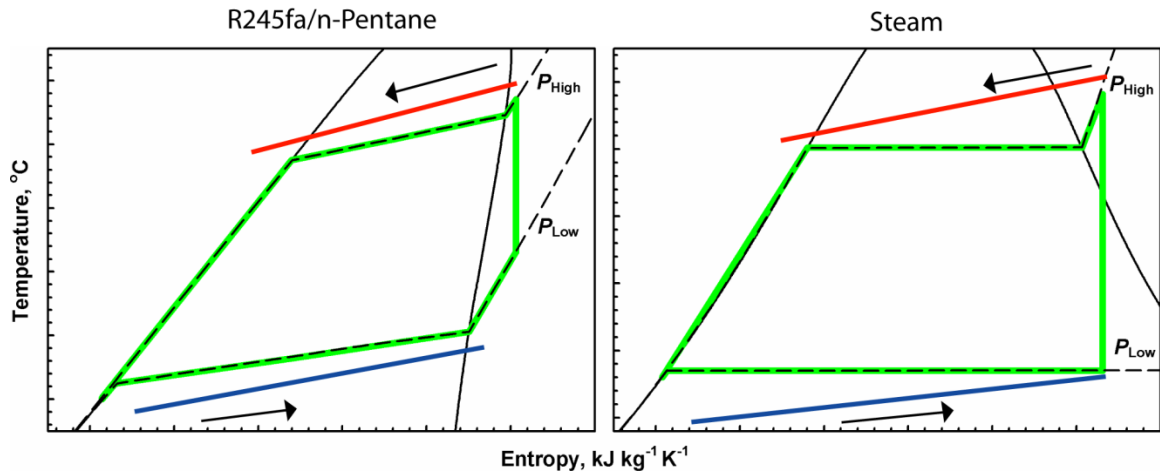
Figure 1.2. Idealized zeotropic mixure and pure fluid steam cycle comparison

Natural working fluids such as hydrocarbons, and synthetic refrigerants such as R245fa are being considered for use in these processes. While hydrocarbons offer good cycle efficiencies at low GWPs (3 – 5 compared to > 1,000 for typical refrigerants), there are obvious flammability concerns associated with the use of hydrocarbons in HVAC&R and water heating applications. Past computational studies have shown increased efficiencies when using zeotropic hydrocarbon and synthetic refrigerant mixtures while also reducing flammability concerns (with sufficiently high refrigerant concentrations) and maintaining low GWPs (Garg *et al.*, 2013). However, although zeotropic mixtures have thermodynamic advantages, mass transfer resistances in the vapor-phase during condensation limit heat transfer rates. The mass transfer effects on heat transfer in zeotropic hydrocarbon and synthetic refrigerant mixtures are not well understood. The present study is focused on experimentally investigating condensation in single-component and binary zeotropic mixtures for the purpose of designing efficient and economically viable low-grade thermal energy systems.

Condensation studies in the literature have focused primarily on pure refrigerants, pure hydrocarbons, azeotropic, and near-azeotropic mixtures. Mixtures of dissimilar

4

fluids, such as hydrocarbons and refrigerants, are absent from the literature; therefore, a comprehensive investigation of binary fluid mixture condensation of 45% R245fa/55% *n*-pentane (by mass) was conducted in the present study at typical power plant condenser conditions. This specific combination of fluids exhibits ~16°C temperature glide between the dew and bubble points over the range of conditions of interest. Heat transfer coefficients and frictional pressure gradients of the individual components and the mixture are measured as a function of pressure, mass flux, and quality. The results for the mixture are compared with those for the pure component fluids to determine the degradation of overall heat transfer due to mass transfer effects. An estimate of the effects of the mass transfer resistances on the heat transfer process can be obtained using the concentration shift of both phases and the temperature glide from the *T-x-y* diagram for the mixture of interest. The larger the temperature glide and the greater the concentration shifts, the more of an effect mass transfer will have.

Accurate flow regime characterization and void fraction models are vital for the modeling of pressure drop and heat transfer in two-phase flow, and critical to the understanding of condensing hydrocarbon flows in geothermal applications. Such understanding benefits applications in the process industry using propane as a refrigerant or working fluid. Studies in the literature on two-phase flow regimes and void fraction have focused on air-liquid mixtures, steam, refrigerants, and select very low pressure hydrocarbons. In the present study, condensing flow phenomena of the hydrocarbon propane are documented visually using high-speed video recordings at saturation temperatures of 25 to 35°C. The results from the experimental portion of this study include detailed observations and quantitative parameters describing condensing

hydrocarbon propane flows, and frictional pressure drop and heat transfer coefficient measurements of refrigerant R245fa, hydrocarbon *n*-pentane, and a zeotropic binary mixture of these fluids. The observations of the flow mechanisms are used to develop flow regime and void fraction models for hydrocarbon flows. Heat transfer coefficient and frictional pressure drop data are combined with flow regime observations to develop mechanistic frictional pressure drop and heat transfer coefficient models for refrigerant R245fa, hydrocarbon *n*-pentane, and a zeotropic binary mixture of these fluids. The findings of this study are expected to yield improved models for the prediction of frictional pressure drops and heat transfer coefficients of condensing hydrocarbons and their zeotropic mixtures with synthetic refrigerants. Applications such as refrigeration, low-grade heat-driven power generation, and the development of heat exchangers for the chemical and process industries will benefit from these models.

Following this introduction, a review of the relevant literature on two-phase flow regimes, void fraction, frictional pressure drop, and heat transfer for pure fluid and zeotropic mixture effects is presented Chapter 2. In Chapter 3, the experimental approach and test facility used in this study, as well as the test matrix is described. The data analysis methods and associated uncertainty analyses used to reduce experimental pressure drop, heat transfer, and high-speed video data are discussed in Chapter 4, showing how the relevant condensation quantities and flow parameters, including void fraction, film thickness, frictional pressure drop, and heat transfer coefficients are derived from the data. Experimental results and discussion of key trends in the data, followed by comparisons with the predictions of models and correlations from the literature are presented in Chapter 5. Model development, followed by a brief discussion on how to use

these models in condenser design applications for zeotropic mixtures are presented in Chapter 6. Finally, conclusions from this study as well as recommendations for further research are presented in Chapter 7.

CHAPTER 2. LITERATURE REVIEW

This chapter presents a review of the literature pertinent to the present study on condensing hydrocarbons and zeotropic hydrocarbon/refrigerant mixtures. The review is subdivided into four primary sections, two-phase flow regimes, void fraction, pressure drop, and heat transfer. Due to the lack of condensation studies on R245fa, several evaporation studies conducted with R245fa in microchannels are examined briefly at the end of this section.

2.1 Two-Phase Flow Regimes

Proper classification of the two-phase flow regime is critical to the development of accurate models of the condensation process. For the purpose of the present study flow regime studies can be classified into two subcategories: adiabatic and condensing flows.

2.1.1 Adiabatic flows

One of the earliest two-phase flow regime maps was proposed by Baker (1954) for adiabatic air/water flows in 25.4, 50.8, and 101.6 mm diameter tubes. His map classifies flows into bubble, plug, stratified, wavy, slug, annular, and spray regimes based on subjective observations. Although he acknowledges transitions occurring over a range of conditions, specific transition lines are defined for air/water flows. It was observed that flow regime has a strong dependence on liquid and vapor phase mass fluxes: the abscissa is plotted using the ratio of the liquid to vapor phase mass flux and the ordinate axis is plotted using the vapor-phase mass flux. Empirical property corrections using phase density, viscosity, and surface tension were proposed to adjust the axes for fluids other than air/water. Baker noted the importance of flow regime on pressure drop, developing regime-specific two-phase multipliers. Later, Scott (1964) used data from Hoogendoorn

(1959) for air/water and air/oil mixtures in 24 to 140 mm smooth and rough horizontal tubes to modify the Baker (1954) map to include flow regime transition regions.

Wallis and Dobson (1973) studied the wavy to slug transition in square and rectangular channels with hydraulic diameters of 25.4 to 137.7 mm using air/water mixtures for no net liquid flow, counter-current flow, and co-current flows. They found that slug flows occurred when waves grow and reach the top of the channel and the co-current flows transition to slug flow slower than counter-current flows. They found small wave theory to be insufficient in describing the transition. They proposed that slug flow be modeled as large amplitude waves that are pushed up by gas behind it and pulled forward by decreased pressure at the wave crest.

Mandhane *et al.* (1974) developed a flow map using a database of 5,935 flow regime observations for air/water and other fluids in tube diameters ranging from 12.7 to 165.1 mm. They developed empirical transition lines for the 1,178 air/water data. Rather than adjust the axis for fluids other than air/water, empirical fluid property factors, modified from Govier and Aziz (1972), are applied to the transition lines. Superficial liquid velocity and superficial vapor velocity are used to plot the data on the abscissa and the ordinate axes, respectively. They did not observe diameter effects at diameters greater than 12.7 mm, although the use of superficial velocity does include diameter. Their proposed map showed significantly better agreement with air/water data than the other flow regime maps that they examined. When considering all the data, they found better agreement with data for tube diameters below 50.8 mm than for larger diameters. However, overall predictive capability for their proposed map was low, with 80.1% of the air/water data and only 68.2% of all the data properly predicted in the correct regime,

leading them to conclude that further work is necessary with adjustments needed for fluid properties. Mandhane *et al.* (1974) found excellent agreement between the air/water data and the Baker (1954) map for their annular-mist flows, with reasonable agreement with the stratified regime observations. Other regimes observed in their air/water data were not predicted well by the Baker map.

Jones Jr and Zuber (1975) measured time varying area averaged void fractions of air/water mixtures in vertical rectangular channels (4.98 mm × 63.5 mm) using a fast response x-ray. They calculated the associated probability density functions (PDF), which differ significantly for bubbly, slug, and annular flows. They suggested that variations in void fraction measurements with time could be used to distinguish between flow regimes. Specifically, they proposed that the probability density function (PDF) for annular flows will show a single peak at high values of void fraction, bubble flows will show a single peak at low values of void fraction, and slug flows will show dual peaks. They found slug flows to occur for void fractions ranging of ~0.2 to ~0.8. No specific transition criteria were presented.

Taitel and Dukler (1976) derived theoretical dimensionless flow regime boundaries as functions of phase mass fluxes, fluid properties, and tube diameter. They divided the flows into five regimes: intermittent (slug and plug), stratified-smooth, stratified-wavy, dispersed bubble, and annular-annular dispersed. The Taitel and Dukler (1976) map is presented using the Lockhart Martinelli parameter (X_{LM}), which is directly related to the liquid volume fraction, as the abscissa and dimensionless terms F, T, and K as the ordinate axes. Regime transitions are derived starting from stratified flow, analyzing the mechanisms responsible for transitions to other regimes and balancing forces on each

phase. The transition from stratified to wavy flow (K transition) is derived for wave propagation on a quiescent liquid. Stratified-to-intermittent flow transition (F transition) is derived from Kelvin-Helmholtz theory for a wave height equal to half the tube diameter. Intermittent-to-annular flow transition, defined by the condition of insufficient liquid to maintain a slug resulting in annular or annular dispersed flow, is derived assuming a constant liquid height to diameter ratio (h_L/D) of 0.5, which corresponds to a constant $X_{LM} = 1.6$. The intermittent-to-dispersed transition (T transition) is defined by turbulent forces overcoming buoyancy force. For comparison with transition criteria from the literature, they transformed their transition lines to superficial gas velocity (j_v) and superficial liquid velocity (j_l). Taitel and Dukler found reasonable agreement with the empirical map of Mandhane *et al*. (1974), but argue that the superficial velocity axis system used by Mandhane *et al*. does not account for property influences and diameter effects for a tube with an internal diameter greater than 50 mm.

Weisman *et al.* (1979) systematically studied the effects of tube diameter and fluid properties (liquid viscosity, liquid density, vapor density, and surface tension) on flow regime transitions for horizontal flows from 11.5 to 51 mm internal diameter tubes using air/water, air/glycerin, air/oil, and R113. They classified flows as annular, separated, intermittent, and dispersed (Dukler and Hubbard, 1975). For air/water mixtures, Weisman *et al.* (1979) found an equilibrium situation at $L/D = 60$ by examining regime transitions at the beginning, middle, and end of the test section with the first measurement made 203 mm from the mixing location. They found the transitions observed in 11.5 mm tubes to be essentially the same at these three locations. At 25.0 mm, they found only slight variations between the middle and end locations, with transitions observed in the first

location to show wavy to slug transitions at higher liquid flowrates. In an attempt to develop quantifiable indicators to corroborate regime observations, they used fluctuations in pressure drop measurements to distinguish between regimes. Stratified flows show nearly no fluctuations in pressure drop measurements, slug flows show distinct disturbances around the transitions between slug and plug, wavy-annular and dispersed flows show increasing amplitudes of continuous disturbances. Over the range of conditions studied, they observed only slight effects of diameter and fluid properties, confirming the observation of little effect of diameter greater than approximately 10 mm by Mandhane *et al.* (1974). They found that liquid viscosity affects the transition to annular and dispersed flows. They also found surface tension to affect the stratified-to-wavy transition, with an increase in surface tension causing the transition to wavy flow to occur at lower gas-phase mass fluxes. They found that an increase in liquid density delays the separated-to-intermittent transition, and the transition to dispersed flows to higher liquid mass fluxes. Finally, they found that an increase in gas-phase density required a higher gas-phase mass flux to transition to annular flows and a lower gas-phase mass flux to transition from stratified to wavy flows. Using their observations, they proposed a new flow regime map using diameter and property corrections to the superficial velocities. Empirical transition lines for air/water mixtures in 25.4 mm round tubes are presented. Comparisons of their proposed transitions for air/water to the flow regime maps of Baker (1954) as modified by Scott (1964) and Taitel and Dukler (1976) showed good agreement.

Barnea and coworkers extended the theoretical work of Taitel and Dukler (1976) to improve predictive capabilities. Barnea *et al.* (1983) studied air/water flow patterns in 4

to 12.5 mm internal diameter tubes, specifically examining the effect of surface tension on regime transitions as diameters are decreased. They identified four main regimes: dispersed, annular, intermittent, and stratified. Barnea *et al.* (1982) modified the criteria developed by Taitel and Dukler (1976) for the slug-to-annular transition to $h_L/D = 0.35$ rather than 0.5. Except for the stratified-to-annular and intermittent transition, they found that the Taitel and Dukler (1976) transitions, as modified by Barnea *et al.* (1982), predicts the transitions observed in their data well. Observing a dependence on surface tension as diameter decreases below 25 mm, they note that the stratified-to-annular and stratified-to-intermittent transitions developed using the Kelvin-Helmholtz theory proposed by Taitel and Dukler (1976) is no longer valid because surface tension effects cannot be ignored. They propose a modification of the transition between stratified flows and annular and intermittent flows to include surface tension forces through a modified h_G to define the condition for intermittent flow. The resulting equation predicts a constant minimum gas height (h_G) for small tubes that are more likely to exhibit strong surface tension effects. Intermittent flow can be assumed if sufficient liquid is present, namely $h_G < (\pi D)/4$. Later, Barnea and Brauner (1985) expanded the regime map to include a model of the elongated bubble-to-liquid slug transition by balancing the forces of turbulence attempting to break up vapor bubbles and the stabilizing coalescence forces of gravity and surface tension for tubes less than 50 mm internal diameter using air/water. They found good agreement with horizontal and vertical air/water and air/oil flows. They identify a stable slug length of 32D for horizontal flows, twice the stable slug length in vertical tubes.

Jassim (2006) and Jassim *et al.* (2007) developed an automated image analysis program to characterize the flow regime of each image in a series to develop a database of "fraction of time" for each regime for adiabatic horizontal flows of R134a and R410A in 1.74 to 8 mm internal diameter tubes at saturation temperatures of 25 to 49.7°C. They used video at 30 frames per second with a striped background image to distinguish between phases. Each frame is converted to black and white using a greyscale threshold value. The resulting image presents a black vapor-liquid interface with the lines on the background image being distorted at the vapor-liquid interface. Depending on the distortion pattern, regime classification is made. They identified intermittent/liquid, stratified, and annular flows and defined the flows using four probabilities: liquid, intermittent, vapor, and annular regimes. Using the experimental results, Jassim (2006) developed a probabilistic flow regime map. Intended to be used to develop flow-regime-specific void fraction, pressure drop, and heat transfer models, the map proposed by him ensures continuity across the quality range. The probabilities are empirically correlated using fluid properties including the density ratios, Weber number, and Froude number. The map is presented with quality on the abscissa and probability or "fraction of time" on the ordinate. This method has several quality regions that are clearly dominated by a single regime, but includes regions that cannot be classified as one regime.

2.1.2 Condensing flow

Soliman and Azer (1971) developed a flow regime map for condensing flows of R12 in 12.7 mm horizontal tubes. They classified flows into six regimes, spray, annular, semi-annular, wavy, slug, and plug, with three transitional flows, annular-wavy, semi-annular-wavy, and spray-annular. They found that using the Froude number and void fraction to identify flow regime transitions represented their data well. The map presented by Baker

(1954) did not represent their condensation flow data well. Later, Soliman and Azer (1974) expanded the data set to include additional diameters of 4.8 and 15.9 mm for condensing flows of R12 and R113. The new data did not agree well with their previous map (Soliman and Azer, 1971). Using the larger database, they propose a new regime map using the average liquid velocity and a function of void fraction, $(1-\alpha)\ \alpha^{-1}$, as coordinates.

Traviss and Rohsenow (1973) observed flow regimes in an 8 mm internal diameter tube for condensing R12 at saturation temperatures ranging from 10 to 40.6°C and mass fluxes ranging from 100 to 989 kg m^{-2} s^{-1}. They classified the flows into four regimes, dispersed flow, annular flow, semi-annular (similar to wavy flows (Soliman, 1982)), and slug flow. They combined the observations of Soliman and Azer (1971) with their experimental observations for comparison with flow maps from the literature and development of an annular-to-wavy regime transition. Their transition criterion is derived using the von Karman universal velocity profile and the Soliman *et al.* (1968) frictional pressure drop two-phase multiplier. They found that the Baker (1954) map and plots using the Froude number do not represent their data well because these methods lack key parameters.. Traviss and Rohsenow (1973) use liquid Reynolds number, Re$_l$, and *turbulent-turbulent* Lockhart Martinelli parameter, X$_{tt}$, to represent the transition. The resulting transition criterion is shown in Equation (2.1).

$$
\begin{aligned}
\text{Re}_l &= 1.38\text{Ga}^{0.31}\text{Fr}_l^{0.68}\left(f(X_{tt})\right)^{-0.94} & \text{Re}_l &< 50 \\
\text{Re}_l &= 0.474\text{Ga}^{0.34}\text{Fr}_l^{0.68}\left(f(X_{tt})\right)^{-1.02} & 50 &< \text{Re}_l < 1125 \qquad (2.1) \\
\text{Re}_l &= 0.0442\text{Ga}^{0.44}\text{Fr}_l^{0.88}\left(f(X_{tt})\right)^{-1.33} & \text{Re}_l &> 1125
\end{aligned}
$$

A liquid film Froude number, Fr_l, of 45 was found to represent the transition best. Comparing their experimental results and those of Soliman and Azer (1971) with transition criteria available in the literature, they found that adiabatic flow regime maps can be used to predict condensation flow regimes.

The map of Soliman and Azer (1974) was later compared with the data of Traviss and Rohsenow (1973) by Tandon *et al.* (1982), showing moderate agreement for the spray and slug regimes and completely classifying semi-annular flows, as classified by Traviss and Rohsenow (1973), within the wavy regime.

Jaster and Kosky (1976) identified a transition region between annular and stratified flows. They used the stress ratio of axial shear forces to gravitational body forces given by: $F = \left(\tau_{wall} / \rho_l g \delta \right)$. The wall shear stress, τ_{wall}, is obtained from the two-phase multiplier approach of Wallis (1969) while the film thickness, δ, is calculated using the earlier work of Kosky (1971). Combining the stress ratio, wall shear stress, and film thickness, the stress ratio F is shown in Equation (2.2), where δ^+ is given by Equation (2.3). The vapor friction factor, f_v is calculated using the turbulent Blasius friction factor, while M is a function of pressure.

$$F = \frac{\left(1 + X_{tt}^{2/M} \right)^{3M/2} \rho_l q^3 G^3 \left(0.25 f_v \right)^{3/2}}{2 \sqrt{2} \left(\rho_v \rho_l \right)^{3/2} \mu_l \delta^+ g} \tag{2.2}$$

$$\begin{aligned} \delta^+ &= \sqrt{\frac{Re_l}{2}} & Re_l \leq 1250 \\ \delta^+ &= 0.0504 \, Re_l^{0.875} & Re_l > 1250 \end{aligned} \tag{2.3}$$

Using experimental results for steam/water mixtures in a 12.5 mm internal diameter tube at pressures ranging from 20 to 170 kPa, and mass fluxes ranging from 12.6 to 145 kg m^{-2} s^{-1}, they determined that stratified flow occurs for values of F less than 5 and annular flow occurs at values of F greater than 29, with the intermediate region being a transition region.

Breber *et al.* (1979; 1980) proposed a simple straight-line map based on the theoretical transitions proposed by Taitel and Dukler (1976). Breber *et al.* (1979; 1980) identified the Lockhart Martinelli parameter (X_{LM}) parameter and the dimensionless gas velocity, J_G, as proposed by Wallis (1969) (shown in Equation (2.4)), as two key parameters in determining the applicable flow regime.

$$J_G = \frac{Gq}{\sqrt{Dg\rho_v(\rho_l - \rho_v)}} \tag{2.4}$$

The Lockhart Martinelli parameter was chosen because of its relation to void fraction, or liquid inventory. This relationship is described in detail in Section 2.2.4. Using experimental results for R11, R12, R113, steam, and *n*-pentane in 4.8 to 22 mm internal diameter horizontal tubes, the transition lines proposed by Taitel and Dukler (1976) were expanded into transition regions and shifted slightly. The resulting regions are outlined in Table 2.1.

Table 2.1. Breber *et al.* (1979; 1980) flow regime map transition criteria

Regime	X_{LM}	J_G
Annular and Mist	< 1.0	> 1.5
Wavy or Stratified		< 0.5
Slug and Plug	> 1.5	< 1.5
Bubble		> 1.5

17

These transition criteria were found to represent the transitions exhibited by their data well. No transition region exists at the slug and plug to bubble regime transition because bubble flow is limited to high reduced pressure condensation and the same heat transfer model was used for both regimes in the accompanying heat transfer coefficient correlation. Breber *et al.* (1979; 1980) found the theoretical boundaries of Taitel and Dukler (1976), derived for adiabatic flows, to be applicable to condensing flows. The annular-wavy and wavy-stratified boundaries of the Taitel and Dukler (1976) map were found to be in excellent agreement with their data. However, the predictions for other regimes and smaller diameter tubes (≤ 4.8 mm) were not as consistent.

Sardesai *et al.* (1981) identified the transition between shear and gravity controlled flows using a ratio of local condensation heat transfer coefficient between the top and bottom of the tube. Heat transfer coefficient measurements were made at the top, side, and bottom at 10 different axial locations using thermocouple pairs for 800 measurements. A 2.92 m tube-in-tube condenser with an internal stainless steel tube of internal diameter 24.4 mm and a wall thickness of 4.5 mm was used. Assuming a uniform film thickness around the perimeter of the tube for shear dominated regimes, the upper and lower heat transfer coefficients will be similar. The flows are assumed to be stratified when the lower heat transfer coefficient is appreciably lower than the upper heat transfer coefficient. Sardesai *et al.* (1981) found that the annular-dispersed to stratified-wavy transition of the Taitel and Dukler (1976) map accounts for the phenomena dominating the transition well. Using the Taitel and Dukler (1976) transition as a basis, Sardesai (1981) found that $\beta = 1.75$ accounted for the transition in their data better than $\beta = 1$ proposed by Taitel and Dukler (1976). The resulting transition line is parallel to that of

Taitel and Dukler (1976), but identifies a greater portion of flows as stratified. They presented their transition criteria using the Lockhart Martinelli parameter and the dimensionless gas velocity as coordinate axis.

Soliman (1982, 1986) studied the annular-to-wavy and intermittent regime transition for condensing flows of R12, R113, and steam in horizontal tubes with internal diameters ranging from 4.8 to 15.9 mm for saturation temperatures ranging from 27.6 to 62.3°C for the refrigerants and 110°C for steam. He developed the transition criterion using the Froude number similar to the work of Traviss and Rohsenow (1973). The liquid film thickness proposed by Kosky (1971) and two-phase multiplier approach of Lockhart and Martinelli (1949) for frictional pressure drop were used to develop a transitional liquid Reynolds number, shown in Equation (2.5).

$$
\begin{aligned}
\mathrm{Re}_l &= 10.18\mathrm{Ga}^{0.313}\mathrm{Fr}^{0.625}\left(\phi_v \,/\, X_{tt}\right)^{-0.938} && \mathrm{Re}_l \leq 1250 \\
\mathrm{Re}_l &= 0.79\mathrm{Ga}^{0.481}\mathrm{Fr}^{0.962}\left(\phi_v \,/\, X_{tt}\right)^{-1.442} && \mathrm{Re}_l > 1250
\end{aligned}
\tag{2.5}
$$

The two-phase multiplier, ϕ_v, is calculated using the Azer *et al.* (1972) correlation, although the resulting transitional Reynolds number is highly sensitive to the selection of two-phase multiplier. He proposed a transitional Froude number of 7, which was found to provide good agreement with his database that includes data from Soliman and Azer (1971), Traviss and Rohsenow (1973) and Soliman and Azer (1974). Over the narrow range of diameters and fluids examined in this study, he found superficial liquid and vapor velocities were able to reasonably account for diameter. Despite questioning the effectiveness of superficial velocities as coordinates to capturing property and diameter effects over a wide range, as concluded by Mandhane *et al.* (1974), Soliman (1982)

presented the proposed transition using superficial velocity coordinates. Finding property trends similar to those found by Taitel and Dukler (1976) and Weisman *et al.* (1979), Soliman (1982) found that liquid density and surface tension have a negligible effect, but vapor density is important in the transition between annular flows and wavy and intermittent flows. He found the liquid Froude number based transition of Traviss and Rohsenow (1973) to represent the database well for tubes less than 8 mm. Taitel and Dukler (1976) was found to show good agreement for larger tubes but under predict the transition below a diameter of 8 mm. He also found that their transition breaks down for values of $X_{LM} > 0.4$, where the Kelvin-Helmholtz theory may be invalid. Additionally, Soliman (1982) found the transition region between annular and wavy proposed by Breber *et al* (1980) to be too large, suggesting that the transition should include a diameter effect.

Observing the deviations of heat transfer coefficient predictions using annular flow correlations at high mass fluxes and qualities, Soliman (1983) hypothesized that the breakdown of the liquid film on the tube wall causing mist flow can be predicted using a balance between the destructive vapor-phase inertia force and the restoring surface tension and liquid viscous forces. Soliman (1983) proposed a modified Weber number, shown in Equation (2.6), to describe the transition between annular and mist flow, where ϕ_v is given by Equation (2.7)

$$
\begin{aligned}
&\mathrm{We}_{So} = 2.45\,\mathrm{Re}_v^{0.64}\left(\frac{\mu_v^2}{\rho_v \sigma D}\right)^{0.3}\phi_v^{-0.4} && \mathrm{Re}_l \le 1250 \\[2ex]
&\mathrm{We}_{So} = 0.85\,\mathrm{Re}_v^{0.79}\left(\frac{\mu_v^2}{\rho_v \sigma D}\right)^{0.3}\left[\left(\frac{\mu_v}{\mu_l}\right)^2\left(\frac{\rho_l}{\rho_v}\right)\right]^{0.084}\left(\frac{X_{tt}}{\phi_v^{2.55}}\right)^{0.157} && \mathrm{Re}_l > 1250
\end{aligned}
\tag{2.6}
$$

$$\phi_v = 1 + 1.09 X_{tt}^{0.039} \qquad (2.7)$$

Using a combination of heat transfer data and flow regime observations, Soliman (1986) implemented the modified Weber number proposed by Soliman (1983) in their heat transfer correlation, outlined below, identifying annular flow for $We_{So} < 20$ and mist flow for $We_{So} > 30$.

Tandon and coworkers developed a flow regime map for pure and binary mixtures of refrigerants (Tandon *et al.*, 1982; Tandon *et al.*, 1985b). Tandon *et al.* (1982) developed a straight-line map, similar to that of Breber *et al.* (1979; 1980) using data from Soliman and Azer (1971) Traviss and Rohsenow (1973) and Soliman (1974) for R12 and R113 in 4.8 to 15.9 mm internal diameter tubes. Tandon *et al.* (1982) selected the dimensionless gas velocity (J_G), as defined by Wallis (1969) as the ordinate. This coordinate was also used by Breber *et al.* (1979; 1980). Due to the importance of void fraction on two-phase flow, they chose a function of the void fraction, $(1 - \alpha) \alpha^{-1}$, as the abscissa, as was done by Soliman and Azer (1971) and Soliman (1974). The void fraction was calculated using the Smith (1969) correlation. They found that this coordinate system makes differentiation between annular and semi-annular flows difficult. As a result, they combine the annular and semi-annular regimes into a single region. The transition criteria proposed by them, shown in Table 2.2, were found to represent the annular, semi-annular, and wavy flow data well, but showed only fair agreement with spray, slug, and plug flows.

Table 2.2. Tandon *et al.* (1982) flow regime map transition criteria

Regime	$(1-\alpha)\,\alpha^{-1}$	J_G
Spray	≤ 0.5	≥ 6
Annular	≤ 0.5	$< 6; \geq 1$
Wavy	≤ 0.5	< 1
Slug	≥ 0.5	≥ 0.01
Plug	≥ 0.5	< 0.01

For the small diameter tubes of 4.8 mm internal diameter, they found that the wavy regime was predicted poorly by their map. This agrees with the observations of Breber *et al.* (1980), who indicated that accurate classification of wavy flow at this diameter is difficult. However, it is more likely the wavy regime is beginning to be suppressed due to surface tension forces. They found much better agreement for wavy flows in tubes larger than the 4.8 mm tube.

Later, Tandon *et al.* (1985b) investigated flow regimes for condensing binary mixtures of R12 and R22 in three concentrations (25/75, 50/50, and 75/25, by mass) in a 10 mm internal diameter tube. They subsequently used their observations to evaluate existing flow regime transition criteria from the literature. In a comparison of their binary mixture data with several maps from the literature, they found that their earlier map (Tandon *et al.*, 1982) provided the most consistent representation of the data. All of the other maps considered failed in one or more significant ways. Baker (1954) accounted for the mixture data in the annular, slug, and plug regimes well, but no wavy data were properly accounted for. Similarly, Soliman and Azer (1974) failed to account for the semi-annular data well, but showed better agreement in the wavy regime than Tandon *et al.* (1982). Breber *et al.* (1979; 1980) showed good agreement, except that all semi-annular and wavy data were predicted to be in the transition regions.

Dobson *et al.* (1994) conducted flow visualization and heat transfer experiments on R12 and R134a in a 4.57 mm internal diameter horizontal tube at condensing pressures corresponding to saturation temperatures of 35 to 60°C, and over a range of mass fluxes from 75 to 650 kg m^{-2} s^{-1}. The heat transfer model, outlined in a subsequent section, identifies two key regimes: annular and wavy. They found the Froude number based annular to wavy-annular transition proposed by Soliman (1982) to represent their data well, but found a transitional Froude number of 18 to provide improved agreement. They also found the annular-to-mist transition (We$_{So}$ > 30) of Soliman (1983) to provide reasonable agreement. They observed that the transition to mist flow was accompanied by a decrease in the rate of increase of the pressure drop with increasing quality. Later, Dobson and Chato (1998) expanded the database of fluids to include R22 and R32/R125 near-azeotropic mixtures in horizontal tubes with internal diameters ranging from 3.14 to 7.04 mm over a slightly higher mass flux range of 25 to 800 kg m^{-2} s^{-1}. They observed that their annular heat transfer correlation predicted their data above a mass flux of 500 kg m^{-2} s^{-1} better than the Nusselt-based wavy correlation. Therefore, they proposed that annular flow exists for all conditions above a mass flux of 500 kg m^{-2} s^{-1}. For mass fluxes below 500 kg m^{-2} s^{-1}, a transitional Froude number of 20, rather than 18 as proposed by Dobson *et al.* (1994), was found to better delineate the annular and wavy-annular regimes. Furthermore, they observed no diameter or fluid property effects below mass fluxes of 75 kg m^{-2} s^{-1}. They found the flow regime map of Mandane *et al.* (1974) represented their data, primarily due to the use of air/water data in the development of the map poorly. However, a simple kinetic energy multiplier modification to the superficial velocities to account for the difference between refrigerant liquid and vapor phase

densities and the density of water and air, respectively, improved the agreement dramatically. The theoretical map of Taitel and Dukler (1976) was found to under-predict the size of the slug flow region and failed to account for the wavy region between slug and annular flows. Shao and Granryd (1998) found a Froude number transition region of $15 < Fr_{So} < 20$, similar to Dobson and Chato (1998).

Coleman and Garimella (Coleman and Garimella, 1999; Coleman, 2000; Coleman and Garimella, 2000b, a; Coleman and Garimella, 2003) used video recordings to observe air/water and condensing R134a flows in small diameter round, square, and rectangular tubes with hydraulic diameters ranging from 1 to 5.5 mm over a range of mass fluxes from 150 to 750 kg m^{-2} s^{-1}. They used these experimental results to develop a regime map that classified flows into four regimes, intermittent, wavy, annular, and dispersed, with several different flow patterns within each regime. The dimensional mass flux and local quality were chosen for the coordinates of their map because neither require additional assumptions or empirical correlations for secondary parameters, such as void fraction or slip ratio. Comparison of their regime map with the two-phase flow studies of Weisman *et al.* (1979) and Wang *et al.* (1997) for refrigerants shows good qualitative agreement. They showed that for tubes with diameters less than 10 mm (Mandhane *et al.* (1974) and Weisman *et al.* (1979)), pipe diameter and surface tension are important in determining flow regime transitions. These effects may extend to include tubes with diameters less than 10 mm (Mandhane *et al.* (1974) and Weisman *et al.* (1979)).

Cavallini *et al.* (2002a) proposed flow regime transition criteria developed using their previous heat transfer and frictional pressure drop data (Cavallini *et al.*, 2001) for R22, R134a, R125, R32, R236ea, R407C and R410A in 8 mm internal diameter tubes for

saturation temperatures ranging from 30 to 50°C, and mass fluxes ranging from 100 to 750 kg m^{-2} s^{-1}. They identified four regimes: stratified, slug, annular, and bubbly. For dimensionless gas velocities, J_G, greater than 2.5, flows are identified as annular flow. For values of dimensionless gas velocity less than 2.5, stratified and slug flows are delineated using the *turbulent-turbulent* Lockhart-Martinelli parameter, X_{tt}, of 1.6, identical to the theoretical transition Taitel and Dukler (1976) used to distinguish annular dispersed flow from intermittent and dispersed bubble flows.

El Hajal *et al.* (2003) adapted the evaporation flow regime map developed by Kattan *et al.* (1998a), which is ultimately derived from the Taitel and Dukler (1976) transitions, and applied it to condensation flows at high reduced pressure. They identify six regimes, fully-stratified, stratified-wavy, intermittent, annular, mist, and bubbly. They define the transition criteria with expressions based on mass flux and quality. They identify an unduly large intermittent regime, but include in this regime large amplitude waves that wash the top of the tube. These large amplitude waves may be classified as wavy flow in other studies. The most notable change from the Kattan *et al.* (1998a) regime map is the elimination of dry-out considerations in the annular regime using an adapted wavy transition of Zurcher *et al.* (2002). Without dry-out, the annular regime extends from the intermittent regime through a quality of unity with mist flow developing at higher mass fluxes. Bubble flows, identified separately from intermittent flows, are confined to very high mass fluxes. The stated range of applicability is for internal diameter tubes between 3.14 and 21.4 mm, for reduced pressures between 0.02 and 0.8, mass fluxes ranging from 16 to 1,532 kg m^{-2} s^{-1} and for fluids ammonia, R11, R12, R22, R32, R123, R125, R134a, R236ea, R32/R125, R402A, R404A, R407C, R410A, R502, propane, *n*-butane, and

propylene. Qualitative comparisons were made between their transition lines and several transition lines and regime maps from the literature. The mass flux dependence of the flow regime transitions is incorporated within the void fraction, with a decreasing contribution for mass fluxes greater than approximately 300 kg m^{-2} s^{-1}. Reduced pressure is predicted to have a significant effect on the intermittent-to-annular transition and the transition to mist flow. Between diameters of 3 and 22 mm, the diameter has a slight effect on the stratified regime transition and a significant effect on the mist transition. El Hajal *et al.* (2003) make somewhat generously positive qualitative assessments of their flow regime transitions as compared to the results of Breber *et al.* (1979; 1980), Tandon *et al.* (1982), Sardesai *et al.* (1981), and Cavallini *et al.* (2002c) maps, and state that reasonable agreement is found. However, most maps show some discrepancy with the intermittent-to-annular transition. The flow transition criteria of Dobson and Chato (1998) were found not to agree well with their map. They found 83% of the flow observations of Shao and Granryd (1998) to agree with the El Hajal *et al.* (2003) map.

In an attempt to develop a simple but accurate heat transfer coefficient model, Cavallini *et al.* (2006) proposed a shear-to-gravity controlled flow transition criterion based on the dependence of the heat transfer coefficient on the temperature difference between the fluid saturation temperature and the wall temperature. Using known annular flow heat transfer data, an empirical annular flow correlations was developed, shown in Equation (2.65). Deviations of the ratio of measured heat transfer coefficients to the annular flow correlation predictions from unity were used to define the transition criteria. The data used to develop the transition criteria consisted of synthetic refrigerants (R22, R134a, R125, R32, R236ea), synthetic refrigerant mixtures (R410A, R407C,

R125/236ea, R32/R125, R502, R507A, R404a, R142b, R744, R717, and R718), hydrocarbons (propane, butane, isobutane, propylene) and hydrocarbon mixtures (propane/butane, propane/isobutane) at mass fluxes ranging from 24 to 2,240 kg m^{-2} s^{-1} and saturation temperatures ranging from -15 to 302°C. As was done by Sardesai *et al.* (1981), an empirical transitional dimensionless gas velocity was defined using observed trends in the data, as shown in Equation (2.8), where C_c is dependent on the fluid with C_c = 1.6 for hydrocarbons and C_c = 2.6 for refrigerants, carbon dioxide, ammonia, and water.

$$J_G^T = \left(\left(\frac{7.5}{4.3 X_{tt}^{1.111} + 1} \right)^{-3} + C_c^{-3} \right)^{-1/3} \tag{2.8}$$

Citing inadequate agreement with data of Jiang and Garimella (2003) for high pressure R404A near the critical point, they limit the applicability of the transition and heat transfer correlation to reduced pressures less than 0.8.

Nema *et al.* (2014) developed transition criteria based on the flow regime database of Coleman and Garimella (2003) for condensing R134a in 1 to 4.91 mm hydraulic diameter tubes over a range of mass fluxes from 150 to 750 kg m^{-2} s^{-1}. They used dimensionless parameters that describe the physical transition mechanisms. Examining the key dimensionless parameters which include gravitational, diameter, surface tension, viscous, and inertia effects and examining the transition mechanisms, they found the vapor Weber number (We$_v$ = 6) and Lockhart-Martinelli parameter to predict the transition to the intermittent regime from both the wavy and annular regimes. The critical bond number was used to identify which regime was transitioning to the intermittent regime. The vapor

Weber number ($We_v > 700$) and Lockhart-Martinelli parameter were also used to identify the transition from annular to mist flow. Lacking sufficient dispersed regime data, they recommend the transition criterion of Taitel and Dukler (1976).

2.1.3 <u>Summary</u>

As discussed above, a variety of flow regime maps and transition lines have been proposed using visual observations and trends in heat transfer and pressure drop data. A summary of these studies is provided in Table 2.3. The observations have been correlated using a range of dimensional and dimensionless parameters, including mass flux, quality, superficial velocities, Reynolds numbers, void fraction, Weber number, Froude number, modified Froude number, dimensionless gas velocity, and Lockhart Martinelli parameter (X_{LM} and X_{tt}), to name a few. However, there is a significant amount of disagreement on the effectiveness of each variable to accurately represent the pertinent transitions. This is compounded by the subjectivity of the researcher in classifying the flows into the annular, stratified, wavy, and intermittent regimes. A variety of fluids and fluid mixtures have been classified optically including mostly air/water, synthetic refrigerants and synthetic refrigerant mixtures, and air-hydrocarbon mixtures. However, flow regime transition criteria for other fluids, including hydrocarbons, have sometimes been inferred using heat transfer and other data.

Table 2.3. Flow regime literature review summary table

Investigators	Hydraulic diameter (mm)	Fluids	Orientation / conditions	Range / applicability	Techniques, basis, observations
Flow Regime Studies: Adiabatic Flows					
Baker (1954)	25.4 - 101.6 mm	Air/water	Adiabatic Horizontal		• Developed empirical regime transitions based on observations • Recognized the importance of tube diameter on flow regime and pressure drop
Scott (1964)	24 - 140 mm	Air/water Air/oil	Adiabatic Horizontal Smooth tubes Rough tubes		• Added transition regions to Baker (1954) map
Wallis and Dobson (1973)	25.4 - 137.7 mm	Air/water	Horizontal Square Rectangular		• Slug flow occurs when waves grow and reach the top of the tube • Found small wave growth theory insufficient, model as large wave pushed by surrounding gas
Mandhane *et al.* (1974)	12.7 - 165.1 mm	Various	Horizontal Vertical Inclined	$705 < \rho_1 < 1{,}009 \text{ kg m}^{-3}$ $0.8 < \rho_v < 50.5 \text{ kg m}^{-3}$ $0.0003 < \mu_1 < 0.09 \text{ kg m}^{-1}\text{ s}^{-1}$ $1\times10^{-5} < \mu_v < 22\times10^{-6} \text{ kg m}^{-1}\text{ s}^{-1}$ $9\times10^{-4} < j_1 < 7.3 \text{ m s}^{-1}$ $0.04 < j_v < 170.7 \text{ m s}^{-1}$	• Developed property correction and applied to transition lines • Observed no diameter effect above 12.7 mm internal diameter

Table 2.3. Flow regime literature review summary table - Continued

Investigators	Hydraulic diameter (mm)	Fluids	Orientation / conditions	Range / applicability	Techniques, basis, observations
Flow Regime Studies: Adiabatic Flows - Continued					
Jones Jr and Zuber (1975)	4.98×63.5 mm	Air/water	Vertical Rectangular Adiabatic		• Probability density function response used to distinguish bubbly, slug, and annular flows • Slug flows can be considered transitional and occupied $0.2 < \alpha < 0.8$
Taitel and Dukler (1976)		Air/water			• Derived theoretical approach to flow regime mapping using a momentum balance on a stratified flow pattern
Weisman *et al.* (1979)	11.5 - 51 mm	Air/water, air/oil, air/ glycerin, R113	Horizontal Adiabatic		• Systematically varied fluid properties D, μ_l, ρ_l, ρ_v, σ to observe effects on flow regime transitions • Found little diameter effect above 10 mm
Barnea *et al.* (1982, 1983, 1985)	4 - 12.5 mm	Air/water	Horizontal Vertical Adiabatic		• Replace Kelvin-Helmholtz instability transition of Taitel and Dukler (1976) with surface tension for stratified-to-intermittent transition in small diameter tubes • Modified the slug-to-annular transition of Taitel and Dukler (1976) • Derived theoretical boundary between elongated bubble and liquid slug regimes balancing turbulence with gravity and surface tension

Table 2.3. Flow regime literature review summary table - Continued

Investigators	Hydraulic diameter (mm)	Fluids	Orientation / conditions	Range / applicability	Techniques, basis, observations
Flow Regime Studies: Adiabatic Flows - Continued					
Jassim (2006), Jassim *et al.* (2007)	1.74 - 8.00 mm	R134a, R410A	Horizontal Adiabatic	$100 < G < 600$ kg m^{-2} s^{-1} $25 < T_{sat} < 50°C$	• Developed probabilistic flow regime map
Flow Regime Studies: Condensing Flows					
Soliman and Azer (1971, 1974)	4.8 - 15.9 mm	R12, R113	Horizontal Condensing		• Proposed map using average liquid-phase velocity and void fraction function $(1-\alpha)\alpha^{-1}$
Traviss and Rohsenow (1973)	8 - 12.7 mm	R12	Horizontal Condensing	$100 < G < 989$ kg m^{-2} s^{-1} $10 < T_{sat} < 40.6°C$ $0.02 < q < 0.96$ $558 < Re_l < 10{,}400$	• Transition occurs at a constant value of liquid film Froude number ($Fr_l = 45$) • Plot using Re_l vs. X_{tt}
Jaster and Kosky (1976)	12.5 mm	Steam	Horizontal Condensing	$12.6 < G < 145$ kg m^{-2} s^{-1} $20 < P < 170$ kPa	• Annular-to-stratified transition based on stress ratio • Film thickness calculated using Kosky (1971) • Empirical transition values from experimental data
Breber *et al.* (1979; 1980)	4.8 - 22.0 mm	R11, R12, R113, steam, *n*-pentane	Horizontal Condensing	$108.2 < P < 1{,}250$ kPa $17.6 < G < 1{,}600$ kg m^{-2} s^{-1}	• Simple transition criteria using X_{LM} and J_G based on theoretical transitions of Taitel and Dukler (1976) • Transition zones between regimes

Table 2.3. Flow regime literature review summary table - Continued

Investigators	Hydraulic diameter (mm)	Fluids	Orientation / conditions	Range / applicability	Techniques, basis, observations
Flow Regime Studies: Condensing Flows - Continued					
Sardesai *et al.* (1981)	24.4 mm	R113, steam, propanol, methanol, *n*-pentane	Horizontal Condensing		• Modified Taitel and Dukler (1976) with $\beta = 1.75$
Soliman (1982, 1986)	4.8 - 15.9 mm	R12, R113, steam	Horizontal Condensing	$100 < G < 989$ kg m^{-2} s^{-1} $27.6 < T_{sat} < 110°C$ $0.02 < q < 0.957$ $558 < Re_l < 10,400$	• Annular to Wavy and Intermittent transition represented by modified Froude number $Fr_{So} = 7$ • Found significant effect of vapor density on transition but only minor diameter effects • Found annular to wavy transition in Breber *et al.* (1979, 1980) map did not capture diameter effect
Soliman (1983, 1986)	7.4 - 12.7 mm	Steam, R113, R12	Horizontal Vertical Condensing	$80 < We_{So} < 140$ $21 < T_{sat} < 310°C$ $0.2 < q < 0.95$ $1 < Pr_l < 7.7$ $80 < G < 1,610$ kg m^{-2} s^{-1}	• Modified Weber number transition from annular-to-mist transition • Balanced destructive inertia forces and restorative surface tension and liquid viscous forces • Annular at $We_{So} < 20$ and Mist at $We_{So} > 30$

Table 2.3. Flow regime literature review summary table - Continued

Investigators	Hydraulic diameter (mm)	Fluids	Orientation / conditions	Range / applicability	Techniques, basis, observations
Flow Regime Studies: Condensing Flows - Continued					
Tandon *et al.* (1982, 1985)	4.8 - 15.9 mm	R12, R113, R12/R22	Horizontal	$100 < G < 989$ kg m^{-2} s^{-1} $10 < T_{sat} < 40.6$°C $0.001 < q < 0.96$ $558 < \mathrm{Re_l} < 10{,}400$	• Dimensionless gas velocity vs. stretched void fraction $(1-\alpha)/\alpha$ • Empirical regime transitions • Tandon et al. (1982) found map proposed by Tandon *et al.* (1982) to represent binary mixture data well
Dobson *et al.* (1994)	4.57 mm	R12, R134a	Horizontal	$75 < G < 800$ kg m^{-2} s^{-1} $35 < T_{sat} < 60$°C $0.1 < q < 0.9$	• $Fr_{So} = 18$
Dobson and Chato (1998)	3.14 - 12.5 mm	R12, R22, R134a, R32/R125	Horizontal	$25 < G < 1{,}540$ kg m^{-2} s^{-1} $0.1 < q < 0.9$ $0.21 < P_r < 0.57$ $1.8 < \Delta T_{wall} < 4$°C $35 < T_{sat} < 60$°C	• $Fr_{So} = 20$ • All annular flow for mass fluxes greater than 500 kg m^{-2} s^{-1}
Cavallini *et al.* (2002a)	3 - 21 mm	R22, R134a, R125, R32, R236ea, R407C, R410A	Horizontal Condensing	$100 < G < 750$ kg m^{-2}s^{-1} $30 < T_{sat} < 50$°C $0 < q < 1$ $P_r < 0.75$ $\rho_l/\rho_v > 4$	• Proposed regime map in conjunction with heat transfer and pressure drop models • J_G and X_{tt} used for transition criteria • Merged bubbly and annular flows

Table 2.3. Flow regime literature review summary table - Continued

Investigators	Hydraulic diameter (mm)	Fluids	Orientation / conditions	Range / applicability	Techniques, basis, observations
Flow Regime Studies: Condensing Flows - Continued					
El Hajal *et al.* (2003)	3.14 - 21.4 mm	Ammonia, R11, R12, R22, R32, R123, R125, R134a, R236ea, R32/R125, R402A, R404A, R407C, R410A, R502, propane, n-butane, propylene	Horizontal Condensing	$16 < G < 1{,}532\ \mathrm{kg\,m^{-2}\,s^{-1}}$ $0 < q < 1$ $0.02 < P_r < 0.8$ $76 < (We/Fr)_l < 884$	• Modified Kattan *et al.* (1998) for condensing flows and high reduced pressures • Large intermittent regime

Table 2.3. Flow regime literature review summary table - Continued

Investigators	Hydraulic diameter (mm)	Fluids	Orientation / conditions	Range / applicability	Techniques, basis, observations
Flow Regime Studies: Condensing Flows - Continued					
Cavallini *et al.* (2006)	3.1-17.0 mm	R22, R134a, R410A, R125, R32, R236ea, R407C, R125/R236ea, R32/R125, R502, R507A, R404a, R142b, R744, R717, R718, propane, butane, isobutane, propylene, propane/ butane, propane/ isobutane	Horizontal Condensing	$P_r < 0.8$ $24 < G < 2{,}240 \text{ kg m}^{-2}\text{ s}^{-1}$ $-15 < T_{sat} < 302°C$ $0.6 < \Delta T < 28.7°C$	• Classified all flow regimes as ΔT-dependent or ΔT-independent • Use J^T_G, similar to Sardesai *et al.* (1981) • Derived using deviation of h from annular correlation • Large database, hydrocarbons differ from all other fluids
Nema *et al*. (2014)	1 - 4.91 mm	R134a	Horizontal Condensing	$150 < G < 750 \text{ kg m}^{-2}\text{ s}^{-1}$ $1.8 < \text{Bo} < 67.5$ $0.02 < X_{tt} < 12.4$ $0.1 < \text{We}_v < 6{,}000$ $0.05 < \text{Fr}_{So} < 28$	• Vapor Weber number and Lockhart-Martinelli parameter distinguish intermittent from annular and wavy flows • Critical Bond number distinguishes between wavy and annular • Vapor Weber number identifies mist from annular flows

35

2.2 Void Fraction

Void fraction is defined as the ratio of the volume of vapor to the total volume of the cross-section. Void fraction has long been understood to affect pressure drop and heat transfer. A detailed review of void fraction measurement and modeling techniques is presented in Winkler *et al.* (2012b). To define the equations governing the two-phase flow domain, three methods are commonly used.

1. The homogeneous model assumes the two-phases behave as a single, homogeneous fluid with thermo-physical properties representative of the flow at the local quality. This approach results in equal phase velocities for both the liquid and vapor phase. While not applicable for many two-phase flow conditions, this model is a reasonable approximation in some specific cases such as when fluids approach the critical point.

2. The separated-flow model assumes that the vapor and liquid phases flow as two separate phases, each occupying a portion of the tube cross-section. Each phase is allowed to flow at different velocities, thus the two phases are said to "slip" past one another. The separated flow model is made up of six conservation equations (mass, momentum, and energy), one for each of the two phases. Constitutive equations for the interface must be defined. Assumptions included in the interface constitutive equations determine the validity and accuracy of this approach.

3. The drift-flux model simplifies the separated-flow model by replacing the six conservation equations with three mixture conservation equations (mass, momentum, and energy). It does this by assuming the fluid behaves as a

mixture, with one kinetic conservation equation accounting for the relative motion between the two phases.

As described in Winkler *et al.* (2012b), six categories of models have been developed based on these three approaches: homogeneous, multiplier, implicit, Lockhart-Martinelli parameter, slip-ratio, and drift-flux. Following a discussion of the literature in each of these categories, flow characteristic models and experimental void fraction measurement techniques are discussed.

2.2.1 <u>Homogeneous void fraction model</u>

The homogeneous model assumes the two-phases behave as a single, homogeneous, fluid with quality weighted thermo-physical properties. This approach results in equal phase velocities for both the liquid and vapor phase. The slip ratio, *S*, is defined as the ratio of the vapor to the liquid phase velocity. Under the homogeneous flow assumption, the slip ratio is unity. Therefore, the homogeneous void fraction, *β*, is defined as shown in Equation (2.9).

$$
\alpha = \left[1 + S \left(\frac{1-q}{q} \right) \frac{\rho_{\mathrm{v}}}{\rho_{\mathrm{l}}} \right]^{-1}
$$
$$
\beta = \left[1 + \left(\frac{1-q}{q} \right) \frac{\rho_{\mathrm{v}}}{\rho_{\mathrm{l}}} \right]^{-1}
$$

(2.9)

The homogeneous void fraction can be accurately applied near the critical point, where the difference in phase properties between liquid and vapor phase becomes small. Another condition where the homogeneous model can be used, though not applicable to the present study, is in very small channels, where the two phases are confined to flow at the same velocity (Triplett *et al.*, 1999b).

37

2.2.2 Simplified multiplier models and correlations

Using air/water mixtures, Armand (1946) suggested that the void fraction can be correlated using the homogeneous void fraction, β, and a multiplier, C_a, as shown in Equation (2.10), where C_a is a function of pressure and there is a linear relationship between the void fraction and the homogeneous void fraction. He found a value of $C_a =$ 0.833 to represent his air/water data well for $\beta < 0.9$.

$$\frac{\alpha}{\beta} = C_a \qquad (2.10)$$

Bankoff (1960) found that the homogeneous and separated models do not represent mixed regimes, such as bubbly flow (of which annular and homogeneous flows are treated as special cases). He derived an equation identical in form to Armand (1946) for flow through a pipe using a power law distribution of velocity and void fraction with radius, where vapor occupies the center of the cross section and both phases are assumed to travel at the same velocity at a specified radius. The resulting equation is shown in Equation (2.11).

$$\frac{\alpha}{\beta} = K \qquad (2.11)$$

The flow parameter K (equivalent to C_a proposed by Armand (1946)) is a function of the exponents in the velocity and void fraction distribution equations as shown in Equation (2.12).

$$K = \frac{2(m+n+mn)(m+n+2mn)}{(n+1)(2n+1)(m+1)(2m+1)} \qquad (2.12)$$

He found that reasonable values of K should be confined to be between 0.6 and 1.0 and should be functions of Reynolds number, Froude number, and Weber number. He found that a pressure dependence given by $K = 0.71 + 0.0145\ P$ led to good agreement with steam/water data for a range of pressures from 100 to 13,800 kPa. Later, Zuber (1960) assessed the validity of the vapor-phase distribution assumption made by Bankoff (1960) using data for vertical intermittent flow of air/water and steam/water in 25 to 76 mm diameter round tubes. He found the range of K ($0.5 \leq K \leq 1.0$) to be in good agreement with his experimental results.

Using data for air/liquid and air/water in horizontal and vertical tubes with diameter ranging from 15.8 to 63.5 mm, Hughmark (1962) found the overall model proposed by Bankoff (1960) to be applicable to all flow regimes in both horizontal and vertical tubes, although his equation for K did not represent air/liquid systems well. Hughmark (1962) correlated the flow parameter, K, in terms of Reynolds number, Froude number, and the homogeneous void fraction, β, finding that the Weber number had little effect. The correlation proposed by him showed good agreement with air/liquid and air/water results. He found similar agreement between his correlation and the pressure dependent correlation proposed by Bankoff (1960) when compared with his data.

2.2.3 Implicit models

Levy (1960) developed a theoretical void fraction model known as the momentum exchange model for both horizontal and vertical flows. He used a momentum balance on each phase, assuming that the pressure drops in the liquid and vapor phases are equal. The resulting equation is a function of void fraction (α), quality (q), and fluid properties as shown in Equation (2.13).

$$q = \frac{\alpha(1-2\alpha) + \alpha\sqrt{(1-2\alpha)^2 + \alpha\left[2\dfrac{\rho_1}{\rho_v}(1-\alpha)^2 + \alpha(1-2\alpha)\right]}}{2\dfrac{\rho_1}{\rho_v}(1-\alpha)^2 + \alpha(1-2\alpha)}$$ (2.13)

The equal pressure drop assumption is only applicable if variations in the flowrate of each phase, due to a change in quality or phase density because of pressure change, occur slowly. In most cases this is not an accurate representation of the flow', therefore, Levy (1960) adds a non-equilibrium term but does not include an expression for the added term. Comparison with data for steam/water at pressures ranging from 82 to 13,800 kPa shows that the model tends to under predict the data by 20 to 40%. He determined that the under prediction was due to rapid quality changes, thus violating the equal phase pressure drop assumption.

Fujie (1964) used a force balance on annular flow considering three regions (a liquid, a vapor, and a liquid/vapor region in between to compensate for phase change) to derive four theoretical void fraction models (vertical and horizontal, for both adiabatic and evaporating conditions). Liquid entrainment in the vapor-phase is neglected. Considering steam/water mixtures at pressures from 690 kPa to 7,000 kPa, he makes several simplifications and introduces an empirically determined coefficient. The simplifications made are as follows: $(\rho_1/\rho_v)(1-\alpha)$ is assumed to be much greater than a, and the range of application is limited to liquid-only velocities less than 9.1 m s^{-1}. The resulting simplified equation is shown in Equation (2.14), where a is found to be 10 from data.

$$q = \frac{\alpha}{(\rho_1/\rho_v)(1-\alpha)}\left[1 + \frac{\alpha^{0.25}}{1-\sqrt{\alpha}}\sqrt{\frac{a}{P(0.143\,\mathrm{PSI/kPa})}}\right]$$ (2.14)

2.2.4 Lockhart-Martinelli parameter based models and correlations

The Lockhart-Martinelli parameter, shown in Equation (2.33), relates the two-phase pressure drop to the liquid and vapor single-phase pressure drops. When both phases are turbulent, the Lockhart-Martinelli parameter can be written as shown in Equation (2.15). The models and correlations in this section are shown to use a form similar to that of the *turbulent-turbulent* Lockhart-Martinelli parameter.

$$X_{tt} = \left(\frac{1-q}{q}\right)^{0.9}\left(\frac{\rho_v}{\rho_l}\right)^{0.5}\left(\frac{\mu_l}{\mu_v}\right)^{0.1} \tag{2.15}$$

Baroczy (1965) tabulated liquid hold-up, $1 - \alpha$, against the *turbulent-turbulent* Lockhart-Martinelli parameter for vertical upward flow of nitrogen/liquid mercury and air/water mixtures. Baroczy (1966) later found that his earlier model did not account for an apparent mass flux dependence.

Butterworth (1975) showed that several models from the literature (Homogeneous, Zivi (1964), Lockhart and Martinelli (1949), Turner-Wallis (Wallis, 1969), Thom (1964), and Baroczy (1965)) could be approximated by a single equation with different coefficients and exponents, shown in Equation (2.16). The coefficient, *A*, and exponents, *a*, *b*, and *c*, are summarized in Table 2.4.

$$\frac{1-\alpha}{\alpha} = A\left(\frac{1-q}{q}\right)^{a}\left(\frac{\rho_v}{\rho_l}\right)^{b}\left(\frac{\mu_l}{\mu_v}\right)^{c} \tag{2.16}$$

Table 2.4. Butterworth (1975) correlation coefficient and exponent values

Author(s), Correlation, Model	A	a	b	c
Homogeneous Model	1	1	1	0
Lockhart and Martinelli (1949)	0.28	0.64	0.36	0.07
Thom (1964)	1	1	0.89	0.18
Baroczy (1965)	1	0.74	0.65	0.13
Turner-Wallace (Wallace 1969)	1	0.72	0.4	0.08
Zivi (1964)	1	1	0.67	0

Several approximations to the original models were made to fit into the form shown in Equation (2.16). In particular, the approximation used to simplify the correlation of Baroczy (1965) is only valid up to a quality of 0.9. Examining trends predicted by these correlations, as a fluid approaches the critical point, i.e. $\rho_l \approx \rho_v$ and $\mu_l \approx \mu_v$, the void fraction should tend to the quality. Thus, the coefficient A and exponent a should equal unity; however, based on the coefficients and exponents proposed by them, several of these correlations are not applicable as the critical point is approached. Furthermore, Butterworth also acknowledges the lack of a mass flux term or flow regime dependence as deficiencies to this approach.

Tandon *et al.* (1985c) derive an analytical model for determining void fraction in annular flow assuming an axisymmetric liquid annulus and no entrainment. Both phases are assumed to be turbulent with the von Karman universal velocity profile for the liquid phase velocity, which was simplified in the same manner as Traviss *et al.* (1973). The resulting void fraction model is a piecewise function of the liquid Reynolds number and *turbulent-turbulent* Lockhart-Martinelli parameter. The Tandon *et al.* (1985c) model was found to predict the data of Isbin *et al.* (1957; 1959) (among others) within ±15%. Isbin *et al.* (1957; 1959) used the gamma radiation attenuation method to measure void

fractions in 12.3 to 22.1 mm diameter horizontal and vertical round tubes for steam/water

flows at pressures ranging from 100 to 6,900 kPa and measured void fractions at values

of $L/D = 110$. The correlation of Smith (1969) shows slightly better agreement, especially

below qualities of 0.008, with most data predicted within $\pm 10\%$. The correlation of Zivi

(1964) showed unsatisfactory agreement below qualities of 0.02. They also observed

slightly better agreement with data for pressures less than of 2,100 kPa.

2.2.5 Slip-ratio based models and correlations

Zivi (1964) developed a theoretical model for void fraction by assuming: a

minimization of entropy generation for the annular flow regime, no liquid entrainment in

the vapor phase, negligible time variations of the flow, and negligible energy dissipation

due to wall friction. The rate of kinetic energy flowing per unit area, referred to as kinetic

energy flux, is minimized, resulting in the simplified void fraction correlation shown in

Equation (2.17).

$$\alpha = \left[1 + \left(\frac{1-q}{q} \right) \left(\frac{\rho_{\mathrm{v}}}{\rho_{\mathrm{l}}} \right)^{2/3} \right]^{-1} \qquad (2.17)$$

He considers the effect of wall friction and liquid entrainment as extensions of the

simplified analysis. The inclusion of wall friction was found to cause a reduction in the

void fraction, and therefore an increase in the slip ratio. Liquid entrainment was varied

from no entertainment, as in the simplified case, to total entrainment. He found liquid

entrainment to exhibit a greater effect on void fraction than wall friction. Examining the

effect of pressure on void fraction, the void fraction was found to show more variation at

low pressure than at high pressure, where the void fraction approaches the homogeneous

void fraction. He found Equation (2.17) to define a lower bound on the void fraction with

the homogeneous void fraction representing the upper bound. The liquid entrainment should be used to interpolate between these two bounds. His comparison with void fraction data for steam/water flows at pressures ranging from 100 to 8,200 kPa in vertical and horizontal tubes of various diameters including 12.7 mm showed that models for the annular flow regime should include liquid entrainment.

Thom (1964) proposed a void fraction formulation based on the premise that the slip ratio is defined as $S = \rho_1 \rho_v^{-1} \gamma^{-1}$, where the slip factor, γ, is constant for a given pressure. This results in a simple continuous function across all quality points. He used steam/water void fraction data in a horizontal 25.7 mm internal diameter tube at pressures ranging from 101 kPa to the critical point of water (22,100 kPa) with a focus on qualities below 0.5. He used gamma radiation attenuation to tabulate the density ratio, slip factor, and slip ratio at different pressures. He found his proposed model agreed well with the data presented by Levy (1960) and the form of his equation to be similar to the correlation of Bankoff (1960), although the Bankoff correlation does not approach reasonable values at qualities of zero and one.

Smith (1969) proposed a slip ratio model assuming annular flow with two regions, a liquid phase and homogeneous mixture of liquid and vapor, flowing with equal pressure head, i.e. $\rho_1 U_1^2 = \rho_m U_m^2$. He also indicates that thermal equilibrium exists and the homogeneous mixture phase behaves as a single fluid with variable density. He suggests that the model, shown in Equation (2.18), is applicable to all regimes, pressures, mass velocities, qualities as well as during phase-change.

$$\alpha = \left\{ 1 + \frac{\rho_v}{\rho_l}\left(\frac{1-q}{q}\right)K + \frac{\rho_v}{\rho_l}\left(\frac{1-q}{q}\right)(1-K)\left[\frac{\frac{\rho_l}{\rho_v} + K\left(\frac{1-q}{q}\right)}{1 + K\left(\frac{1-q}{q}\right)} \right]^{1/2} \right\}$$ (2.18)

The ratio of liquid in the vapor/liquid region to the total liquid flowing is defined to be K. Examining the limits of $K = 0$ and $K = 1$, he noted that the $K = 1$ case represented the no-slip condition and $K = 0$ to be equivalent to equal velocity pressure head. The actual values of K must be empirically determined. A value of $K = 0.4$ was found to represent data well for heavy water, steam/water, and air/water mixtures in 6 to 38 mm internal diameter tubes with mass fluxes ranging from 50 to 2,050 kg m^{-2} s^{-1}, pressures up to 14,500 kPa, and qualities from 0 to 0.53, although a range of K values from 0.3 to 0.5 was observed. Over the range of conditions examined, he found no identifiable trend with mass flux. Smith (1969) found the models of Bankoff (1960) and Thom (1964) to be in good agreement at qualities of less than 0.1 (0.02 to 0.06 in the case of the Thom model). The correlation of Levy (1960) shows good agreement only at high pressures.

Premoli *et al.* (1970) proposed an empirical slip-ratio correlation for vertical upward flow under adiabatic conditions that includes the Weber number, as shown in Equation (2.19), where F_1 and F_2 are given by Equation (2.20). The addition of the Weber number incorporates mass flux, diameter, and surface tension effects.

$$\alpha = \left[1 + \left(1 + F_1 \left(\frac{(\beta/(1-\beta))}{1+F_2} - F_2 \right)^{1/2} \right) \left(\frac{1-q}{q}\right)\frac{\rho_v}{\rho_l} \right]^{-1}$$ (2.19)

$$F_1 = 1.578 \, \mathrm{Re}_l^{-0.19} \left(\frac{\rho_l}{\rho_v} \right)^{0.22}$$

$$F_2 = 0.0273 \mathrm{We}_{LO} \, \mathrm{Re}_{LO}^{-0.51} \left(\frac{\rho_l}{\rho_v} \right)^{-0.08} \tag{2.20}$$

2.2.6 Drift-flux based models and correlations

Zuber and Findlay (1965) derive a generalized void fraction model, known as the drift-flux model as shown in Equation (2.21).

$$\langle \alpha \rangle = \frac{\langle \beta \rangle}{C_0 + \bar{v}_{vj}/\langle j \rangle} = \frac{\langle \beta \rangle}{C_0 + \langle \alpha \bar{V}_{vj} \rangle / (\langle \alpha \rangle \langle j \rangle)} \tag{2.21}$$

The drift-flux model simplifies the separated flow model, as described above, where the relative velocities of the two-phases are incorporated through the weighted mean drift velocity, $\bar{v}_{Vj}$. The drift-flux model also extends the homogeneous flow model by including non-uniform flow velocities and vapor distribution within the cross-section through the distribution parameter, C_0. With the correct assumptions about phase interactions incorporated within C_0 and $\bar{v}_{Vj}$, the drift-flux model can be applied to any flow regime. When the weighted mean drift velocity is neglected, the phases are assumed to flow at the same velocity and the distribution parameter is the inverse of the simplified multiplier parameters of Bankoff (1960) and Hughmark (1962). Further simplification, by assuming one-dimensional flow, reduces the drift-flux model to the homogeneous model. To close the model, they derive a distribution parameter for axisymmetric vertical flows and present empirical weighted mean velocity equations for churn-turbulent, bubbly, and slug flows. This generic form of the void fraction represents a significant improvement over the homogeneous, simple multiplier, and separated flow

models. A comparison of their model with data showed good agreement for air/water, air/glycerin, and steam/water mixtures in vertical tubes with internal diameters ranging from 50.8 to 153 mm. However, the use of empiricism within the distribution parameter and weighted mean velocity equations limits the applicability of this model to other flow regimes.

Rouhani and Axelsson (1970) modified the Zuber and Findlay (1965) void fraction model, (Equation (2.22)), to couple with heat transfer calculations for multiple subcooled boiling regimes. They found the distribution parameter, C_0, to be 1.12 for their data, except at low mass fluxes ($G < 200$ kg m^{-2} s^{-1}) where they found C_0 to be 1.54.

$$\alpha = \frac{q}{\rho_v} \left[C_0 \left(\frac{q}{\rho_v} + \frac{1-q}{\rho_l} \right) + \frac{1.18(1-q)\left(g\sigma(\rho_l - \rho_v)\right)^{0.25}}{G\rho_l^{0.5}} \right]^{-1}$$ (2.22)

They found good agreement between their void fraction model and data for subcooled boiling at low qualities ($q < 0.18$) using heavy water and steam/water at pressures ranging from 1,900 to 13,800 kPa and mass fluxes ranging from 130 to 1,610 kg m^{-2} s^{-1} in round and rectangular tubes. Steiner (1993) later modified the Rouhani and Axelsson (1970) model for R12 and R22 to include a quality dependence in place of C_0, as shown in Equation (2.23).

$$\alpha = \frac{q}{\rho_v} \left[\left(1 + 0.12(1-q)\right)\left(\frac{q}{\rho_v} + \frac{1-q}{\rho_l} \right) + \frac{1.18(1-q)\left(g\sigma(\rho_l - \rho_v)\right)^{0.25}}{G\rho_l^{0.5}} \right]^{-1}$$ (2.23)

Ishii *et al.* (1976) extend the drift-flux analysis of Zuber and Findlay (1965) by defining the drift velocity for annular flows including gravitational effects, interfacial

47

shear stress and roughness, and flow regime of the liquid phase. The laminar liquid film equation is shown in Equation (2.24), while the turbulent film equation is shown in Equation (2.25) where the liquid volumetric flux is given by Equation (2.26) and the subscript *m* denotes the mixture properties.

$$\bar{V}_{vj}^2 = \frac{16\alpha}{\rho_v f_i \xi} \left[\frac{\mu_l j_f}{D} + \frac{(\rho_l - \rho_v) g D (1-\alpha)^3}{48} \right] \tag{2.24}$$

$$\bar{V}_{vj}^2 = \frac{\alpha (1-\alpha)^3 D}{\rho_v f_i \xi} \left[\left(\frac{0.0791}{\mathrm{Re}_l^{0.25}} \right) \frac{\rho_l j_f |j_f|}{D(1-\alpha)^3} + \frac{(\rho_l - \rho_v) g}{3} \right] \tag{2.25}$$

$$j_f = (1-\alpha) v_m - \frac{\alpha \rho_v}{\rho_m} \bar{V}_{vj} \tag{2.26}$$

The interfacial friction factor used in the derivation of Equations (2.24) and (2.25) was proposed by Wallis (1969). They found agreement within 30% for values of drift velocity, $\bar{V}_{vj}$, between 0.2 and 2.5 m s^{-1} when confined to annular flows for air/water, argon/water, and argon/ethyl alcohol in vertical tubes with internal diameters ranging from 15 to 31.8 mm at pressures ranging from 100 to 2,160 kPa. When significant liquid entrainment was present, they found that their model over predicted the data. A detailed overview of the drift-flux model and constitutive equations, including those discussed in this section, for several flow regimes can be found in Ishii (2011).

Chexal *et al.* (1992) highlight the issue that numerical instabilities and uncertainties in specification of the interfacial interaction terms are major disadvantages of the separated flow models. Therefore, they propose an empirical drift-flux correlation for vertical and horizontal flows of steam/water, air/water, R11, R12, R22, R113, R114, and

oxygen in tubes with hydraulic diameters ranging from 5 to 450 mm, mass fluxes ranging from 0.01 to 5,500 kg m^{-2} s^{-1}, and pressures ranging from 100 to 18,000 kPa, across the entire quality range. Emphasis was placed on not requiring knowledge of the flow regime *a priori* and developing closure equations (C_0 and $\overline{V}_{vj}$) such that the functions are continuous, produce void fractions between zero and unity, and produce expected results as the pressure approaches the critical pressure. The resulting set of equations is quite complex with correlating coefficients for the distribution parameter that differ depending on the fluid and tube orientation. They found good agreement with air/water and steam/water flows, and reasonable agreement with refrigerant flows. For improved agreement, they suggest further refinement of the Chexal-Lellouche fluid parameter.

More recently, El Hajal *et al.* (2003) defined a logarithmic mean void fraction for use with the heat transfer model of Thome *et al.* (2003). The homogeneous void fraction, α_h, and the drift flux models of Rouhani and Axelsson (1970) as modified by Steiner (1993) for horizontal flow given by Equation (2.23), α_{ra}, are combined using a logarithmic mean as shown in Equation (2.27).

$$\alpha = \frac{\alpha_h - \alpha_{ra}}{\ln\left(\dfrac{\alpha_h}{\alpha_{ra}}\right)} \tag{2.27}$$

The void fraction model was verified using annular flow (as classified by El Hajal *et al.* (2003)) heat transfer coefficient data from Cavallini *et al.* (2001) for R22, R134a, R410A, R125, R32, and R236ea in an 8 mm internal diameter tube for temperatures ranging from 30 to 60 °C, reduced pressures of 0.02 to 0.8, and mass fluxes ranging from 65 to 750 kg m^{-2} s^{-1}. The drift flux model of Rouhani and Axelsson (1970) was chosen

because it includes mass flux and surface tension effects and offers good reliability at low and medium pressures. The weighted average allows the resulting model to span the entire pressure range from very low pressure all the way to the critical point where the void fraction approaches the homogeneous void fraction. When combined with the accompanying flow regime map, the use of the logarithmic mean void fraction shows a slight change in the transition lines of about 20 kg m^{-2} s^{-1} for the stratified-wavy to intermittent/annular regime and 50 kg m^{-2} s^{-1} in the transition to mist flow from the intermittent and annular regimes. Wojtan *et al.* (2004) used the flow visualization method developed in Ursenbacher *et al.* (2004) to measure the void fraction in an adiabatic section following evaporation at low mass fluxes ranging from 70 to 300 kg m^{-2} s^{-1} for R22 and R410A in a 13.6 mm internal diameter tube. They found good agreement of their data with the Rouhani and Axelsson (1970) model. Additionally, Wojtan *et al.* (2004) found the slug frequency model of Tronconi (1990) to over predict their data by two to three times. The discrepancy was attributed to the difference between air/water and refrigerant properties.

2.2.7 Other void fraction and flow mechanism models

Several studies measured void fraction or used a database of void fraction data to recommend correlations that represent the data well within each regime identified in a flow regime map.. Other studies model key flow characteristics such as bubble frequency or liquid entrainment. These studies are discussed in this section.

Assessing the predictive capability of several correlations available in the literature, Rice (1987) found the models of Hughmark (1962), Baroczy (1965), Premoli *et al.* (1970), and Tandon *et al.* (1985c) to predict the total charge of refrigerant (R12, R22)

systems well. He noted that the majority of the liquid inventory, and therefore system mass, is located in the condensing unit.

Tronconi (1990) developed a slug frequency model assuming that the slug frequency is inversely proportional to the period of the waves, τ, which are precursors to slug flow. Two conditions are assumed to decrease the frequency: 1) not all waves will form slugs and 2) some slugs may be unstable and break apart after formation. To account for these effects, a constant, $C_1 = 0.5$, is introduced, $\omega = C_1/\tau$, reasoning that only half of the waves formed result in sustained slugs. The wave properties, used to calculate the wave period, are estimated using the method first proposed by Kordyban and Ranov (1970) for rectangular channels. By neglecting the effects of surface tension, they arrived at the slug frequency model shown in Equation (2.28).

$$\omega = 0.61\frac{\rho_v}{\rho_l}\frac{U_v}{h_G} \tag{2.28}$$

The equilibrium gas height, h_G, and vapor-phase velocity, U_v, are calculated using an approach similar to Taitel and Dukler (1976; 1977) to account for liquid phase roughness but maintain simplicity of original equation by using $f_i/f_v = 1$ for laminar liquid films and $f_i/f_v = 2$ for turbulent liquid films. When comparing the predictions of their equation with a database of data air/water, air/polyethylene oxide, CO_2/water, mineral oil/kerosene flows in 12.7 to 51.5 mm internal diameter tubes, he found good agreement over most conditions with an absolute average deviation of 8.9 to 16.7%, except for the 12.7 mm diameter tube data, which were over predicted by ~50%. He concluded that this was because surface tension was neglected in the model and is applicable to two-phase

51

flows inside 12.7 mm internal diameter tubes, resulting in a limited range of applicability of 15 to 50 mm internal diameter tubes. They found, as other researchers have found, that the slug frequency increases with increasing liquid viscosity and decreasing diameter. They also observed a maximum near the laminar-turbulent transition of the vapor phase, which was also noted by Taitel and Dukler (1977). An overview of studies focusing on slug formation and evolution can be found in Kordyban (1990).

Hewitt and Govan (1990) present a method for determining the entrainment and deposition rate of liquid droplets in the vapor core of annular flow for adiabatic, evaporating (including dry-out conditions), and condensing flows. They found good agreement between their model and steam/water and R12 data in transient dry-out conditions in 7.72 to 10.8 mm internal diameter tubes at pressures ranging from 1,200 to 7,000 kPa. They also found that the liquid entrainment in the vapor phase differs significantly from the liquid inventory in the liquid film for condensing flows when compared to adiabatic or evaporating flows. Condensing flows may exhibit a thicker liquid film because of the influx of condensing liquid toward the wall.

Jassim *et al.* (2008) developed a flow regime specific void fraction model using the probabilistic two-phase flow map of Jassim (2006). Several correlations were tested using refrigerant condensation, adiabatic, and evaporation data for R11, R12, R134a, R22, R410A in 4.26 to 9.58 mm internal diameter tubes with mass fluxes ranging from 70 to 900 kg m^{-2} s^{-1}. The empirical correlation of Graham (1998), given by Equation (2.29), was found to represent the intermittent regime well. Here, *Ft* is the Froude rate, given by Equation (2.30).

$$\alpha = \begin{cases} 1-\exp\left\{-1-0.3\ln\left[Ft\right]-0.0328\left[\ln\left(Ft\right)\right]^2\right\} & Ft > 0.01032 \\ 0 & Ft < 0.01032 \end{cases} \qquad (2.29)$$

$$Ft = \left[\frac{q^3 G^2}{\rho_v^2 gD(1-q)}\right]^{1/2} \qquad (2.30)$$

The empirical separated flow Lockhart-Martinelli parameter and Froude rate based correlation of Yashar *et al.* (2001), shown in Equation (2.31), was found to fit the stratified regime well.

$$\alpha = \left(1 + \frac{1}{Ft} + X_{tt}\right)^{-0.321} \qquad (2.31)$$

The Steiner (1993) modified Rouhani and Axelsson (1970) correlation was found to fit the annular regime data best. Using this set of correlations, their data were predicted within an absolute average deviation of 3.5%.

2.2.8 <u>Experimental void fraction measurement techniques and studies</u>

Void fractions and film thicknesses have been measured using several different techniques, including quick-closing valves (Koyama *et al.*, 2004), electrical conductance (Fukano, 1998), gamma radiation attenuation (Jiang and Rezkallah, 1993), neutron radiography (Mishima and Hibiki, 1998), index of refraction (Aprin *et al.*, 2007), and various forms of photography (Hewitt *et al.*, 1990; Triplett *et al.*, 1999b; Ursenbacher *et al.*, 2004; Keinath and Garimella, 2010; Winkler *et al.*, 2012a).

One of the oldest methods of measuring void fraction is the use of quick closing valves. Recently, this method has been used to measure void fractions in microfin tubes with various refrigerants (Yashar *et al.*, 2001; Koyama *et al.*, 2004). Quick closing vales

are located on either side of the test section and closed simultaneously to trap the fluid in the test section. A by-pass line is simultaneously opened to allow the system to continue to operate. The fluid in the test section is removed and weighed. Knowing the volume of the test section and weight of fluid in the test section, the void fraction can be calculated. This method is well suited for microfin geometries where other methods of measuring void fraction cannot be implemented. Ensuring complete removal of all the fluid from within the test section remains a limitation of this method. Koyama *et al.* (2004) address this concern by accounting for the vapor remaining in the test section by measuring temperature and pressure, assuming all the liquid has been removed. Another major disadvantage of this method is that is yields no information regarding the distribution of the two phases within the cross section.

The electrical conductance method relates the ability of the liquid film to conduct electricity to the thickness of the film and thus, the void fraction. Fukano (1998) developed an improved method called the constant-electric-current method. This method has advantages over the previous electrical conductance method, because the output increases as the film gets thinner, rather than a decrease to zero, allowing for better resolution of thin films. The output is, therefore, similar for a given void fraction, irrespective of the distribution of the vapor phase. Previous conductance methods were sensitive to the location of the vapor relative to the electrodes. The method used by Fukano (1998) yields better accuracy in the void fraction measurement, but does not account for fluid distribution. To use this method, the test fluid must be electrically conductive and the tube in which the electrodes are placed must be non-conductive. Due to the flammability of hydrocarbons, this method is not well suited for void fraction

54

measurement of hydrocarbon fluids because an electric current is applied directly to the test fluid.

Two methods that operate using the interaction of radiation with different types of matter are gamma attenuation, as outlined by Jiang and Rezkallah (1993) and high-frame-rate neutron radiography, as described by Mishima and Hibiki (1998). Both can be used to measure void fraction; however, neutron radiography produces images of the flow. The primary limitations of these methods are the availability of a radioactive source, and the need for a difference in neutron attenuation behavior between phases, which makes this method best for dissimilar phases such as air-water mixtures.

Several different techniques using photography and video recordings for observing two-phase flows have been reported in the literature. Hewitt *et al.* (1990) studied the liquid films in annular flow using refractive index matching for air/water flows in a 32 mm internal diameter tube. High-speed video was used to record the images at 6,000 frames per second where the vapor phase appears dark and the liquid phase appears light. They found significant entrainment of vapor bubbles in the liquid films and the vapor-liquid interface is characterized by both smooth and rough patches rather than continuously rough as previously thought. They hypothesize that vapor entrainment, breakup and release of vapor bubbles due to the rolling motion of the waves should enhance the heat and mass transfer processes.

Toda and Hori (1993) developed a video analysis program for measuring void fractions of steam/water flows in a vertical 14 mm internal diameter tube near atmospheric pressure while examining condensation of vapor in a subcooled liquid. They

recorded gray scale images at 60 frames per second. They determine a gray scale threshold value that they apply to the image. The resulting black and white image identifies the vapor-liquid interface. Isolated dots from uneven lighting are filtered.

Hurlburt and Newell (1996) used a He-Ne laser and a video camera to record liquid film thicknesses in 25.4 mm internal diameter tubes for air/water flows. The method uses the difference in the index of refraction between the two phases and the tube wall to measure the liquid film thickness. They found high standard deviations in the liquid film thickness, indicating the film thickness varies significantly for given conditions. They also measured wave speed using two pairs of an LED and a photo cell, spaced axially down the tube. With a sufficiently small spacing (they used 50 mm), a wave would result in a set of peaks at each location. Knowing the time and spacing between peaks, the wave speed can be calculated. One of the drawbacks of this method is that it relies on waves maintaining their structure along the axial distance between the sensor pairs.

Wilmarth and Ishii (1997) obtain video at 30 frames per second of air/water mixtures flowing in vertical rectangular channels of 1×20 mm and 2×15 mm. They used an image processing technique similar to that of Toda and Hori (1993) but with a few additional steps. They located the channel edges to quantify the scale and averaged the background image to clarify the vapor-liquid interface.

Triplett *et al.* (1999a; 1999b) used photography analysis to observe flow regimes and measure void fractions of air/water flows in circular tubes ranging from 1.1 to 1.45 mm internal diameter, and triangular tubes with hydraulic diameters ranging from 1.09 to 1.49 mm. They used a digital camera and strobe light to record images of the flow, analyzing

multiple images per condition. Several assumptions about flow characteristics were made: bubbles were cylindrical, spherical, or a combination of the two, slug/annular flows were not included in the void fraction calculations, and churn flow was assumed to have a local void fraction of 0.5 for regions with the gas phase dispersed in the liquid phase. Uncertainties were estimated to be 15% by using the minimum and maximum apparent boundaries with about 10% change and a 10% from image to image at the same conditions.

Ursenbacher *et al.* (2004) present a method of image analysis for accurately measuring cross-sectional dry angles and void fractions. To do this, they observe the vapor-liquid interface in stratified flows through a round horizontal sight-glass of internal diameter of 13.6 mm and outer diameter of 16 mm for R22 and R410A. They use a monochromatic laser sheet and fluorescent powder (Rhodamine-B) suspended in the liquid phase to illuminate the cross-section of the liquid phase. A calibration grid was used to reconstruct the image by adjusting for distortion of the tube wall and angle of observation. Using the calibration image and the actual size of the grid, the resulting images can be transformed to recreate the undistorted image. An upper film thickness would distort this calibration. Therefore this method is limited to stratified flows with no liquid entrainment or upper film. Similarly, vapor bubbles entrained in the liquid phase can obscure the interface. These conditions limit the range of conditions to low mass fluxes and low qualities.

Schubring *et al.* (2010b) investigated waves in air-water flows for vertical 23.7 mm internal diameter tubes using high-speed video. They used a backlit quartz glass test section with backlighting in five locations. The grayscale video frame was segmented

into five segments using Matlab (one for each back light location) to detect wave motion. Darkening of the segment was used to identify a wave. They identified two types of waves: large, coherent waves and smaller, piece waves. Coherent waves were more likely to occur at low flow rates, while piece waves occurred at high flow rates. Using the same experimental setup but with a slightly smaller fluorinated ethylene propylene test section of 22.4 mm internal diameter, Schubring *et al.* (2010a) added Rhodamine-B to the water and used a planar laser to induce fluorescence in the liquid phase. The concentration of Rhodamine-B was minimized to prevent significant fluid property changes. This technique is similar to that of Ursenbacher *et al.* (2004), but rather than illuminating the cross section, Schubring *et al.* illuminated the axial direction to capture the liquid film thickness. The images were smoothed and blurred using Matlab image processing functions to remove distortion and allow for measurement of the liquid film thickness. The sample images do not appear to be distorted from the original image to the final processed image. They found the liquid film to exhibit a more pronounced positive skew, indicating the presence of larger amplitude waves at higher liquid film velocities. They also observed the film thickness and standard deviation of the film thickness to increase with increasing liquid film velocity and decrease with increasing air velocity.

In part two of a two-part study by Winkler *et al.* (2012a; 2012b), void fractions for condensing R134a collected by Coleman and Garimella (2003) at a nominal pressure of 1,400 kPa in round, square, and rectangular channels with hydraulic diameters ranging from 2 to 4.91 mm over a range of mass fluxes from 150 to 750 kg m^{-2} s^{-1}. They observed flows in the annular, wavy, intermittent, and dispersed regimes. Due to the method of analysis, only flows in the intermittent, wavy, and intermittent-to-wavy transition region

could be analyzed. They modified an image processing tool developed by Killion and Garimella (2004) for gravity driven falling-films to analyze horizontal flows inside tubes. A user defines the tube wall location and a region-of-interest near the vapor-liquid interface for a single frame. The Canny (1986) edge detection algorithm was then used to identify the vapor-liquid interface and a spline was fit to the boundary. A threshold value was identified for each frame based on lighting conditions such that the edge detection algorithm accurately located the edge. The user sets several parameters, such as closed vs. open spline and vapor-phase geometric shape, which are determined from the observed flow regime (intermittent or wavy). A statistical method was used to define the regime in the intermittent-to-wavy transition region. This method was later modified by Keinath and Garimella (2010), for measuring void fractions in 0.508 to 3.00 mm internal diameter round tubes over a range of mass fluxes from 200 to 800 kg m^{-2} s^{-1} and reduced pressures from 0.38 to 0.77 for R404A. They added the ability to measure bubble velocity, bubble frequency, slug frequency, bubble dimensions, and liquid film thicknesses using the method employed to identify the vapor-liquid interface. Both Winkler *et al.* (2012a) and Keinath and Garimella (2010) developed regime-specific void fraction models. However, due to the small dimensions of tubes considered in these two studies, they are not discussed in detail.

The primary deficiency in the use of any of the above photography and high-speed video analysis methods to deduce void fraction is the inability to accurately know the shape of the vapor-liquid interface in 3-D for a given cross section, and the lack of precise liquid entrainment information.

2.2.9 <u>Summary</u>

As detailed above, there are several methods for modeling void fraction, with differing levels of empiricism required for each method. The accuracy of the void fraction predictions is dependent on the vapor-liquid interface shape and flow regime assumptions used for closure of the model or correlation, as well as the accuracy of the method used to measure the void fraction. This highlights the importance of accurate measurement of void fraction. Early experimental studies of void fraction were focused on boiling flows for the nuclear industry. More recently, void fraction measurements have been made on refrigerants for HVAC applications. To date, little experimental work has been done to measure void fractions for hydrocarbon flows, especially at above ambient pressures. Those void fraction models that have been compared to hydrocarbon void fractions have been done so by inferring a void fraction from experimental heat transfer data. A summary of the literature discussed in this section can be found in Table 2.5.

Table 2.5. Void fraction literature review summary table

Investigators	Hydraulic diameter (mm)	Fluids	Orientation / conditions	Range / applicability	Techniques, basis, observations
Simple multiplier models and correlations					
Armand (1946)		Air/water			• Proposed simple multiplier method • Linear relationship between void fraction and homogeneous void fraction
Bankoff (1960)		Steam/water	Horizontal Vertical	$100 < P < 13,800$ kPa	• Derived simple multiplier method using power laws of velocity and void fraction • K parameter a function of Reynolds, Froude, and Weber numbers • Proposed pressure dependent K
Zuber (1960)	25 - 76 mm	Air/water, steam/water, and vapor/mercury		$0.1 < U_{water} < 1.6$ m s^{-1}	• Found good agreement with the range of K proposed by Bankoff (1960) • Slip-ratio a function of void fraction only over experimental range
Hughmark (1962)	15.8 - 63.5 mm	Air/water, air/oil, air/kerosene, air/benzene	Horizontal Vertical	$100 < P < 20,600$ kPa	• Correlated Bankoff (1960) flow parameter, K, in terms of Reynolds and Froude number and homogeneous void fraction

Table 2.5. Void fraction literature review summary table - Continued

Investigators	Hydraulic diameter (mm)	Fluids	Orientation / conditions	Range / applicability	Techniques, basis, observations
Implicit models					
Levy (1960)		Steam/water	Horizontal Vertical	$82 < P < 13,800$ kPa	• Derived theoretical equations governing slip effects • Momentum balance on each phase assuming steady flow such that phase quality changes slowly
Fujie (1964)		Steam/water	Horizontal Vertical	$690 < P < 7,000$ kPa	• Theoretical equations for void fraction using three-region force balance • Derived four models, vertical and horizontal both considering adiabatic and evaporating flows
Lockhart-Martinelli parameter based models and correlations					
Baroczy (1965)		Nitrogen/liquid mercury, air/water	Vertical		• Tabulated $(1-\alpha)$ against X_{tt}
Butterworth (1975)					• Approximated several models using a common form in terms of the Lockhart-Martinelli parameter
Tandon *et al.* (1985b)	6.1 - 22 mm	Steam/water, Heavy Water	Vertical Evaporation	$700 < P < 6,000$ kPa $380 < G < 2,050$ kg m^{-2} s^{-1}	• Derived an analytical model for void fraction under annular flow • Assumed von Karman profile in liquid phase

Table 2.5. Void fraction literature review summary table - Continued

Investigators	Hydraulic diameter (mm)	Fluids	Orientation / conditions	Range / applicability	Techniques, basis, observations
Slip-ratio based models and correlations					
Zivi (1964)	Various, 12.7 mm	Steam/water	Horizontal Vertical	$100 < P < 8{,}200$ kPa	• Derived theoretical void fraction model for annular flow regime by minimizing entropy generation
Thom (1964)	25.5 mm	Steam/water	Horizontal	$100 < P < 22{,}100$ kPa	• Proposed void fraction model where slip ratio is constant with pressure
Smith (1969)	6 - 38 mm	Steam/water, heavy water, air/water		$100 < P < 14{,}500$ kPa $50 < G < 2{,}050$ kg m^{-2} s^{-1} $0 < q < 0.53$	• Derived equal velocity head model accounting for liquid entrainment • Observed no trend in void fraction with mass flux
Premoli (1970)			Vertical		• Empirical slip-ratio model with the addition of liquid Weber number
Drift-flux based models and correlations					
Zuber and Findlay (1965)	50.8 - 153 mm	Air/water, air/glycerin, steam/water	Vertical		• Developed the drift-flux approach to modeling void fraction • Accounted for non-uniform velocity profiles and vapor-phase distribution • Accounted for relative velocities between the two phases • Applicable to all regimes with proper formulation of interface definition

63

Table 2.5. Void fraction literature review summary table - Continued

Investigators	Hydraulic diameter (mm)	Fluids	Orientation / conditions	Range / applicability	Techniques, basis, observations
Drift-flux based models and correlations - Continued					
Rouhani and Axelsson (1970)		Steam/water, Heavy water	Rectangular Round Tube Evaporation	$1{,}900 < P < 13{,}800$ kPa $180 < q'' < 1{,}200$ kW m^{-2} $0 < q < 0.18$ $130 < G < 1{,}610$ kg m^{-2} s^{-1}	• Predicted void fraction in subcooled boiling regime using modified Zuber and Findlay (1965)
Ishii *et al.* (1976)	15.0 - 31.8 mm	Air/water, Argon/water, Argon/ethyl alcohol	Vertical	$100 < P < 2{,}160$ kPa	• Defined drift-flux kinematic constitutive equation for annular flow • Include gravitational, interfacial shear, interfacial roughness, and liquid phase regime
Chexal *et al.* (1992)	5 - 450 mm	Steam/water, air/water, R11, R12, R22, R113, R114, and oxygen	Vertical Horizontal Adiabatic and diabatic	$100 < P < 18{,}000$ kPa $0.01 < q < 0.99$ $0.01 < G < 5{,}500$ kg m^{-2} s^{-1}	• Developed generalized closure equations for drift-flux model • Accounted for tube orientation and fluid pair in calculating distribution parameter and drift velocity
Thome and Coworkers	8 - 13.6 mm	R22, R134a, R410A, R125, R32, and R236ea	Adiabatic and condensing	$65 < G < 750$ kg m^{-2} s^{-1} $30 < T_{sat} < 60°C$ $0 < q < 1$ $0.02 < P_r < 0.8$	• Developed logarithmic mean void fraction using homogeneous model and Steiner (1998) modified Rouhani and Axelsson (1970) • Comparison with heat transfer data and wavy regime observations • Good agreement over entire pressure range

Table 2.5. Void fraction literature review summary table - Continued

Investigators	Hydraulic diameter (mm)	Fluids	Orientation / conditions	Range / applicability	Techniques, basis, observations
Void fraction measurement techniques					
Isbin *et al.* (1957, 1959)	12.3 - 22.1 mm	Steam/water	Horizontal Vertical	$100 < P < 6{,}900$ kPa $0 < q < 0.6$	• Used Gamma radiation attenuation method • Measured at $L/D = 110$
Tronconi (1990)	12.7 - 51.5 mm	Air/water, Air/ polyethylene oxide, CO_2/water, mineral oil/kerosene	Horizontal		• Investigated the onset of slugging as a function of phase flowrates, diameter, vapor density, and liquid viscosity • Slug frequency proportional to inverse of wave period • Slug frequency increases with increasing liquid phase viscosity and decreasing diameter • Surface tension effects applicable at 12.7 mm, can be neglected above 15 mm
Hewitt and Govan (1990)	7.72 - 10.8 mm	Steam/water, R12	Adiabatic Evaporation Condensation	$1{,}200 < P < 7{,}000$ kPa	• Liquid entrainment in vapor-phase and deposition rate equations for adiabatic, evaporating, and condensing annular flows • Found significant difference in entrained liquid of condensing flows vs. evaporating flows

Table 2.5. Void fraction literature review summary table - Continued

99

Investigators	Hydraulic diameter (mm)	Fluids	Orientation / conditions	Range / applicability	Techniques, basis, observations
Void fraction measurement techniques - Continued					
Hewitt *et al.* (1990)	32 mm	Air/water	Horizontal	$17 < j_v < 44$ m s^{-1} $0.09 < j_1 < 0.22$ m s^{-1}	• Observed liquid film thickness using index of refraction matching and high-speed video • Found the liquid film is characterized by both smooth and rough patches
Toda and Hori (1993)	14 mm	Steam/water	Vertical		• Developed an automated image analysis program from gray-scale images • Converted to B&W image using threshold value, obtain void fraction from identified interfaces
Hurlburt and Newell (1996)	25.4 mm	Air/water	Horizontal		• Measured film thickness using a laser and video camera • Measured wave speed using two pairs of LEDs and photo cell
Wilmarth and Ishii (1997)	1×20 mm 2×15 mm	Air/water	Vertical		• Improved image processing by averaging background image and using tube edges to calibrate length scale
Yashar *et al.* (2001)	7.3 - 8.9 mm	R134a, R410A	Horizontal Microfinned	$75 < G < 700$ kg m^{-2} s^{-1}	• Found the Froude rate captures trends in condensation data better than X_{tt}

Table 2.5. Void fraction literature review summary table - Continued

Investigators	Hydraulic diameter (mm)	Fluids	Orientation / conditions	Range / applicability	Techniques, basis, observations
Void fraction measurement techniques - Continued					
Jassim *et al.* (2008)	4.26 - 9.48 mm	R11, R12, R134a, R22, R410A, R32/R125	Horizontal Adiabatic Evaporation Condensation	$70 < G < 900$ kg m^{-2} s^{-1}	• Void fraction within probabilistic flow regime map • Fit models of Graham (1998), Yashar *et al.* (2001), and Steiner-Rouhani and Axelsson (1970) to intermittent, stratified, and annular flow
Keinath and Garimella (2010)	0.508 - 3 mm	R404A	Horizontal Condensation	$0.38 < P_r < 0.77$ $200 < G < 800$ kg m^{-2} s^{-1} $0 < q < 1$	• High-speed video with manual edge detection • Statistics of void fraction, film thickness, and bubble frequency
Schubring *et al.* (2010a, b)	22.4 - 23.7 m	Air-water	Vertical	$P = 101$ kPa $G < 340$ kg m^{-2} s^{-1}	• High-speed video with automated wave detection • Laser-induced flourescence to measure film thickness with automated image processing • Statistics of wave frequency and film thickness
Winkler *et al.* (2012a, b)	2 - 4.91 mm	R134a	Horizontal Condensation	$P = 1,400$ kPa $150 < G < 750$ kg m^{-2} s^{-1} $0 < q < 1$	• High-speed video with manual edge detection

2.3 Frictional Pressure Gradient

Extensive work has been done on measuring and modeling the frictional component of the pressure gradient for a range of fluids, tube diameters, and orientations.

Lockhart and Martinelli (1949) identify four flow types based on the liquid- and vapor- regime: *turbulent-turbulent, laminar-turbulent, turbulent-laminar, and laminar-laminar*. Assuming that the two-phase pressure drop can be directly related to the corresponding single-phase liquid or vapor pressure drop, Lockhart and Martinelli (1949) proposed the two-phase multiplier approach, which can take either of the forms shown in Equation (2.32).

$$\left(\frac{\Delta P}{\Delta L}\right)_{TP} = \phi_v^2 \left(\frac{\Delta P}{\Delta L}\right)_v = \phi_l^2 \left(\frac{\Delta P}{\Delta L}\right)_l \tag{2.32}$$

They tabulate the multipliers, ϕ_v and ϕ_l, for adiabatic air/benzene, air/kerosene, air/water, and air/oil mixtures in horizontal round tubes with internal diameters ranging from 1.48 to 25.83 mm as functions of the Lockhart-Martinelli parameter, X_{LM}, for each of the four flow types, where X_{LM} is defined as shown in Equation (2.33).

$$X_{LM}^2 = \left(\frac{\Delta P}{\Delta L}\right)_l \bigg/ \left(\frac{\Delta P}{\Delta L}\right)_v \tag{2.33}$$

The liquid and vapor two-phase multipliers were shown to be reflections about an X_{LM} of unity. In the derivation of the above equations, the phases are assumed to be at the same pressure and the sum of the volume of vapor and volume of liquid equals the total tube volume, at all points. The multipliers were presented in graphical form, making the results unwieldy for use in design applications.

Chisholm (1967) later curve fit the tabulated two-phase multipliers presented by Lockhart and Martinelli (1949) using the theoretical form of the two-phase multiplier shown in Equation (2.34) where values of *C* are shown in Table 2.6.

$$\phi_l^2 = 1 + \frac{C}{X_{LM}} + \frac{1}{X_{LM}^2} \qquad (2.34)$$

Table 2.6. Chisholm (1967) two-phase multiplier coefficients

Flow Type (Liquid – Vapor)	*C*
turbulent – turbulent	20
laminar – turbulent	12
turbulent – laminar	10
laminar – laminar	5

The curve fit by Chisholm (1967) was found to reproduce the two-phase multipliers presented by Lockhart and Martinelli (1949) well. However, the *C* coefficients in Table 2.6 are limited to use with fluids with a density ratio close to that of air/water systems.

Soliman *et al.* (1968) outlined a curve fit in terms of the *turbulent-turbulent* Lockhart-Martinelli parameter, shown in Equation (2.35), which represents the data of Lockhart and Martinelli well. This model was used in the development of their heat transfer model, discussed below and is applicable for X_{tt} from 0 to 1.

$$\phi_v = 1 + 2.85 X_{tt}^{0.523} \qquad (2.35)$$

Chisholm (1973) later extended the analysis of Lockhart and Martinelli (1949) as well as his earlier analysis (Chisholm, 1967, 1970) by showing that Equation (2.34) could be transformed into Equation (2.36). For evaporating flows in smooth tubes, he proposed a modified Lockhart and Martinelli (1949), X_{LM}, parameter based on vapor- and liquid-

only single-phase pressure drops, defined as Γ. The coefficient, B, is adapted from prior work in determining C in Equation (2.34).

$$\phi_{LO}^2 = 1 + \left(\Gamma^2 - 1\right)\left(B \cdot q^{\frac{2-n}{2}} \left(1 - q\right)^{\frac{2-n}{2}} + q^{2-n} \right) \qquad (2.36)$$

His correlation asymptotically approaches the pressure drop for liquid-only and vapor-only flows at qualities of 0 and 1, respectively, as is expected of the actual flow. However, depending on fluid properties and mass flux, B can contain a discontinuity at Γ = 9.5, which results in an abrupt change in predicted pressure drop. A comparison with evaporating steam flow data in horizontal and vertical smooth tubes at pressures between 1,030 and 13,800 kPa and mass fluxes up to 6,700 kg m^{-2} s^{-1}, showed reasonable agreement with most data, but the correlation did tend to over predict some air/water channel data for mass fluxes less than 700 kg m^{-2} s^{-1}.

Friedel (1979, 1980) developed a widely used empirical two-phase multiplier correlation using a large database (25,000 data points) of adiabatic frictional pressure drop measurements of single- and multi-component fluids, consisting predominantly of water, R12, air/water and air/oil two-phase flow in horizontal and vertical round, rectangular, and annular cross section tubes with hydraulic diameters ranging from 12 to 49 mm. Mass flux, quality, diameter, fluid properties and gravity were found to be significant in determining frictional pressure drop, while flow regime was considered to be of secondary importance. An empirical curve fit of these relevant fluid properties and flow parameters, shown in Equation (2.37), was derived using approximately one-third of the available data.

$$\phi_{\text{LO}} = (1-q)^2 + q^2 \left(\frac{\rho_{\text{l}} f_{\text{VO}}}{\rho_{\text{v}} f_{\text{LO}}} \right)$$

$$+ 3.43 q^{0.685} (1-q)^{0.24} \left(\frac{\rho_{\text{l}}}{\rho_{\text{v}}} \right)^{0.8} \left(\frac{\mu_{\text{v}}}{\mu_{\text{l}}} \right)^{0.22} \left(1 - \frac{\mu_{\text{v}}}{\mu_{\text{l}}} \right)^{0.89} \text{Fr}_{\text{l}}^{-0.047} \text{We}_{\text{l}}^{-0.0334}$$

(2.37)

The Friedel (1979, 1980) correlation was designed to asymptotically approach the liquid and vapor single-phase pressure drops at qualities of zero and unity, respectively. The large database used for development of their correlation allowed their model to account for a much wider range of fluid properties, including surface tension, than previous studies. He found better agreement with single component fluid results than with multi-component mixtures. This could be because single-component fluid data were used in the development of his correlation.

Müller-Steinhagen and Heck (1986) developed an empirical correlation, shown in Equation (2.38), using a database of 9,300 data points, including data from Friedel (1979), and frictional pressure drop data for water, R11, R12, air/water, air/oil, hydrocarbons, argon, neon, and nitrogen. Based on their observations, frictional pressure drop increases linearly with quality until a quality of 0.7, reaches a maximum at approximately 0.85, and then approaches pure vapor flow at a quality of 1.

$$\phi_{\text{VO}} = \frac{(dP/dL)_{\text{LO}}}{(dP/dL)_{\text{VO}}} (1-q)^{1/3} + 2q(1-q)^{1/3} \left(1 - \frac{(dP/dL)_{\text{LO}}}{(dP/dL)_{\text{VO}}} \right) + q^3$$

(2.38)

They found rather poor agreement with their correlation and the database of experimental results, predicting only 49.5% of the data within ±30%. However, of the fourteen other correlations examined, none predicted greater than 59.9% of the data within ±30%. The correlation of Lockhart and Martinelli (1949) was found to provide

71

better agreement, predicting 52.4% of the data within ±30% with a tendency to consistently over predict their data. Friedel (1979, 1980) predicted 44.6% of data within ±30% with a tendency to over predict the data, particularly at low qualities. They found Friedel (1979), among other correlations, to predict values orders of magnitude greater when the vapor-phase pressure drop, $dP/dL|_{VO}$ is less than the liquid phase pressure drop, $dP/dL|_{LO}$. They also found poor agreement when liquid Reynolds numbers were less than 100 and for high viscosity ratios (μ_l / μ_v). While their correlation does not provide an improvement from previous correlations in the literature, they showed that correlations from the literature were unable to provide accurate results when applied to fluids significantly different from those that were used in the development of their respective correlations.

Singal *et al.* (1983) measured pressure drop of R12 and R12/R13 mixtures in a horizontal 9.52 mm internal diameter round tube at mass fluxes ranging from 234 to 720 kg m^{-2} s^{-1} and saturation temperatures ranging from -9 to 5°C. They found the pressure drop to be a function of concentration when comparing their data to the correlation of Martinelli and Nelson (1948), which increasingly under predicted the data with increasing R13 concentration. They developed two concentration adjustments, as shown in Equation (2.39), to modify the correlation of Martinelli and Nelson (1948), $\Delta P_{f,\text{MN1948}}$, for increasing R13 concentration (X_{R13}).

$$\Delta P_f = 0.86\Delta P_{f,\text{MN1948}}\left(1+x_{\text{R13}}\right)^{2.86}$$
$$\Delta P_f = 0.88\Delta P_{f,\text{MN1948}}\left(1-x_{\text{R13}}\right)^{-2.28}$$

(2.39)

Jung and Radermacher (1989) found correlations developed for the nuclear industry to be insufficient for refrigerant and refrigerant mixture applications. They measured pressure drop for evaporating R12, R22, R114, and R152a, and R22/R114 and R12/R152a zeotropic and azeotropic mixtures in a horizontal 9.1 mm internal diameter round tube at reduced pressures ranging from 0.08 to 0.16 and mass fluxes ranging from 250 to 720 kg m^{-2} s^{-1}. They proposed a simplified two-phase multiplier correlation for annular flows in terms of X_{tt}. They used a simplification to write X_{tt} in terms of the reduced pressure which requires only the liquid density and viscosity, quality and reduced pressure to calculate the two-phase pressure drop. This simplification was found to result in less than 5% error over a range of reduced pressures from 0.06 to 0.7. They found the proposed correlation to predict their pure fluid and mixture data within 8.4%. They also observed no mixture effects in their pressure drop results when comparing the pure fluid behavior with that of the zeotropic mixtures. This finding appears to be in direct contradiction to the findings of Singal *et al.* (1983).

Chen *et al.* (2001) measured frictional pressure drop for air/water mixtures and R410A in 1.02 to 9.0 mm internal diameter horizontal round tubes at temperatures ranging from 5 to 25°C and mass fluxes ranging from 50 to 600 kg m^{-2} s^{-1}. They found the correlations of Chisholm (1967) and Friedel (1979) predicted their data poorly. They concluded that while Friedel includes surface tension and gravity effects through the Weber number and the Froude number, respectively, the exponents are too small. They propose an empirical multiplier, shown in Equation (2.40), to adjust the Friedel correlation for these effects. Comparison with their data showed an average deviation of 19.8%.

$$\nabla P_\mathrm{f} = \nabla P_\mathrm{Friedel} \Omega$$

$$\Omega = \begin{cases} \dfrac{0.0333\,\mathrm{Re}_\mathrm{LO}^{0.45}}{\mathrm{Re}_\mathrm{v}^{0.09}\left(1+0.4e^{-Bo}\right)} & \text{for } \mathrm{Bo} < 2.5 \\[2em] \dfrac{\mathrm{We}^{0.2}}{2.5+0.06\mathrm{Bo}} & \text{for } \mathrm{Bo} \geq 2.5 \end{cases} \qquad (2.40)$$

Cavallini *et al.* (2002a) proposed an empirical two-regime pressure drop correlation based on the Friedel (1979, 1980) correlation using heat transfer data for R22, R134a, R125, R32, R236ea, R407C and R410A in an 8 mm internal diameter tube for saturation temperatures ranging from 30 to 50°C and mass fluxes ranging from 100 to 750 kg m^{-2} s^{-1}. For annular flows ($J_\mathrm{G} > 2.5$), a modified Friedel (1979, 1980) correlation is proposed and the unmodified version is recommended for wavy and slug flows. The modified Friedel empirical fit was deduced from heat transfer coefficient data in the annular regime and the annular heat transfer correlation proposed by Kosky and Staub (1971). They found good agreement of the combined model with the data of Cavallini *et al.* (2001) with the exception of data for R32, which were under predicted by 30%. No explanation for this discrepancy was provided, highlighting one of the weaknesses of such an approach.

Garimella *et al.* (2002; 2003b) measured frictional pressure drop in round tubes and parallel microchannel arrays with hydraulic diameters ranging from 0.5 to 4.91 mm over mass fluxes ranging from 150 to 750 kg m^{-2} s^{-1}. They modeled intermittent flow pressure drop for small channels by summing the contributions of the liquid slug, vapor bubble, and transitions at the slug and bubble interface fore and aft of the bubble. An empirical bubble frequency was fit to the data to determine the frequency of the bubbles. They found losses in the liquid slug to account for over half the total pressure drop with the

transitional losses accounting for 35%. Garimella *et al.* (2003a) extended this work to model pressure drop in the annular regime. Using an idealized annular flow model with uniform film thickness and equating the pressure gradients in both phases, the annular frictional pressure gradient was then modeled in terms of the interfacial shear stress using Equation (2.41), where the interfacial diameter, D_i can be written in terms of the void fraction and the interfacial friction factor, as shown in Equation (2.42).

$$\frac{\Delta P}{L} = \frac{1}{2} f_i \rho_v U_v^2 \frac{1}{D_i} = \frac{1}{2} f_i \frac{G^2 q^2}{D \rho_v \alpha^{2.5}} \tag{2.41}$$

$$\frac{f_i}{f_1} = a \mathrm{X}_{LM} \mathrm{Re}_1 + b \mathrm{Re}_1 + c \mathrm{X}_{LM} \tag{2.42}$$

The coefficients *a*, *b*, and *c* were found for the laminar and turbulent cases based on their data. Garimella *et al.* (2005) modified the intermittent and annular regime models. The intermittent model was expanded by including the discrete wave flow region into the intermittent model and fitting a new slug frequency (unit cell length). The annular model was expanded to include surface tension using the dimensionless parameter, $\Psi = j_1 \mu_1 / \sigma$, proposed by Lee and Lee (2001), where the interfacial friction factor is calculated using Equation (2.43).

$$\frac{f_i}{f_1} = A \mathrm{X}_{LM}^a \mathrm{Re}_1^b \Psi^c \tag{2.43}$$

The coefficient *A* and exponents *a*, *b*, and *c* were found for the laminar and turbulent cases from their data.

Mitra (2005) modified the exponents on the correlation of Friedel (1979) using his data and the data of Jiang (2004) for near-critical pressures ($P_r \geq 0.8$) R410A and R404A in 6.2 to 9.4 mm internal diameter tubes at mass fluxes ranging from 200 to 800 kg m^{-2} s^{-1}. Later, Andresen (2007) investigated condensing R-410A at near-critical and super-critical pressures in horizontal tubes ranging in diameter from 0.76 to 3.05 mm. He found that the correlation developed by Mitra over predicted the pressure drop in the smaller diameter channels. Using his data and the data of Mitra and Jiang, Andresen developed a condensing flow pressure drop model accounting for the liquid-phase, vapor-phase, and combination region as shown in Equation (2.44). He found good agreement with the larger data set, with 76% of the data predicted within ±25%.

$$\Delta P = \Delta P_l + C\left[\Delta P_l \Delta P_v\right] + \Delta P_v$$

$$C = 24\,\mathrm{Re}_l^{-0.3}\left[\frac{1}{D}\left(\frac{\sigma}{g(\rho_l - \rho_v)}\right)^{0.5}\right]^{-0.4} \tag{2.44}$$

Dalkilic *et al.* (2010) conducted an experimental study on R134a in an 8.1 mm internal diameter vertical tube and isobutane in a horizontal 4.0 mm internal diameter round tube at mass fluxes ranging from 75 to 400 kg m^{-2} s^{-1} and saturation conditions ranging from 30 to 50°C. They collected data in the annular flow regime, as predicted by the Tandon *et al.* (1982) map, as well as through visual confirmations. This limited the data to qualities in the range of 0.7 to 0.95 and 0.45 to 0.9 for R134a and isobutane, respectively. They found the correlation of Cavallini *et al.* (2002a) to predict the R134a data well, predicting all the data within ±20%. They found that the Chen *et al.* (2001) correlation predicted both the R134a and isobutane data well, predicting all the R134a data within ±20% and most of the isobutane data within ±30%.

Xu and Fang (2013) compiled experimental frictional pressure drop results from several researchers for R22, R32, R125, R134a, R236ea, R410A, isobutane, propane, and ammonia in circular, rectangular and square channels with hydraulic diameters ranging from 0.1 to 10.1 mm, mass fluxes ranging from 20 to 800 kg m^{-2} s^{-1}, and qualities up to 0.92 for comparison with the literature. They found the correlations of Friedel (1979), Müller-Steinhagen and Heck (1986), and Cicchitti et $al.$ (1960) to provide the best agreement with the compiled database, with all three predicting the data within 30%. The correlation of Friedel (1979) showed slightly better agreement with the microchannel data, while the latter two showed better agreement with the larger tube data. However, all three were found to slightly under-predict the data. They proposed a modification to the correlation of Müller-Steinhagen and Heck (1986) by considering the relative importance of gravitational, inertia, and surface tension effects by incorporating the Froude and Weber numbers. Including their empirical exponents, the resulting correlation is shown in Equation (2.45), where the two-phase Froude and Weber numbers are the same as those defined by Friedel (1979)

$$\phi_{\text{LO}}^2 = \frac{(dP/dL)_{\text{LO}}}{(dP/dL)_{\text{VO}}}q^3 + \left(1-q^{2.59}\right)^{0.632}\left[\begin{matrix}1+2q^{1.17}\left(\dfrac{(dP/dL)_{\text{LO}}}{(dP/dL)_{\text{VO}}}-1\right)\\ +0.00775q^{-0.475}\text{Fr}_{\text{tp}}^{0.535}\text{We}_{\text{tp}}^{0.188}\end{matrix}\right] \qquad (2.45)$$

They found their correlation to predict the data with an absolute average deviation of 19.4%. The good agreement of the Friedel correlation with small diameter tubes is in contradiction to the findings of Chen et $al.$ (2001), who found unsatisfactory agreement with small diameter channels.

2.3.1 <u>Summary</u>

As discussed above, frictional pressure drop has been studied for a variety of fluids, fluid pairs, operating conditions and tube diameters. There have been some studies examining the effects zeotropic mixtures of like fluids, i.e. refrigerant/refrigerant and hydrocarbon/hydrocarbon, have on frictional pressure drop with contradicting conclusions. However, it is not expected that mixture effects should influence pressure drop for these cases. While good agreement is still found with the classical models, the specific fluids and fluid pairs become increasingly important as the thermodynamic and transport properties of new fluids differ from those used to develop the correlation. Furthermore, the differences in fluid properties between hydrocarbons and refrigerants may lead to inaccuracies in predictions when extrapolating empirical models to new fluids or mixtures.

Table 2.7. Frictional pressure drop literature review summary table

Investigators	Hydraulic diameter (mm)	Fluids	Orientation / conditions	Range / applicability	Techniques, basis, observations
Pressure Drop Studies					
Lockhart and Martinelli (1949)	1.48 - 25.83 mm	Air/benzene, air/kerosene, air/water, air/oils	Adiabatic Horizontal	Annular or wavy flow	• Correlated ΔP using two-phase multiplier, which is a function of laminar and turbulent phase conditions • Defined X_{LM} as the square root of the ratio of liquid-to-vapor phase pressure drops • Tabulate f_1 as a function of X_{LM} for experimental results
Chisholm (1967)				$\rho_v/\rho_1 \approx 0.001$	• Curve fit f_1 as a function of X_{LM} based on tabulated values of Lockhart and Martinelli (1949)
Chisholm (1973)		Steam	Vertical Horizontal	$1{,}030 < P < 13{,}800$ kPa $G > 700$ kg m^{-2} s^{-1}	• Transformed theoretical multiplier equation of Chisholm (1967) for evaporating flows using C values of Chisholm (1967) and Baroczy (1966) Lockhart and Martinelli (1949)
Friedel (1979, 1980)		Water, R12, air/water, air/oil	Adiabatic Horizontal Vertical Circular Rectangular	Annular	• Developed empirical f_{LO} based on 25,000 point database • Accounted for relevant fluid properties and dimensionless parameters • Included surface tension effects

Table 2.7. Frictional pressure drop literature review summary table - Continued

Investigators	Hydraulic diameter (mm)	Fluids	Orientation / conditions	Range / applicability	Techniques, basis, observations
Pressure Drop Studies - Continued					
Singal *et al.* (1983)	9.52 mm	R12, R12/R13	Horizontal Evaporating	$234 < G < 454$ kg m^{-2} s^{-1} $-9 < T_{sat} < 5°C$ $5 < q'' < 17$ kW m^{-2}	• Found composition effect in pressure drop for binary mixtures
Müller-Steinhagen and Heck (1986)	14.0 - 24.3 mm	Water, R11, R12, Air / water, Air / oil, hydrocarbons, Argon, Neon, Nitrogen		$50 < G < 2,490$ kg m^{-2} s^{-1} $0.01 < q < 0.91$ $Re_{LO} > 100$ $dP/dL|_{VO} > dP/dL|_{LO}$	• Developed empirical f_{VO} based on 9,300 point database • Found Friedel (1979,1980) to predict data poorly, especially for $Re_{LO} < 100$ and $dP/dL|_{VO} > dP/dL|_{LO}$
Jung and Rademacher (1989)	9.1 mm	R12, R22, R114, R152a, R22/R114, R12/R152a	Horizontal Evaporating	$250 < G < 720$ kg m^{-2} s^{-1} $0.08 < P_r < 0.16$ $10 < q'' < 45$ kW m^{-2}	• Proposed a simplified two-phase multiplier based on simplified X_{tt} • Found no composition effect on pressure drop for zeotropic mixtures
Chen *et al.* (2001)	1.02 - 9.0 mm	Air/water, R410A	Horizontal Round	$50 < G < 600$ kg m^{-2} s^{-1} $5 < T_{sat} < 25°C$ $0.1 < q < 0.9$	• Modified the Friedel correlation to include stronger surface tension and gravity effects
Cavallini *et al.* (2002a)	3 - 21 mm	R22, R134a, R125, R32, R236ea, R407C, R410A	Horizontal	$100 < G < 750$ kg m^{-2}s^{-1} $30 < T_{sat} < 50°C$ $0 < q < 1$ $P_r < 0.75$ $\rho_l/\rho_v > 4$	• Modified Friedel (1979) correlation fit using experimental h in Kosky and Staub (1971) • Recommend Friedel (1979) for wavy flows ($J_G < 2.5$)

Table 2.7. Frictional pressure drop literature review summary table - Continued

Investigators	Hydraulic diameter (mm)	Fluids	Orientation / conditions	Range / applicability	Techniques, basis, observations
Pressure Drop Studies - Continued					
Garimella *et al.* (2002, 2003, 2005)	0.5 - 4.91 mm	R134a	Horizontal	$150 < G < 750$ kg m^{-2}s^{-1}	• Developed an intermittent flow model summing the contributions of the slug, bubble, and transitions using an empirical bubble frequency • Slug contributes over half of the total pressure drop in the intermittent regime • Annular flow can be modeled using the interfacial friction factor which is correlated using Re_l, X_{LM}, and surface tension term of Lee and Lee (2001)
Jiang (2004) and Mitra (2005)	6.2 - 9.4 mm	R404A, R410A		$200 < G < 800$ kg m^{-2} s^{-1} $0.8P_{crit} < P < 1.2P_{crit}$	• Modified Friedel correlation for near critical pressures
Andresen (2007)	0.76 - 9.4 mm	R404A, R410A		$200 < G < 800$ kg m^{-2} s^{-1} $0.8P_{crit} < P < 1.2P_{crit}$	• Model liquid and vapor pressure drop individually
Xu and Fang (2013)	0.1 - 10.1 mm	R22, R32, R125, R134a, R236ea, R410A, isobutane, propane, ammonia	Condensing Horizontal Circular Rectangular Square	$20 < G < 800$ kg m^{-2} s^{-1}	• Found Friedel (1979) correlation predicts microchannel data well • Found Müller-Steinhagen and Heck (1986) predicts large tube data well • Modified Müller-Steinhagen and Heck (1986) to include Froude and Weber number effects

2.4 Condensation Heat Transfer

There has been extensive work on measuring, modeling, and correlating heat transfer coefficients for condensing fluids, with several detailed reviews of heat transfer fundamentals (Rose, 1998), prominent literature for pure fluid condensation (Cavallini *et al.*, 2003; Dalkilic and Wongwises, 2009), condensation of hydrocarbons (Miyara, 2008; Thonon, 2008), and condensation of fluid mixtures (Wang and Chato, 1995; Fronk and Garimella, 2013). Some of the key papers are discussed here. The literature is divided into two categories: pure fluid models and correlations, and zeotropic mixture models and correlations.

2.4.1 Pure-fluid condensation studies

Pure fluid condensation studies can be divided into two main categories: models and correlations for a single flow regime, and models and correlations that cover multiple regimes. This section also includes studies of azeotropic and near-azeotropic mixtures, because these mixtures behave similar to pure fluids during the condensation process.

2.4.1.1 Single-regime studies

Carpenter and Colburn (1951) measured heat transfer coefficients for condensing steam, methanol, ethanol, toluene, and trichloroethylene in 11.7 mm internal diameter vertical tubes. They hypothesized that the condensate layer became turbulent at lower Reynolds numbers due to increasing vapor shear at higher qualities and that the laminar sublayer of the liquid film presented the major thermal resistance. They found that the heat transfer coefficient is a function of fluid properties and the wall shear stress. The shear stress is comprised of friction, momentum, and gravitational (for vertical flows) contributions. Soliman *et al.* (1968) later found their momentum term to be incorrect.

Chato (1962) derived a result similar to the Nusselt (1916) falling-film analysis for laminar films at the top of horizontal and inclined tubes in stratified flows using the energy and momentum equations, resulting in Equation (2.46), where K is a correction for low Prandtl numbers.

$$h = 0.468K \frac{g\rho_l (\rho_l - \rho_v) i_{fg} \left(1 + 0.68\left(Cp_l \Delta T / i_{fg}\right)\right) k_l^3}{\mu_l (D/2) \Delta T} \tag{2.46}$$

He neglects condensation in the bottom portion of the tube, but considers the additional sensible cooling contribution due to the temperature difference between saturation and the wall temperature. To simplify the analysis, he suggests a constant liquid angle of 120° to replace an integrated solution around the tube circumference with changing void fraction, finding that the angle varied by only ±8° for nearly horizontal tubes. The angle assumption of 120° was later verified by Rosson and Meyers (1965), who measured temperatures at several locations around the perimeter for condensing methanol and acetone in 7.75 mm internal diameter horizontal tubes. He observed that for horizontal flows, the discharge end of the tube can have a significant effect on the depth of the liquid pool for stratified flows. He observed air/water flows using a clear test section and later conducted heat transfer experiments using R113. Depending on the conditions of the experiment, he found the optimum tube inclination angle from horizontal to be 10 to 20°.

Soliman *et al.* (1968) adapted the method proposed by Carpenter and Colburn (1951) by modifying the approach for calculating wall shear stress. A semi-empirical correlation, shown in Equation (2.47), was developed for annular flow assuming no slip at the vapor-

liquid interface and that the laminar sublayer of the condensate film is the dominant resistance to heat transfer.

$$h = 0.036 \frac{\rho_l^{0.5} k_l}{\mu_l} \mathrm{Pr}_l^{0.65} F_o^{0.5}$$ (2.47)

The wall shear force, F_o, is the sum of the frictional, momentum and gravitational shear forces. The frictional shear forces are calculated using the approach of Lockhart and Martinelli (1949) for *turbulent-turbulent* flow. The multiplier is calculated using a curve fit to the data of Lockhart and Martinelli (1949), where Φ_v is a function of X_{tt}, as shown in Equation (2.35). Soliman *et al.* (1968) determined that the frictional forces dominate the momentum and gravitational forces at mid- and high- qualities. However, they concluded that momentum effects cannot be neglected in deriving the heat transfer coefficient, particularly at high liquid-to-vapor density ratios and low qualities. Soliman *et al.* (1968) recommend the similar analysis of Rufer and Kezios (1966) for stratified flows.

Kosky and Staub (1971), an extension of Altman *et al.* (1960), derive an analytical turbulent film heat and momentum transfer analogy model, neglecting entrainment and surface waves. Following Altman *et al.* (1960), the Nusselt number is given by Equation (2.48), where the dimensionless temperature is defined by Equation (2.49).

$$\mathrm{Nu} = \frac{\rho_l D C_{p,l} u^*}{k_l T^+}$$ (2.48)

For $\delta^+ < 5$

$$T^+ = \delta^+ \left[\text{Pr}_l \right]$$

For $5 \leq \delta^+ < 30$

$$T^+ = \delta^+ \left(\frac{5}{\delta^+} \right) \left[\text{Pr}_l + \ln \left\{ 1 + \text{Pr}_l \left(\frac{\delta^+}{5} - 1 \right) \right\} \right] \tag{2.49}$$

For $\delta^+ \geq 30$

$$T^+ = \delta^+ \left(\frac{5}{\delta^+} \right) \left[\text{Pr}_l + \ln \left\{ 1 + \text{Pr}_l \left(\frac{\delta^+}{5} - 1 \right) \left(\frac{5}{\delta^+/5 - 1} \right) \right\} + \ln \left(\frac{\delta^+}{30} \right) \right]$$

A 1/7th power law velocity distribution for the liquid film was assumed to calculate the liquid film thickness. The resulting dimensionless film thickness, δ^+, is written as a function of liquid Reynolds number. Their model is compared with data for steam and R22 in a 12.6 mm internal diameter horizontal tube for mass fluxes up to 850 kg m^{-2} s^{-1}, pressures ranging from 3.5 to 1,460 kPa, and for qualities ranging from 0.01 to 0.92, with the upper bounds of these conditions associated with the R22 data. They note that the use of axially averaged heat transfer coefficients, spanning a large quality range, may not be sufficient when the condensing side thermal resistance is significant, and local calculations may be required for accurate modeling due to the large change in heat transfer coefficient.

Traviss *et al.* (1973) proposed an annular flow model based on the heat and momentum analogy using the von Karman universal velocity profile in the liquid film, shown in Equation (2.50).

$$\text{Nu} = f \left(X_{tt} \right)^a \frac{\text{Pr}_l \text{Re}_l^{0.9}}{F_2} \tag{2.50}$$

85

The frictional portion of the pressure drop is calculated using the two-phase multiplier of Soliman *et al.* (1968), which is found from:

$$f\left(X_{tt}\right) = 0.15\left(1 / X_{tt} + 2.85X_{tt}^{-0.476}\right) \tag{2.50}$$

The exponent, *a*, was derived to be unity but was subsequently changed to 1.15 for values of $f\left(X_{tt}\right)$ greater than two to better fit the data for R12 and R22 in an 8 mm internal diameter round tube over a range of mass fluxes from 161 to 1,533 kg m^{-2} s^{-1} and pressures corresponding to saturation temperatures of 25 to 58.3°C. The three layers of the von Karman velocity profile are contained in F_2, which is a function of Re$_l$ and Pr$_l$. Simplifications made in the analysis of the turbulent region of the liquid sublayer restricts the range of applicability to fluids with liquid Prandtl numbers greater than 3, which is reasonable for many refrigerant applications. Mist flow was not thought to cause significant deviations from the annular flow model because the major portion of the thermal resistance is in the laminar sublayer, however, their model consistently under predicated the data.

Shah (1979) adapted the evaporation correlation he developed earlier (Shah, 1976) to convective condensation. Shah (1979) concluded that the reduced pressure, P_r, provides a better representation of the data than vapor-to-liquid density ratio for a range of data from 21 sources on condensation data for water, R11, R12, R22, R113, methanol, ethanol, benzene, toluene, and trichloroethylene in 4 to 40 mm internal diameter vertical, horizontal, and inclined round tubes. The resulting widely used empirical correlation is shown in Equation (2.51), where the liquid-only heat transfer coefficient, h_{LO}, is calculated using the Dittus and Boelter (1930) correlation as shown in Equation (2.52).

$$h = h_{LO}\left[(1-q)^{0.8} + \frac{3.8q^{0.76}(1-q)^{0.04}}{P_r^{0.38}}\right] \tag{2.51}$$

$$h_{LO} = \frac{k_l}{D} 0.023 \, \text{Re}_{LO}^{0.8} \, \text{Pr}_l^{0.4} \tag{2.52}$$

At qualities greater than 0.85, Shah (1979) noticed that his correlation under predicted the data. He concluded that this could be due to entrance effects, liquid entrainment, or a breakdown of the liquid film that was assumed in the development of the correlation. He recommends the correlation for all flow regimes.

Soliman (1986) proposed a semi-empirical correlation for mist flow assuming that the mist region is a homogeneous mixture in thermodynamic equilibrium, and that heat transfer occurs only at the wall. His correlation is based on the heat and momentum analogy for single-phase turbulent flow, modified to incorporate the temperature difference between saturation and the wall, as shown in Equation (2.53), where the mixture Reynolds number is defined as $\text{Re}_m = GD\left((q/\mu_v) + ((1-q)/\mu_l)\right)$.

$$\text{Nu} = 0.00345 \, \text{Re}_m^{0.9} \left(\frac{\mu_v i_{fg}}{k_v \Delta T}\right)^{1/3} \tag{2.53}$$

A modified Weber number of 30, as defined by Soliman (1983) (Equation (2.6)), is used to identify the lower bound of the mist flow region. For values of $\text{We}_{So} < 20$, Soliman (1986) found good agreement with the correlation of Akers *et al.* (1959) and with the refrigerant data of Traviss *et al.* (1973), but found the steam data of Ananiev *et al.* (1961) and Goodykoontz and Dorsch (1967) to be in poor agreement. These findings

led Soliman (1986) to conclude that the correlation of Traviss *et al.* (1973) has limited applicability beyond the fluids for which it was developed.

Moser *et al.* (1998) found the equivalent Reynolds number model with the assumption of equal interfacial and wall friction factors made by Akers *et al.* (1959) to be invalid and subsequently reformulated the model using the heat and momentum analogy. They assumed that two-phase annular flow can be modeled as a single-phase flow with an equivalent Reynolds number that is a function of the liquid only Reynolds number and the frictional pressure gradient. They recommend the Petukhov (1970) correlation to calculate the single-phase heat transfer coefficient for closure. The two-phase heat transfer coefficient can then be calculated using Equation (2.54), where the single phase heat transfer coefficient is corrected using an empirical correction *F* that accounts for the difference in the driving temperature between the bulk (single-phase) and the saturation (two-phase) temperatures.

$$h_{tp} = \frac{T_{bulk} - T_{wall}}{T_{int} - T_{wall}} h_{single\text{-}phase} = Fh_{single\text{-}phase} \qquad (2.54)$$

Plotting curves of the resulting correlation, they found that increasing Reynolds number causes the single-phase temperature difference to approach the two-phase temperature difference, with low liquid Reynolds numbers and low liquid Prandtl numbers having greater single-phase temperature differences. Their model was applied to a large database of refrigerant data (R12, R22, R113, R134a, R410A) in 3.14 to 12.7 mm internal diameter tubes over a range of mass fluxes from 87 to 862 kg m^{-2} s^{-1}, and saturation temperatures ranging from 22 to 52°C. They found that their model showed improved agreement as compared to the predictions of the Shah (1979) and Traviss *et al.*

(1973) models, but slightly under predicted the data. They hypothesized that the under

prediction was a result of two-phase pressure drop model used and some measurements

being outside the annular regime (liquid entrainment in the vapor core and stratification

of the annular flow).

2.4.1.2 Multi-regime studies

In combination with their annular-to-wavy regime transition criterion, discussed

above, Jaster and Kosky (1976) modeled the wavy regime using a classical Nusselt film

condensation approach. The heat and momentum analogy based heat transfer coefficient

derived by Kosky and Staub (1971) is used for the annular regime. A simplified Nusselt

model is used for the stratified regime where the liquid pool angle is calculated from the

Zivi (1964) correlation for void fraction. Heat transfer in the liquid pool is neglected. The

resulting stratified flow regime correlation is shown in Equation (2.55).

$$ h = 0.725 \frac{k_1}{D} \left(\frac{\rho_1 (\rho_1 - \rho_v) i_{fg} g D^3 \alpha^3}{k_1 \mu_1 \Delta T} \right)^{1/4} \tag{2.55} $$

In accordance with their regime map, a linear interpolation with F between the

annular regime ($F > 29$) and stratified regime ($F < 5$) is used to calculate the heat transfer

coefficient in the transition region. They found experimental heat transfer coefficient

results from Kosky and Staub (1971) and new steam results (described above) for the

transition and stratified flow regimes. The data were found to be in reasonable agreement

with the proposed interpolation and correlations.

In conjunction with their flow regime map, outlined above, Breber *et al.* (1979; 1980)

proposed regime-specific heat transfer correlations: a convective correlation for shear

controlled flows, and a Nusselt-type film condensation correlation for gravity controlled flows. A forced-convective heat transfer coefficient, h_s, (shown in Equation (2.56)) is calculated using the two-phase multiplier proposed by Chisholm (1967).

$$h_s = h_l \left(\phi_l^2 \right)^m \tag{2.56}$$

In most cases, $m = 0.5$. However, Breber *et al.* (1979; 1980) recommend a conservative exponent of $m = 0.45$ for design applications. The Nusselt-type gravity-controlled heat transfer coefficient correlation is shown in Equation (2.57), where F_g is defined to be 0.79.

$$h = F_g \left(\frac{k_l^3 \rho_l \left(\rho_l - \rho_v \right) g i_{fg}}{4 \mu_l \Delta T_{wall} D} \right)^{0.25} \tag{2.57}$$

Using the regime definitions in Table 2.1, Equation (2.56), was proposed for the annular and mist flow regimes, and for lack of a better model, the authors also suggest this model for the slug and plug, and bubble flow regimes. A linear interpolation using X_{LM} and J_G, as appropriate, was proposed for the transition regions.

Tandon *et al.* (1995) proposed a two part empirical correlation for shear- and gravity-controlled flows using a modification to the earlier model of Akers and Rosson (1960). Data for R12 and R22 in a 10 mm internal diameter tube at saturation temperatures ranging from 20 to 40°C and mass fluxes ranging from 175 to 560 kg m^{-2} s^{-1} were observed to have a change in slope at $Re_v \approx 30,000$ when plotted against $Nu \cdot Pr_l^{-1/3} \left(i_{fg} / C_{p,l} \Delta T \right)^{-1/6}$. Previously, Tandon *et al.* (1985a) recommended Equation (2.58) for condensation in the annular and semi-annular regimes. This equation was

applied to shear-controlled flows ($Re_v > 30{,}000$), while Equation (2.59) was proposed for gravity-controlled flows ($Re_v < 30{,}000$).

$$Nu = 0.084 \, Pr_l^{1/3} \left(i_{fg} / C_{p,l} \Delta T \right)^{1/6} Re_v^{0.67} \tag{2.58}$$

$$Nu = 23.1 \, Pr_l^{1/3} \left(i_{fg} / C_{p,l} \Delta T \right)^{1/6} Re_v^{1/8} \tag{2.59}$$

They found agreement within ±15% for the R12 data and ±20% for the R22 data.

Dobson *et al.* (1994) conducted flow visualization and heat transfer experiments using R12 and R134a in a 4.57 mm internal diameter horizontal tube at condensing pressures corresponding to saturation temperatures of 35 to 60°C, and over a range of mass fluxes from 75 to 650 kg m^{-2} s^{-1}. Their proposed Froude number transition from annular to wavy-annular flow is discussed above. To model the wavy regime, they extended the Nusselt-based correlation of Chato (1962) by accounting for a varying void fraction with quality. This is similar to the modification made by Jaster and Kosky (1976). Observing wavy regime heat transfer coefficients to be insensitive to mass flux, indicating negligible convective heat transfer effects, they neglected any convective heat transfer in the liquid pool. They found that most of their wavy data were predicted within ±15%. Annular heat transfer coefficients were correlated using a Lockhart-Martinelli based two-phase multiplier, arguing that the theoretical basis is similar to the heat and momentum transfer analogy. The annular regime correlations of Cavallini and Zecchin (1974), Shah (1979), and Traviss *et al.* (1973) were found to over-predict the data of Dobson *et al.* (1994) by 18, 20, and 31%, respectively. Finally, they conclude that the mechanisms that dominate convective condensation are similar to those that dominate

convective evaporation. Dobson and Chato (1998) extended the correlation proposed by Dobson *et al.* (1994) by modifying the wavy and annular heat transfer coefficient correlation based on additional data for R22 and near-azeotropic R32/R125 mixtures in 3.14 to 7.04 mm internal diameter horizontal tubes. Contrary to Dobson *et al.* (1994), Dobson and Chato (1998) found heat transfer coefficients in the wavy regime to be a function of quality and mass flux as well as being dependent on temperature difference between saturation and the wall. The shear-dominated (annular) regime was found to be independent of temperature difference but dependent on mass flux and quality. They also noted that diameter has little impact on heat transfer coefficient in both regimes down to 3.14 mm. They used a detailed analysis of the theoretical approach of Traviss *et al.* (1973) to show the validity of a two-phase multiplier approach to heat transfer. The annular regime heat transfer coefficient is calculated using a modified Dittus-Boelter correlation, as shown in Equation (2.60).

$$\mathrm{Nu} = 0.023\mathrm{Re_l}^{0.8}\mathrm{Pr_l}^{0.4}\left(1 + \frac{2.22}{\mathrm{X_{tt}}^{0.89}}\right) \tag{2.60}$$

The wavy regime correlation of Dobson *et al.* (1994) was expanded by including convective condensation in the liquid pool, using the void fraction to determine the pool angle and the film condensation in the top portion of the tube, as shown in Equation (2.61).

$$\mathrm{Nu} = 0.23\frac{\mathrm{Re_{vo}}^{0.12}}{1 + 1.11\mathrm{X_{tt}}^{0.58}}\left(\frac{Ga\mathrm{Pr_l}}{Ja_l}\right)^{0.25} + \left(1 - \frac{\theta}{\pi}\right)h_f \tag{2.61}$$

The angle subtended from the top of the tube, θ, is calculated following an approach similar to that of Jaster and Kosky (1976) using the Zivi (1964) correlation to calculate the void fraction. The forced-convective heat transfer coefficient for the liquid pool, h_f, is given by a modified Dittus-Boelter correlation. As indicated above, flow regime transitions defined by $G = 500$ kg m^{-2} s^{-1} and a modified Froude number of 20 were used to specify the appropriate correlation. The resulting correlations, when applied in conjunction with the regime transitions, are shown to predict their data within a mean deviation of 4.4 to 6.1%, predicting data from other authors within 13.7% for R12 and R22 up to diameter of 12.5 mm and mass fluxes up to 1,540 kg m^{-2} s^{-1}.

In conjunction with their flow regime map and frictional pressure drop correlation outlined above, Cavallini *et al.* (2002a) proposed a multi-regime heat transfer coefficient correlation for halogenated refrigerants based on data for R22, R134a, R125, R32, R236ea, R407C and R410A in an 8 mm internal diameter tube for saturation temperatures ranging from 30 to 50°C and mass fluxes ranging from 100 to 750 kg m^{-2} s^{-1}. They proposed using the approach of Kosky and Staub (1971) with the modified Friedel (1979, 1980) pressure drop correlation outlined above to correlate the annular regime. The stratified flow regime is calculated using Nusselt film theory along the top portion of the tube, with forced convection in the liquid pool. The stratification angle is related to void fraction, as proposed by Jaster and Kosky (1976). The slug regime is calculated using the empirical slug flow correlation of Cavallini *et al.* (2002b). Due to the independent development of each regime, transition regions are identified to help smooth the abrupt regime transitions. The annular-to-stratified flow transition is smoothed using the dimensionless gas velocity. The stratified-to-slug flow transition is smoothed to the

liquid-only single-phase heat transfer coefficient using quality. They found the slug transition to result in a slight over prediction of 8%. Similar to Breber *et al*. (1979; 1980), bubbly flow was merged with annular flow for predicting heat transfer and pressure drop. This transition in particular results in an abrupt change in slope of the predicted heat transfer coefficient with decreasing quality. A comparison with 600 new data points and 2,164 HCFC, HFC, and CFC data from the literature found their proposed model to predict the data with an absolute average deviation of 10.4%. This led the authors to expand the range of applicability for all halogenated refrigerants to tube diameters of 3 to 21 mm, for fluids with reduced pressures up to 0.75, and liquid-to-vapor density ratios of greater than 4. For data other than those used in the development of their correlation, high pressure refrigerants were found to have an absolute average deviation of 10%, while low pressure refrigerants were found to have an absolute average deviation of 11%. Cavallini *et al.* (2002a) found annular correlations from the literature, including Cavallini and Zecchin (1974), Dobson and Chato (1998), and Shah (1979) to be limited in their range of applicability, particularly for high pressure fluids. The Shah (1979) correlation was the only of these correlations with a wide enough range of applicability to encompass a significant number of their data that also provided reasonable predictions. The Dobson and Chato (1998) correlation was found to provide reasonable agreement with stratified flow data, again breaking down as the reduced pressure increases. The Jaster and Kosky (1976) correlation was found to provide an unsatisfactory agreement with experimental results in the stratified regime due to their neglecting heat transfer in the liquid pool and non-constant temperature difference along the tube perimeter, both of which are addressed in their correlation.

94

Thome *et al.* (2003) extend the convective boiling correlation of Kattan *et al.* (1998b) to condensation. They proposed a semi-empirical three-regime (annular, stratified-wavy, fully-stratified) correlation using the regime transitions proposed by El Hajal *et al.* (2003). Empirical coefficients were obtained using a database of refrigerant (R11, R12, R22, R32, R113, R125, R134a, R236ea, R404A, R410A, and a R32/R125 near-azeotropic mixture) and hydrocarbon (propane, *n*-butane, isobutane, and propylene) data for mass fluxes ranging from 24 to 1,022 kg m^{-2} s^{-1}, reduced pressures ranging from 0.02 to 0.80, and internal tube diameters of 3.1 to 21.4 mm from several researchers. Axial convective condensation is assumed around the entire perimeter for annular, mist and intermittent flows (similar to the correlation proposed by Breber *et al.* (1979; 1980)) and in the liquid pool for stratified flows. The upper portion of the tube in stratified-wavy and fully stratified flows is assumed to be a uniform thin laminar falling film. The convective condensation region is modeled using Equation (2.62), where *C*, *n* and *m* are empirical coefficients. The Reynolds number is calculated using the film thickness and void fraction and f_i is an empirical interfacial roughness correction factor.

$$h_c = \frac{k_l}{\delta} C f_i \mathrm{Re}_l^{\,n} \mathrm{Pr}_l^{\,m}$$
(2.62)

A simplified flow structure for the stratified-wavy and fully stratified regimes is used. Here, the pool of liquid at the bottom of the tube is modeled as a thick annular ring over the stratification angle. As such, the overall heat transfer coefficient in the stratified-wavy and fully-stratified regimes is a combination of Nusselt falling-film theory and convective condensation (Equation (2.62)), each contributing a proportional quantity according to the stratification angle. The stratification angle is calculated using geometric

relationships and a log-mean void fraction presented in El Hajal *et al.* (2003). The liquid film heat transfer coefficient is calculated using Equation (2.63).

$$h_f = 0.728 \left(\frac{\rho_l (\rho_l - \rho_v) g i_{fg} k_l^3}{\mu_l D \Delta T_{wall}} \right)^{1/4}$$

(2.63)

Thome *et al.* (2003) proposed a mass flux based interpolation of the stratification angle between the annular and fully-stratified regimes resulting in smooth *h* curves across flow regimes. They found the resulting correlation to compare reasonably well with experimental results, with 75% of the hydrocarbon data predicted within ±20%, and 85% of refrigerant data within ±20%. The model shows a tendency to significantly over predict hydrocarbon data at mass fluxes below 100 kg m^{-2} s^{-1}.

Mitra (2005) proposed a two-regime model using his data and the data of Jiang (2004) for near-critical R410A and R404A in 6.2 to 9.4 mm internal diameter tubes at mass fluxes ranging from 200 to 800 kg m^{-2} s^{-1} for $P_r \geq 0.8$. A modified Froude number (Soliman, 1982) of 18 was used to identify the transition between wavy and annular flows, as proposed by Dobson *et al.* (1994). For near-critical pressures, the annular regime was modeled using a two-phase multiplier approach assuming a turbulent liquid film. The resulting correlation is shown in Equation (2.64).

$$Nu = 0.0134 \, Re_l^{0.84} \, Pr_l^{0.3} \left[1 + \left(\left(\frac{q}{1-q} \right) \left(\frac{\rho_l}{\rho_v} \right) \right)^{0.8} \right] \left(\frac{D}{0.0094 \, mm} \right)^{-0.32}$$

(2.64)

The wavy regime was modeled by combining film condensation in the upper portion of the tube and forced convection in the liquid pool. The condensate film term is modeled

using an energy and momentum balance on a differential element and integrating across the film while the convective term is modeled similar to Equation (2.64). A smoothing approach for the transition between modified Froude numbers of 14 to 24 was used. Andresen (2007) used a nearly identical approach to extended the analysis of Mitra to include his data for R410A in channels ranging in diameter from 0.76 to 3.05 mm at near-critical pressures and mass fluxes ranging from 200 to 800 kg m^{-2} s^{-1}. The transition region is defined using the transition criteria presented by Cavallini *et al.* (2002a).

Cavallini *et al.* (2006) fit an empirical two-part heat transfer coefficient correlation to data consisting of refrigerants (R22, R134a, R125, R32, R236ea), refrigerant mixtures (R410A, R407C, R125/236ea, R32/R125, R502, R507A, R404a, R142b, R744, R717, and R718), hydrocarbons (propane, butane, isobutane, propylene) and hydrocarbon mixtures (propane/butane, propane/isobutane) at mass fluxes ranging from 24 to 2,240 kg m^{-2} s^{-1} and saturation temperatures ranging from -15 to 302°C. Using the transitional dimensionless gas velocity, J_G^T, as outlined above, two regions are defined based on the dependence of the heat transfer coefficient on temperature difference between the fluid and the wall. Temperature-difference-independent or shear-controlled flows, identified by $J_G > J_G^T$, are correlated using an empirical two-phase multiplier approach, shown in Equation (2.65).

$$h_I = h_{LO}\left(1 + 1.128 q^{0.817}\left(\frac{\rho_l}{\rho_v}\right)^{0.3685}\left(\frac{\mu_l}{\mu_v}\right)^{0.2363}\left(1 - \frac{\mu_v}{\mu_l}\right)^{2.144} Pr_l^{-0.1}\right) \qquad (2.65)$$

Identical to Shah (1979), Cavallini *et al.* (2006) define the liquid-only heat transfer coefficient, h_{LO}, using Equation (2.52), with a Prandtl number exponent of 0.4. Their

temperature-difference-dependent or gravity controlled region, identified by $J_G < J_G^T$, is correlated using an empirical stratified flow correlation with a weighted transition based on the dimensionless gas velocity region as shown in Equation (2.66), where the stratified heat transfer coefficient, h_{ST}, is calculated using Equation (2.67).

$$h = \left(h_I \left(\frac{J_G^T}{J_G} \right)^{0.8} - h_{ST} \right) \left(\frac{J_G}{J_G^T} \right) + h_{ST} \qquad (2.66)$$

$$h_{ST} = 0.725 \left(1 + 0.741 \left(\frac{1-q}{q} \right)^{0.3321} \right)^{-1} \left(\frac{k_l^3 \rho_l (\rho_l - \rho_v) g i_{fg}}{\mu_l D \Delta T_{wall}} \right)^{0.25} + \left(1 - q^{0.087} \right) h_{LO} \quad (2.67)$$

As noted above, they limit the applicability of the transition and heat transfer correlation to reduced pressures below 0.8, citing inadequate agreement with data of Jiang and Garimella (2003) for high pressure R404A near the critical point. They also found poor agreement with the limited ammonia data included in the database. For pure fluid and azeotropic mixture data within the range of applicability, they found an absolute average deviation of 15% with an average deviation of 1%. They found the earlier correlation of Cavallini *et al.* (2002a) to be unable to accurately predict HFC refrigerant data due to the use of HCFC and CFC data in the development of the correlation.

Jassim *et al.* (2008) found data for R11, R12, R134a, R22, R410A, R32/R125 in 3.14 to 9.58 mm internal diameter horizontal tubes to be predicted well by several correlations from the literature when applied within their probabilistic regime map. The Dittus and Boelter (1930) equation was fit to intermittent flows, the Chato (1962) model was fit to stratified flows, and both the model of Dobson and Chato (1998) and the annular portion of the Thome *et al.* (2003) model were found to fit the annular regime. The agreement

98

with both annular models were comparable with the Dobson and Chato (1998) model, predicting 80.8 % of all data within ±20%, and the Thome *et al.* (2003) model predicting 82.4 % of all data within ±20%. Each of these correlations was slightly better for certain refrigerants. However, neither accounted for the R32/R125 mixture data particularly well with 21.1% and 57.8% of the data within ±20% for the Dobson and Chato and Thome *et al.* models, respectively.

Table 2.8. Heat transfer literature review summary table

Investigators	Hydraulic diameter (mm)	Fluids	Orientation / conditions	Range / applicability	Techniques, basis, observations
Heat Transfer Studies: Pure fluid single-regime condensation studies					
Chato (1962)	14.5 mm	Air/water, R113	Horizontal Inclined Finned tube	$Pr_l > 1$	• Derived a laminar condensation model for stratified flow • Neglected convection in liquid pool • Considered temperature difference between saturation and wall
Soliman *et al.* (1968)	7.44 - 11.66 mm	Steam, R113, R22, ethanol, methanol, toluene, trichloro-ethylene	Horizontal Vertical	$6 < U_v < 305$ m s^{-1} $1 < Pr_l < 10$ $0.03 < q < 0.99$	• Modified Carpenter and Colburn (1951) shear stress equation • h derived using wall shear stress, fit with experimental data • h independent of momentum at mid and high qualities • Momentum effects cannot be neglected at low q and high ρ_l/ρ_v
Kosky and Staub (1971)	12.6 mm	Steam, R22		$G < 850$ kg m^{-2} s^{-1} $3.5 < P < 1{,}460$ kPa $0.01 < q < 0.92$	• Heat–momentum transfer analogy (annular flow) with two-phase multiplier for shear stress

Table 2.8. Heat transfer literature review summary table - Continued

Investigators	Hydraulic diameter (mm)	Fluids	Orientation / conditions	Range / applicability	Techniques, basis, observations
Heat Transfer Studies: Pure fluid single-regime condensation studies - Continued					
Traviss *et al.* (1973)	8 mm	R12, R22	Horizontal Vertical Inclined	$161 < G < 1{,}533$ kg m^{-2} s^{-1} $25 < T_{sat} < 58.3$°C $Pr_l > 3$	• Annular Flow: heat–momentum analogy with von Karman velocity profile in film • Three-region turbulent film model • ∇P_f two-phase multiplier from Soliman *et al.* (1968)
Shah (1979)	7 - 40 mm	Water, R11, R12, R22, R113, methanol, ethanol, benzene, toluene, trichloro-ethylene	Horizontal Vertical Inclined Condensation	$11 < G < 1{,}600$ kg m^{-2} s^{-1} $Pr_l > 0.5$ $0.002 < P_r < 0.44$ $Re_{LO} > 350$ $21 < T_{sat} < 310$°C $3 < U_v < 300$ m s^{-1}	• Developed using database of 473 points from 21 sources • Widely used empirical correlation • Two-phase multiplier applied to h_{LO} based on q and P_r • P_r gives better representation of data than ρ_v/ρ_l
Soliman (1986)	7.4 - 12.7 mm	Steam, R113, R12	Horizontal Vertical	$We_{So} > 30$ $21 < T_{sat} < 310$°C $0.2 < q < 0.95$ $1 < Pr_l < 7.7$ $80 < G < 1{,}610$ kg m^{-2} s^{-1}	• Developed correlation for mist flow • Based on heat-momentum analogy for single-phase flow • Reynolds number based on mixture viscosity

Table 2.8. Heat transfer literature review summary table - Continued

Investigators	Hydraulic diameter (mm)	Fluids	Orientation / conditions	Range / applicability	Techniques, basis, observations
Heat Transfer Studies: Pure fluid single-regime condensation studies - Continued					
Moser *et al.* (1998)	3.14 - 12.7 mm	R12, R22, R113, R134a, R410A	Horizontal	$87 < G < 862$ kg m^{-2} s^{-1} $22 < T_{sat} < 52°C$	• Extended Akers *et al.* (1959) by including unequal friction factors between the interface and liquid phase • Combined equivalent Reynolds number and heat-momentum analogy for annular regime
Heat Transfer Studies: Pure fluid multi-regime condensation studies					
Jaster and Kosky (1976)	12.5 mm	Steam	Horizontal	$12.6 < G < 145$ kg m^{-2} s^{-1} $20 < P < 170$ kPa	• h from Kosky and Staub (1971) (Annular) and Nusselt method with pool angle related to α (Stratified) • Developed regime transition with linear interpolation of h using stress ratio
Breber *et al.* (1979; 1980)	4.8 - 22.0 mm	R11, R12, R113, steam, *n*-pentane	Horizontal	$108.2 < P < 1,250$ kPa $17.6 < G < 1,600$ kg m^{-2} s^{-1}	• Forced-convective correlation with Chisholm (1967) two-phase multiplier for annular, intermittent and bubbly flow • Nusselt-type equation for stratified–wavy • Coupled with flow map, linear interpolation with X_{LM} and J_G in transition zones, as appropriate

Table 2.8. Heat transfer literature review summary table - Continued

Investigators	Hydraulic diameter (mm)	Fluids	Orientation / conditions	Range / applicability	Techniques, basis, observations
Heat Transfer Studies: Pure fluid multi-regime condensation studies - Continued					
Dobson *et al.* (1994)	4.57 mm	R12, R134a	Horizontal	$75 < G < 800$ kg m^{-2} s^{-1} $35 < T_{sat} < 60°C$ $0.1 < q < 0.9$	• Wavy *h:* modified Nusselt-type based on Chato (1962), not *G* dependent, includes variation of α • Annular *h:* two-phase multiplier based on heat-momentum transfer analogy
Tandon *et al.* (1995)	10 mm	R12, R22	Horizontal	$20 < T_{sat} < 40°C$ $175 < G < 560$ kg m^{-2} s^{-1} $0.1 < q < 0.99$	• Modified Akers-Rosson correlation • Sharp transition in *h* exists between shear and gravity flows at Re$_v$ = 30,000
Dobson and Chato (1998)	3.14 - 7.04 mm	R12, R22, R134a, R32/R125	Horizontal	$75 < G < 800$ kg m^{-2} s^{-1} $0.1 < q < 0.9$ $0.21 < P_r < 0.57$ $1.8 < \Delta T_{wall} < 4°C$ $35 < T_{sat} < 60°C$	• Extension of Dobson *et al.* (1994) • Wavy regime *h:* include liquid pool convective condensation and void fraction based pool angle, dependent on *G* • *D* effects on *h* insignificant down to 3.14 mm

Table 2.8. Heat transfer literature review summary table - Continued

Investigators	Hydraulic diameter (mm)	Fluids	Orientation / conditions	Range / applicability	Techniques, basis, observations
Heat Transfer Studies: Pure fluid multi-regime condensation studies - Continued					
Cavallini *et al.* (2002a)	3 - 21 mm	R22, R134a, R125, R32, R236ea, R407C, R410A	Horizontal	$100 < G < 750$ kg m^{-2}s^{-1} $30 < T_{sat} < 50°C$ $0 < q < 1$ $P_r < 0.75$ $\rho_l/\rho_v > 4$	• Annular *h:* based on Kosky and Staub (1971) with modified Friedel (1979) pressure drop • Stratified *h:* Nusselt-film and force convective flow in pool • Slug *h:* based on Cavallini *et al.* (2002b) • J_G and X_{tt} used as transitions • Bell and Ghaly (1973) correction used for mixtures
Thome *et al.* (2003)	3.1 - 21.4 mm	R11, R12, R22, R32, R113, R125, R134a, R236ea, R404A, R410A, R32/R125, propane, *n*-butane, isobutane, and propylene	Horizontal	$24 < G < 1,022$ kg m^{-2} s^{-1} $0.02 < P_r < 0.8$ $0.03 < q < 0.97$ $23.1 < T_{sat} < 65.2°C$ $1 < \Delta T < 32.7°C$	• Annular flow and stratified liquid pool *h*: modeled as turbulent film • Stratified flow film *h*: modeled as Nusselt falling film • Regime transitions from El Hajal *et al.* (2003) • Mist and intermittent flows treated as annular flow • Interfacial roughness correction factor applied to annular *h* • Continuous *h* across regimes using interpolation based on *G*

Table 2.8. Heat transfer literature review summary table - Continued

Investigators	Hydraulic diameter (mm)	Fluids	Orientation / conditions	Range / applicability	Techniques, basis, observations
Heat Transfer Studies: Pure fluid multi-regime condensation studies - Continued					
Jiang (2004) and Mitra (2005)	6.2 - 9.4 mm	R404A, R410A		$200 < G < 800$ kg m^{-2} s^{-1} $0.8 P_{crit} < P < 1.2 P_{crit}$	• Annular h: modeled using two-phase multiplier • Wavy h: modeled both film and convection terms • Modified Froude number used to smooth transition
Andresen (2007)	0.76 - 3.05 mm	R410A		$200 < G < 800$ kg m^{-2} s^{-1} $0.8 P_{crit} < P < 1.2 P_{crit}$	• Extended analysis of Mitra to small tube diameters
Cavallini *et al.* (2006)	3.1-17.0 mm	R22, R134a, R410A, R125, R32, R236ea, R407C, R125/R236ea, R32/R125, R502, R507A, R404a, R142b, R744, R717, R718, propane, butane, isobutane, propylene, propane/butane, propane/isobutane	Horizontal	$P_r < 0.8$ $24 < G < 2{,}240$ kg m^{-2} s^{-1} $-15 < T_{sat} < 302°C$ $0.6 < \Delta T < 28.7°C$	• Classified all flow regimes as ΔT-dependent or ΔT-independent • ΔT-independent region: two-phase multiplier with h_{LO} • ΔT-dependent region: h combination of h for stratified flow and h from ΔT-independent region, based on J^T_G • Bell and Ghaly (1973) correction used for zeotropic mixtures • Satisfactory predictions for natural fluids; suggest further validation
Jassim *et al.* (2008)	3.14 - 9.58 mm	R11, R12, R134a, R22, R410A, R32/R125	Horizontal	$24 < G < 900$ kg m^{-2} s^{-1} $24.9 < T_{sat} < 46.4°C$ $1.1 < \Delta T_{wall} < 9.9°C$	• Fit Dittus-Boelter to intermittent flows, Chato (1962) to stratified, and Dobson and Chato (1998) or Thome *et al.* (2003) to annular regimes

2.4.2 <u>Zeotropic mixture studies</u>

Zeotropic mixture studies can be classified into two categories: application-specific studies and fundamental condensation studies. Application-specific studies, which investigate how zeotropic mixtures behave within a system level application or cycle model, will be discussed first. This is followed by a discussion of fundamental heat transfer studies investigating the effects of mass transfer on the heat transfer process.

2.4.2.1 *Application-specific studies*

Wu (1985) investigated the use of zeotropic mixtures in energy conversion cycles. He found zeotropic mixtures of R12/R114 to provide an increase in performance of 4.4 and 9.2% over pure R12 and R114 systems, respectively.

Chang *et al.* (2000) investigated the cooling capacity and COP of pure hydrocarbons (propane, *n*-butane, isobutane, and propylene) and zeotropic hydrocarbon mixtures (propane/*n*-butane and propane/isobutane) as alternatives to R12 in heat pump applications with 8 mm internal diameter tubes. The system was designed for R12, but in both heating and cooling mode, propane and propylene were both found to have better COPs than R12, making these fluids potential alternatives. For the mixtures, the COPs for intermediate concentrations were found to be higher than the values predicted by a linear interpolation between the values for the two pure fluids. In cooling mode, increases in COP of 7% and 11% were found for propane/isobutane mixtures of 50/50 and 75/25 by mass, respectively. In the heating mode, the mixture COPs were found to be lower than the COP for R12. The COP of the isobutane system was found to be lower than that of the R12 system for both heating and cooling modes.

Sekhar *et al.* (2004) conducted an experimental study on R134a heavy mixtures with small concentrations (7 to 11%) of a 45/55 by mass propane/isobutane hydrocarbon mixture as a possible drop-in replacement for R12 in heat pump systems. This combination was studied because the presence of the hydrocarbons improves miscibility of R134a in mineral oils. Two identical systems were compared, one with the R134a/hydrocarbon mixture and the second with R12. They found COP improvements of 3 to 8 % using the zeotropic mixture.

Heberle *et al.* (2012) simulated geothermal power cycles using zeotropic isobutene/isopropane and R227ea/R245fa mixtures. They found that for low temperature systems ($T_{source} < 180°C$), the mixtures of R227ea/R245fa have the highest cycle efficiencies.

Chys *et al.* (2012) simulated and analyzed a large variety of fluids (hydrocarbons, refrigerants, and hydrocarbon/refrigerant mixtures) as pure fluids and binary and ternary mixtures (including hydrocarbon/refrigerant mixtures) in low temperature ($150 < T_{source} < 250°C$) organic Rankine cycles. They optimized the concentration of each fluid pair for optimal performance. In all cases, they found that a zeotropic mixture provides a performance enhancement over pure fluids with an increase of 15.7% in cycle efficiency and 12.3% increase in generated electricity at the lower temperature ($T_{source} = 150°C$) end among the sources examine. They also found that adding a third component does further increase performance, but not substantially.

Garg *et al.* (2013) simulated and analyzed a power cycle with R245fa, isopentane, and a mixture of R245fa/isopentane (30/70 by mole or 44/56 by mass) for low

temperature ($106 < T_{source} < 152°C$) sources. Using conservative efficiencies of the pump and turbine, they found that the mixture of R245fa/isopentane had an efficiency of 13% compared to a Carnot efficiency of 27% for the upper temperature limit and a 35°C ambient. They found a minimum irreversibility at compression ratios of 8 to 10 and also found that the mixture reduces flammability concerns of pure isopentane and GWP concerns of pure R245fa.

2.4.2.2 Condensation studies

Zeotropic mixtures exhibit both a phase concentration shift and temperature glide during the phase-change process as shown in the *T-x-y* diagram in Figure 2.1, where the R245fa concentration is shown by mass. During the condensation process, the less volatile component condenses first, resulting in an increase in vapor-phase concentration of the more volatile component at the vapor-liquid interface. Referring to Figure 2.1, a superheated vapor at A is cooled to point B (the dew point line), where the mixture becomes saturated and begins to condense. At equilibrium, the condensate concentration (B') is low in the more volatile component (R245fa). As the mixture continues to condense to C and C', the condensing temperature decreases, the vapor-phase R245fa concentration increases as the *n*-pentane is depleted by being condensed, and the condensate R245fa concentration increases. As the fluid becomes completely condensed at D' (the bubble point line), the condensate returns to the bulk mixture concentration. The mixture is then subcooled to point E.
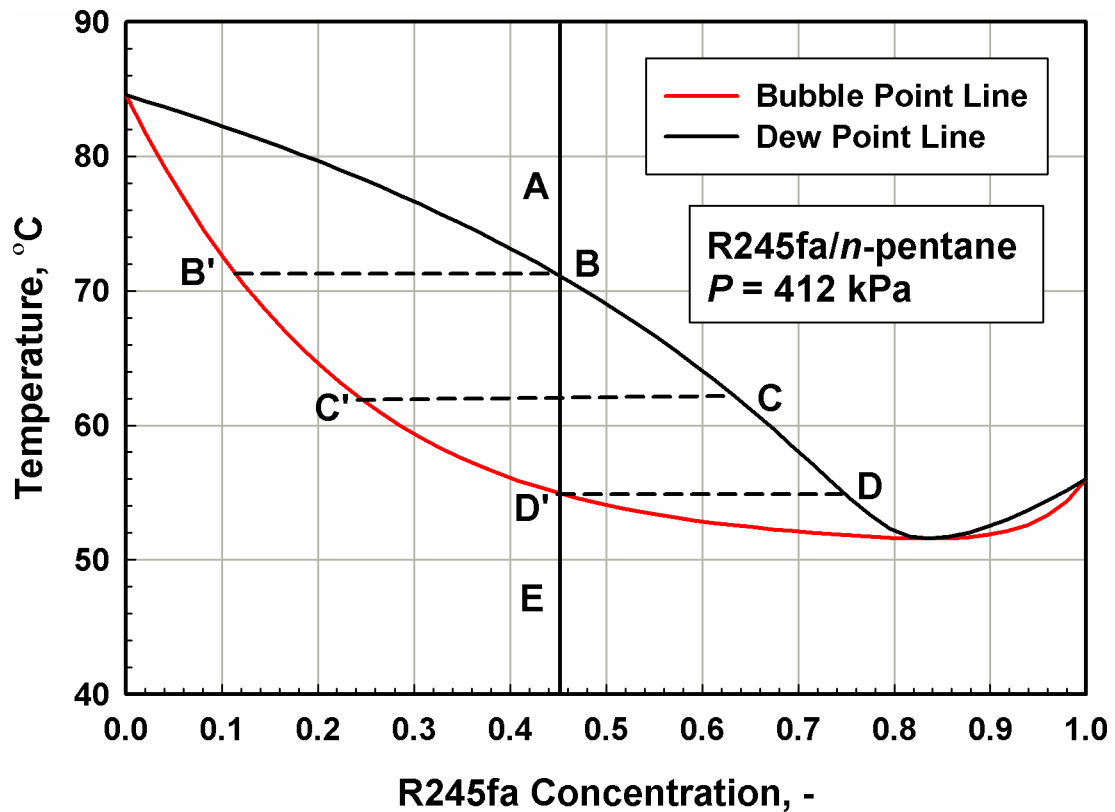
Figure 2.1. Zeotropic mixture phase diagram with sample points

The increased vapor-phase concentration at the interface adds a mass transfer resistance to the condensation process. Two methods are commonly used to account for the additional mass transfer resistance impact on the condensation heat transfer coefficient. These are the approximate method developed by Silver (1947) and Bell and Ghaly (1973), and the more fundamental approach developed by Colburn and Drew (1937) and Price and Bell (1974).

Colburn and Drew (1937) analyze the theoretical approach to condensation of a binary vapor mixture that is miscible in the liquid phase for all concentrations. The total condensation heat duty is assumed to be comprised of the sum of the sensible heat of the condensate, latent heat of the condensing fluid (all of which occurs at the interface), and sensible heat of the vapor. Their analysis assumes that the liquid and vapor phase

concentrations and temperatures at the vapor-liquid interface are in local equilibrium, which will probably differ from bulk equilibrium conditions. The driving temperature difference for the overall heat transfer coefficient is between the vapor-liquid interface and the wall temperatures. The total molar condensing flux is calculated using Equation (2.68), where $\dot{N}_{\text{T}}$ is the net molar rate of condensation per unit area, $\tilde{z}$ is the ratio of the condensation rate of the more volatile fluid to the net rate of condensation and F is a function of fluid properties and flow conditions, given by Chilton and Colburn (1934).

$$\dot{N}_{\text{T}} = F \ln \left(\frac{\tilde{z} - \tilde{y}_{\text{int}}}{\tilde{z} - \tilde{y}_{\text{v}}} \right) \tag{2.68}$$

The flux of each component can be calculated using $\tilde{z}$ and $\dot{N}_{\text{T}}$. They note that the concentration variation in the liquid phase can often be neglected due to negligible error and the difficulty in determining the liquid F coefficient.

The approximate method proposed by Silver (1947), and Bell and Ghaly (1973) accounts for mass transfer resistances in multi-component condensation through an over-estimation of the heat transfer resistance in the vapor phase. Four assumptions are made; 1) phase concentrations are in bulk equilibrium at the vapor temperature, 2) phase enthalpies are in equilibrium at the vapor temperature, 3) vapor-phase sensible cooling is achieved by convection to the vapor-liquid interface, and 4) the latent heat and sensible cooling of vapor and liquid phases occurs across the entire liquid film. Calculation of the vapor-phase convection heat transfer coefficient assumes that the vapor flows alone at the local vapor flow rate. The first and second assumptions differ from an actual system in that the interface is at local equilibrium and the liquid condensate is subcooled and vapor

is superheated relative to the interface. The third assumption is the key assumption for the approximate method. Over estimation of the vapor-phase heat transfer resistance is used to account for added mass transfer resistances. For a finite segment condenser design, the method of Bell and Ghaly (1973) can be expressed as a thermal resistance between the vapor and wall as shown in Equation (2.69).

$$R_{\mathrm{T}} = \frac{1}{h_{\mathrm{pure}}} + \left(\frac{\Delta Q_{\mathrm{v}}}{\Delta Q_{\mathrm{mix}}} \right) \frac{1}{h_{\mathrm{v}}} \tag{2.69}$$

The second term accounts for the additional vapor-phase resistance. The resulting approximate method can be used to adjust any pure fluid condensation heat transfer correlation, h_{pure}, for mass transfer resistances. The approximate method was compared with heat transfer data from the Heat Transfer Research, Inc. (HTRI) database for air/n-pentane, n-pentane/methane, n-pentane/n-heptane, n-pentane/n-xylene, and gasoline in horizontal tubes, outside ideal tube banks, and on the shell-side of horizontal shell-and-tube condensers with exit qualities ranging from 0 to 90%. The comparison with data found that the predicted values in some cases showed that 90% of the data were predicted within 30% with a tendency to under predict the data by up to 50%.

Price and Bell (1974) later formulated the equations developed by Colburn and Drew (1937) into a computational design tool for condensing binary mixtures in a counter flow heat exchanger. The net condensing flux $\dot{N}_{\mathrm{T}}$ is combined with a mass, species, and energy balance on both phases and several simplifying assumptions were made. These assumptions include: 1) the coolant has a constant specific heat, 2) the liquid and vapor phase properties are known, and 3) the condensing fluid thermal resistance is the only

unknown resistance. The liquid condensate film is assumed to be isobaric and well mixed, eliminating concentration gradients in the liquid film. The interface is at local equilibrium at the interface temperature and local pressure, which can differ from the bulk equilibrium of the mixture. All heat and mass transfer resistances in the vapor phase occur in a thin boundary layer adjacent to the interface. A condensation heat transfer coefficient correlation or model from the literature is used to calculate the liquid-film heat transfer coefficient. As in the Colburn and Drew (1937) analysis, the driving temperature difference for the liquid film is from the interface to the wall temperature and neglects the condensate film sensible heat. Using the computational framework developed in their paper, Price and Bell (1974) found for mixtures of 43% methanol/57% water and 18% n-butane/82% n-octane in a 21.1 mm internal diameter vertical tube, that the approximate method proposed by Bell and Ghaly (1973) tends to over predict the concentration of the more volatile component in the vapor bulk and over predict the heat transfer area required for condensation, therefore, under estimating the effective heat transfer coefficient.

Webb et $al.$ (1996) recommend the film method of Colburn and Drew (1937) over the approximate method of Silver (1947) and Bell and Ghaly (1973) for all applications. They found the vapor Lewis number, the ratio of thermal to mass diffusion coefficients, to provide a reliable indication of the accuracy of the approximate method. Using the film method as the baseline, Webb et $al.$ (1996) determined that the approximate method provides reasonable agreement for vapor Lewis numbers, Le_v , of 0.6 to 0.8, but over predicts the heat transfer coefficient at values of Le_v greater than unity, and under predicts heat transfer coefficients at small values of Le_v. They also noted that using the

112

approximate method within a segmented rather than differential approach improves the agreement with the film method results. They found the error associated with the use of the approximate method within design applications to be decreased when the condensation resistance is small relative to the other resistances. Finally, Webb *et al.* (1996) proposed a modification to the Bell and Ghaly (1973) correction; however, the modified correction requires knowledge of several values calculated within the film method such as the interface temperature, condensing molar flux, and binary diffusion coefficient, making the application of the revised correction factor just as limited as the application of the Colburn and Drew (1937) film method.

Shao and Granryd (1998) investigated heat transfer characteristics of condensing mixtures of R32/R134a in a 6 mm internal diameter tube over a range of mass fluxes from 131 to 369 kg m^{-2} s^{-1} and a range of saturation temperatures from 23 to 40°C. They found that the error associated with using the UA-LMTD method for calculating heat transfer coefficient for mixtures is affected by the non-linear temperature-enthalpy curves. If the profile is convex, the LMTD is lower than the actual value, thus over-predicting the heat transfer coefficient. If the profile is concave, the opposite is true. Thus, they conclude that if small segments, with approximately linear profiles in the condensing region are used, the UA-LMTD method is acceptable. They also observed that lower heat fluxes and mass fluxes result in greater heat transfer degradation. A similar trend was also observed by Stoecker and Kornota (1985), who found greater degradation in the wavy flow regime as compared to the annular regime. They conclude that concentration gradients, non-ideal properties, and slip between the phases are the primary causes for degradation of the heat transfer coefficients of zeotropic mixtures.

Thonon and Bontemps (2002) measured condensation heat transfer coefficients of pure hydrocarbons *n*-pentane, butane, and propane and zeotropic butane/propane mixtures in compact plate heat exchangers at pressures ranging from 150 to 1,800 kPa. They proposed using the method of Silver (1947) and Bell and Ghaly (1973) to account for mixture effects. They found that this method agreed well with their data for cases when the Reynolds number is in the turbulent regime ($Re_{eq} > 1500$); however, when the flow was laminar, the Silver, Bell, and Ghaly method tended to over predict their data.

Cavallini *et al.* (2002a) found that the approximate method of Bell and Ghaly (1973), combined with their pure fluid heat transfer coefficient correlation, provided good agreement with heat transfer data for the zeotropic mixture R407C, but resulted in a slight under prediction at high mass fluxes due to the large correction factor in this range.

Cavallini *et al.* (2002c) measured heat transfer coefficients of condensing zeotropic mixtures of R125 and R236ea in three concentrations in a horizontal 8 mm internal diameter tube over mass fluxes ranging from 400 to 750 kg m^{-2} s^{-1} and saturation conditions ranging from 40 to 60°C. High mass fluxes were chosen to keep the flow in the annular regime. Cavallini *et al.* (2002c) compared their data to predictions from a segmented model based on the Price and Bell (1974) framework using the model of Cavallini and Zecchin (1974) for the calculation of the liquid-film heat transfer coefficient. They found good agreement between their data and the computational results with most data predicted within 10%. However, the water-side resistance was found to be on average 40% of the total resistance, limiting the effect of mass transfer resistances.

Del Col *et al.* (2005) extended the pure fluid regime-specific correlation of Thome *et al.* (2003), outlined above, to zeotropic mixtures. Del Col *et al.* (2005) use an approximated Bell and Ghaly (1973) correction, shown in Equation (2.70), to modify the convective condensation term, h_c shown in Equation (2.62), and a film-condensation term, h_f shown in Equation (2.63).

$$\frac{1}{h} = \frac{1}{h_{\text{pure}}} + qC_{\text{p,v}} \left(\frac{\Delta T_{\text{Glide}}}{\Delta i} \right) \frac{1}{h_{\text{v}}} \tag{2.70}$$

The pure fluid heat transfer coefficient, h_{Pure}, is calculated using the Thome *et al.* (2003) heat transfer coefficient correlation. The convective condensation term in the pure fluid correlation is modified further by multiplying the vapor-phase heat transfer coefficient, h_v, in Equation (2.70), by the interfacial roughness coefficient, f_i, defined in Thome *et al.* (2003). Non-equilibrium effects are incorporated into the film condensation term using an empirical non-equilibrium factor multiplied by the heat transfer coefficient calculated using Equation (2.70). A comparison of the heat transfer coefficients, calculated using the modified convective and film condensation terms within the flow regime dependent interpolation identified in Thome *et al.* (2003) showed good agreement with refrigerant and hydrocarbon zeotropic mixture data. A database of zeotropic mixtures R407C, R125/R236ea, R22/R124, and propane/butane temperature glides ranging from 3.6 to 21.9°C in 7.5 to 8 mm internal diameter horizontal tubes over a range of mass fluxes from 57 to 755 kg m^{-2} s^{-1} was used for comparison.

In conjunction with their flow regime transition and heat transfer model, Cavallini *et al.* (2006) indicate that their proposed correlation, Equation (2.65) - (2.67), can be used within the Price and Bell (1974) framework for calculating the film heat transfer

coefficient for zeotropic mixtures with reasonable accuracy. However, they recommend using the more easily implemented approximate method of Bell and Ghaly (1973) for zeotropic mixtures, citing an absolute average deviation of 12% and average deviation of 5% between their correlation and experimental results.

2.4.3 <u>Summary</u>

As detailed above, there has been a significant amount of theoretical and experimental analysis of pure fluid heat transfer and analysis of zeotropic mixture effects. A summary of pure fluid heat transfer studies for both single- and multi-regime studies is provided above in Table 2.8. The importance of accurately capturing the dominant heat transfer processes in the significant flow regimes has been documented. A wide variety of pure fluids have been used to experimentally validate models, including refrigerant and hydrocarbons. However, there remains some uncertainty in the use of models outside the range for which they are developed, even when validated using a range of fluids and accounting for multiple regimes as done in Cavallini *et al.* (2006). This is especially important when applied to fluid types different from those used in the development of the respective models and correlations, such as HFC and CFC. Finally, zeotropic hydrocarbon/refrigerant mixtures have been gaining increasing interest in cycle modeling and limited system level testing. However, the mixture effects on the heat transfer coefficient can be significant and have not been explored in detail for zeotropic hydrocarbon/refrigerant mixtures. A summary of application specific and fundamental heat transfer studies is provided in Table 2.9.

Table 2.9. Zeotropic mixture literature review summary table

Investigators	Hydraulic diameter (mm)	Fluids	Orientation / conditions	Range / applicability	Techniques, basis, observations
Zeotropic Mixture Studies: Application Specific					
Wu (1985)		R12/R114	Energy Conversion		• Found zeotropic mixtures to provide 4.4 to 9.1% increase in conversion efficiencies
Chang *et al.* (2000)	8 mm	R22, propane, butane, propane/ butane	Horizontal Heat Pump		• Zeotropic mixtures show h degradation • Propane and propylene show better COP than R-12 • COPs of mixtures greater than linear interpolation between pure fluid COPs
Sekhar *et al.* (2004)		R12, R134a/ propane/ isobutane	Heat pump		• Mixture could serve as drop in replacement for R-12 • Mixture showed 3 to 8% COP improvement
Thonon & Bontemps (2002)	1 - 10 mm	Pentane, butane, propane, butane/ propane	Compact welded plate	$150 < P < 1,800$ kPa $100 < \text{Re}_{LO} < 2,000$	• Forced-convective correlation with two-phase multiplier for pure fluids • Bell and Ghaly (1973) correction used for mixtures • Pure hydrocarbon fluids exhibit similar trends in h
Heberle *et al.* (2012)		isobutane/ isopropane, R227ea/ R245fa	Simulated geothermal power cycle		• Found refrigerant mixture to have higher conversion efficiencies

Table 2.9. Zeotropic mixture literature review summary table - Continued

Investigators	Hydraulic diameter (mm)	Fluids	Orientation / conditions	Range / applicability	Techniques, basis, observations
Zeotropic Mixture Studies: Application Specific - Continued					
Chys *et al.* (2012)		Hydrocarbon, refrigerants, and variety of binary and ternary mixtures	Simulated low temperature	$150 < T_{source} < 250°C$	• Investigated pure fluid and binary and ternary mixtures in low temperature ORCs for efficiency improvements • Found 15.7% increase in cycle efficiency using binary mixtures • Found 12.3% increase in generated power using binary mixtures
Garg *et al.* (2013)		R245fa, isopentane, R245fa/ isopentane	Simulated low temperature	$106 < T_{source} < 152°C$	• Found mixture of 44% R245fa/55% isopentane can reduce GWP and flammability concerns with pure fluids • Found conservative efficiency of 13% achievable for mixture, compared to 27% Carnot efficiency
Heat Transfer Studies: Zeotropic mixtures					
Colburn and Drew (1937)		81% methanol/ 19% water	Vertical Plate	$0 < T < 77°C$	• Derived theoretical mass transfer equations for condensing vapors • Derived molar vapor to interface flux equation • Iterative and requires mass diffusion coefficient in vapor phase

Table 2.9. Zeotropic mixture literature review summary table - Continued

119

Investigators	Hydraulic diameter (mm)	Fluids	Orientation / conditions	Range / applicability	Techniques, basis, observations
Bell and Ghaly (1973)		air/*n*-pentane, *n*-pentane/ methane, *n*-pentane/ *n*-heptane, *n*-pentane/ *n*-xylene, gasoline	Horizontal tube Horizontal tube bank Shell-side		• Assumed equilibrium conditions in vapor and liquid phases • Heat transfer occurs between liquid-vapor interface and coolant • Mass transfer resistance accounted for using over estimation of the heat transfer resistance • Developed computational framework for single- and multi-pass condenser design
Price and Bell (1974)	21.1 mm	Methanol/ Water *n*-butane/*n*-octane	Vertical tube		• Adapted Colburn and Drew (1937) equations into iterative computational model for counter flow tube-in-tube condenser of mixtures • Assumed well mixed condensate film
Webb *et al*. (1996)	40 mm	Benzene/ Nitrogen, Toluene/ Nitrogen	Downward		• Colburn and Drew (1937) film method preferable • Bell and Ghaly (1973) correction reasonable for Lewis numbers of 0.6 to 0.8, under prediction of *h* occurs for Le > 1 • Developed a new correction for Silver, Bell and Ghaly method for condensation in the presence of non-condensable gas

Table 2.9. Zeotropic mixture literature review summary table - Continued

Investigators	Hydraulic diameter (mm)	Fluids	Orientation / conditions	Range / applicability	Techniques, basis, observations
Heat Transfer Studies: Zeotropic mixtures - Continued					
Shao and Granryd (1998)	6 mm	R32, R134a, R32/R134a	Horizontal	$131 < G < 369$ kg m^{-2} s^{-1} $23 < T_{sat} < 40°C$	• Concentration gradients, non-ideal properties, and slip are primary causes of heat transfer degradation in zeotropic mixtures • Low heat and mass flux conditions show higher degradation
Cavallini *et al.* (2002c)	8 mm	R125/R236ea	Horizontal	$400 < G < 750$ kg m^{-2} s^{-1} $19 < \Delta T_{Glide} < 21°C$ $780 < P_{sat} < 1,420$ kPa $40 < T_{sat} < 60°C$	• Good agreement with Price and Bell (1974) framework • Film h calculated using Cavallini and Zecchin (1974) • Data limited to annular flow regime
Del Col *et al.* (2005)	7.5 - 8 mm	R407C, R125/R236ea, R22/R124, propane/ butane	Horizontal	$57 < G < 755$ kg m^{-2} s^{-1} $3.6 < \Delta T_{Glide} < 21.9°C$ $2.8 < \Delta T < 19.3°C$	• Modified Thome *et al*. (2003) with modified Bell and Ghaly (1973) correction for application to zeotropic mixtures • Non-equilibrium correction factor to film condensation term • Interfacial roughness factor to convective condensation term

120

2.5 R245fa Evaporation Studies

In an attempt to qualitatively analyze the flow and heat transfer behavior of R245fa compared to other refrigerants, several evaporation studies are reviewed in this section.

Kedzierski (2006) measured the difference in temperature between the saturation temperature and the wall temperature on an enhanced surface for pool boiling of R245fa, R123, and a mixture of R245fa/isopentane (99.5/0.5 by mass) at a saturation condition of 4°C, over a range of heat fluxes up to 125 kW m^{-2}. He found for a given temperature difference, that the heat flux of the mixture was up to 11% higher for the mixture relative to pure R245fa for heat fluxes greater than 72 kW m^{-2}. At heat fluxes lower than 72 kW m^{-2}, the boiling performance of the mixture was degraded. He hypothesized that the addition of isopentane to the R245fa could have a "seeding" effect, increasing the areas of active boiling.

Revellin and Thome (2007a; 2007b) measured flow characteristics using lasers of evaporating R134a and R245fa in 0.509 and 0.790 mm diameter microchannels over a range of mass fluxes from 200 to 2,000 kg m^{-2} s^{-1} at saturation conditions of 26, 30 and 35°C. They conclude that the mechanisms that control flow regimes for R134a also apply to R245fa. However, they note that the transitions between regimes occur at lower qualities for R245fa than R134a and show smaller changes in transition quality with increasing mass flux. Due to high pressure drops and the low operating pressure of R245fa (at $T = 20$°C, $P_{sat} = 122$ kPa), limited annular flow data for R245fa were collected to prevent approaching a vacuum in the test loop. Revellin and Thome (2007a) determined that the transition mechanisms of R245fa are similar to those of R134a, although the transitions of R245fa are less dependent on mass flux.

Consolini and Thome (2009) studied flow boiling of R245fa, R134a, and R236fa in microchannels with internal diameters of 0.51 mm and 0.79 mm over a range of mass fluxes from 200 to 2,000 kg m^{-2} s^{-1} and heat fluxes less than 200 kW m^{-2} but below the critical heat flux. An adiabatic visualization section was used to record the flow regime present at the outlet of the heated test section. They observed bubbly, slug, churn, and annular flows in their R134a experiments. At low flowrates, the R245fa data were observed to be in the churn regime rather than the bubbly or slug regimes that were observed for R134a at similar conditions. With constant mass flux and increasing heat flux, they found the heat transfer coefficient trends of R245fa to differ from the trends observed for R134a and R236fa. Most notably, heat transfer coefficients of R245fa were found to increase with increasing heat flux up to a quality of between 0.15 and 0.35, depending on the heat flux. After this point, the heat transfer coefficient was found to be independent of heat flux. The independence of heat transfer coefficient with increasing heat flux shown in R245fa was found primarily in the annular flow regime and was not predicted by any of the models examined. They also found flow instabilities to detrimentally impact the heat transfer coefficient of R245fa more significantly than for R134a or R236fa.

Bertsch *et al.* (2009) conducted boiling heat transfer experiments in microchannels with hydraulic diameters ranging from 0.54 to 1.09 mm for R134a and R245fa at low mass fluxes ranging from 20 to 350 kg m^{-2} s^{-1}, temperatures ranging from 8 to 30°C, and for a range of heat fluxes up to 220 kW m^{-2}.Flow within the channels was observed using a clear top test section. Flow of R134a was found to be more uniform than that ofR245fa at the onset of boiling. Heat transfer coefficients were measured in small quality

increments. The heat flux and mass flux were adjusted simultaneously to maintain a constant quality change of 0.2 in the test section. Single-phase heat transfer coefficient data of the two fluids, conducted for experimental setup verification, were found to be accounted for well by the Dittus and Boelter (1930) and Gnielinski (1976) correlations. Both R134a and R245fa exhibited expected trends with increasing quality: an abrupt increase in heat transfer coefficient at the onset of nucleate boiling, followed by a decrease with increasing quality. The peak occurred significantly later ($q = 0.5$) for R245fa than for R134a ($q = 0.1$) and the rate of increase and decrease was more gradual for R245fa as compared to that of R134a. Both fluids exhibited similar trends with increasing heat flux; the heat transfer coefficient is relatively insensitive to heat flux except in the range of 2 to 10 kW m^{-2}. Channel diameter was found to have a less significant impact than mass flux and heat flux. A slight increase in heat transfer coefficient with increasing saturation pressure, up to a quality of 0.7, was observed. Similar to the findings of Consolini and Thome (2009), Bertsch *et al.* (2009) found the measured heat transfer coefficients of R245fa to be significantly lower than those of R134a at similar conditions. With the exception of the last point, these results seem to contradict the earlier results of Consolini and Thome (2009); however, these studies investigate different influences. Consolini and Thome (2009) investigated trends with heat flux and mass flux, while Bertsch *et al.* (2009) investigated trends with increasing quality. Because they span slightly different mass flux regions, a direct comparison of the two data sets is difficult. Both studies found reasonably good agreement between R134a and R245a with some exceptions. R134a was found by the authors of both studies to be a more stable fluid than R245fa. Maldistibution at the onset of nucleate boiling and the

123

observation of a larger churn regime for R245fa were attributed to the fluid instability. Also, R245fa was found to be insensitive to heat flux for high values of heat flux.

2.5.1 <u>Summary</u>

A summary of experimental studies on the evaporation of R245fa is presented in Table 2.10. The studies mentioned above demonstrate that the behavior of R245fa does differ from that of other refrigerants, such as R134a. Not only does R245fa differ in the magnitude of the expected heat transfer coefficient, but also the results show that R245fa can also deviate from the expected trends for certain conditions. This can pose a significant problems when applying correlations and models developed for other refrigerants to flows of R245fa.

Table 2.10. R245fa experimental studies literature review summary table

Investigators	Hydraulic diameter (mm)	Fluids	Orientation / conditions	Range / applicability	Techniques, basis, observations
Evaporation studies					
Kedzierski (2006)		R245fa, R123, R245fa/ isopentane	Pool boiling Enhanced surface	$T = 4°C$ $10 < q'' < 125$ kW m^{-2}	• Mixture showed up to an 11% increase in q'' for $q'' > 72$ kW m^{-2} • Showed degradation in q'' at low q''
Revellin and Thome (2007)	0.51 - 0.79 mm	R134a, R245fa	Horizontal Evaporation	$200 < G < 2,000$ kg m^{-2} s^{-1} $3.2 < q'' < 422$ kW m^{-2} $26 < T_{sat} < 35°C$	• Two-phase mechanisms in micro channels are the same between R134a and R245fa • R245fa transitions less influenced by mass flux than R134a, yet have similar mechanisms
Bertsch *et al.* (2009)	0.54 - 1.09 mm	R134a, R245fa	Horizontal Evaporation	$20 < G < 350$ kg m^{-2} s^{-1} $8 < T_{sat} < 30°C$ $q'' < 220$ kW m^{-2}	• At ONB: Exhibited in single-phase region for R245fa not for R134a
Consolini and Thome (2009)	0.51 - 0.79 mm	R134a, R236fa, R245fa	Horizontal Evaporation	$300 < G < 2,000$ kg m^{-2} s^{-1} $q'' < 200$ kW m^{-2}	• For R245fa: Bubbly and slug regimes less evident; exhibit churn characteristics • R245fa trends differed from conventional refrigerant (R134a) trends • For R245fa: h independent of q'' at high q (annular regime), dependent on q'' at low q • For R134a and R236fa: h dependent on q'' at all q

2.6 Specific Research Needs

It has long been understood that heat transfer and pressure drop are dependent on flow regime and void fraction. The classification of flow regimes can vary significantly between authors. As outlined above, there has been a significant amount of work on characterizing two-phase flow and modeling void fraction, frictional pressure drop, and heat transfer coefficients, for pure fluids as well as for zeotropic mixtures of fluids. However, there are several areas of interest in geothermal power generation and the process industy that are in need of further investigation. While some studies have investigated two-phase flows of hydrocarbons, the majority have been conducted using air/water mixtures and steam. There remains a need for further research to characterize two-phase flows, including flow regime mapping and measurement and modeling of void fraction for hydrocarbon flows, particularly at pressures above ambient pressure.

After obtaining a qualitative understanding of two-phase hydrocarbon flows, a fundamental study on pressure drop and heat and mass transfer of zeotropic hydrocarbon/refrigerant mixtures is necessary. These mixtures are being explored literature for possible efficiency gains of energy conversion systems. However, realizing these gains is dependent on the ability to accurately predict pressure drop and heat transfer coefficient during the design phase. These two deficiencies will be explored in the present study.

2.7 Objectives of the Present Study

The objectives of the present study address two primary needs. The first is to gain a fundamental and quantitative understanding of hydrocarbon flows, specifically propane, at elevated pressures. The second is to understand the pressure drop and heat transfer

characteristics and mass transfer effects of zeotropic hydrocarbon/refrigerant mixtures undergoing condensation. The specific tasks of the present study are as follows.

- Visualize two-phase flows of propane in 7.0 and 15.0 mm internal diameter horizontal round tubes at mass fluxes ranging from 75 to 450 kg m^{-2} s^{-1} and operating pressures of 952 and 1218 kPa ($0.22 < P_r < 0.29$; $25 < T_{sat} < 35$°C).

- Determine flow regime transitions and quantitatively analyze the visualization results to obtain local void fraction and film thicknesses for propane with changing quality, mass flux, pressure, and tube diameter.

- Experimentally determine local heat transfer coefficients and frictional pressure gradients at small quality increments ($\Delta q \sim 0.1$) for condensing flows of:

  o Pure R245fa in a 7.75 mm internal diameter horizontal round tube for mass fluxes ranging from 150 to 600 kg m^{-2} s^{-1} and operating pressures ranging from 122 to 610 kPa ($0.03 < P_r < 0.17$; $20 < T_{sat} < 70$°C).

  o Pure n-pentane in 7.75 mm and 14.45 mm internal diameter horizontal round tubes for mass fluxes ranging from 100 to 450 kg m^{-2} s^{-1} and operating pressures ranging from 136 to 215 kPa ($0.04 < P_r < 0.06$; $45 < T_{sat} < 60$°C).

  o Zeotropic mixtures of 45% R245fa/55% n-pentane in a 7.75 mm internal diameter horizontal round tube for mass fluxes ranging from 150 to 600 kg m^{-2} s^{-1} and operating pressures ranging from 198 to 763 kPa ($0.06 < P_r < 0.24$).

- Develop flow-regime-specific void fraction, pressure drop, and heat transfer models based on the insights gained from the present study. Develop models for predicting condensation of zeotropic mixtures of dissimilar fluids.

CHAPTER 3. EXPERIMENTAL APPROACH

The phase-change test facility used for conducting the experimental portion of the present study is shown in Figure 3.1. This facility was originally used for flow visualization and pressure drop experiments by Coleman and Garimella (2000b) and Garimella *et al*. (2002), and subsequent heat transfer experiments by Bandhauer *et al*. (2006) for condensation of R134a in channels with hydraulic diameters in the range of 0.4 to 5 mm. It has also been used, with appropriate modifications, to conduct condensation heat transfer, pressure drop, and flow visualization experiments for R404A by Keinath and Garimella (2010) and other investigators for R404A and R410A at high reduced pressures in 6.22 and 9.40 mm round tubes (Jiang, 2004; Mitra *et al.*, 2005; Jiang *et al.*, 2007). In the present work, additional modifications were made to this facility to accommodate the fluids under consideration and the required range of conditions. The test facility and test sections used for pressure drop, heat transfer, and high-speed flow visualization experiments are described in detail, followed by a description of the testing procedures.

3.1 Phase-Change Experiments

In this section, the experimental facility and test sections used for pressure drop and heat transfer experiments on the pure fluids and the zeotropic mixture under consideration are outlined in detail. A discussion of the thermal amplification technique, mixture measurements, and the test matrix for this portion of the study follows.

Figure 3.1. Experimental phase-change test facility photograph

3.1.1 <u>Test Facility</u>

A schematic drawing of the test facility is shown in Figure 3.2. The facility consists of a test flow loop constructed of ½-inch 316 stainless steel tubing with a wall thickness of 0.035", a primary coolant loop also constructed of ½-inch 316 stainless steel tubing, and several closed coolant water loops constructed of ½-inch copper tubing. The closed coolant loops were coupled to the laboratory chilled water supply through a large shell-and-tube heat exchanger that was replaced part way through the study with two plate heat exchangers to increase the cooling capacity.
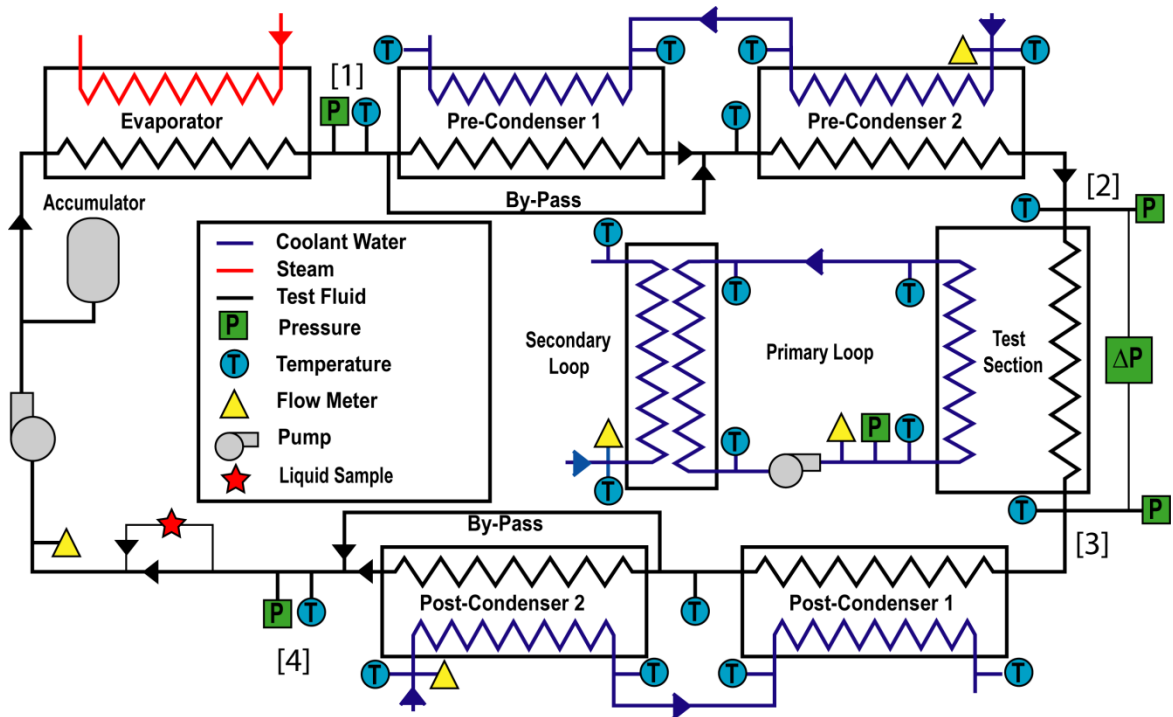
Figure 3.2. Experimental phase-change test facility schematic

The experimental facility included twenty three temperature measurements with an additional four redundant temperature measurements at the test section for the mixture experiments, six flowrate measurements, six absolute pressure measurements, and three differential pressure measurements. Instrumentation signals were recorded using a National Instruments Data Acquisition System (DAQ), LabView, and a PC. Detailed specifications of the data acquisition system are provided in Table 3.1.

Table 3.1. Summary of data acquisition system specifications

Instrument	Manufacturer	Model Number	Serial Number	Range
DAQ Chassis	National Instruments	NI SCXI-1000	14223AE	
16 Bit Digitizer for USB	National Instruments	NI SCXI-1600	1423DE9	
32 Channel Thermocouple Amplifier	National Instruments	NI SCXI-1102	142E214	0 - 24 V
Terminal Block		NI SCXI-1303	13C86A6	0 - 24 V
32 Channel Analog Voltage	National Instruments	NI SCXI-1102	142E1EF	0 - 24 V
Terminal Block		NI SCXI-1303	13F2AE6	0 - 24 V

Referring to Figure 3.2, subcooled liquid was pumped (Micro Pump GC M23-JVSEN3 Serial #1074767 (0 – 2.5 L min^{-1}) or Tuthill TWS8.0EEET7WN00000 (2 – 27.6 L min^{-1})) through a Coriolis flow meter to a steam-coupled tube-in-tube evaporator (Exergy, Inc. Model 00528; Serial # 13890), where the fluid was evaporated and superheated to state point [1]. The superheated state was verified using temperature and pressure measurements. The fluid was partially condensed in the pre-condenser to establish the desired quality at the inlet to the test section [2]; this was achieved by controlling the coupling fluid water flowrate and temperature and the heat transfer area of the pre-condenser. Two pre-condensers (Exergy, Inc. Series 35; Model 00256-1; Serial #s 30178 and 16870) were configured in series. A by-pass line for the first pre-condenser allowed the superheated vapor to directly enter the second pre-condenser if necessary, thus decreasing the heat transfer area and enabling a high vapor quality at the test section inlet. An energy balance on the coupling fluid water and the superheated state was used to calculate the test section inlet quality. Upon leaving the test section at state point [3], the fluid was subcooled in the post-condenser to state point [4]. A two post-condenser (Exergy, Inc. Series 35; Model 00256-1; Serial #'s 33819 and 33560) configuration similar to the pre-condensers was used to control the heat transfer capabilities downstream of the test section. However, the second post-condenser was rarely by-passed in the tests. The subcooled state at state point [4] was verified by temperature and pressure measurements, and also visually verified using a sight glass (Pressure Products Bulls-Eye ½" NPT Serial #SCGQ8510). An energy balance on the post-condenser coupling fluid water and the subcooled state was used to calculate the test section outlet quality.

Coolant water was circulated through the pre- and post-condenser using centrifugal pumps (AMT 3680-975-95 #1105 and 1106, respectively). Two sets of rotameters were used to control the flowrate through the pre- and post-condenser independently. One of two magnetic tube flow meters (Rosemount 8711 Serial #0168079 (1 – 14 L min^{-1}) and #0071955 (0 – 2.5 L min^{-1})) was used to measure the pre-condenser coolant flowrate. A single magnetic tube flow meter (Rosemount 8711 Serial #0168080 (1 – 14 L min^{-1}) was used to measure the post-condenser coolant flowrate. A summary of the heat exchangers in the test facility is provided in Tables 3.2 and 3.3.

Table 3.2. Summary of heat exchanger dimensions

Exergy, Inc Model	Serial Number	Tube Length, mm	Heat Transfer Area, m^2	Shell		Tube		Tube / Baffle Count
				Outer Diameter, mm	Wall Thickness, mm	Outer Diameter, mm	Wall Thickness, mm	
Pre-Condenser 1								
35-00256-1	30178	508	0.27	38.1	1.65	3.18	0.032	55/11
Pre-Condenser 2								
35-00256-1	16870	508	0.27	38.1	1.65	3.18	0.032	55/11
Post-Condenser 1								
35-00256-1	33819	508	0.27	38.1	1.65	3.18	0.032	55/11
Post-Condenser 2								
35-00256-1	33820	508	0.27	38.1	1.65	3.18	0.032	55/11
Primary-to-Secondary								
23-00540-6	33560	406	0.08	25.4	1.25	3.18	0.032	19/18

Table 3.3. Summary of evaporator dimensions

Evaportator Tube-in-Tube		
Exergy, Inc : Model 00528; Serial Number: 13890		
Inner Tube	Outer Diameter, mm	12.70
	Wall Thickness, mm	1.65
Outer Tube	Outer Diameter, mm	25.4
	Wall Thickness, mm	1.65
Length, m		5.9

3.1.1.1 Facility Instrumentation

All temperature measurements were made using T-type thermocouples (Omega Engineering Model# TMQSS-125G-6). Calibration of all thermocouples was conducted using a temperature controlled calibration bath (Hart Scientific Model# 7340 Serial # A57096) with calibration bath silicone oil 200.10 (Hart Scientific Model# 5012) and high accuracy Platinum RTD (Hart Scientific Model# 5612 Serial# 748503; ±0.012°C) with a Tweener PRT readout (Hart Scientific Model# 1502A Serial# A57032). The thermocouple calibrations were entered into LabView® software, which linearly interpolates between calibration points. The maximum uncertainty of the thermocouples was calculated to be 0.3°C, which was applied to all thermocouple measurements.

Flowrates were measured using two Coriolis flow meters and four magnetic flow meters. The test fluid flowrate was measured using a Coriolis flow meter (MicroMotion CMF025 series). The secondary coolant water flowrate for the thermal amplification technique was measured using the second Coriolis flow meter (MicroMotion DS006 series). Four magnetic flow meters (Rosemount 8711 series) were used to measure three coolant water flowrates. Specifications and uncertainties of the flow meters are presented in Table 3.5. Test fluid pressure measurements were made using four absolute pressure transducers (Rosemount 3051 series). Because of the range of saturation pressure of the fluids of interest in this study, transducers with different absolute pressure spans were used for different fluids to reduce experimental uncertainty. Test section pressure drops were measured using two differential pressure transducers. The absolute pressures of the primary loop and coolant lines were measured to ensure that the fluid remains in the liquid phase. A differential pressure transducer measured the pressure drop in the primary

loop. Specifications and uncertainties of absolute and differential pressure transducers are

shown in Table 3.4.

Table 3.4. Summary of pressure transducer specifications

Instrument	Device Manufacturer and Model Number	Serial Number	Range	Accuracy
Main Flow Loop Pressure Transducers				
Pre-Condenser Inlet - Absolute	Rosemount 3051TA4A2B21AE5M5	1019352	0 - 3447 kPa	5.17 kPa (0.15% F.S.)
Test Section Inlet - Absolute	Rosemount 3051TA4A2B21AE5M5	1019351	0 - 500 kPa	2.15 kPa (0.43% F.S.)
			0 - 3447 kPa	5.17 kPa (0.15% F.S.)
Test Section Outlet - Absolute	Rosemount 3051TA4A2B21AE5M5	1019353	0 - 500 kPa	2.15 kPa (0.43% F.S.)
			0 - 3447 kPa	5.17 kPa (0.15% F.S.)
Post-Condenser Outlet - Absolute	Rosemount 3051TA4A2B21AE5M5	1021623	0 - 500 kPa	2.15 kPa (0.43% F.S.)
			0 - 3447 kPa	5.17 kPa (0.15% F.S.)
Test Section - Differential	Rosemount 3051CD3A22A1AB4M5	0687134	0 - 62.6 kPa	0.088 kPa (0.14% F.S).
	Rosemount 3051CD1A22A1AM5	0687133	0 - 6.26 kPa	0.014 kPa (0.22% F.S).
Coolant Loop Pressure Transducers				
Coolant Loops - Absolute	Rosemount 2088A3M22A1M7	138877	0 - 2413 kPa	2.4 kPa
Primary Loop - Absolute	Rosemount 2088A3M22A1M7	138874	0 - 5516 kPa	5.5 kPa
Primary Loop - Differential	Rosemount 3051CD4A22A1AB4M5E5	2251309	0 - 2068 kPa	N/A
Gas Chromatograph Calibration	Rosemount 2088A3M22A1M7	138875	0 - 5516 kPa	5.5 kPa

Table 3.5. Summary of flow meter specifications

	Model Number	Serial Number	Range	Accuracy
Main Loop - Coriolus (MicroMotion)				
Sensor	CMF025M319NU	0326974	0 - 100.0 g sec^{-1}	±0.10% of Reading
Transmitter	IFT9701R6D3U	0366359		
Secondary Loop - Coriolus (MicroMotion)				
Sensor	DS006S100SU	0205104	0 - 15.1 g sec^{-1}	±0.15% of Reading
Transmitter	IFT9701R6D3U	0366366		
Pre-Condenser - Magnetic Tube (Rosemount)				
Sensor	8711ASA30FR1E5G1	0168079	0 - 14.0 L min^{-1}	±0.25% of Reading & ±0.005 L min^{-1}
Transmitter	8712ESR1A1N5M4	0310126		
Pre-Condenser - Magnetic Tube (Rosemount)				
Sensor	8711RRE15FS1	0071955	0 - 2.5 L min^{-1}	±0.5% of Reading OR ±0.0034 L min^{-1}
Transmitter	8712CT12M4	63610		
Post-Condenser - Magnetic Tube (Rosemount)				
Sensor	8711ASA30FR1E5G1	0168080	0 - 14.0 L min^{-1}	±0.25% of Reading & ±0.005 L min^{-1}
Transmitter	8712ESR1A1N5M4	0310125		
Primary Loop - Magnetic Tube (Rosemount)				
Sensor	8705TSA005S1W0N0M4	0870119434	0 - 15.0 L min^{-1}	±0.5% of Reading
Transmitter	8732CT03N0M4	0860199499		

3.1.1.2 *Hazardous Fluid Safety Equipment*

Because the experimental facility was originally designed for refrigerant experiments, the system was modified to accommodate flammability concerns associated with testing hydrocarbons. As shown in Figure 3.1, the facility was surrounded by a Plexiglas® wall that extended down to the floor. Because the hydrocarbon vapors are more dense than air, leaks were expected to lead to accumulation of hydrocarbons near the floor. At the center of the facility was an exhaust vent (orange and black duct in Figure 3.1) that exhausted up to 2,000 cubic feet per minute from two locations near the bottom of the facility. This prevented any buildup of hydrocarbons in the event of a small leak. Also located below the test fluid loop were two flammable gas sensors that continuously monitor for the presence of flammable gases. The flammable gas sensors had a local and remote alert to

the university Environmental Health and Safety Department. During the course of the present study, the alarms were not set off.

Electrical connections were also a consideration addressed though facility modifications. The pressure sensors, flow meters, and electric motors located within the containment wall were all sealed such that there were no open electrical connections. The controls and pumps not connected to the test fluid were located outside the containment wall. The electrical box can be observed down the left side of the experimental facility in Figure 3.1.

3.1.2 Test Section

Two heat transfer test sections were used as part of the pressure drop and heat transfer experiments conducted in this study: one with a 7.75 mm internal diameter and one with a 14.45 mm internal diameter. The test sections were designed as counter-flow tube-in-tube heat exchangers, shown schematically in Figure 3.3.
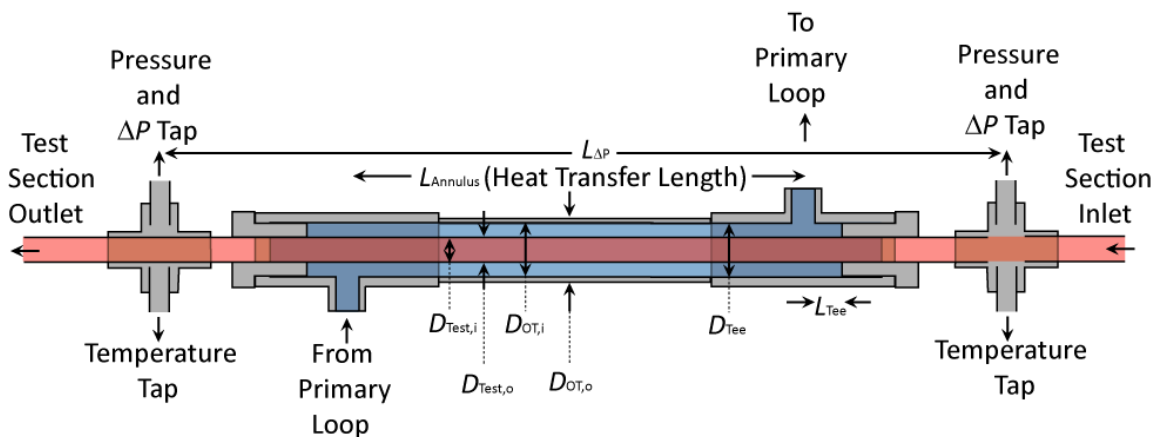
Figure 3.3. Pressure drop and heat transfer test section schematic

A thin walled copper tube with the desired inner diameter was used as the inner tube to maintain a low thermal resistance across the tube wall. The outer tube was sized such

that the annulus formed by the inner and outer tubes results in an annulus-side heat transfer coefficient high enough to present a low thermal resistance relative to the condensation resistance. Dimensions of the two test sections, including end fittings, used in this study are shown in Table 3.6.

Table 3.6. Pressure drop and heat transfer test section dimensions

Heat Transfer Test Sections		Test Section	
Dimension	Variable	7.75 mm	14.45 mm
Test Section Inner Diameter, mm	$D_{Test,i}$	7.75	14.45
Test Section Outer Diameter, mm	$D_{Test,o}$	9.5	15.9
Outer Tube Inner Diameter, mm	$D_{OT,i}$	11.1	17.4
Outer Tube Outer Diameter, mm	$D_{OT,o}$	12.7	19.1
Annulus Length, mm	$L_{Annulus}$	530	530
Differential Pressure Length, mm	L_{DP}	746	746
Tee Length, mm	L_{Tee}	13.2	15.0
Internal Diameter of Tee, mm	D_{Tee}	10.4	16.8

3.1.3 Thermal Amplification Technique

The condensation heat duty in the test section must be obtained while also maintaining the condensation resistance as the dominant thermal resistance. Accurate measurement of test section heat duty was essential to maintain low uncertainties of the heat transfer coefficients. Possible methods to measure the test section heat duty were to infer the heat duty using the coupling fluid temperature rise and flowrate or use the thermal amplification technique. Accurate measurement of the test section heat duty using the coupling fluid temperatures and flowrate requires a large temperature difference, which in turn results in a low annulus flowrate. A low flowrate results in a high thermal resistance on the annulus side. Conversely, maintaining a high coolant flowrate, which presents a low thermal resistance, would result in a high uncertainty in

measured heat duty. The thermal amplification technique, described in detail in Bandhauer *et al*. (2006), decouples the conflicting requirements of measuring heat transfer rate and heat transfer coefficient. Referring to Figure 3.4, this technique involves removing the heat of condensation by a primary coolant at a high flowrate; the high flowrate coolant poses a low thermal resistance, enabling accurate deduction of the condensation heat transfer resistance from the measured overall test section heat transfer resistance. The high flowrate through the test section annulus results in only a small temperature rise in the coolant. Therefore, a secondary cooling fluid at a much lower thermal capacitance rate was used to exchange heat with the primary coolant. This lower flowrate coolant results in an accurately measurable temperature rise in the secondary coolant. Dimensions of the primary loop are summarized in Table 3.7.
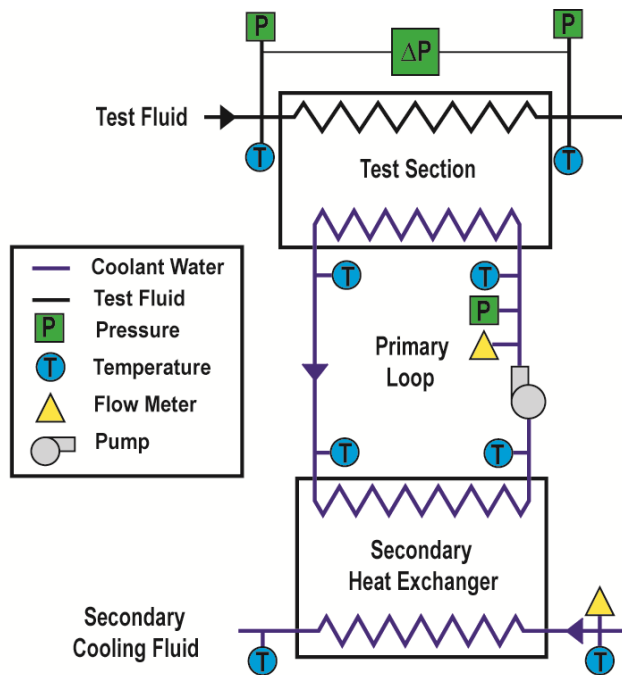
Figure 3.4. Thermal amplification technique schematic

The water in the primary loop was circulated using a positive displacement pump (Micro Pump Model 5000.750/50C, Serial #365623). A magnetic flow meter (Rosemount

139

8705 Serial #0870119434; ±0.5% reading) was used to measure the volumetric flowrate. The primary loop pressure was measured using an absolute pressure transducer (Rosemount 2088 Serial #138874; ±5.5 kPa). The differential pressure across the pump, which is equal to the pressure drop through the primary loop, was measured using a differential pressure transducer (Rosemount 3051CD Serial #2251309; ±0.065%). Four temperature measurements were made in the primary loop at the inlets and outlets of the test section and the secondary loop heat exchanger. The primary loop was coupled to the secondary loop using a shell-and-tube heat exchanger (Exergy Model #00540-06 Serial #33560). The measured secondary loop water temperature and mass flowrate (measured using a Coriolis flow meter (Micro Motion DS006S100SU Serial #0205104; ±0.15% of reading) were used to calculate the secondary loop heat duty. The secondary loop water flowrate was controlled by controlling the pump speed (Micropump 74011-21 Serial # 912334 (0 – 10 L min^{-1})).

Table 3.7. Primary loop dimensions

Dimension	Variable	Length
Actual Primary Loop Length	$L_{Pri,Actual}$	2.94
Equivalent Primary Length for Heat Transfer	$L_{Pri, Effective}$	5.70
Primary Loop Plumbing Inner Diameter	$D_{Pri,i}$	10.2
Primary Loop Plumbing Outer Diameter	$D_{prim,o}$	12.7

3.1.4 Zeotropic Mixture Concentration Measurement

An in-line gas chromatograph (Shimadzu Scientific GC-2014 DualPac TCD no D/S, Part # 220-94624-00, Serial #C11484939600, ±0.0023 concentration) was used to measure the bulk concentration of the mixture prior to taking each data point. Helium was used as the carrier gas because the thermal conductivity of helium is significantly

different from that of R245fa and *n*-pentane. For example, at a pressure of 101 kPa and temperature of 100°C, the thermal conductivity of helium is 0.181 W m^{-1} K^{-1}, while the thermal conductivities of R245fa and *n*-pentane are 0.019 and 0.022 W m^{-1} K^{-1}, respectively. The thermal conductivity of nitrogen, another carrier gas option, is 0.031 W m^{-1} K^{-1}. The greater the difference in thermal conductivity between the carrier gas and the test fluid, the more sensitive the thermal conductivity detector becomes to the measured fluid, resulting in increased accuracy.
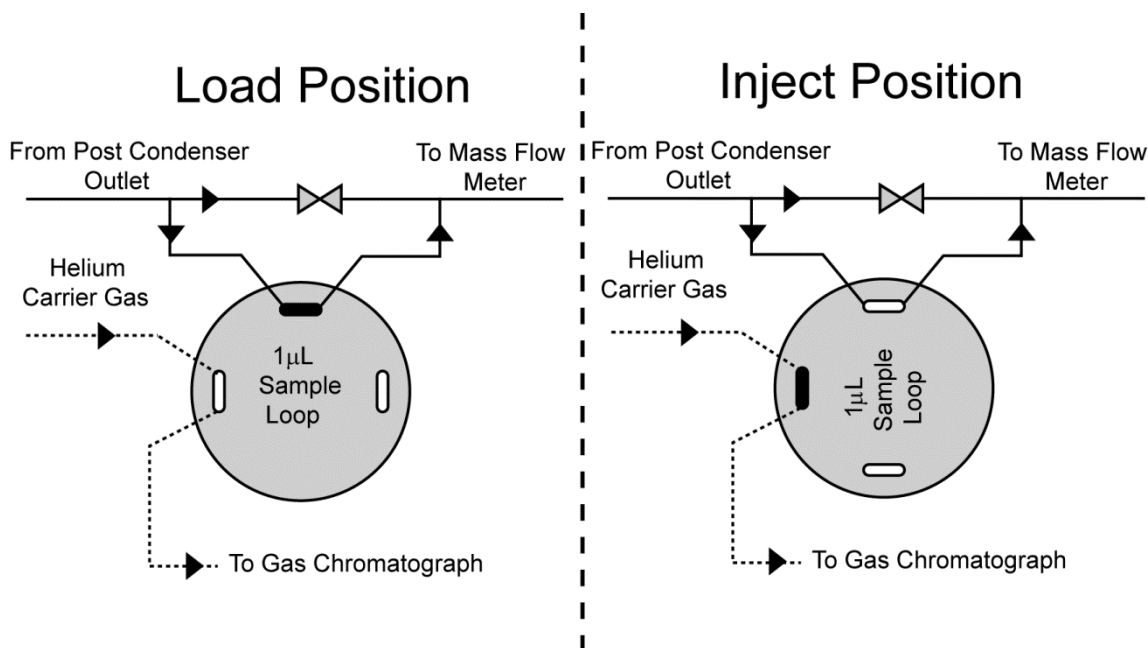
Figure 3.5. Gas chromatograph liquid sample loop schematic

A wide-bore capillary column (ResTek Rt-Alumina BOND/CFC; 30 m, 0.53 mm internal diameter, df = 10 µm; Serial # 962866) was used to separate the R245fa from *n*-pentane. An electrically actuated liquid sampling valve (Valco ED4CI4UWE1/2 Serial #11S-1052V) with a 1 µL sampling loop was used to draw the bulk liquid sample from the system during operation with negligible disturbance to the steady state. The plumbing and valve configuration in the load and inject positions are shown schematically in Figure

3.5. The thermal conductivity detector response was recorded and analyzed using Shimadzu LabSolutions Version 5.42 SP1 (Part #223-07822-91). The nominal temperature, pressure, and flowrate set points of the gas chromatograph are provided in Table 3.8. The uncertainty of the gas chromatograph at these conditions was conservatively estimated to be 2% of the measured mass of each fluid, resulting in a concentration uncertainty at the nominal concentration of 45 ± 0.9% and 55 ± 1.1% for R245fa and n-pentane, respectively. A summary of the gas chromatograph calibration is provided in Appendix A.

Table 3.8. Gas chromatograph configuration

Gas Chromatograph Configuration	
Temperatures	
Liquid sampling valve, °C	26
Injector, °C	120
Column, °C	150
Pre-heater, °C	155
TCD, °C	155
Pressures	
Carrier gas inlet, kPa	730
Right make-up gas, kPa	127
TCD reference, kPa	157
Flow rates	
Left carrier gas, mL min^{-1}	0
Right carrier gas, mL min^{-1}	15

3.1.5 Test Matrix

The test matrix for the pressure drop and heat transfer portion of this study is shown in Table 3.9. As described in Chapter 1, the ability to recover low-temperature energy from waste heat or geothermal sources for the production of electricity is the motivation for including zeotropic mixtures as part of the present study. As such, the test matrix was identified based on condenser conditions relevant to grid-scale geothermal power

generation applications. The selection of an optimum design condition including condenser orientation, tube diameter, fluid concentration, and mass flux was conducted by United Technologies Research Center. The test matrix for this study was developed to provide a range of conditions around the design point. The *n*-pentane portion of the test matrix was defined by conditions relevant to the process industry: saturation temperatures of 45 and 60°C, and mass fluxes up to 450 kg m^{-2} s^{-1}. Due to facility limitations caused by the low absolute pressure of *n*-pentane, the test matrix for the 14.45 mm tube was extended to an additional saturation condition and lower mass flux. The R245fa test matrix and *n*-pentane 600 kg m^{-2} s^{-1} mass flux in the 7.75 mm internal diameter tube were added to facilitate comparison with the zeotropic mixture results.

Table 3.9. Pressure drop and heat transfer test matrix

		R245fa/*n* -pentane Mixture			Pure R245fa			Pure *n* -pentane				
	D, mm	7.75			7.75			7.75		14.45		
	T$_{Sat}$, °C	30*	55*	80*	20	45	70	45	60	45	60	75
Mass Flux, kg m^{-2} s^{-1}	75									■	■	
	150	■	■	■	■	■	■	■	■	■	■	■
	300	■	■	■	■	■	■	■	■	■	■	■
	450/500	■	■	■	■	■	■	■	■			■
	600	■	■	■	■	■	■	■	■			
* Indicates Bubble point temperature												

3.2 High-Speed Video Experiments

The test facility, camera setup, and test section details for the flow visualization experiments are described in this section. The flow visualization test matrix follows that description.

3.2.1 Test Facility

The modified experimental facility used for the visualization portion of the present study is shown in Figure 3.6. Comparing the visualization experimental setup to the pressure drop and heat transfer test facility, described in Section 3.1, facility modifications to accommodate the visualization test section occurred only between state points [2] and [3]. The heat transfer test section, primary loop, and secondary loop used in the pressure drop and heat transfer experimental facility were replaced by a visualization test section, lighting, and a high-speed camera. The test fluid, steam, and pre- and post-condenser configurations remained unchanged. In addition to the visualization test section, a test section by-pass between [2] and [3] was installed with three pneumatic isolation valves: one valve was used to close the by-pass and the remaining two were at the inlet and outlet of the test section. The valves were set to default with flow through the by-pass and isolation of the test section.
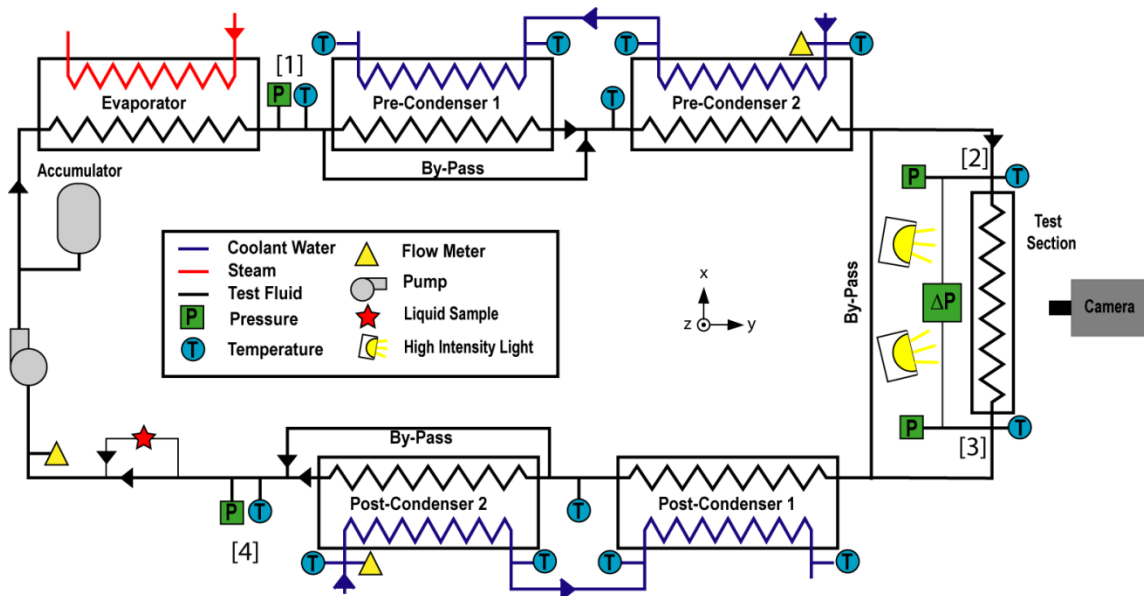
Figure 3.6. Flow visualization test facility schematic

144

3.2.2 High-Speed Video Camera Setup

The high-speed visualization test section configuration is shown from a side view and the camera view in Figure 3.7. A high-speed video camera (Photron FASTCAM SA4 Serial # 364435125 with Nikon Micro-NIKKOR 105 mm f/2.8 Serial # 224551) was aligned perpendicularly to the flow direction and vertically level with the visualization test section as shown in the side view. The test section was back-lit using two high intensity lights (Lowel OMNI Lights 500W). To produce two-phase flow images with distinguishable vapor-liquid interfaces, the lights were positioned such that the light was incident at a slight vertical angle relative to the camera location, as shown in the schematic. A light box with white interior was used to surround the test section on the top and two sides. An additional barrier that separated the camera from the light sources was used to prevent light from directly entering the camera lens, as shown in the camera view of Figure 3.7. In combination with the light box, a light diffusion screen was placed behind the test section to increase the diffusion of the light and provide a uniform background in the images. The high-speed video camera was connected using an Ethernet cable to the data acquisition computer. The Photron FASTCAM viewer software (version 3.2.8.0) recorded the video and allowed control of shutter speed, frame rate, image resolution, and exported the captured video to a file.

Viewing was only conducted using the horizontal viewing angle in the present study. Several complexities limited the ability to obtain multiple viewing angles. First, the position of the light box, such that high quality images could be obtained from the horizontal view, obstructed the ability to obtain simultaneous images from multiple angles. Second, because the present study had multiple parts, including heat transfer and visualization, the ability to change between test facilities and back again was very

important. Experimental instrumentation, including pressure transducers and a portion of the thermal amplification technique, as well as a portion of the exhaust system, would have to be permanently removed to accommodate recording video from the vertical angle. Furthermore, the entire visualization test matrix would have had to be repeated. As such, obtaining a second angle was beyond the scope of the present study.
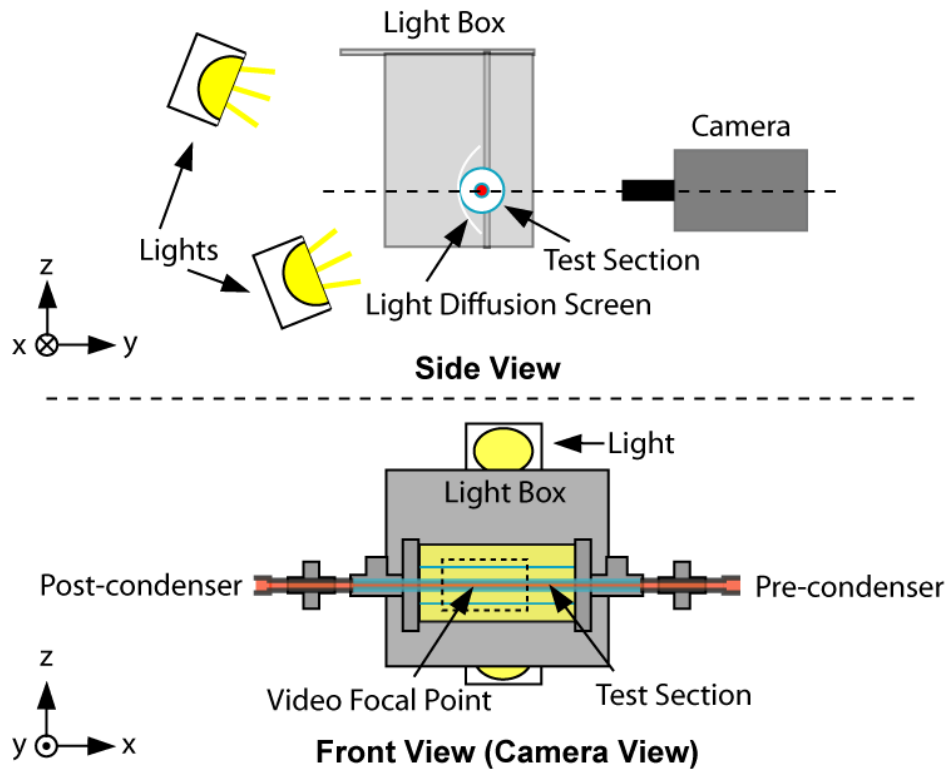
Figure 3.7. Flow visualization lighting setup

3.2.3 Test Section

Two test sections were used for visualization, one with an internal diameter of 7.0 mm and the second with an internal diameter of 15.0 mm. The 7.0 and 15.0 mm test sections, shown schematically in Figures 3.8 and 3.9, were constructed using a fused quartz glass inner tube (Technical Glass Products D_i = 7 and D_o = 10.4 and D_i = 15 and D_o = 18) epoxied using Devcon 2 Ton® Epoxy into stainless steel Swagelok fittings at

146

either end as shown in Figure 3.10. A Teflon spacer was used to align the glass tube within the inlet tube. Surrounding the inner tube was a round outer pressure chamber (Pressure Products ¾-inch and 1-inch Full-View sight flow indicator). The annulus between the inner tube and the outer pressure chamber was pressurized to reduce the differential pressure across the inner tube wall. This allowed higher pressures to be achieved inside the inner tube. The smaller 7.0 mm internal diameter test section was pressurized using nitrogen to approximately 550 kPa. The larger 15.0 mm internal diameter test section was filled with water and pressurized to 550 kPa. The water was necessary to produce a distinguishable inner and outer tube wall during the visualization. An emergency vent, consisting of a pressure relief valve and analog pressure gage, was used to ensure safety. The pressure relief valve was set at approximately 800 kPa. The relief side of the valve was vented to the exterior of the building. Because of the safety precautions and pressure requirements in the outer chamber, no active cooling was provided to the test section. A summary of the test section dimensions is provided in Table 3.10. A calibration procedure was used to account for any potential distortion effects due to the use of round tubes and round outer annuli. A description of the calibration procedure is provided in Appendix B. Additionally, as described in the data analysis section (Chapter 4), the video frames were analyzed compared to a static, liquid filled tube image. The combination of these two procedures ensured the validity of this approach for flow visualization.

Table 3.10. Flow visualization test section dimensions

Flow Visualization Test Sections		Test Section	
Dimension	Variable	7.0 mm	15.0 mm
Test Section Inner Diameter, mm	$D_{Test,i}$	7.0	15.0
Test Section Outer Diameter, mm	$D_{Test,o}$	10.4	18.0
Outer Tube Inner Diameter, mm	$D_{OT,i}$	35.6	41.2
Outer Tube Outer Diameter, mm	$D_{OT,o}$	44.5	50.8
Glass Tube Length, mm	L_{glass}	510	610
Differential Pressure Length, mm	$L_{\Delta P}$	610	622
Inlet Length, mm	$L_{Test,Inlet}$	115	114
Outlet Length, mm	$L_{test,Outlet}$	95	114
Inlet Diameter, mm	D_1	7.75	14.45
Outlet Diameter, mm	D_2	7.75	14.45
Loop Diameter at Test Section Inlet, mm	D_{Loop}	10.9	10.9
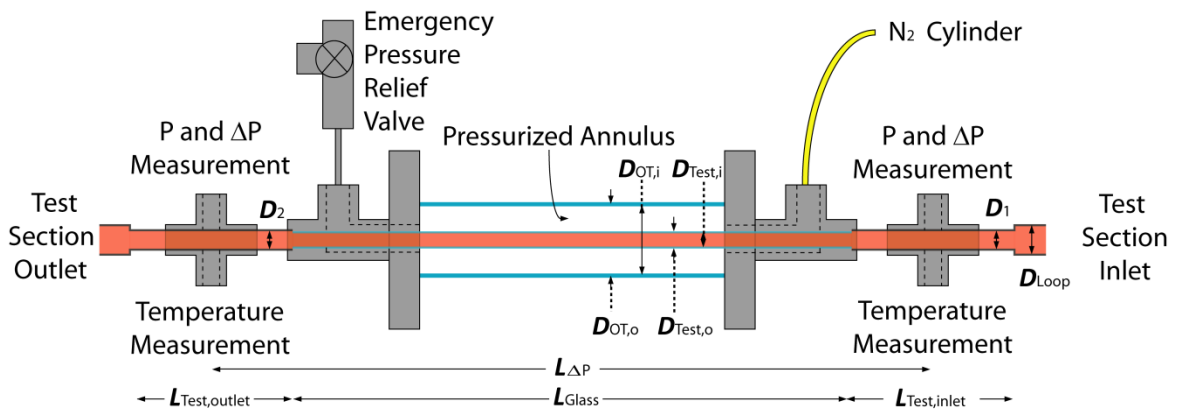
Figure 3.8. Flow visualization test section schematic

148
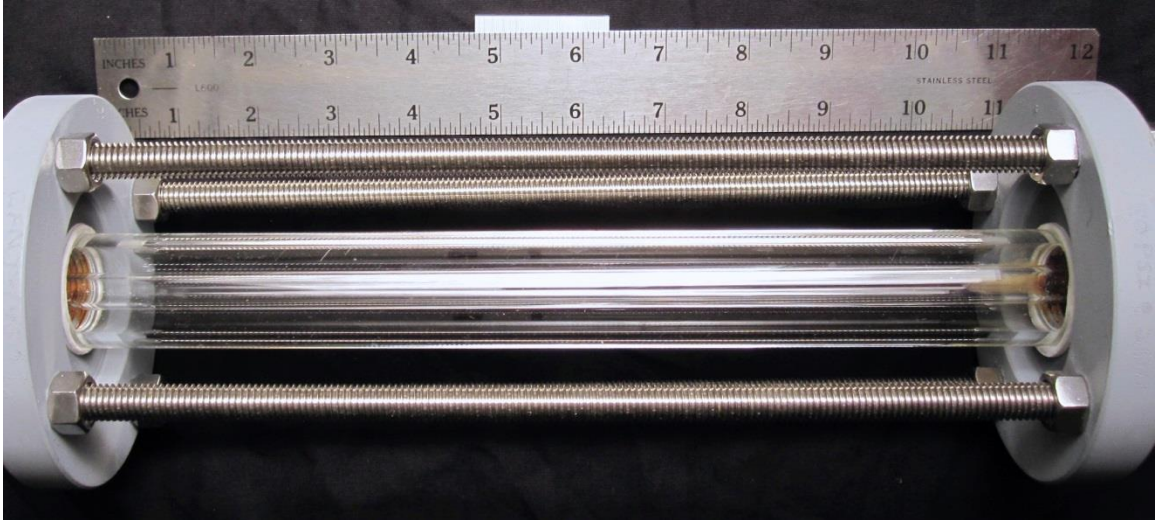
Figure 3.9. Flow visualization test section photograph
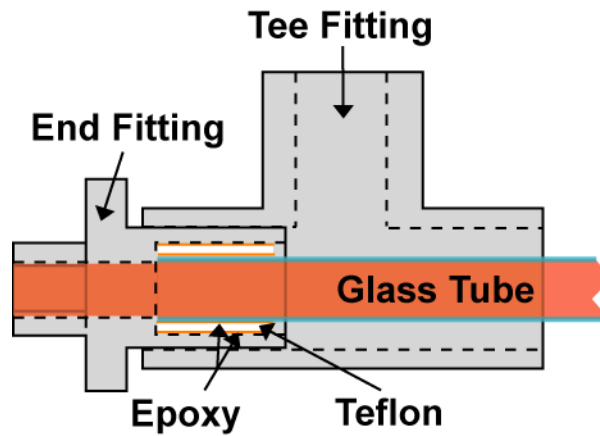
Figure 3.10. Flow visualization test section end connection schematic

3.2.4 Test Matrix

A set of conditions similar to those used for the condensation pressure drop and heat transfer experiments was considered for the visualization portion of the present study. The conditions investigated in the present study are summarized in Table 3.11.

Table 3.11. Flow visualization test matrix

		Propane Visualization			
	D, mm	7.0		15.0	
	$T_{sat,}$ °C	25	35	25	35
Mass Flux, kg $m^{-2} s^{-1}$	75	■	■	■	■
	150	■	■	■	■
	300	■	■	■	■
	450	■	■		

3.3 Test Procedures

The experimental procedures used to prepare the system for testing and conduct the experiments are described in this section. The procedures for the condensation pressure drop and heat transfer experiments, as well as the flow visualization, are similar for the entire test matrix, and the differences in the procedure are noted.

3.3.1 Leak Checking

Once the desired test section was installed in the test loop, the test fluid loop was pressurized to 1,700 kPa using nitrogen. If necessary, the span on the pressure transducers was increased for this process. A pressure of 1,400 kPa was used for the visualization test sections due to limitations of the glass test section. With the system pressurized, leaks were initially located using soapy water. With most leaks identified, the system was filled with R404A and further pressurized with nitrogen, again to 1,700 kPa or 1,400 kPa as appropriate, and slow leaks were identified using a refrigerant leak detector (Yellow Jacket AccuProbe® Leak Detector with heated sensor Model: 686800-69365) capable of detecting HFC leaks down to 1.7 g yr^{-1}. The system was then monitored for a minimum of 8 hours to verify that the system was sealed.

3.3.2 Charging the Experimental Loop

The procedure used to charge the experimental facility with the test fluid is detailed in this section. The procedure for charging pure components differs slightly from the procedure to charge multi-component fluids.

3.3.2.1 Charging the Loop with Pure-Component Fluids

Once the loop was verified to be leak free, the test loop was opened to atmosphere and evacuated using a vacuum pump (JB Industries INC. Platinum series Serial #0610). The charging port had three interconnected ports. The first was connected to the fluid cylinder, which was placed inverted on a scale (Wey-Tek Refrigerant Charging Scale 100 kg) to ensure that the liquid phase was drawn from the tank. The vacuum pump was connected to the second port, and the vacuum gage was connected to the third port. The vacuum pump was allowed to run until a vacuum below 300 microns was achieved and verified using a vacuum gage (Thermal Engineering Co. Model #14571 Serial #TR2573). Isolating the vacuum pump and vacuum gauge, the liquid valve on the fluid cylinder was opened and the charging lines filling with liquid while the test loop remained at a vacuum. The tare function on the scale was then used to set the reading to zero. The mass charged into the system was calculated using the liquid phase density, an estimate of the volume of the main fluid loop (0.00155 m^3), and a portion of the 1.5 L of the liquid storage tanks (0.7 L or 0.0007 m^3). For example, the mass of propane charged was calculated using a total system volume of 0.00225 m^3 and liquid phase density at 20°C of 500.1 kg m^{-3} to be 1.13 kg.

In some cases, the coupling fluid loops were used to provide cooling to the main fluid loop, which would draw additional fluid from the cylinder to the main fluid loop. Once

the desired mass was charged into the test loop, the fluid cylinder and charging line isolation valve were closed and the cylinder removed.

3.3.2.2   *Charging the Loop with Zeotropic Mixtures*

The procedure for charging multi-component fluids was nearly identical to the procedure for charging a pure component, outlined in the previous section. The main difference was the two components were charged to the system individually from different cylinders. This required pre-calculating the required mass of each component to achieve the desired bulk concentration once mixed in the system. The lower pressure fluid (*n*-pentane) was charged first using a procedure identical to that used for the pure fluid. After the desired mass of the first component was charged, the system was cooled and the first cylinder was disconnected. The second fluid cylinder was connected and connecting lines were evacuated before the desired mass of the second fluid was added. Unlike the pure fluid, the two fluids needed to be well mixed to provide assurance that the circulating fluid was near the nominal concentration. To achieve mixing, the system was started and shut down approximately five times to cycle fluid into and out of the storage cylinders. The system was then allowed to sit overnight with all internal isolation valves open to allow additional mixing by diffusion. With the system running, the gas chromatograph was used to verify the bulk concentration. If necessary, the concentration was adjusted slightly by adding additional mass of the needed component.

3.3.3   Pressure Control

Pressure control was achieved by controlling fluid inventory in the main fluid loop and cooling rates provided in the pre- and post- condensers. Material compatibility issues prevented the use of the bladder accumulator used previously by Keinath and Garimella (2010). To maintain a sealed system for safety considerations, stainless steel cylinders

were selected to store excess fluid. Two liquid storage cylinders (1.0 L and 0.5 L), shown in Figures 3.11 and 3.12, were used to store excess liquid to achieve the desired test section quality. Liquid was removed from the test fluid loop through a throttling valve. Isolation valves on each cylinder as well as in parallel with the throttling valve were used for startup and shutdown. The 0.5 L cylinder was opened at startup to allow excess liquid to be stored when the steam was turned on. The capacity of 0.5 L capacity prevented the system from over shooting the desired quality during startup. Pre- and post-condenser flowrates were adjusted to achieve the desired operating pressure. Upon reaching the desired test section quality, as verified using a short 30 second data point, the main fluid loop was completely isolated from the cylinders and allowed to come to steady state. At low qualities, the pre-condenser was primarily used to control pressure, while the post-condenser flowrate was varied to improve experimental uncertainty of the outlet quality. At high qualities, the post-condenser was primarily used for pressure control, while the pre-condenser was used for fine control of test section inlet quality.
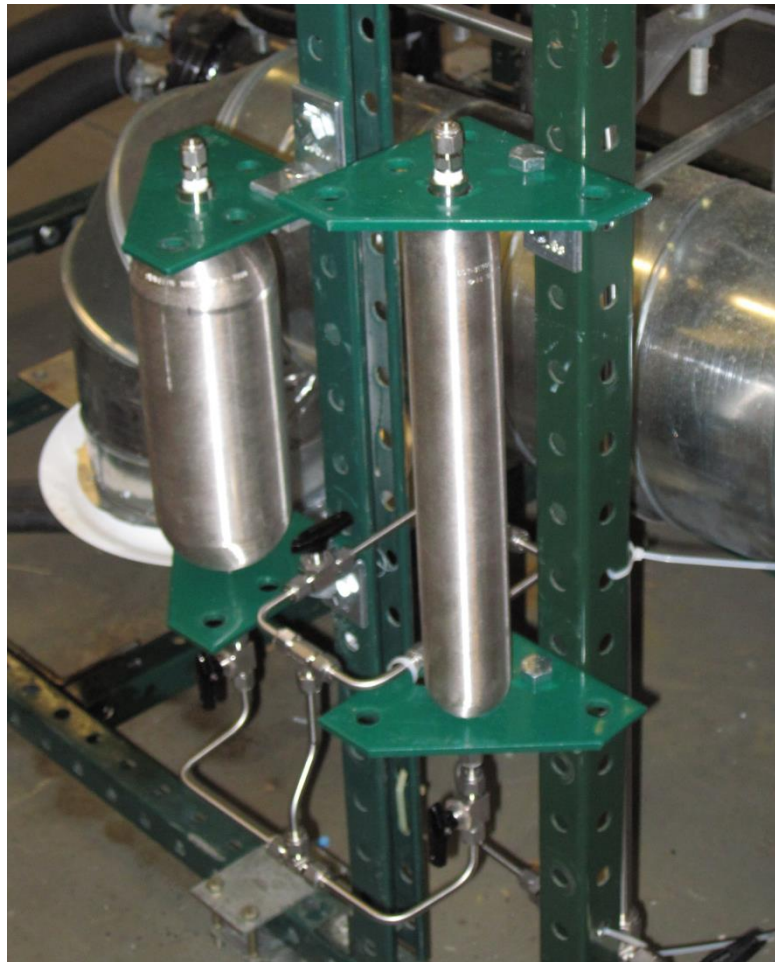
Figure 3.11. Pressure control liquid storage cylinders photograph
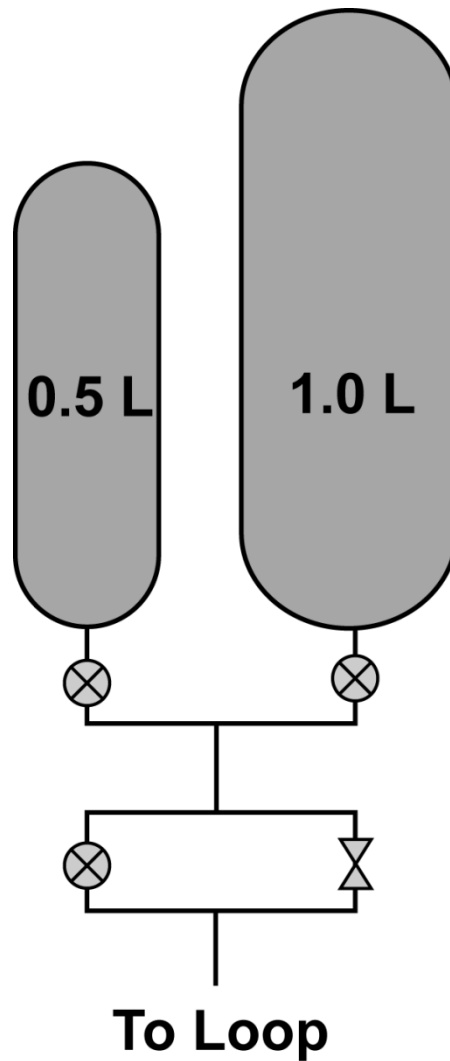
Figure 3.12. Pressure control liquid storage cylinders schematic

3.3.4 <u>System Startup and Shutdown</u>

To start the system, the lab chiller was turned on and allowed to reach the desired set

point. The facility cooling pumps were turned on with the flowrates of the pre- and post-

condensers set high to provide maximum cooling. The main fluid loop pump was turned

on and the test fluid was circulated and cooled at a mass flux of approximately 100 kg m⁻

^{2} s^{-1}. The isolation valve on the smaller of the two liquid storage cylinders was opened,

while the larger cylinder valve remained closed. The steam was turned on to a low

pressure, approximately 110 kPa or 102°C. This sudden addition of heating caused a

spike in system pressure pushing excess liquid into the storage cylinder. The high cooling rates in the pre- and post-condenser, as well as limited volume of the smaller cylinder, limited the amount of liquid removed from the main fluid loop. This ensured that low quality points at the test section could still be obtained. Once the system stabilized, data collection began.

At the completion of the data set, the system contained the largest amount of vapor than at any point during the test run. To shut down the system, liquid was drawn back into the loop by reducing the system pressure below the saturation pressure of the test fluid at ambient temperature. Ensuring that the by-pass was open and test section was closed for the flow visualization tests, the cooling of the post-condenser was increased to the maximum flowrate and the main fluid loop flowrate was decreased. Once the system pressure was decreased sufficiently, the cylinders were opened. The pre-condenser cooling was slowly increased, as increasing the flowrate too quickly caused vapor to enter the pump. The test section inlet temperature was observed until a subcooled liquid condition was achieved at this point. The pre-condenser flowrate was further increased and the steam was turned off.

3.3.5 Data Point Transition, Stability, and Capture

Once the system was started, the throttling valve on the storage cylinder was opened slightly in small increments to let fluid into the liquid cylinders. Simultaneously, the pre-condenser flowrate was decreased until a quality of 0.1 at the desired pressure was obtained in the test section. Short 15 to 30 second data samples were used to determine when this condition was met. The LabView® interface contained several continuous plots of the temperature, pressure, and flowrate measurements with a five minute history.

Visual observation of the temperature, pressure, and flowrate plots were indicative of a steady-state condition. This typically occurred within 2 to 20 minutes of reaching the desired point, depending on the specific operating conditions. Following the recording of the data point, a qualitative assessment of the data point quality was made using a comparison of the evaporator duty, calculated using the subcooled and superheated states, to the sum of the test loop heat exchanger duties. A difference of less than 2% was considered acceptable. Each data point was captured at three samples per second over a five minute (360 second) period. The file was named with the test identifying information including date, nominal flowrate, nominal pressure, and data point number. If fluctuation in the temperature, pressure or flowrate plots occurred during the data collection or the energy balance was significantly off, the data collection procedure was repeated. The final data point was then averaged over the data run and analyzed in EES.

3.3.6 <u>Zeotropic Mixture Concentration Measurements</u>

For mixture experiments, the bulk concentration was measured immediately prior to the initiation of the data collection. Within the LabSolutions® software, the electronic liquid sample valve, shown in Figure 3.5, was switched to inject the liquid sample onto the column. The software then recorded the readout from the TCD detector and converted the TCD response to a sample concentration based on the calibration shown in Appendix A. A run time of three and a half minutes was required for the sample to be completely processed. The processing for the concentration sample and the recording of the temperature, pressure, and flowrate measurements occurred simultaneously. To verify the stability of the system concentration, twenty six consecutive concentration measurements were taken with the experimental facility running at steady state, over the course of

several hours. The resulting concentration measurements were stable, with an average

difference from the first measurement of 0.225%, and a maximum difference of 0.229%.

3.3.7 <u>High-Speed Video Recording</u>

Once the data collection process was initiated, the high-speed video was recorded.

The high intensity lights were turned on and good video quality was visually confirmed

using the live output on the FASTCAM Viewer software. A single four to eight second

8-bit grayscale video was recorded at a resolution of 1024 by 512 pixels, a frame rate of

1000 frames per second, a shutter speed of 1/25,000 second, and the lens aperture set at

5.6. Two videos were saved into AVI format for each data point from the original

recording, a one-second video at 1000 fps, and a four-second video at 333 fps by saving

every third captured frame over four seconds. The second video increased duration of the

video, while limiting disk space requirements. Both AVI files were opened and verified

to be of good quality prior to transitioning to the next data point.

CHAPTER 4. DATA ANALYSIS

Calculation of heat transfer coefficients, frictional pressure gradients, and their respective uncertainties from experimental measurements is presented in this section. Calculations were conducted using Engineering Equation Solver (EES) (Klein, 2011). Fluid properties including those of pure fluid, mixture, water, and ambient air properties were calculated using REFPROP Version 9.1 (Lemmon *et al.*, 2013). Metal properties were calculated using EES (Klein, 2011). Uncertainty analyses were conducted using the EES uncertainty propagation function, (Equation (4.1)), which assumes that individual measurements are uncorrelated and random (Taylor and Kuyatt, 1994).

$$U_y = \sqrt{\sum_i \left(\frac{\partial Y}{\partial X_i} \right)^2 U_{X_i}^2} \tag{4.1}$$

The frictional pressure gradient and heat transfer coefficient and their uncertainties for pure component and binary mixtures were calculated using similar approaches. The mixture analysis required the concentration and concentration uncertainty in addition to the two independent properties from the pure fluid analysis. For clarity, analysis of a representative mixture data point for the case of 45% R245fa / 55% *n*-pentane by mass, $G = 507.4$ kg m^{-2} s^{-1}, $P_{AVG} = 405.9$ kPa and $q_{AVG} = 0.39$ is presented here. Details of the uncertainty propagation analysis are shown in Appendix D.

4.1 In-Tube Condensation Analysis

The analysis detailed in this section presents the evaluation of the test section inlet and outlet conditions using values for a representative data point. Additional details of the calculations are provided in Appendix D.

4.1.1 Average Test Section Quality

Measured temperatures and pressures of the mixture and coupling fluids are reported in Tables 4.1 and 4.2. Referring to the test facility schematic, reproduced in Figure 4.1, superheated vapor exits the evaporator and enters the pre-condenser at [1]. In the representative case under consideration here, smaller heat transfer areas were necessary to achieve the desired inlet conditions. Thus, pre-condenser 1 was by-passed and the superheated vapor entered pre-condenser 2. The superheated state was verified by calculating the dew point temperature at the pre-condenser inlet pressure compared to the measured temperature:

$$T_{\text{f,Pre,in,Dew}} = f\left(449.4\,\text{kPa}, q=1\right) = 74.3°\text{C}$$
$$\Delta T_{\text{f,Pre,in,Sup}} = 103.7°\text{C} - 73.12°\text{C} = 29.4 \pm 0.7°\text{C}$$
(4.2)

After verifying that the fluid was sufficiently superheated at the inlet of the pre-condenser, the inlet mixture enthalpy was calculated using the measured temperature, measured pressure, and bulk concentration:

$$
\begin{aligned}
i_{\text{f,Pre,in}} &= f\left(P_{\text{f,Pre,in}}, T_{\text{f,Pre,in}}, x_{\text{R245fa}}\right) \\
&= f\left(449.4\,\text{kPa}, 103.7°\text{C}, 0.454\right) \\
&= 484.4 \pm 0.5\,\text{kJ}\,\text{kg}^{-1}
\end{aligned}
$$
(4.3)

The enthalpies of the coolant water of the pre-condenser and post-condenser were calculated using the respective inlet and outlet temperatures and a measured coolant loop pressure of 225.2 ± 2.4 kPa. The pre- and post- condenser flowrates were calculated using the water densities at the inlet temperatures of the respective streams and the coolant loop pressure. The resulting enthalpies and mass flowrates are summarized in Table 4.3. The pre-condenser heat duty was calculated using the water-side parameters:

$$\dot{Q}_{Pre} = \dot{m}_{w,Pre}\left(i_{w,Pre,out} - i_{w,Pre,in}\right) + \dot{Q}_{loss,Pre}$$

$$= 0.0187\,\text{kg s}^{-1}\left(316.2\,\text{kJ kg}^{-1} - 31.0\,\text{kJ kg}^{-1}\right) + 2.0\,\text{W} \qquad (4.4)$$

$$= 5248 \pm 51\,\text{W}$$
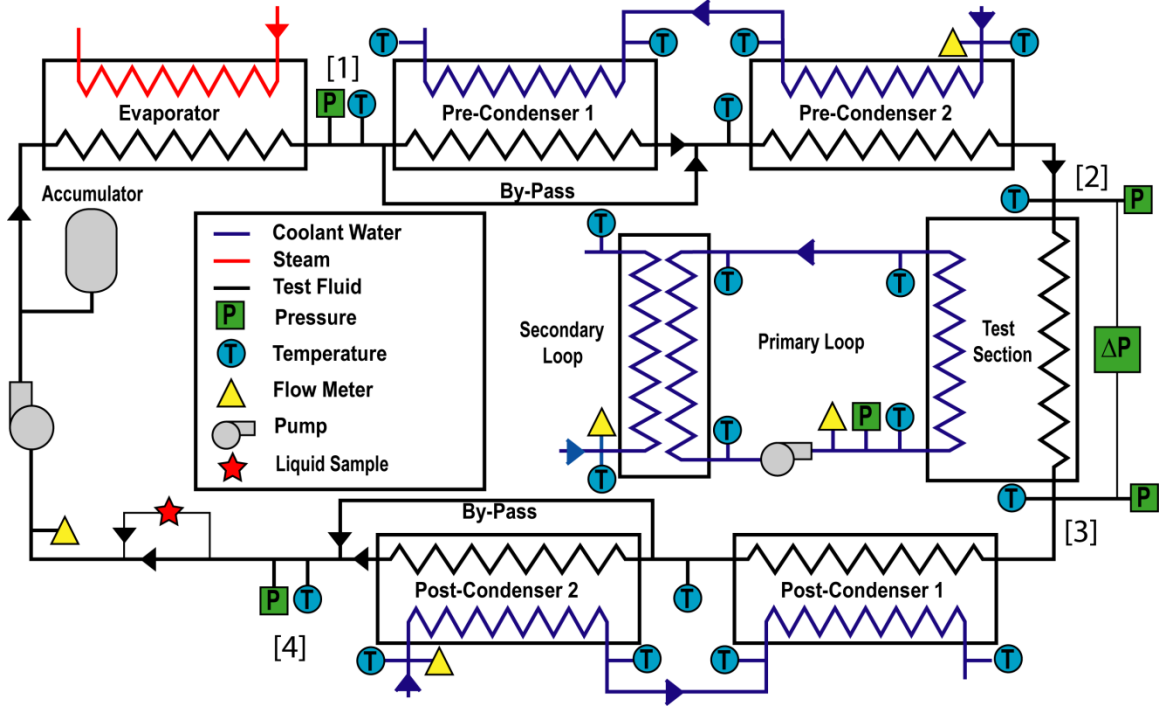
Figure 4.1. Test facility schematic

The ambient loss calculation is presented in the following section with details of each loss calculation shown in Appendix E. Using the inlet state of the mixture at the pre-condenser and the pre-condenser heat duty, the test section inlet, [2], enthalpy was calculated as follows:

$$i_{f,Test,in} = i_{f,Pre,in} - \frac{\dot{Q}_{Pre}}{\dot{m}_f} - \frac{\dot{Q}_{loss,Pre\,to\,Test}}{\dot{m}_f}$$

$$= 484.5\,\text{kJ kg}^{-1} - \frac{5248\,\text{W}}{0.0239\,\text{kg s}^{-1}} - \frac{2.7\,\text{W}}{0.0239\,\text{kg s}^{-1}} \qquad (4.5)$$

$$= 265 \pm 2.2\,\text{kJ kg}^{-1}$$

The test section inlet quality was calculated using the calculated enthalpy, measured pressure, and bulk concentration:

$$q_{f,\text{Test,in}} = f\left(i_{f,\text{Test,in}}, P_{f,\text{Test,in}}, x_{\text{R245fa}}\right)$$
$$= f\left(265\,\text{kJ kg}^{-1}, 411.2\,\text{kPa}, 0.454\right) \quad (4.6)$$
$$= 0.442 \pm 0.01$$

Similar to the above analysis, the subcooled mixture state at the post-condenser outlet, [4], and post-condenser energy balances were used to calculate the test section outlet quality, [3]. For the representative data point here, the outlet quality was calculated to be 0.346 ± 0.01. The average test section quality was calculated using the inlet and outlet qualities obtained from the pre- and post-condenser energy balances:

$$q_{f,\text{Test,Avg}} = \frac{\left(q_{f,\text{Test,in}} + q_{f,\text{Test,out}}\right)}{2} = \frac{\left(0.442 + 0.346\right)}{2} = 0.394 \pm 0.007 \quad (4.7)$$

The corresponding test section average pressure and enthalpy were calculated to be 405.9 ± 3.7 kPa and 252.0 ± 2.2 kJ kg^{-1}, respectively.

Table 4.1. Representative data point fluid-side conditions

		Temperature		Pressure	
		Symbol	°C	Symbol	kPa
Pre-Condenser	**Inlet**	$T_{f,\text{Pre,in}}$	103.7 ± 0.3	$P_{f,\text{Pre,in}}$	449.4 ± 5.17
	Outlet	$T_{f,\text{Pre,out}}$	60.8 ± 0.3	$P_{f,\text{Test,in}}$	411.2 ± 5.17
Test Section	**Inlet**	$T_{f,\text{Test,in,meas}}$	59.5 ± 0.3		
	Outlet	$T_{f,\text{Test,out,meas}}$	57.2 ± 0.3	$P_{f,\text{Test,out}}$	400.6 ± 5.17
Post-Condenser	**Inlet**	$T_{f,\text{Post,in}}$	56.1 ± 0.3		
	Outlet	$T_{f,\text{Post,out}}$	12.7 ± 0.3	$P_{f,\text{Post,out}}$	392.7 ± 5.17

Table 4.2. Representative data point water-side conditions

		Temperature		Flowrates	
		Symbol	°C	Symbol	L min^{-1}
Pre-Condenser	**Inlet**	$T_{w,Pre,in}$	8.6 ± 0.3	$\dot{V}_{w,Pre}$	$1.13 \pm$
	Outlet	$T_{w,Pre,out}$	75.5 ± 0.3		0.01
Post-Condenser	**Inlet**	$T_{w,Post,in}$	7.3 ± 0.3	$\dot{V}_{w,Post}$	$1.60 \pm$
	Outlet	$T_{w,Post,out}$	40.2 ± 0.3		0.01

Table 4.3. Representative data point water-side enthalpies and flowrates

		Enthalpy		Mass Flowrate	
		Symbol	kJ kg^{-1}	Symbol	kg s^{-1}
Pre-Condenser	**Inlet**	$i_{w,Pre,in}$	36.3 ± 1.3	$\dot{m}_{w,Pre}$	$0.0187 \pm$
	Outlet	$i_{w,Pre,out}$	316.2 ± 1.3		0.0001
Post-Condenser	**Inlet**	$i_{w,Post,in}$	31.0 ± 1.3	$\dot{m}_{w,Post}$	$0.0266 \pm$
	Outlet	$i_{w,Post,out}$	168.5 ± 1.3		0.0002

4.1.2 <u>Heat Losses to Ambient</u>

To minimize ambient losses, low thermal conductivity insulation (0.04 W m^{-1} K^{-1}) was used to wrap the entire experimental facility, including pure fluid, mixture, and coolant lines. For this representative ambient loss calculation, the resistance network is shown schematically in Figure 4.2. The ambient losses were calculated between the average internal fluid temperature of the segment (in this case the average pre-condenser coolant water temperature) through the wall and insulation layer and to the ambient by radiation and natural convection. The fluid-side resistance, identified in the schematic as R_f, was assumed to be small relative to the other thermal resistances and was neglected.
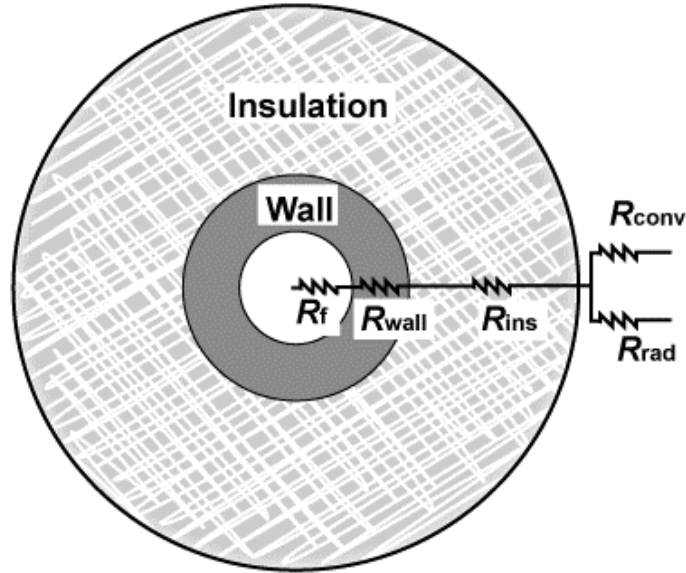
Figure 4.2. Ambient loss resistance network schematic

A representative ambient loss calculation is presented here for the ambient losses in the pre-condenser; additional details and the remaining ambient loss calculations are presented in Appendix E. An uncertainty of 50% was applied to each net heat loss term. The internal wall temperature was assumed to be equal to the average of the pre-condenser coolant temperatures identified in Table 4.2, or 42.0°C. The thermal resistance across the outer shell of the pre-condenser heat exchanger was calculated as follows:

$$
\begin{aligned}
R_{\text{wall}} &= \frac{\ln\left(D_{\text{Pre,o}} / D_{\text{Pre,i}}\right)}{2\pi k_{\text{wall}} L_{\text{Pre}}} \\
&= \frac{\ln\left(38.1\,\text{mm} / 34.8\,\text{mm}\right)}{2\pi \cdot 13.07\,\text{W}\,\text{m}^{-1}\,\text{K}^{-1} \cdot 0.508\,\text{m}} \\
&= 0.0022\,\text{K}\,\text{W}^{-1}
\end{aligned}
\tag{4.8}
$$

The thermal resistance across the insulation layer was calculated as follows:

$$R_{\text{ins}} = \frac{\ln\left(D_{\text{ins,o}} / D_{\text{Pre,o}}\right)}{2\pi k_{\text{ins}} L_{\text{Pre}}}$$

$$= \frac{\ln\left(100\,\text{mm} / 38.1\,\text{mm}\right)}{2\pi \cdot 0.04\,\text{W}\,\text{m}^{-1}\,\text{K}^{-1} \cdot 0.508\,\text{m}}$$

$$= 7.1\,\text{K}\,\text{W}^{-1}$$

(4.9)

The outer insulation temperature was solved iteratively to be 26.8°C. The path for heat loss from the outer insulation surface was the combination of the radiation and convection contributions in parallel. The radiation resistance was calculated as follows:

$$R_{\text{rad}} = \frac{1}{\varepsilon_{\text{ins}} \pi D_{\text{ins,o}} L_{\text{Pre}} \sigma_{\text{SB}} \left(T_{\text{ins}}^{2} + T_{\text{amb}}^{2}\right)\left(T_{\text{ins}} + T_{\text{amb}}\right)}$$

$$= \frac{1}{\left[\begin{array}{c} 0.85 \cdot \pi \cdot 0.1\,\text{m} \cdot 0.508\,\text{m} \cdot 5.67 \times 10^{-8}\,\text{W}\,\text{m}^{-2}\text{K}^{-4} \\ \cdot\left(300.0\text{K}^{2} + 298.1\text{K}^{2}\right)\left(300.0\text{K} + 298.1\text{K}\right) \end{array}\right]}$$

$$= 1.2\,\text{K}\,\text{W}^{-1}$$

(4.10)

Transport properties of air were calculated at the film temperature, calculated to be 25.8°C. The convective resistance was calculated using the Churchill and Chu (1975) correlation for a horizontal cylinder, as shown in Equations (4.11) and (4.12).

$$Ra_{\text{air}} = \frac{g\beta\left(T_{\text{ins}} - T_{\text{Amb}}\right)\left(D_{\text{ins,o}}\right)^{3}}{\nu\alpha} = Ra_{\text{air}} = 173,000$$

(4.11)

$$h_{\text{nat,conv}} = \frac{k_{\text{air}}}{D_{\text{ins,o}}} Nu_{\text{D}} = \frac{k_{\text{air}}}{D_{\text{ins,o}}} \left(0.60 + 0.387 \frac{Ra_{\text{air}}^{1/6}}{\left(1 + \left(0.559 / \text{Pr}\right)^{9/16}\right)^{8/27}}\right)^{2} =$$

$$= \frac{0.0259\,\text{W}\,\text{m}^{-1}\,\text{K}^{-1}}{0.1\,\text{m}} 9.0 = 2.33\,\text{W}\,\text{m}^{-2}\,\text{K}^{-1}$$

(4.12)

The convective resistance was then calculated as follows:

$$R_{conv} = \frac{1}{h_{nat,conv} \pi D_{ins,o} L_{Pre}} = \frac{1}{2.33 \, \text{W m}^{-2}\,\text{K}^{-1} \cdot \pi \cdot 0.1\text{m} \cdot 0.508\text{m}} = 2.7 \, \text{K W}^{-1} \qquad (4.13)$$

Combining the above thermal resistances, the total loss from the pre-condenser was calculated in an iterative manner to be 2.0 ± 1.0 W.

$$\begin{aligned}
\dot{Q}_{loss} &= \frac{T_{wall,i} - T_{amb}}{R_{wall} + R_{ins} + \dfrac{R_{conv} R_{rad}}{\left(R_{conv} + R_{rad}\right)}} \\[2mm]
&= \frac{42.0°\text{C} - 24.9°\text{C}}{0.0022 \, \text{K W}^{-1} + 7.1\text{K W}^{-1} + \dfrac{2.7 \, \text{K W}^{-1} \cdot 1.2 \, \text{K W}^{-1}}{\left(2.7 \, \text{K W}^{-1} + 1.2 \, \text{K W}^{-1}\right)}} \\[2mm]
&= 2.2 \pm 1.1 \, \text{W}
\end{aligned} \qquad (4.14)$$

4.1.3 Heat Loss in Test Section

For this segment of the test loop, in addition to the ambient losses from the test section, there are also ambient losses from the primary loop and heat exchanger, which couples the secondary and the primary coolant loops that are part of the thermal amplification technique. The losses to ambient from the secondary-to-primary loop heat exchanger were calculated using the above-described procedure to be 1.5 ± 0.75 W. Using the dimensions of the test section, the ambient loss from the test section was calculated in a manner similar to that described above. However the annulus thermal resistance, $R_{Annulus,o}$, was included in this case, as shown in Figure 4.3 and Equation (4.15). The heat duties in the pre- and post-condensers are significantly larger than that of the test section. As such, the ambient losses in the test section become more significant as a percentage of the total duty. Therefore, the convective resistance on the annulus-side of the test section is included rather than simply assuming that the inner wall temperature is equal to the average fluid temperature.

166

$$\dot{Q}_{\text{loss,Test}} = \frac{T_{\text{wall,i}} - T_{\text{amb}}}{R_{\text{Annulus,o}} + R_{\text{wall}} + R_{\text{ins}} + \dfrac{R_{\text{conv}}R_{\text{rad}}}{\left(R_{\text{conv}} + R_{\text{rad}}\right)}} \qquad (4.15)$$

The annulus thermal resistance was calculated to be 0.0027 K W^{-1} using the annulus heat transfer coefficient calculated in Section 4.2.1. Due to the high flowrate in the annulus in which the coolant flows, the thermal resistance was small (on the same order as the wall thermal resistance) relative to the other terms. Thus, including the annulus thermal resistance had a negligible effect on the ambient loss from the test section. The resulting ambient loss from the test section was calculated to be 1.4 ± 0.7 W

Finally, the ambient loss from the primary loop was evaluated as the sum of the ambient losses from the primary loop tubing, the pump, and the flow meter. To simplify the analysis, the heat transfer area of the three components was measured and converted to an effective length of tubing that would yield an equivalent heat loss area for the ambient loss calculation. The actual measured length of ½-inch tubing in the primary loop was 2.94 m. The equivalent length of tubing for the pump and flow meter, as described by Mitra (2005), were 1.29 m and 1.48 m, respectively. The total loss to ambient from the primary loop was then calculated as described in the previous section to be 15.4 ± 7.7 W. Thus, the total ambient loss from the test section and primary loop was 18.3 ± 9.2 W.
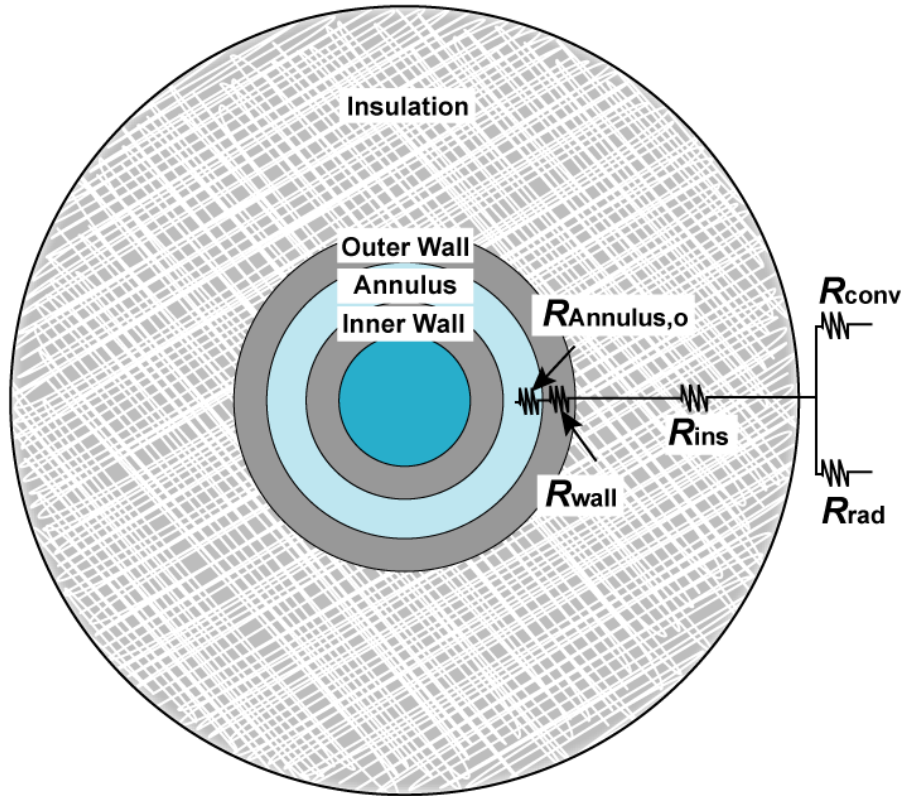
Figure 4.3. Test section ambient loss schematic

4.1.4 Primary Cooling Loop Pump Heat Addition

Use of the thermal amplification technique to improve the accuracy of the test section heat duty calculation developed by Garimella and Bandhauer (2001) relies on detailed knowledge of the primary loop contributions. The calculation of the loss to ambient was explained in the previous section. The heat addition to the primary loop due to the pump for the representative case is described here. Pump heat addition, as a function of volumetric flowrate, was measured using single-phase experiments (Personal Communication, 2013). Additional details of the pump heat addition calculation are provided in Appendix C. The conditions in the primary loop are summarized in Table 4.4. The pump heat addition to the primary loop was calculated as a function of volumetric flow rate using Equation (4.16) to be 36.8 W.

$$\dot{Q}_{\text{Pump}} = 0.1401\dot{V}^3_{\text{w,Pri}} + 0.9598\dot{V}^2_{\text{w,Pri}} + 3.025\dot{V}_{\text{w,Pri}} \tag{4.16}$$

An uncertainty of ±50% was assigned to the pump heat addition obtained from this curve fit. Thus, the pump heat addition is 36.8 ± 18.4 W.

Table 4.4. Representative data point primary loop conditions

		Temperature		Flowrates	
		Symbol	°C	Symbol	L min^{-1}
Primary Loop	Inlet	$T_{\text{w,Pri,Test,in}}$	45.6 ± 0.3	$\dot{V}_{\text{w,Pri}}$	4.02 ± 0.02
	Outlet	$T_{\text{w,Pri,Test,out}}$	47.8 ± 0.3		

4.1.5 Test section Heat Duty

The test section heat duty was calculated using the secondary loop energy balance, ambient losses in the primary loop, and pump heat addition as shown in Equation (4.17).

$$\dot{Q}_{\text{Test}} = \dot{Q}_{\text{Sec}} + \dot{Q}_{\text{loss,Amb}} - \dot{Q}_{\text{Pump}} \tag{4.17}$$

Using the measured secondary loop temperatures shown in Table 4.5 and the water loop pressure of 225.2 ± 2.4 kPa, the inlet and outlet enthalpies of the secondary coolant loop were calculated and are shown in Table 4.6. The secondary loop heat duty was then calculated as follows:

$$\begin{aligned} \dot{Q}_{\text{Sec}} &= \dot{m}_{\text{w,Sec}}\left(i_{\text{w,Sec,out}} - i_{\text{w,Sec,in}}\right) \\ &= 0.0036\,\text{kg}\,\text{s}^{-1}\left(197.1\,\text{kJ}\,\text{kg}^{-1} - 31.4\,\text{kJ}\,\text{kg}^{-1}\right) \\ &= 595.6 \pm 6.5\,\text{W} \end{aligned} \tag{4.18}$$

Combining the secondary loop heat duty, primary loop pump heat addition of 36.8 ± 18.4 W, and total ambient losses of 18.3 ± 9.2 W, the test section heat duty was

calculated using Equation (4.17) to be 577.1 ± 21.5 W. The test section heat duty can also

be approximated using the primary loop flowrate and temperature change of the coolant:

$$
\begin{aligned}
\dot{Q}_{\text{Test,Alt}} &= \dot{m}_{\text{pri}} C_{P\text{w,pri}} \left(T_{\text{w,pri,test,out}} - T_{\text{w,pri,test,in}} \right) \\
&= 0.66\,\text{kg}\,\text{s}^{-1}\,4.1\,\text{kJ}\,\text{kg}^{-1}\,\text{K}^{-1} \left(47.8°\text{C} - 45.6°\text{C} \right) \\
&= 617.1 \pm 118\,\text{W}
\end{aligned}
\tag{4.19}
$$

The large uncertainty of 19% in measured test section heat duty using the coolant

energy balance highlights the need to use the thermal amplification technique, where the

uncertainty in measured heat duty was just 4%.

Table 4.5. Representative data point secondary loop measurements

		Temperature		Flowrate	
		Symbol	°C	Symbol	kg s^{-1}
Secondary Loop	Inlet	$T_{\text{w,Sec,in}}$	7.4 ± 0.3	$\dot{m}_{\text{w,Pre}}$	0.0036 ± 5.4×10^{-6}
	Outlet	$T_{\text{w,Sec,out}}$	47.0 ± 0.3		

Table 4.6. Representative data point secondary loop enthalpies

		Enthalpy	
		Symbol	kJ kg^{-1}
Secondary Loop	Inlet	$i_{\text{w,Sec,in}}$	31.4 ± 1.3
	Outlet	$i_{\text{w,Sec,out}}$	197.1 ± 1.3

The net heat added in the evaporator between the subcooled and superheated states

was 9,517 W, and the sum of the heat transfer rates in the coolant heat exchangers,

including ambient losses/gains, was 9,481 W, which resulted in a difference between the

two methods of 36.1 ± 97.8 W or 0.4% of the evaporator duty. A positive difference

indicates that the sum of the measured heat exchanger contributions was less than the net

heat addition in the evaporator. The uncertainties in the pre- and post-condenser flowrates

and temperatures dominated the uncertainty associated with the calculation of the evaporator duty using the subcooled and superheated states.

4.2   Heat Transfer Coefficient Calculation

The heat transfer coefficient of the mixture was calculated using a resistance network between the condensing fluid and the coolant water flowing through the annulus. Use of the thermal amplification technique allows the thermal resistance on the water side to be maintained low relative to the condensation resistance. In this section, the annulus heat transfer coefficient is calculated first. Then the heat transfer coefficient of the condensing mixture is calculated in two ways: a) assuming equilibrium of the mixture at the inlet and outlet using a log-mean-temperature-difference (LMTD) from the fluid to the coolant and b) accounting for non-equilibrium at the test section outlet by using the Price and Bell (1974) framework. Heat transfer coefficient results using both methods are compared in Chapter 5 to analyze the effect of mass transfer on the interface temperature and heat transfer coefficient as well as the assumption of equilibrium in design applications. Detailed reduction of the data for a representative data point to calculate heat transfer coefficients for the LMTD equilibrium method and the corresponding calculations for the Price and Bell (1974) non-equilibrium method are presented in Appendix E.

4.2.1   <u>Annulus-side and Test Section Wall Thermal Resistance</u>

The annulus heat transfer coefficient was calculated using the correlation of Garimella and Christensen (1995) for water flows in annuli. Thermodynamic and transport properties of the annulus-side water were calculated at the average test section annulus temperature of 46.7°C and the primary loop pressure of 405.8 kPa. The annulus Reynolds number was calculated to be 7,100, which is above the upper critical Reynolds number of 3,300, indicating turbulent flow. The turbulent Nusselt number was calculated

using Equation (4.20), which resulted in an annulus heat transfer coefficient of $20,300 \pm 5,070$ W m^{-2} K^{-1}. A conservative uncertainty of $\pm 25\%$ was assumed for this heat transfer coefficient.

$$
\begin{aligned}
\mathrm{Nu}_{\text{Annulus}} &= 0.025\left(\mathrm{Re}_{\text{Annulus}}{}^{0.78}\mathrm{Pr}^{0.48}r^{*-0.14}\right) \\
&= 0.025\left(7,094^{0.78}\,3.78^{0.48}\,0.86^{-0.14}\right) \\
&= 48.7
\end{aligned}
\tag{4.20}
$$

Relatively stagnant water was present in two regions inside the tee fittings used to seal the end of the coolant annulus of the test section as shown schematically in Figure 4.4.
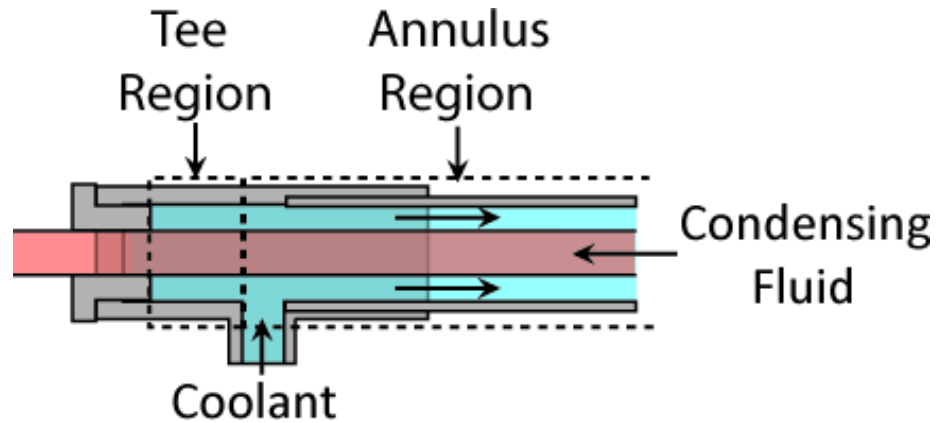
Figure 4.4. Tee region schematic

However, these sections still contributed to the cooling duty of the test section. Therefore, the effective thermal resistance accounting for these end sections was accounted for using Equation (4.21).

$$
R_{\text{Conv,eq}} = \left(\frac{1}{R_{\text{Annulus,i}}} + 2\frac{1}{R_{\text{Tee}}}\right)^{-1}
\tag{4.21}
$$

The annulus thermal resistance was calculated using the annulus-side heat transfer coefficient calculated above to be 0.0031 W K^{-1} using Equation (4.22).

$$R_{\text{Annulus,i}} = \frac{1}{h_{\text{w,Annulus}} \pi D_{\text{Test,o}} L_{\text{Annulus}}} \tag{4.22}$$

The thermal resistance for the fluid inside the end fittings, R_{Tee}, was calculated using Equation (4.23), where the effective thermal conductivity of the water was calculated using Equation (4.24), as presented in Incropera and DeWitt (2007).

$$R_{\text{Tee}} = \frac{\ln\left(D_{\text{Tee}} / D_{\text{Test,o}}\right)}{2\pi k_{\text{Tee,Effective}} L_{\text{Tee}}} \tag{4.23}$$

$$\text{For } Ra^* < 100 : k_{\text{Tee,Effective}} = k_{\text{w,Pri}}$$

$$\text{For } Ra^* > 100 : k_{\text{Tee,Effective}} = k_{\text{w,Pri}} 0.386 \left(\frac{\text{Pr}_{\text{w,Pri}}}{0.861 + \text{Pr}_{\text{w,Pri}}}\right)^{0.25} Ra^{*0.25} \tag{4.24}$$

The outer tube wall temperature was calculated iteratively to be 48.6°C, which resulted in a value of Ra L^{-3} of 8.79×10^{10} m^{-3}. Ra$^*_{\text{Tee}}$ is calculated using Equation (4.25) as follows:

$$
\begin{aligned}
Ra^*_{\text{Tee}} &= \frac{Ra}{L^3} \frac{\left(\ln\left(D_{\text{Tee}} / D_{\text{Test,o}}\right)\right)^4}{\left(\left(D_{\text{Test,o}}\right)^{-3/5} + \left(D_{\text{Tee}}\right)^{-3/5}\right)^5} \\
&= 8.79 \times 10^{10} \, \text{m}^{-3} \frac{\left(\ln\left(0.0104\text{m} / 0.00953\text{m}\right)\right)^4}{\left(\left(0.00953\text{m}\right)^{-3/5} + \left(0.0104\text{m}\right)^{-3/5}\right)^5} \\
&= 0.16
\end{aligned}
\tag{4.25}
$$

The resulting modified Rayleigh number was low, indicating that any convective effects due to fluid movement would have a minimal effect on the thermal conductivity

of the liquid phase. This was due to the small gap between the two tubes of approximately 0.5 mm. Therefore, the effective conductivity of the relatively stagnant liquid was equal to the thermal conductivity of water (0.640 W m^{-1} K^{-1}). The thermal resistance in the tee was calculated to be 1.7 K W^{-1}. This term had a negligible influence on the effective convective thermal resistance, which was calculated to be 0.0031 K W^{-1}. In this case, the total test section duty was measured to be 577.1 W with 575.0 W transferred in the annulus and 2.2 W (1.1 W each) transferred through the relatively stagnant water in the Tee regions. (It should be noted that the annulus and Tee regions do not sum to the total duty here due to rounding.)

The thermal resistance of the copper test section tube wall was calculated as follows:

$$
\begin{aligned}
R_{\text{Test,wall}} &= \frac{\ln\left(D_{\text{Test,o}} / D_{\text{Test,i}}\right)}{2\pi k_{\text{Test,wall}}\left(L_{\text{Annulus}} + 2L_{\text{Tee}}\right)} \\
&= \frac{\ln\left(9.525\,\text{mm} / 7.75\,\text{mm}\right)}{2\pi \cdot 398.5\,\text{W m}^{-2}\,\text{K}^{-1}\left(0.53\,\text{m} + 2\cdot 0.013\,\text{m}\right)} \\
&= 0.00015\,\text{K W}^{-1}
\end{aligned}
\tag{4.26}
$$

In most cases, the thermal resistance of the wall was negligible.

4.2.2 Pure Fluid and Equilibrium Zeotropic Mixture Analysis

Thermodynamic equilibrium of the mixture or pure fluid was assumed at the inlet and outlet of the test section. The heat transfer coefficient was calculated using the LMTD between the mixture equilibrium temperatures or pure fluid saturation temperatures and the coolant water temperatures as shown in Equation (4.27).

$$\text{LMTD} = \frac{\left(T_{f,\text{Test,in}} - T_{w,\text{Test,out}}\right) - \left(T_{f,\text{Test,out}} - T_{w,\text{Test,in}}\right)}{\ln\left(\dfrac{T_{f,\text{Test,in}} - T_{w,\text{Test,out}}}{T_{f,\text{Test,out}} - T_{w,\text{Test,in}}}\right)}$$

$$= \frac{\left(60.0°\text{C} - 47.8°\text{C}\right) - \left(57.3°\text{C} - 45.6°\text{C}\right)}{\ln\left(\dfrac{60.0°\text{C} - 47.8°\text{C}}{57.3°\text{C} - 45.6°\text{C}}\right)} \tag{4.27}$$

$$= 11.9 \pm 0.6\,\text{K}$$

Using the test section heat duty calculated in Section 4.1.5, the overall condensing fluid thermal resistance, UA_f in Equation (4.28), was calculated to be 48.3 ± 2.9 W K^{-1}.

$$UA_f = \frac{\dot{Q}_{\text{Test}}}{\text{LMTD}} \tag{4.28}$$

The resistance network for the test section was comprised of three resistances in series, the condensation resistance of interest, the wall resistance, and the equivalent convective resistance on the annulus side, as shown in Equation (4.29).

$$UA_f = \frac{1}{\left(R_f + R_{\text{Test,wall}} + R_{\text{Conv,eq}}\right)} \tag{4.29}$$

After the test section wall and the annulus equivalent convective thermal resistances were calculated, the condensing fluid-side thermal resistance, and therefore the equilibrium heat transfer coefficient, were calculated using Equation (4.28). The condensing fluid resistance was calculated to be 0.017 ± 0.001 K W^{-1}. The equilibrium heat transfer coefficient was calculated using Equation (4.30) to be $4{,}231 \pm 355$ W m^{-2} K^{-1}.

$$R_{\mathrm{f}} = \frac{1}{h_{\mathrm{f}} \pi D_{\mathrm{Test,i}} \left(L_{\mathrm{Annulus}} + 2L_{\mathrm{Tee}} \right)}$$

$$= \frac{1}{h_{\mathrm{f}} \cdot \pi \cdot 0.00775\,\mathrm{m} \cdot \left(0.53\,\mathrm{m} + 2 \cdot 0.013\,\mathrm{m} \right)} \qquad (4.30)$$

$$= 0.00113\,\mathrm{K\,W^{-1}}$$

To ensure that the thermal resistance on the condensation side was the dominant resistance in the test section, the resistance ratio was calculated as shown in Equation (4.31) to be 5.4. A resistance ratio greater than two was considered acceptable.

$$R_{\mathrm{Ratio}} = \frac{R_{\mathrm{f}}}{R_{\mathrm{Test,wall}} + R_{\mathrm{Conv,eq}}}$$

$$= \frac{0.017\,\mathrm{K\,W^{-1}}}{0.00010\,\mathrm{K\,W^{-1}} + 0.0031\,\mathrm{K\,W^{-1}}} \qquad (4.31)$$

$$= 5.4$$

4.2.3 Non-Equilibrium Zeotropic Mixture Analysis

The non-equilibrium zeotropic mixture analysis was conducted using the approach developed by Colburn and Drew (1937) and Price and Bell (1974). The idealized flow schematic is shown in Figure 4.5 and consists of the condensate liquid film and condensing vapor being analyzed. The Price and Bell (1974) procedure was used in the present study to determine the condensation rate and interface temperatures while accounting for mass transfer, assuming annular flow. The film heat transfer coefficient was calculated in this analysis using the interface temperature rather than the bulk equilibrium temperature.
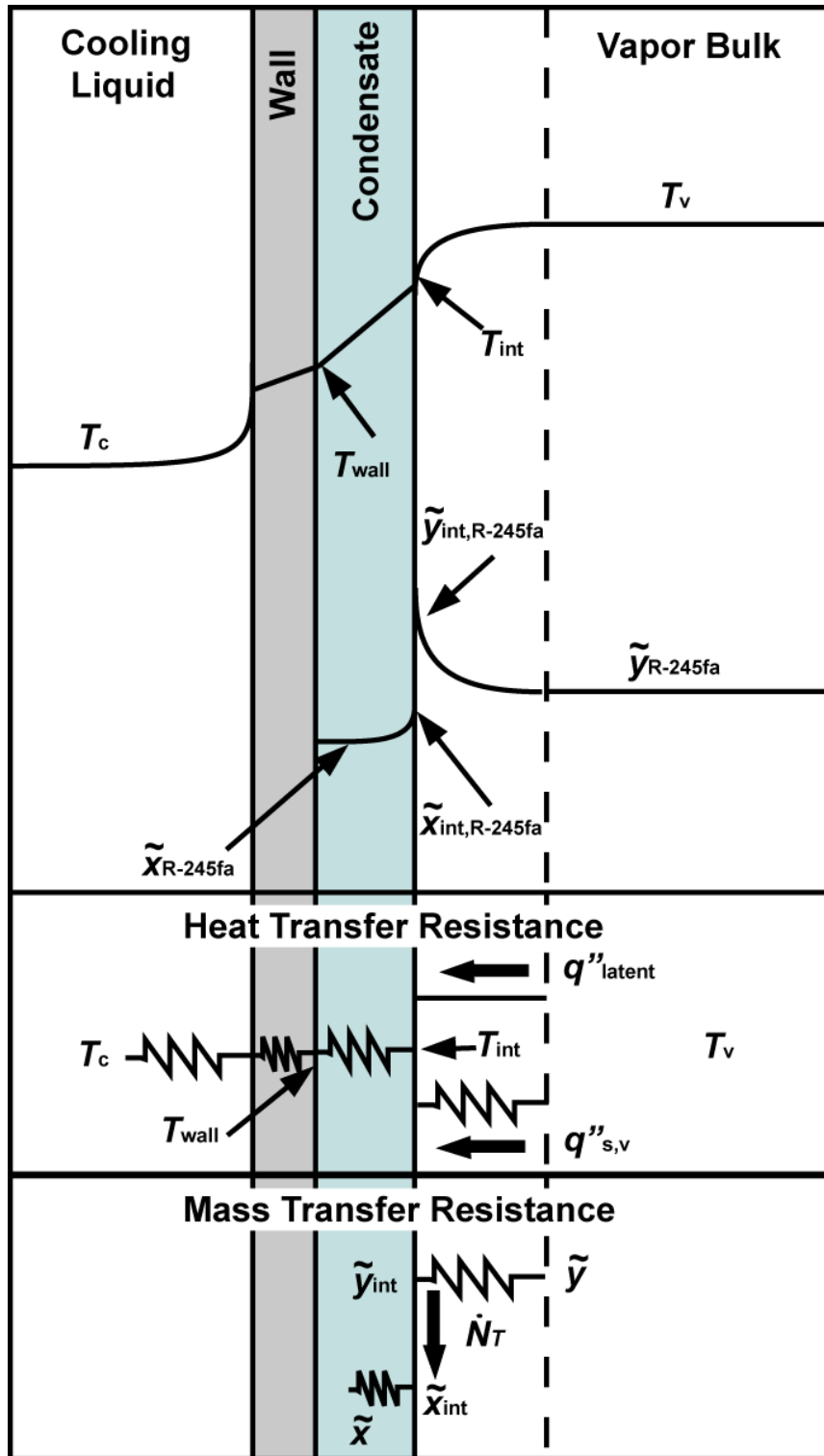
Figure 4.5. Colburn and Drew (1937) and Price and Bell (1974) thermal resistance and mass transfer resistance schematic

The test section inlet and outlet conditions are measured directly from the pre- and post-condenser analyses. As described previously, the thermal amplification technique was used over these measured values to determine the test section heat duty for improved accuracy. High accuracy of the inlet and outlet conditions is also desirable for the non-equilibrium analysis of the zeotropic mixtures because slight changes in the inlet and outlet conditions can affect the mass transfer rate. Results from the analysis of the primary loop and the average test section conditions are used to calculate the inlet and outlet conditions to improve the accuracy over values obtained from the pre- and post-condenser analyses. Specifically, the average test section conditions are calculated from the measured pre- and post- condenser conditions. The new inlet condition is calculated using the average test section enthalpy, the test section heat duty and the mass flowrate using Equation (4.31) to be 264 ± 2.2 kJ kg^{-1}. In this case, the pre-condenser energy balance enthalpy and uncertainty were nearly identical at 265.0 ± 2.2 kJ kg^{-1}.

$$i_{\text{f,Test,in,Pri}} = i_{\text{f,Test,Avg}} + \frac{\dot{Q}_{\text{Test}}}{2\dot{m}_{\text{f}}}$$

(4.31)

Similarly, the primary loop based outlet enthalpy was calculated to be 239.9 ± 2.2 kJ kg^{-1}. An improvement in uncertainty was achieved compared to a post-condenser based enthalpy of 239.4 ± 3.5 kJ kg^{-1}.

The importance of using the primary loop results over the pre- and post- condenser values is shown in Figure 4.6, where the temperature and concentration profiles from the inlet to the outlet of the test section using both methods are compared. The slight changes in the inlet and outlet conditions observed in the representative data point discussed here appreciably affect the phase temperature and concentration profile in the test section.

	Vapor-phase		Liquid-phase	
	Temperature	Concentration	Temperature	Concentration
Primary Loop	——	——	——	——
Pre- Post-Condenser	— — —	— — —	— — —	— — —
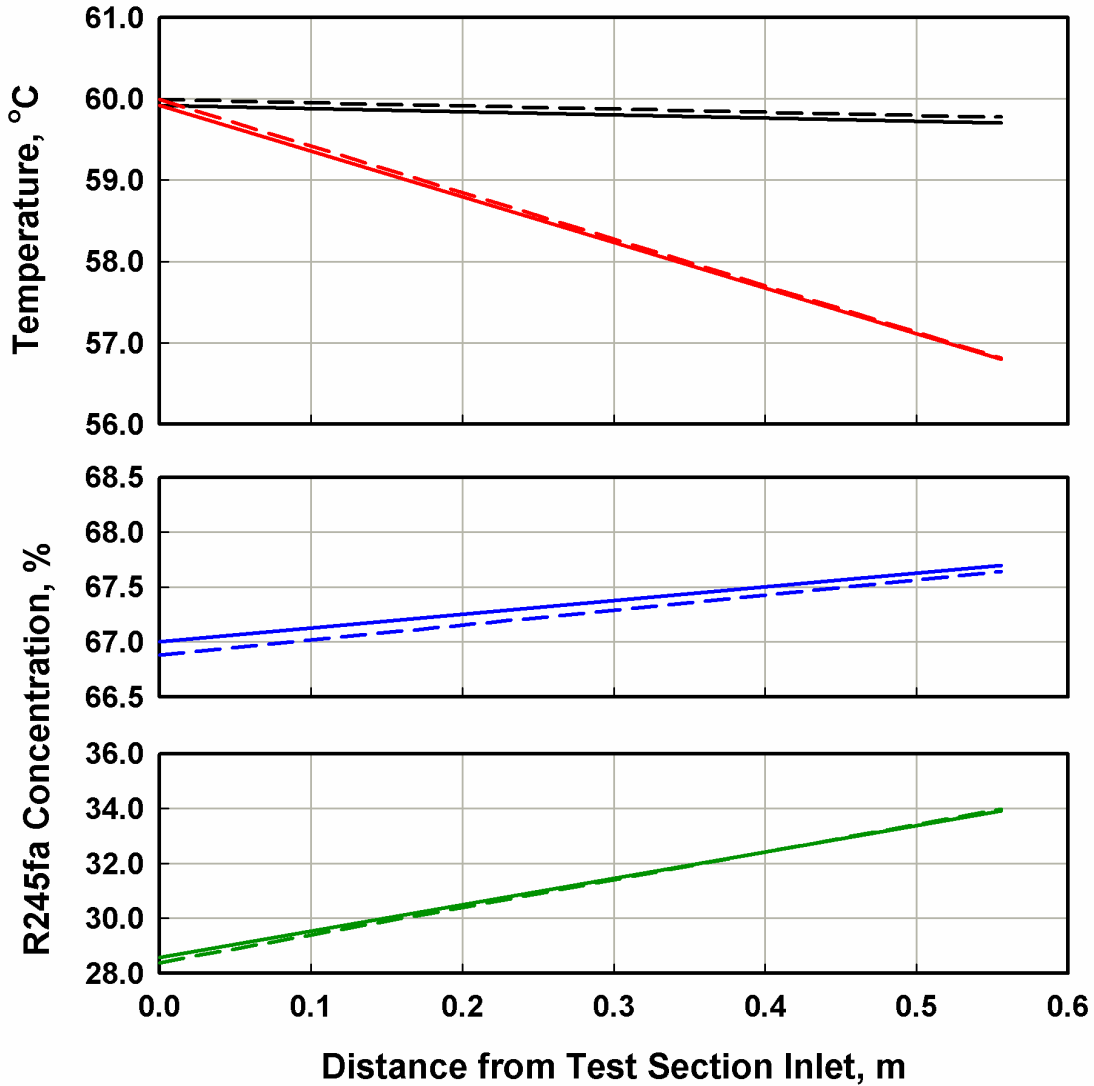
Figure 4.6. Comparison of test section temperature and concentration profiles

The following calculation is iterative; however, values obtained iteratively are introduced as necessary to facilitate discussion. Key steps are presented here, with additional details of the calculations available in Appendix E. A schematic of the non-equilibrium analysis is presented in Figure 4.7.

179
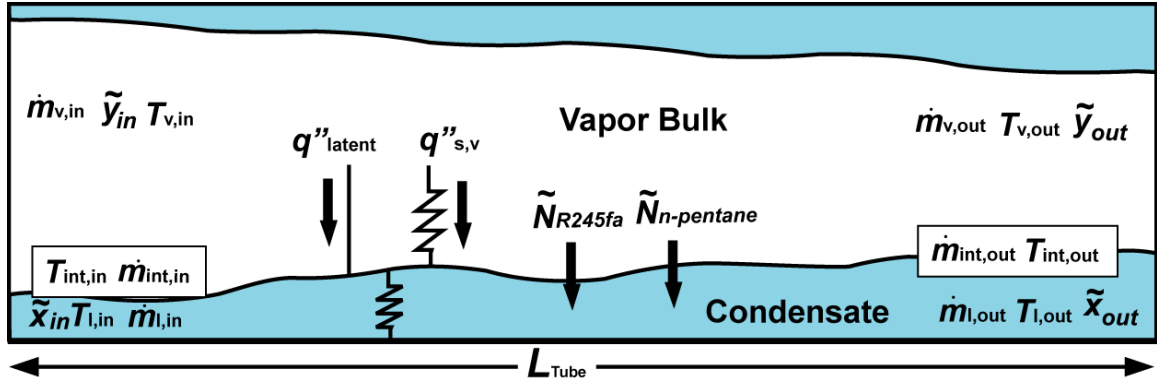
Figure 4.7. Non-equilibrium analysis schematic

The cooling duty of the vapor-phase, $q''_{s,v}$ in Figure 4.7, and the outlet vapor-phase temperature were calculated for single-phase vapor flowing through the vapor core (calculated using the Baroczy (1965) void fraction model), as shown in Equation (4.32). The single-phase vapor heat transfer coefficient was calculated using the Churchill (1977a) correlation.

$$
\begin{aligned}
\dot{Q}_v &= h_v \pi D_{\text{Test,i}} \left(L_{\text{Annulus}} + 2L_{\text{Tee}} \right) \sqrt{\alpha} \, \text{LMTD}_v \\
\dot{Q}_v &= \dot{m}_{v,\text{Avg}} C_{pv,\text{in}} \left(T_{f,\text{Test,in,Pri}} - T_{v,\text{out}} \right)
\end{aligned}
\tag{4.32}
$$

The vapor-phase temperature difference, LMTD$_v$, was calculated between the inlet and outlet vapor temperatures and the inlet and outlet interface temperatures. Because the inlet was assumed to be at equilibrium ($\Delta T_{\text{lv,in}} = 0$ K), the temperature difference between the vapor and interface at the inlet, $\Delta T_{\text{lv,in}}$, was assumed to have an infinitesimal temperature difference of 0.001 K. This is well below the experimental uncertainty and near zero while still allowing the computation to proceed. A 75% uncertainty was applied to this value.

$$\text{LMTD}_v = \frac{\left(\Delta T_{lv,in}\right) - \left(T_{v,out} - T_{int,out}\right)}{\ln\left(\dfrac{\Delta T_{lv,in}}{T_{v,out} - T_{int,out}}\right)} = 0.3\,\text{K} \tag{4.33}$$

Using the iteratively solved interface outlet temperature of 56.8°C, the cooling duty of the vapor-phase and outlet vapor-phase temperature were calculated to be 2.7 W and 59.7°C, respectively.

The binary diffusion coefficient was calculated to be 8.9×10^{-7} m^2 s^{-1} using the Chapmann-Enskog diffusion coefficient correlation as presented by Poling (2001). An uncertainty of 25% was assigned to this term. The net molar condensation flux was calculated to be 0.00182 ± 0.00026 kmol m^{-2} s^{-1} using Equation (4.34), where $C_T = P_{f,test,avg} / (R_u\, T_{v,avg})$ and $\beta_v = \text{Sh}_v\, D_{12} / D_{Test,i}$.

$$\tilde{N}_T = \beta_v C_T \ln\left(\frac{\tilde{z} - \tilde{y}_{R245fa,int,Avg}}{\tilde{z} - \tilde{y}_{R245fa,Avg}}\right) \tag{4.34}$$

The condensing flux of each component was calculated using $\tilde{N}_{R245fa} = \tilde{z}\tilde{N}_T$ and $\tilde{N}_{Pentane} = \left(1 - \tilde{z}\right)\tilde{N}_T$. The resulting R245fa and n-pentane fluxes were calculated to be 0.00090 kmol m^{-3} and 0.00092 kmol m^{-3}, respectively.

The outlet conditions were calculated using phase mass balances (Equation(4.35)), phase species balances (Equation (4.36)) and an energy balance over the outlet control surface (Equation (4.37)).

$$
\begin{aligned}
\dot{m}_{v,out} &= \dot{m}_{v,in} - \left(\tilde{N}_{R245fa} MW_{R245fa} + \tilde{N}_{n\text{-pentane}} MW_{n\text{-pentane}}\right) A_{HT} \\
\dot{m}_{l,out} &= \dot{m}_{l,in} + \left(\tilde{N}_{R245fa} MW_{R245fa} + \tilde{N}_{n\text{-pentane}} MW_{n\text{-pentane}}\right) A_{HT}
\end{aligned}
\tag{4.35}
$$

$$\hat{y}_{\text{R245fa,out}} \dot{m}_{\text{v,out}} = \hat{y}_{\text{R245fa,in}} \dot{m}_{\text{v,in}} - \tilde{N}_{\text{R245fa}} MW_{\text{R245fa}} A_{\text{HT}}$$

$$\hat{x}_{\text{R245fa,out}} \dot{m}_{\text{l,out}} = \hat{x}_{\text{R245fa,in}} \dot{m}_{\text{l,in}} + \tilde{N}_{\text{R245fa}} MW_{\text{R245fa}} A_{\text{HT}} \quad (4.36)$$

$$\dot{m}_{\text{f}} i_{\text{f,Test,out,Pri}} = \dot{m}_{\text{v,out}} i_{\text{v,out}} + \dot{m}_{\text{l,out}} i_{\text{l,out}} \quad (4.37)$$

The outlet liquid- and vapor-phase mass flowrates were calculated to be 0.0158 kg s^{-1} and 0.008 kg s^{-1}, respectively. The outlet liquid- and vapor-phase mass concentrations of R245fa were calculated to be 0.339 and 0.677, respectively. The outlet liquid-phase temperature was calculated to be 56.8°C. With a bulk equilibrium outlet temperature of 57.3°C, the vapor-phase temperature at 59.7°C was higher than the equilibrium condition by 2.4°C and the liquid-phase at 56.8°C was below the equilibrium temperature by 0.5°C. With the inlet and outlet conditions completely defined, the heat transfer coefficient was calculated. Remembering that the heat transfer coefficient was calculated from the interface rather than the bulk temperature, the LMTD was calculated to be 11.7 ± 0.5 K using Equation (4.38).

$$\text{LMTD}_{\text{l}} = \frac{\left(T_{\text{f,Test,in,Pri}} - T_{\text{w,Pri,Test,out}}\right) - \left(T_{\text{int,out}} - T_{\text{w,Pri,Test,in}}\right)}{\ln\left(\dfrac{T_{\text{f,Test,in,Pri}} - T_{\text{w,Pri,Test,out}}}{T_{\text{int,out}} - T_{\text{w,Pri,Test,in}}}\right)} \quad (4.38)$$

Using the measured test section heat duty of 577.1 W and the LMTD of 11.7 K, the film heat transfer coefficient was calculated to be 4,350 ± 364 W m^{-2} K^{-1} using Equations (4.39) to (4.41).

$$\dot{Q}_{\text{Test}} = UA_{\text{f,PB}} \text{LMTD}_{\text{l}} \quad (4.39)$$

$$UA_{PB} = \frac{1}{\left(R_{film} + R_{Test,wall} + R_{Conv,eq}\right)} \tag{4.40}$$

$$R_{film} = \left(\frac{1}{h_{f,PB} \pi D_{Test,i} \left(L_{Annulus} + 2L_{Tee}\right)}\right)^{-1} \tag{4.41}$$

The film heat transfer coefficient was slightly higher than the equilibrium heat transfer coefficient calculated in Section 4.2.2 of $4{,}231 \pm 355$ W m^{-2} K^{-1}. The mass transfer resistance in the vapor-phase caused the liquid phase to be cooled below the equilibrium temperature at the outlet.

The sensitivity of the calculated heat transfer coefficients to the binary diffusion coefficient was assessed by comparing several other binary diffusion coefficients from the literature. Over the range of conditions observed in this study, the correlation of Gilliland (1934) for diffusion of gases in air was found to predict diffusion coefficients on average 225% higher than those predicted using the Chapmann-Enskog diffusion coefficient used in this analysis. Two semi-empirical correlations of Fuller *et al.* (1966; 1969) were both found to predict binary diffusion coefficients which differed from the Chapmann-Enskog diffusion coefficient by an average of 11%, with a maximum difference of 14%. The correlations of Fuller *et al.* (1966; 1969) were developed using a range of fluid pairs including hydrocarbons, halogenated hydrocarbons, and various other gases. Their correlation has been recommended by several authors (Hines, 1985; Reid, 1987) and is considered a better estimate for these fluids than the correlation of Gilliland (1934). The heat transfer coefficients calculated using the above analysis with the Fuller *et al.* (1969) diffusion coefficient correlation was found to be an average of 0.2% lower

than those calculated using the Chapmann-Enskog diffusion coefficient. The maximum difference was -1%. Therefore, the use of the Chapmann-Enskog diffusion coefficient as presented by Poling (2001) with a 25% uncertainty should incorporate any error associated with using this model. The resulting diffusion coefficient values predicted by the Chapmann-Enskog model were also increased by a factor of 10 to include the prediction of the Gilliland (1934) correlation and assess the sensitivity of the results to the diffusion coefficient. The heat transfer coefficients were found to be an average of - 6% lower than the unaltered values with a maximum of 29% difference. While 29% is a noticeable difference, it is due to substantially higher assumed diffusion coefficient. Therefore, it can be concluded that this particular mixture, at the conditions of interest in the present study, is relatively insensitive to the diffusion coefficient.

4.3   Frictional Pressure Gradient Calculations

The frictional pressure gradient was calculated from the measured pressure drop using Equations (4.42) and (4.43). The deceleration due to condensation must be calculated to separate the frictional component of the pressure drop from the total measured pressure drop.

$$\Delta P_{\text{f,Measured}} = \Delta P_{\text{fr}} + \Delta P_{\text{f,Decel}} \tag{4.42}$$

$$\nabla P_{\text{fr}} = \frac{\Delta P_{\text{fr}}}{L_{\Delta P}} \tag{4.43}$$

The deceleration term was calculated using Equation (4.44), as outlined in Carey (2008).

$$\Delta P_{f,Decel} = \left[G^2 \left(\frac{q^2}{\rho_{v,out} \alpha} + \frac{(1-q)^2}{\rho_{l,out}(1-\alpha)} \right) \right]_{\substack{\alpha=\alpha_{f,Test,out} \\ q=q_{f,Test,out,Pri}}} - \left[G^2 \left(\frac{q^2}{\rho_{v,in} \alpha} + \frac{(1-q)^2}{\rho_{l,in}(1-\alpha)} \right) \right]_{\substack{\alpha=\alpha_{f,Test,in} \\ q=q_{f,Test,in,Pri}}} \quad (4.44)$$

The void fraction correlation of Baroczy (1965) was used to calculate the inlet and outlet void fractions as shown in Equation (4.45). At the inlet conditions, as determined by the average conditions and the primary loop, the inlet and outlet void fractions were calculated to be 0.86 and 0.83, respectively.

$$
\begin{aligned}
\alpha_{f,Test,in} &= \left(1 + \left(\frac{1-q_{f,Test,in,Pri}}{q_{f,Test,in,Pri}} \right)^{0.74} \left(\frac{\rho_{v,in}}{\rho_{l,in}} \right)^{0.65} \left(\frac{\mu_{l,in}}{\mu_{v,in}} \right)^{0.13} \right)^{-1} \\
&= \left(1 + \left(\frac{1-0.44}{0.44} \right)^{0.74} \left(\frac{17.5\,\mathrm{kg\,m^{-3}}}{676.1\,\mathrm{kg\,m^{-3}}} \right)^{0.65} \left(\frac{1.6\times10^{-4}\,\mathrm{kg\,m^{-1}\,s^{-1}}}{1.05\times10^{-5}\,\mathrm{kg\,m^{-1}\,s^{-1}}} \right)^{0.13} \right)^{-1} \quad (4.45) \\
&= 0.86
\end{aligned}
$$

The deceleration term was calculated to be -1.08 kPa. A conservative uncertainty of 50% was applied to the deceleration term. The negative deceleration term indicates a pressure recovery due to condensation. Using the measured pressure drop across the test section of 9.80 kPa and the calculated deceleration term, the frictional component of the pressure drop was calculated to be 10.9 kPa. Over the distance between the differential pressure transducer measurements of 0.746 m, the frictional pressure gradient was calculated to be 14.6 ± 0.7 kPa m^{-1}. To ensure that acceptable accuracy in the frictional pressure drop was obtained, the frictional and deceleration pressure drop terms are expressed in terms of the measured pressure drop. In this case, the frictional and deceleration contribution were 111% and 11% of the measured, respectively, indicating good accuracy in determining the frictional contribution.

4.4 High-Speed Video

A representative data point is discussed here for the 7.0 mm internal diameter tube propane visualization at an average test section pressure of 954.6 kPa and mass flux of 146.8 kg m^{-2} s^{-1}. The determination of the inlet and outlet qualities using the pre- and post- condensers remains unchanged from the procedure outlined in Section 4.1. The test section, secondary, and primary loop were replaced by a visualization test section. Using energy balances on the pre- and post-condensers, the inlet and outlet qualities were calculated to be 0.27 ± 0.02 and 0.28 ± 0.02, respectively. This resulted in an average test section quality of 0.27 ± 0.01. In this case, the outlet quality is measured to be slightly higher than the inlet quality. With no active cooling, the test section is essentially adiabatic. The apparent increase is due to experimental uncertainty from the pre- and post- condensers in calculating the test section conditions. Additionally, in some cases, the pressure change in the test section causes a change in saturation conditions from the inlet to the outlet. In this case, the pressures at the inlet and outlet of the test section are 954.8 kPa and 954.3 kPa, respectively.

4.4.1 Test Section Calculations

Although no active cooling was provided, the ambient loss from the visualization test section was calculated. A schematic of the resistance network for the ambient loss from the visualization test section is shown in Figure 4.8. The inner and outer tubes were quartz glass with a thermal conductivity of 1.4 W m^{-1} K^{-1}. Using the procedure identified in Section 4.1.2, the thermal resistances due to conduction in the inner and outer glass tubes were calculated to be 0.088 and 0.047 K W^{-1}, respectively. The radiation and natural convection resistances were calculated to be 2.18 and 8.27 K W^{-1}, respectively.

As in the previous ambient loss calculations, the internal thermal resistance, R_f, was neglected.
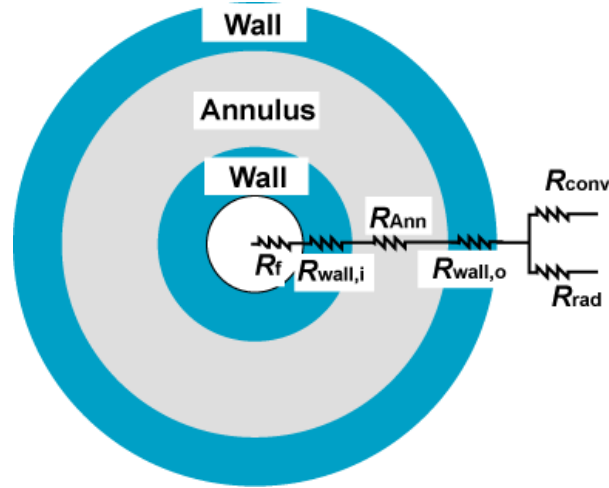
Figure 4.8. Visualization test section ambient loss schematic

The natural convection heat transfer across the pressurized annulus thermal resistance was calculated using the correlation of Hollands *et al.* (1975) as presented in Incropera and DeWitt (2007). As discussed in Chapter 3, the annulus was filled with pressurized nitrogen for the 7.0 mm data and pressurized water for the 15.0 mm data. The properties in the pressurized annulus were calculated at 550 kPa using air for the 7.0 mm data, and water at the same conditions for the 15.0 mm data. The characteristic length was calculated using Equation (4.46), to be 0.0087 m.

$$L_c = 2 \frac{\left(\ln \left(D_{\text{OT,i}} / D_{\text{test,o}} \right) \right)^{4/3}}{\left(\left(D_{\text{w,o}} \left| \frac{0.001 \frac{\text{m}}{\text{mm}}}{2} \right| \right)^{-3/5} + \left(D_{\text{OT,i}} \left| \frac{0.001 \frac{\text{m}}{\text{mm}}}{2} \right| \right)^{-3/5} \right)^{5/3}} \tag{4.46}$$

The Rayleigh number was calculated to be 1,252 using Equation (4.47).

$$Ra_{c} = \frac{g\beta_{air}\left(T_{test,o} - T_{OT,i}\right)L_{c}^{3}}{\nu_{air}\alpha_{air}} \qquad (4.47)$$

The effective thermal conductivity of the air in the annulus was calculated to be 0.049 W m^{-1} K^{-1} using Equation (4.48). The increase in effective air thermal conductivity over the base value of 0.026 W m^{-1} K^{-1} is due to the contribution of natural convection in the annulus.

$$k_{Effective,Annulus} = k_{air}\left(0.386\left(\frac{Pr_{air}}{0.861+Pr_{air}}\right)^{0.25} Ra_{c}^{0.25}\right) \qquad (4.48)$$

The thermal resistance was calculated as shown in Equation (4.49) to be 8.72 W K^{-1}.

$$R_{Effective,Annulus} = \frac{T_{test,o} - T_{OT,i}}{\dot{Q}_{Annulus}} = \frac{\ln\left(D_{OT,i} / D_{test,o}\right)}{2\pi L_{Annulus} k_{Effective,Annulus}} \qquad (4.49)$$

Thus, the ambient heat transfer from the test section was calculated using (4.50) to be a slight gain of 0.1 W. In this case, the ambient heat transfer is a gain to the test section because the room temperature was 25.9°C, while the saturation temperature of the propane at 954.6 kPa is 24.9°C.

$$
\begin{aligned}
\dot{Q}_{Test} &= \frac{T_{wall,i} - T_{amb}}{R_{wall,i} + R_{Effective,Annulus} + R_{wall,o} + \dfrac{R_{conv}R_{rad}}{\left(R_{conv} + R_{rad}\right)}} \\[2mm]
&= \frac{25.9°C - 25.1°C}{0.088\,\mathrm{K\,W^{-1}} + 8.73\,\mathrm{K\,W^{-1}} + 0.047\,\mathrm{K\,W^{-1}} + \dfrac{8.27\,\mathrm{K\,W^{-1}} \cdot 2.18\,\mathrm{K\,W^{-1}}}{\left(8.27\,\mathrm{K\,W^{-1}} + 2.18\,\mathrm{K\,W^{-1}}\right)}} \\[2mm]
&= -0.1 \pm 0.04\,\mathrm{W}
\end{aligned}
\qquad (4.50)
$$

The net heat added in the evaporator between the subcooled and superheated states was 3,030 W, while the sum of the coolant heat exchangers, including ambient losses/gains, was 3,040 W, resulting in a difference between the two methods of -12 ± 52 W or -0.4 percent of the evaporator duty.

4.4.2 Video Frame Analysis

The video processing procedure used to convert the flow videos to flow parameters including flow regime, void fraction, and film thicknesses is presented here. The video processing was conducted using the MatLab software package and *Image Processing Toolbox* (Mathworks, 2013) using some of the approaches of Toda and Hori (1993) and Wilmarth and Ishii (1997). First, the flow video was converted to a binary representation of the vapor (white) and liquid (black) regions using empirically adjusted threshold values. The vapor-liquid interface identified in the binary images was used to calculate the flow parameters. The data reduction procedure discussed here for the 7.0 mm data was nearly identical to the procedure used for the 15.0 mm videos. The difference between the analyses for the two diameters pertains to the horizontal length calibration and was discussed in the previous chapter and Appendix B.

The following section presents the analysis for a single two-phase flow image relative to the average image of the stagnant liquid video. The conversion procedure described in the following section is summarized in Figure 4.9. The following procedure is repeated for each frame of the two-phase flow videos, for a total of 2,335 frames analyzed for each data point. Every two-phase video frame is converted to two binary images: a binary flow image that identifies the vapor regions and a binary film image that removes the vapor entrained in the liquid phase from the binary flow image.
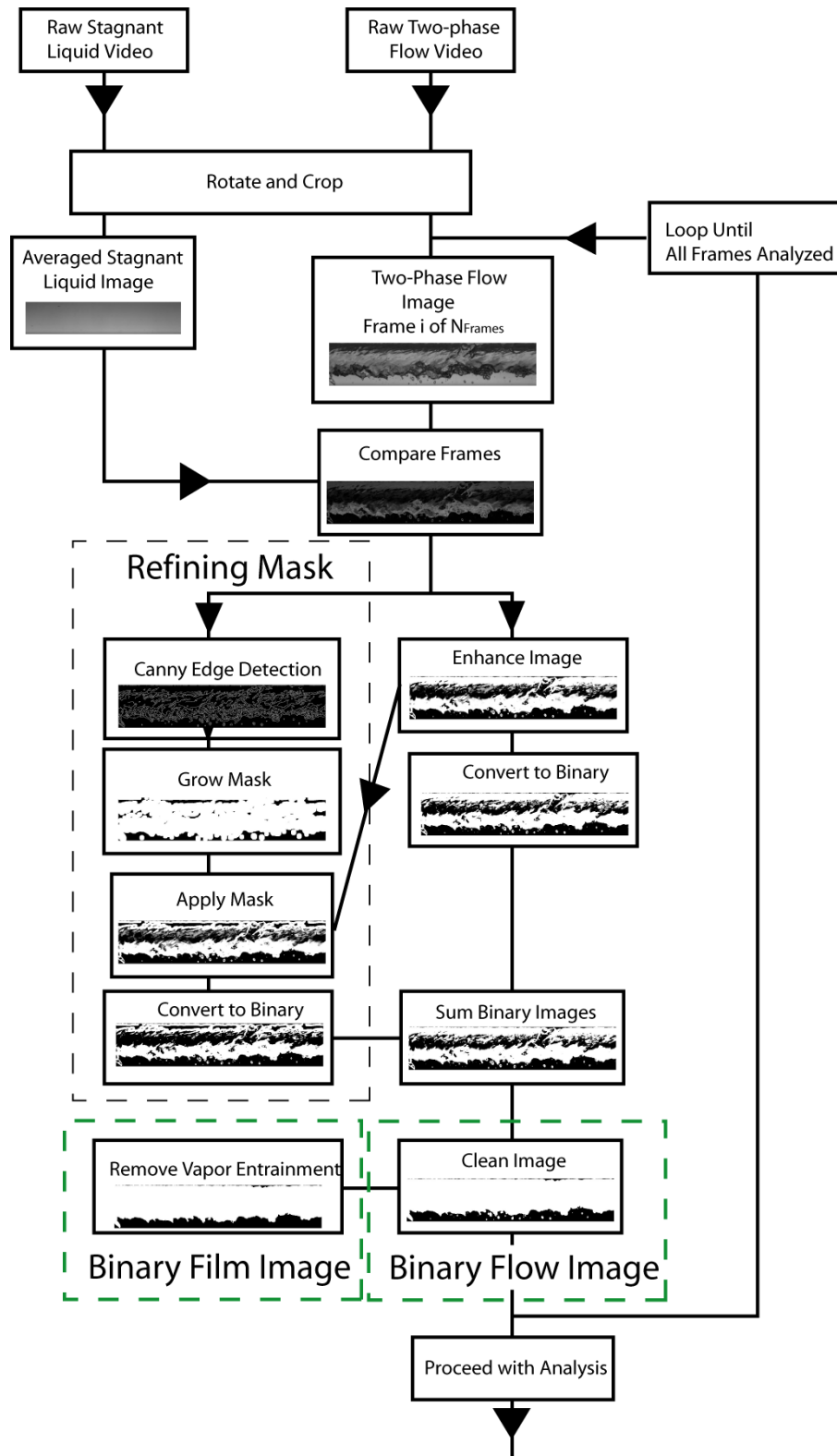
Figure 4.9. Conversion to binary image flow chart

4.4.2.1 Raw videos

To conduct the analysis, a two-phase flow video frame (shown in Figure 4.10 and referred to as the two-phase flow video) and a no-flow liquid filled tube video frame (shown in Figure 4.11 and referred to as the stagnant liquid video) were utilized. As indicated in Chapter 3, the flow videos were captured at 1,000 fps and 1024×512 pixels and output into two videos. This corresponds to 22×43 mm and 23×46 mm frames for the 7 and 15 mm test sections, respectively or approximately 0.033 mm per pixel. The first video was output at 1,000 fps for one second while the second video was output at 333 fps for four seconds. The one-second videos (each with 1,001 frames) were used for the flow regime and void fraction analyses. The four-second videos (with 1,334 frames each) were analyzed as part of the uncertainty analysis to quantify the sensitivity to the length of the video.

The two-phase flow and stagnant liquid videos were separated into sets of 8-bit grayscale images and stored in the system memory for processing. The two-phase flow image, shown in Figure 4.10, is the first frame in the representative flow video. The selected video is representative of the image quality obtained across all the videos in the test matrix. The stagnant liquid image, shown in Figure 4.11, is the first image in the liquid filled video set.
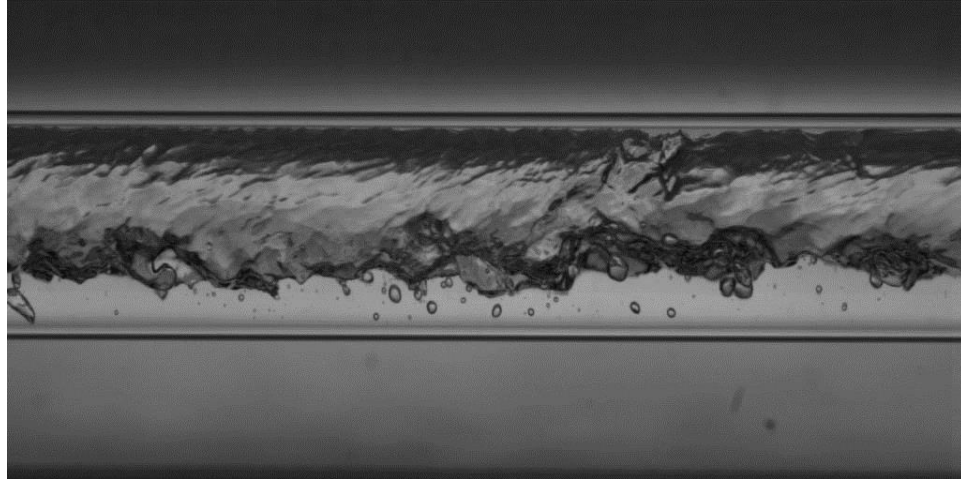
Figure 4.10. Two-phase flow video image
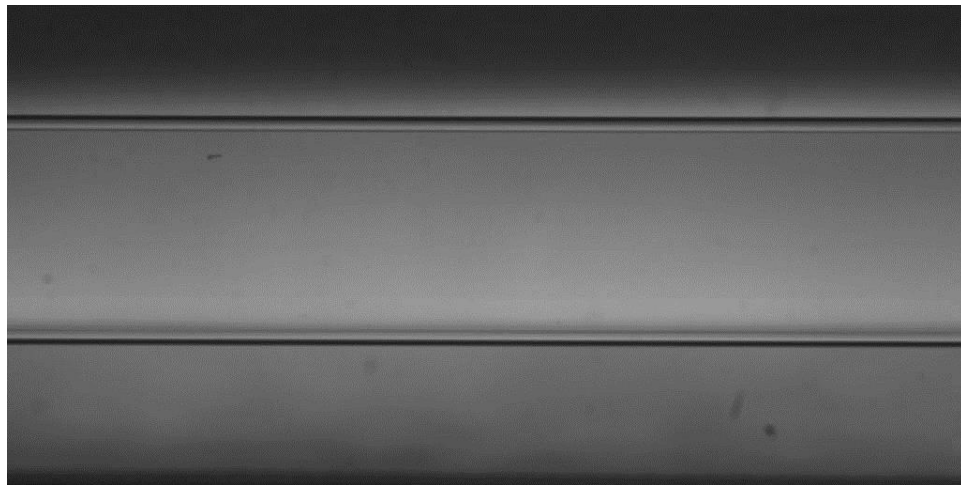
Figure 4.11. Stagnant liquid filled image

4.4.2.2 Locate tube edge, rotate, and crop videos

The automated procedure used to identify the tube wall locations and crop the videos to focus on the flow area is described here. The main steps in this procedure include rotating the image, locating the tube walls, aligning the liquid and flow videos, and cropping the images to focus only on the flow area. The image origins (1,1) are located in the upper left corners. As observed in both the representative images, there is a significant amount of background at the top and bottom of the images. To reduce required computational power, 100 pixels were initially removed from the top and bottom

192

of the images, reducing the frame size from 1024×512 to 1024×312 pixels. The stagnant liquid image was used to locate the inner and outer tube wall locations. Referring to Figure 4.12, the outer and inner edges of the top and bottom of the tube can be observed. To ensure that the frame is horizontal relative to the tube, the image was rotated relative to the outer edges of the outer tube walls. Twenty five pixels from the left end and the right end of the tube, highlighted in yellow in Figure 4.12, were used to identify the tube wall locations and rotate the images. The pixels from each end were averaged into a single array, 312 wide, using the *mean* function. The discrete Laplacian was calculated for both ends of the tube using the *del2* function. The Laplacian for each end are plotted in Figure 4.13. Two groupings of peaks were observed near the tube walls. The Laplacian was found to locate the outer edge of the outer tube wall and inner edges of the inner tube walls better than an average or gradient. It was important to locate edges of the walls for accurately cropping the frame to the flow area and determining the length calibrations. Referring to Figure 4.14, the average of each column from the 1024×312 pixel stagnant liquid image and the Laplacian were normalized to allow plotting on the same figure. The first and last significant negative peaks near each wall were used to define the tube wall regions. Within these regions, the first and last zero of the Laplacian identifies the outer and inner edges of the tube wall. The inner most zeros represent the inner edge of the inner tube walls while the outer zeros represent the outer tube walls.

To rotate the image, the location of the upper outer tube wall was located at both ends of the image using an average of 25 pixels at each end. In this case, the top outer tube wall at the left and right ends of the tube were located at pixels 19 and 21, respectively. Remembering that the numbering starts from the top of the tube, the right end of the tube

was lower than the left end by 2 pixels. This can be observed upon close inspection of Figure 4.13. The curves were nearly identical in shape with the left end (Blue) slightly above the right end (Red). The rotation angle was determined using the arctangent of offset (2 pixels) divided by the distance between the centers of the shaded regions (1024 pixels − 25 pixels = 999 pixels). The rotation angle for the stagnant liquid frame was determined to be 0.115 degrees. The rotation angle for the two-phase flow image was also determined independently to be 0.115 degrees.
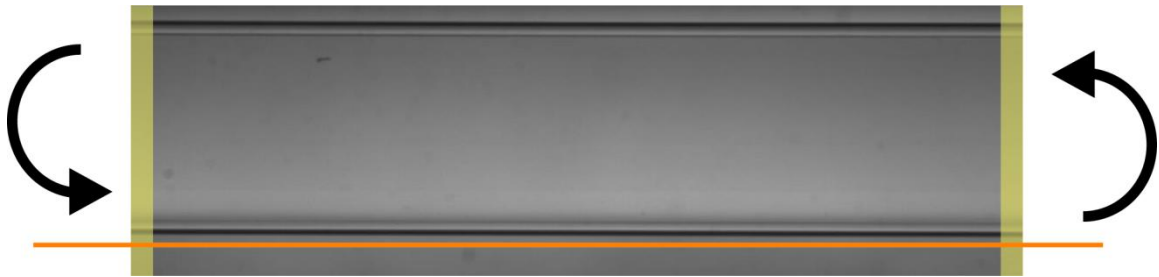
Figure 4.12. Stagnant liquid filled image with rotation sum regions highlights

The stagnant liquid image was used to determine the wall locations. For this calculation, the full 1024×512 image was used and the wall locations were applied to the two-phase flow image using the same coordinates. The entire rotated stagnant liquid image was averaged into a 512 long array. The zeros of the Laplacian were used to locate the inner and outer wall edges. The inner and outer wall locations of the top of the tube were identified to be at pixel 119 and pixel 136, respectively. The inner and outer tube walls of the bottom of the tube were identified to be at pixels 347 and 363, respectively. Non-integer zeros were rounded to the nearest integer. These points were manually verified for the representative stagnant liquid image by zooming in on the zeros in Figure 4.14. The difference between the outer tube walls was used to determine the horizontal length calibration, as shown in Equation (4.51) and detailed in Appendix B. In the 15 mm

194

analysis, the horizontal length calibration was 76.8% of this value due to a magnification effect. This scaling was not necessary for the 7 mm test section.
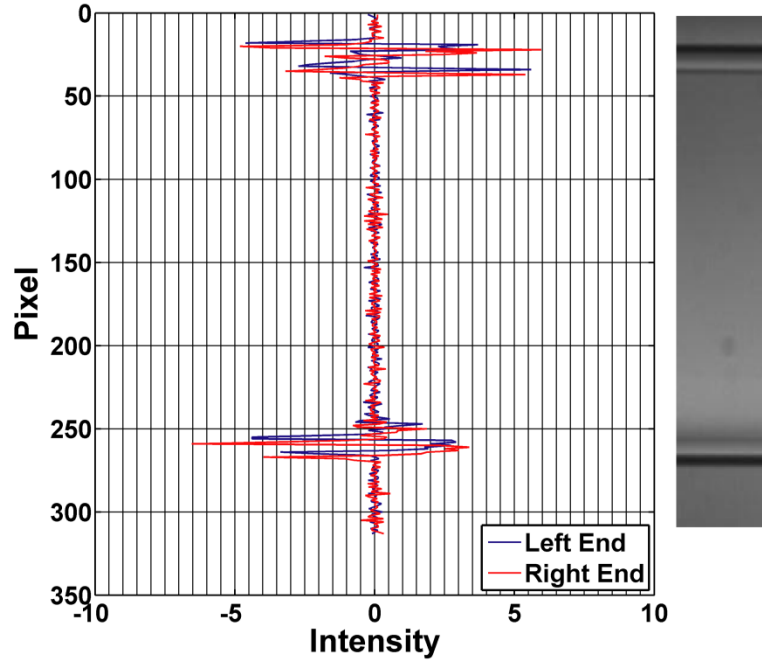
Figure 4.13. Determine rotation angle to rotate images

$$\Delta L = \frac{D_{\text{o}}}{Px_{\text{Tube,B}} - Px_{\text{Tube,T}} + 1}$$
$$= \frac{10.4\,\text{mm}}{362 - 119 + 1} = 4.26 \times 10^{-5}\,\text{m Px}^{-1}$$

(4.51)

The difference between the inner tube wall locations was used, as shown in Equation (4.52), to determine the length calibration in the diameter direction.

$$\Delta D = \frac{D_{\text{i}}}{Px_{\text{B}} - Px_{\text{T}} + 1}$$
$$= \frac{7.75\,\text{mm}}{347 - 136 + 1} = 3.30 \times 10^{-5}\,\text{m Px}^{-1}$$

(4.52)
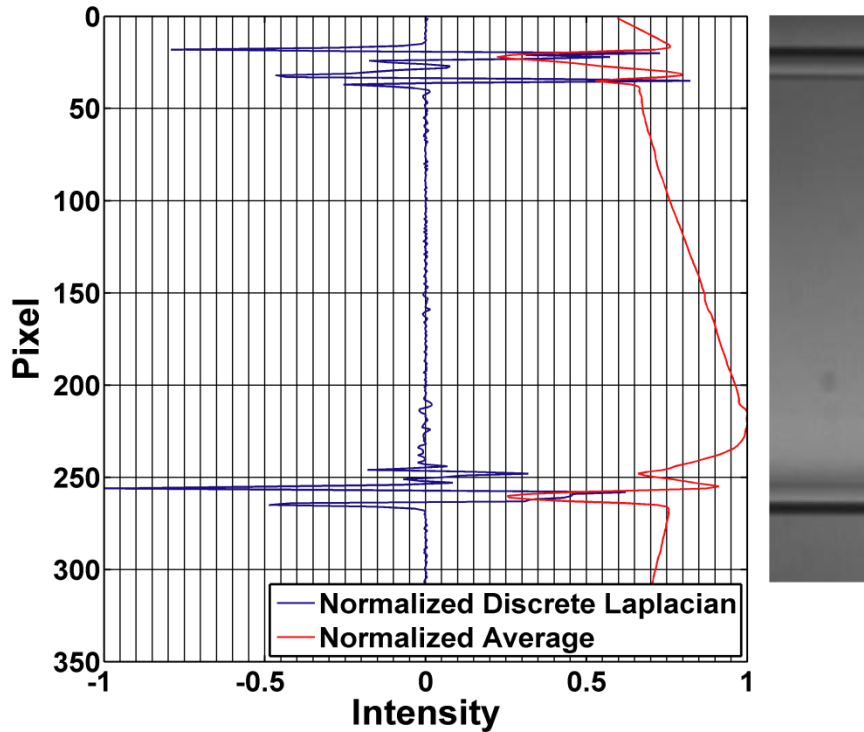
Figure 4.14. Locate tube walls using stagnant liquid image

Before the wall locations found in the stagnant liquid image were applied to the two-phase flow image, the two images were aligned using the outer tube wall locations. Again, zeros of the Laplacian for the two-phase flow image and stagnant liquid images were used, shown in Figure 4.15. The difference in the upper tube wall location between the stagnant liquid and two-phase flow images was used to determine if the camera shifted between the stagnant liquid video capture and the two-phase flow image capture. A shift of 1 pixel in both wall locations was found for the representative two-phase flow image relative to the stagnant liquid image.

196
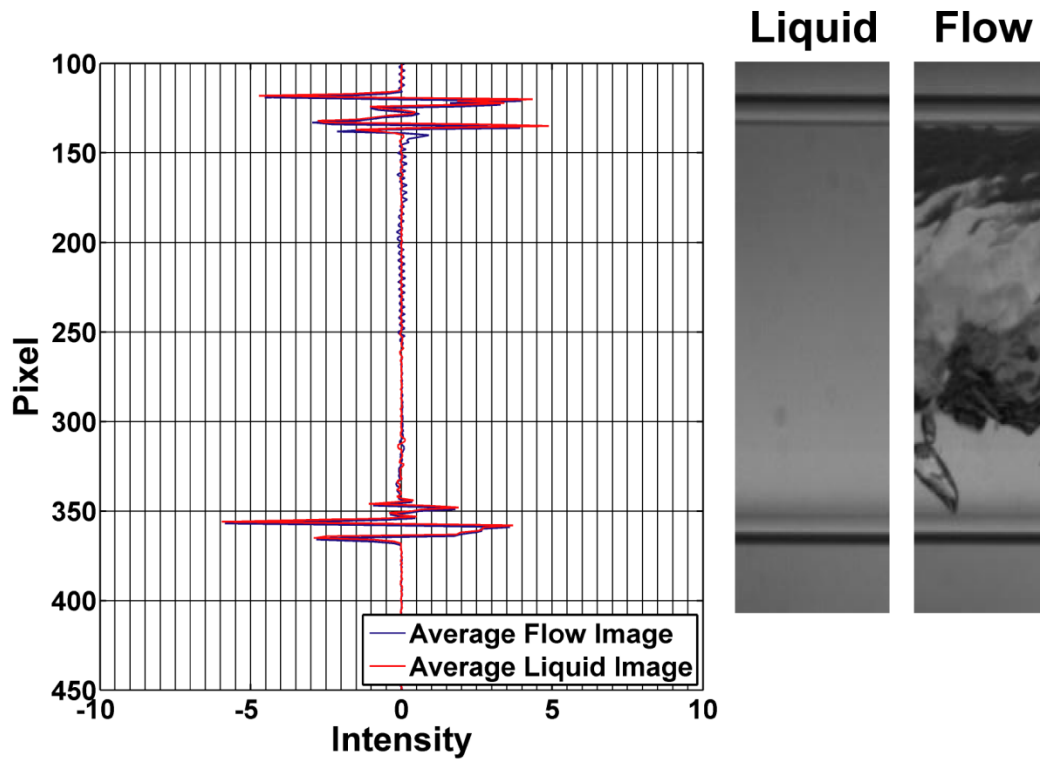
Figure 4.15. Align stagnant liquid filled and two-phase flow image

The inner tube wall locations identified for the stagnant liquid image were shifted by one pixel to be located at pixels 137 and 348. To confirm the locations, the outer wall locations and the last pixels included in the flow area were drawn over half of the two-phase flow image in Figure 4.16. As can be observed, the four edges were located quite well. Using the edge locations, the two-phase flow images were cropped at between pixels 137 and 348 and the stagnant liquid images between 136 and 347, resulting in two images 1024×212 pixels. The cropped two-phase flow and stagnant liquid images are show in Figures 4.17 and 4.18, respectively.
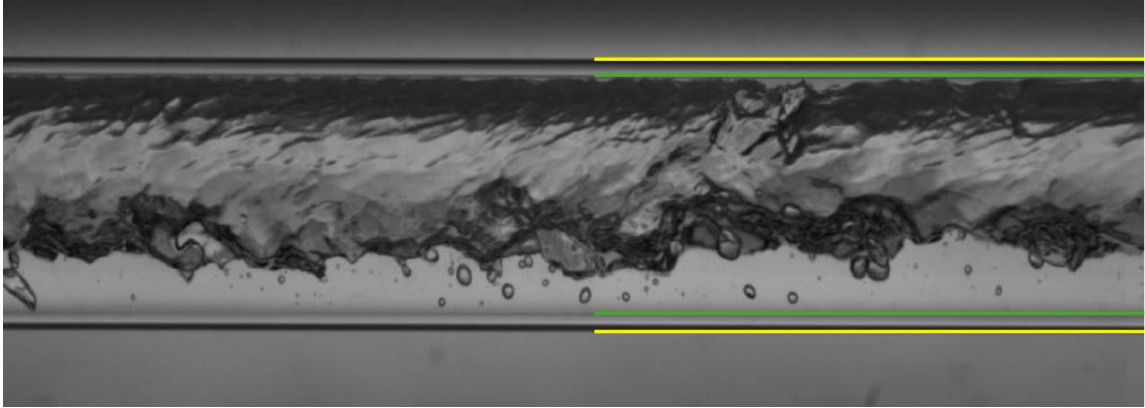
Figure 4.16. Representative two-phase flow image with located edges drawn
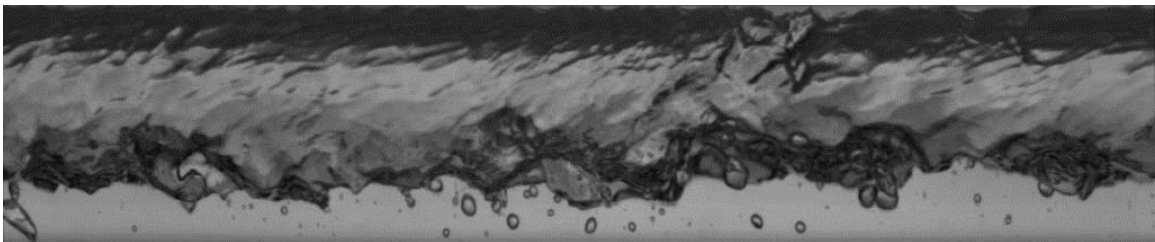
Figure 4.17. Cropped two-phase flow image
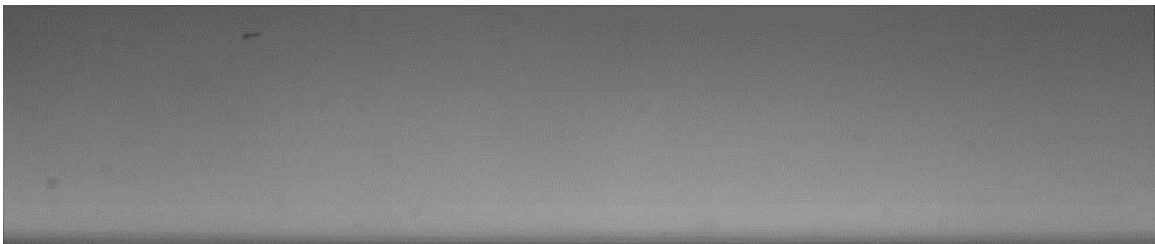
Figure 4.18. Cropped stagnant liquid image

4.4.2.3 Compare video frames

In the following sections, the conversion from the two grayscale images to a binary image representative of the liquid and vapor regions is presented. This procedure was repeated for each frame in the video.

The absolute difference between the cropped 8-bit liquid and flow grayscale images was calculated using the *imabsdiff* function in the Matlab *Image Processing Toolbox* (Mathworks, 2013). This method resulted in any pixel within the two-phase flow image that was darker or brighter (lower or higher in grayscale value) than the corresponding

198

pixel in the stagnant liquid image to appear bright, while locations that appear close to the stagnant liquid image in brightness to appear nearly black. The resulting image is shown in Figure 4.19. This approach reduces any effects of background variations.
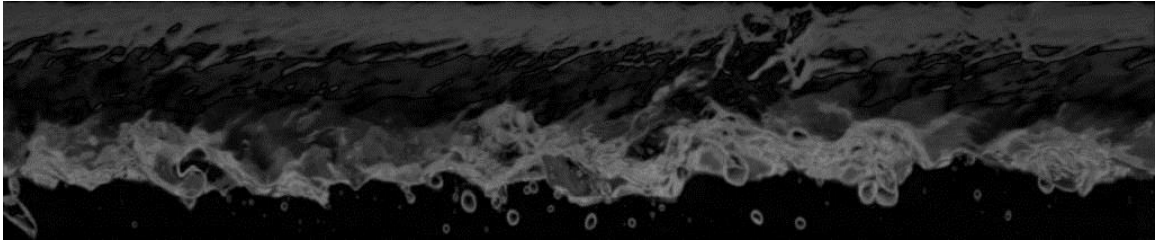
Figure 4.19. Absolute difference between two-phase flow and stagnant liquid image

4.4.2.4 Enhance image

Referring to the absolute difference image (Figure 4.19), the *graythresh* function was used to define a threshold for each grayscale image. This function is designed to provide a threshold value that will convert the grayscale image to a binary image. Here, the threshold calculated using the *graythresh* function was 0.157. However, this value was found to indicate an upper bound on the threshold, while 50% of the threshold represents a value below ideal threshold value. To improve the accuracy of the conversion, the image was enhanced using the *imadjust* function. Grayscale values below 50% of the threshold value were clipped and set to zero. Values above the threshold value were clipped and set to unity. The values between 50% and 100% of the threshold were stretched between 0 and 1, resulting in the enhanced image, shown in Figure 4.20. The result is an image that exhibits a well-defined vapor-liquid interface.

Figure 4.20. Conversion to binary - enhanced image

4.4.2.5 Convert to binary image

To convert the enhanced image shown in Figure 4.20 to a binary image, a conversion threshold value was calculated for the enhanced image, again using the *graythresh* function. The enhanced image threshold in the representative case was calculated to be 0.473. An empirically determined multiple of the enhanced image threshold value was determined for each of the liquid videos used due to the lack of a significant upper film. The 7.0 mm videos showed a noticeable upper film with significant darkening of the vapor-phase. Therefore, a single liquid video could be used because any slight changes in the intensity or angle of the back lighting had little effect on the quality of the conversion. The 15.0 mm test sections were far more sensitive to the liquid video used. Therefore three stagnant liquid videos were used in the conversions with four of the six 15.0 mm data sets using the 2/20/2013 stagnant liquid video and the remaining two data sets each using the their own stagnant liquid video for comparison. The enhanced image threshold multiples used for each stagnant liquid video are shown in Table 4.7. These threshold multiples were applied to the frame analysis of the two-phase flow videos. The sensitivity of the analysis to these empirical threshold values is quantified in Section 4.4.4 by modifying each threshold by $\pm 25\%$.

200

Table 4.7. Binary image conversion threshold multiples

Tube Diameter	Liquid Video Date	Threshold Multiple
7.0 mm	1/6/2013	0.70
15.0 mm	2/20/2013	0.28
15.0 mm	2/27/2013	0.30
15.0 mm	3/1/2013	1.00

A very slight 120 Hz frequency variation in the background intensity was observed due to the 60 Hz electrical frequency of the back lighting. A slight correction was made for this variation in the applied threshold. In the representative image, the correction was -0.002. The *im2bw* function was used to convert the enhanced grayscale image, shown in Figure 4.20, to an initial binary image, shown in Figure 4.21. The enhanced threshold multiplied by the threshold with the 120 Hz correction added was used as the *im2bw* threshold. Thus, the enhanced image threshold calculation for the representative image was $0.7 \times 0.473 - 0.002 = 0.329$

Figure 4.21. Binary image after initial conversion

4.4.2.6 Refining mask

For most videos, this conversion was sufficient for defining the vapor-liquid interface. However, in some low mass flux, low quality points in the 15.0 mm tube, the edge needs additional refinement. This was necessary when significant darkening of the vapor region or significant disturbance of the vapor-liquid interface did not occur. Therefore, an interface refining procedure was used. Although not necessary for the

conversion of the representative image, for consistency, the procedure is applied to all images and is described here.

In this procedure, a lower threshold was applied to a focused area around identified boundaries for frames with few edges. Applying a lower threshold value to the entire image resulted in breakup of the liquid regions. The Canny edge detection algorithm (Canny, 1986) was used to locate edges in the absolute difference between two-phase flow and stagnant liquid image (Figure 4.18). The edge locations identified by the Canny edge detection algorithm are shown in Figure 4.22. The *imdilate* function was used to expand the located edges to an edge refining region of interest, shown in Figure 4.23. For the representative image, the majority of the image was defined to be in the region of interest. However, in the images that require refinement, the region of interest was a thin horizontal band across the image.
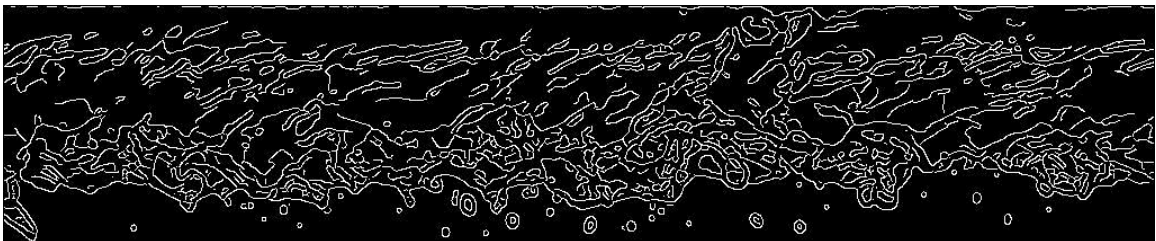
Figure 4.22. Representative image Canny edge detection

Figure 4.23. Representative two-phase flow image edge refining region of interest

The region of interest identified in Figure 4.23 was used to mask the enhanced image, shown in Figure 4.20. The masked image is shown in Figure 4.24. Valid threshold values

202

range from zero to unity. Because the purpose of the refined edge detection was to locate edges in images with few edges, the average of the binary region of interest image was used as the threshold. The average of the region of interest image was found to be proportional to the percentage of the image that was identified as a region of interest. An empirical reduction multiple of 0.8 for the 7.0 mm videos, and 0.7 for all 15.0 mm videos was applied. As discussed above, the slight change for the 120 Hz frequency was applied. For the representative image, the resulting threshold of 0.665 was applied. In this case, a significant portion of the two-phase flow image differs from the stagnant liquid image and was identified as containing an edge. The application of the interface refining procedure was not necessary to detect the vapor-liquid interface, thus the refining threshold was actually higher than the conversion threshold. Again applying the refining threshold using the *im2bw* function, the refining region of interest binary image is shown in Figure 4.25. To quantify the sensitivity of the threshold values and empirical multiples on measured quantities, the threshold multiples were varied in the uncertainty analysis.

Figure 4.24. Enhanced two-phase flow image with region of interest mask applied

Figure 4.25. Binary image derived using refining region of interest

4.4.2.7 Combine the binary images

The two binary images, Figure 4.21 and Figure 4.25 were added together to a single binary image shown in Figure 4.26. The liquid-phase is shown as black, while the vapor-phase is shown white.

Figure 4.26. Combination of converted binary images

4.4.2.8 Clean binary image for analysis

As can be observed in Figure 4.25, there are "liquid" regions internal to the vapor regions. Because liquid entrained in the vapor-phase cannot be identified using this conversion technique, these areas are not actually liquid. The *bwmorph* function with an infinite "*bridge*" was used to remove thin liquid bridges that connect the false liquid region in the vapor core to the liquid film. The *imfill* and *bwareaopen* function were used to remove the black regions that were completely surrounded by white. For this conversion, the right and left end of the tube are considered to be vapor. The two-phase flow image (Figure 4.17) is reproduced in Figure 4.27, while the resulting binary two-phase flow image is shown in Figure 4.28.
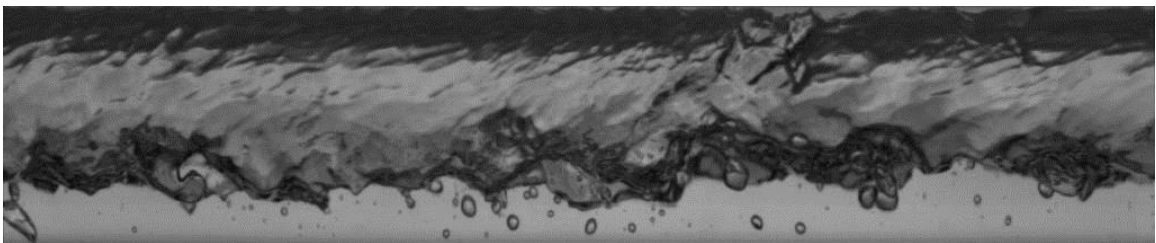
Figure 4.27. Reproduced cropped two-phase flow image
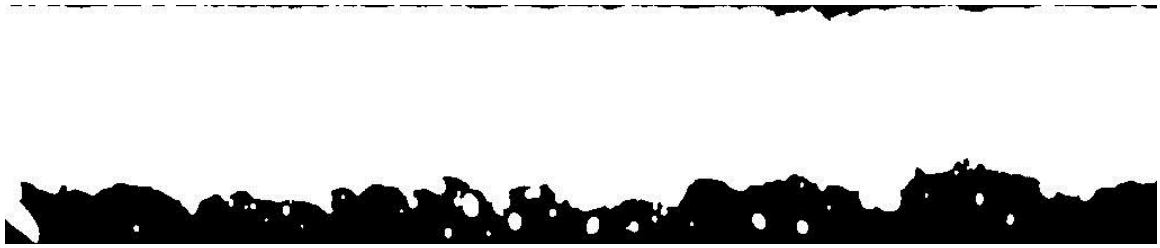
Figure 4.28. Binary two-phase flow image

To measure film thickness and quantify of vapor entrained in the liquid phase, the small bubbles entrained in the liquid film are removed from the binary two-phase flow image to create a second binary image, called the binary film image. Small bubbles, defined as vapor regions with an area equivalent to a circle with a diameter less than 3 mm were removed from the liquid film. The resulting binary film image is shown in Figure 4.29.
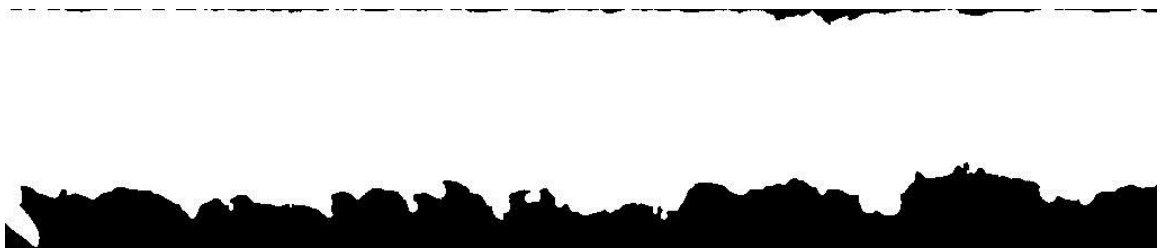
Figure 4.29. Binary film image

4.4.3 Analysis and Interpretation of Processed Images

The binary images obtained from the two-phase flow images were processed to determine quantitative values that identify the flow. A flow diagram for the video analysis is shown in Figure 4.30, and the process is described in this section. Every frame of the one-second and four-second two-phase flow videos was analyzed individually using the procedure described here. . The binary film image (without vapor entrainment) was used to quantitatively define the flow regime, measure the liquid film thicknesses, and film void fraction. The binary two-phase flow image was used to measure the total void fraction. The binary image is shown schematically in (A) of Figure 4.31. The frame

205

averaged quantities were averaged over each video to determine the flow regime, void fraction, and film thicknesses for the data point.
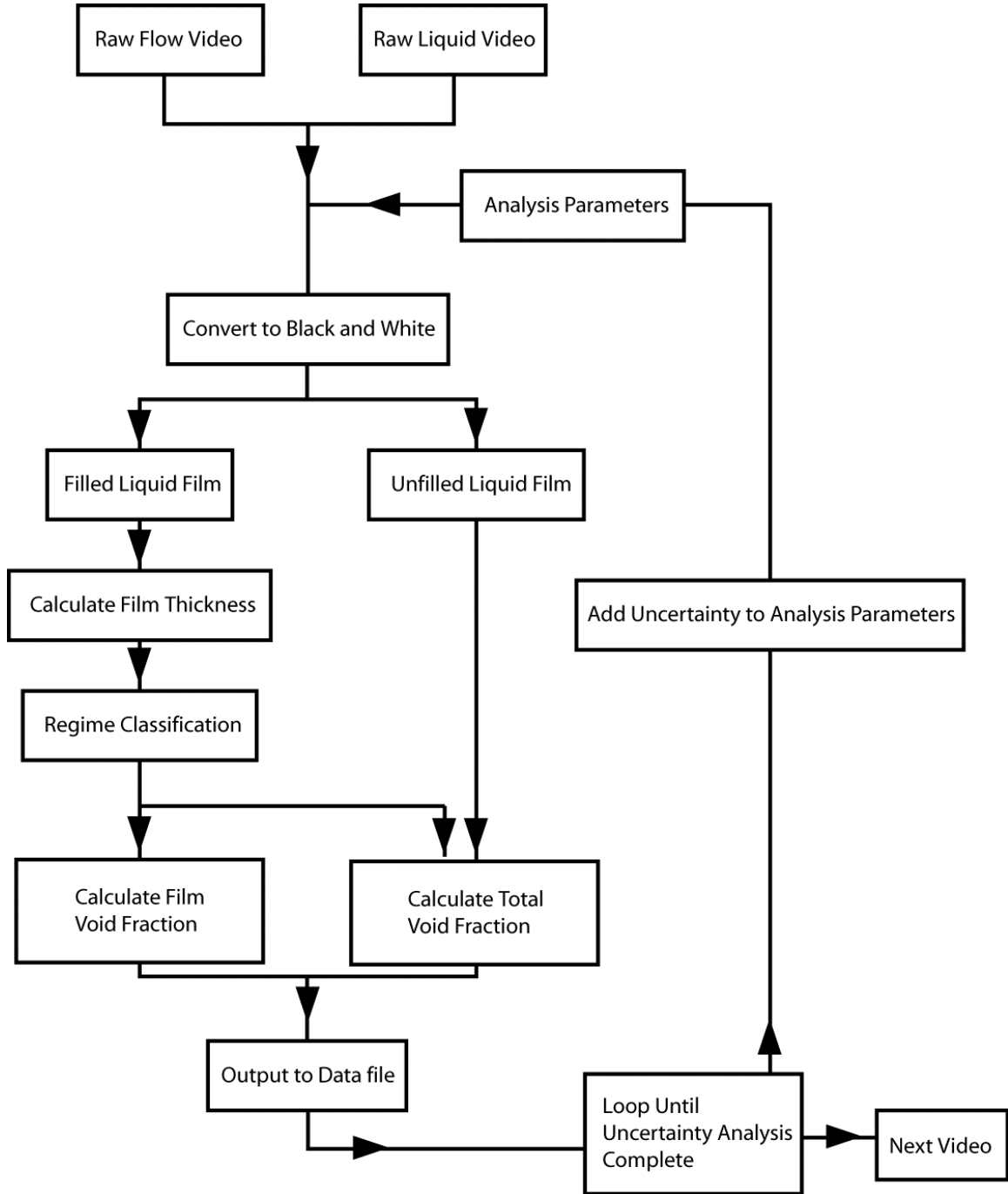
Figure 4.30. Video analysis calculation flow diagram
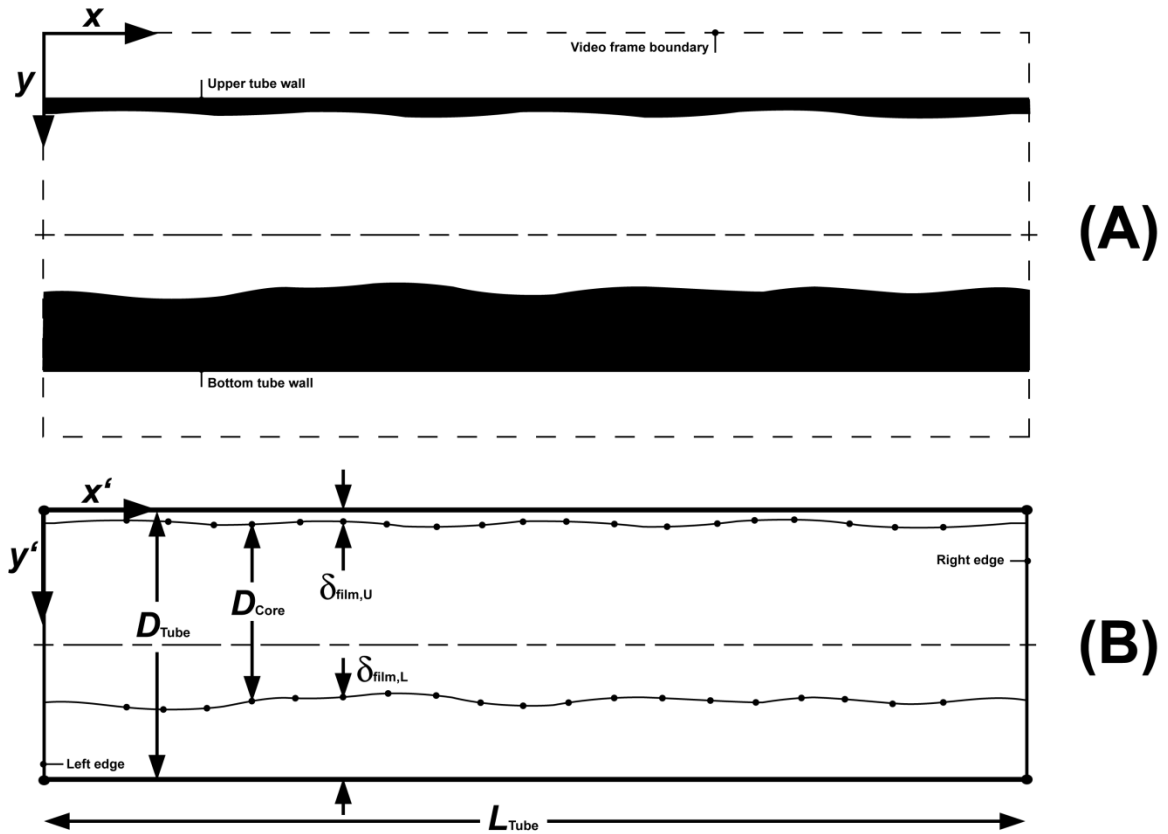
Figure 4.31. Location of vapor-liquid interface from binary image

The image was subdivided into 1024 vertical slices, one for each pixel, and scanned for the coordinates (x',y') of the vapor liquid interface as shown in (B) of Figure 4.31. The vapor-liquid boundary was identified using the vapor (white) pixel locations. The identified vapor-liquid interface based on (x',y') coordinates overlaid on the cropped 1024 × 212 image is shown in Figure 4.32. For the first column of the representative image (left edge), the vapor region started at the first pixel, i.e., no liquid film was present at the top of the image. The last pixel in the vapor region was pixel 190. There was only one vapor region in this column. The lower liquid film was 22 pixels (212 – 190) thick.
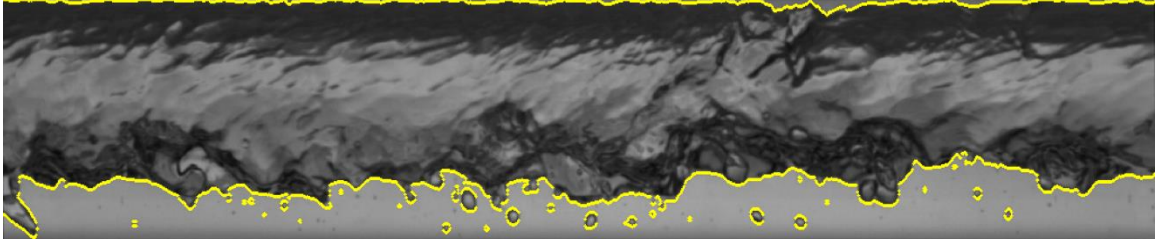
Figure 4.32. Identified vapor-liquid interface overlaid on representative frame

Using the vertical length calibration determined from the edge location (3.30×10^{-5} m Px^{-1}), the lower film thickness of the first column (the left most edge of Figure 4.32 and 4.33) was calculated to be 0.00073 m. Repeating this for all slices in the image, the average upper and lower liquid film thicknesses were calculated to be 6.75×10^{-5} m and 0.0015 m, respectively. Repeating this procedure for the entire binary film video, the average upper and lower liquid film thicknesses were calculated to be 7.1×10^{-5} m and 0.0012 m, respectively. The local film thickness and frame-average film thickness are shown in Figure 4.33. Using the local film thicknesses for each frame, the standard deviation of the film thicknesses was determined. The standard deviations of the upper and lower film thickness for the representative frame were calculated to be 6.88×10^{-5} and 0.00040 m, respectively. Averaging the standard deviation from each frame over the entire video, the standard deviations of the upper and lower film thickness for the video were calculated to be 4.99×10^{-5} and 0.00043 m, respectively.
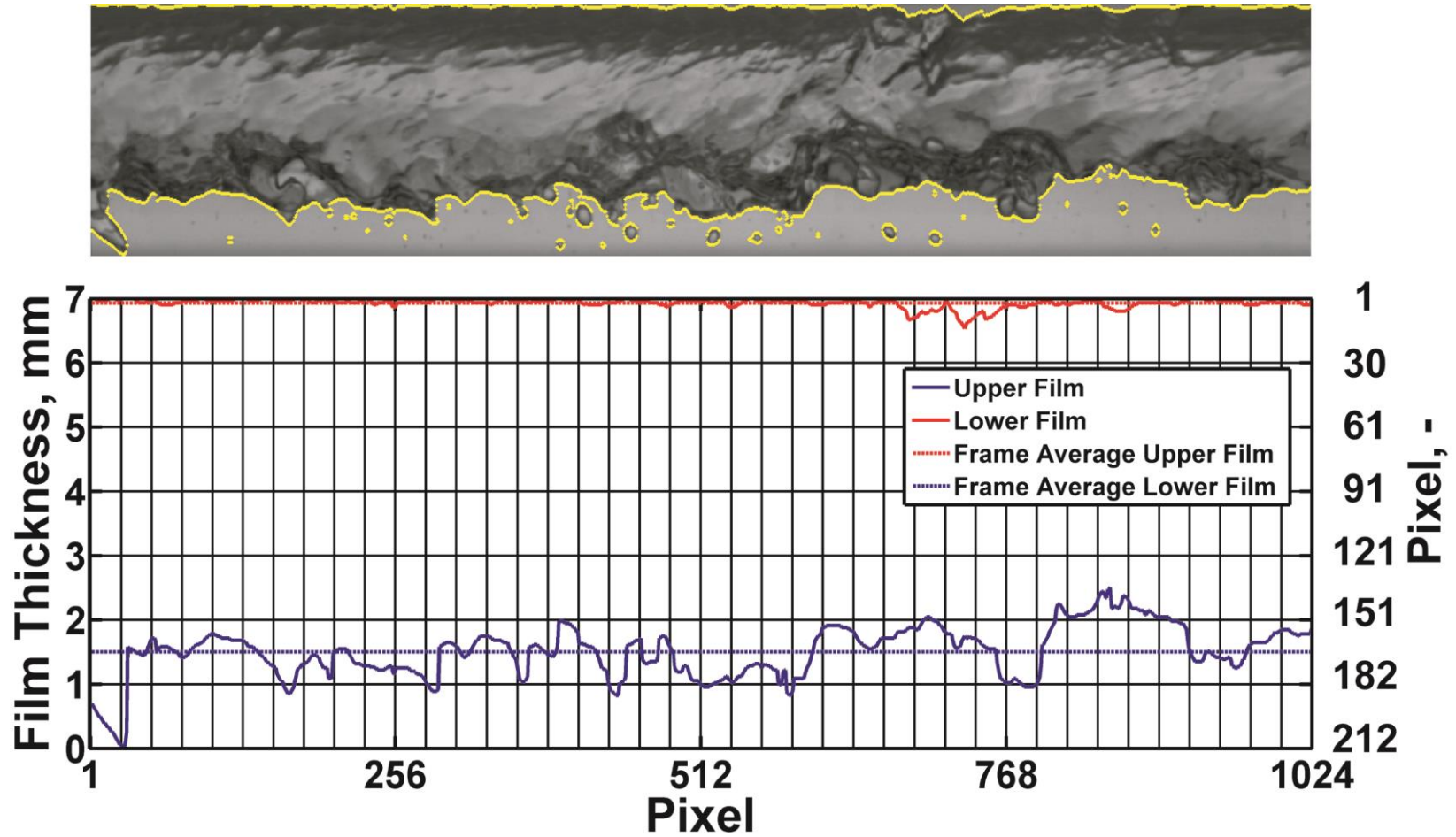
Figure 4.33. Cross sectional film thicknesses with representative two-phase flow image

Once the film thickness has been determined for each frame, the frame was quantitatively characterized into one of four flow regimes: liquid, intermittent, wavy, and annular. The frame was classified as liquid if the frame, less small bubbles, was completely liquid. It was classified as intermittent flow if the liquid bridges from the bottom to the top of the tube for more than 5 pixels. If the flow was not liquid or intermittent, the flow was classified as annular or wavy. If the lower liquid film was less than 5% of the diameter, the flow was classified as annular flow. To validate the annular flow assumption, a comparison was made of calculated void fractions using both the truncated circle and circular assumptions, as shown in Figure 4.34. Depending on the upper film thickness, the ratio of the circular void fraction to the truncated circle void fraction ranges from 0.98 ($\delta_{\text{Film,U}} = 0$) to 1 ($\delta_{\text{Film,U}} = 2\%$ D_i) indicating a small-to-negligible difference between the two calculations.
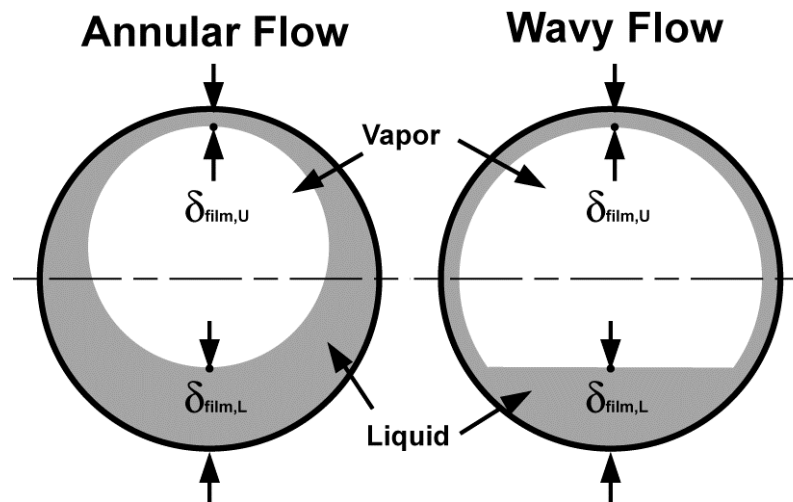
Figure 4.34. Comparison of void fraction assumptions

For the representative data point, the entire video was classified as wavy flow. However, every video frame for any case does not necessarily have a single regime classification across all the frames. In some cases, multiple regimes were found in a

single video, which indicates a transition region. This type of frame-by-frame classification was used by Jassim (2006). In the present study, a data point was classified as the dominant regime when 75% of the frames were classified as a single regime. Otherwise, the data point was classified as a transitional point.

The two void fractions were calculated next: one using the binary film image (without vapor entrained in the liquid phase) and one using the binary two-phase flow image. With video from a single angle and no cross sectional images, assumptions about the three dimensional vapor-liquid interface were required. Both void fraction calculations were made using the same assumptions given in Figure 4.35:

A. Small bubbles, defined as having a diameter in the cross-sectional plane less than 3 mm, were assumed to have a circular cross section. Location within the cross section is not considered to be significant for this assumption as shown in i to iii.

B. Regime-specific assumptions based on frame regime classification:

 iv. Annular flow was assumed to have a circular vapor core cross section

 v. All other regimes were assumed to have a vapor core that could be approximated as a truncated circle
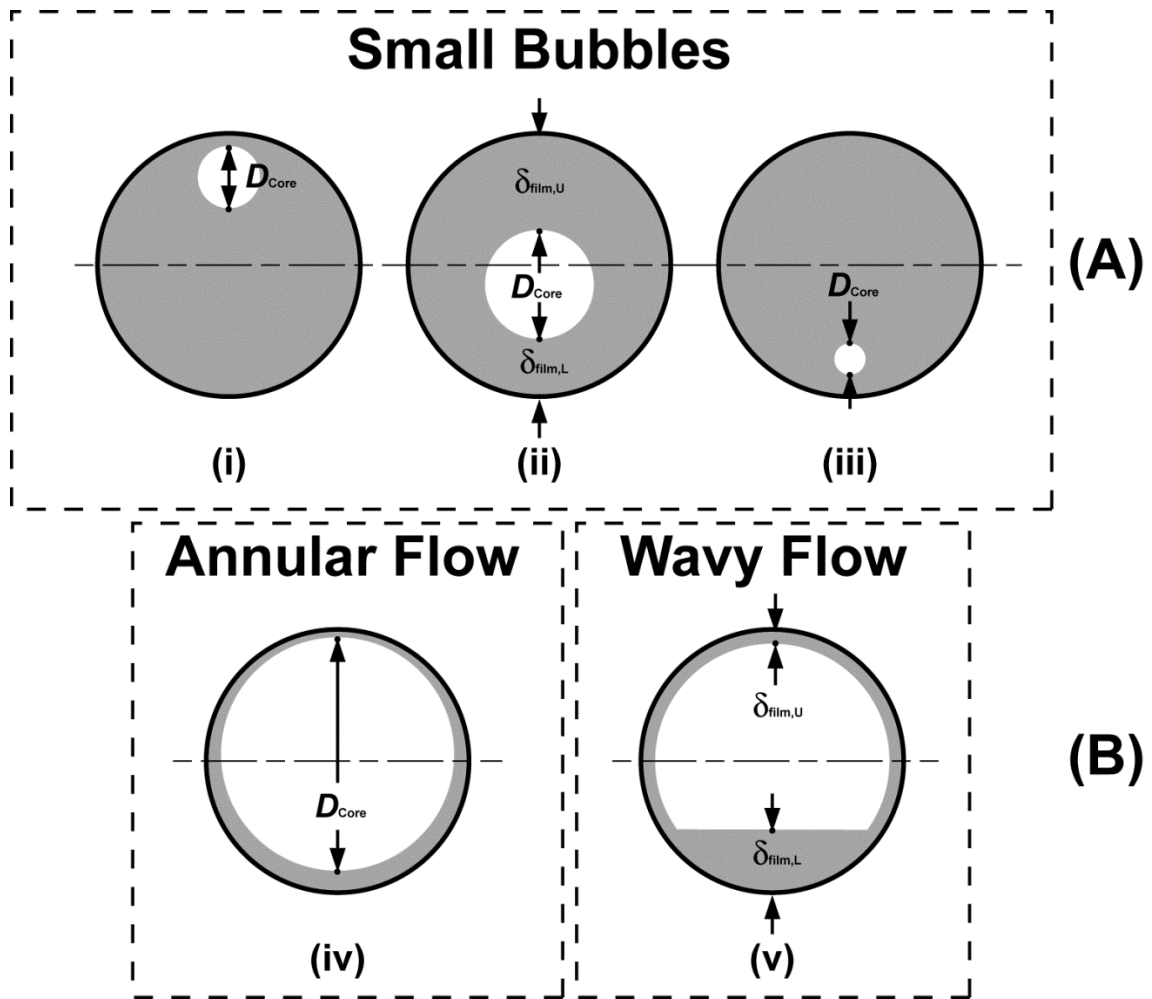
Figure 4.35. Void fraction assumptions

The areas of the circular cross section in assumptions (i) to (iv) were calculated by using $1 + (y'_{top} - y'_{bottom})$ pixels (Figure 4.31) as the diameter of the circular vapor core region. For example, in the first column of the representative film image, the vapor region starts at pixel 1 and ends at pixel 190. Based on this approach, the core diameter would be 190 pixels. The truncated circle approximation was calculated as shown in Figure 4.36. First the core diameter, D_{core}', was calculated assuming a uniform film thickness equal to the upper film thickness as shown in i. In the case of the first column of the representative frame, the core diameter was equal to the total diameter (212 pixels), resulting in an area of 35,300 square pixels. Second the area corresponding to the lower

liquid film was removed using the idealizations shown in (ii) (portion of a circle) and (iii) (triangle above the pool). The segment area, $A_{Segment}$, was calculated to be 7,370 square pixels using Equations (4.53) to (4.55).

$$h = \frac{D_{core}'}{2} - \delta_{film,L} = \frac{212}{2} - 22 = 84 \qquad (4.53)$$

$$\theta = 2 arc\cos\left(\frac{2h}{D_{core}'}\right) = 1.36\,\text{radians} \qquad (4.54)$$

$$A_{Segment} = \frac{\theta}{2\pi}\frac{\pi}{4}\left(D_{core}'\right)^2 = 7,370 \qquad (4.55)$$

The triangle area was calculated using the cord length, l_{cord}, as shown in Equation (4.56) to be 5,430 square pixels.

$$l_{cord} = 2\sqrt{\left(\frac{D_{core}'}{2}\right)^2 - h^2} = 5,430 \qquad (4.56)$$

Using the core diameter area, segment area, and triangle area, the truncated cross section was calculated to be 33,360 square pixels:

$$\begin{aligned} A_{Trunc} &= A_{Circle} - A_{Segment} + A_{Triangle} \\ &= 35,300 - 7,370 + 5,430 = 33,360 \end{aligned} \qquad (4.57)$$
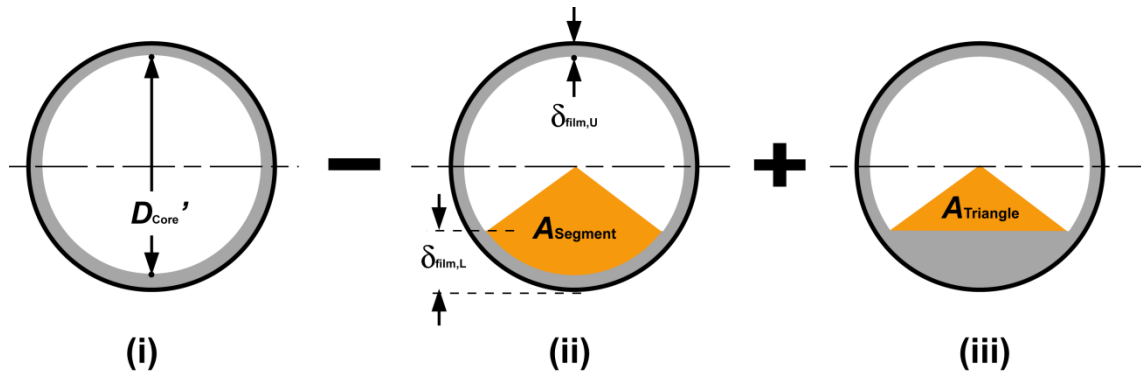
Figure 4.36. Truncated circle area calculation

Using the length calibrations, 3.30×10^{-5} m Px^{-1} in the diameter direction and 4.24×10^{-5} m Px^{-1} in the horizontal direction, the void area was calculated to be 3.64×10^{-5} m^2. This compares to the total tube cross sectional area of 3.85×10^{-5} m^2. The void and total tube cross sectional areas were multiplied by 4.24×10^{-5} m Px^{-1}, resulting in a void volume of 1.55×10^{-9} m^3 and tube cross sectional volume of 1.64×10^{-9} m^3. Using the void and cross sectional volumes, the film void fraction in the first segment was calculated to be 0.94.
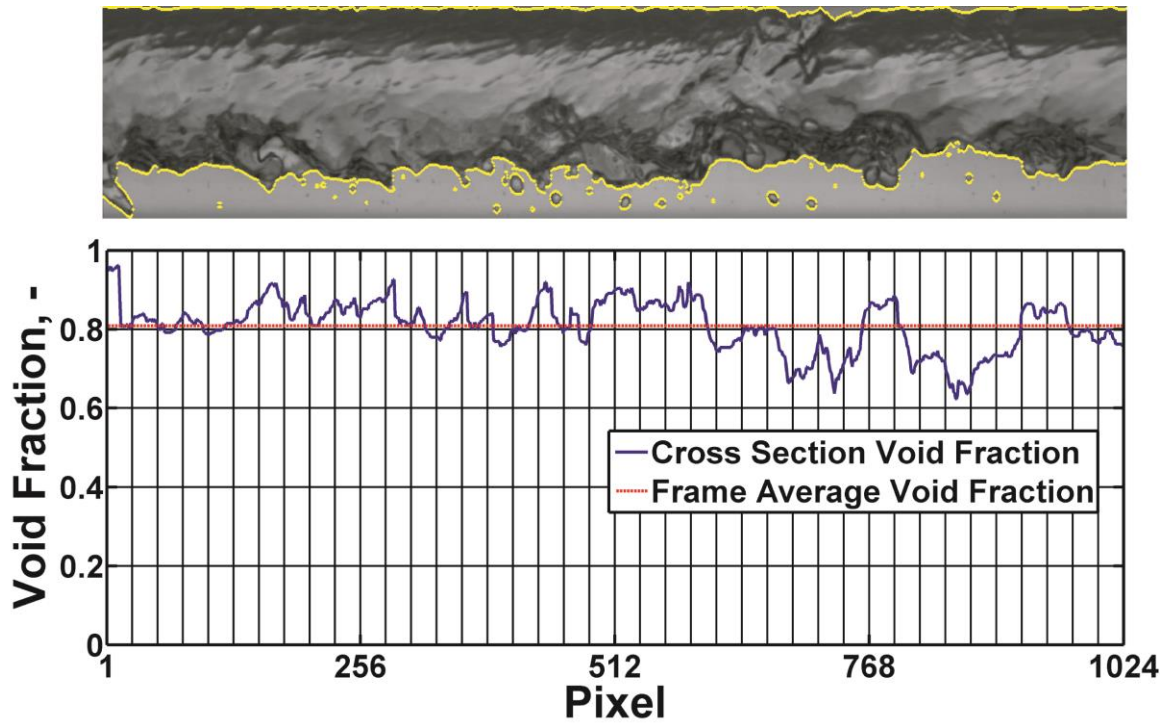
Figure 4.37. Cross sectional void fraction with representative two-phase flow image

This procedure was repeated for each horizontal pixel. The local void fraction with frame average is shown in Figure 4.37. Because no small vapor bubbles in the first column of the two-phase flow image were suppressed when creating the film image, the representative segment flow void fraction was also 0.94. The average film void fraction for the first frame and the entire set of 1,001 video frames were calculated to be 0.808 and 0.851, respectively. The average flow void fraction for the first frame and the video were calculated to be 0.809 and 0.851, respectively.
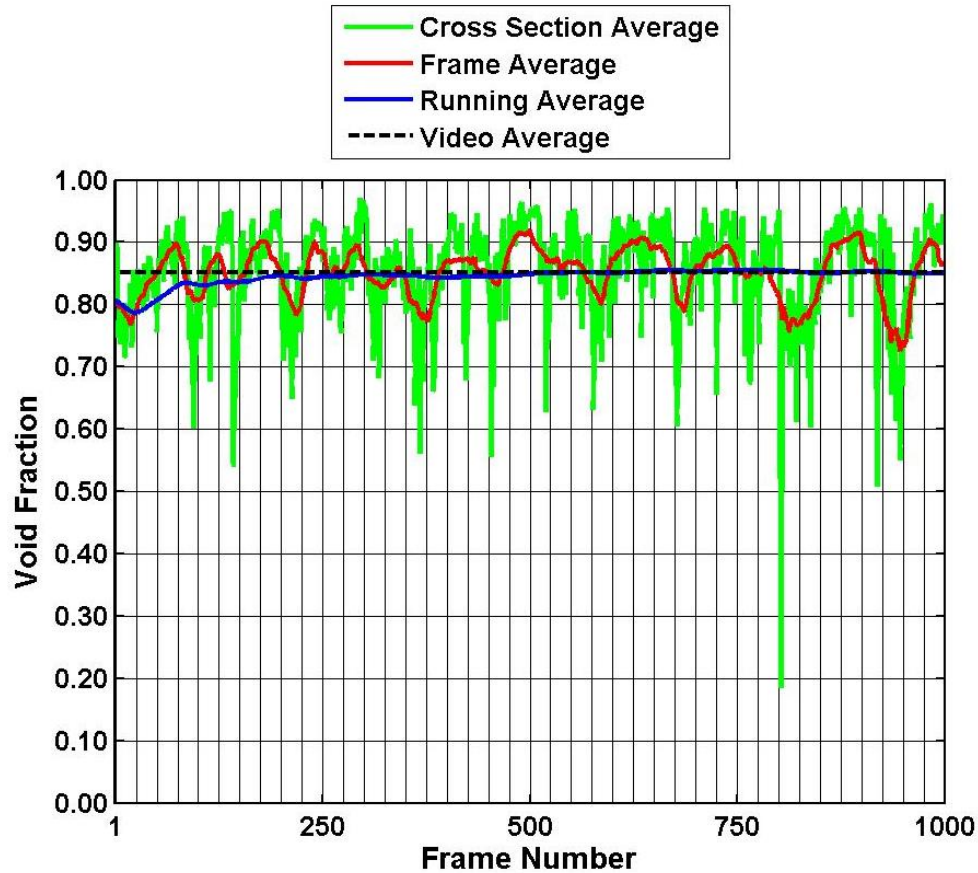
Figure 4.38. Void fraction by video frame

The cross section void fraction at pixel 500, frame average, running average, and video average for the representative data point are shown in Figure 4.38. As would be expected, the cross section average varies significantly due to the dynamic nature of two-phase flows. The frame average shows less variation. The running average approaches the frame average by approximately frame 500, indicting the analysis results in an accurate average void fraction.

Of interest for heat transfer applications is the amount of liquid contained in the liquid pool and the percentage of the liquid that is contained in the liquid pool rather than the upper film. Because the total inventory of vapor contained in the liquid film was already evaluated, the binary film images were used to calculate the amount of liquid in the liquid

pool, neglecting entrained vapor. The cross sectional area of the liquid pool, A_{Pool} in Figure 4.39, was calculated in a manner similar to that of the wavy regime void fraction, shown in Figure 4.36, except the upper film thickness was assumed to be zero. For the first column of the representative image, the segment area was 7,370 square pixels and the triangle area was 5,430 square pixels. The cross sectional area and volume were calculated to be 2.11×10^{-6} m^2 and 9.01×10^{-11} m^3, respectively using the length calibrations. The fraction of liquid to total volume in the representative cross section was 5.5%. Because the upper film thickness was zero, the cross section void and liquid pool sum to account for 100% of the cross section. When the upper film thickness was nonzero, subtracting the fraction of liquid in the liquid pool from the total volume yields the percentage of liquid contained in the upper liquid film. For the entire video, the percentage of the volume in the liquid film was 12%, while the percentage of the liquid contained in the liquid pool was 79%. The total liquid fraction in the cross section was 0.149.
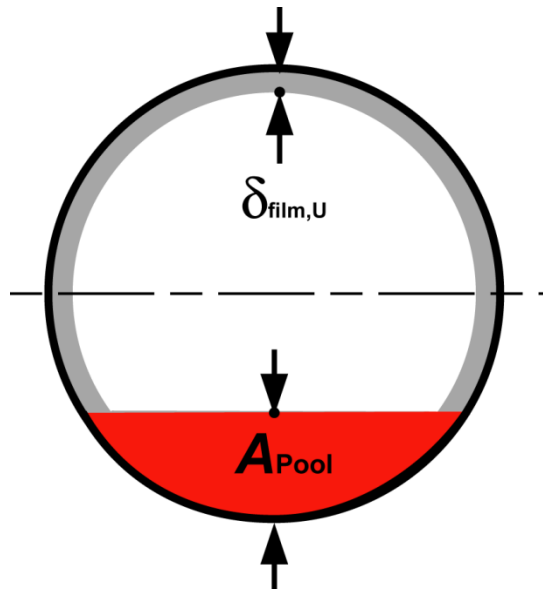
Figure 4.39. Liquid inventory in liquid pool schematic

4.4.4 <u>Accuracy of Analysis</u>

The accuracy of the visualization analysis in determining void fraction, and upper and lower film thickness was quantified in three ways:

1) By varying the empirically determined threshold multiples by ±25% to quantify the sensitivity of the analysis to these threshold multiples.

2) By altering the binary image vapor-liquid boundary by shrinking and expanding the liquid region by 1 pixel in every location, as shown in Figure 4.40, to quantify the sensitivity of the results to the resolution of the videos.
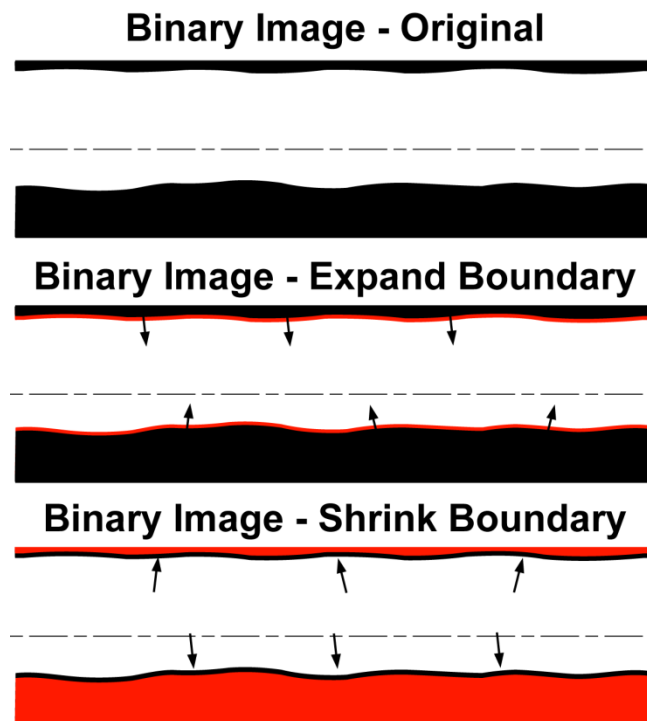
Figure 4.40. Video resolution sensitivity schematic

3) By comparing the analysis results of the one-second video to the four-second low frame rate videos that were processed using the unaltered thresholds

Every frame in the one-second video was processed five times: once for the original analysis, twice for the threshold sensitivity (once with +25% and once with -

25%), and twice for the resolution sensitivity. Each analysis produced a set of results (flow regime, void fraction, film thicknesses, etc.) The difference between the results of the original analysis of the one-second video and the four uncertainty analyses of the one-second video from 1) and 2) was used to quantify the reliability of the analysis procedure. To quantify the sensitivity of the results to the duration of the video and the frame rate, the difference between the results of the one-second and the longer and lower frame rate four-second video is calculated. However, earlier, it was shown that the running average values approach the video averages by approximately frame 500, see Figure 4.38. The total uncertainty in the flow void fraction for the representative void fraction was then calculated to be 0.041 as shown in Equation (4.58). In this case, the uncertainty associated with decreasing the vapor region by one pixel had the greatest effect on uncertainty.

$$
\begin{aligned}
U_{\alpha_{\text{Flow}}} &= \sqrt{\left(\Delta_{\alpha_{\text{Flow,125\%}}}\right)^2 + \left(\Delta_{\alpha_{\text{Flow,75\%}}}\right)^2 + \left(\Delta_{\alpha_{\text{Flow,+1}}}\right)^2 + \left(\Delta_{\alpha_{\text{Flow,-1}}}\right)^2 + \left(\Delta_{\alpha_{\text{Flow,Long}}}\right)^2} \\
&= \sqrt{\left(-0.002\right)^2 + \left(0.003\right)^2 + \left(0.017\right)^2 + \left(-0.038\right)^2 + \left(0.003\right)^2} \\
&= 0.851 \pm 0.041
\end{aligned}
\tag{4.58}
$$

In most cases, the results of the five analyses on the one-second video and the analysis of the four-second video were very close to one another. Excluding data points classified as a transition point, the percentage of frames in each regime differed by an average of 1% between the two videos. The average lower film thicknesses and void fractions varied by an average of 5% and 1%, respectively.

CHAPTER 5. RESULTS AND DISCUSSION

In this chapter, the experimental results from the present study are presented followed by a comparison of the data with predictions of correlations from the literature.

5.1 Experimental Results

The two-phase flow regime and flow characteristics of propane are presented first. Frictional pressure gradient and heat transfer coefficient results for *n*-pentane, R245fa, and R245fa/*n*-pentane follow.

5.1.1 <u>Flow Regime and Flow Characteristics</u>

Two-phase propane flow visualization results are presented in this section. Flow regime results are presented first, followed by void fraction and film thickness results. Sample video frames for $G \sim 150$ kg m^{-2} s^{-1}, $P \sim 952$ kPa and qualities ranging from 0.02 to 0.9 in the 7.0 and 15.0 mm internal diameter (ID) tubes are shown in Figures 5.1 and 5.2, respectively. In both cases, the flow was observed to be shear-dominated annular flow at high qualities. As the quality decreases, the flow transitions to gravity controlled wavy flow. In some cases, intermitted flow was observed at very low qualities where the liquid inventory was sufficient to bridge the liquid pool to the top of the tube.
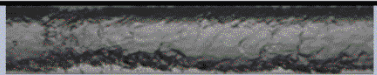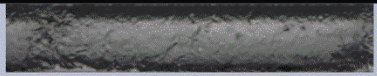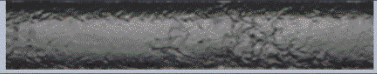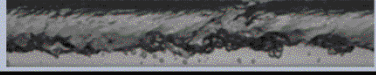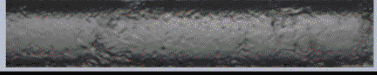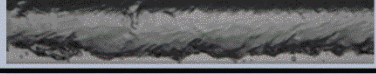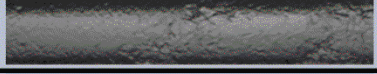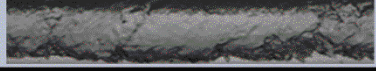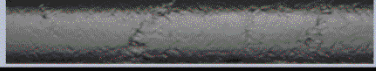
Quality		Quality	
0.02		0.52	
0.09		0.61	
0.21		0.69	
0.27		0.8	
0.35		0.85	
0.44		0.9	

Figure 5.1. Sample set of 7.0 mm ID tube videos at $G = 150$ kg m^{-2} s^{-1} and $P = 952$ kPa
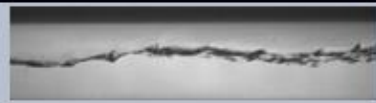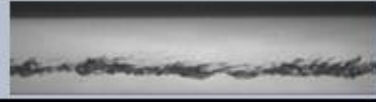
Quality		Quality	
0.06		0.49	
0.11		0.59	
0.2		0.73	
0.29		0.79	
0.4		0.89	

Figure 5.2. Sample set of 15.0 mm ID tube videos at $G = 150$ kg m^{-2} s^{-1} and $P = 952$ kPa

Results for both diameters are compared in Figure 5.3 at three similar qualities with the binary images of the vapor-liquid interface also shown. Referring to Figure 5.3or comparing Figures 5.1 and 5.2, significant differences in flow pattern were observed with increasing diameter. Substantial disturbances were clearly observable in the upper film in the 7.0 mm results at qualities below 0.5. In the 15.0 mm tube, very slight disturbances

221

were observed only at the highest mass fluxes at qualities below 0.5. Additionally, the 7.0

mm diameter results show a significant and well defined upper film in the wavy regime.

The 15.0 mm ID data does not show the same well defined upper film in the wavy

regime.

$G = 300$ kg m^{-2} s^{-1} $P = 1218$ kPa				
Flow Images				
Quality	**7.0 mm**	**Quality**	**15.0 mm**	
0.19		0.20		
0.45		0.46		
0.73		0.75		
Binary Images				
Quality	**7.0 mm**	**Quality**	**15.0 mm**	
0.19		0.20		
0.45		0.46		
0.73		0.75		
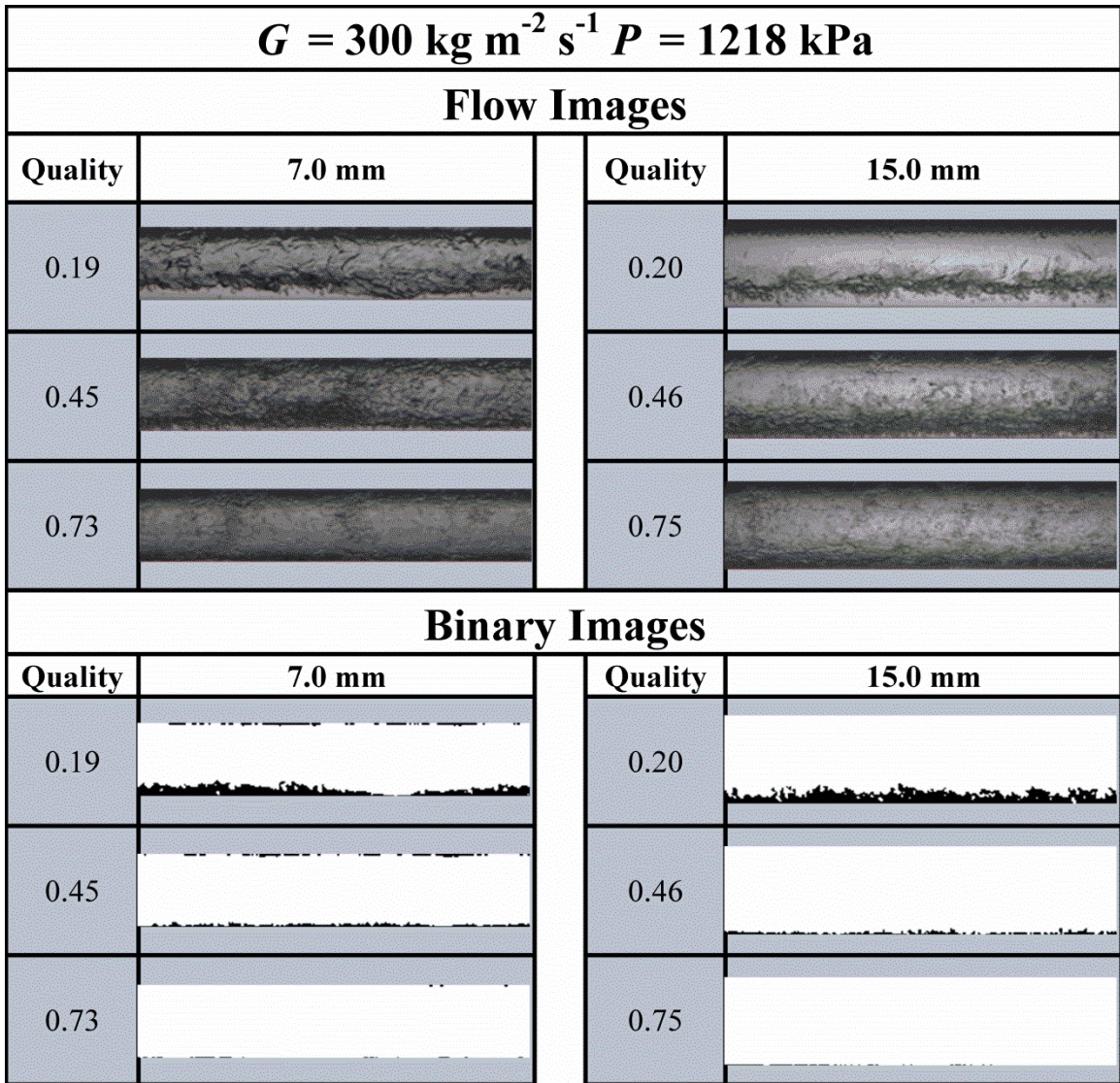
Figure 5.3. Comparison of flow videos for 7.0 and 15.0 mm ID tubes

At certain conditions, very low quality ($q < 0.05$) and low mass flux ($G \sim 75$ kg m^{-2} s^{-1}), mid to high quality ($q > 0.5$) and high mass flux ($G \sim 300$ kg m^{-2} s$^{-1)}$, a well defined and significant upper film was observed, indicating that the difference observed over the

remainder of the flow is a characteristic of the flow and not a limitation of the video analysis. In the 7.0 mm ID tube, surface tension and inertia forces are sufficient to maintain an upper film while in the 15.0 mm tube, gravitational forces deplete the film liquid inventory by causing the liquid to pool at the bottom of the tube. Relevant dimensionless parameters describing these forces are the Bond number (Bo = $\rho\ g\ D^2\ \sigma^{-1}$), liquid only Weber number (We$_{lo}$ = $G^2\ D\ \rho_l^{-2}\ \sigma^{-1}$), and dimensionless gas velocity or modified Froude number (J_G^* = $G\ q\ (D\ g\ \rho_v\ (\rho_l - \rho_v)^{-0.5}$). Comparing the 7.0 and 15.0 mm ID tubes, for otherwise identical conditions, the Bond number increases by 4.6 times in the 15 mm ID tubes, indicating higher gravitational effects relative to surface tension. Similarly, the Weber number increases by 2.1 times, indicating higher inertia effects relative to surface tension. The dimensionless gas velocity decreases to 0.7 times the 7.0 mm tube value, indicating higher gravitational effects relative to inertia. At P = 952 kPa, the Bond number decreases from 150 in the 15.0 mm tube to 30 in the 7.0 mm tube. The Weber number ranges from 12 to 500 in the 7.0 mm tube, and 24 to 460 in the 15.0 mm tube. The dimensionless gas velocity ranges from 0.13 to 15.4 in the 7.0 mm tube, and 0.06 to 6.3 in the 15.0 mm tube.

5.1.1.1 *Flow Regime*

As discussed in Chapter 4, each frame was classified into a flow regime using the lower film characteristics. The number of frames in each regime, as a percentage of the total number of frames, is shown in Figure 5.4for each 952 kPa data point in the 7 mm tube. From the right end of each figure, approaching a quality of one, annular flow was observed in every case. As the quality decreased, the flow transitioned to wavy flow. Finally, intermittent flow was observed at low qualities in a portion of the frames for each of these cases. However, only the 150 kg m^{-2} s^{-1} mass flux case had greater than the

223

threshold of 75% of the frames in the intermittent regime to be classified as an intermittent data point. The lowest quality points for the other three mass flux cases shown in Figure 5.4 were classified as transitional.
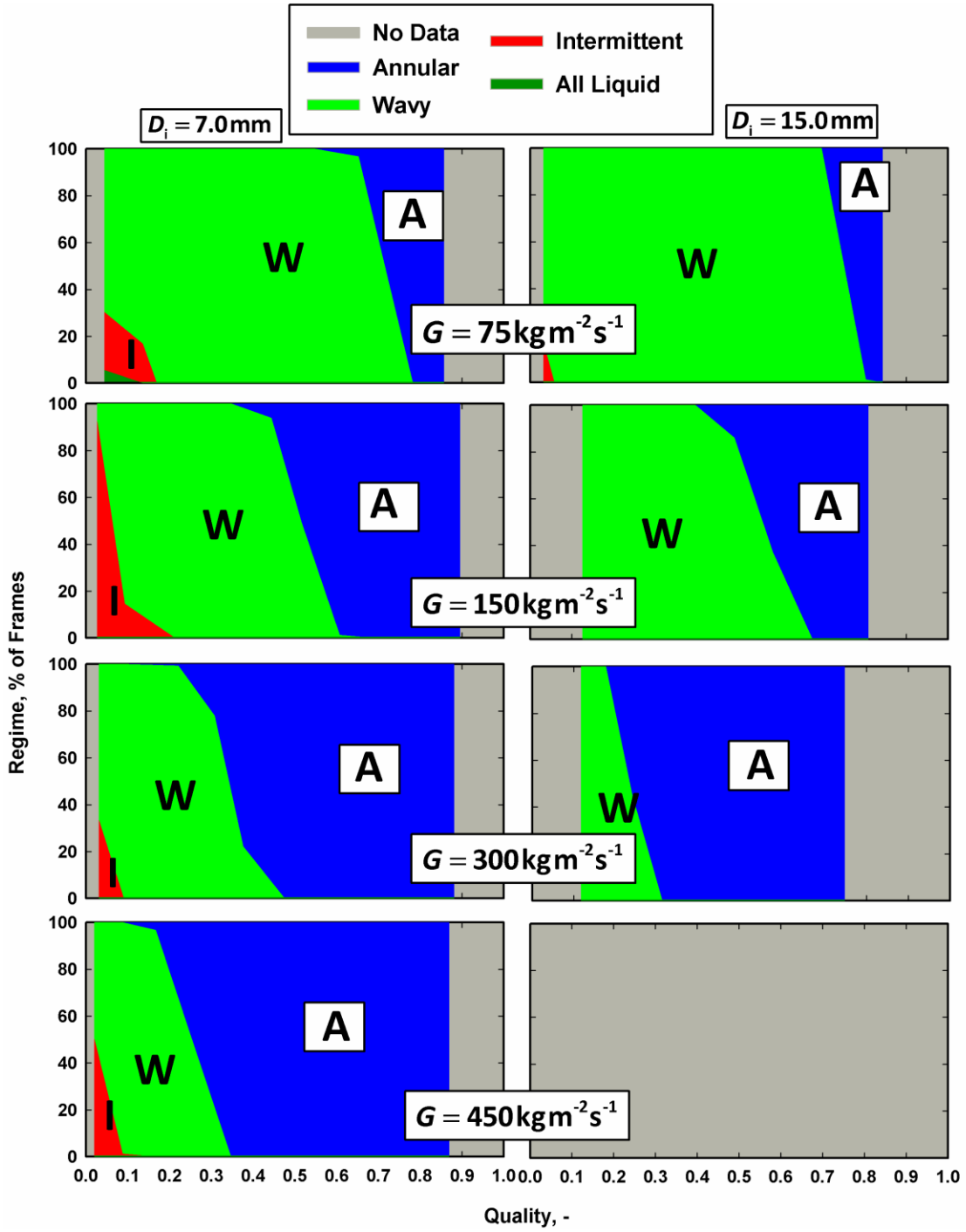
Figure 5.4. Flow regime versus quality for 7.0 mm ID propane data at 952 kPa

The vapor-phase velocity decreased as the fluid was condensed, reducing the ability of the flow to uniformly distribute around the circumference of the tube which resulted in pooling of the liquid at the bottom of the tube and the transition from annular to wavy flow. For example, in the 7.0 mm tube at P_{avg} ~ 952 kPa, G ~ 150 kg m^{-2} s^{-1}, the superficial vapor velocity, j_v, decreased from 6.6 m s^{-1} at q_{avg} = 0.90 to 4.9 m s^{-1} at q_{avg} = 0.61. With the decrease in vapor velocity the vapor-phase Reynolds number, Re$_v$, decreased from 110,000 to 76,000 and the dimensionless gas velocity J_G^*, decreased from 5.0 to 3.7 over the same range. Further decreases of the vapor quality resulted in an increased liquid inventory, resulting in further liquid pooling at the bottom of the tube. For example, in the 7.0 mm tube at P_{avg} ~ 952 kPa, G ~ 150 kg m^{-2} s^{-1}, the superficial vapor velocity decreased from 4.3 m s^{-1} at q_{avg} = 0.52 to 0.7 m s^{-1} at q_{avg} = 0.09. With the decrease in vapor velocity, the vapor-phase Reynolds number decreased from 65,000 to 12,000 and the dimensionless gas velocity decreased from 3.0 to 0.5 over the same range, indicating that gravitational effects become more significant.

With increasing mass flux, the flows exhibited greater inertial effects, as evidenced by higher phase Reynolds numbers and dimensionless gas velocity at a given quality. This delayed the transition from annular to wavy flow to lower vapor qualities as shown in Figure 5.4. For example, in the 7.0 mm tube at P_{avg} ~ 952 kPa, when increasing from a mass flux of G ~ 150 kg m^{-2} s^{-1} to G ~ 300 kg m^{-2} s^{-1}, the transition from annular to wavy flow decreased from q_{avg} ~ 0.5 where Re$_v$ ~ 65,000 and J_G^* ~ 3 to q_{avg} ~ 0.35 where Re$_v$ ~ 85,000 to J_G^* ~ 4.

When a single regime was observed in 75% or more of the frames, the data point was classified as that regime. When the second regime exceeded 25% or more of the frames,

225

the data point was classified as a transitional point. The regime classifications for both

pressures and tube diameters are shown in Figure 5.5. The trends observed in Figure

5.4with decreasing quality and increasing mass flux were also observed at both pressures

and tube diameters.
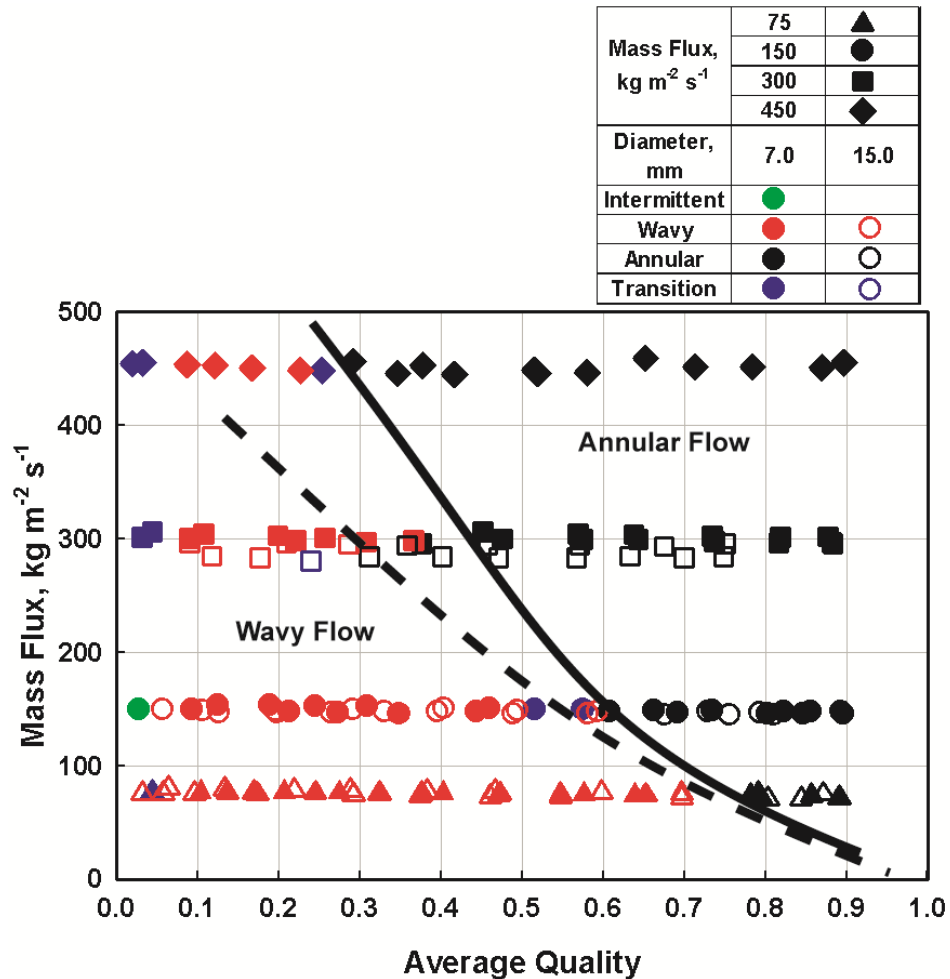
Figure 5.5. Summary of flow regime classifications with mass flux versus quality; Approximate wavy-to-annular transitions overlay: Solid line (7.0 mm) and Dashed line (15.0 mm)

The transition from annular to wavy flow was delayed to lower qualities with

increasing reduced pressure. For the 7.0 mm ID tube, at $G \sim 300$ kg m^{-2} s^{-1} and $q_{avg} =$

0.37, the flow was classified as annular at $P = 952$ kPa and wavy at $P = 1218$ kPa. The

decrease in vapor-phase density and liquid-to-vapor density ratio contribute to the delay

in transition. As the vapor-phase density and density ratio decrease with increasing pressure, the high shear force between the two phases decreases. Here, the liquid-to-vapor density ratio decrease from 24 at $P = 952$ kPa to 18 at $P = 1218$ kPa. However, because the range of reduced pressure in the present study is small, the shift in the transition point with increasing pressure was a few percent quality at most over the range of conditions considered.

At $G \leq 200$ kg m^{-2} s^{-1}, the transition from annular flow to wavy flow occurs at higher qualities in the 15.0 mm ID tube than the 7.0 mm tube. For example, at $G \sim 75$ kg m^{-2} s^{-1} and $P \sim 952$ kPa the dimensionless gas velocity in the 7.0 mm tube increased from 0.13 at $q_{avg} = 0.04$ to 2.4 at $q_{avg} = 0.86$, whereas in the 15.0 mm tube, the dimensionless gas velocity increased from 0.06 at $q_{avg} = 0.03$ to 1.6 at $q_{avg} = 0.84$. At low mass fluxes, a larger portion of the quality range was within the region where gravitational forces were more significant than inertial forces.

As mass flux is increased above $G \sim 200$ kg m^{-2} s^{-1}, inertia forces become more dominant over much of the quality range. For otherwise identical conditions, both phase Reynolds numbers increase by a factor of 2.1 between the 7.0 to 15.0 mm diameter tubes. The increased phase Reynolds numbers result in a more turbulent liquid film and vapor core, both of which contribute to a breakdown of the lower liquid film. Thus, the flow remains annular, as classified by a lower film thickness of less than 5% of the diameter, to lower qualities for the 15.0 mm tube than the 7.0 mm tube. The change in the transition to annular flow is shown in Figure 5.5.

5.1.1.2 *Void Fraction*

Because high-speed video analysis is unable to track liquid entrainment in the vapor core, the void fraction results presented here do not include liquid entrained in the vapor core. While the image analysis technique could not quantify the liquid entrainment, the presence of liquid entrainment can be visually observed by watching the video. Each flow video was visually analyzed to approximate the significance of liquid entrainment in the vapor core. A representative set of images is shown in Figure 5.6 for the three visual classification categories. The results are shown in Figure 5.7 where the points within the green region showed a limited quantity of entrainment. Data points within the red region were observed to show a significant amount of entrainment. A yellow region between the two was identified for data showing some entrainment.
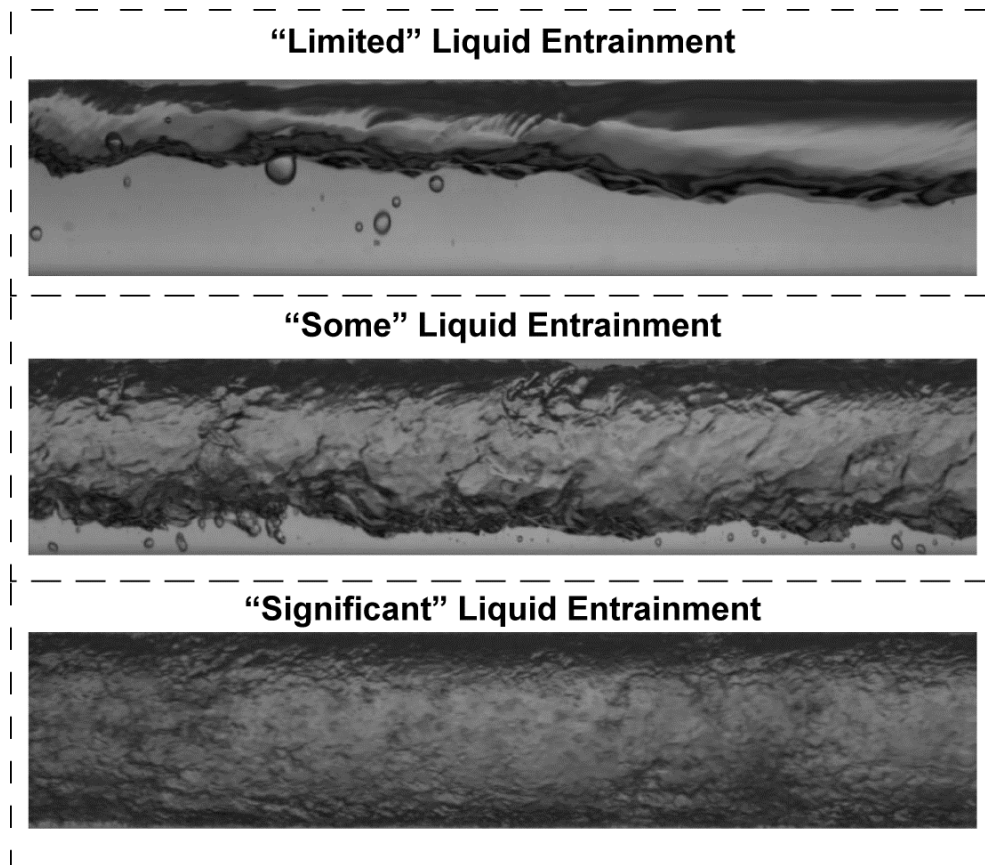
Figure 5.6. Representative entrainment quantification images

		Pressure, kPa	
		952	1218
Mass Flux, kg m^{-2} s^{-1}	75	▼	▽
	150	●	●
	300	■	■
	450	◆	◆
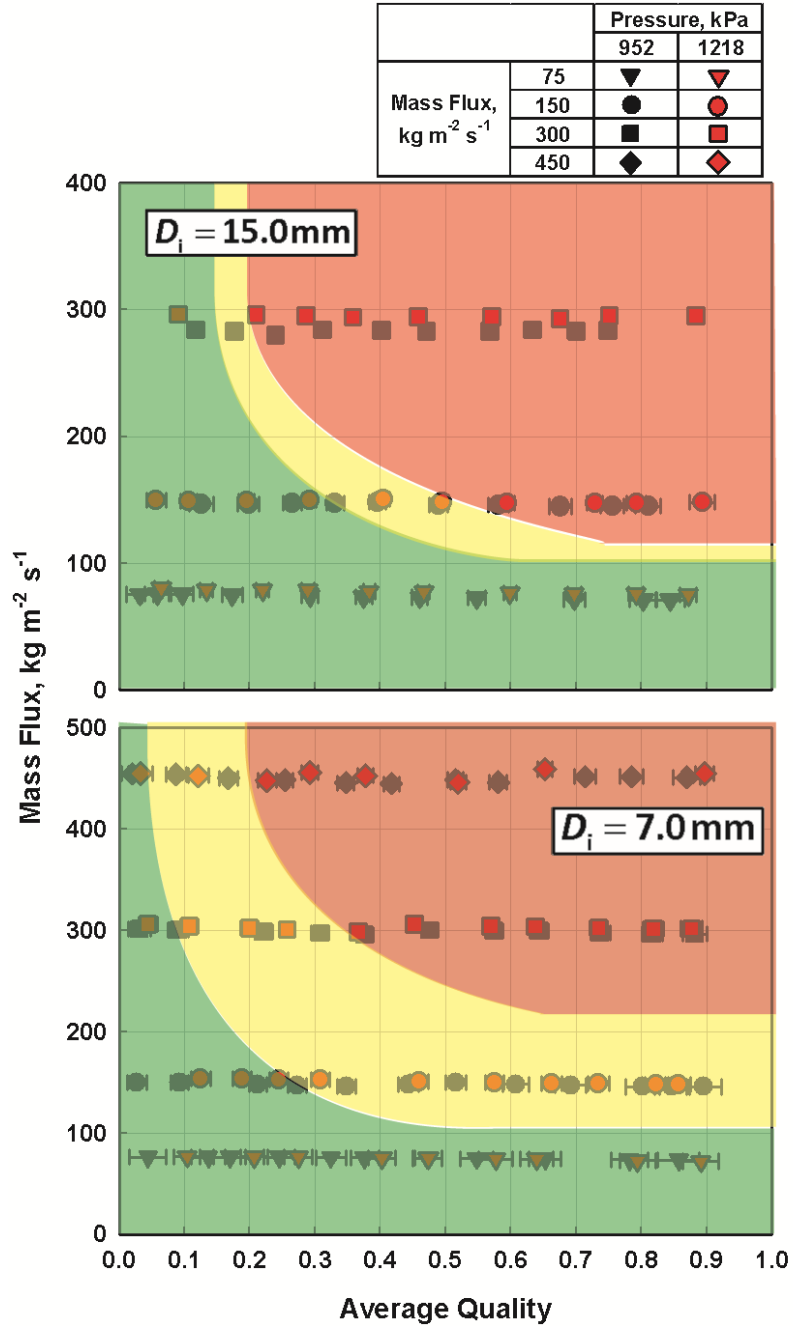
Figure 5.7. Assessment of the significance of liquid entrainment in the vapor core; green – limited entrainment; yellow – some entrainment; red – significant entrainment

The void fraction measurements for data points within the red region will not include a significant portion of the liquid contained in the cross section. The average void fractions calculated from the video analysis, as described in Chapter 4, are shown in

229

Figure 5.8, distinguished based on pressure and diameter. Referring to Figure 5.8, the measured void fractions range from 0.31 at P_{avg} = 937 kPa, G = 149 kg m^{-2} s^{-1}, and q_{avg} = 0.03 to 0.99 at P_{avg} = 921 kPa, G = 451 kg m^{-2} s^{-1}, and q_{avg} = 0.87 in the 7.0 mm ID tube, and from 0.33 at P_{avg} = 913 kPa, G = 75 kg m^{-2} s^{-1}, and q_{avg} = 0.03 to 1 at P_{avg} = 1194 kPa, G = 295 kg m^{-2} s^{-1}, and q_{avg} = 0.88 in the 15.0 mm ID tube.

As expected, the measured void fraction increases with increasing quality in an asymptotic fashion to a void fraction of one at a quality of one. Because the liquid density is significantly higher than the vapor density at the conditions of the present study, small quantities of vapor in the cross section at low qualities result in a rapidly increasing void fraction with increasing quality. For example, in the 7.0 mm tube at G ~ 150 kg m^{-2} s^{-1} and P ~ 952 kPa, the void fraction increased from 0.31 at q_{avg} = 0.03 to 0.58 at q_{avg} = 0.09.Further increasing the quality to q_{avg} = 0.27 increases the void fraction to 0.85.

The void fraction was observed to increase with increasing mass flux. With increasing mass flux, the vapor core velocity increases, resulting in increased interfacial shear between the phases, which thins the liquid film and increases liquid entrainment in the vapor core. This in turn, results in a higher measured void fraction. For example, in the 7.0 mm tube at q_{avg} ~ 0.35 and P ~ 952 kPa, the void fraction increased from 0.89 at G = 146 kg m^{-2} s^{-1} to 0.91 at G = 445 kg m^{-2} s^{-1}. As observed in Figure 5.9, the void fraction approaches a value greater than 0.9 more rapidly with increasing mass fluxes. As presented in Figure 5.7, the liquid entrainment becomes more significant with increasing mass flux. Therefore, it is possible the mass flux effect is exaggerated by the inability to track liquid entrainment.
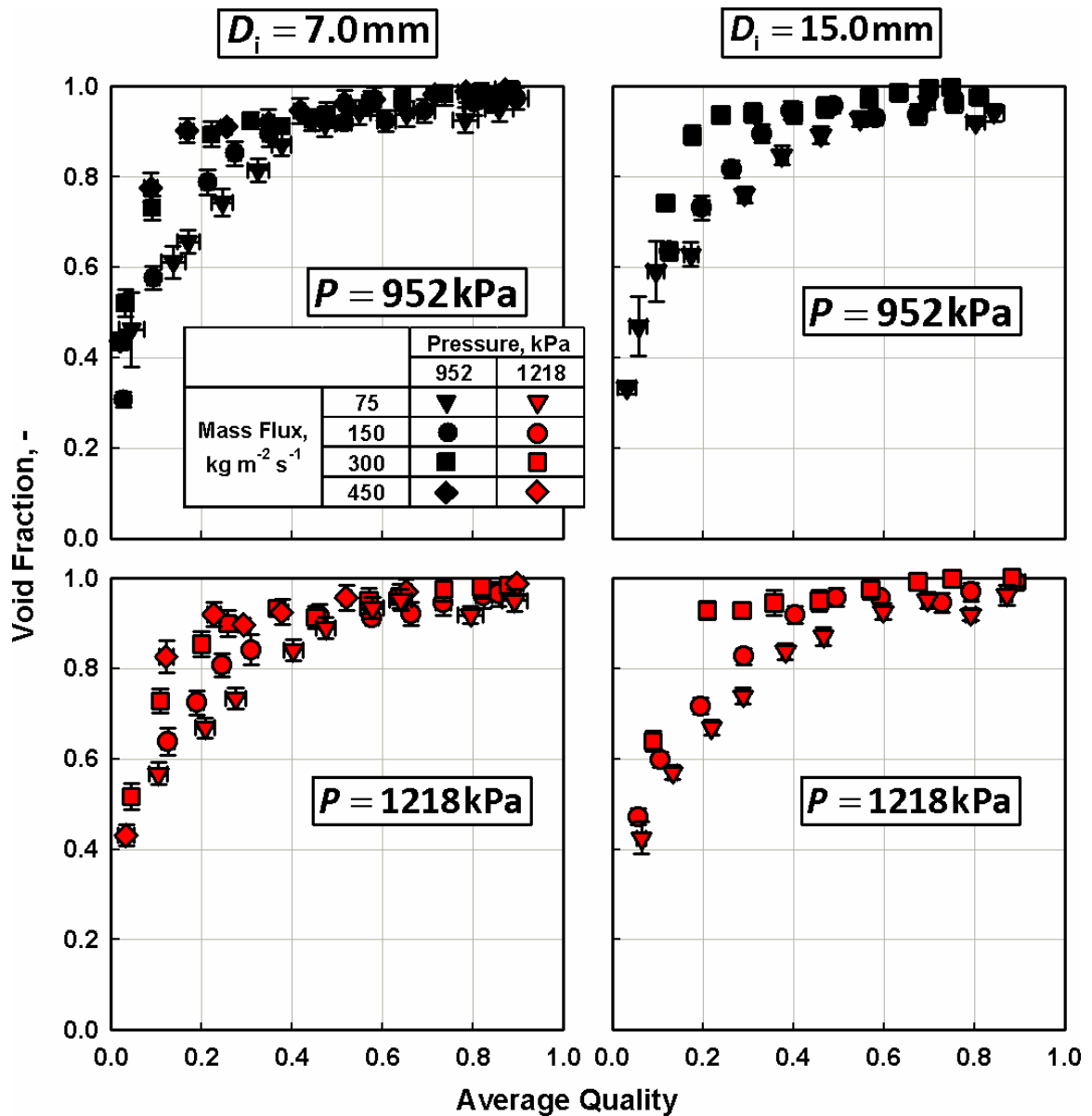
Figure 5.8. Void fraction versus quality for propane in 7 and 15 mm ID tubes

The void fraction was observed to decrease with increasing pressure. As indicated above, the liquid-to-vapor density ratio decreases with increasing pressure. The increasing vapor-phase density and decreasing liquid-phase density lead to the liquid occupying more of the cross section. Additionally, the vapor velocity decreases with increasing pressure, resulting in a thicker liquid film, for otherwise identical conditions. For example, in the 7.0 mm tube at $G \sim 300$ kg m^{-2} s^{-1} and at $q_{avg} \sim 0.37$, the void fraction

decreases from 0.93 at $P = 1174$ kPa to 0.91 at $P = 947$ kPa. For these conditions, the superficial vapor velocity decreases from 5.4 m s^{-1} at $P = 947$ kPa to 4.3 m s^{-1} at $P = 1174$ kPa.

The videos clearly indicate a difference in the distribution of the vapor between the 7.0 and 15.0 mm tubes (Figure 5.3). In addition, the void fraction was observed to increase with increasing tube diameter, particularly in the annular regime. For example, at $G \sim 150$ kg m^{-2} s^{-1}, $P \sim 952$ kPa and $q_{avg} \sim 0.8$ the void fraction increased from 0.96 to 0.98 with an increase in diameter from 7.0 to 15.0 mm. The variation in the void fraction between tube diameters was established by approximating the quantity of liquid contained in the liquid pool as discussed in Chapter 4. The results for both tube diameters are shown in Figure 5.9. For example at $G \sim 150$ kg m^{-2} s^{-1} and P ~ 1218 kPa in the 7.0 mm ID tube, the fraction of liquid in the pool increases from 6% at $q_{avg} = 0.86$ to 91% at $q_{avg} = 0.13$.

In the 15.0 mm ID tube, the liquid pool contained nearly 100% of the liquid in the cross section within the wavy regime. At low qualities, the fraction of liquid in the pool decreases because the liquid contained in liquid slugs are not considered to be contained in the pool. With a reduction of liquid contained in the upper film for the 15.0 mm tube, the total liquid inventory at a given cross section decreases, resulting in a higher void fraction. In the stratified regime, the significant upper film in the 7.0 mm ID tube resulted in the liquid fraction in the wavy regime to be dependent on mass flux. As the mass flux was increased, the shear between the phases increases thinning of the liquid pool at the bottom and distributes a larger portion of the liquid phase around the upper tube wall, resulting in a decrease in the fraction of liquid in the pool. Referring to Figure 5.10, in the

7.0 mm ID tube at $P \sim 1218$ kPa and $q_{avg} \sim 0.20$, the fraction of liquid in the pool decreased from 96% at $G = 75$ kg m^{-2} s^{-1} to 72% at $G = 300$ kg m^{-2} s^{-1}. Similarly, at the same conditions in the 15.0 mm tube, the fraction of liquid in the pool decreased from 99.5% at $G = 75$ kg m^{-2} s^{-1} to 87% at $G = 300$ kg m^{-2} s^{-1}.
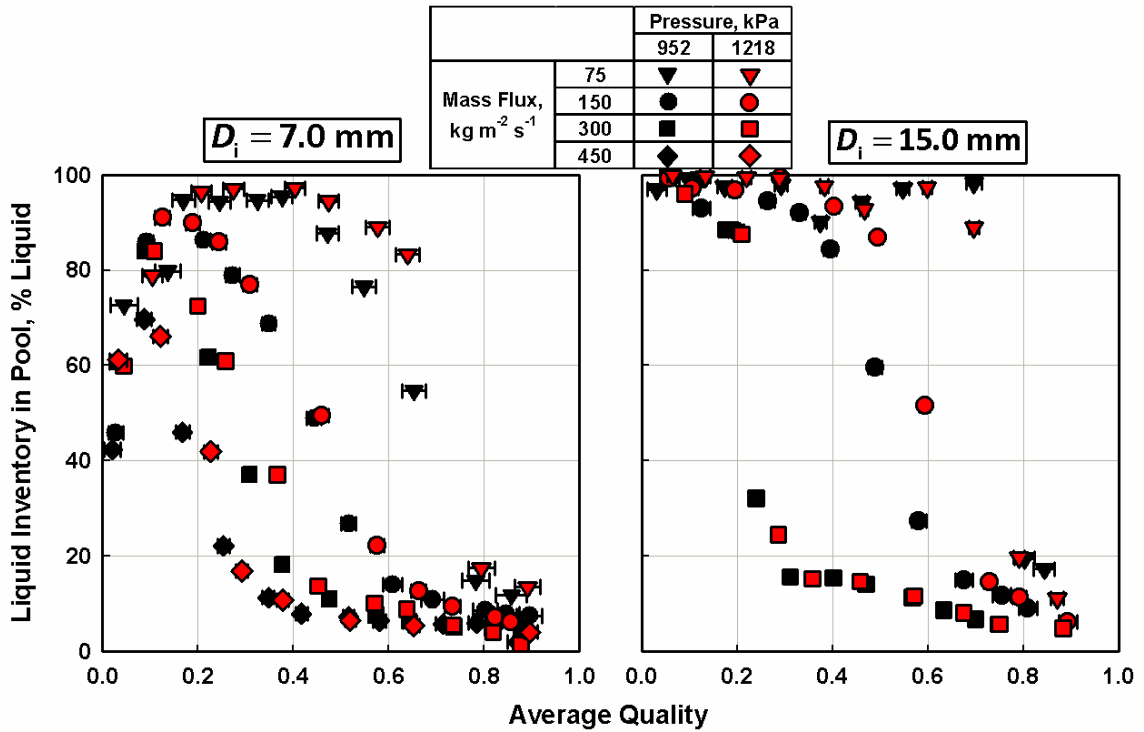
Figure 5.9. Liquid inventory in lower liquid pool versus quality
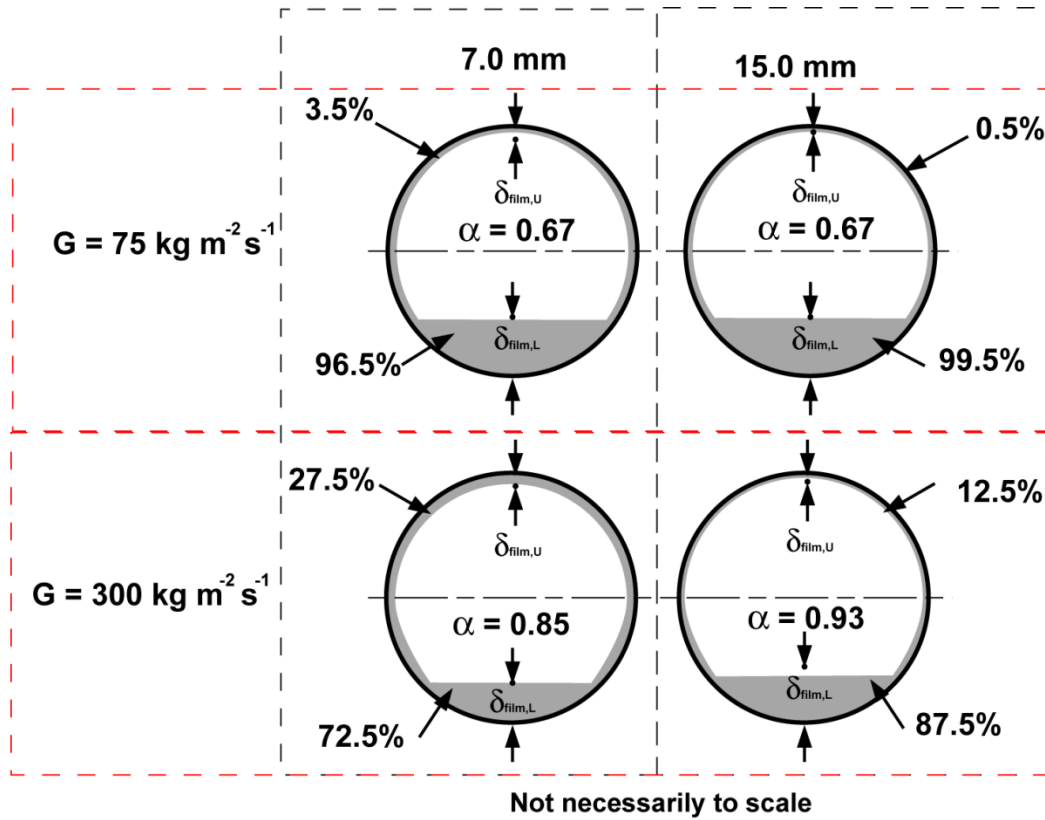
Figure 5.10. Liquid-phase distribution schematic for changing tube diameter and mass flux

5.1.1.3 Film Thickness

The measured lower film thicknesses from the lower tube wall to the lower vapor-liquid interface are shown as a percentage of the diameter in Figure 5.11. Because the film thickness was used to calculate the void fraction, the lower film thickness shows trends similar to those of the void fraction with increasing mass flux and quality for reasons discussed in the previous section. For example, in the 7.0 mm tube at $P \sim 1218$ kPa and $G \sim 75$ kg m^{-2} s^{-1}, the average lower film thickness decreased from 2.1 mm at $q_{avg} = 0.27$ to 1.1 mm at $q_{avg} \sim 0.47$. When increasing the mass flux to $G \sim 300$ kg m^{-2} s^{-1} at $q_{avg} = 0.25$, the average lower film thickness decreased further to 0.8 mm.

234
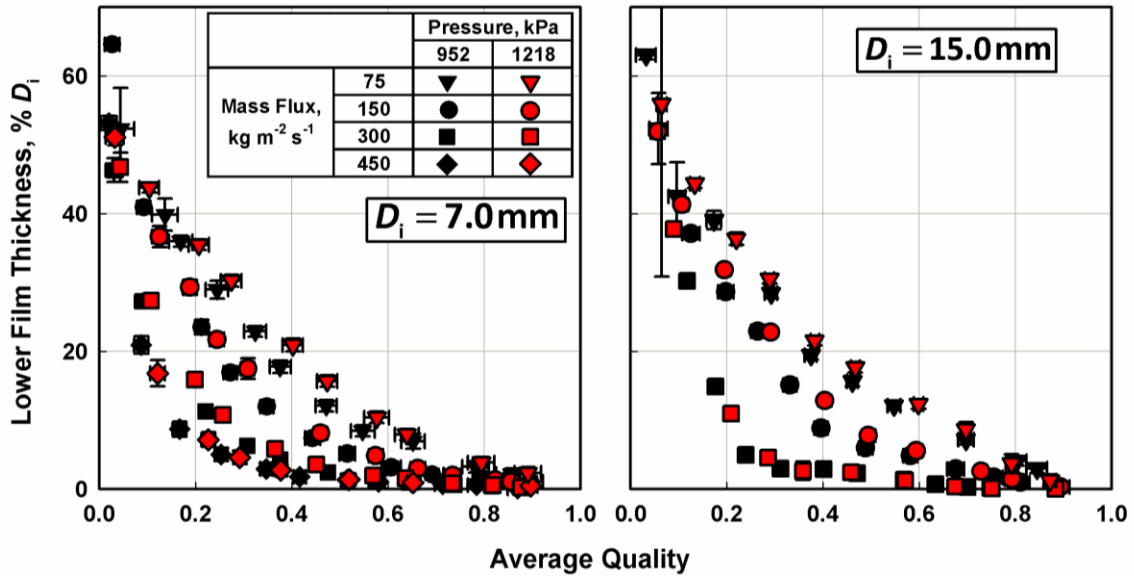
Figure 5.11. Measured lower film thickness as percent of diameter versus quality

Referring to Figure 5.11, the lower film thickness divided by the ID of the tube showed a slight increase with increasing internal tube diameter, but shows the same trend. For example, at $P \sim 1218$ kPa, $G \sim 150$ kg m^{-2} s^{-1}, and $q_{avg} = 0.19$, the average lower film thickness is 29% of the internal tube diameter in the 7.0 mm tube, whereas in the 15.0 mm ID tube, the average film thickness is 32% of the ID. The larger annular regime in the 15.0 mm tube noted above resulted in the relative film thickness to decrease more rapidly in the 15.0 mm tube than in the 7.0 mm tube at lower qualities.

As noted above, no identifiable upper film was observed in the 15.0 mm tube. The average upper film thickness in the 7.0 mm tube, shown in Figure 5.12 on a logarithmic scale, decreases quickly with increasing quality; thus, the film thickness is presented on a log scale. While the average upper film thickness was small, the film exhibited small identifiable waves. Thus, the accuracy in the average film thickness was fairly high. The average upper film thickness was observed to be insensitive to mass flux and pressure over much of the quality range, with the exception of the $G \sim 75$ kg m^{-2} s^{-1} case. In the G

~ 75 kg m^{-2} s^{-1} case in the 7.0 mm tube, the upper film was observed to thin more quickly than at higher mass fluxes. In this case, the gravitational forces thin the upper film while the inertia forces are insufficient to support the upper film. The lower phase velocities resulted in lower inertia forces resulting in the liquid pooling at the bottom of the tube. The reduction in phase velocities also results in fewer waves generated in the lower film; as a result fewer liquid droplets are flung to the top of the tube after being sheared from a wave.
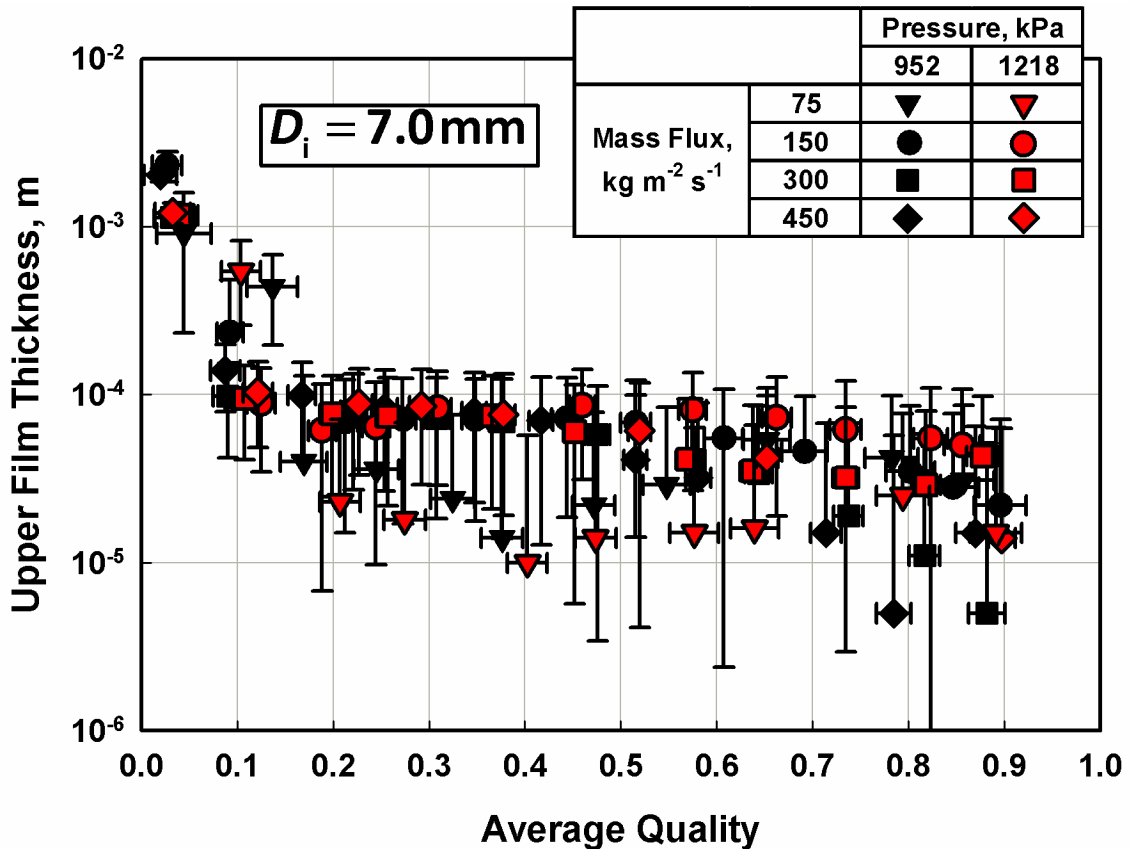
Figure 5.12. Upper film thickness versus quality

Finally, the standard deviation of the lower film thickness, shown in Figure 5.13, was determined on a frame-by-frame basis and averaged for each data point as discussed in Chapter 4. The standard deviation of the lower film thickness indicates the relative

variation of the film at different conditions. In the annular regime, the lower film contains a relatively small amount of liquid and the rapidly moving vapor core maintains a relatively stable and uniform film. As the liquid pool height increases and the flow transitions to a wavy regime, the variation in the film thicknesses increases. Because the forces that maintain an upper film and thin the lower film were lower at $G = 75$ kg m^{-2} s^{-1} than those at the higher mass fluxes, the variation in film thickness increased in the $G = 75$ kg m^{-2} s^{-1} case first. However, the standard deviation in the film thickness approaches between 0.4 and 0.6 mm for both tube diameters through the wavy regime. This indicated that the liquid film thickness variation is only slightly dependent on the tube diameter. The variation in the film thickness in the annular regime was also found to be independent of diameter with standard deviations less than 0.1.
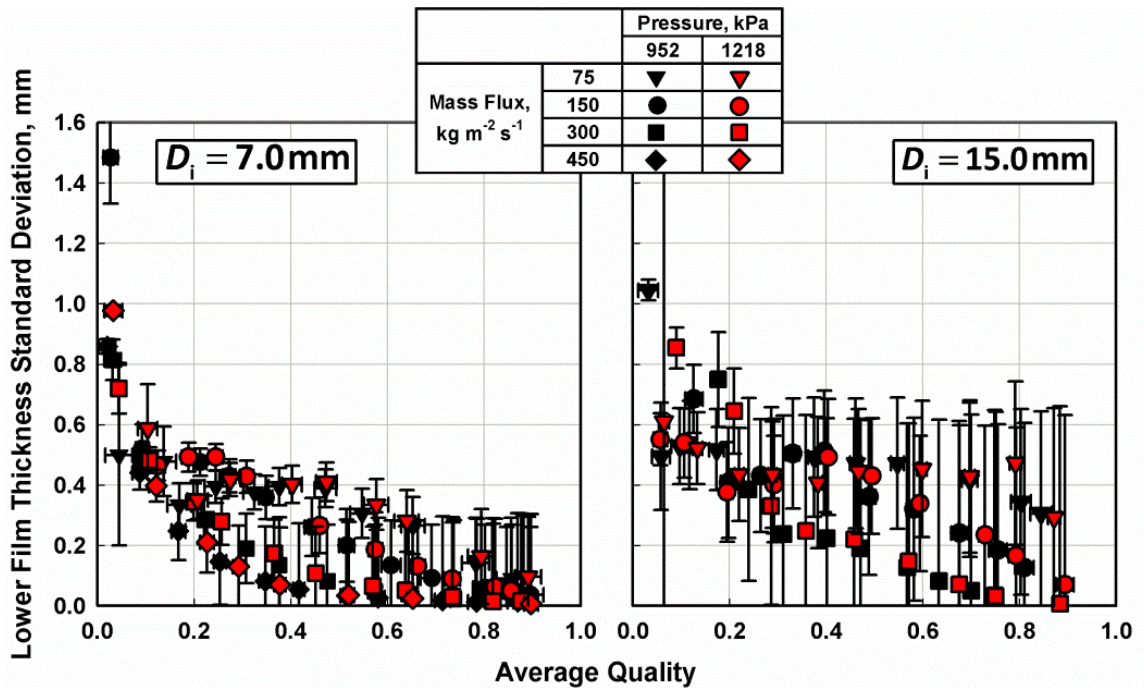
Figure 5.13. Lower film thickness standard deviation versus quality

5.1.2 Frictional Pressure Gradient

An overview of the frictional pressure gradient data is presented first. The experimental results for n-pentane in the 7.75 and 14.45 mm ID tubes are presented next to assess general trends of the frictional pressure gradient with mass flux, quality, and diameter. Finally, frictional pressure gradient results in the 7.75 mm tube for n-pentane, R245fa, and the zeotropic R245fa/n-pentane mixtures are presented with a discussion of pressure and fluid property effects on frictional pressure gradient.

For the purpose of this discussion, the pressure drop is defined as the inlet pressure minus the outlet pressure. Therefore, a positive value for ΔP_f, ΔP_{meas}, and ΔP_{Decel} indicates that the test section inlet pressure is greater than the test section outlet pressure or the pressure decreases along the test section. Conversely, a negative value for ΔP_f, ΔP_{meas}, and ΔP_{Decel} indicates that the outlet is higher than the inlet. The frictional pressure gradient was deduced from the measured pressure drop and calculated deceleration pressure recovery due to condensation (Equation (5.1)).

$$\Delta P_f = \Delta P_{meas} + \Delta P_{Decel} \tag{5.1}$$

In most cases ΔP_{Decel} was negative, which indicates a pressure recovery due to phase change as is expected for condensation. Thus, the frictional pressure drop term was greater than the measured pressure drop. However, in a very few cases, ΔP_{Decel} was positive, which is unexpected for condensation. This occurred at low reduced pressures when the quality change was small and pressure drop in the test section was large. In these cases, the void fraction at the outlet of the test section is greater than at the inlet, and the large pressure change across the test section caused the saturated state and the

238

properties to change dramatically. For example, at P_{avg} = 141 kPa, G = 457 kg m^{-2} s^{-1}, and

q_{avg} = 0.34, the measured test section quality change (Δq) is 0.03 and the measured

pressure change from inlet to outlet is +33.3 kPa. At these conditions, the inlet void

fraction is 0.911, while the outlet void fraction is 0.914. Additionally, the significant

pressure decrease causes the vapor-phase density to decrease from 4.6 kg m^{-3} at P =

159.3 kPa to 3.6 kg m^{-3} at P = 124 kPa. Due to the combination of the increase in void

fraction and decreasing vapor density, the flow slightly accelerates, with a ΔP_{Decel} =

+0.48 kPa calculated using Equation 4.45. Therefore, the frictional pressure drop (ΔP_f) is

calculated to be 32.8 kPa. This behavior is seen in the minority of the data, with most

deceleration terms calculated to be negative. As a percentage of the measured pressure

drop, the deceleration pressure drop ranges from 3.5%, indicating an acceleration of the

flow, to -124.8%. The former occurred in the 7.75 mm ID tube n-pentane data set at P_{avg}

= 234 kPa, G = 589 kg m^{-2} s^{-1}, and q_{avg} = 0.74, where the quality change was 0.08 and the

measured pressure drop was 64.7 kPa. The latter occurred in the 14.45 mm n-pentane

data set at P_{avg} = 221 kPa, G = 299 kg m^{-2} s^{-1}, and q_{avg} = 0.08, where the quality change

was 0.06 and the measured pressure drop was 0.3 kPa. Because the LMTD was

maintained at approximately 10K and the heat transfer coefficient increases with

increasing quality, the quality change, shown in Figure 5.14, also increased with

increasing average quality. A representative plot of the deceleration term as a percent of

the measured pressure drop is shown in Figure 5.15. The data points with a significant

deceleration term correspond to low mass flux, high quality, and large quality change

data points. For example, in the representative 7.75 mm n-pentane data set shown, the

deceleration term was -30.2% at P_{avg} = 141 kPa, G = 148 kg m^{-2} s^{-1}, and q_{avg} = 0.84

where the quality change was 0.26. At P_{avg} = 138 kPa, G = 148 kg m^{-2} s^{-1}, and q_{avg} = 0.12, the quality change was 0.09 and the deceleration term decreased to -15.6%.
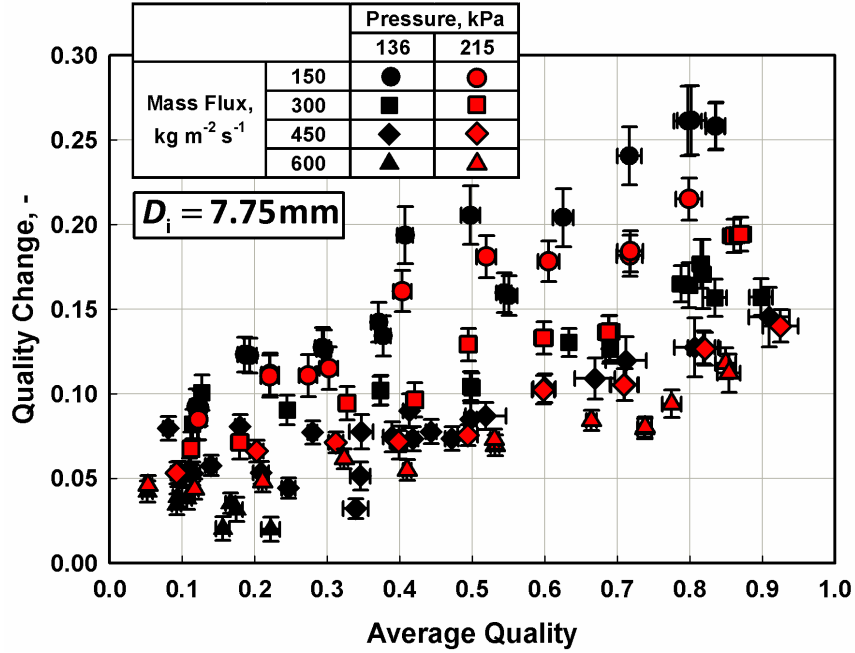
Figure 5.14. Quality change versus average quality for *n*-pentane in 7.75 mm ID tube
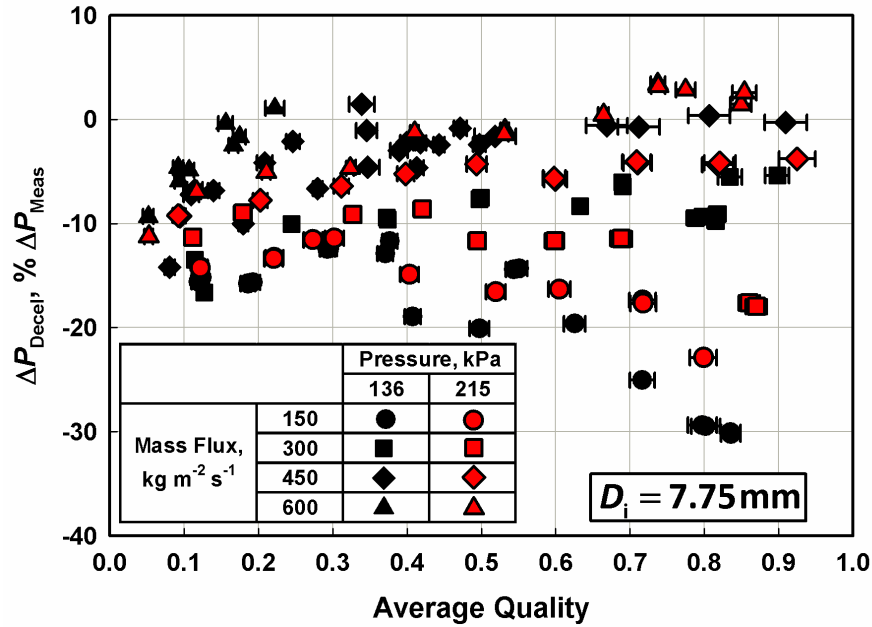
Figure 5.15. Deceleration contribution for *n*-pentane in 7.75 mm ID tube

Over the entire data set, the average deceleration contribution as a percentage of the measured pressure drop was -17%. A summary of the deceleration contribution by fluid and saturation condition is shown in Table 5.1. Because the frictional pressure gradient in the 14.45 mm ID n-pentane data was significantly lower than the corresponding term for the 7.75 mm data, the deceleration term was significantly larger as a percent of the measured pressure drop than in the 7.75 mm data. The pure fluid data show an increasing average deceleration contribution with increasing average quality change. For example, in the representative 7.75 mm ID n-pentane data shown, the average quality change at T_{sat} = 45°C was 0.112, while at T_{sat} = 45°C, the average quality change was 0.107. The average deceleration contributions at these two conditions were -9.2% and -8.2%, respectively. Because the deceleration term and the measured pressure drop were the only terms used to calculate the frictional pressure drop, the frictional pressure drop was, in most cases, greater than 100% of the measured pressure drop.

Table 5.1. Summary of the frictional pressure gradient data

Fluid	Diameter	T_{Bub}/T_{Sat}	P_r	Number	ΔP_f	ΔP_{Decel}	$U \nabla P_f$
	mm	°C	-	of Data	% ΔP_{meas}	% ΔP_{meas}	% ∇P_f
R245fa		20	0.03	41	105.6%	-5.6%	2.7%
		45	0.08	34	117.3%	-17.3%	7.2%
		70	0.17	27	117.0%	-17.0%	7.2%
n-pentane	7.75	45	0.04	65	109.2%	-9.2%	4.1%
		60	0.06	48	108.2%	-8.2%	4.9%
45% R245fa/ 55% n-pentane		30	0.05	35	109.6%	-9.6%	4.3%
		55	0.11	41	110.5%	-10.5%	4.8%
		80	0.21	37	111.4%	-11.4%	5.3%
n-pentane	14.45	45	0.04	35	136.7%	-36.7%	13.3%
		60	0.06	27	144.0%	-44.0%	14.1%
		75	0.10	38	135.7%	-35.7%	12.5%
Average					117.0%	-17.0%	6.8%

The primary contributions to the uncertainties in the pressure gradient were the uncertainty associated with the measured value and the conservative 50% uncertainty assigned to the deceleration term, and not the measured conditions. The uncertainties in the pressure gradients were typically dominated by the uncertainty assigned to the deceleration term. Thus, data with a high deceleration contribution had greater uncertainties. The uncertainty as a percentage of the frictional pressure gradient is summarized in Table 5.1 and shown for n-pentane in the 7.75 mm ID tube in Figure 5.16. For example, considering the R245fa data, the average deceleration contribution was 5.6% at 20°C and increased to -17.3% at 45°C. The corresponding uncertainties in the frictional pressure gradient at these conditions were 2.7% and 7.2%, respectively. This trend held true for each condition, except for the 7.75 mm n-pentane data set. Considering the 7.75 mm n-pentane data, with a deceleration contribution of 8.2%, the average uncertainty at 60°C was 4.9%. Despite having a greater average deceleration contribution of 9.2%, the average uncertainty for the 45°C data was 4.1%. This occurs because five of the 48 data points in the 60°C data exceeded the range of the low uncertainty differential pressure transducers, requiring the difference between the absolute pressure transducers to be used, which results in a greater uncertainty.
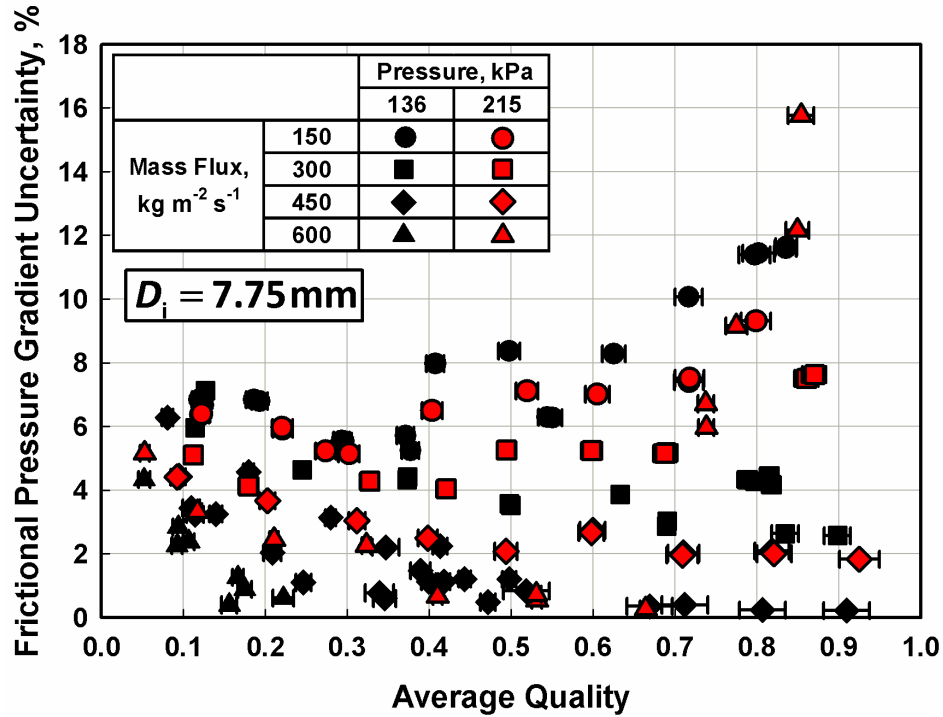
Figure 5.16. Frictional pressure gradient uncertainty for *n*-pentane in 7.75 mm ID tube

5.1.2.1 *Effects of mass flux, quality, and diameter – n-pentane results*

Referring to Figures 5.17 and 5.18, the measured frictional pressure gradients for *n*-pentane range from 1.4 kPa m^{-1} at P_{avg} = 220 kPa, G = 155 kg m^{-2} s^{-1}, and q_{avg} = 0.08 to 95.0 kPa m^{-1} at P_{avg} = 248 kPa, G = 603 kg m^{-2} s^{-1}, and q_{avg} = 0.85 in the 7.75 mm ID tube. In the 14.45 mm ID tube, they range from 0.18 kPa m^{-1} at P_{avg} = 140 kPa, G = 108 kg m^{-2} s^{-1}, and q_{avg} = 0.06 to 10.5 kPa m^{-1} at P_{avg} = 309 kPa, G = 292 kg m^{-2} s^{-1}, and q_{avg} = 0.81. As the mass flux increases, the respective phase velocities also increase. Because the pressure drop is a function of the square of the velocity, an increase in the mass flux results in a much larger increase in pressure drop. Increasing pressure gradient with increasing mass flux is shown in Figure 5.17 for *n*-pentane for both tube diameters and each pressure under consideration in the present study. For example, with increasing mass flux in the 7.75 mm ID tube at P ~ 215 kPa and q ~ 0.3, the frictional pressure

gradient increased from 3.5 kPa m^{-1} at $G = 148$ kg m^{-2} s^{-1} to 42.7 kPa m^{-1} at $G = 602$ kg m^{-2} s^{-1}. As would be expected, the same trend was observed in the 14.45 mm ID tube. For example, with increasing mass flux at $P \sim 323$ kPa and $q \sim 0.1$, the gradient increased from 0.2 kPa m^{-1} at $G = 157$ kg m^{-2} s^{-1} to 1.0 kPa m^{-1} at $G = 431$ kg m^{-2} s^{-1}. Furthermore, the increased phase velocities caused an increase in turbulence in the respective phases. Over the range of conditions investigated for n-pentane, in the 7.75 mm ID tube, the liquid Reynolds number increased from 1024 at $P_{avg} = 141$ kPa, $G = 148$ kg m^{-2} s^{-1}, and $q_{avg} = 0.84$, to 27,493 at $P_{avg} = 217$ kPa, $G = 612$ kg m^{-2} s^{-1}, and $q_{avg} = 0.05$, while the vapor Reynolds number increased from 18,338 at $P_{avg} = 138$ kPa, $G = 148$ kg m^{-2} s^{-1}, and $q_{avg} = 0.09$ to 500,305 at $P_{avg} = 248$ kPa, $G = 603$ kg m^{-2} s^{-1}, and $q_{avg} = 0.85$. In the 14.45 mm ID tube, the liquid Reynolds number increased from 971 at $P_{avg} = 133$ kPa, $G = 94.6$ kg m^{-2} s^{-1}, and $q_{avg} = 0.87$, to 38,053 at $P_{avg} = 323$ kPa, $G = 430.7$ kg m^{-2} s^{-1}, and $q_{avg} = 0.11$, while the vapor Reynolds number increased from 18,622 at $P_{avg} = 140$ kPa, $G = 108$ kg m^{-2} s^{-1}, and $q_{avg} = 0.09$ to 454,522 at $P_{avg} = 348$ kPa, $G = 296$ kg m^{-2} s^{-1}, and $q_{avg} = 0.88$.
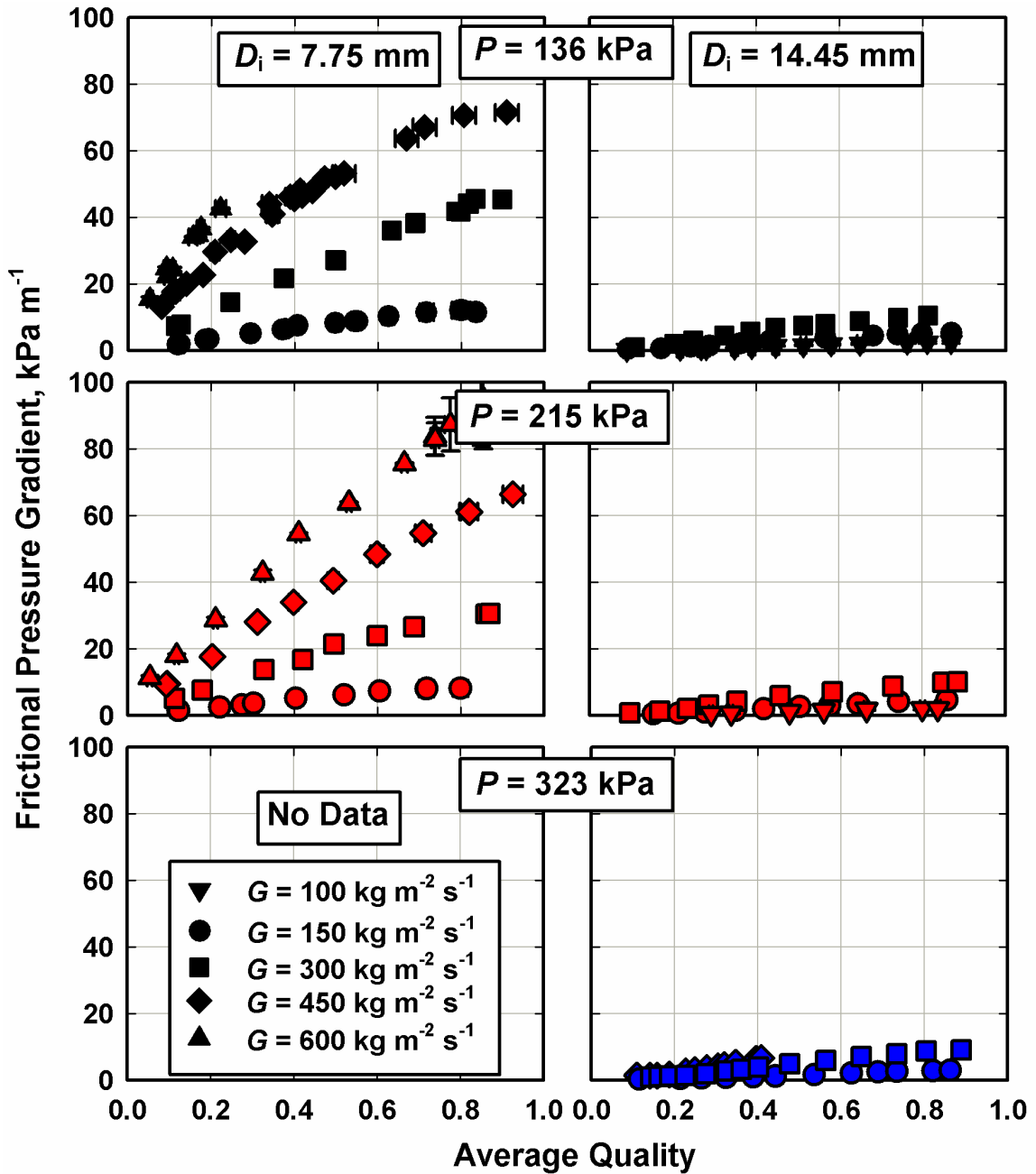
Figure 5.17. *n*-pentane experimental frictional pressure gradient versus quality for increasing mass flux
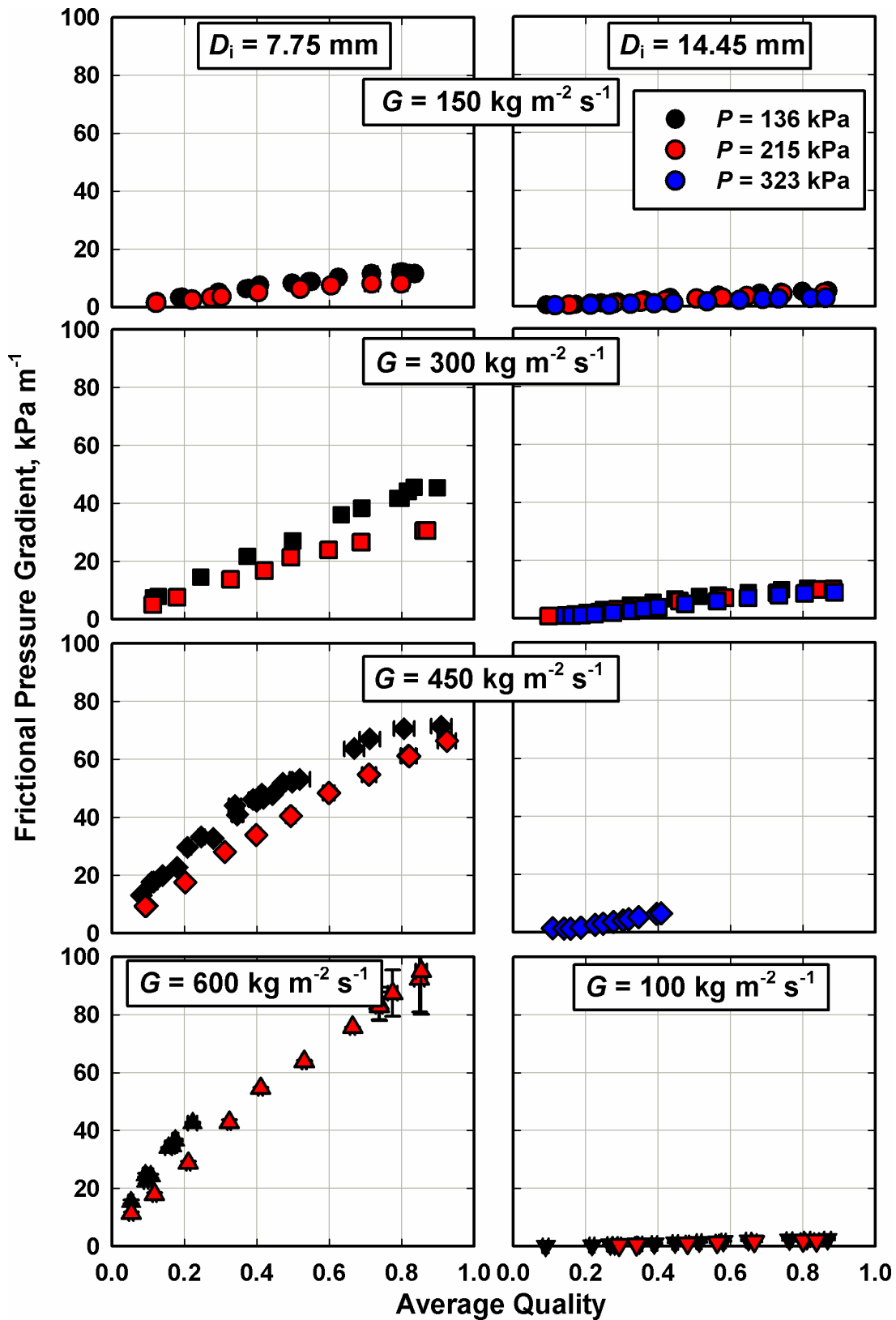
Figure 5.18. *n*-pentane experimental frictional pressure gradient versus quality for increasing pressure

The vapor-phase velocity also increases as quality increases, causing an increase in the frictional pressure gradient. For example, in the 7.75 mm ID tube at $G \sim 300$ kg m^{-2} s^{-1} and $P \sim 215$ kPa, the frictional pressure gradient increased from 5.0 kPa m^{-1} at $q_{avg} = 0.11$ to 30.7 kPa m^{-1} at $q_{avg} = 0.87$. At these conditions, the superficial vapor velocity increased from 5.6 m s^{-1} to 43.0 m s^{-1}, while the superficial liquid velocity only decreased from 0.42 m s^{-1} to 0.06 m s^{-1}.

The frictional pressure gradient decreased with increasing tube diameter for a given mass flux, pressure, and quality. As the diameter increases, the phases were able to separate which decreased the interactions between the phases. The single-phase frictional pressure drop in a tube, $\Delta P = 0.5\, f_i\, G^2\, L\, \rho^{-1}\, D^{-1}$, is proportional to D^{-1}. Thus, increasing the tube diameter, while keeping mass flux, pressure, and quality the same, decreases the single-phase pressure drop. Furthermore, the friction factor is proportional to D^{-a}, where a is less than unity. Therefore, the friction factor decreases with increasing diameter which further decreases the pressure drop. For example, at $P_{avg} \sim 215$ kPa, $G \sim 300$ kg m^{-2} s^{-1}, and $q_{avg} \sim 0.32$, the frictional pressure gradient decreased from 13.8 kPa m^{-1} in the 7.75 mm tube to 4.5 kPa m^{-1} in the 14.45 mm ID tube. The decrease in pressure drop with increasing diameter for each mass flux is shown in Figure 5.18 with the 7.75 mm data on the left and the 14.45 mm data on the right.

5.1.2.2 Effects of fluid properties and reduced pressure

A comparison of the data in the 7.75 mm ID tube for *n*-pentane, R245fa, and the zeotropic mixture of R245fa/*n*-pentane are presented here. A summary of the thermodynamic and transport properties of each fluid at the saturation conditions investigated in the present study is shown in Tables 5.2 and 5.3. The reduced pressures

under consideration in the present study range from 0.03 to 0.21. These conditions

correspond to absolute pressures ranging from 123 kPa to 768 kPa and saturation

temperatures ranging from 20°C to a dew point temperature of 96.1°C. Referring to

Figure 5.19, data for pure R245fa and the zeotropic mixture exhibited identical trends in

fictional pressure gradient with increasing mass flux and quality. The measured frictional

pressure gradients in the R245fa data range from 0.40 kPa m^{-1} at $P_{avg} = 601.1$ kPa, $G =$

168.3 kg m^{-2} s^{-1}, and $q_{avg} = 0.23$, to 62.2 kPa m^{-1} at $P_{avg} = 198.1$ kPa, $G = 598.0$ kg m^{-2} s^{-1}, and $q_{avg} = 0.91$. The measured frictional pressure gradients in the R245fa/n-pentane

data range from 0.25 kPa m^{-1} at $P_{avg} = 764.4$ kPa, $G = 155.5$ kg m^{-2} s^{-1}, and $q_{avg} = 0.08$, to

68.6 kPa m^{-1} at $P_{avg} = 257.0$ kPa, $G = 602.6$ kg m^{-2} s^{-1}, and $q_{avg} = 0.91$. It should be noted

that these extrema correspond to the data points for which minimum and maximum

values of heat transfer coefficient (discussed in a subsequent section) were observed,

demonstrating the coupled nature of two-phase heat transfer and pressure drop.

Table 5.2. Comparison of thermodynamic properties

	Thermodynamic Properties				
	$T_{Bub/Sat}$	ΔT_{Glide}	P	P_r	i_{fg}
	°C	°C	kPa	-	kJ kg^{-1}
R245fa	20	-	123	0.03	193
	45	-	294	0.08	178
	70	-	610	0.17	160
***n*-pentane**	45	-	136	0.04	350
	60	-	215	0.06	337
	75	-	323	0.10	323
45% R245fa/ 55% *n*-pentane	30	16.1	198	0.05	285
	55	16.2	412	0.11	267
	80	15.9	768	0.21	244

Table 5.3. Comparison of transport properties relevant to frictional pressure gradient

	Transport Properties						
	P_r	ρ_l	ρ_v	$\rho_l\,\rho_v^{-1}$	μ_l	μ_v	σ
	-	kg m^{-3}	kg m^{-3}	-	kg m^{-1} s^{-1}	kg m^{-1} s^{-1}	N m^{-1}
R245fa	0.03	1352	7	189	4.29×10^{-4}	1.03×10^{-5}	0.014
	0.08	1282	17	78	3.08×10^{-4}	1.11×10^{-5}	0.011
	0.17	1204	34	36	2.25×10^{-4}	1.21×10^{-5}	0.008
n-pentane	0.04	601	4	153	1.85×10^{-4}	7.44×10^{-6}	0.013
	0.06	585	6	97	1.64×10^{-4}	7.84×10^{-6}	0.012
	0.10	568	9	63	1.46×10^{-4}	8.26×10^{-6}	0.010
45% R-245fa/ 55% *n*-pentane	0.05	794	7	109	2.17×10^{-4}	9.24×10^{-6}	0.014
	0.11	754	15	51	1.71×10^{-4}	1.00×10^{-5}	0.011
	0.21	709	27	26	1.36×10^{-4}	1.10×10^{-5}	0.008
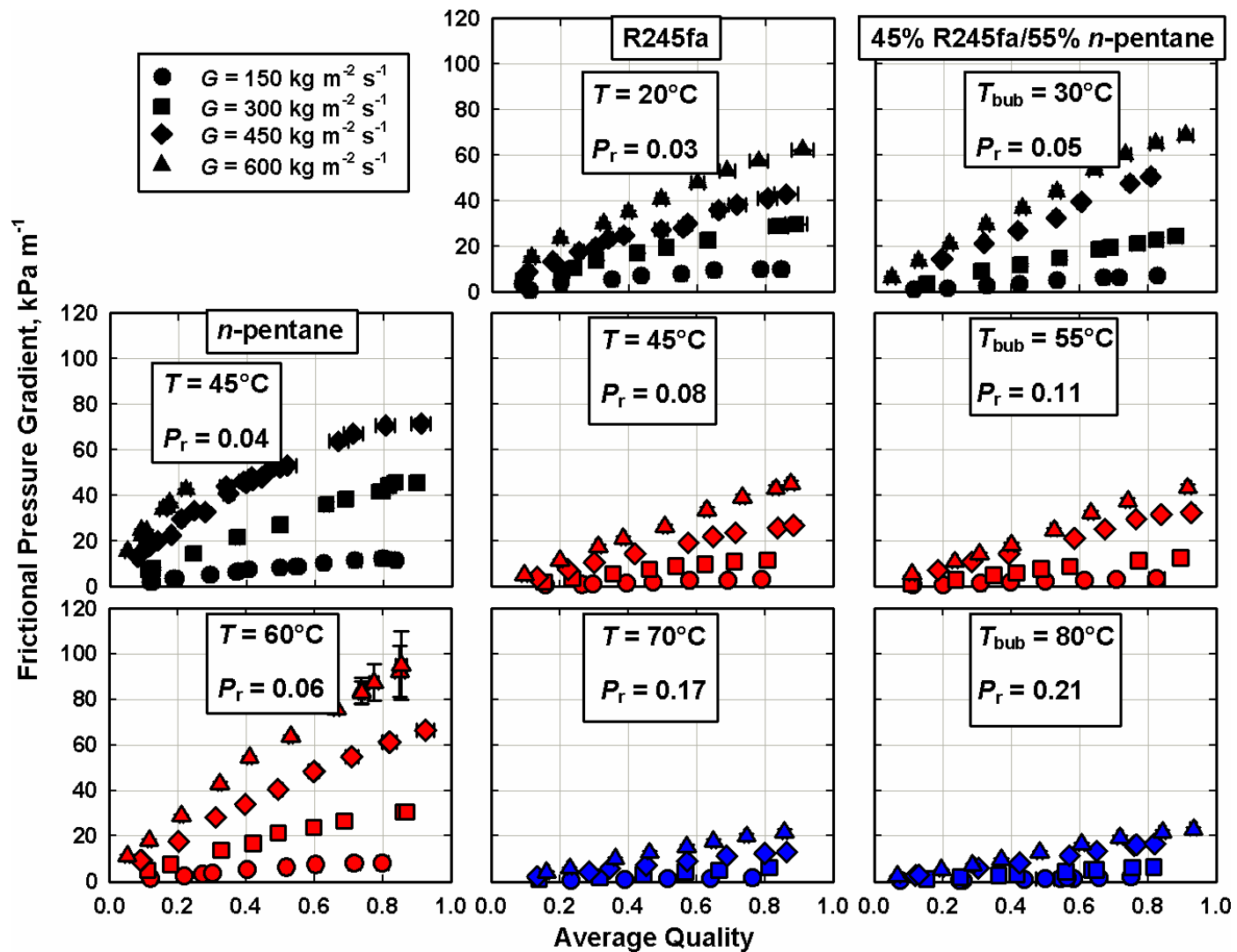
Figure 5.19. Experimental frictional pressure gradient in 7.75 mm tube versus quality for increasing mass flux

The transport properties of these fluids at the same conditions are summarized in Table 5.3. The low reduced pressures considered in the present study correspond to a wide range of liquid-to-vapor density ratios from 26 at the highest reduced pressure of 0.21 for the zeotropic mixture to 189 at the lowest reduced pressure of 0.03 for R245fa. While the density ratio decreases with increasing reduced pressure, the phase densities differ significantly by fluid type. Synthetic refrigerants, specifically R245fa, have greater phase densities than hydrocarbons, specifically n-pentane. Because the phase densities affect the phase velocities at similar mass flux and quality conditions, the difference in phase densities and density ratios between reduced pressures and fluids has a significant effect on the frictional pressure gradient. As the reduced pressure is increased, the pressure gradient decreases in part due an increase in the vapor phase density, which causes a reduction in the vapor phase velocity. For example, the liquid densities of R245fa range from 1,204 kg m^{-3} at $P_{avg} = 610$ kPa to 1,352 kg m^{-3} at $P_{avg} = 123$ kPa while the liquid densities of n-pentane range from 585 kg m^{-3} at $P_{avg} = 215$ kPa to 601 kg m^{-3} at $P_{avg} = 136$ kPa. However, the vapor densities of R245fa exhibit much larger changes, ranging from 34 kg m^{-3} at $P_{avg} = 610$ kPa to 7 kg m^{-3} at $P_{avg} = 123$ kPa. Similarly, the vapor density of n-pentane changes from 4 kg m^{-3} at $P_{avg} = 215$ kPa to 9 kg m^{-3} at $P_{avg} = 136$ kPa. Other secondary effects that tend to increase the pressure drop are the increase in the vapor viscosity. The decrease in liquid-phase viscosity and surface tension contribute to the decrease in pressure drop with increasing pressure.

Due to the larger phase densities of R245fa, the phase velocities of R245fa are lower than those of n-pentane, at otherwise comparable conditions. Therefore, the frictional pressure gradients of R245fa were less than those for n-pentane. For example, at a

nominal saturation temperature of 45°C, the reduced pressure of R245fa and *n*-pentane were 0.08 and 0.04, respectively. At $G \sim 300$ kg m^{-2} s^{-1} and $q_{avg} = 0.35$, the frictional pressure gradients of R245fa and *n*-pentane were 5.7 kPa m^{-1} and 27.1 kPa m^{-1}, respectively. At these conditions, the vapor and liquid superficial velocities of *n*-pentane were 37.5 m s^{-1} and 0.25 m s^{-1}, respectively, while the superficial liquid and vapor velocities of R245fa were only 6.5 m s^{-1} and 0.15 m s^{-1}, respectively.

Referring to Figure 5.20, the effect of reduced pressure in the zeotropic mixture on the frictional pressure gradient is slightly more complex than the effect of reduced pressure in the pure fluids. For example, for the R245fa/*n*-pentane data at $G \sim 500$ kg m^{-2} s^{-1} and $q = 0.4$, the frictional pressure gradient decreased from 26.7 kPa m^{-1} at $P_{avg} = 214$ kPa to 8.4 kPa m^{-1} at $P_{avg} = 756$ kPa. As discussed above, the liquid and vapor densities change significantly over the range of pressures in the present study. At $G \sim 500$ kg m^{-2} s^{-1} and $q \sim 0.4$, the superficial vapor velocity decreased as a results of changing phase densities from 21.6 m s^{-1} at $P_{avg} = 213.7$ kPa to 6.8 m s^{-1} at $P_{avg} = 756$ kPa, leading to lower pressure drop with increasing pressure. Also, at $q = 0.4$, the liquid viscosity decreased from 0.0020 kg m^{-1} s^{-1} at $P = 198$ kPa to 0.0013 kg m^{-1} s^{-1} at $P = 763$ kPa, with this increase contributing to an increased pressure drop, although the net effect is dominated by the change in vapor-phase density.
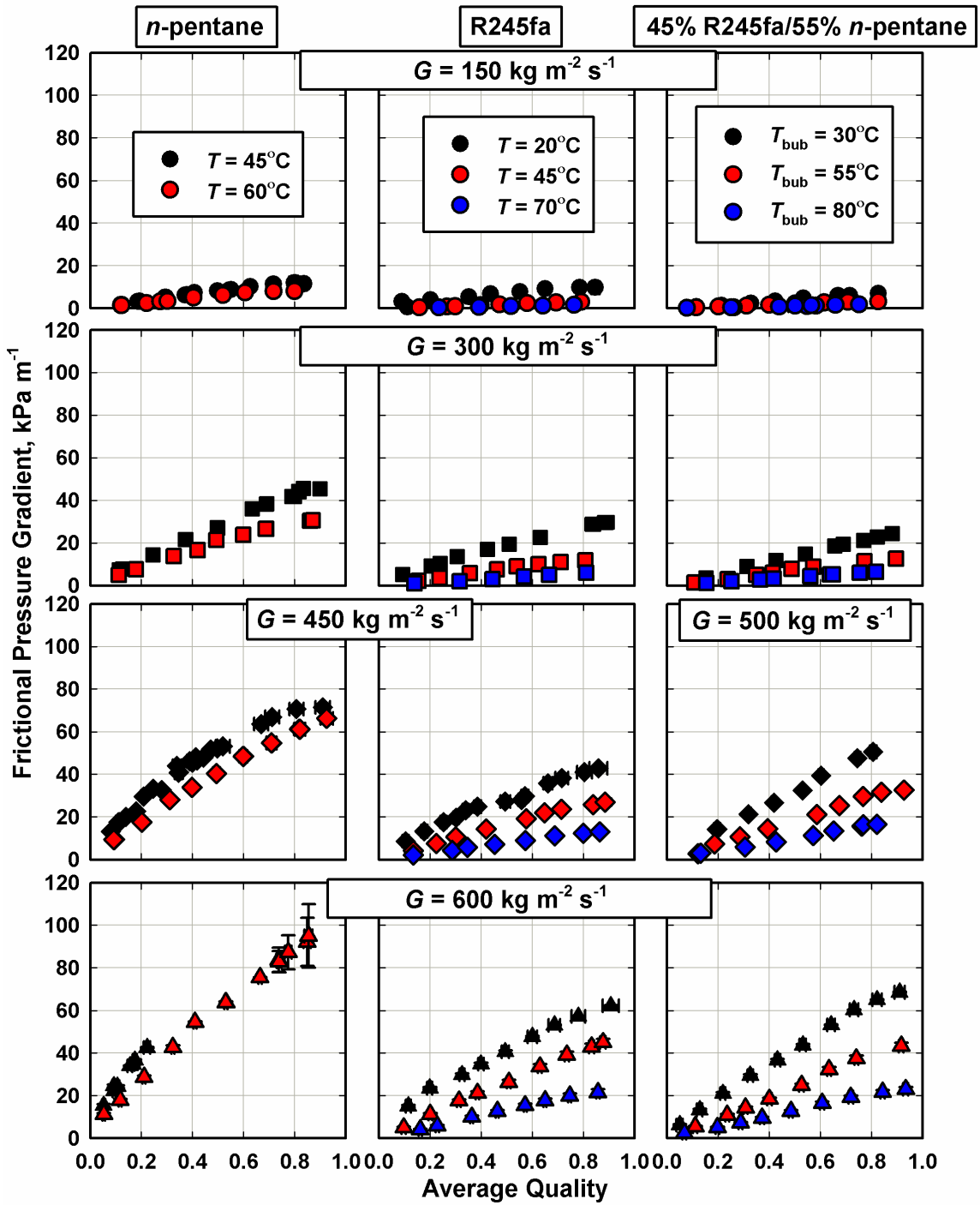
Figure 5.20. Experimental frictional pressure gradient in 7.75 mm tube versus quality for increasing pressure

In addition to the decrease in pressure gradient with increasing pressure due to changing phase density effects, there is a subtle density effect due to changing phase concentrations. The phase concentrations of R245fa are shown in Figure 5.21 versus quality. As shown in the figure, the liquid-phase is rich in *n*-pentane at high qualities, while the vapor-phase is rich in R245fa at low qualities.
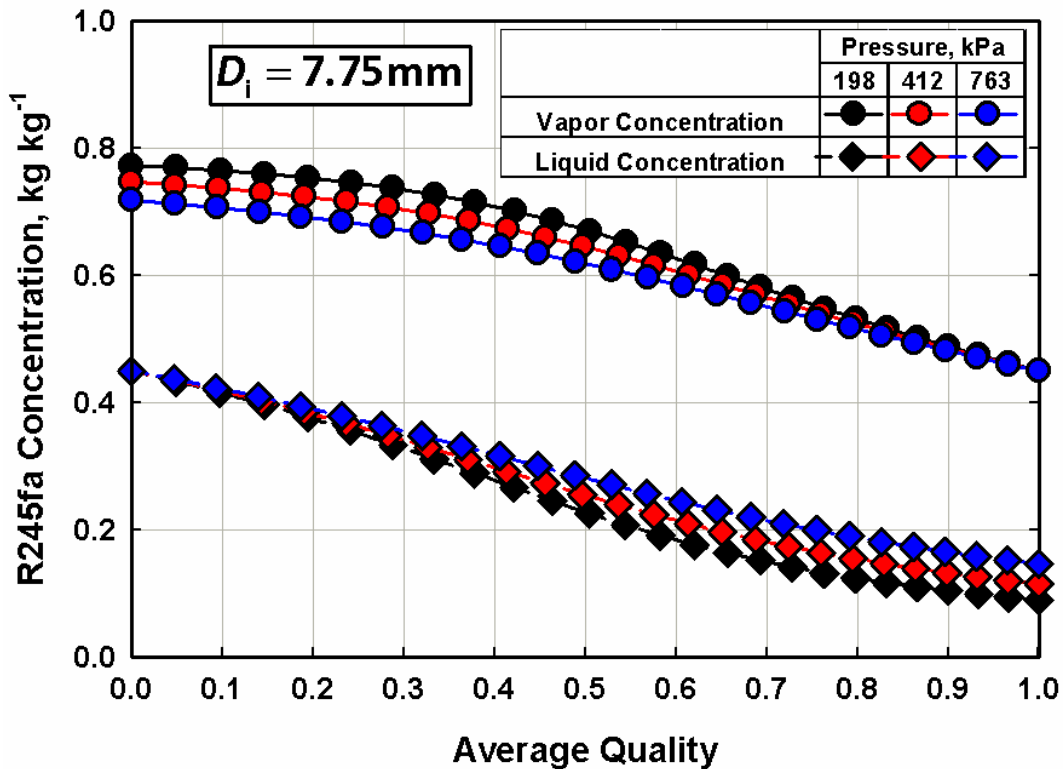
Figure 5.21. Phase concentration versus quality

The phase densities of the zeotropic mixture vary significantly over the quality range as shown in Figure 5.22. The change in phase densities occurs because of the difference in liquid- and vapor-phase density of the two components of the mixture, R245fa and *n*-pentane, and the composition shift in each phase that occurs during the phase-change process. At high qualities, the liquid has properties similar to those of a hydrocarbon, while the vapor has properties similar to those of the mixture. At low qualities, the vapor

has properties similar to those of a refrigerant, while the liquid has properties similar to those of the mixture. For this mixture, the density ratio, shown in Figure 5.23, initially decreases with increasing quality before reaching a minimum at $q_{avg} \sim 0.45$ then increasing with increasing quality. The decrease in phase densities of the mixture with increasing quality also contributed to increase in the pressure gradient. For example, at q = 0.9 and P = 198 kPa, 412 kPa, and 763 kPa, the density ratios are 84.5, 40.5, and 21.1, respectively. It should be noted that this differs from the bulk liquid-to-vapor density ratios of 109 and 27 at P = 198 kPa and P = 763 kPa, respectively. This is due to the phase concentration change of the liquid and vapor phase with quality. For a 45% R245fa/55% n-pentane mixture at P = 198 kPa and q = 0.8, the equilibrium liquid-phase composition is 12% R245fa/88% n-pentane, while the equilibrium vapor-phase composition is 53% R245fa/47% n-pentane. In contrast, at P = 198 kPa and q = 0.2, the equilibrium liquid-phase composition is 37% R245fa/63% n-pentane, while the equilibrium vapor-phase composition is 75% R245fa/25% n-pentane. At P = 198 kPa, pure R245fa and pure n-pentane have liquid-phase densities of 1316 kg m^{-3} and 588 kg m^{-3}, respectively, and vapor-phase densities of 11 kg m^{-3} and 6 kg m^{-3}, respectively. With these individual phase compositions, a 45% R-245fa/55% n-pentane mixture at P = 198 kPa has liquid- and vapor-phase densities of 793 kg m^{-3} and 7 kg m^{-3}, respectively. As the reduced pressure decreases, and the liquid-to-vapor density ratio increases, the shear force between the phases increases as the vapor occupies more of the tube and at an increased velocity, in turn increasing the probability of annular flow.
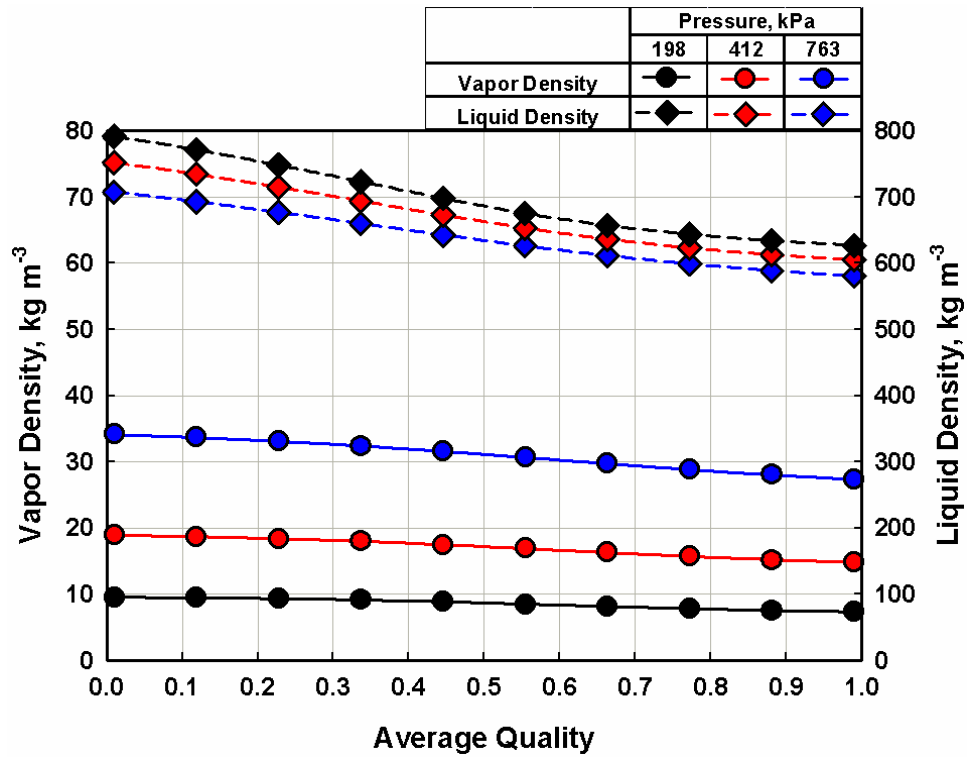
Figure 5.22. Zeotropic mixture phase densities versus quality
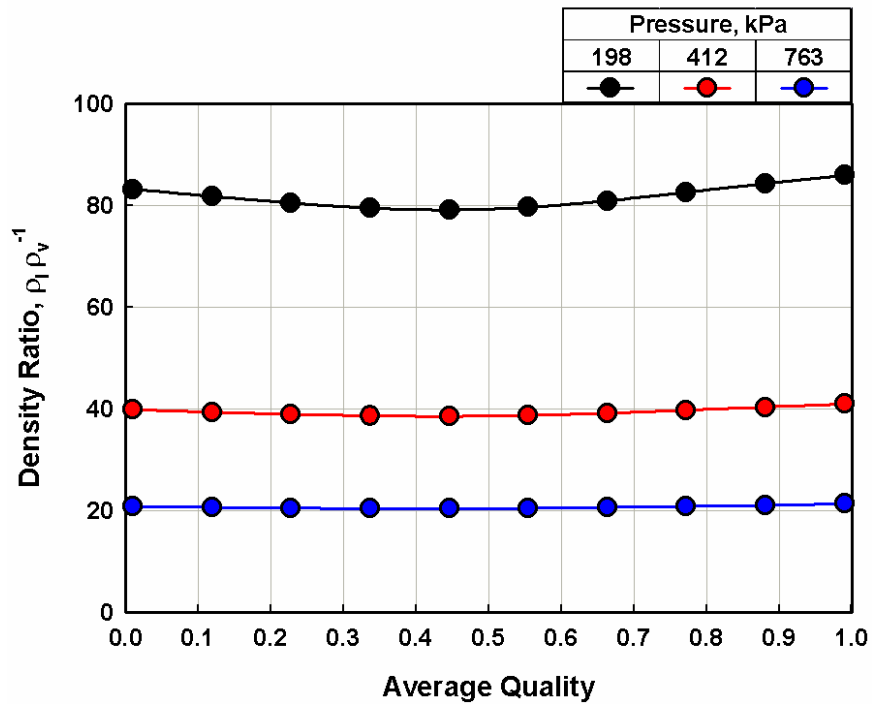
Figure 5.23. Zeotropic mixture density ratio versus quality

256

The liquid-phase viscosities of both pure fluids and the mixture decrease with increasing pressure. For example, the liquid-phase viscosity of R245fa decreased from 4.29×10^{-4} kg m^{-1} s^{-1} at $P_{avg} = 123$ kPa to 2.25×10^{-4} kg m^{-1} s^{-1} at $P_{avg} = 610$ kPa. Decreasing liquid viscosity with increasing pressure results in an increase in liquid Reynolds number. This tends to increase the frictional pressure gradient with increasing pressure. However, the increase in pressure gradient with increasing pressure due to viscosity effects is small relative to the increasing density effects resulting in a net decrease.

Comparing the pure fluid to the zeotropic mixture, at bubble point temperatures of 30°C and 55°C, the reduced pressures of the R245fa/n-pentane mixture were 0.05 and 0.11, respectively. At $G \sim 300$ kg m^{-2} s^{-1} and $q_{avg} = 0.35$, the frictional pressure gradients were 9.0 kPa m^{-1} and 5.8 kPa m^{-1} at $T_{Bub} = 30$°C and 55°C, respectively. At $G \sim 300$ kg m^{-2} s^{-1}, $q_{avg} = 0.35$, and $T_{Bub} = 30$°C and 55°C, the superficial liquid velocities were 0.55 m s^{-1} and 0.28 m s^{-1}, respectively, while the superficial vapor velocities were 20.5 m s^{-1} and 5.9 m s^{-1}, respectively. When compared to the pure n-pentane and pure R245fa at T_{Sat} = 45°C, the pressure drops for the representative mixture data points lie between those of the two pure fluids. The superficial liquid and vapor velocities at $T_{Bub} = 30$°C also lie between the two corresponding pure fluid values.

5.1.3 Pure Fluid Heat Transfer Coefficient
The discussion of the heat transfer coefficient data from the present study is divided into two sections. The pure fluid data are presented and discussed here. The zeotropic mixture heat transfer coefficient data are presented and discussed in the next section. As discussed in Chapter 4, the heat transfer coefficient was calculated from the test section

heat duty as determined by the thermal amplification technique and the thermal resistance network of the test section. The primary and secondary loops were intentionally controlled to a nominal temperature difference of 10K between the test fluid and coolant fluid. A representative set of LMTDs for the *n*-pentane 7.75 mm ID is shown in Figure 5.24. In this data set, the LMTDs range from 7.8 to 14.3K with an average of 10.3K. The average LMTDs for each pure fluid at each saturation condition are summarized in Table 5.4. Due to system limitations, namely the freezing point of the coolant water (0°C), the LMTD in the 20°C R245fa data is lightly lower than 10K with an average of 6.5K.
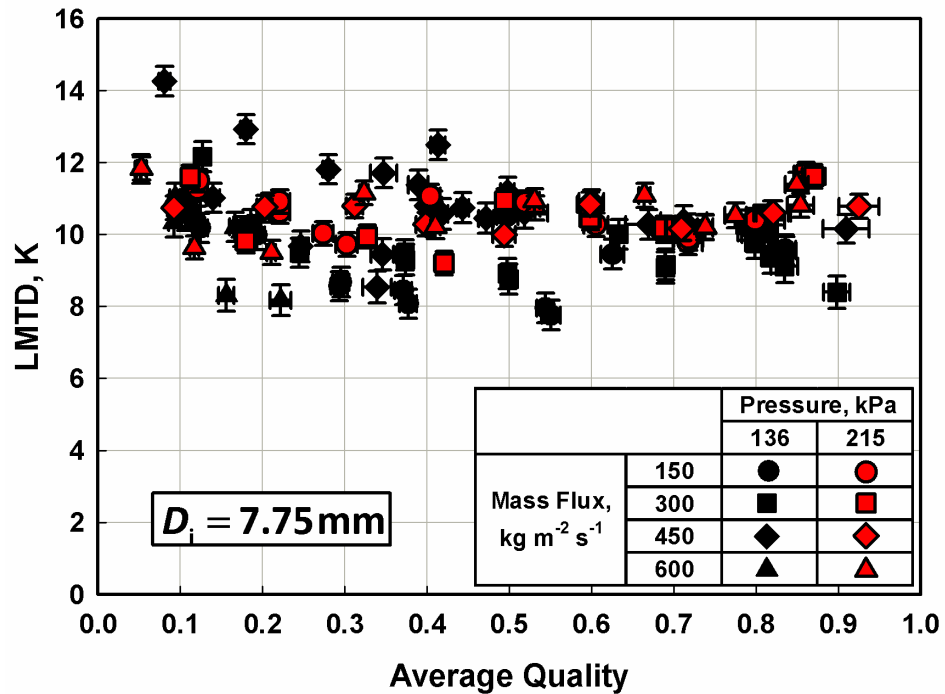
Figure 5.24. Representative LMTD versus quality for *n*-pentane in 7.75 mm ID tube

Table 5.4. Summary of pure fluid heat transfer coefficient data

Fluid	D_i	T_{Sat}	P_r	Number of Data	LMTD	Δq	R_{ratio}	$\dot{Q}_{Pump}$	$U\,h_f$
	mm	°C	-		K	-	-	% $\dot{Q}_{Test}$	% h_f
R245fa	7.75	20	0.03	41	6.5	0.09	5.2	19.5%	21.6%
		45	0.08	34	10.5	0.14	5.9	7.0%	9.0%
		70	0.17	27	10.7	0.13	8.6	9.1%	8.7%
n-pentane		45	0.04	65	10.1	0.11	5.1	12.8%	11.1%
		60	0.06	48	10.6	0.11	6.5	13.3%	10.6%
n-pentane	14.45	45	0.04	35	11.2	0.10	4.8	6.8%	8.5%
		60	0.06	27	12.5	0.11	4.7	5.1%	7.5%
		75	0.10	38	11.6	0.07	4.6	4.9%	7.6%
Average					10.4	0.11	5.6	10.5%	10.9%

To ensure accurate calculation of the condensation heat transfer coefficient, the condensation thermal resistance must be the dominant thermal resistance. The resistance ratio, $R_f\,(R_{wall} + R_{conv,eq})^{-1}$, should be high while minimizing the pump heat addition as a percentage of the test section heat duty. The wall thermal resistance was fixed by the construction of the test section. The equivalent convective resistance on the annulus side and the pump heat addition are coupled. These two factors were balanced during testing to minimize uncertainty, and 25% and 50% uncertainties were applied to the convective resistance and the pump heat addition, respectively. In the representative 7.75 mm ID *n*-pentane data set, the average resistance ratio was 5.7 while the average pump heat addition was 13.0% of the measured tests section heat duty. The uncertainty in the test section heat duty ranged from 4.1% to 13.5% with an average of 6.9%. In general, high resistance ratios were easily obtained at low qualities and low mass flux conditions, at which the test fluid heat transfer coefficient was low. Referring to Figure 5.25, the maximum resistance ratio in the representative data set occurred at $P_{avg} = 220.1$ kPa, $G =$

155.0 kg m^{-2} s^{-1}, and q_{avg} = 0.12. The lowest resistance ratio of 2.6 in the representative

data set occurred at P_{avg} = 132.7 kPa, G = 298.3 kg m^{-2} s^{-1}, and q_{avg} = 0.90. At this point,

the pump heat addition was 10.1% of the measured test section heat duty. The resulting

uncertainty in the heat transfer coefficient was 14.2%. Over the range of conditions in the

representative data set, the average uncertainty in the heat transfer coefficient was 10.9%.

Referring to Figure 5.26, the minimum uncertainty in measured heat transfer coefficient

of 8.2% occurred at P_{avg} = 143.6 kPa, G = 450.8 kg m^{-2} s^{-1}, and q_{avg} = 0.08, while the

maximum of 15.3% occurred at P_{avg} = 140.3 kPa, G = 305.5 kg m^{-2} s^{-1}, and q_{avg} = 0.82.

The average resistance ratio, pump heat addition contribution, and uncertainty in the heat

transfer coefficient are summarized in Table 5.4.
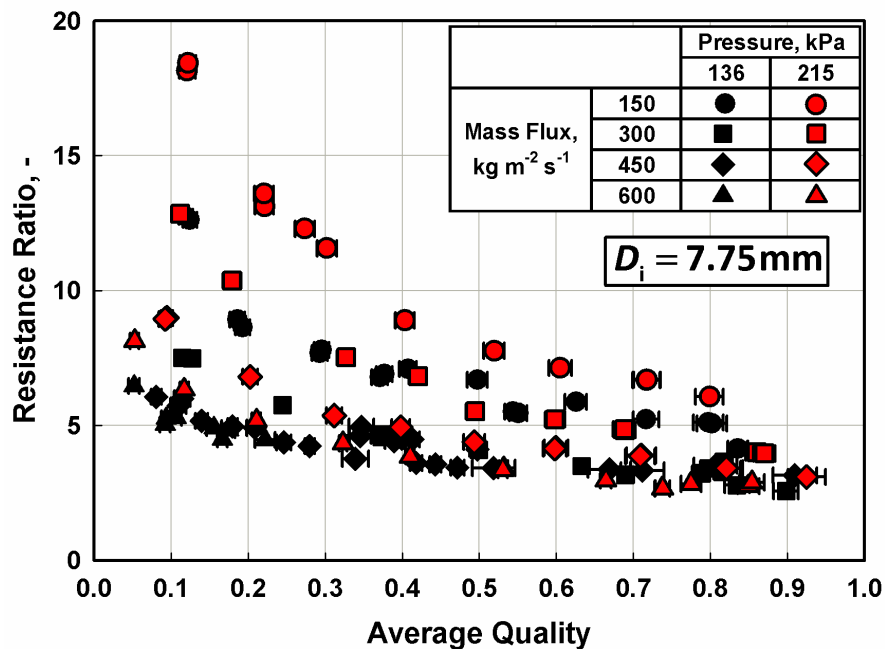
Figure 5.25. *n*-pentane resistance ratio
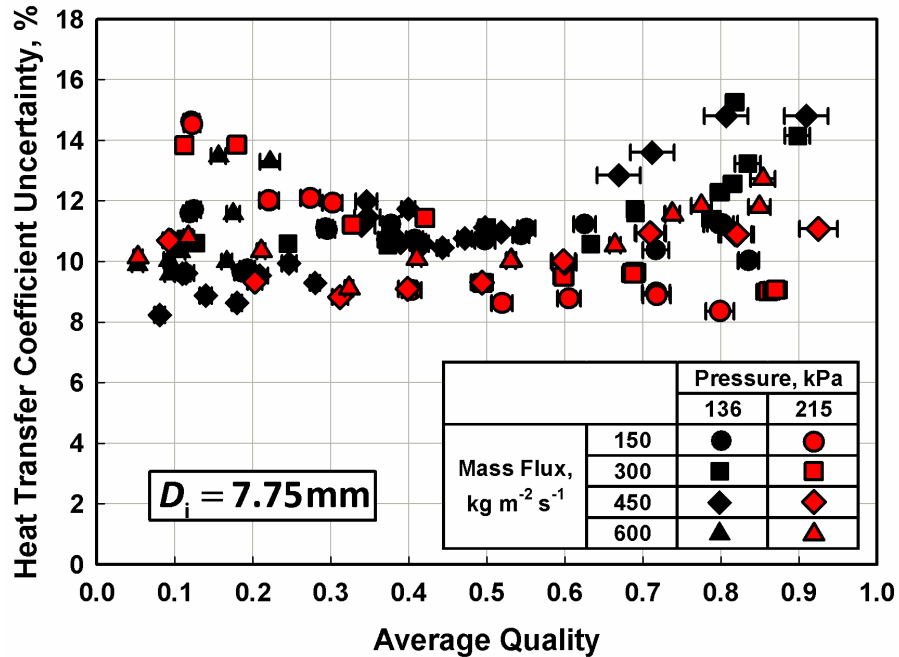
Figure 5.26. Representative uncertainty in measured heat transfer coefficient versus quality for *n*-pentane in 7.75 mm ID tube

5.1.3.1 General trends and effect of diameter– n-pentane results

The measured heat transfer coefficients in Figures 5.27 and 5.28 range from 1.43 kW m^{-2} K^{-1} at P_{avg} = 220 kPa, G = 155 kg m^{-2} s^{-1}, and q_{avg} = 0.12 to 14.6 kW m^{-2} K^{-1} at P_{avg} = 248 kPa, G = 603 kg m^{-2} s^{-1}, and q_{avg} = 0.85. Because of the coupled nature of two-phase heat transfer coefficient and pressure gradient, the heat transfer coefficient shows trends with increasing mass flux, quality, and pressure similar to those for the frictional pressure gradient. Increasing mass flux and quality result in increasing shear forces at the vapor-liquid interface as the vapor velocity increases, causing a thinning of the liquid film along the wall and entraining liquid in the vapor core as predicted by Soliman (1986). The thinning liquid layer decreases the thermal resistance of the liquid film, resulting in an increased heat transfer coefficient and exposing the vapor to a lower temperature liquid interface, thus increasing the driving temperature difference for condensation.
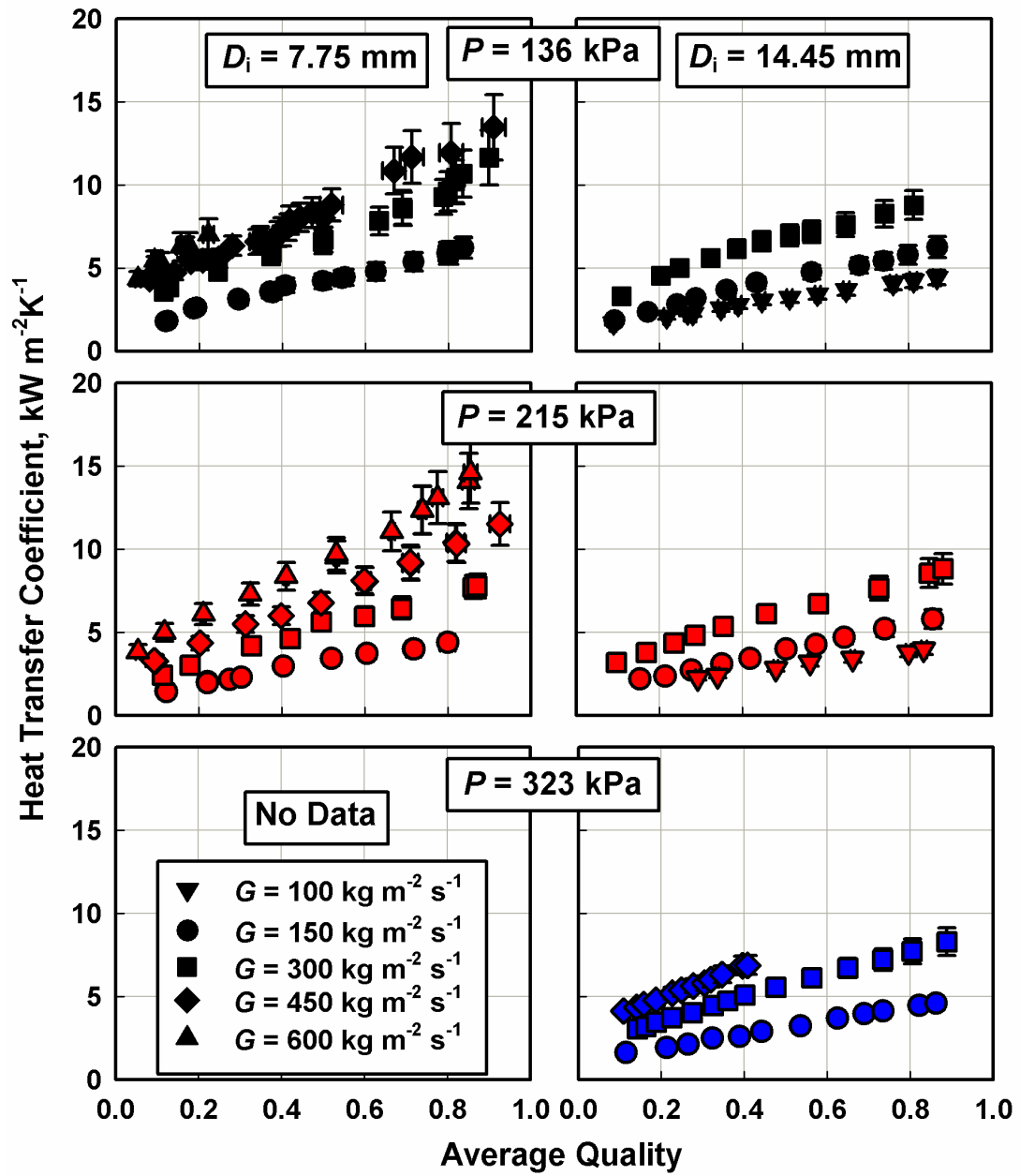
Figure 5.27. *n*-pentane experimental heat transfer coefficient versus quality for increasing mass flux

262
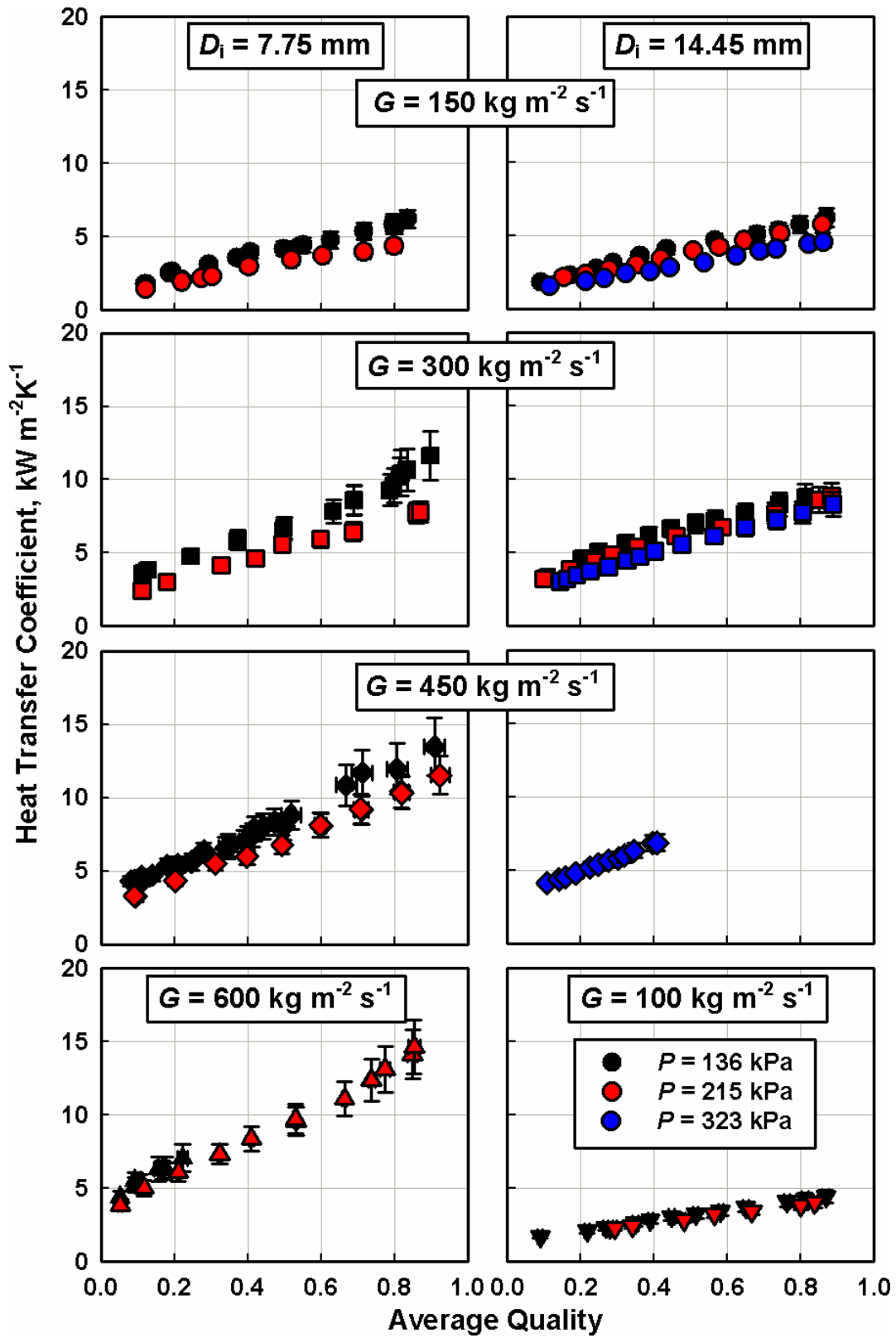
Figure 5.28. *n*-pentane experimental heat transfer coefficient versus quality for increasing pressure

The lower vapor density at low pressures further compounds these effects resulting in higher heat transfer coefficients at lower pressures. For example, in the 14.45 mm ID tube at $G \sim 300$ kg m^{-2} s^{-1}, and $q \sim 0.45$, the heat transfer coefficients were 5.5 kW m^{-2} K^{-1} at P_{avg} = 371 kPa and 6.5 kW m^{-2} K^{-1} at P_{avg} = 255 kPa. The latent heat decreases with increasing pressure. For example, the latent heat is 350 kJ kg^{-1} at P = 136 kPa, and 323 kJ kg^{-1} at P = 323 kPa. The decrease in latent heat means less energy is released at higher pressures for a given quality change, thereby resulting in lower heat transfer coefficients. Additionally, the liquid thermal conductivity decreases with increasing pressure. For example, the liquid thermal conductivity was 0.094 W m^{-1} K^{-1} at P = 323 kPa and 0.104 W m^{-1} K^{-1} at P = 136 kPa. Because the thermal conductivity of the liquid phase decreases with increasing pressure, the thermal resistance due to conduction in the liquid film increases, resulting in an lower heat transfer coefficient with increasing pressures.

The changes in liquid-phase viscosity and surface tension tend to destabilize the flow with increasing pressure. For example, the liquid-phase viscosity is 1.46×10^{-4} kg m^{-1} s^{-1} at P = 323 kPa, and 1.85×10^{-4} kg m^{-1} s^{-1} at P = 136 kPa, while the surface tension decreases from 0.013 N m^{-1} at P = 136 kPa to 0.010 N m^{-1} at P = 323 kPa to. While these effects would tend to decrease the heat transfer coefficient with increasing pressure due to an increase in turbulence in the liquid film and more unstable liquid-vapor interface, the effects of higher vapor density and lower latent heat and liquid-phase thermal conductivity are stronger, resulting in a net decrease in heat transfer coefficient with increasing pressure.

Because of the coupled nature of the two-phase heat transfer coefficient and pressure gradient, the heat transfer coefficient was expected to show a significant decrease

increasing tube diameter. Referring to Figure 5.28, a slight decrease occurred for some points but not all. For example, at $P_{avg} \sim 136$ kPa, $G = 150$ kg m^{-2} s^{-1}, and $q_{avg} = 0.2$ the measured heat transfer coefficient in the 7.75 mm ID tube was 2.6 kW m^{-2} K^{-1}, while in the 14.45 mm ID tube, the measured heat transfer coefficient was 2.3 kW m^{-2} K^{-1}. However, in many cases the measured heat transfer coefficients in the 14.45 mm ID tube were substantially similar or larger than those seen for the 7.75 mm ID tube. For example, at $P_{avg} \sim 215$ kPa, $G \sim 300$ kg m^{-2} s^{-1}, and $q_{avg} \sim 0.32$ the measured heat transfer coefficient in the 7.75 mm ID tube was 4.2 kW m^{-2} K^{-1}, while in the 14.45 mm ID tube, the measured heat transfer coefficient was 5.6 kW m^{-2} K^{-1}. Because the absolute pressure at the outlet of the post-condenser was maintained above approximately 100 kPa, the average test section pressure in the 14.45 mm ID tube increased away from the nominal condition with increasing quality. For example, at $P_{avg} \sim 215$ kPa, $G \sim 300$ kg m^{-2} s^{-1} the pressure at $q_{avg} = 0.10$ was 221.1 kPa, while the pressure at $q_{avg} = 0.88$ in the same data set increased to 348 kPa. Therefore, a direct visual comparison of the nominal conditions in Figures 5.27 and 5.28 does not show the diameter effect due to the increasing pressure. Mandane *et al.* (1974) and Weisman *et al.* (1979) both observed an elimination of diameter effect on flow regime above approximately 10 mm. As noted in the propane visualization results section above, the 7.0 mm ID tube exhibits a significant upper liquid film in the wavy regime across the conditions examined. The 15.0 mm ID showed no such upper film in the wavy regime. Additionally, the higher void fractions in the annular regime in the 15.0 mm tube indicate a thinner liquid film relative to the tube diameter. The presence of an upper film in the 7.0 mm tube and no film in the 15.0 mm tube even

in the annular regime would explain an increased heat transfer coefficient in the larger tube.

5.1.3.2 *Effect of working fluid*

The effect of changing the fluid from *n*-pentane to R245fa in a 7.75 mm ID tube is discussed in this section. The measured heat transfer coefficients for R245fa in Figures 5.29 and 5.30 range from 1.42 kW m^{-2} K^{-1} at P_{avg} = 601 kPa, G = 168 kg m^{-2} s^{-1}, and q_{avg} = 0.23 to 11.1 kW m^{-2} K^{-1} at P_{avg} = 198 kPa, G = 598 kg m^{-2} s^{-1}, and q_{avg} = 0.91. The measured heat transfer coefficients for *n*-pentane range from 1.43 kW m^{-2} K^{-1} at P_{avg} = 220 kPa, G = 155 kg m^{-2} s^{-1}, and q_{avg} = 0.12 to 14.6 kW m^{-2} K^{-1} at P_{avg} = 248 kPa, G = 603 kg m^{-2} s^{-1}, and q_{avg} = 0.85. The general trends of increasing heat transfer coefficient with increasing mass flux and quality and decreasing heat transfer coefficient with increasing pressure were also observed in the R245fa data. As discussed in the pressure gradient section, the properties differ significantly by fluid type, and a summary of transport properties relevant to heat transfer is presented in Table 5.5. The lower densities of *n*-pentane relative to R245fa, discussed above, result in higher phase velocities of *n*-pentane that result in thinning of the liquid film as well as increased mixing as described previously. Therefore, the heat transfer coefficients of R245fa were lower than those of *n*-pentane. For example at T_{Sat} = 45°C, G = 300 kg m^{-2} s^{-1}, and q_{avg} = 0.3 the measured heat transfer coefficient for *n*-pentane was 4.2 kW m^{-2} K^{-1}, while the measured heat transfer coefficient for R245fa was 1.8 kW m^{-2} K^{-1}.
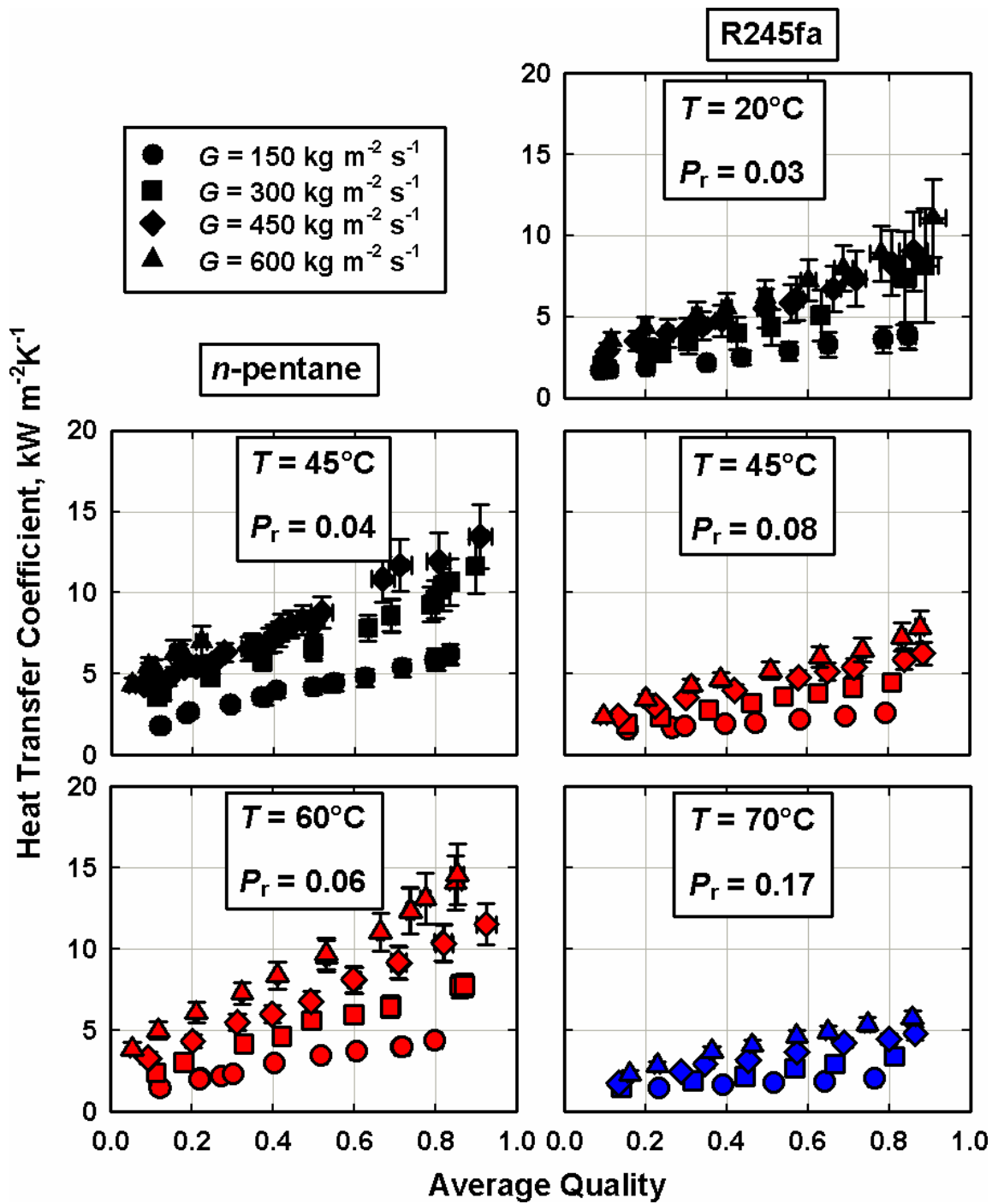
Figure 5.29. Pure fluid experimental heat transfer coefficient versus quality for increasing mass flux
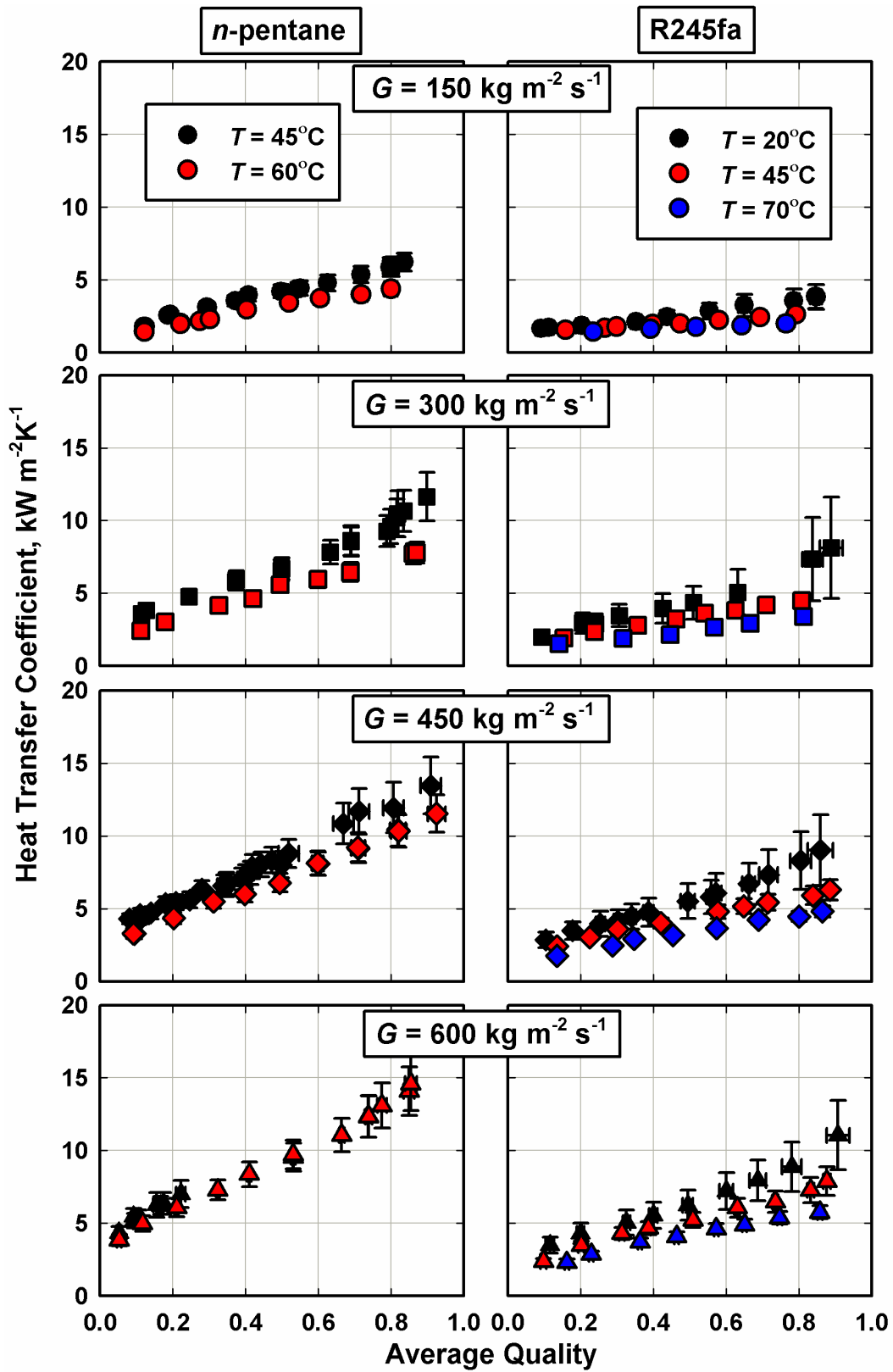
Figure 5.30. Pure fluid experimental heat transfer coefficient versus quality for increasing pressure

Table 5.5. Comparison of transport properties relevant to heat transfer coefficient

Fluid	P_r	i_{fg}	k_1	ρ_1	ρ_v	$\rho_1 \rho_v^{-1}$	μ_1	σ
					Transport Properties			
	-	kJ kg^{-1}	W m^{-1} K^{-1}	kg m^{-3}	kg m^{-3}	-	kg m^{-1} s^{-1}	N m^{-1}
R245fa	0.03	193	0.090	1352	7	189	4.29×10^{-4}	0.014
	0.08	178	0.082	1282	17	78	3.08×10^{-4}	0.011
	0.17	160	0.074	1204	34	36	2.25×10^{-4}	0.008
***n*-pentane**	0.04	350	0.104	601	4	153	1.85×10^{-4}	0.013
	0.06	337	0.099	585	6	97	1.64×10^{-4}	0.012
	0.10	323	0.094	568	9	63	1.46×10^{-4}	0.010

Lower latent heats and liquid-phase thermal conductivities, and higher liquid viscosities of R245fa compared to those of *n*-pentane also contribute to the lower heat transfer coefficients observed in R245fa relative to *n*-pentane. The latent heats of R245fa range from 193 kJ kg^{-1} at P_{avg} = 123 kPa to 160 kJ kg^{-1} at P_{avg} = 610 kPa, while the latent heats of *n*-pentane were significantly higher, and range from 350 kJ kg^{-1} at P_{avg} = 136 kPa to 337 kJ kg^{-1} at P_{avg} = 215 kPa. The lower latent heat of R245fa results in less energy released per unit mass condensed than *n*-pentane. Additionally, the liquid thermal conductivity of R245fa is lower than that of *n*-pentane. For example, the liquid-phase thermal conductivity of R245fa ranges from 0.090 W m^{-2} K^{-1} at P_{avg} = 123 kPa to 0.074 W m^{-2} K^{-1} at P_{avg} = 610 kPa while the liquid-phase thermal conductivity of *n*-pentane ranges from 0.104 kg m^{-3} at P_{avg} = 136 kPa to 0.099 W m^{-2} K^{-1} at P_{avg} = 215 kPa. The lower thermal conductivity of R245fa results in a greater thermal resistance in the liquid film. Furthermore, the stabilizing effects of the liquid-phase viscosity are higher for R245fa, which results in lower heat transfer coefficients of R245fa due to higher liquid-phase viscosity. The surface tension for both fluids ranges from 0.008 to 0.014 N m^{-1},

therefore, surface tension is not a significant parameter in determining heat transfer coefficients for these two fluids.

5.1.4 Zeotropic Mixture Heat Transfer Coefficient

As discussed in Chapter 4, two methods for calculation of the heat transfer coefficient were used for the zeotropic mixture data. Across the 113 data points in this study, an average difference of 11.9% between the two calculation methods was seen, with a range of 0.04% to 57.7%. The largest differences occur at high mass flux, high quality, and low pressure conditions where the heat transfer rates were largest and the mass transfer effects were high, resulting in the greatest departure from equilibrium.

Measured heat duties and heat transfer coefficients are discussed in this section. There was a total of 113 data points taken at the nominal conditions outlined in Table 5.6. Of the 113 data points, 35 were at nominal conditions of $P = 198$ kPa, 41 were at $P = 412$ kPa, and 37 at $P = 763$ kPa. The results from both analysis methods are presented with the Price and Bell (1974) method denoted by an asterisk. Similar to the pure fluid data, the LMTD between the fluid and the coolant was maintained at a nominal value of 10K. The LMTDs between the bulk equilibrium temperatures and the measured coolant temperatures, defined in Figure 5.31, are shown on the left in Figure 5.32. The LMTDs between the vapor-liquid interface temperature and the measured coolant temperatures, as calculated using the Price and Bell (1974) method, are shown on the right in Figure 5.32. Because non-equilibrium effects cause the interface temperature to be below the bulk equilibrium temperature, the LMTDs for the Price and Bell (1974) method tend to be slightly lower. As discussed in the pure fluid heat transfer coefficient section, a balance between a low thermal resistance on the annulus side and the pump heat addition was

made to maintain low uncertainties. The pump heat addition as a percentage of the total test section heat duty and the annulus side resistance were fixed by system conditions and therefore identical for both analysis methods. Because the LMTD was smaller for the non-equilibrium analysis and the heat duty was the same at a given condition, the film heat transfer coefficient (calculated between the vapor-liquid interface and the coolant temperatures using the non-equilibrium analysis) was higher than the apparent heat transfer coefficient (calculated between the fluid equilibrium and the coolant temperatures using the equilibrium analysis). Additionally, the resistance ratio was lower for the non-equilibrium analysis than the equilibrium analysis, as shown in Figure 5.33. A trend of decreased resistance ratio with increasing quality that was observed in the pure fluids was also present in the mixture data. The lower resistance ratios and LMTD in the non-equilibrium analysis as well as the additional uncertainties applied within the non-equilibrium analysis procedure lead to higher uncertainties for the non-equilibrium analysis. The average LMTD, resistance ratio, pump heat addition, and heat transfer coefficient uncertainty are summarized in Table 5.6.

Table 5.6. Summary of zeotropic mixture heat transfer coefficient results

Fluid	D_i	T_{Bub}	P_r	Number of Data	LMTD	Δq	R_{ratio}	$\dot{Q}_{Pump}$	Uh_f
	mm	°C	-		K	-	-	% $\dot{Q}_{Test}$	% h_f
45% R245fa/ 55% _n_ -pentane	7.75	30	0.05	35	10.8 / 9.6*	0.09	5.2 / 4.6*	7.7%	11.3% / 13.3%*
		55	0.11	41	11.0 / 10.1*	0.09	6.5 / 6.0*	7.0%	9.2% / 10.3%*
		80	0.21	37	11.1 / 10.4*	0.09	10.7 / 10.0*	9.4%	11.4% / 11.8%*
Average					11.0 / 10.1*	0.09	7.5 / 6.9*	8.0%	10.6% / 11.8%*
* Denotes Price and Bell (1974) Heat Transfer Coefficient Results									
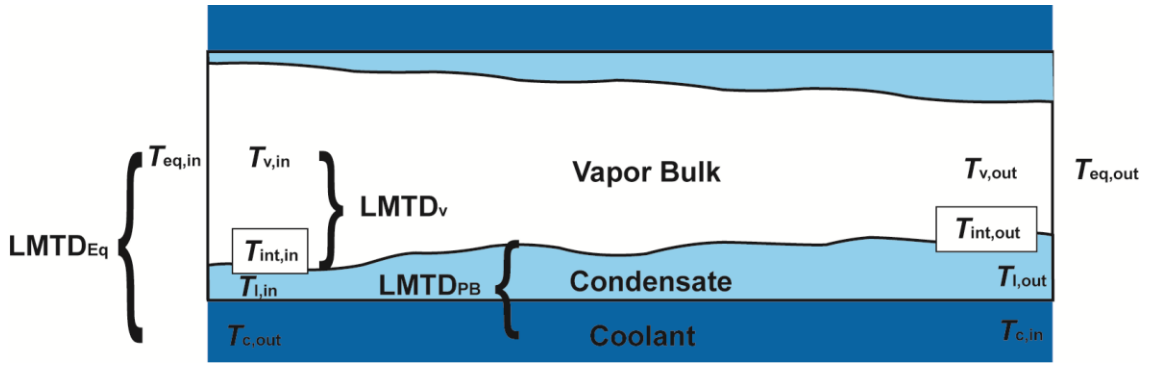
Figure 5.31. Test section schematic with LMTD definitions
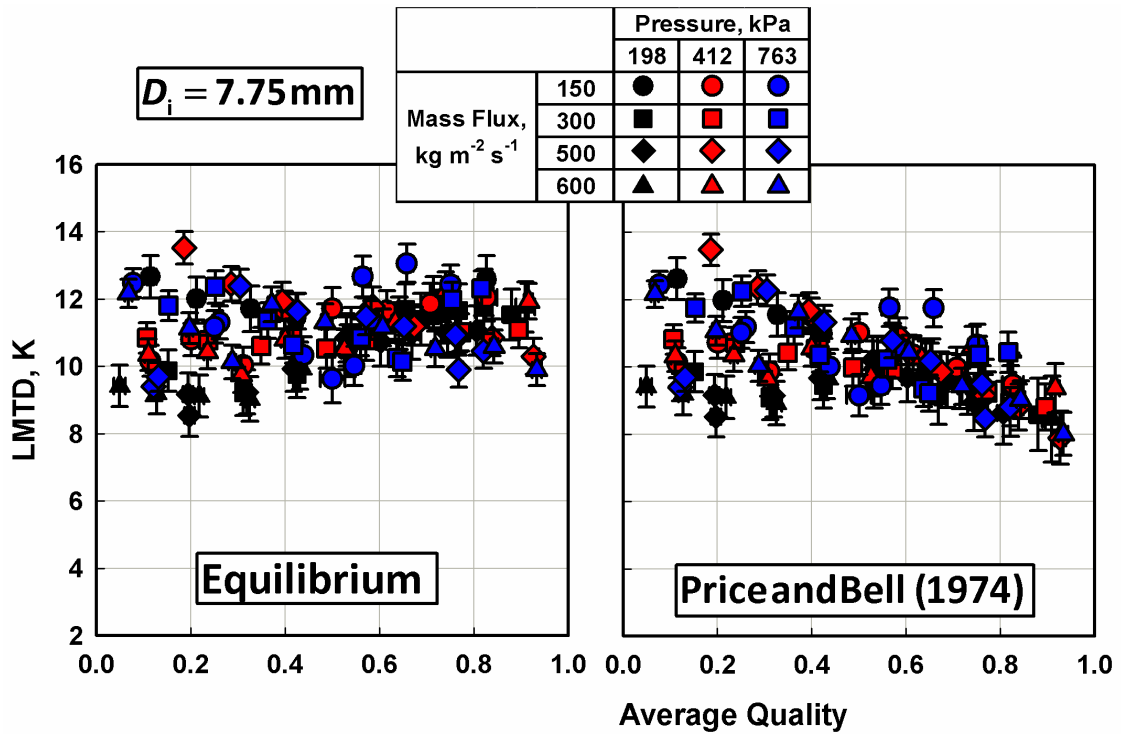
Figure 5.32. LMTDs using the equilibrium and Price and Bell (1974) methods
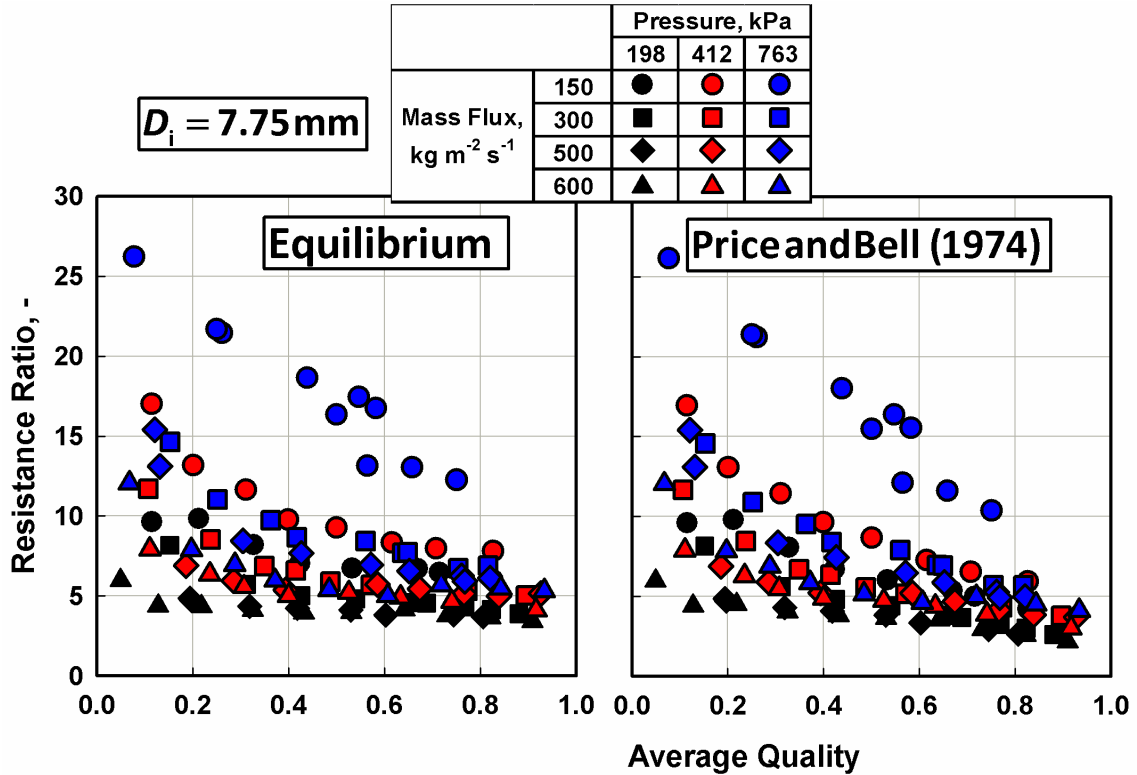
Figure 5.33. Resistance ratios for equilibrium LMTD and Price and Bell (1974) methods

The temperature glide in the test section due to the quality change and the pressure drop is shown in Figure 5.34. Using the temperature glide at equilibrium and a nominal quality change of 0.1, the temperature glide in the test section at constant pressure was approximately 2K. However, because the test section pressure drop was substantial at low pressures and high mass fluxes as discussed above, the equilibrium temperature change in the test section exceeded 8K in some cases. The change in temperature of the interface between the inlet and outlet of the test section as calculated using the Price and Bell (1974) method is also shown in Figure 5.34. At high qualities, there was a noticeable difference between the equilibrium and non-equilibrium temperature glide. For example, at P_{avg} = 407 kPa, G = 149 kg m^{-2} s^{-1}, and q_{avg} = 0.82, the equilibrium and non-equilibrium temperature glides were 2.9K and 7.6K, respectively. The difference in

temperature glide between the equilibrium and non-equilibrium analysis for each data point is shown in Figure 5.35. The magnitude of the temperature glide for both methods decreases with increasing pressure. For example, at $G \sim 500$ kg m^{-2} s^{-1} and $q_{avg} = 0.75$ the equilibrium and non-equilibrium temperature glides were 6.7K and 10.0K at $P_{avg} = 219.1$ kPa, respectively and 2.2K and 4.9K at $P_{avg} = 738.6$ kPa, respectively. However, the non-equilibrium effects show much less dependence on the pressure than the temperature glide. For example, at $G \sim 500$ kg m^{-2} s^{-1} and $q_{avg} = 0.75$ the change in glide between the equilibrium and non-equilibrium analysis methods were 3.3K at $P_{avg} = 219.1$ kPa and 2.7K at $P_{avg} = 738.6$ kPa.
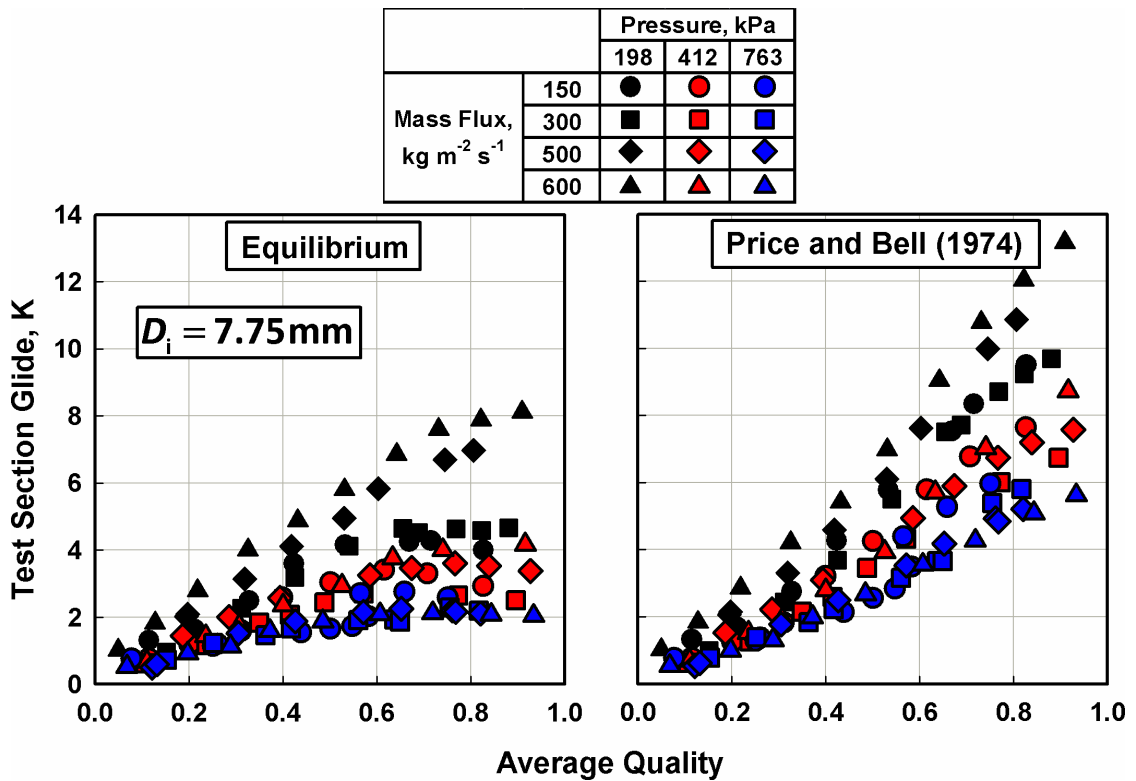
Figure 5.34. Test section temperature glide
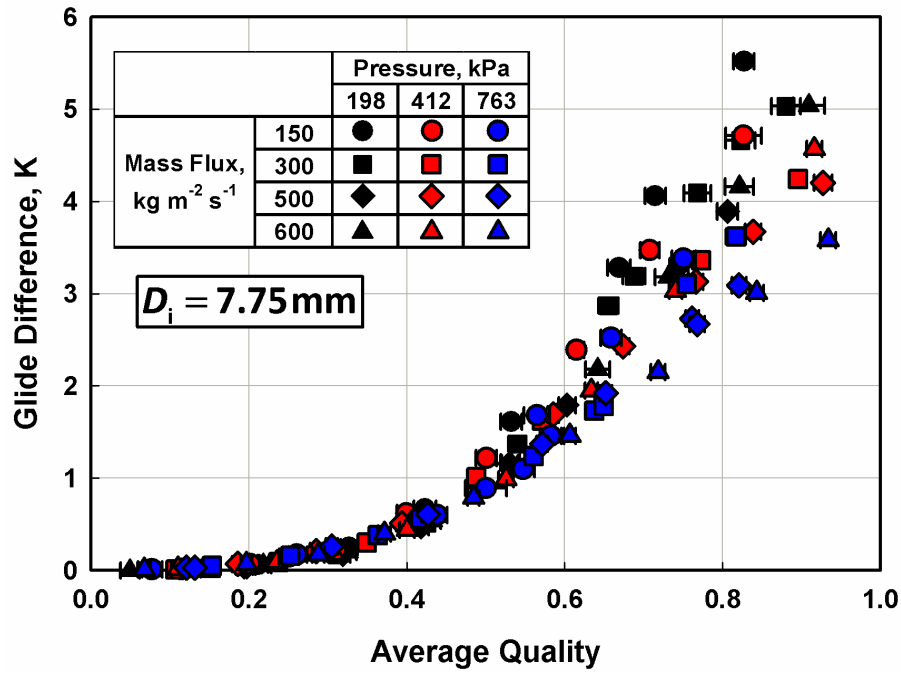
Figure 5.35. Change in temperature glide between equilibrium and non-equilibrium analysis

The temperature changes across the test section had a significant effect on the sensible cooling of each phase in the low pressure, high mass flux conditions. Referring to Figure 5.31, the sensible cooling of the vapor- and liquid-phases are calculated as shown in Equation (5.2).

$$\dot{Q}_{sv} = m_{v,avg} C_{pv} \left(T_{v,out} - T_{v,in} \right)$$
$$\dot{Q}_{sl} = m_{l,avg} C_{pl} \left(T_{l,out} - T_{l,in} \right)$$

(5.2)

Referring to Figure 5.36, the sensible cooling of the vapor phase, as a percentage of the total heat duty, was found to range from 0 % to 2.9%. The sensible cooling of the liquid phase was found to range from 4.5% to 33.4%. The average sensible vapor and liquid contributions were 0.9% and 14.2%, respectively. Thus, neglecting the sensible cooling of the liquid phase in the non-equilibrium model would cause significant errors.

The analysis method used in the present study accounts for the sensible contribution by conducting an energy balance using the outlet enthalpies.
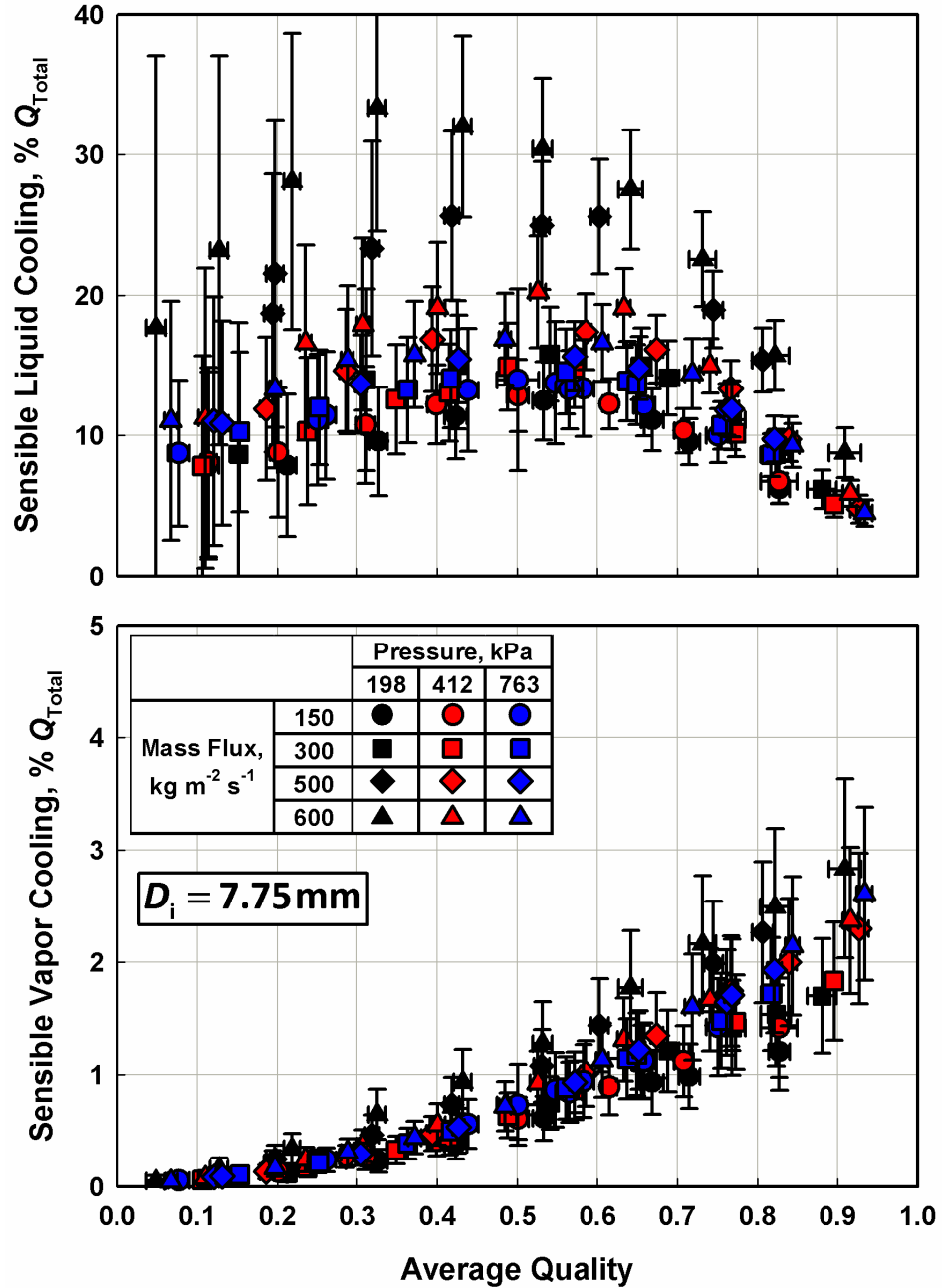
Figure 5.36. Sensible cooling duties of liquid and vapor phases in non-equilibrium analysis

5.1.4.1   Comparison with pure fluid results – Equilibrium analysis

For the equilibrium method, the measured heat transfer coefficients (apparent h) in Figure 5.37 ranged from 0.79 kW m^{-2} K^{-1} at P_{avg} = 764.5 kPa, G = 156 kg m^{-2} s^{-1}, and q_{avg} = 0.08 to 8.3 kW m^{-2} K^{-1} at P_{avg} = 257 kPa, G = 603 kg m^{-2} s^{-1}, and q_{avg} = 0.91. These zeotropic mixture apparent heat transfer coefficients follow trends with mass flux, quality, and pressure similar to those of the pure fluids. However, as expected, a reduction in heat transfer coefficients of the zeotropic mixture, relative to the pure components, was observed due to the additional mass transfer resistances. As discussed in the pressure gradient section, the pure fluid results at T_{Sat} = 45°C were compared with the zeotropic mixture results at bubble point temperatures of 30°C and 55°C. Referring to Figure 5.38, at G ~ 300 kg m^{-2} s^{-1} and q_{avg} = 0.35, the pure fluid heat transfer coefficients were 5.8 kW m^{-2} K^{-1} and 2.8 kW m^{-2} K^{-1} for n-pentane and R245fa, respectively. At T_{Bub} = 30°C and 55°C, the apparent heat transfer coefficients for the mixture were 3.2 kW m^{-2} K^{-1} and 2.7 kW m^{-2} K^{-1}, respectively. In the absence of the mass transfer resistances, the heat transfer coefficients of the mixture would be expected to be substantially closer to the concentration weighted average of the two pure fluids (~4.5 kW m^{-2} K^{-1}) based on the governing fluid properties and flow conditions. However, the mixture results show that the mixture heat transfer coefficients were significantly closer to the R245fa results, confirming the degradation of the heat transfer coefficient due to mass transfer resistances.
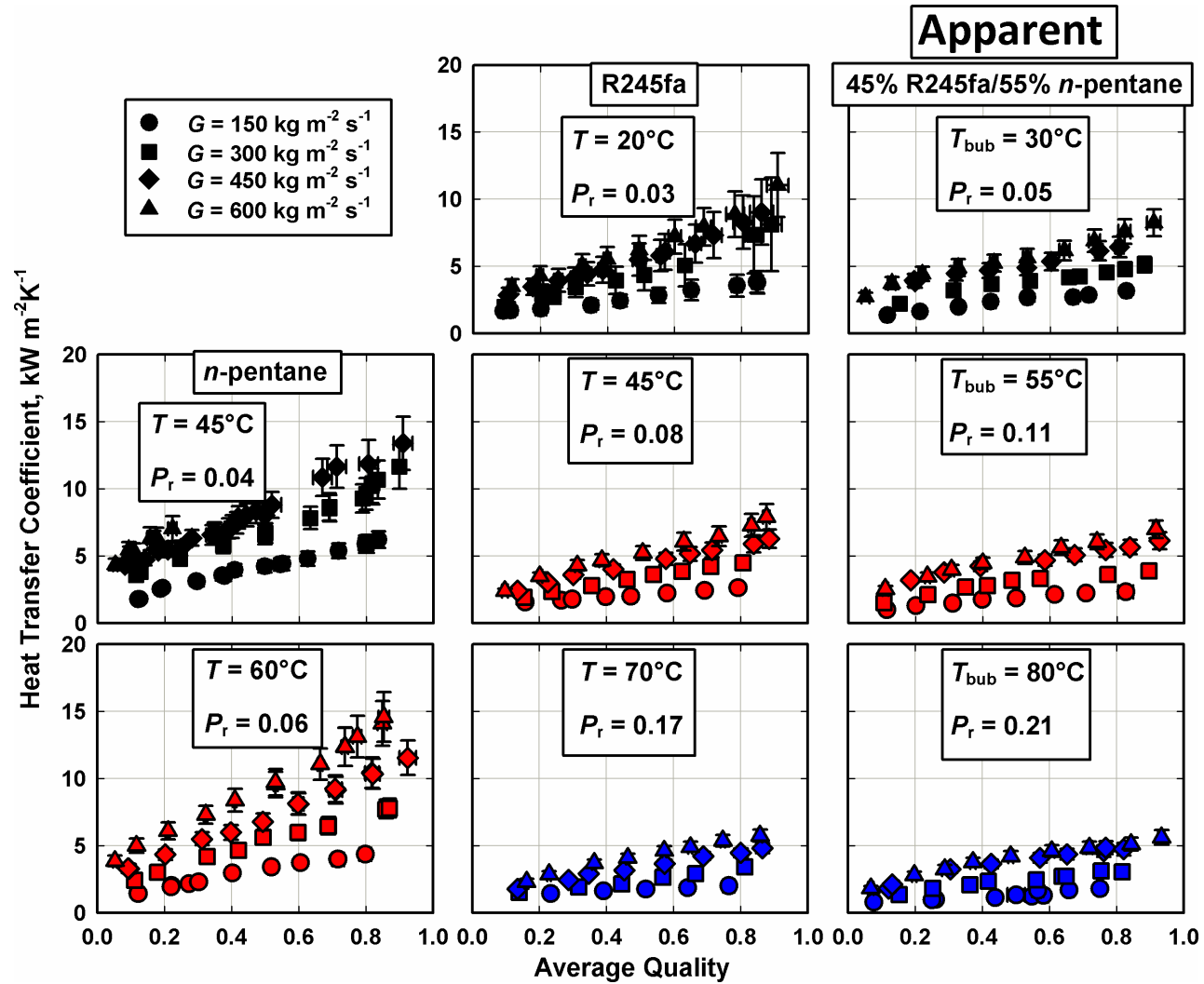
Figure 5.37. Experimental heat transfer coefficients versus quality for increasing pressure

278
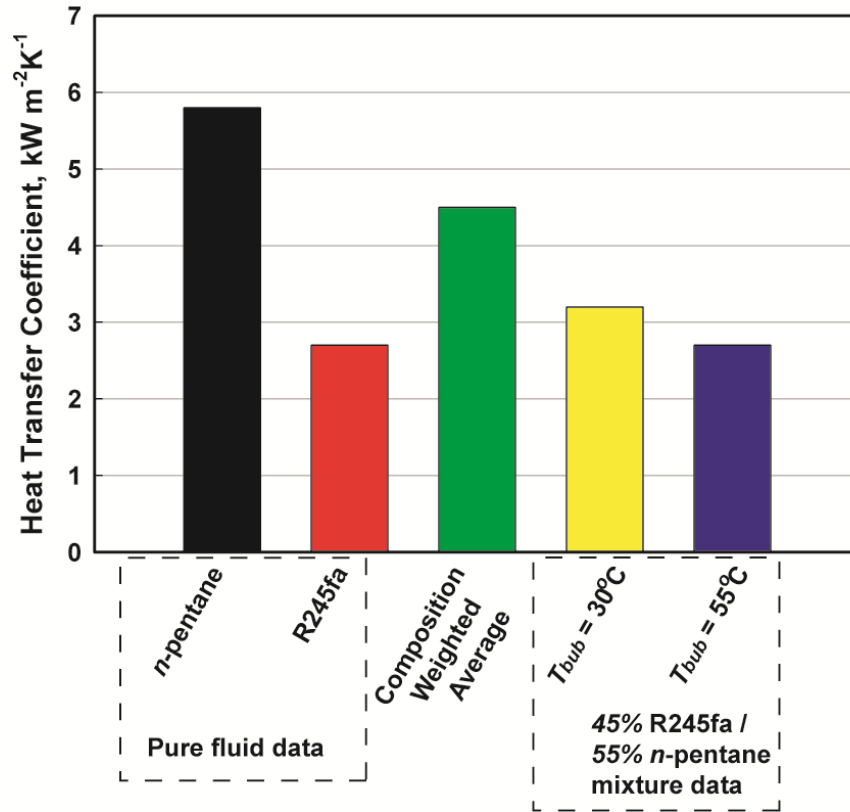
Figure 5.38. Representative mass transfer resistance degradation of heat transfer coefficient

5.1.4.2 *Comparison of analysis methods*

Referring to Figures 5.39 and 5.40, the liquid film heat transfer coefficients calculated

from the data using the Price and Bell (1974) approach range from 0.8 kW m^{-2} K^{-1} at P_{avg}

= 765 kPa, G = 156 kg m^{-2} s^{-1}, and q_{avg} = 0.08 to 13.0 kW m^{-2} K^{-1} at P_{avg} = 257 kPa, G =

603 kg m^{-2} s^{-1}, and q_{avg} = 0.91. It should be noted that these operating conditions at which

the maxima and minima in heat transfer coefficients were observed are the same as those

for which the apparent heat transfer coefficients obtained using the equilibrium approach

exhibit similar maxima and minima. The heat transfer coefficients obtained from the two

different approaches differ in value, but show the same trends with increasing quality and

mass flux, and decreasing pressure. For example, for increasing quality at $G \sim$ 500 kg m^{-2}

s^{-1} and $P \sim 198$ kPa, the film heat transfer coefficient increases from 3.9 kW m^{-2} K^{-1} at

$q_{avg} = 0.19$ to 9.0 kW m^{-2} K^{-1} at 0.8. For increasing mass flux at $P \sim 198$ kPa and $q \sim 0.4$,

the film heat transfer coefficient increases from 2.5 kW m^{-2} K^{-1} at $G = 149.8$ kg m^{-2} s^{-1} to

5.4 kW m^{-2} K^{-1} at 599.2 kg m^{-2} s^{-1}. For increasing pressure at $G \sim 500$ kg m^{-2} s^{-1} and $q \sim$

0.5, the film heat transfer coefficient decreases from 5.3 kW m^{-2} K^{-1} at $P_{avg} = 221.4$ kPa

to 4.4 kW m^{-2} K^{-1} at $P_{avg} = 776.9$ kPa.
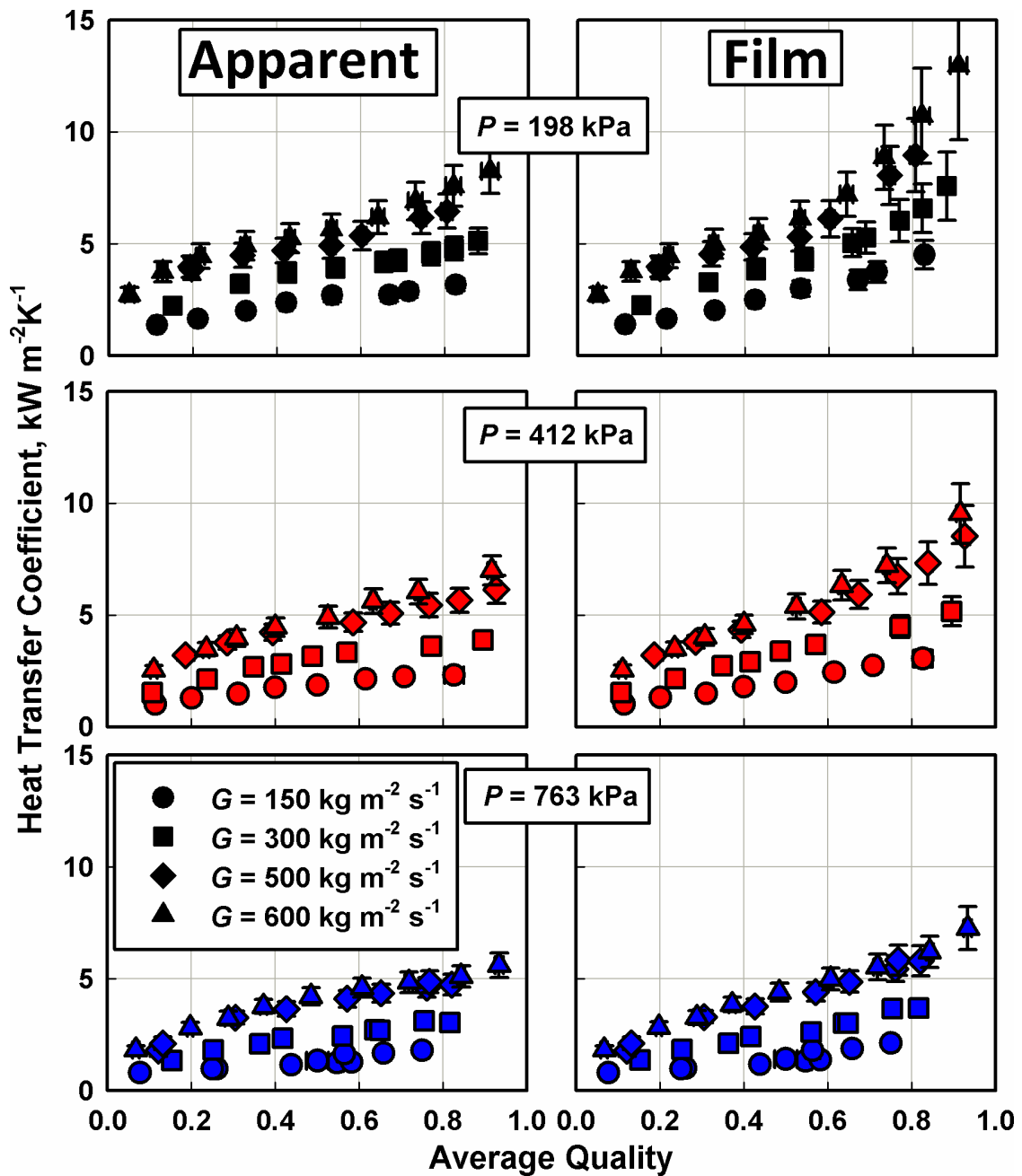
Figure 5.39. R245fa/*n*-pentane experimental heat transfer coefficient versus quality for increasing mass flux
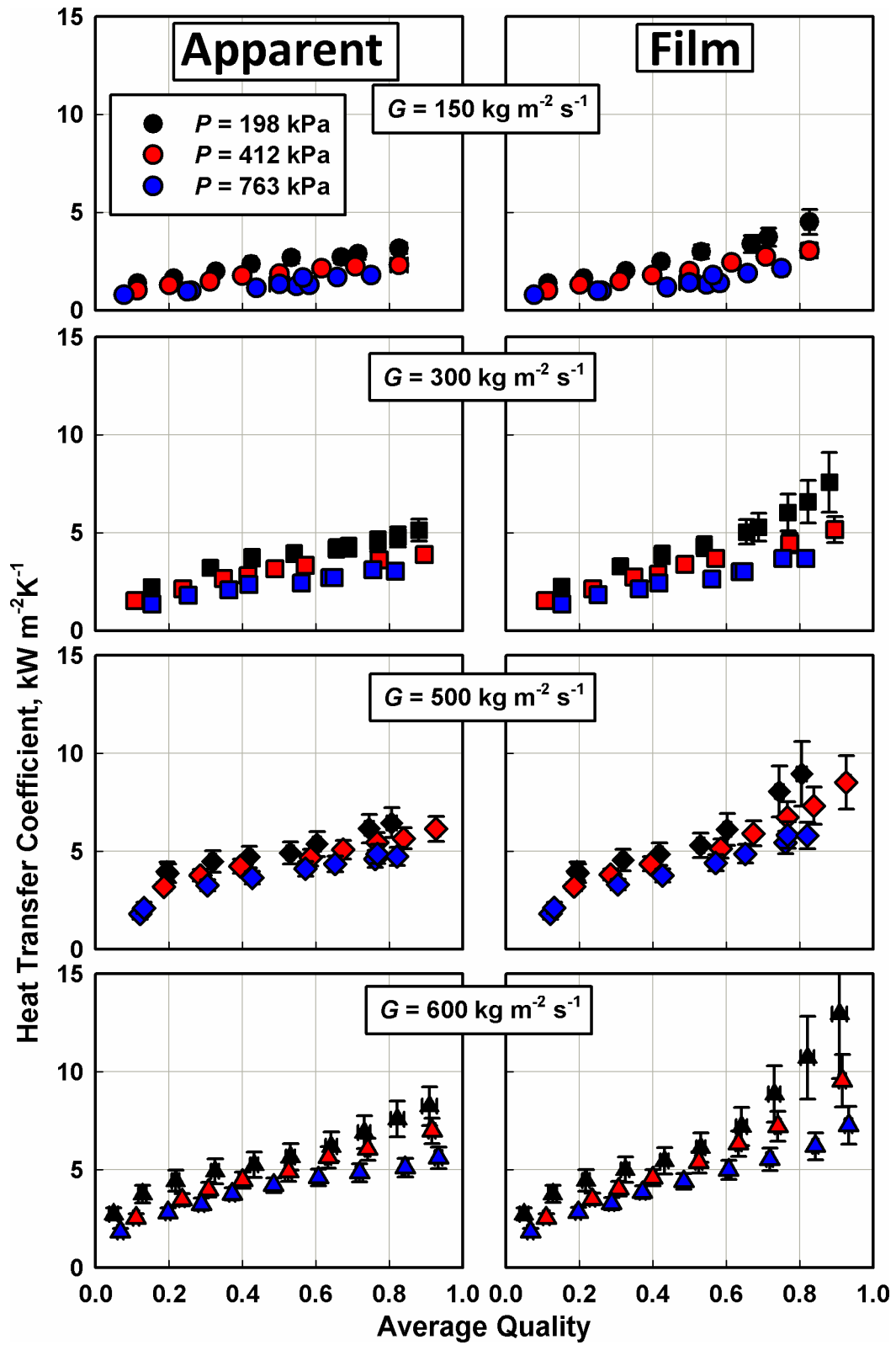
Figure 5.40. R245fa/*n*-pentane experimental heat transfer coefficient versus quality for increasing pressure

Because the film heat transfer coefficient is defined using the liquid film temperature and the apparent heat transfer coefficient is defined using the bulk fluid equilibrium temperature, the two heat transfer coefficients are not directly comparable. The film heat transfer coefficients based on the Price and Bell (1974) approach are up to 57.2% higher than the apparent heat transfer coefficient calculated using the equilibrium approach. The bulk fluid equilibrium temperature and the vapor-phase and interface/liquid temperature (shown in Figure 5.31) calculated using the non-equilibrium analysis method are shown in Figure 5.41. Because the mass transfer effects cause the interface temperature to be cooled below the bulk equilibrium temperature, the Price and Bell (1974) analysis yields a lower LMTD between the interface temperature and the wall temperature for the same heat duty and surface area; therefore, the heat transfer coefficient must be higher. As noted above, the Price and Bell (1974) approach had higher uncertainties in these heat transfer coefficients. Based on the comparison with the pure fluid data, and the difference between the two analysis methods, it is clear the zeotropic mixture of interest in the present study shows significant mass transfer effects.
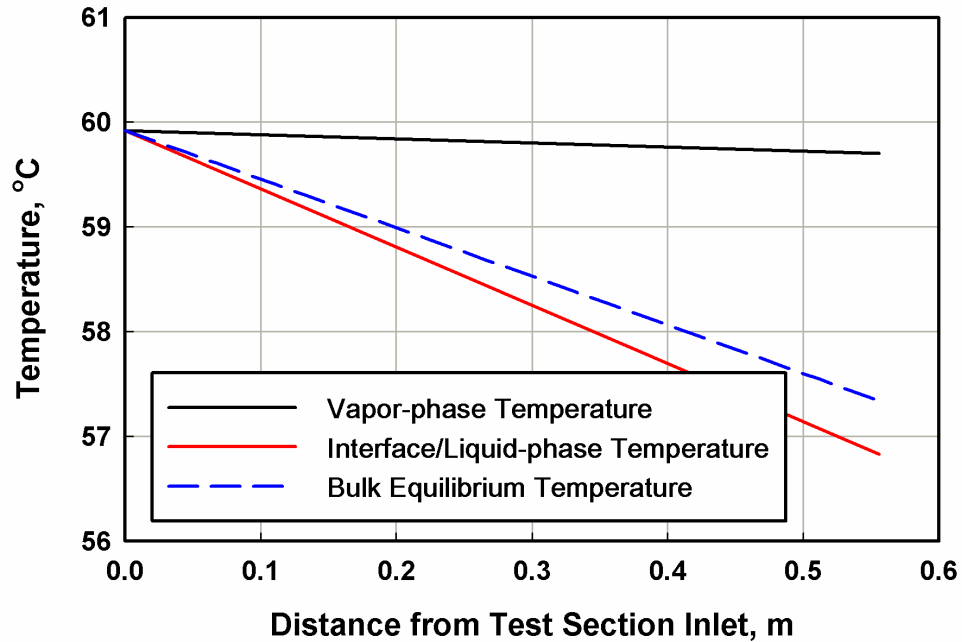
Figure 5.41. Representative test section temperature profiles

5.2 Comparison with the Literature

In this section, the experimental results discussed in the previous section are compared with predictions of models and correlations from the literature. Comparisons with flow regime predictions are discussed first, followed by a discussion of void fraction, frictional pressure drop, and heat transfer coefficient predictions. The average deviation (AD), average absolute deviation (AAD), and quantification of the percentage of data predicted within ±25% are used to compare the data from this study with predictions of the correlations from the literature. The AD and AAD are defined in Equation (5.3), where *n* is the number of data points within the set. In the following sections, the value predicted by the model is greater than the measured value when the AD is positive.

$$\text{AD} \equiv \frac{1}{n} \sum_{i=1}^{n} \frac{predicted - measured}{measured}$$

$$\text{AAD} \equiv \frac{1}{n} \sum_{i=1}^{n} \left| \frac{predicted - measured}{measured} \right|$$

(5.3)

5.2.1 Flow Regime

The observed local flow regime characterizations from the present study were compared with flow regime maps and transition criteria from the literature. Because regime characterizations can be subjective, differences in characterization of the regimes are noted as applicable. Comparison of flow regime transitions was done only for the annular to wavy regime due to the regimes exhibited by the data points in the present study. A total of 143 regime characterizations were done in the present study. Of these, 70 points were classified as wavy flow, with 36 in the 7.0 mm tube and 34 in the 15.0 mm tube. Sixty-two data points were classified as annular flow, with 38 in the 7.0 mm tube and 24 in the 15.0 mm tube. One data point in the 7.0 mm tube was characterized as completely intermittent flow. The remaining 10 data points were transition points between intermittent and wavy flow or wavy and annular flow. A summary of the agreement with transition criteria discussed in this section is presented in Table 5.7. Agreement between the data and predictions are classified in three ways: correctly predicted (the percentage of data in each regime properly predicted by the criteria), false positives (the percentage of all other data inside of the predicted regime) and false negatives (the percentage of data within each regime outside of the predicted regime). Data points classified as a transitional point are not included in this discussion.

Table 5.7. Summary of regime agreement

Author	Prediction	Measured	
		Annular	
		Annular	**Wavy**
Taitel and Dukler (1976)	Correctly Predicted	100%	0%
	False Positive	41%	0%
	False Negative	0%	100%
Breber *et al*. (1979)	Correctly Predicted	98%	1%
	False Positive	23%	0%
	False Negative	2%	99%
Soliman (1982)	Correctly Predicted	100%	56%
	False Positive	33%	0%
	False Negative	0%	44%
Dobson and Chato (1998)	Correctly Predicted	92%	97%
	False Positive	3%	7%
	False Negative	8%	3%
El Hajal *et al*. (2003)	Correctly Predicted	69%	96%
	False Positive	9%	21%
	False Negative	31%	4%
	Percent of each regime properly predicted		
	Percent of other data improperly predicted within range		
	Percent of data outside of predicted range		

Taitel and Dukler (1976) proposed several theoretical regime boundaries based on the mechanisms that governed each transition. Sardesai *et al.* (1981) later modified the stratified wavy-to-annular transition criterion. Both maps are overlaid on the present data in Figure 5.42. The intermittent-to-annular transition of Taitel and Dukler (1976) showed good agreement with the 7.0 mm data with all the intermittent and wavy-to-intermittent transition data points falling within the predicted intermittent region. The 15.0 mm tube did not exhibit intermittent flow over the range of conditions studied here; however, several data points were predicted to be in intermittent flow. This indicates that the Lockhart Martinelli parameter, which remains constant with diameter, does not properly capture the effect of diameter for the transition to intermittent flow in these maps. While

all the annular flow data points were properly identified, both the original Taitel and Dukler (1976) map and the modified stratified-to-annular transition criterion proposed by Sardesai *et al.* (1981) did not identify a wavy regime between the intermittent and annular regime, as observed in the present study.

		Intermittent	Wavy	Annular	Transition
Mass Flux, kg m⁻² s⁻¹	75		🔺	▲	🔺
	150	🟢	🔴	⚫	🔵
	300		🟥	⬛	🟦
	450		🔴◆	◆	🔷
──		Sardesai *et al.* (1981) - 952 kPa			
─ ─		Sardesai *et al.* (1981) - 1218 kPa			
──		Taitel and Dukler - 952 kPa			
─ ─		Taitel and Dukler - 1218 kPa			
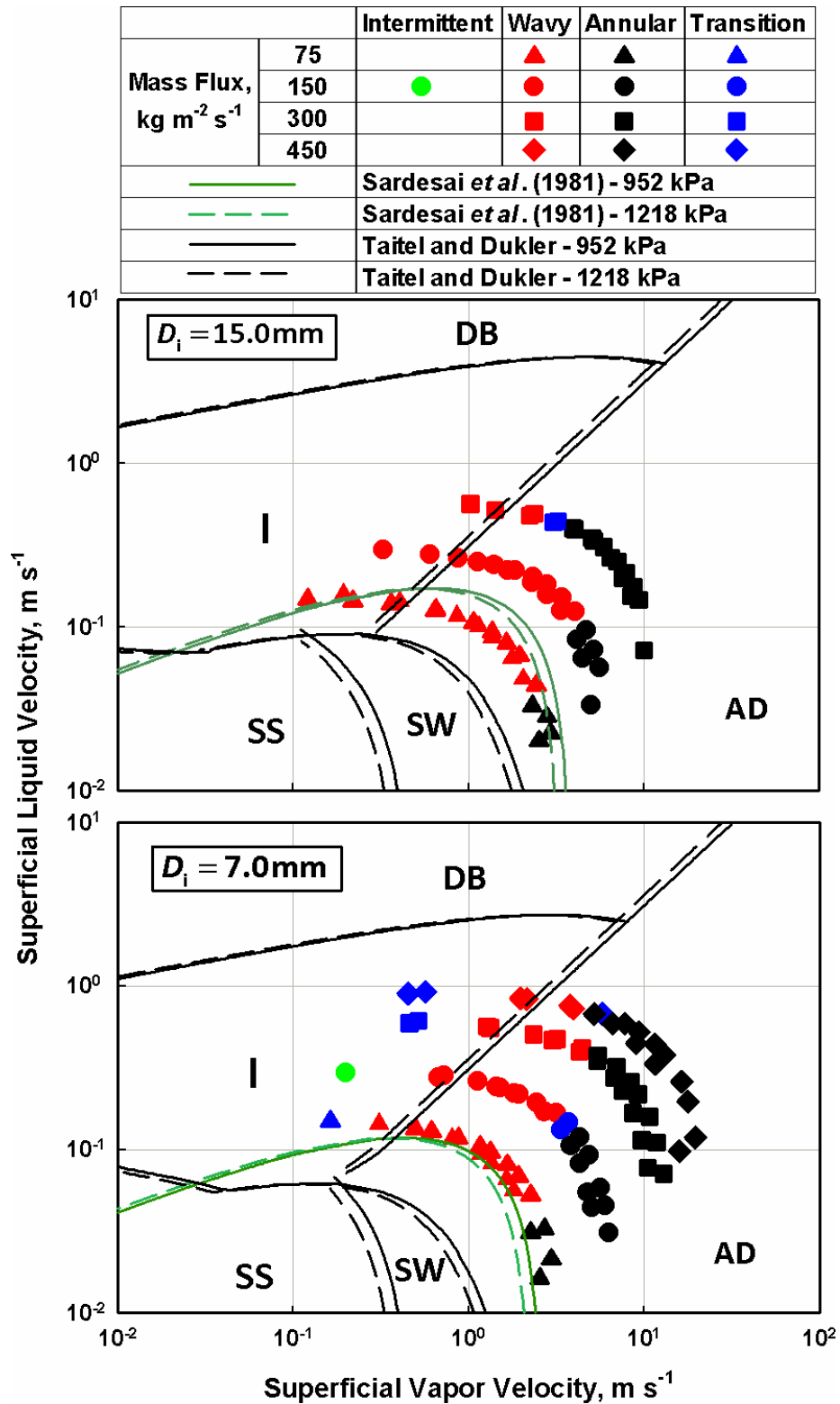
Figure 5.42. Comparison of flow regime observations with Taitel and Dukler (1976) and Sardesai *et al.* (1981) maps; DG – Dispersed Bubble, I – Intermittent, AD – Annular-Dispersed, SW – Smooth Wavy, SS – Smooth Stratified

The Breber *et al.* (1979; 1980) map is overlaid on the data in Figure 5.43. The Breber *et al.* map (also derived from the theoretical boundaries of Taitel and Dukler (1976)), accurately predicts 98% of the data within the annular regime. However, 23% of the annular regime predictions were false positives. As with the Taitel and Dukler (1976) map, data in the wavy regime were not properly characterized as wavy flow, with only 1% of the wavy regime data properly classified. Twenty three percent of the wavy data were classified within the transition regions. Eight wavy data points were improperly characterized as slug and plug flow in the 15.0 mm tube. In the 7.0 mm tube, all seven intermittent and wavy-to-intermittent data were classified as slug and plug flow. The Breber *et al.* (1979; 1980) map was developed using flow regime data for R11, R12, R113, steam, and *n*-pentane in 4.8 to 22 mm ID horizontal tubes similar to those of interest in the present study. However, their simplified transition regions have been noted in the literature to be too large and lack the necessary diameter effect described by Soliman (1982). Additionally, because the 7.0 mm data in particular showed significant convective film effects in the wavy regime, these points could have been considered transitional by Breber *et al*.

		Intermittent	Wavy	Annular	Transition
Mass Flux, kg m^{-2} s^{-1}	75		▲	▲	▲
	150	●	●	●	●
	300		■	■	■
	450		◆	◆	◆
———————		Breber *et al*. (1979)			
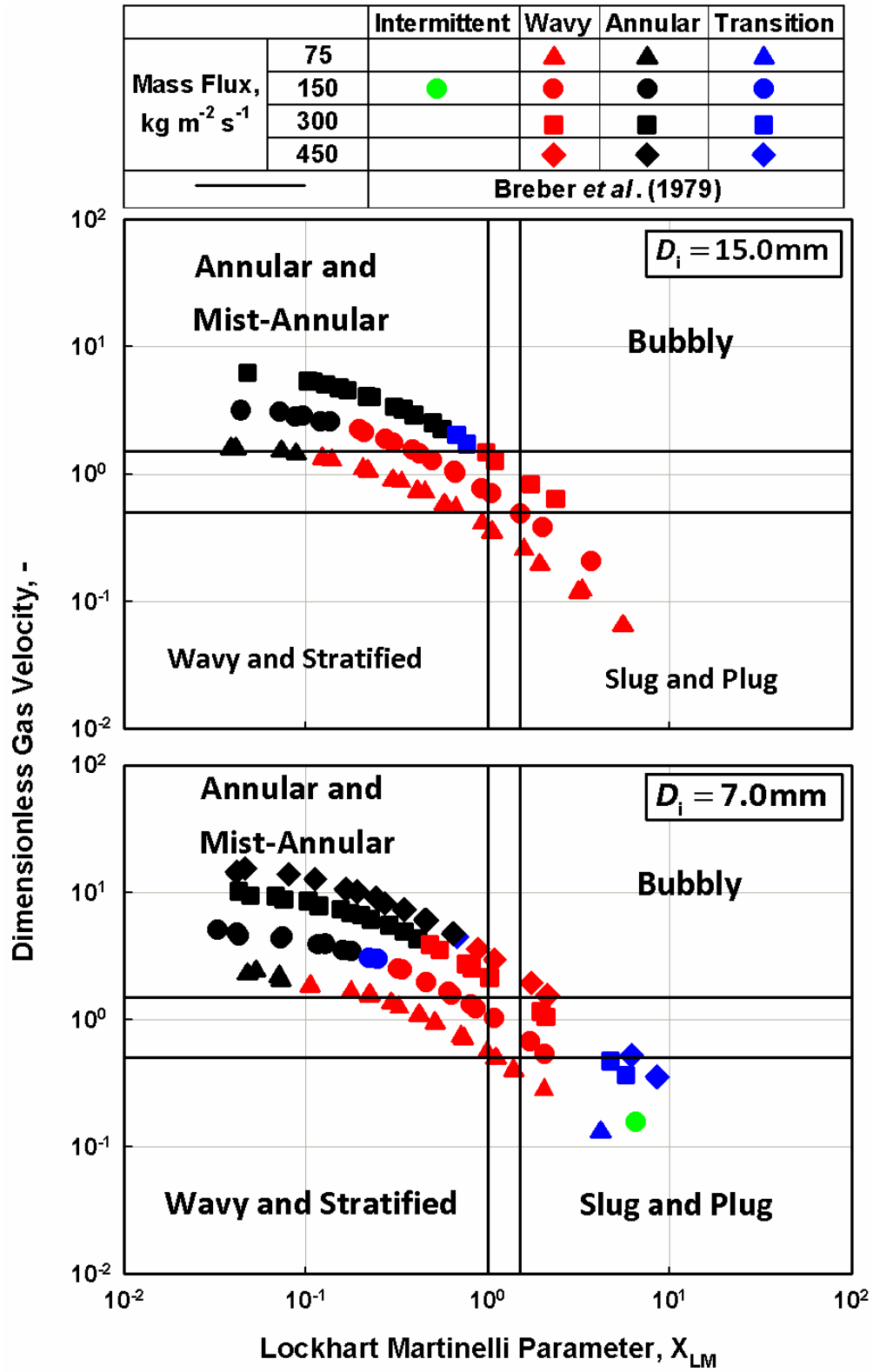
Figure 5.43. Comparison of flow regime observations with Breber *et al.* (1979) map

The wavy-to-annular flow and annular-to-mist flow transitions proposed by Soliman (1982, 1983) are overlaid on the data in Figure 5.44. The combination of his two transitions suggests that the annular flow regime is actually quite limited, particularly in the 15.0 mm tube. The Froude number based stratified-to-annular flow transition proposed by Soliman (1982) qualitatively shows the correct trend in transition with varying mass flux and predicts 100% of the annular flow properly. However, the transition is offset, with 33% of the annular predictions being false positives and only 56% of the wavy flow data properly characterized. While his transition is theoretically based on the transition mechanisms, the empirical transitional Froude number of 7 was developed for condensing flows of R12, R113, and steam in horizontal tubes with IDs ranging from 4.8 to 15.9 mm for saturation temperatures of 110°C for steam and ranging from 27.6 to 62.3°C for the refrigerants. Although mist flow was not directly characterized as part of the present study, entrainment was observed in much of the flow. The Soliman (1983) transition suggests that 48 of the annular flow data points were actually mist using a Weber number based transition criterion as shown in Figure 5.44. Many of the data predicted as being in the mist flow region showed entrainment of liquid in the vapor phase as shown in Figure 5.7.
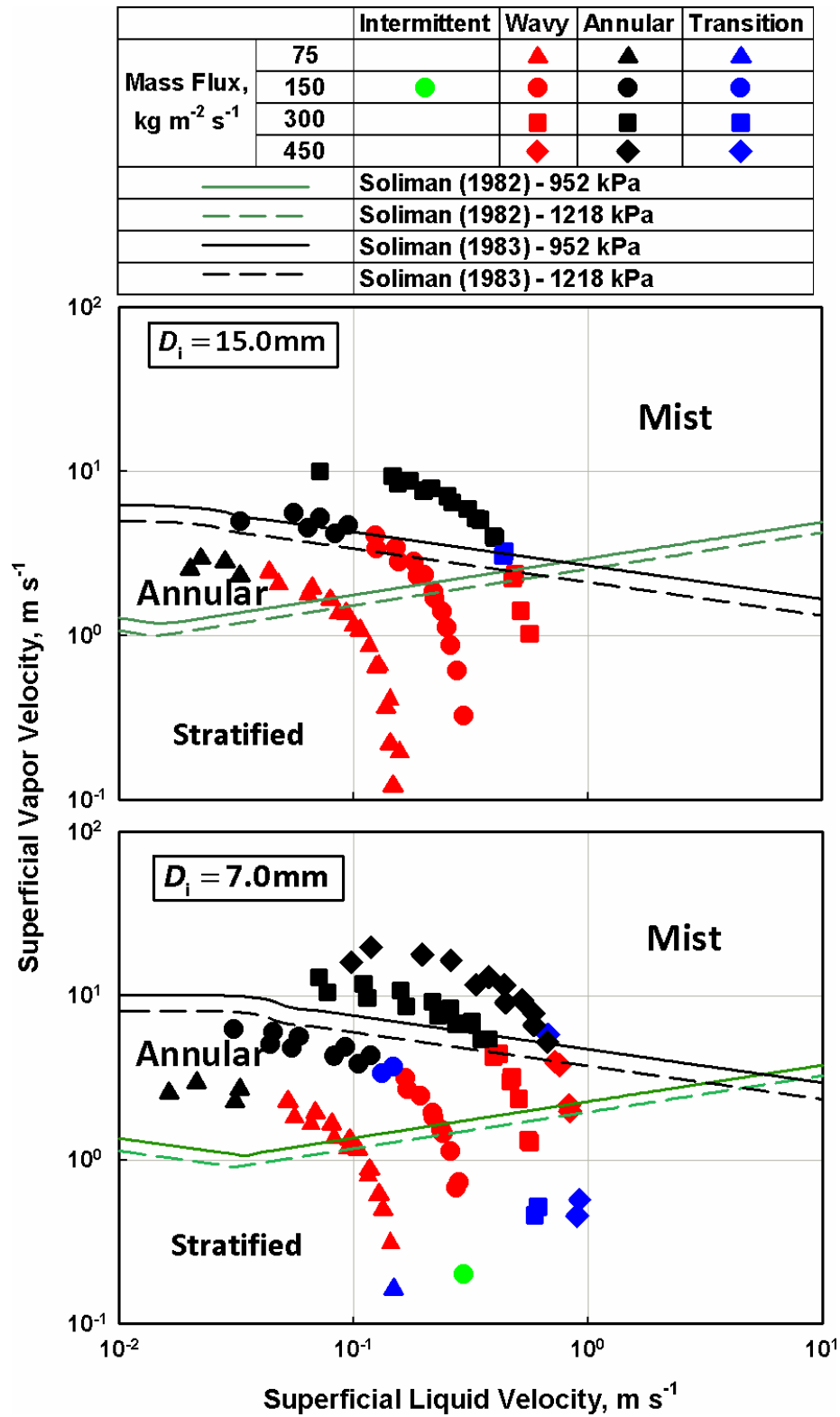
Figure 5.44. Comparison of flow regime observations with Soliman (1982, 1983) criteria

Dobson *et al.* (1994) and Dobson and Chato (1998) both proposed slight changes to the Froude number transition proposed by Soliman (1982). As shown in Figure 5.45, the modified transitions showed a significant improvement in the agreement with the present data. In the 7.0 mm ID tube, their map properly identified 100% of the annular flow and 94% of the wavy flow data. In the 15.0 mm ID tube, 100% of the wavy flow data were properly identified, while 79% of the annular flow data were properly identified. Overall, 3% and 7% of the predictions were false positives in the annular and wavy regimes, respectively. The transitions reported by Dobson and Chato were developed from data on refrigerants and refrigerant mixtures in tubes with a maximum diameter of 7 mm. Thus, the difference in prediction from the data for the larger tube is not unreasonable. Overall, the agreement is quite good, properly characterizing 92% and 97% of the annular and wavy flow data, respectively. Combining the transition criteria of Soliman (1982) and Dobson and Chato (1998) with the data from the present study, it appears that the transitional Froude number may be somewhat dependent on diameter. Thus larger tube data are predicted better with a smaller transitional Froude number.
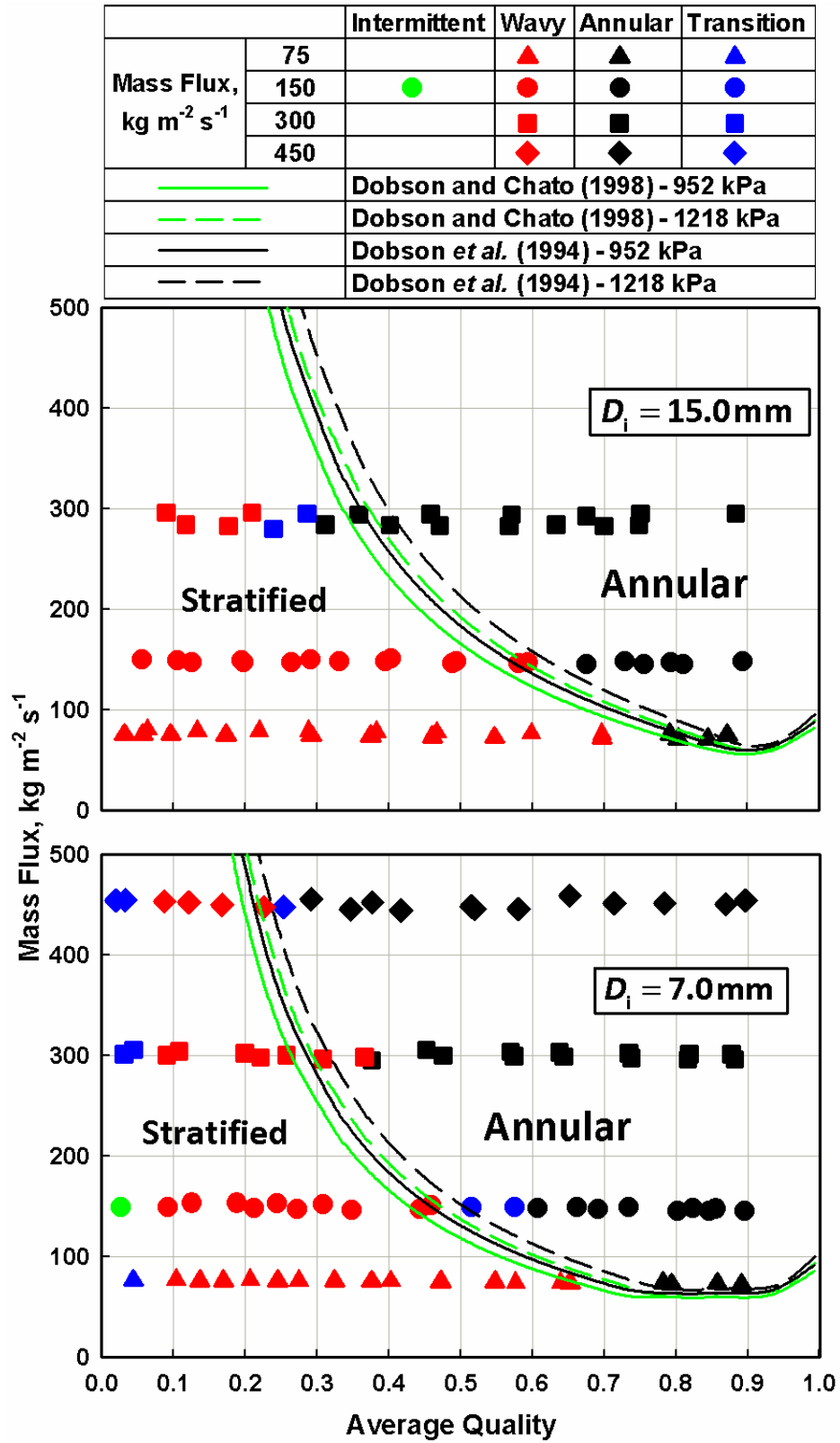
Figure 5.45. Comparison of flow regime observations with Dobson *et al.* (1994, 1998) map

El Hajal *et al.* (2003) proposed a map for condensing two-phase flow regimes, modifying their earlier work on boiling. Their map for propane for each diameter at $G = 150$ kg m^{-2} s^{-1} and $P = 952$ kPa is overlaid on the data from the present study in Figure 5.46. Because their regime map is calculated using the local conditions of the flow, the transitions are only plotted at one condition. The classification of each data point was determined using their map calculated for the local conditions, which may differ slightly from those shown in Figure 5.46. Their criteria correctly characterize 73% of the annular flow data in the 7.0 mm tube. However, in the 15.0 mm tube, only 63% of the annular flow points are properly identified as annular. As noted in Chapter 2, the extent of the intermittent flow regime in their map is believed to be too large, predicting intermittent flow even for qualities up to 0.4. No other maps from the literature predict intermittent flow at such high qualities. El Hajal *et al.* (2003) include large amplitude waves in the intermittent regime. Including wavy data characterized as intermittent flow, the regime map properly characterizes 100% and 91% of the wavy flow data from the 7.0 mm and 15.0 mm tubes, respectively. Alternatively, considering that the accompanying heat transfer model of Thome *et al.* (2003) predicts intermittent heat transfer coefficients using the annular flow correlation, the intermittent flow points can be considered as annular flow. In this case, only 59% of the wavy flow data are properly identified, with 21% of the predictions being false positives. The disagreement between the map predictions and data may originate in the use of a boiling map as the basis for the proposed transitions and the lack of hydrocarbons visualization results in its development.
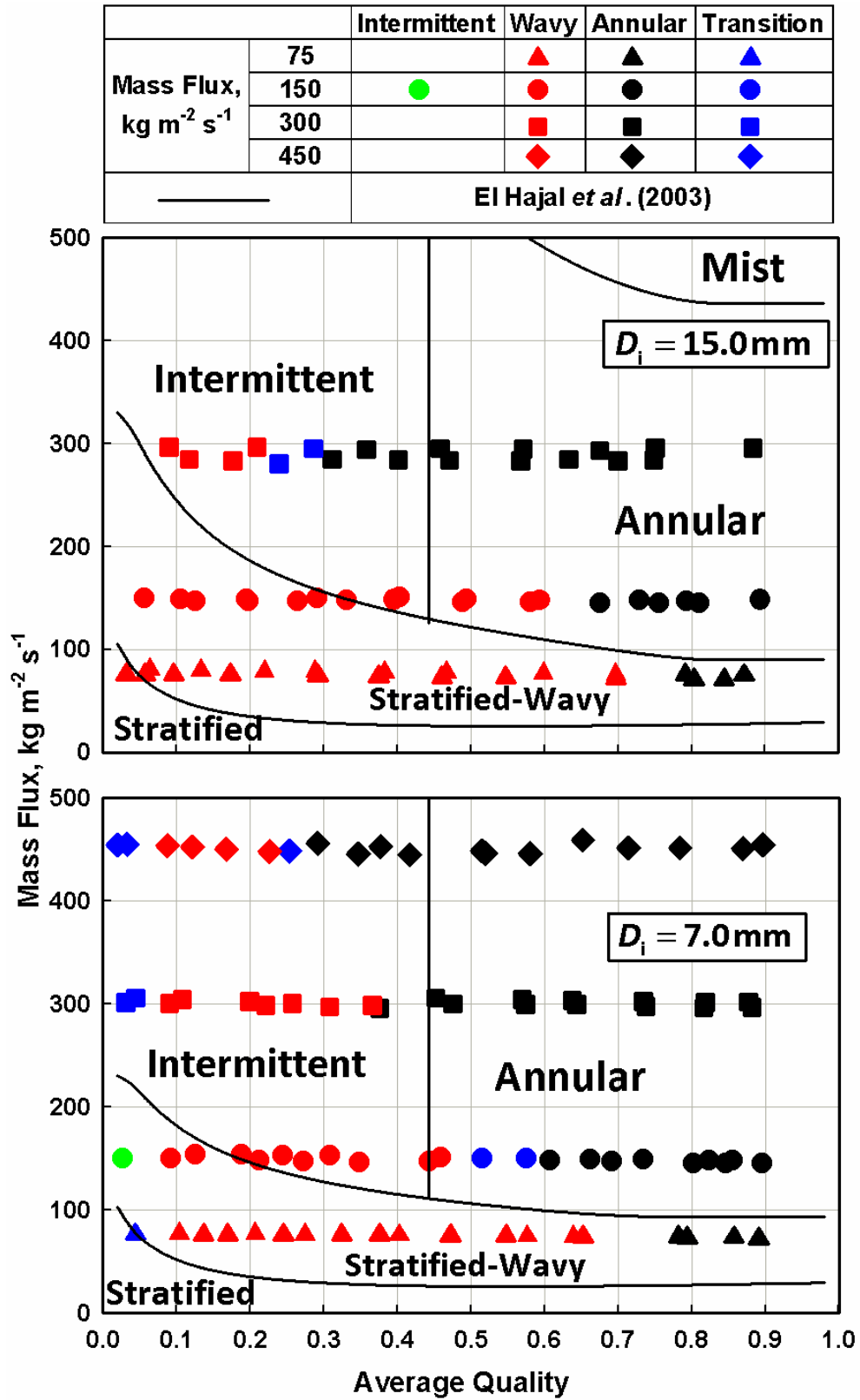
Figure 5.46. Comparison of flow regime observations with El Hajal _et al_. (2003) map

The other maps considered as part of the present study also suggest significantly larger annular regions than those observed in the present study. Of all the considered studies, the transition criteria of Dobson *et al.* (1994) and Dobson and Chato (1998) showed the best agreement with the data from the present study. The flow regime map of Breber *et al.* (1979; 1980) was found to show reasonable agreement with the intermittent and annular regimes, but classified most of the wavy flow data as transitional flows.

5.2.2 Void Fraction

Void fractions measured in the present study are compared with the predictions of several correlations and models from the literature in this section. These comparisons are shown in Figure 5.47. Because 61% of the measured void fractions are greater than 0.9 and 76% of the data are greater than 0.8, trends in the predictions capabilities are difficult to discern from Figure 5.47. Additionally, because the void fraction only takes values between zero and unity, the agreement between the measured void fraction and predicted void fraction are generally quite good in terms of AD and AAD. Therefore, the correlation predictions are overlaid on the data for comparison in Figures 5.48 to 5.51 for the correlations that show very good agreement with the data. The agreement of the selected correlations discussed below with the data from the present study is summarized in Table 5.8. It is important to remember that the measured void fraction neglects liquid entrained in the vapor core, which may lead to significant differences between predictions and data. For data points where significant liquid entrainment in the vapor phase occurs, the measured void fraction is greater than the actual void fraction. At the transition between wavy and annular flow, specifically at the highest mass fluxes, there is an abrupt change in slope of the data. This is due to a combination of the liquid entrained in the vapor phase and the vapor-liquid interface shape assumptions in both regimes.

		Pressure, kPa			
		952	1218	952	1218
		D_i = 7 mm		D_i = 15 mm	
Mass Flux, kg m^{-2} s^{-1}	75	▼	▼	▽	▽
	150	●	●	○	○
	300	■	■	□	□
	450	◆	◆		
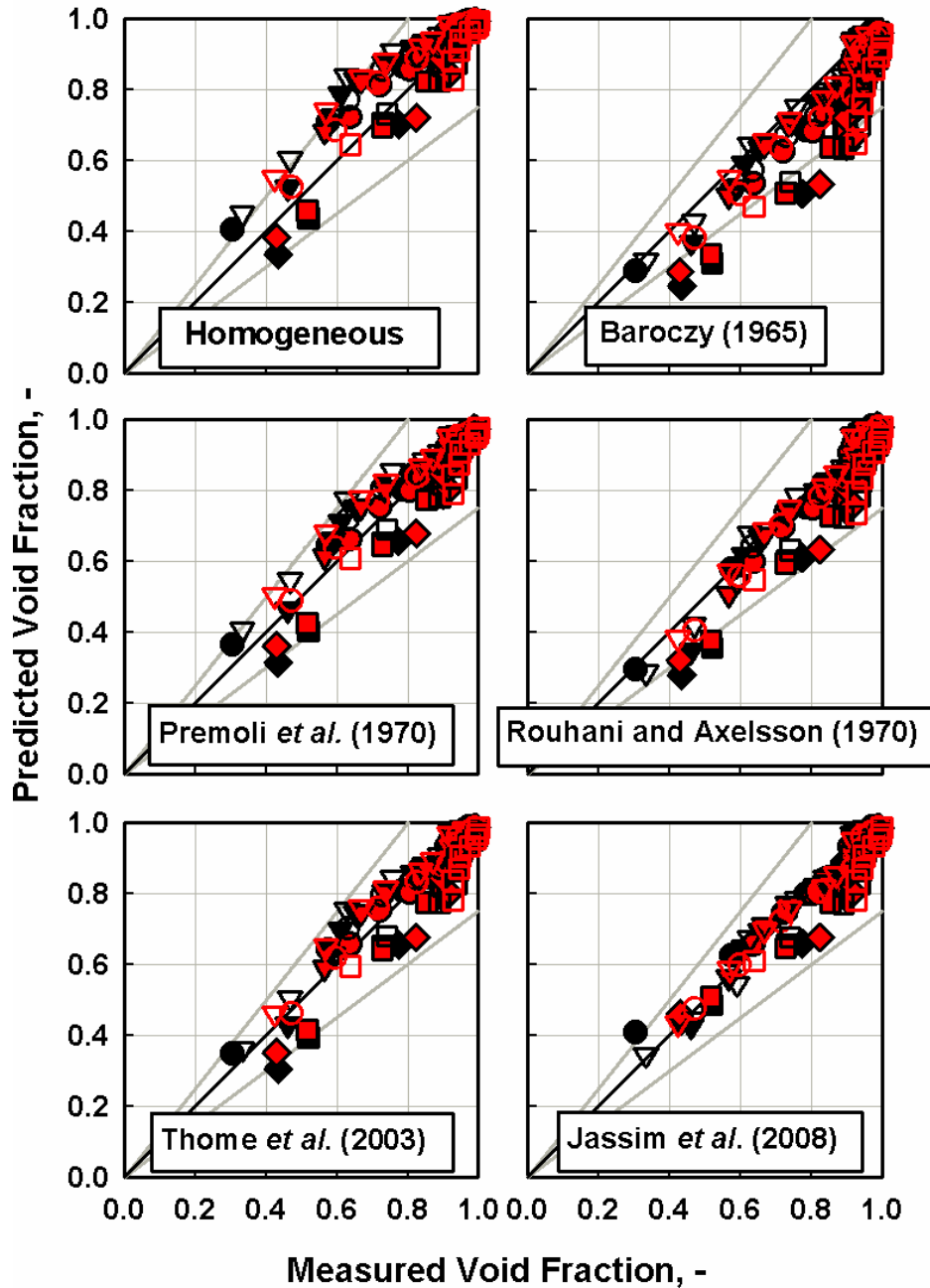
Figure 5.47. Comparison of correlations from the literature with measured void fraction

Table 5.8. Summary of comparisons with the literature – void fraction

Author	Average Deviation	Average Absolute Deviation	R^2	Absolute Average Deviation 7.0 mm	15.0 mm
Homogeneous	5%	7%	0.85	6%	8%
Baroczy (1965)	-11%	11%	0.84	12%	10%
Premoli *et al*. (1970)	-1%	6%	0.89	5%	6%
Rouhani and Axelsson (1970)	-6%	7%	0.91	7%	6%
Thome *et al*. (2003)	-1%	5%	0.90	5%	5%
Jassim *et al*. (2008)	-1%	4%	0.93	4%	4%

Referring to Figure 5.47, the correlation of Baroczy (1965) consistently under predicted the data with an AD of -11% and an AAD of 11%. The agreement was slightly better at low mass fluxes with data in the nominal 75 and 150 kg m^{-2} s^{-1} cases, showing an AD of -7% and AAD of 7%, while for mass fluxes greater than 150 kg m^{-2} s^{-1}, the AD and AAD were -17% and 17%, respectively. Because a mass flux effect was observed in the present data and the correlation of Baroczy (1965) does not account for mass flux, agreement was expected to differ. A portion of the disagreement is likely to be from the entrainment of liquid in the vapor phase, which is not captured in the measurements.

The predictions of the homogeneous void fraction model are overlaid on the data in Figure 5.48. The homogeneous model predicted the data from the present study with an AD of 5% and AAD of 7%, with 94% of the data predicted within ±25%. As shown in Figure 5.48, the homogeneous void fraction significantly over predicted the void fractions from the present study at low mass fluxes and slightly over predicts the data at the highest mass fluxes. For $G < 150$ kg m^{-2} s^{-1}, the AD was -10%, with an AAD of 10%, while at $G > 150$ kg m^{-2} s^{-1}, the AD was -3% and the AAD was 3%. In the annular

regime, the AD and AAD are 1% and 2%, respectively, while in the wavy regime, the

AD and AAD are 8% and 11%, respectively.
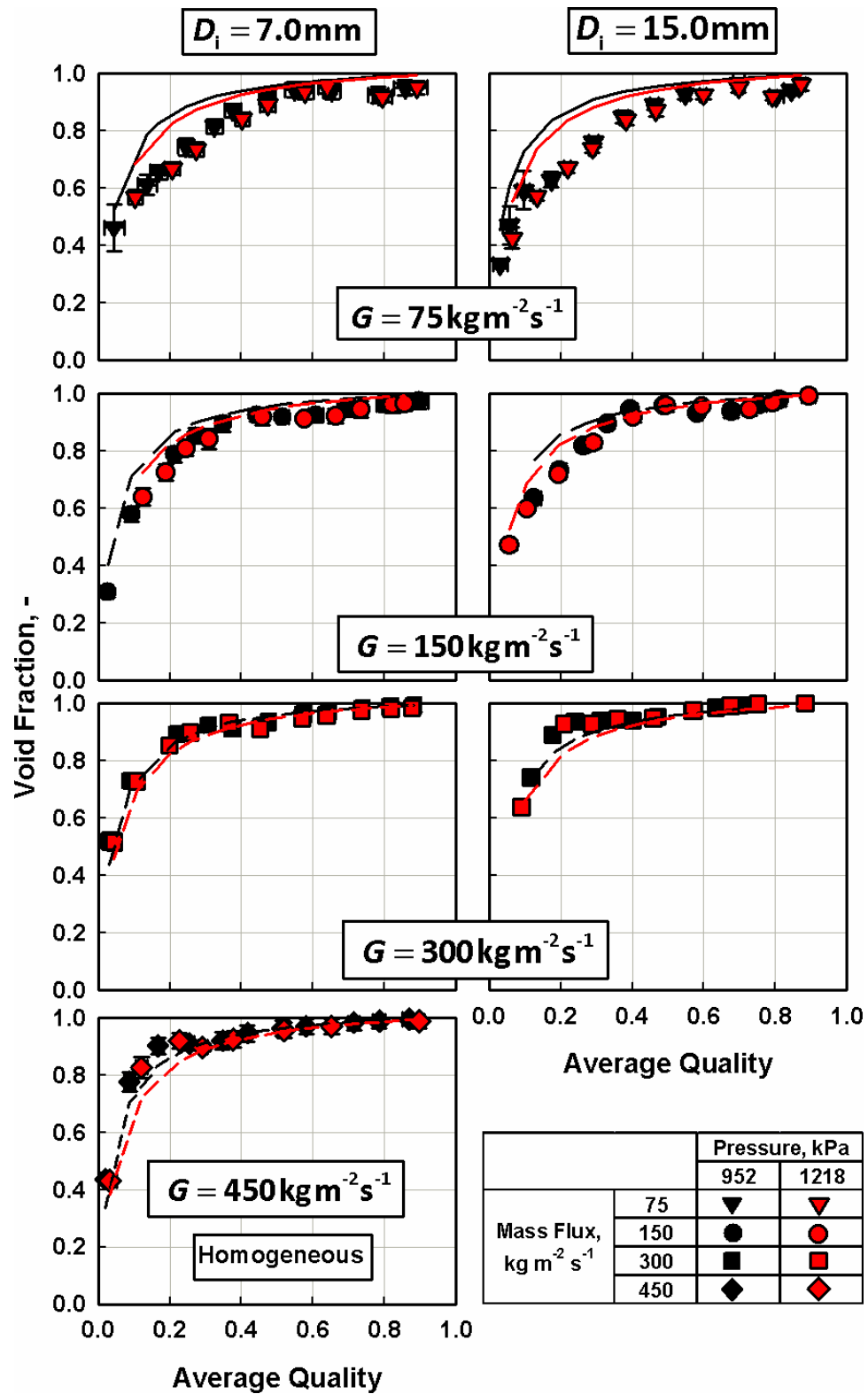
Figure 5.48. Comparison of the homogeneous void fraction model with the present data

301

The predictions of the Premoli *et al.* (1970) correlation are shown in Figure 5.49. The AD was -1% while the AAD was 6%. Despite accounting for mass flux through the Reynolds and Weber number, the Premoli *et al.* (1970) correlation does not properly capture the trends in the void fraction with increasing mass flux, although their correlation does include a mass flux term for qualities less than 0.5. However, the overall agreement was found to be better than those of other correlations considered here. At $q <$ 0.5, the AD was 0%, with an AAD of 8%, while for $q > 0.5$, the AD was -1%, with an AAD of 2%. A slight under prediction occurs in the annular regime, with an AD of -2% and AAD of 3%. There is more scatter in the wavy regime with an AD and AAD of 1% and 7%, respectively. Because this empirical correlation was developed for vertical flow, the inability to capture wavy flow trends well can be expected.
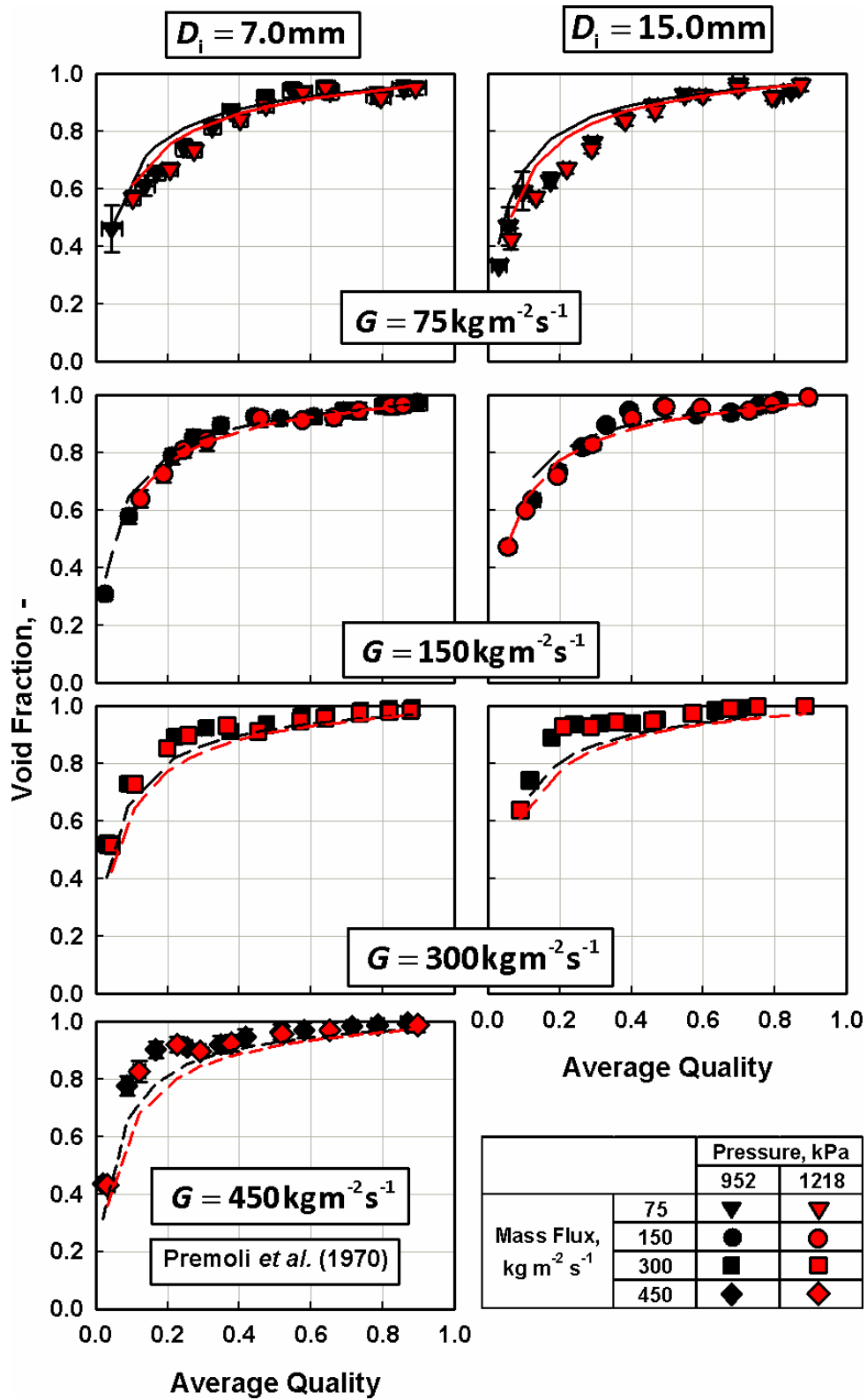
Figure 5.49. Comparison of the Premoli *et al*. (1970) void fraction correlation with the present data

For their heat transfer model, Thome *et al.* (2003) and El Hajal *et al.* (2003) proposed that the void fraction should be modeled as a logarithmic average of the Rouhani and Axelsson (1970) correlation and the homogeneous model to capture the trend as the pressure approaches the critical pressure. Because the reduced pressures are low in the present study (P_r = 0.22 and 0.29) the El Hajal *et al*. and Rouhani and Axelsson models are considered together in the form proposed by Thome *et al.* (2003). The model predictions are overlaid on the data in Figure 5.50. The AD and AAD for this correlation were -1% and 5%, respectively. As with the previously discussed correlations, the predictions of the Thome *et al.* (2003) correlation did not properly capture the increasing void fraction with increasing mass flux that was observed in the present study. At low mass fluxes ($G \leq 150$ kg m^{-2} s^{-1}), the AD and AAD were 3% and 4%, respectively. At high mass fluxes ($G \geq 300$ kg m^{-2} s^{-1}), the AD and AAD were -6% and 6%, respectively. Additionally, at qualities less than q = 0.5 the model predicts the data with an AD of -1% and AAD of 8% but at qualities greater than q = 0.5, the AD and AAD were 0% and 2%, respectively. This correlation predicted both tube diameters and pressures with similar accuracy, with an AAD of 5% in both tubes and for both pressures.
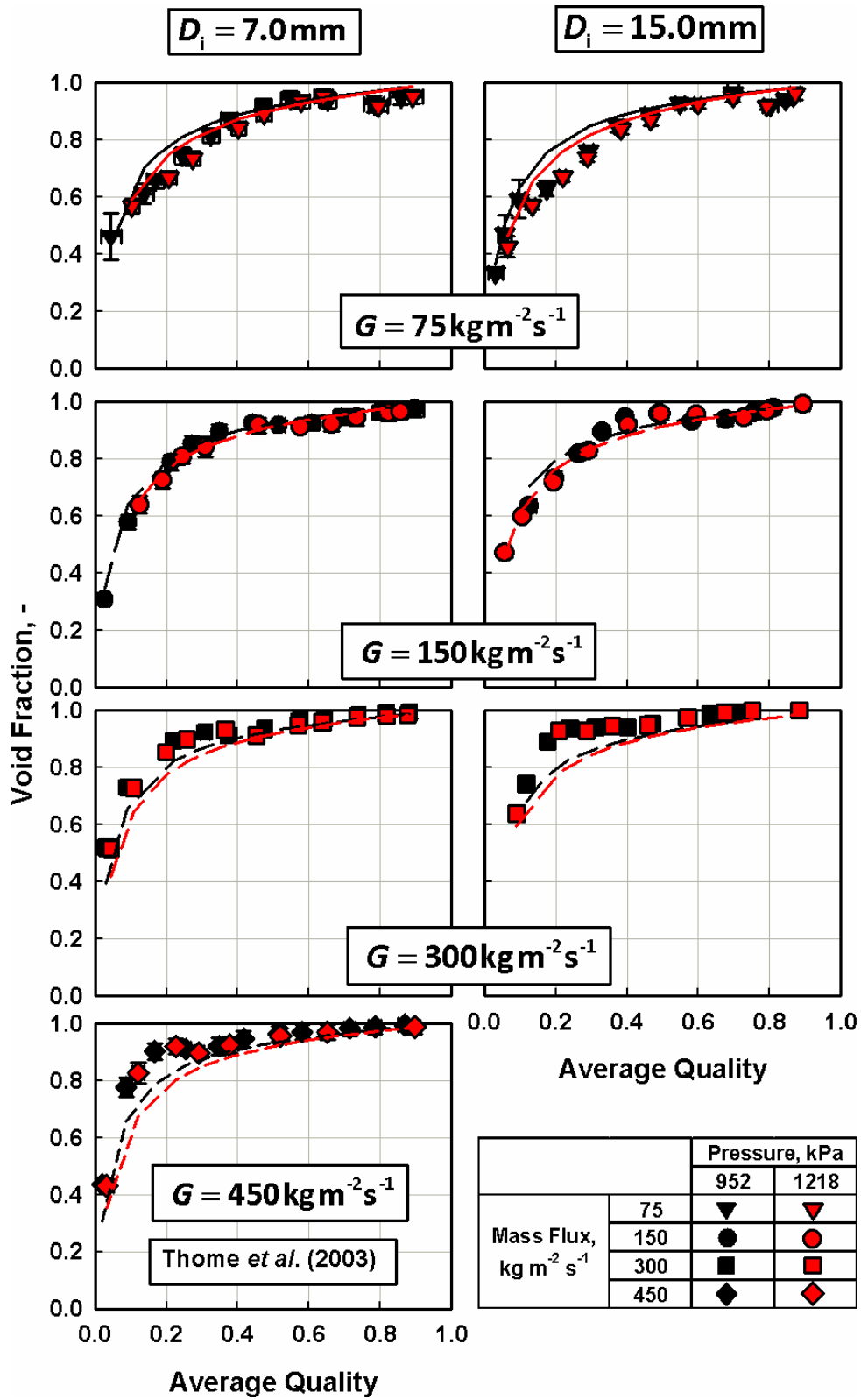
Figure 5.50. Comparison of the Thome *et al*. (2003) void fraction correlation with the present data

Jassim *et al.* (2008) combine the void fraction correlations of Thome *et al.* (2003) for annular flow and Graham (1998) for wavy flow using the flow transition criteria of Jassim (2006). In the present study, the Graham (1998) correlation showed better agreement for wavy flow compared to the Thome *et al.* (2003) correlation. Therefore, the overall agreement with the Jassim *et al.* (2008) model predictions was better than what was seen with the Thome *et al.* model. The model predictions are overlaid on the data in Figure 5.51. The AD and AAD were -1% and 4%, respectively. Slightly better agreement was observed at low mass fluxes ($G \leq 150$ kg m^{-2} s^{-1}), with an AD and AAD of 1% and 3%, respectively. At high mass fluxes ($G \geq 300$ kg m^{-2} s^{-1}), the Jassim *et al.* model consistently under predicted the data, with an AD and AAD of -5% and 5%, respectively. As with the Thome *et al.* (2003) correlation, similar agreement was observed for both diameters and pressures, with an AAD of 4% for both tube diameters and for both pressures.
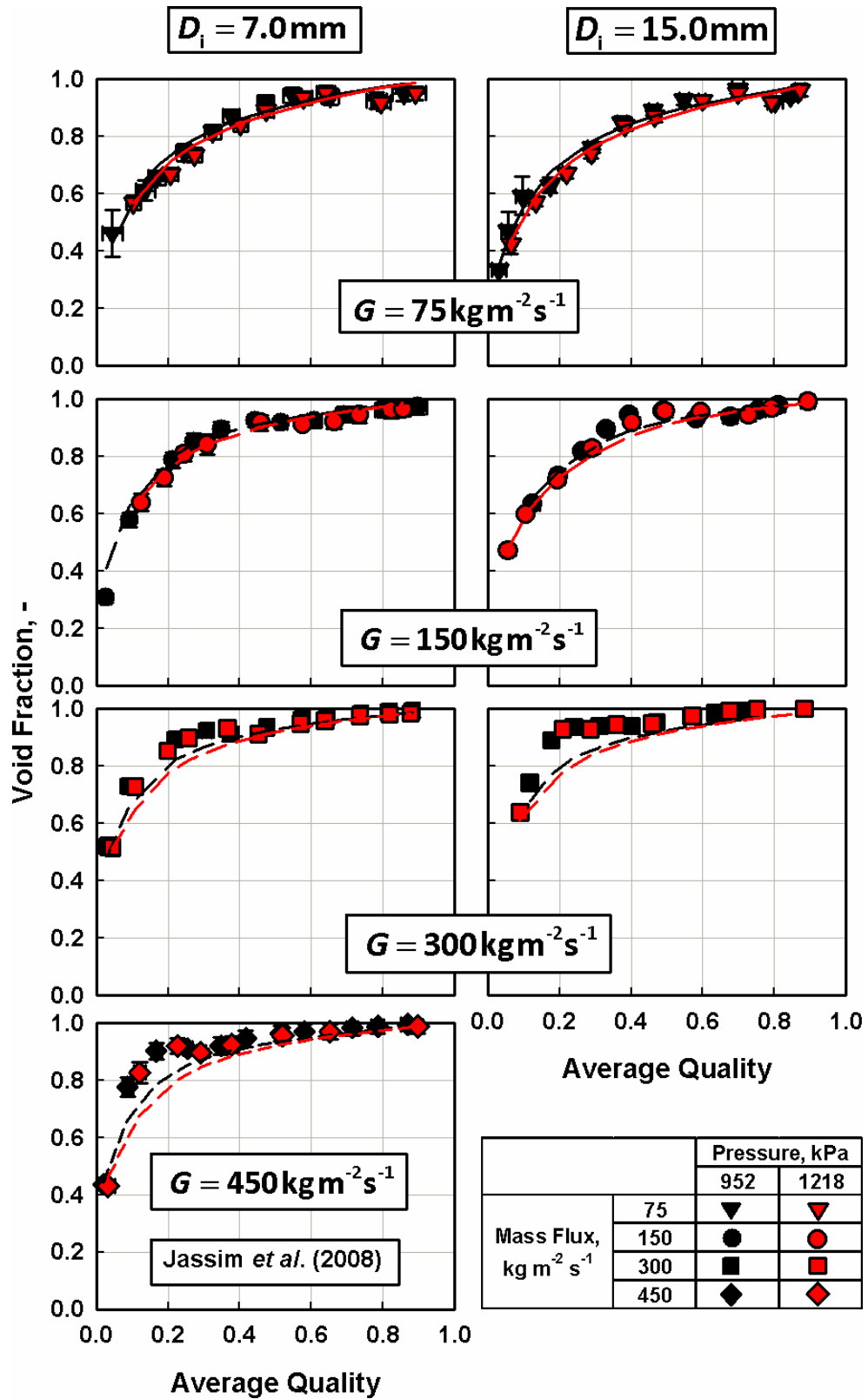
Figure 5.51. Comparison of the Jassim _et al._ (2008) void fraction correlation with the present data

Overall, the void fraction models considered here showed good agreement with the data from the present study based on AD and AAD. The correlation of Jassim *et al.* (2008) showed the best agreement, while the Baroczy (1965) correlation showed the worst agreement among the correlations discussed here. The AD for each of the correlations discussed here is shown in Figure 5.52, with the overall agreement as well as the AD for each tube diameter. These correlations and models do not appear to account for the mass flux dependence observed in the present study. This is most evident at low qualities, when the void fraction is rapidly changing.
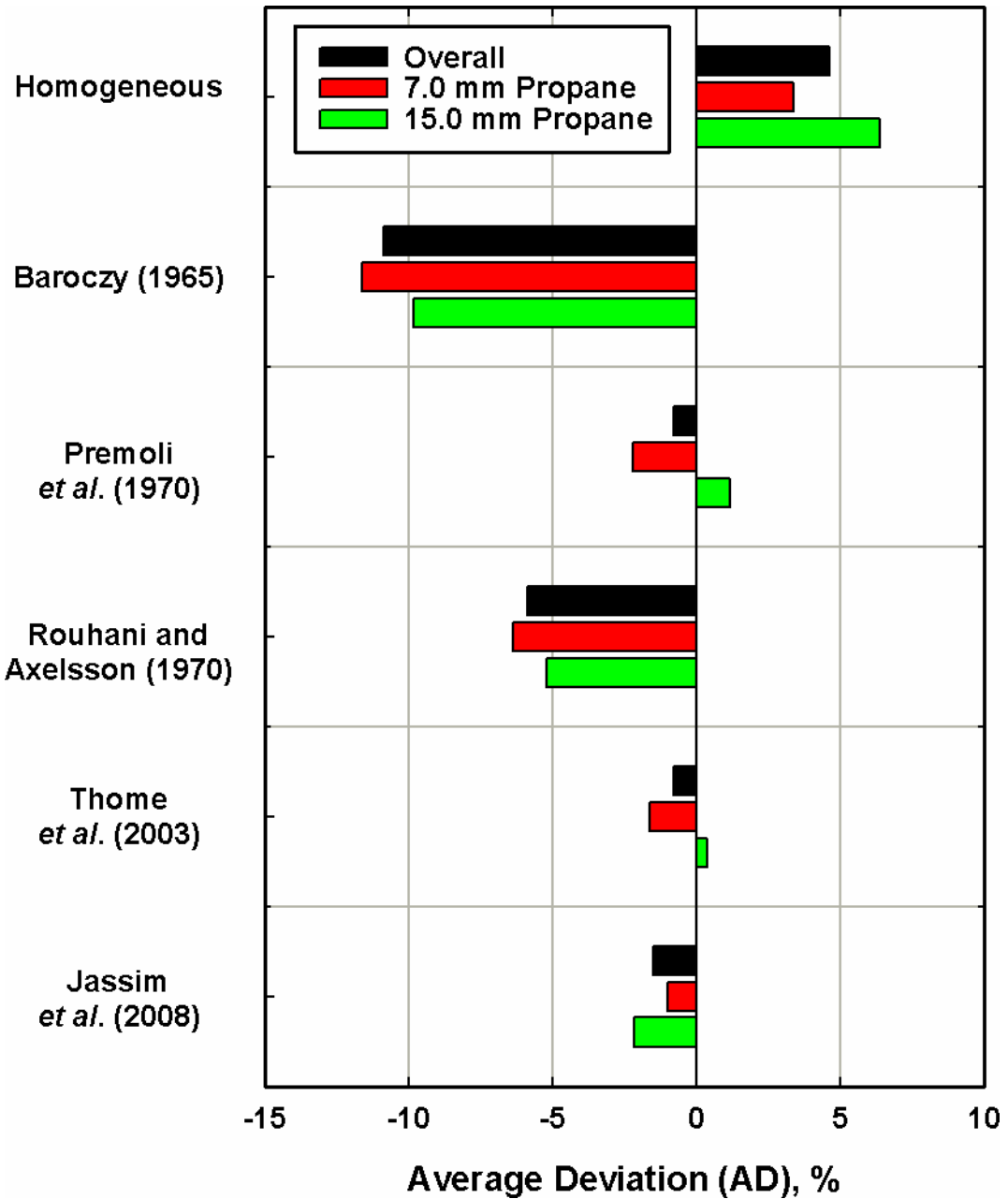
Figure 5.52. Summary of comparisons with the literature – void fraction average deviation

5.2.3 Flow regime classification for *ΔP* and *h* discussion

To facilitate discussion of the agreement of pressure drop and heat transfer correlations from the literature based on flow regime, the Dobson and Chato (1998) annular-to-wavy transition criterion was used to assign the flow regimes to the data points because no visualization results were obtained for the pressure drop and heat

transfer portion of this study. Their transition criterion showed good agreement with the flow visualization of portion of the present study, and was developed for refrigerants at similar conditions and tube diameters to those in the present study. Referring to Table 5.9, the majority of the data were predicted to be in the annular regime. Over the 428 frictional pressure drop and heat transfer coefficient data points, 76% of the data were in the annular regime. The predicted transitions at each pressure for the three fluids are shown together in Figure 5.53. The 14.45 mm ID showed the lowest percentage of the data in the annular regime. A significant number data in the intermittent regime were not expected; therefore, comparisons of ΔP and h with the predictions of correlations in the literature only the wavy and annular flow regimes are discussed here.

Table 5.9. Summary of regime predictions of Dobson and Chato (1998) for ΔP and h data

		Pressure, kPa	# Data Points	Regime	
				Annular	Wavy
7.75 mm	45% R245fa/ 55% *n*-pentane	198	35	89%	11%
		412	41	85%	15%
		763	37	70%	30%
	R245fa	122	65	78%	22%
		294	48	74%	26%
		610	35	63%	37%
	n-pentane	136	27	89%	11%
		215	38	83%	17%
14.45 mm	*n*-pentane	136	41	66%	34%
		215	34	70%	30%
		323	27	66%	34%
Total			428	76%	24%
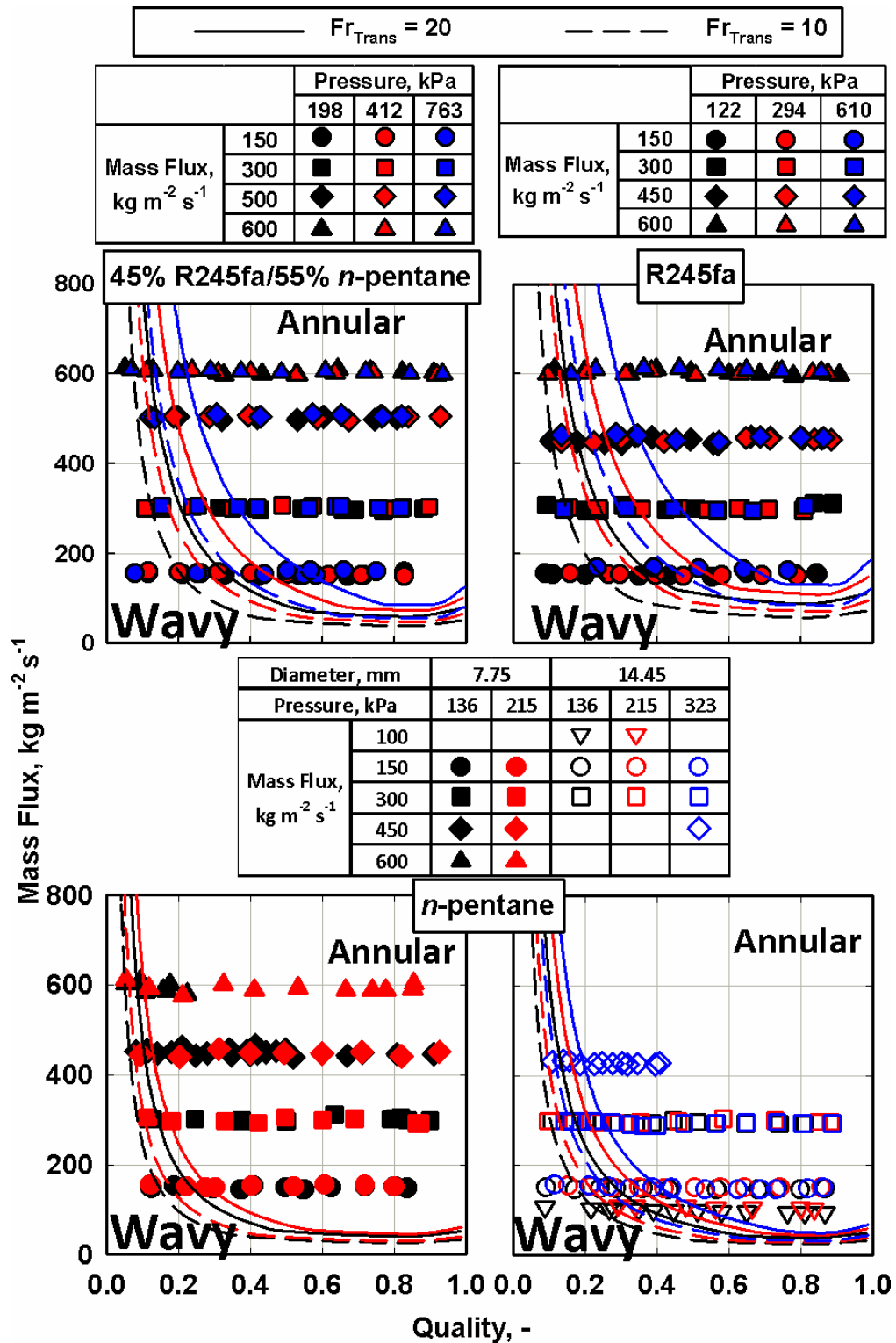
Figure 5.53. Flow regime transition for pressure drop and heat transfer coefficient data

5.2.4 Frictional Pressure Gradient

In this section, the measured frictional pressure gradient data are compared with predictions of representative correlations from the literature.

Referring to Figure 5.54, the Lockhart and Martinelli (1949) correlation over predicted the data, with an AD of 18% and an AAD of 40%, predicting only 53% of the data from the present study within ±25%. The agreement was observed to be dependent on fluid and diameter. For example, for *n*-pentane in the 7.75 mm ID tube, the AD and AAD were -14 and 19%, respectively, while for the 14.45 mm *n*-pentane data, the AD and AAD were 49 and 67% respectively. Additionally, the degree of agreement depended strongly on operating pressure. For example, in the R245fa data set, their correlation under predicted the 122 kPa data with an AD of -23%, while over predicting the 294 and 610 kPa data with an AD of 10% and 46%, respectively. Because this correlation was developed using data for various liquids with air under adiabatic conditions, the data from the present study are considered to be outside its range of applicability. Most of the present data were in the turbulent-turbulent regime. Therefore, no assessment of the laminar portion of their correlation was made.
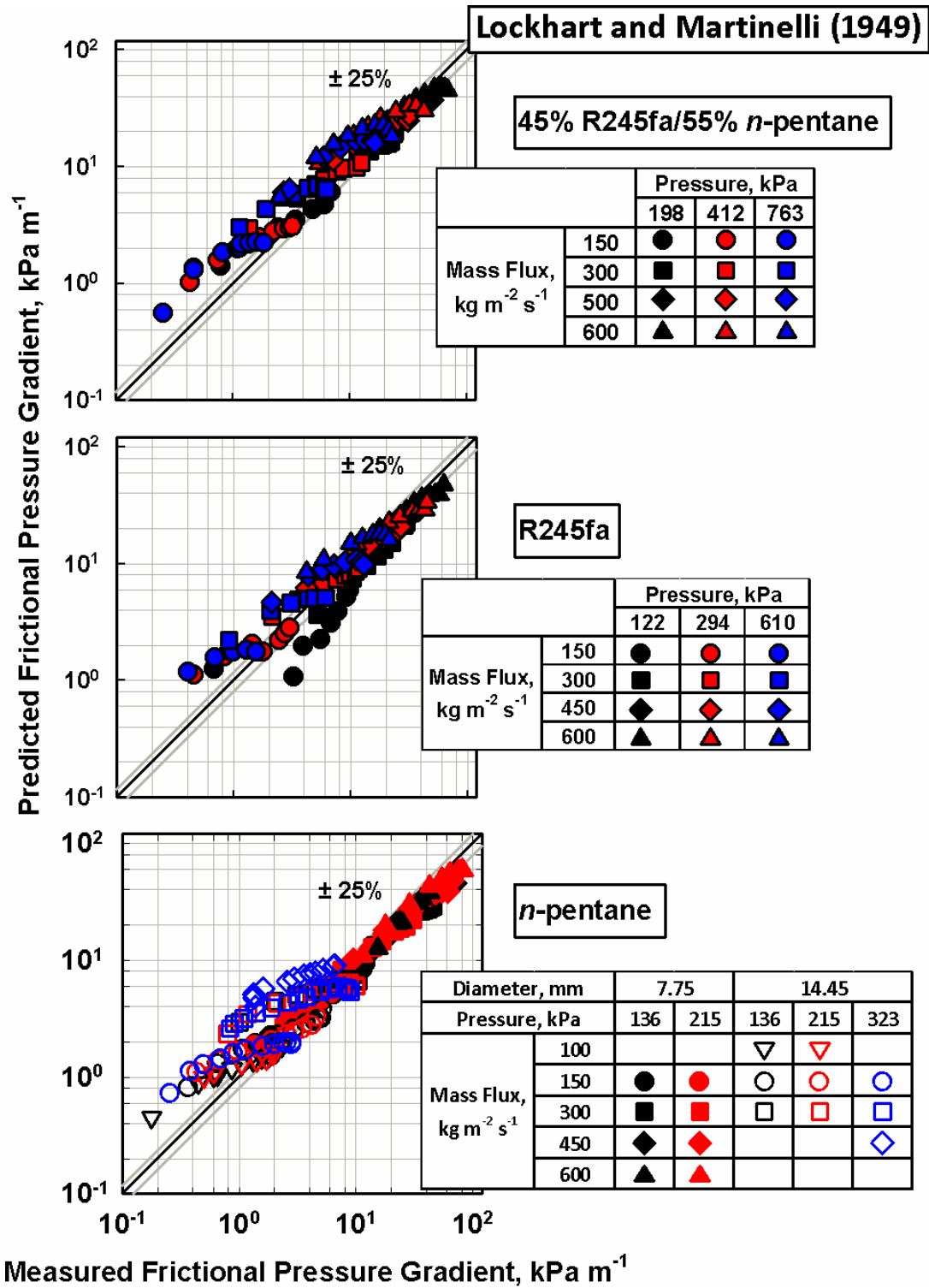
Figure 5.54. Comparison of frictional pressure gradient data from the present study with predictions of the Lockhart and Martinelli (1949) correlation

313

Chisholm (1973) used the two-phase multiplier data from Lockhart and Martinelli (1949) and Baroczy (1966) for the development of his correlation. As shown in Figure 5.55, this correlation showed poor agreement with the present data, with an AD of 30%, an AAD of 49%, and 40% of the data predicted within ±25%. The degree of agreement did not appear to show any systematic dependence on pressure or fluid type. Similar to the Lockhart and Martinelli (1949) correlation, the Chisholm (1973) correlation showed better agreement with the data for the smaller tube, n-pentane data than with the data for the larger tube. Considering the n-pentane data, the AD and AAD for the 7.75 mm ID tube were 14% and 31%, respectively, while for the 14.45 mm tube, the AD and AAD were 84% and 100%, respectively. Because the Chisholm (1973) correlation was developed using the same data as the Lockhart and Martinelli (1949) correlation discussed above, it is expected that these two models would show similar trends.
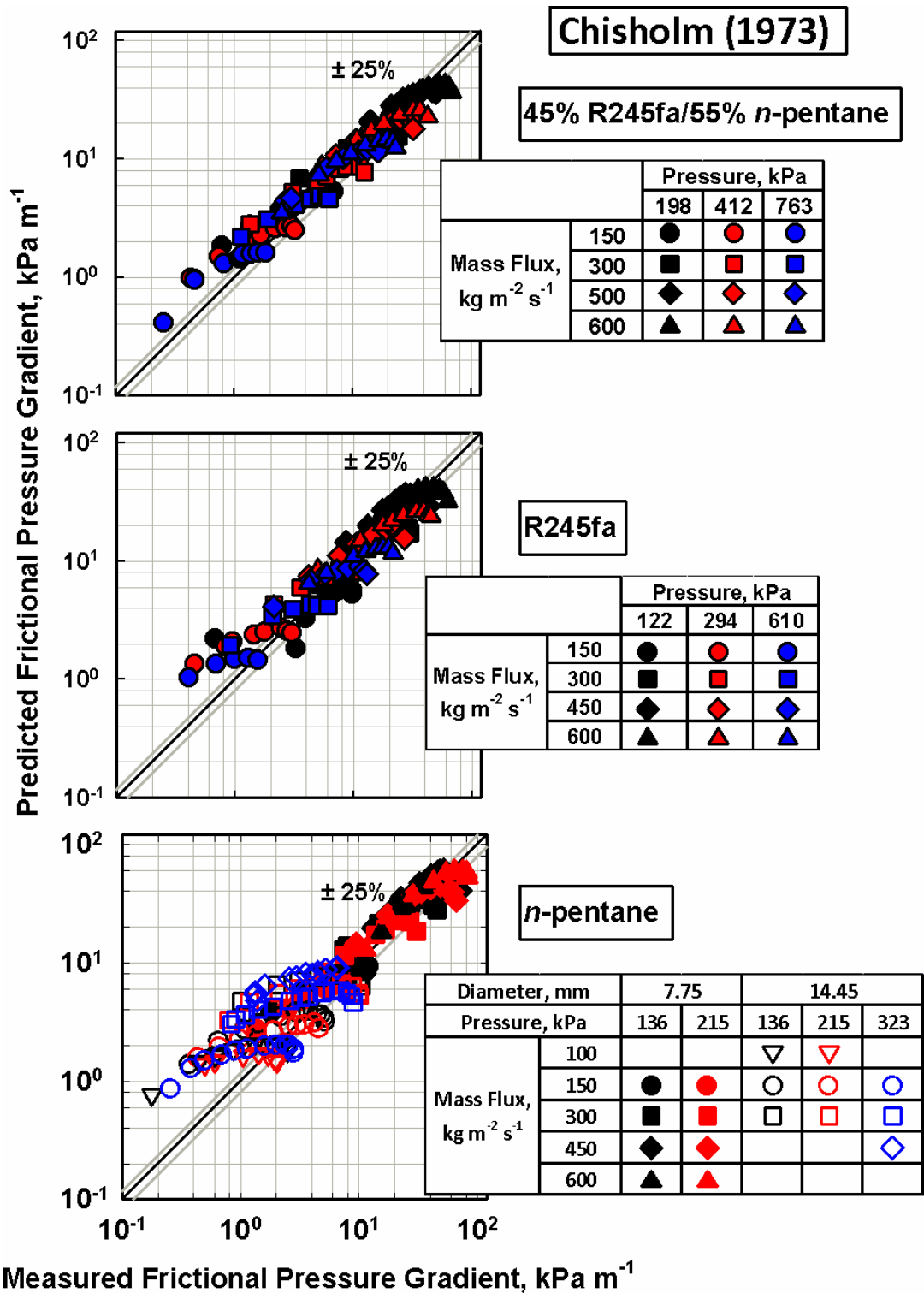
Figure 5.55. Comparison of frictional pressure gradient data from the present study with predictions of the Chisholm (1973) correlation

Although the Friedel (1979) correlation was developed using a large database of adiabatic frictional pressure drop measurements for a variety of fluids consisting predominantly of water, R12, air/water, and air/oil two-phase flow in horizontal and vertical round, rectangular, and annular cross section tubes with hydraulic diameters ranging from 12 to 49 mm. His correlation tends to significantly under predict the data from the present study with an AD of -24% (Figure 5.56.) The AAD was slightly higher at 35%, with 21% of the present data predicted within ±25%. This correlation predicts the data at higher operating pressures better than those at the lowest pressure. In the R245fa data set at P = 122 kPa, the AD is -40%, whereas at P = 610 kPa, the AD is -17%. Tube diameter had a significant effect on the agreement with the n-pentane data. Both show similar AAD with a value of 39% for the 7.75 mm data and 36% for the 14.45 mm data. However, because the 14.45 mm data exhibited more scatter, the AD of the 14.45 mm data was -2% while the 7.75 mm data were consistently under predicted, with an AD of -39%.
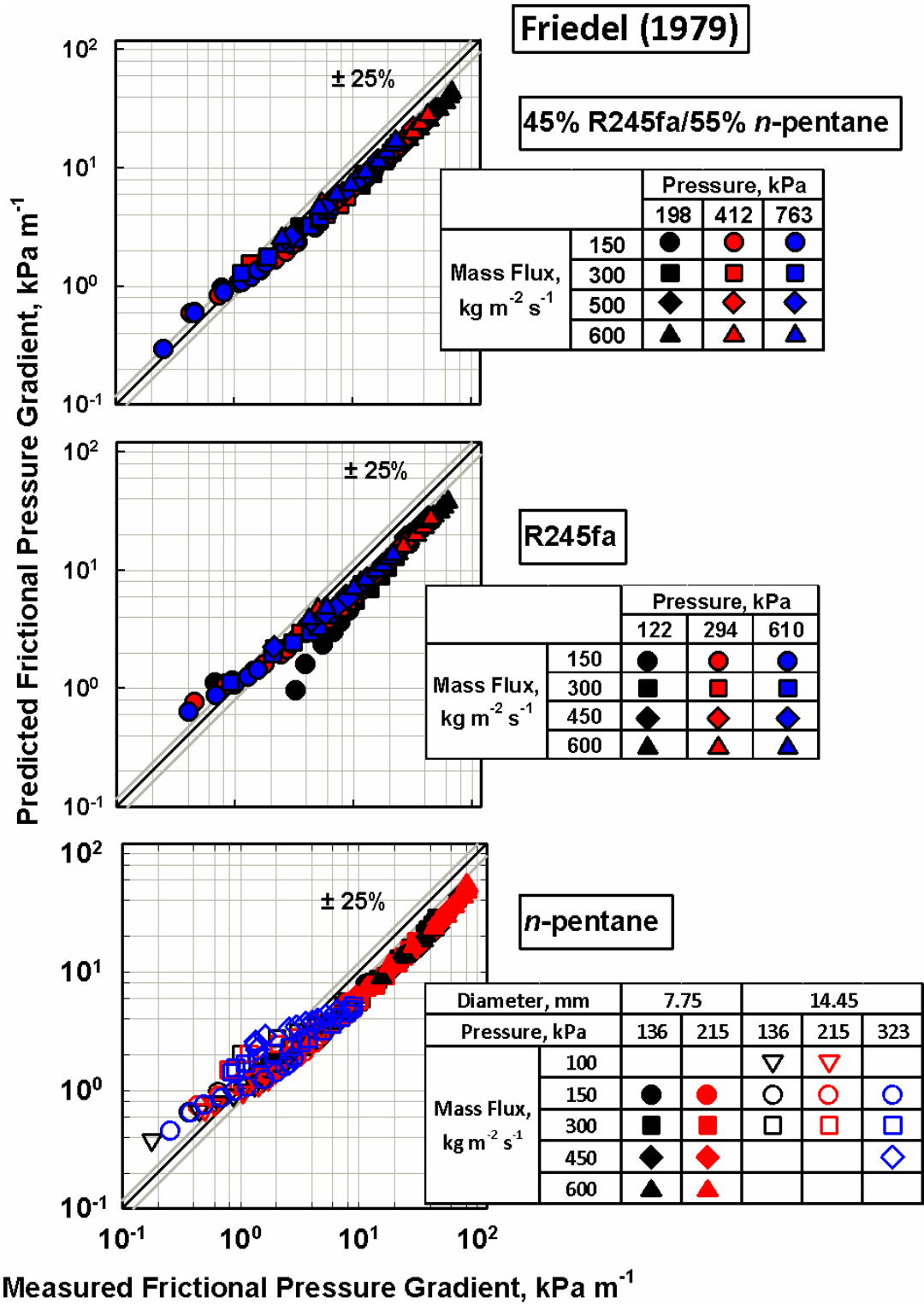
Figure 5.56. Comparison of frictional pressure gradient data from the present study with predictions of the Friedel (1979) correlation

Other authors have noted similar disagreement with the Friedel correlation for condensing flows, including Cavallini *et al.* (2002a) who recommended a modified version (Figure 5.57) of the Friedel (1979) correlation for the annular regime and the original Friedel (1979) correlation for non-annular cases. Compared to the Friedel (1979) correlation, slightly better agreement with the present data was observed with the correlation of Cavallini *et al.* (2002a), with an AD of 20%, an AAD of 30%, and 41% of the data from the present study predicted within ±25%. As was the case with the Friedel (1979) correlation, the agreement of the present data with the predictions of the Cavallini *et al.* (2002a) correlation generally improves with increasing pressure. However, the most noticeable improvement was observed in the pure R245fa data, most probably because their correlation was developed using similar fluids including R236ea. For the pure refrigerant data, the AD and AAD were -8% and 16%, respectively. For the lowest pressure of $P = 122$ kPa, the AD was -15%, while the AD for $P = 294$ kPa and $P = 610$ kPa were -3 and -4%, respectively. Overall, 85% of the data were predicted within ±25%. Of the 148 data points in the R245fa data set predicted to be in the annular regime by the Dobson and Chato (1998) flow map, the AAD is 11%. Over the same subset of data, the Friedel (1979) correlation predicts the data with an AAD of 36%. This indicates that the modifications to the Friedel (1979) correlation proposed by Cavallini *et al.* (2002a) provided a slight improvement in the prediction of the data from the present study overall.
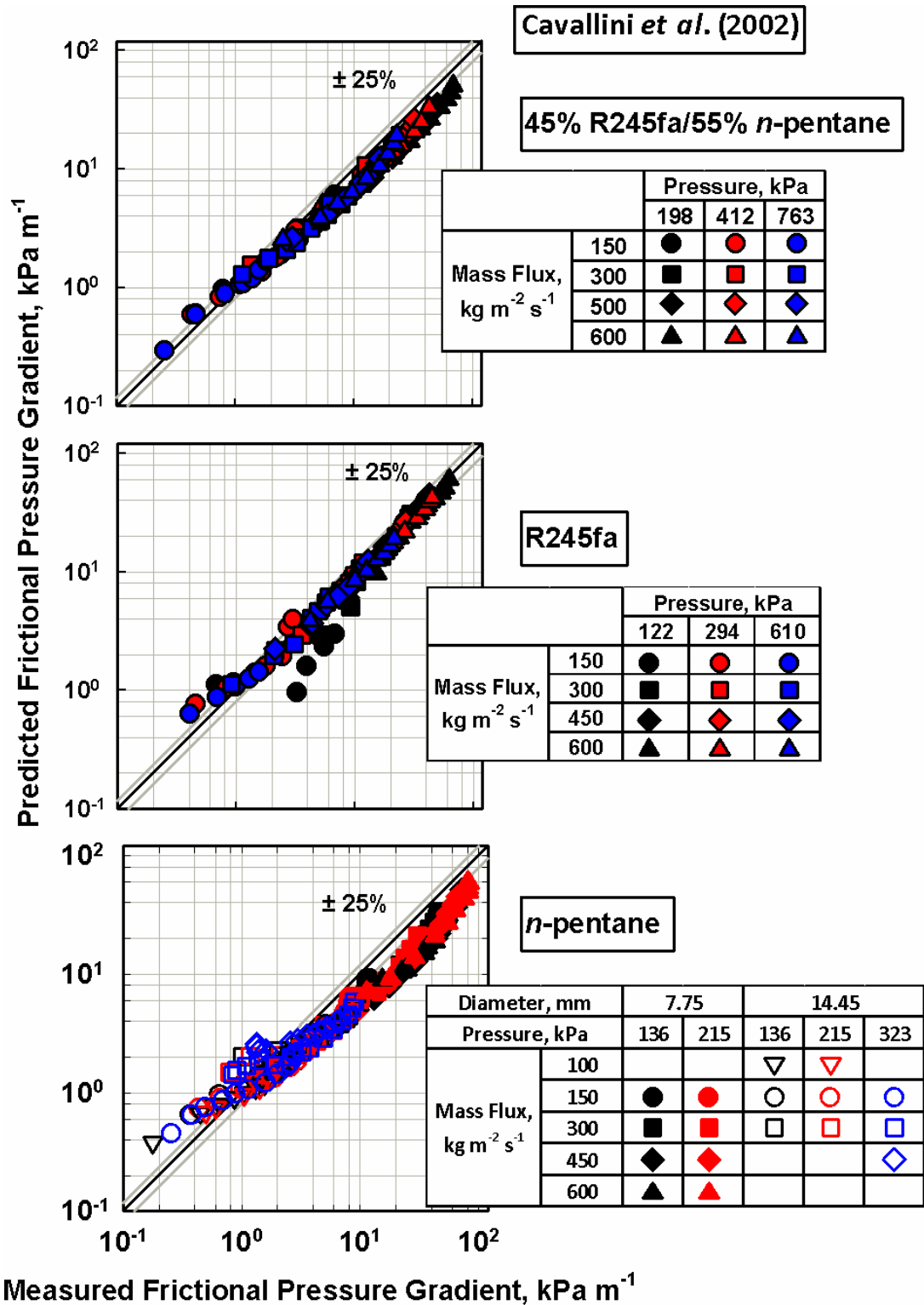
Figure 5.57. Comparison of frictional pressure gradient data from the present study with predictions of the Cavallini *et al.* (2002) correlation

The Müller-Steinhagen and Heck (1986) correlation consistently under predicted the data from the present study (Figure 5.58,) with an AD of -29% and an AAD of 34%. Due to the consistent under prediction, only 14% of the data from the present study were predicted within ±25%. Müller-Steinhagen and Heck (1986) assumed that over most of the quality range, the change in frictional pressure drop was linear, which was a reasonable assumption. In general, the Müller-Steinhagen and Heck (1986) correlation showed better agreement at higher reduced pressure. In the R245fa data set at $P = 122$ kPa, the AD was -41%, whereas at $P = 610$ kPa, the AD is -29%.

The correlation of Soliman *et al.* (1968) showed good agreement with data from the present study (Figure 5.59) with an AD of -4% and AAD of 28%, and with 51% of the data predicted within ±25%. While showing overall good agreement, the Soliman *et al.* (1968) correlation did not account for changes in reduced pressure accurately. In the R245fa data set at $P = 122$ kPa, the AD was –34%, whereas at $P = 610$ kPa, the AD was 15%. The lowest reduced pressure ($P_r < 0.1$) data tended to be under predicted, while the higher reduced pressure data tend to be over predicted.
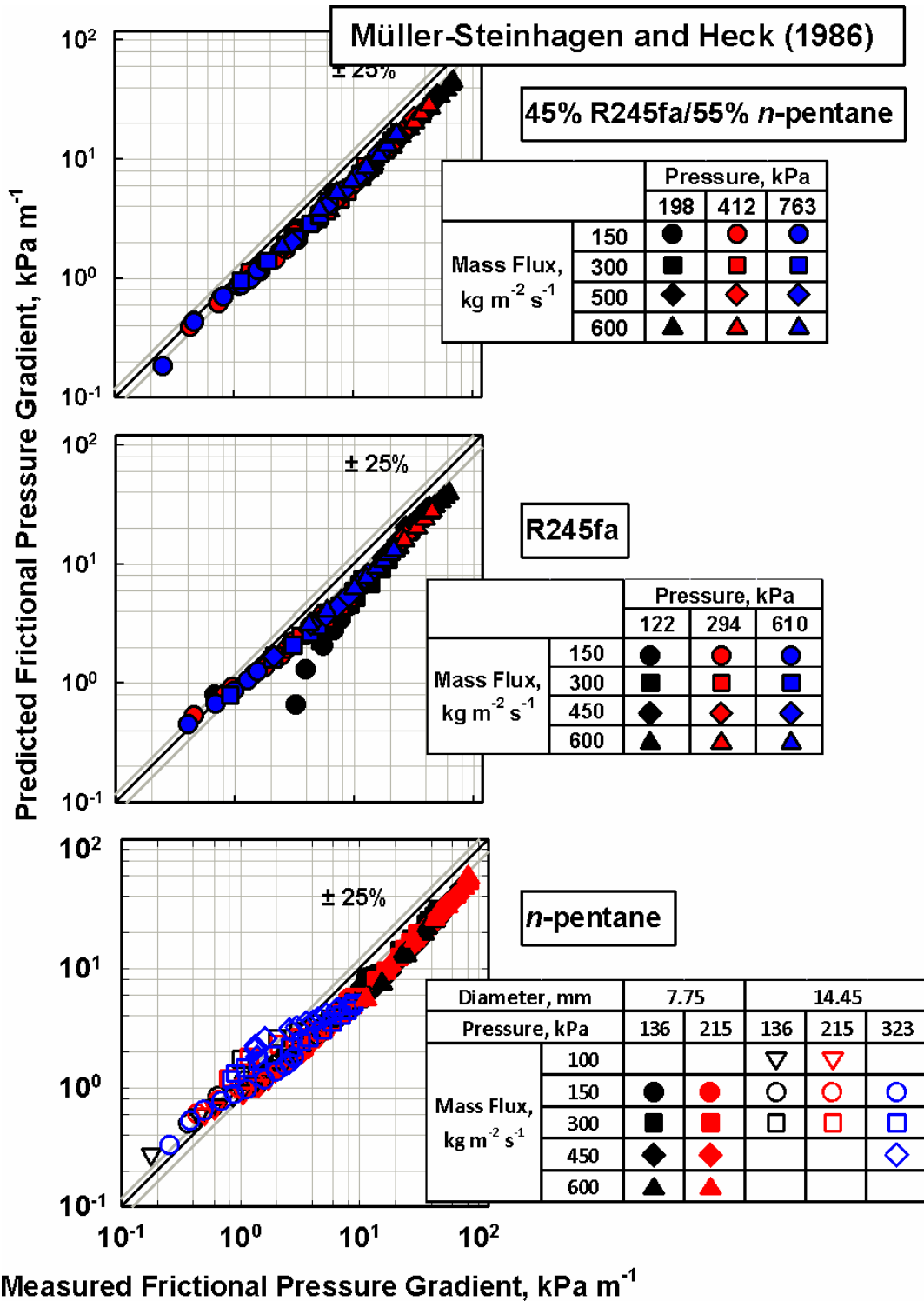
Figure 5.58. Comparison of frictional pressure gradient results to predictions of the Müller-Steinhagen and Heck (1986) correlation
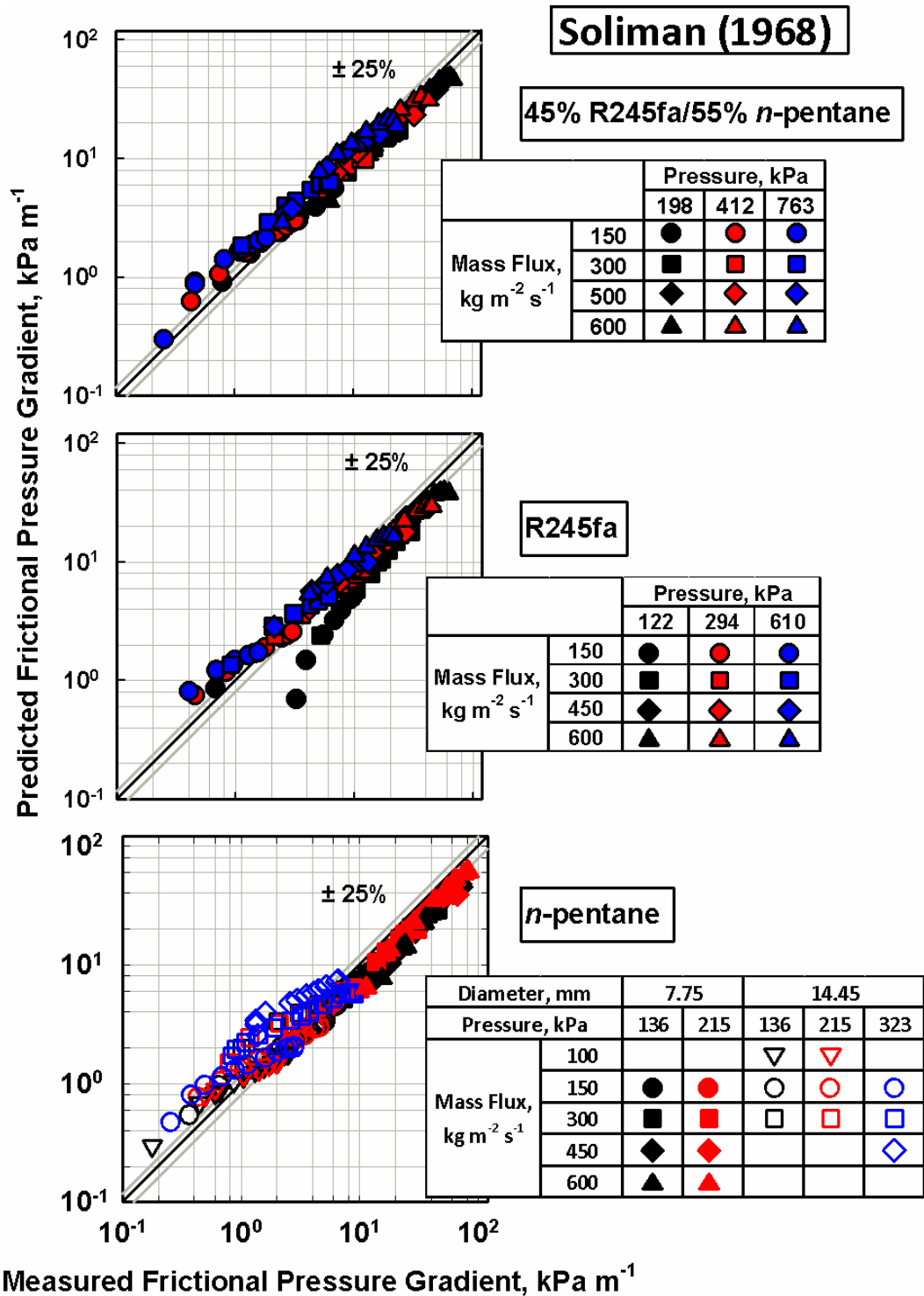
Figure 5.59. Comparison of frictional pressure gradient results to predictions of the Soliman (1968) correlation

A summary of comparison statistics for frictional pressure gradient data from the present study with the predictions of the correlations from the literature is presented in Table 5.10. The AD for all the data and the individual AD for each of the fluids are shown in Figure 5.60. When the models under consideration were developed for similar fluids, such as R236ea, the agreement was quite good. However, none of the models are capable of predicting pressure drop adequately over the wide range of fluid properties and operating conditions under consideration in the present study.

Table 5.10. Summary of comparisons with the literature – frictional pressure gradient results

Author	Average Deviation, %	Absolute Average Deviation, %	% within ±25%
Lockhart and Martinelli (1949)	18%	40%	53%
Soliman (1968)	-4%	28%	51%
Chisholm (1973)	30%	49%	40%
Friedel (1979)	-24%	35%	21%
Müller-Steinhagen and Heck (1986)	-29%	34%	14%
Cavallini *et al*. (2002)	-20%	30%	41%
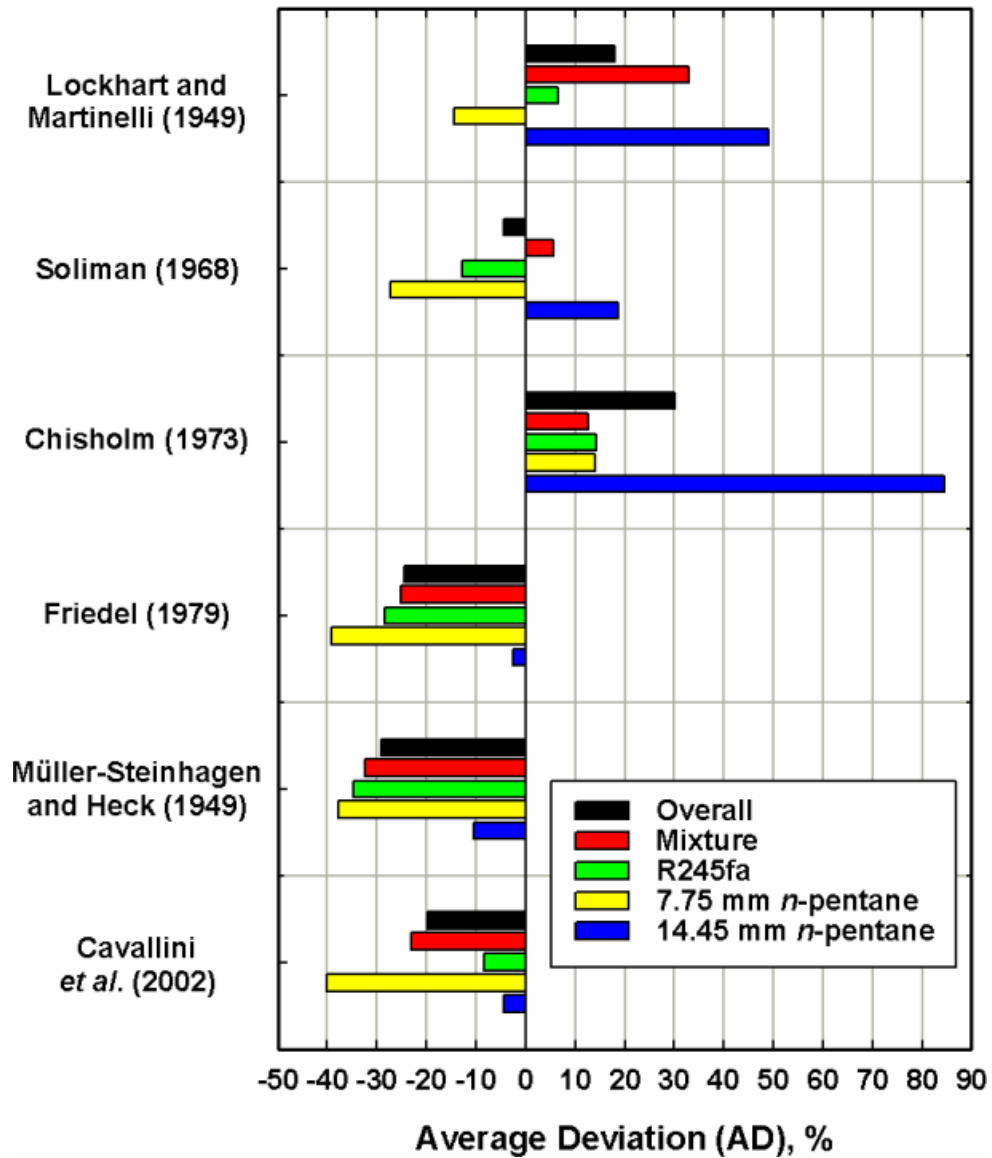
Figure 5.60. Summary of comparisons with the literature – frictional pressure gradient results average deviation

5.2.5 Heat Transfer Coefficient

In this section, heat transfer coefficient data from the present study are compared with selected correlations form the literature that either exhibited good agreement, or are commonly referenced in the literature. The heat transfer coefficients for pure R245fa and pure *n*-pentane are compared with predictions of correlations from the literature. Apparent heat transfer coefficients of the 45% R245fa/55% *n*-pentane zeotropic mixture

obtained using the equilibrium method are compared with correlations in the literature with the correction factor of Bell and Ghaly (1973) (with the exception of the Del Col *et al.* (2005) correlation, which used a modified correction factor.) The Bell and Ghaly comparison is followed by a comparison of the zeotropic mixture measured test section heat duties with those predicted using the non-equilibrium Price and Bell (1974) approach. The liquid film heat transfer coefficient is modeled using condensation models as inputs. Because the Price and Bell (1974) approach calculates the mass transfer effects specific to each set of inlet conditions, operating conditions, and condensation heat transfer rate, the film heat transfer coefficient can significantly alter the calculated outlet conditions. Therefore, comparisons between the zeotropic mixture data and correlations from the literature using the Price and Bell (1974) approach are best conducted based on comparisons of the heat duty. The ability of the correlation to predict heat transfer for different fluid types and the mixture results is discussed.

For the 45% R245fa/55% *n*-pentane zeotropic mixture at $P = 198$ kPa ($T_{\text{Bub}} = 30°$C), the vapor-phase thermal diffusivity is 1.50×10^{-6} m^2 s^{-1} and the binary diffusion coefficient in the vapor phase calculated using the Chapmann-Enskog relation is 1.5×10^{-6} m^2 s^{-1}, resulting in a vapor Lewis number of 0.99. At $P = 763$ kPa ($T_{\text{Bub}} = 80°$C) the vapor Lewis number is 0.87. As noted in Chapter 2, Webb *et al.* (1996) found the Bell and Ghaly (1973) approach to produce accurate results for fluids with vapor Lewis numbers of 0.6 to 0.8. For Lewis numbers greater than unity, they suggest that the method will over predict the heat transfer coefficient. Therefore, in this case, the findings of Webb *et al.* (1996) indicate that a slight over prediction may result from the use of the Bell and Ghaly (1973) approach.

The Traviss *et al.* (1973) correlation (Figure 5.61) systematically over predicted the data. The R245fa data were predicted with an AD of 30%, while the 7.75 mm *n*-pentane data were predicted with an AD of 59%. Thirty six percent of pure fluid heat transfer coefficients from the present study were predicted within ±25%, with an AD of 37% and an AAD of 38%. When including the zeotropic mixture data with the Bell and Ghaly (1973) correction, the Traviss *et al.* (1973) correlation predicted 32% of the data within ±25%, with an AAD of 37%. Using the Price and Bell (1974) approach with the Traviss *et al.* (1973) correlation to predict the test section heat duty, the AD and AAD were both 45%. This correlation was expected to show good agreement in the annular regime as predicted by the Dobson and Chato (1998) criteria. However, the poor agreement might be due to their model being based on fluids different from those in the present study. Replacing the two-phase multiplier based on the Lockhart and Martinelli (1949) data with the measured pressure gradient also resulted in a significant over prediction of the data. Therefore, the film analysis proposed by Traviss *et al*. may not be valid at the high mass fluxes under consideration here due to a significant breakup of the liquid film.

Figure 5.61. Comparison of the present heat transfer data with predictions of the Traviss *et al*. (1973) model

The Shah (1979) correlation (Figure 5.62) predicted 77% of pure fluid heat transfer coefficients from the present study within ±25%, with an AD of 9% and an AAD of 15%. When including the zeotropic mixture data with the Bell and Ghaly (1973) correction, the Shah (1979) correlation predicted 70% of the data within ±25%, with an AAD of 18%. Using the Price and Bell (1974) approach with the Shah (1979) correlation to predict the film heat transfer coefficient, the test section heat duty was predicted with an AD and AAD of 37%. Based on findings of previous research, his correlation was expected to show good agreement in the annular regime, which encompasses the majority of the data in the present study. Better agreement was observed for the *n*-pentane 14.45 mm ID tube with an AD and an AAD of -6% and 7%, respectively whereas the AD and AAD for the 7.75 mm tube were 22 and 23%, respectively. Because the Shah (1979) correlation was developed using data in 7 to 40 mm tube diameter data, better agreement at the larger tube diameter is understandable due to the limited small diameter data. In general, the Shah (1979) correlation tended to increasingly over predict the data with increasing pressure. For example, the R245fa data set had an AAD of 10% at $P = 122$ kPa whereas at $P = 610$ kPa the AAD was 24%.
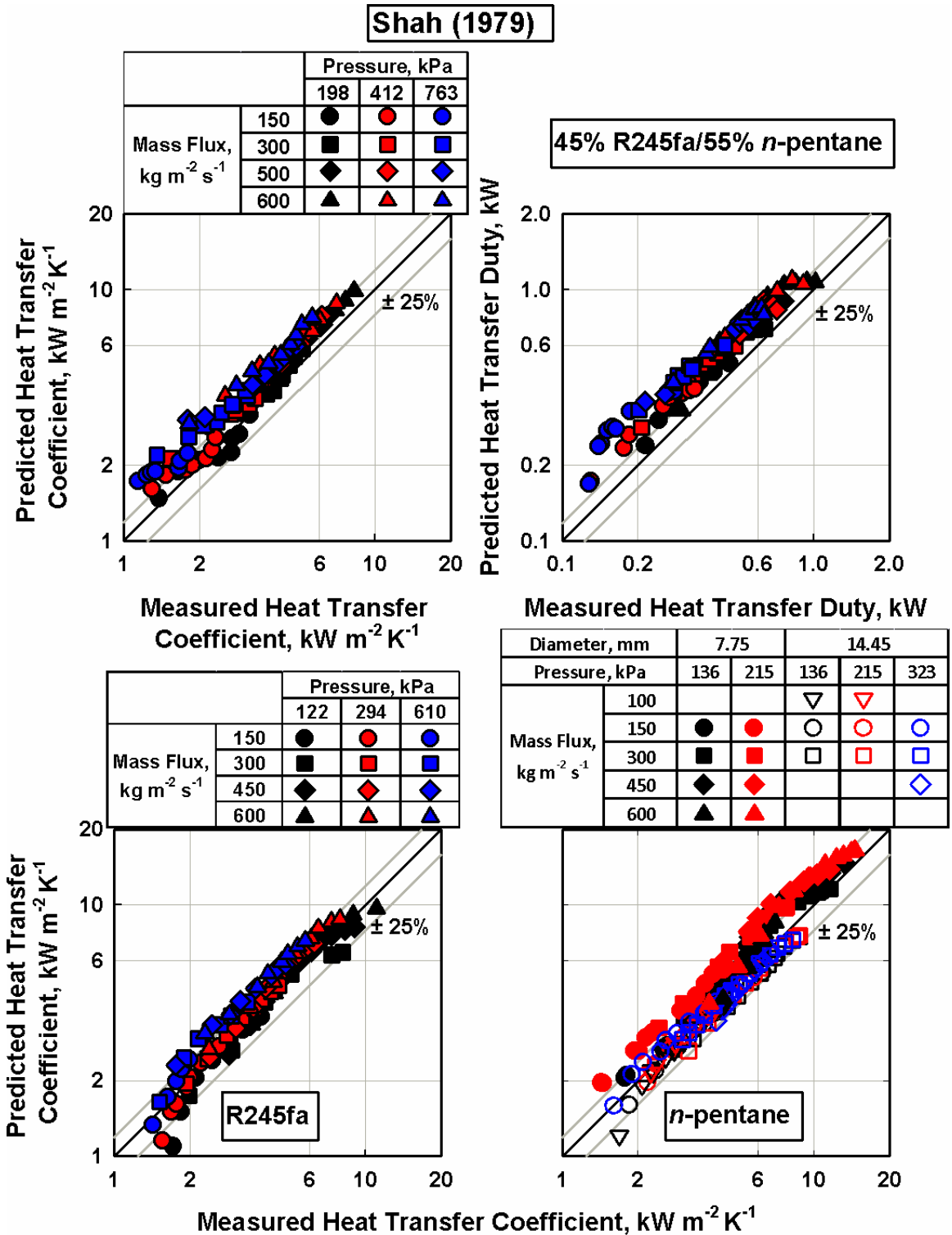
Figure 5.62. Comparison of the present heat transfer data with predictions of the Shah (1979) correlation

The assumption based on the flow regime maps and transitions discussed above is that most of the data points are in the annular flow regime. However, the Soliman (1983) correlation predicted 243 (57%) of the 428 data points in the present study to be mist flow. The predictions of the mist flow correlation of Soliman (1986) (Figure 5.63) showed generally good agreement with the present data in this regime, with AADs for R245fa, 7.75 mm *n*-pentane, 14.45 mm *n*-pentane, and the zeotropic mixture of 14%, 9%, 31% and 8%, respectively with 96% of the 7.75 mm data predicted within ±25%. His correlation based on the heat-momentum analogy for single-phase flow works well in this regime due to the breakdown of the liquid film decreasing the resistance of the film commonly accounted for in annular flow models. The obvious exception is the 14.45 mm tube data which were significantly over predicted. However, he used data from 7.4 to 12.7 mm internal tube diameters which is slightly smaller than the 14.45 mm tube indicating the model may not be valid up to 14.45 mm.
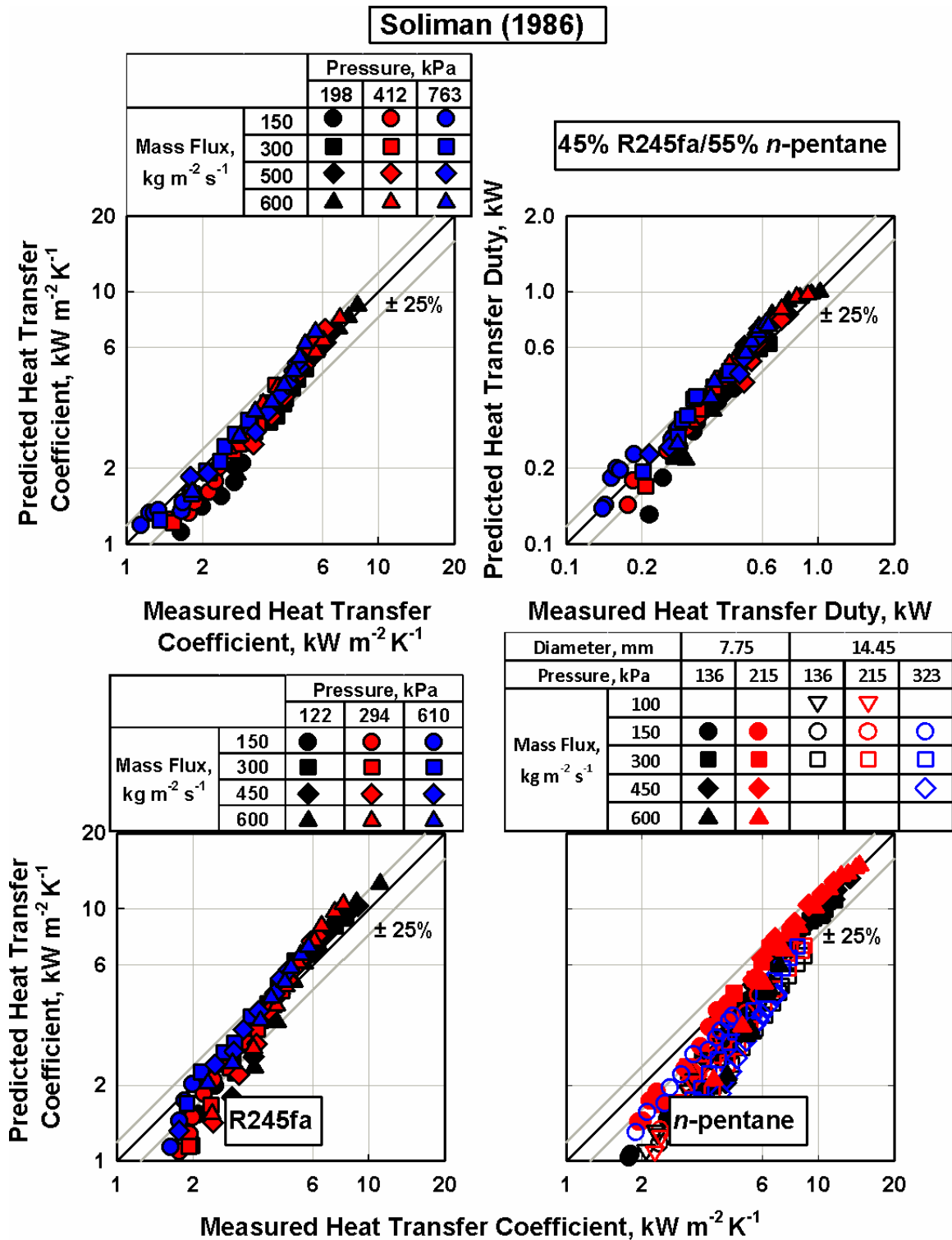
Figure 5.63. Comparison of the present heat transfer data with predictions of the Soliman (1986) correlation

The Dobson and Chato (1998) correlation (Figure 5.64) predicted 50% of the pure fluid data from the present study within ±25%, with an AD of 21% and an AAD of 28%. When including the zeotropic mixture data with the Bell and Ghaly (1973) correction, the Dobson and Chato (1998) correlation predicted 51% of the data within ±25%, with an AAD of 27%. Using the Price and Bell (1974) approach with the Dobson and Chato (1998) correlation to predict the test section heat duty, the AD and AAD were 35 and 36%, respectively. This correlation predicted low pressure data better. For example, for the R245fa data set at $P = 198$ kPa, the AD is 16%, while at $P = 763$ kPa, the AD is 29%. The lack of a transition region between the prediction for wavy and annular regime resulted in an abrupt transition, as observed in Figure 5.64.
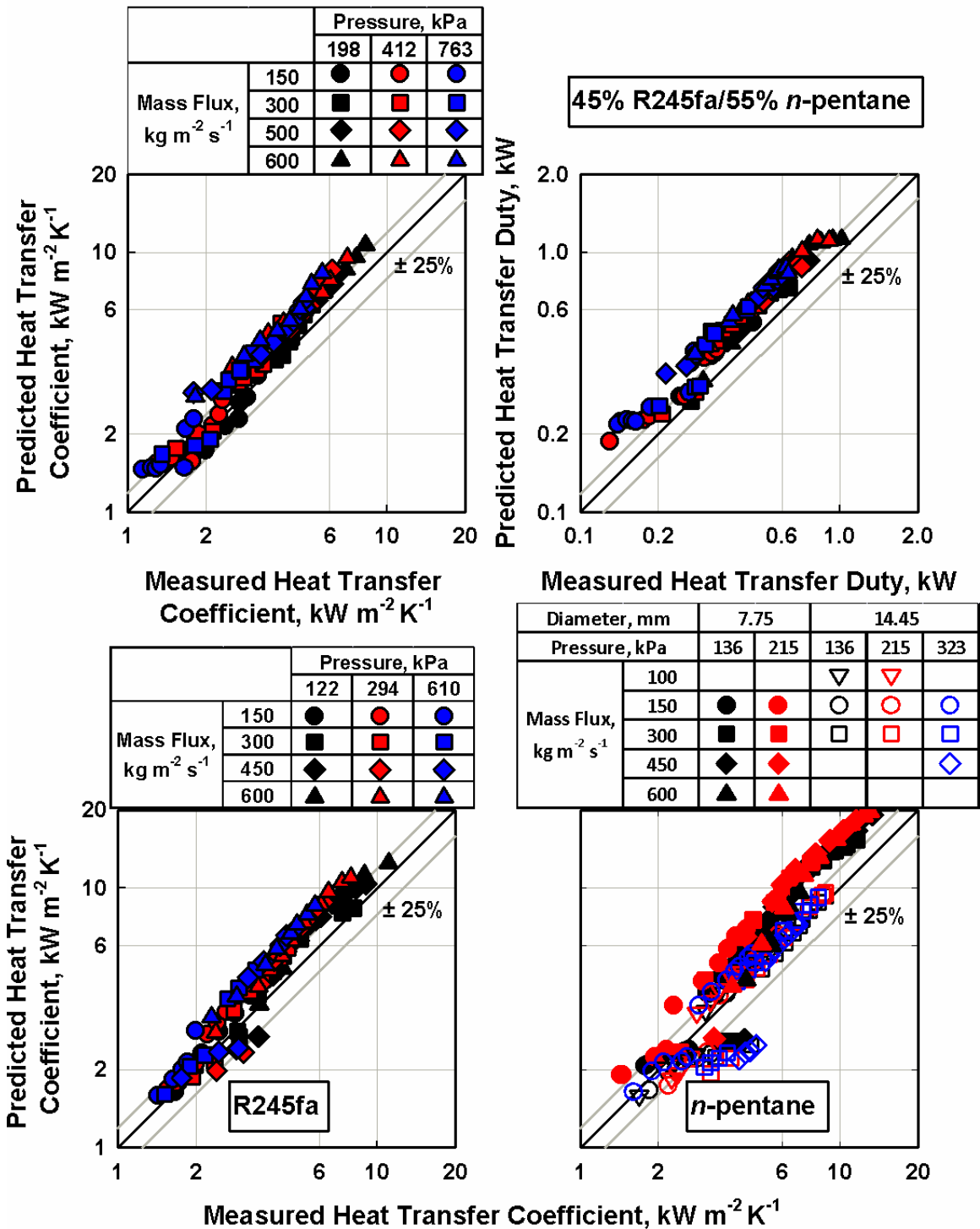
Figure 5.64. Comparison of the present heat transfer data with predictions of the Dobson and Chato (1998) correlation

The Thome *et al.* (2003) correlation (Figure 5.65) predicted 44% of the pure fluid data from the present study within ±25% with an AAD of 31%. When including the zeotropic mixture data with the Bell and Ghaly (1973) correction, the Thome *et al.* (2003) correlation predicted 51% of the data from the present study within ±25% with an AAD of 28%. Using the Price and Bell (1974) approach with the Thome *et al.* (2003) correlation to predict the test section heat duty, the AD and AAD were 35 and 36%, respectively. Del Col *et al.* (2005) (not shown) presented a modified Bell and Ghaly (1973) approximation and non-equilibrium factor to be applied to the Thome *et al.* (2003) correlation. The Del Col *et al.* (2005) approach has an AAD of 32%, with 26% of the data from the present study predicted within ±25%, while the Thome *et al.* (2003) correlation with the unmodified Bell and Ghaly (1973) approximation had an AAD of 30% and predicts 30% of the data from the present study within ±25%. Both over predict the data and show no discernible trend with pressure. The interfacial roughness correction factor does not appear to improve the mass transfer correction factor of Bell and Ghaly (1973) for the zeotropic mixture of interest in the present study. The model of Thome *et al.* (2003) was developed using a large refrigerant and hydrocarbon database, including R236ea, which would indicate reasonable agreement with the R245fa data. For the 7.75 mm pure fluids data, the Thome *et al.* (2003) correlation predicts the R245fa data with an AAD of 32% while the *n*-pentane data are predicted with an AAD of 48%. However, the larger tube 14.45 mm *n*-pentane data were predicted well with an AAD of 15%.
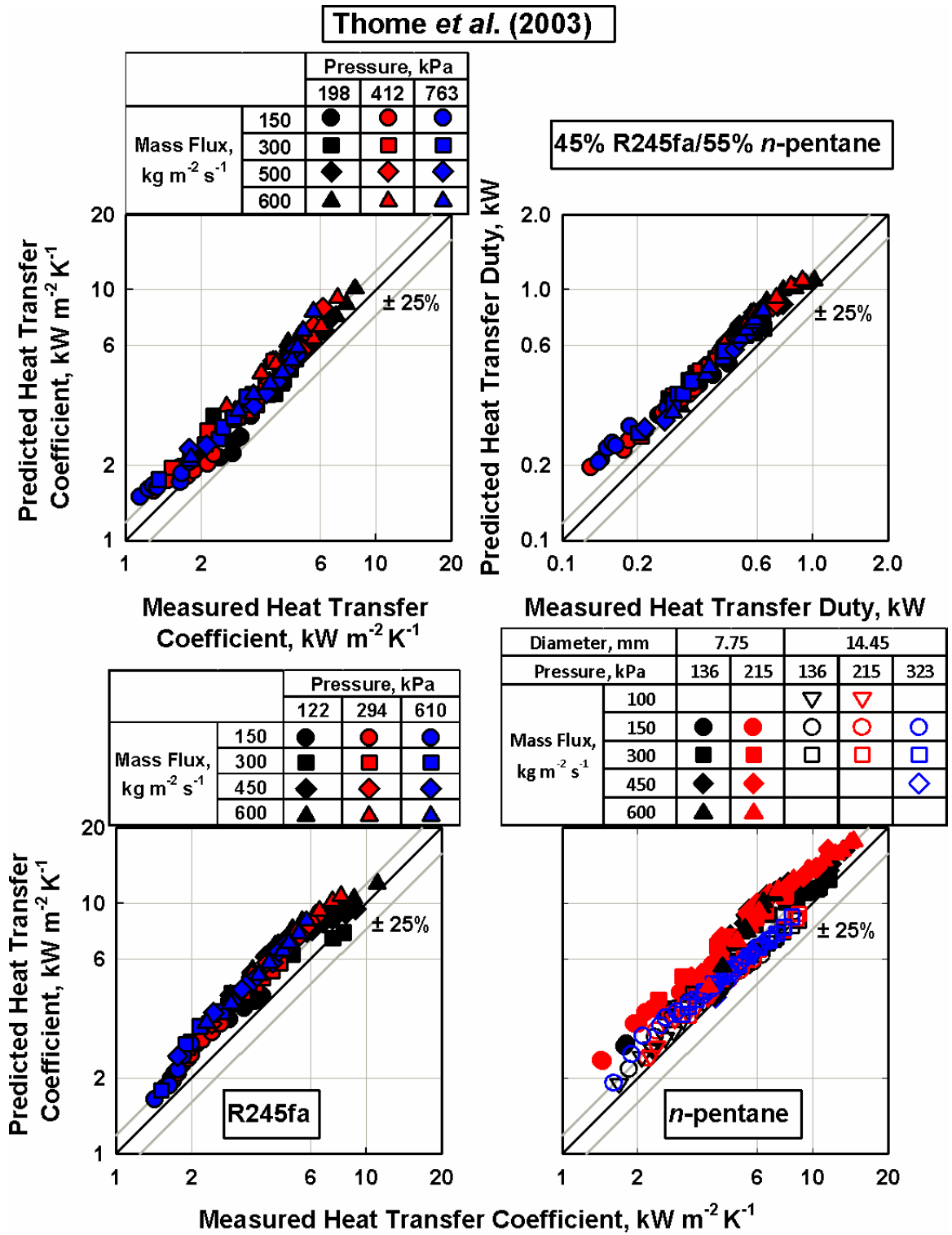
Figure 5.65. Comparison of the present heat transfer data with predictions of the Thome *et al*. (2003) correlation

The predictions of the correlation by Cavallini *et al.* (2006) (Figure 5.66) exhibited the best agreement with the data from the present study. Very good agreement with the pure fluid data was found, with an AD of 8%, AAD of 16% and 79% of the data predicted within ±25%. When including the zeotropic mixture data with the Bell and Ghaly (1973) correction, the Cavallini *et al.* (2006) correlation predicted 82% of the data within ±25%, with an AAD of 15%. Using the Price and Bell (1974) approach with the Cavallini *et al.* (2006) correlation to predict the test section heat duty, the AD and AAD were 20 and 22%, respectively. A slight improvement in agreement was observed in the 7.75 mm tube with decreasing pressure. For example, for the R245fa data set, their correlations predicted the data with an AAD of 11% at $P = 122$ kPa, and an AAD of 22% at $P = 610$ kPa. The slight increase in agreement with decreasing pressure observed in the heat transfer coefficient comparison was amplified in the heat duty comparison with an AAD of 24% for the present data at $P = 764$ kPa and an AAD of 15% for the present data at $P = 198$ kPa. Because of its basis in data for a wide range of fluids, including synthetic refrigerants, hydrocarbons, and mixtures, over a wide range of conditions, this correlation appears to extrapolate to the fluids of interest in the present study well.
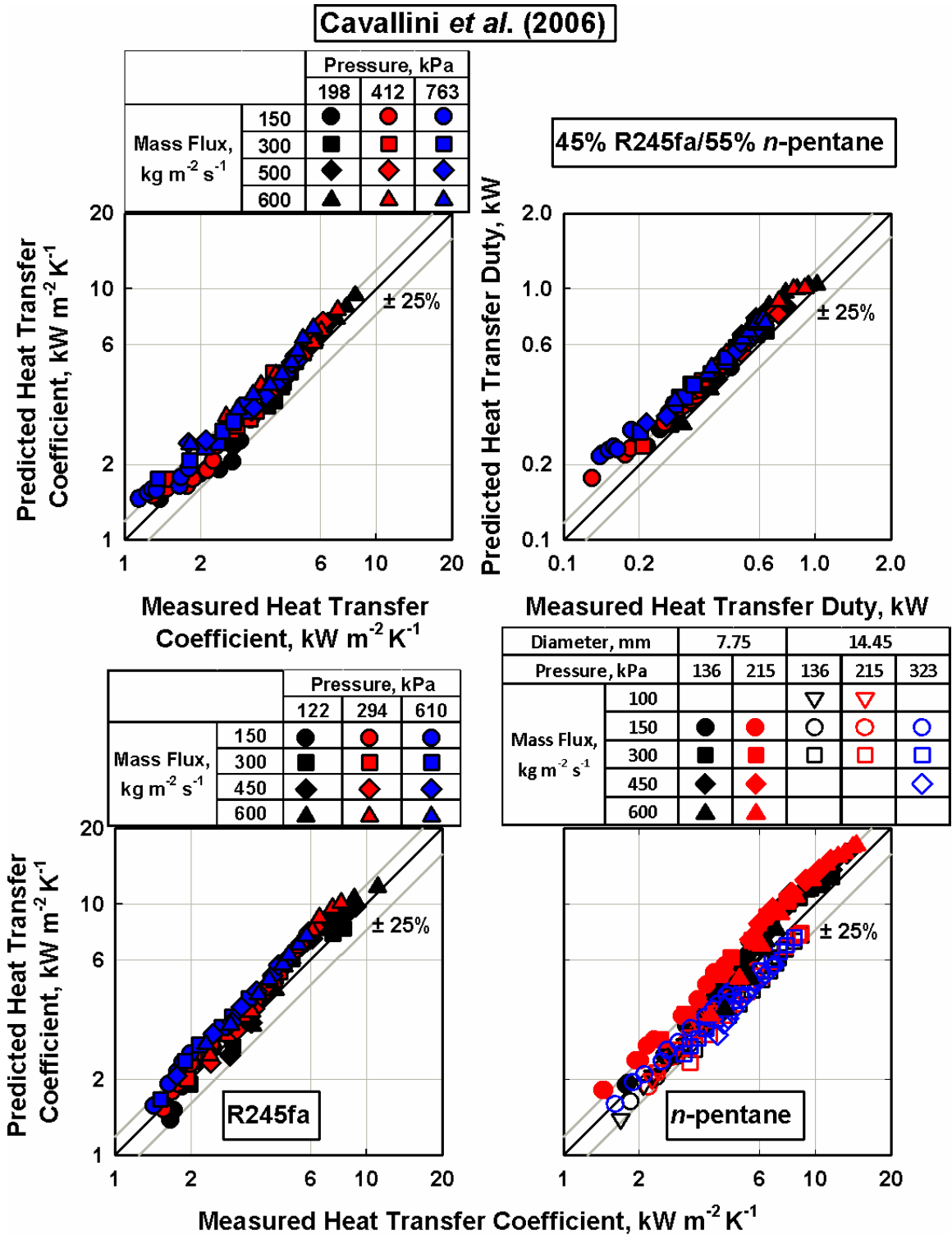
Figure 5.66. Comparison of the present heat transfer data with predictions of Cavallini *et al*. (2006)

A summary of relevant statistics for the correlations from the literature with the heat transfer coefficient from the present study is presented in Table 5.11. Statistics of the mixture comparison between the predictions and the measured heat transfer coefficient and heat duty data from the present study are presented in Table 5.12. The AD for each fluid is shown in Figure 5.67. In general, better agreement with experimental results from the present study was found between correlations in literature with the Bell and Ghaly (1973) approximation rather than with the Price and Bell (1974) approach. The Price and Bell (1974) approach tends to over predict the measured heat duties from the present study. These over predictions are probably due to the correlations being not derived for use with the Price and Bell (1974) framework, liquid film mixing, or other limitations of the Price and Bell analysis. Reasonable agreement was observed for the pure fluid data with the correlations of Shah (1979) and Cavallini *et al.* (2006) with an AAD of 18% and 15%, respectively.

Table 5.11. Summary of comparisons with the literature – pure fluid heat transfer results

	Average Deviation, %	Absolute Average Deviation, %	% within ±25%
Traviss *et al.* (1973)	37%	38%	36%
Shah (1979)	9%	15%	77%
Soliman (1986)	-18%	23%	56%
Dobson and Chato (1998)	21%	28%	50%
Thome *et al*. (2003)	30%	31%	44%
Cavallini *et al*. (2006)	8%	16%	79%

Table 5.12. Summary of comparisons with the literature – zeotropic mixture heat transfer results

	Silver (1947), Bell and Ghaly (1973) Analysis			Price and Bell (1974) Analysis	
	Average Deviation, %	Absolute Average Deviation, %	% within ±25%	Average Deviation, %	Absolute Average Deviation, %
Traviss *et al.* (1973)	37%	37%	32%	45%	45%
Shah (1979)	13%	18%	70%	37%	37%
Soliman (1986)	-14%	20%	64%	5%	12%
Dobson and Chato (1998)	22%	27%	51%	35%	36%
Thome *et al*. (2003)	27%	28%	51%	28%	30%
Cavallini *et al*. (2006)	9%	15%	82%	20%	22%
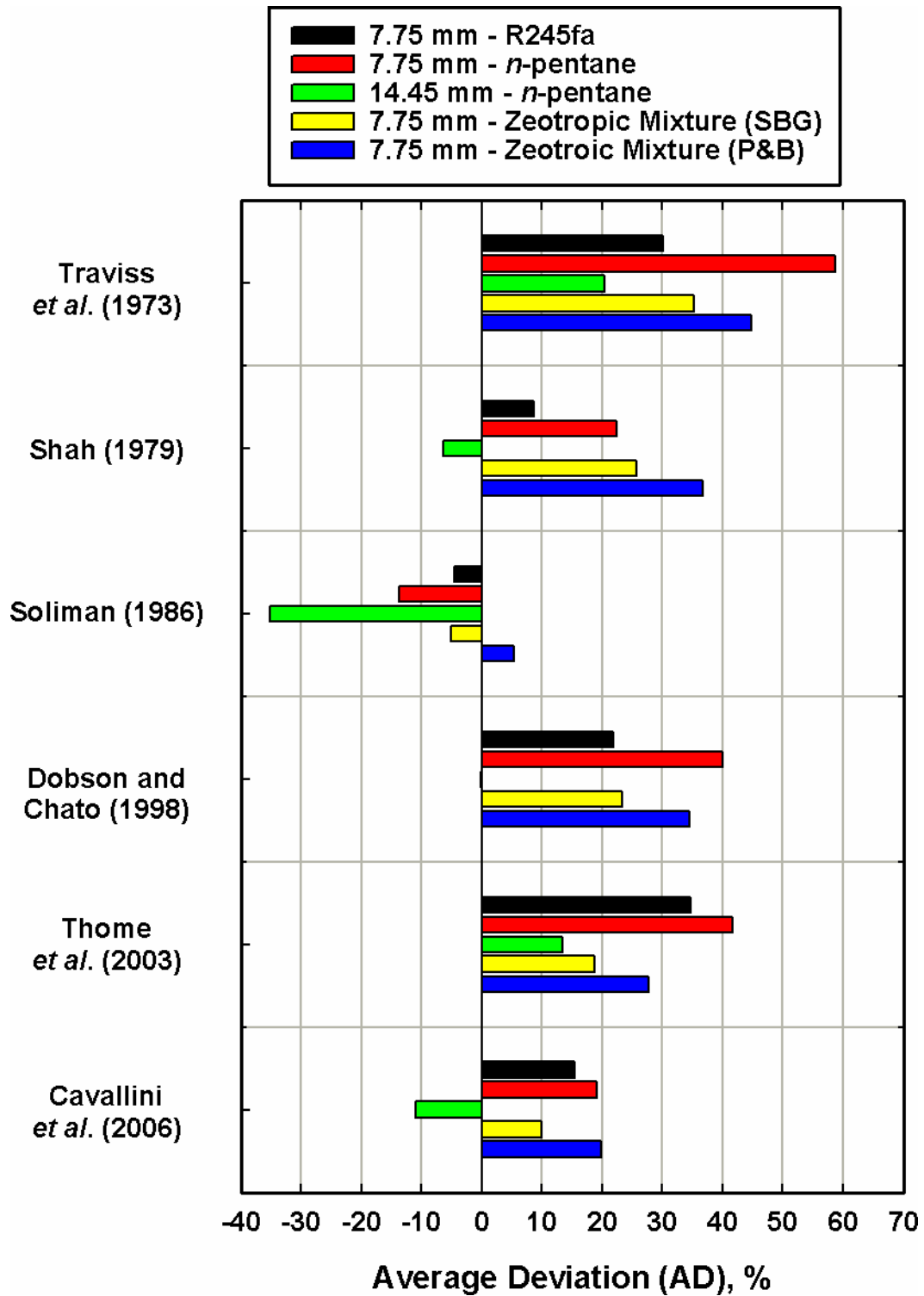
Figure 5.67. Summary of comparisons with the literature - heat transfer results average deviation

CHAPTER 6. MODEL DEVELOPMENT

A comprehensive model for the prediction of flow regimes, void fraction, pressure gradient, and heat transfer coefficient is presented in this chapter.

Two flow regimes dominate the conditions of interest: wavy and annular flow, with a transition region between these. Annular flow is a shear-dominated flow characterized by a thin liquid film supported around the perimeter of the tube by shear forces exerted on the liquid phase by a fast moving vapor core, as shown in Figure 6.1. When the shear force exerted by the vapor core is insufficient to evenly distribute the liquid phase around the perimeter, gravitational forces cause the liquid to pool at the bottom of the tube, resulting in wavy flow. Wavy flow is characterized by the existence of a significant liquid pool at the bottom of the tube and a thin liquid film in the upper portion of the tube, as shown in Figure 6.2.
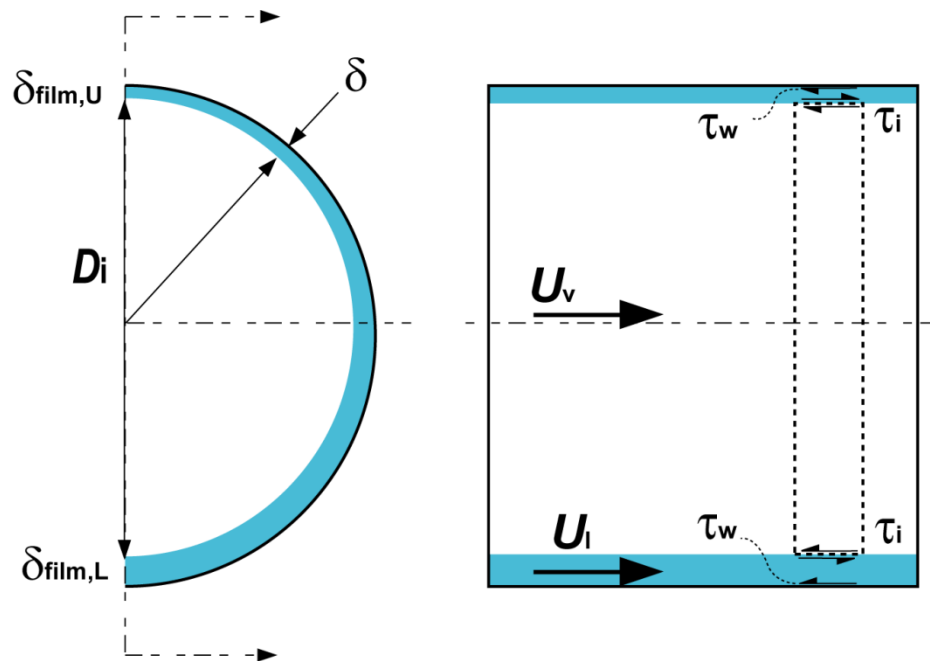
Figure 6.1. Annular flow regime schematic
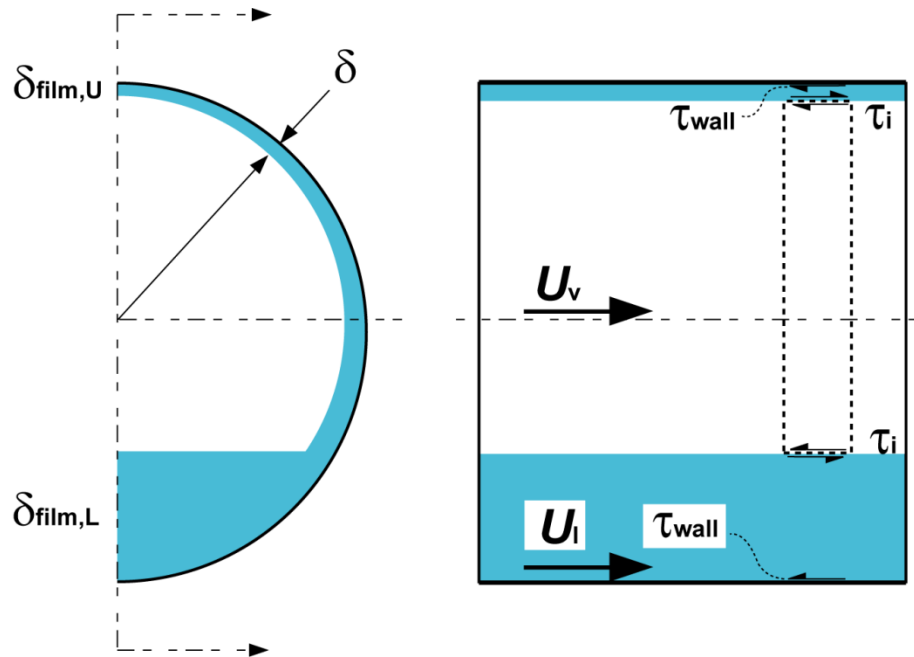
Figure 6.2. Wavy flow regime schematic

A consistent method for modeling both regimes is used in the models described below. Annular flow is modeled with a uniform film flowing along the perimeter of the tube. The vapor core travels faster than the liquid film ($U_v > U_l$) with the interfacial shear stress, τ_i, acting at the vapor liquid interface. Liquid entrained in the vapor core is neglected. The wavy regime component of the frictional pressure drop and heat transfer coefficient models is accounted for by considering contributions from upper film and the liquid pool, shown schematically in Figure 6.3. The specifics of each model are discussed in the following sections. A sample calculation of the model is presented in Appendix F.
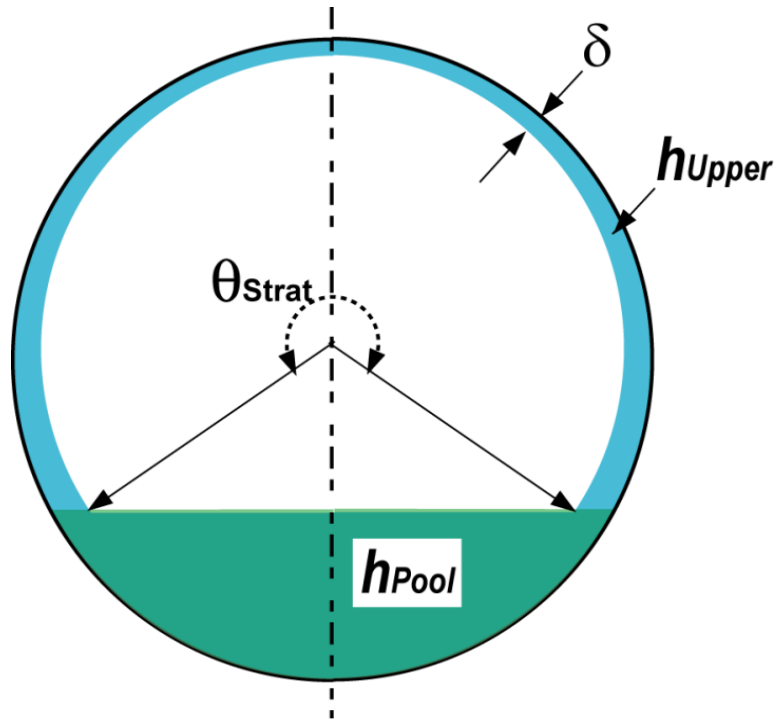
Figure 6.3. Wavy regime model schematic

6.1 Flow Regime Mapping

As identified in Section 5.2.1, the Froude number based annular-to-wavy transition proposed by Dobson and Chato (1998) was found to demarcate the corresponding transition in the present data well. With a slight modification, the annular-to-wavy transition criterion proposed by Dobson and Chato (1998) is used. A summary of the development of the transition criterion is presented here with transitional Froude numbers identified at the end of the section. Their transition criterion was based on the analysis of Soliman (1982), which starts with an annular flow assumption and identifies when gravitational effects cause annular flow to transition to wavy flow, based on the Froude number.

$$\mathrm{Fr} = U_1 \big/ \sqrt{g\delta} \qquad\qquad (6.1)$$

The liquid-phase Reynolds number, Re_l, and dimensionless liquid film thickness, δ^+, are defined using Equations (6.2) and (6.3).

$$Re_l = G(1-q)D/\mu_l \tag{6.2}$$

$$\delta^+ = \delta u^*/U_l \tag{6.3}$$

The friction velocity, u^*, is calculated from the wall shear stress, τ_w, as shown in Equations (6.4) and (6.5).

$$u^* = \sqrt{\tau_w/\rho_l} \tag{6.4}$$

$$\tau_w = D(\nabla P_f)/4 \tag{6.5}$$

The film liquid-phase velocity can be expressed with known terms using a mass balance on the liquid film as shown in Equation (6.6).

$$G(1-q) = 4\rho_l U_l(\delta/D) \tag{6.6}$$

Substituting Equations (6.2), (6.3), and (6.6) into Equation (6.1), yields Equation (6.7).

$$Fr = 0.25\,Re_l\left(u^*/\delta^+\right)^{1.5}/\sqrt{gU_l} \tag{6.7}$$

The equations proposed by Dobson and Chato (1998) show good agreement with observed flow transitions over the range of conditions investigated in the present study. Additionally, this set of equations was found to show good agreement over a larger set of data by Dobson and Chato (1998) using the transitional Froude numbers proposed by

them. Therefore, the correlations for the film thickness and frictional pressure gradient terms originally proposed by Soliman (1982) are used. The dimensionless liquid film thickness is calculated using the correlation proposed by Kosky and Staub (1971), shown in Equation (6.8).

$$\delta^+ = 0.707 \, \text{Re}_l^{0.5} \qquad \text{for Re}_l \leq 1250$$
$$\delta^+ = 0.0504 \, \text{Re}_l^{0.875} \qquad \text{for Re}_l > 1250$$

(6.8)

The two-phase multiplier of Azer *et al.* (1972), shown in Equation (6.9), is used to calculate the frictional pressure gradient.

$$\phi_v = 1 + 1.09 X_{tt}^{0.019}$$

(6.9)

Substituting Equations (6.8) and (6.9) into Equation (6.7), the transitional Froude number is expressed as shown in Equation (6.10) where $\text{Ga} = gD^3 \rho^2 \mu^{-2}$.

$$\text{Fr}_{So} = 0.025 \, \text{Re}_l^{1.59} \left(\frac{1 + 1.09 X_{tt}^{0.039}}{X_{tt}} \right)^{1.5} \frac{1}{\text{Ga}^{0.5}} \qquad \text{for Re}_l \leq 1250$$
$$\text{Fr}_{So} = 1.26 \, \text{Re}_l^{1.04} \left(\frac{1 + 1.09 X_{tt}^{0.039}}{X_{tt}} \right)^{1.5} \frac{1}{\text{Ga}^{0.5}} \qquad \text{for Re}_l > 1250$$

(6.10)

Dobson and Chato (1998) identified annular flow for $\text{Fr}_{So} > 20$ and indicate wavy flow exists below $\text{Fr}_{So} = 10$. These transition criteria are used to identify annular and wavy flow in the present study as well, with a transition region between them. However, the mass flux transition at $G = 500$ kg m^{-2} s^{-1} is not used. The regime transitions are overlaid on the data for *n*-pentane, R245fa, and the zeotropic mixture in Figure 6.4. Using these flow regime criteria, the data in the present study are concentrated in the annular regime, which accounts for 77% of the data. Fourteen percent of the data are in the

transition region, while nine percent are in the wavy regime. The flow regime distribution

of the data for each fluid and pressure is summarized in Table 6.1.
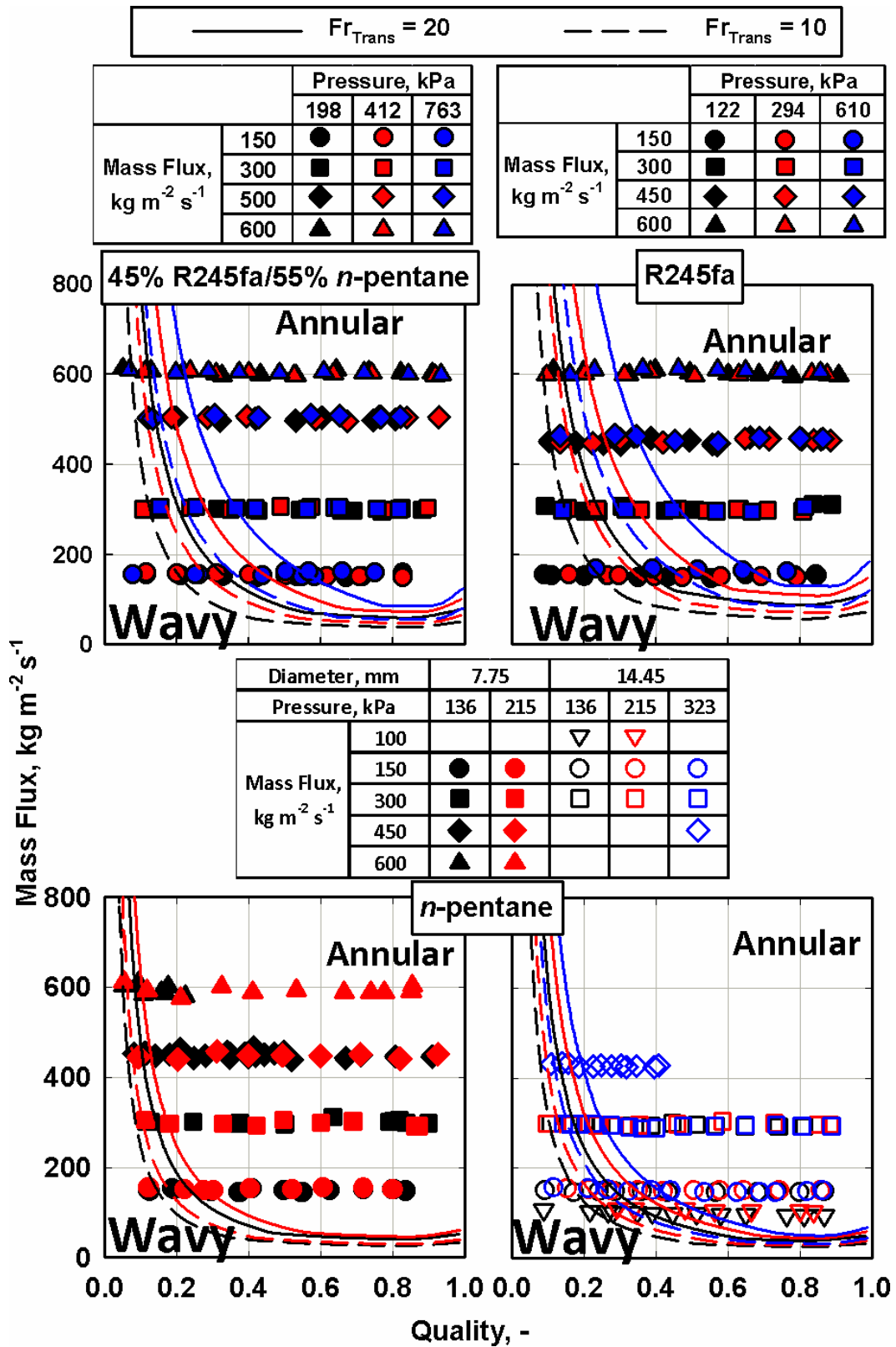
Figure 6.4. Experimental heat transfer and frictional pressure drop data with flow regime transitions

Table 6.1. Summary of flow regime classification

		Pressure, kPa	# Data Points	Regime		
				Annular	Transition	Wavy
7.75 mm	45% R245fa/ 55% *n* -pentane	198	35	89%	6%	6%
		412	41	85%	7%	7%
		763	37	70%	19%	11%
	R245fa	122	41	78%	10%	12%
		294	34	74%	12%	15%
		610	27	63%	22%	15%
	n -pentane	136	65	89%	8%	3%
		215	48	83%	13%	4%
14.45 mm	*n* -pentane	136	35	66%	20%	14%
		215	27	70%	22%	7%
		323	38	66%	24%	11%
Total			**428**	**77%**	**14%**	**9%**

6.2 Model Structure

The void fraction, pressure drop, and heat transfer models described in sections 6.3 to 6.5 are comprised of separate annular and wavy regime models. The predictions from the two models are combined linearly using the transitional Froude number through the transition region as shown in Equation (6.11).

$$
X = \begin{cases}
X_{\text{wavy}} & \text{for Fr}_{\text{so}} < 10 \\
\dfrac{\left(\text{Fr}_{\text{so}} - 10\right) X_{\text{Annular}} + \left(20 - \text{Fr}_{\text{so}}\right) X_{\text{Wavy}}}{10} & \text{for } 10 \leq \text{Fr}_{\text{so}} \leq 20 \\
X_{\text{Annular}} & \text{for Fr}_{\text{so}} > 20
\end{cases}
\qquad (6.11)
$$

The variable X in Equation (6.11) represents by the drift flux velocity ($\bar{V}_{\text{vj}}$), interfacial friction factor (f_i), or heat transfer coefficient (h) as applicable for the void fraction, pressure gradient, and heat transfer coefficient models, respectively. The annular and wavy contributions are calculated at the local conditions and combined using a weighted average. (The annular and wavy contributions in the transition region were also

calculated at the qualities corresponding to the annular and wavy transitions, $Fr_{so} = 20$ and 10, respectively, and interpolated to calculate the values in the transition region. The results found through interpolation were found to yield results nearly identical to those calculated as the weighted average.)

Once the void fraction is calculated, the pressure gradient and heat transfer coefficient models address the wavy regime through upper film and liquid pool contributions. The film and pool contributions are combined using the stratification angle, calculated from the void fraction, as shown in Equation (6.12).

$$X_{\text{wavy}} = \frac{\theta_{\text{Strat}}}{2\pi} X_{\text{upper}} + \left(1 - \frac{\theta_{\text{Strat}}}{2\pi}\right) X_{\text{Pool}} \qquad (6.12)$$

Referring to Figure 6.3, the stratification angle, θ_{Strat}, is calculated iteratively using Equation (6.13). The cross sectional area occupied by the liquid pool is calculated using the void fraction and fraction of the liquid contained in the pool, $(1 - \eta_{\text{Up}})$, which is described next. The area of the liquid segment can also be calculated from geometry. Explicit relationships for the stratification angle can be found in the literature. The explicit relationships eliminate the iterative relationship below but are approximations.

$$A_{\text{Lp}} = \underbrace{A_{\text{c}}(1-\alpha)(1-\eta_{\text{Up}})}_{A_{\text{lp}}} = \left(\underbrace{A_{\text{c}}\left(1 - \frac{\theta_{\text{Strat}}}{2\pi}\right)}_{A_{\text{lp}}+A_{\text{t}}} - \underbrace{A_{\text{c}}\frac{1}{2\pi}\sin\left(2\pi - \theta_{\text{Strat}}\right)}_{A_{\text{t}}}\right) \qquad (6.13)$$
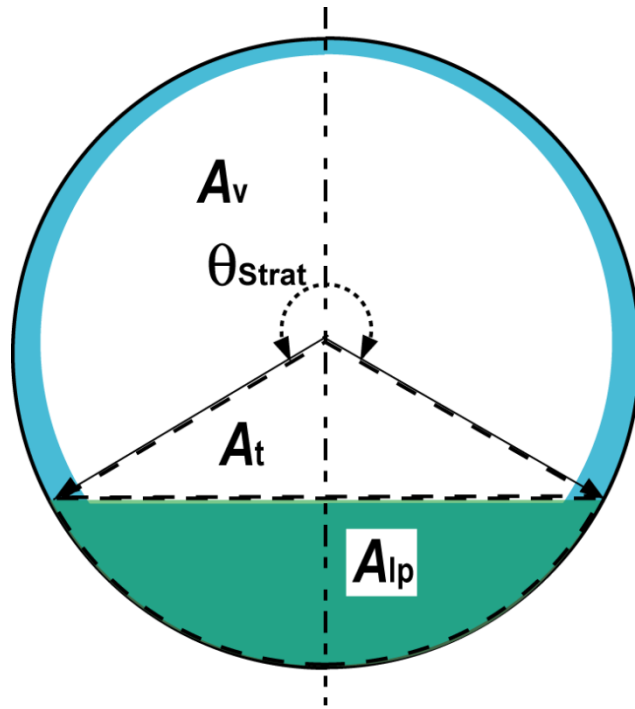
Figure 6.5. Liquid phase distribution and stratification angle schematic

The fraction of liquid in the upper film was measured from the high speed video and a single fraction for each diameter and mass flux pair was identified. The results are shown in Figure 6.4 with the approximate liquid pool fraction ($1-\eta_{Up}$) overlaid. As shown in the figure, a much larger portion of the liquid is contained in the upper film in the 7.0 mm tube than the 15 mm tube.
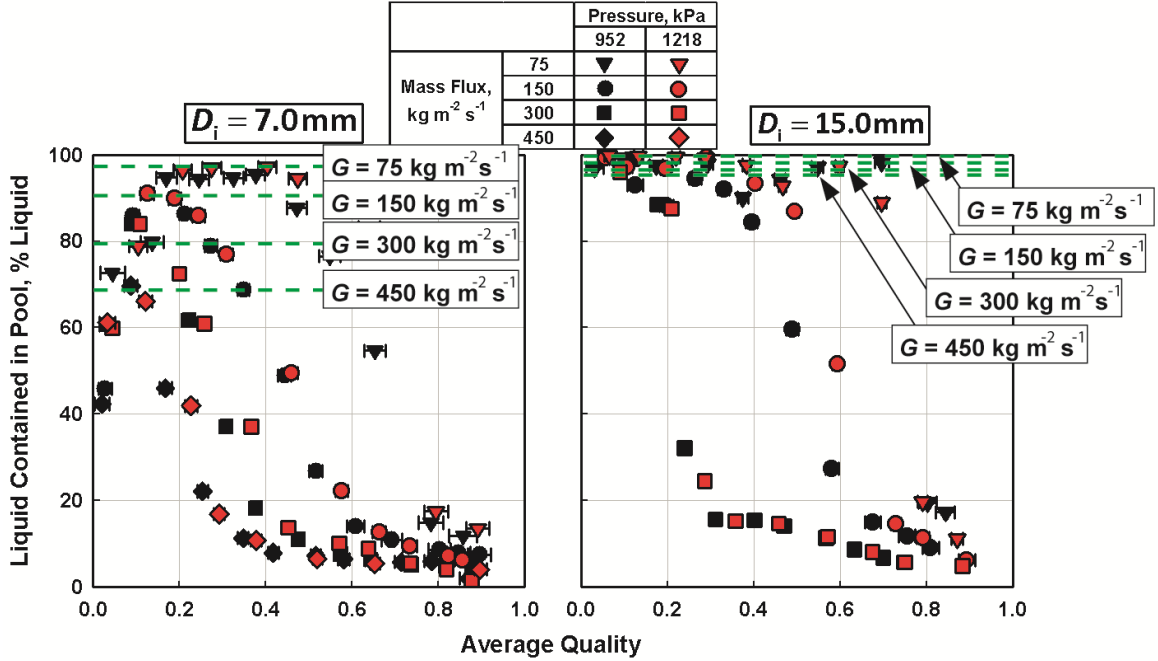
Figure 6.6. Liquid fraction in the stratified pool (1-η_{Up}) with mass flux and diameter effects highlighted

A clear mass flux and diameter effect was observed for the range of conditions in the videos. The fraction of liquid in the upper film scales with G^{a_1} and D^{-a_2} simultaneously while confined between zero and unity. To ensure the calculated liquid fraction was confined to values between zero and unity while capturing the diameter and mass flux effect, the equation was assumed to be of the form: $\eta_{Up} = 1 - \left(1 + a_0 G^{a_1} D^{a_2}\right)^{-1}$. To remove the dimensional effects of the mass flux and diameter, the fraction of liquid in the upper film η_{Up}, is calculated using an equation of the following form:

$$\eta_{Up} = 1 - \left(1 + a_0 \left(\frac{G}{500}\right)^{a_1} \left(\frac{0.007}{D}\right)^{a_2}\right)^{-1} \tag{6.14}$$

A mass flux of 500 kg m^{-2} s^{-1} is chosen to non-dimensionalize the mass flux term; this mass flux value is also used to define transition to annular flow in the original flow

regime map proposed by Dobson and Chato (1998). A diameter of 7.0 mm is chosen to non-dimensionalize the diameter. The visualization was conducted only for a limited range of fluid properties; thus, the upper film percentage term does not attempt to capture property effects. From a regression analysis on the visualization data in the wavy regime, the constants a_0, a_1, and a_2 in Equation 6.3 were determined to be 2.68, 1.06 and 2.08, respectively.

$$\eta_{\mathrm{Up}} = 1 - \left(1 + 0.46 \left(\frac{G}{500}\right)^{1.06} \left(\frac{0.007}{D}\right)^{2.08}\right)^{-1} \tag{6.15}$$

The wavy regime parameters shown in Equation (6.12) can now be calculated using the stratification angle calculated in Equation (6.13).

6.3   Void Fraction Model

The void fraction was modeled using the vapor drift flux velocity following the approach presented by Zuber and Findlay (1965). It should be reiterated here that the void fraction measurements and the resulting model are developed using the liquid film thickness. Therefore, the following model does not include liquid entrained in the vapor phase. The void fraction is related to the vapor phase drift velocity and homogeneous void fraction as shown in Equation (6.16).

$$\alpha = \frac{\beta}{C_0 + \overline{V}_{\mathrm{vj}} / j} \tag{6.16}$$

The distribution parameter, C_0, is set to unity in Equation (6.16). A value of one has been found to be a good approximation for annular flow by Ishii (2011). The distribution parameter is approximated as one here for the wavy regime also. A multi regime drift

flux velocity model is developed here for both the wavy and annular regimes. The void fraction was observed to be dependent on mass flux, pressure, and the distribution of the void fraction (discussed in Section 5.1.1) which indicates there is a surface tension effect. To capture these effects, the form of the drift flux velocity proposed by Zuber and Findlay (1965) (Equation (6.17)) is used as the basis. It should be noted that the superficial velocity, j, is integrated into Equation (6.17) such that the term in parentheses is dimensionless.

$$\frac{\overline{V}_{vj}}{j} = a_0 \left(\frac{g(\rho_l - \rho_v)\sigma}{j^4 \rho_l^2} \right)^{a_1} \tag{6.17}$$

The wavy flow regime drift flux velocity is then written as shown in Equation (6.18).

$$\frac{\overline{V}_{vj,W}}{j} = a_0 \left(\frac{g(\rho_l - \rho_v)\sigma}{j^4 \rho_l^2} \right)^{a_1} \tag{6.18}$$

A regression analysis on the wavy flow regime results yielded a_0 and a_1 values of 1.47 and 0.24, respectively, as shown in Equation (6.19).

$$\frac{\overline{V}_{vj,W}}{j} = 1.47 \left(\frac{g(\rho_l - \rho_v)\sigma}{j^4 \rho_l^2} \right)^{0.27} \tag{6.19}$$

These coefficients are similar to the coefficients presented by Rouhani and Axelsson (1970) of 1.18 and 0.25, respectively. As the result from Equation (6.19) increases, the void fraction decreases and as the result approaches zero, the void fraction approaches the homogeneous void fraction. In this case, as the superficial velocity increases, the void fraction approaches the homogeneous void fraction. Increasing the superficial velocity increases the shear at the interface, which leads to thinning of the liquid film. Thus, the

353

void fraction increases. As the surface tension increases, the liquid film becomes more stable, which prevents breakup of the liquid film. This in turn decreases the void fraction.

The resulting model is physically consistent as quality approaches zero and as the pressure approaches the critical pressure. As quality approaches zero, the homogeneous void fraction approaches zero. Therefore, the void fraction approaches zero. As the pressure approaches the critical pressure, the density difference and therefore Equation (6.19) approach zero. Thus, the void fraction approaches zero.

Equation (6.17) was modified to make the model physically consistent as the quality approaches one by adding $(1 - q)$. A similar approach was also used by Steiner (1993). The resulting form of the drift flux velocity is presented in Equation (6.20).

$$\frac{\bar{V}_{vj,A}}{j} = a_0 \left(1-q\right)^{a_1} \left(\frac{g\left(\rho_1 - \rho_v\right)\sigma}{j^4 \rho_1^2} \right)^{a_2}$$ (6.20)

A regression analysis on the annular flow regime results yielded a_0, a_1, and a_2 values of 49.1, 0.11, and 0.507, respectively, as shown in Equation (6.21).

$$\frac{\bar{V}_{vj,A}}{j} = 49.1\left(1-q\right)^{0.11} \left(\frac{g\left(\rho_1 - \rho_v\right)\sigma}{j^4 \rho_1^2} \right)^{0.507}$$ (6.21)

The result exhibits all the same trends as the wavy portion, and is also physically consistent at a quality of one. As the quality increases, Equation (6.21) approaches zero. Thus, the void fraction approaches the homogeneous void fraction, which approaches unity at a $q = 1$.

The regime-specific drift flux velocities are calculated using Equation (6.11), as shown in Equation (6.22) for the specific case of void fraction. The wavy and annular components are calculated using Equations (6.18) and (6.21), respectively. The annular and wavy contributions in the transiton region are calculated at the local conditions and combined using a weighted average.

$$\bar{V}_{vj} = \begin{cases} \bar{V}_{vj,W} & \text{for } Fr_{so} < 10 \\ \dfrac{\left(Fr_{so} - 10\right)\bar{V}_{vj,A} + \left(20 - Fr_{so}\right)\bar{V}_{vj,W}}{10} & \text{for } 10 \le Fr_{so} \le 20 \\ \bar{V}_{vj,A} & \text{for } Fr_{so} > 20 \end{cases} \qquad (6.22)$$

The model shows good overall agreement with experimental data, as shown in Figure 6.7. It predicts 99% of the data within ±25% with an AD of -2% and AAD of 4%, and an R^2 value of 0.94. The measured void fractions and the model predictions are shown in Figure 6.8. The model predictions are in good agreement in the annular regime with AAD between 0.8% and 2.3% for the 7.0 and 15.0 mm tube diameters, respectively. The AADs for the 7.0 and 15.0 mm tubes in the wavy regime were 5.0 and 5.2%, respectively. The largest errors are introduced at points identified as intermittent or transitional in the visualization results where the AAD is 15.3% in the 7.0 mm tube and 5.6% in the 15.0 mm tube. However, due to the limited number of intermittent points, no intermittent model was developed. The overlay of model predictions on the data shows good ability of the model to follow the trends observed in the data. Notably, the increase in void fraction with increasing mass flux is captured well in both regimes. A summary of model agreement with tube diameter and pressure is presented in Table 6.2.
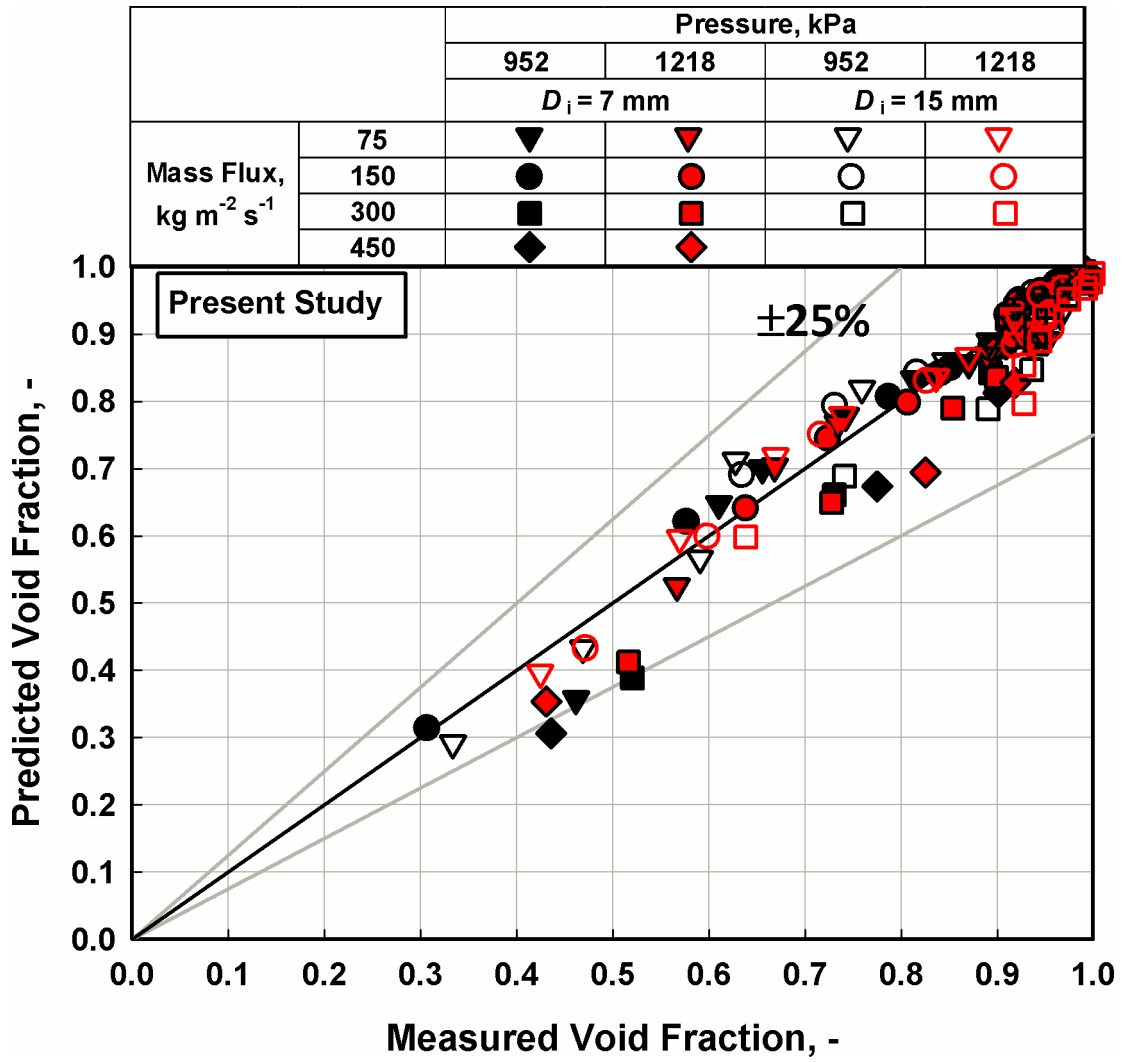
Figure 6.7. Overall void fraction agreement
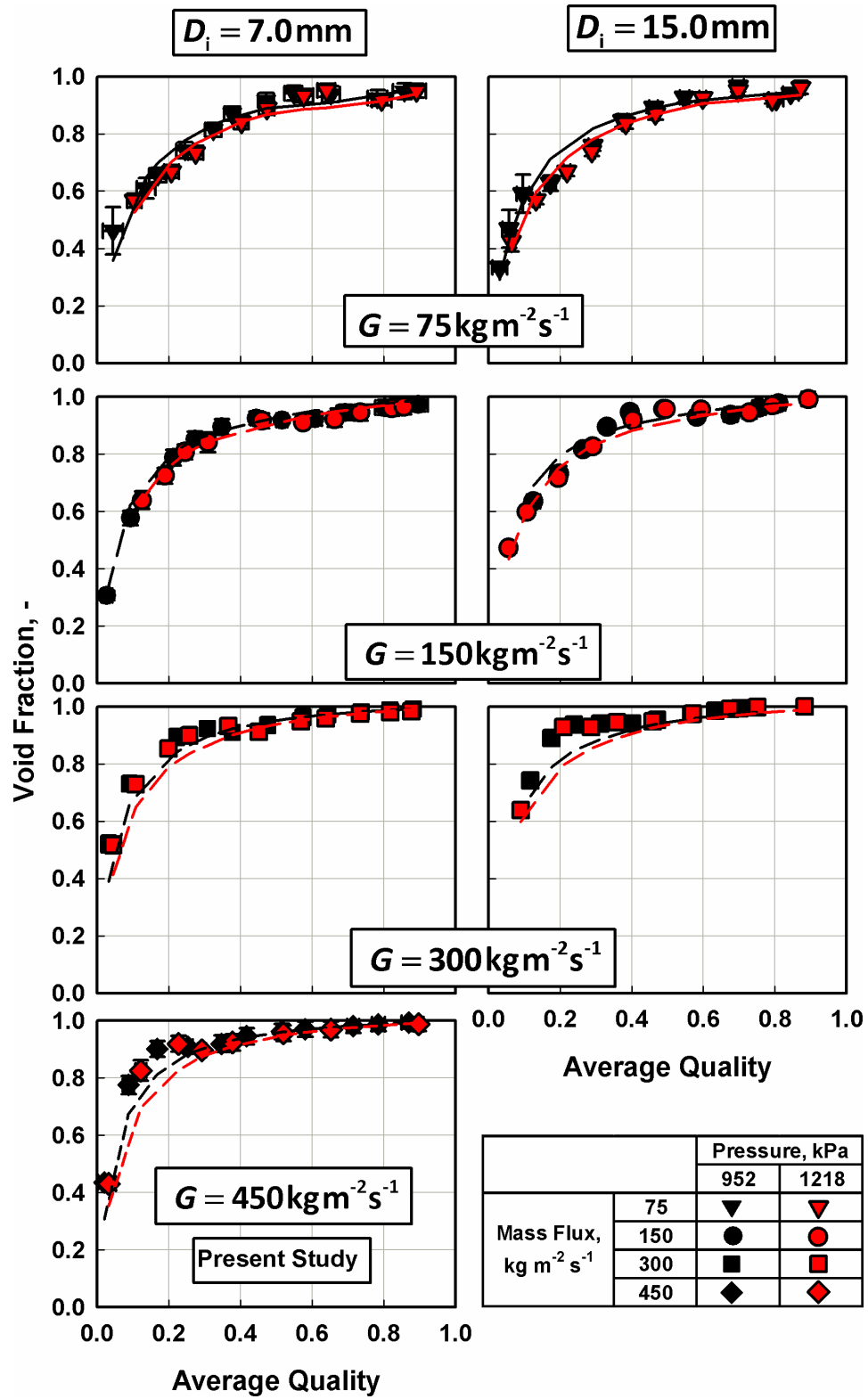
Figure 6.8. Experimental void fraction results with model prediction overlay

Table 6.2. Void fraction model agreement with experimental results

	Pressure, kPa	# Data Points	Agreement				AAD	
			AD	AAD	R^2	% within ±25%	Annular	Wavy
7.0 mm	952	45	-2%	4%	0.95	98%	1%	5%
	1218	38	-3%	4%				
15.0 mm	952	31	-1%	4%	0.94	100%	2%	5%
	1218	29	-2%	4%				
Total		143	-2%	4%	0.94	99%	1%	5%

Trends with varying mass flux, saturation temperature, diameter, and fluid are shown in Figure 6.9. In each plot, the annular and wavy regimes are signified by solid lines and long dashes, respectively, with the transition region signified using a dash dot combination. The void fraction increases with increasing mass flux in both regimes, as observed in the experiments. The void fraction decreases with increasing pressure, as is expected. The four fluids shown in d) span a significant reduced pressure range at 30°C, ranging from 0.02 and 0.04 for *n*-pentane and R245fa, respectively, to 0.19 and 0.25 for R134a and propane, respectively. The predicted void fractions decrease with changing fluid in order of increasing reduced pressure.

The proposed void fraction model is used to determine the void fraction required for the frictional pressure gradient and heat transfer coefficient models.
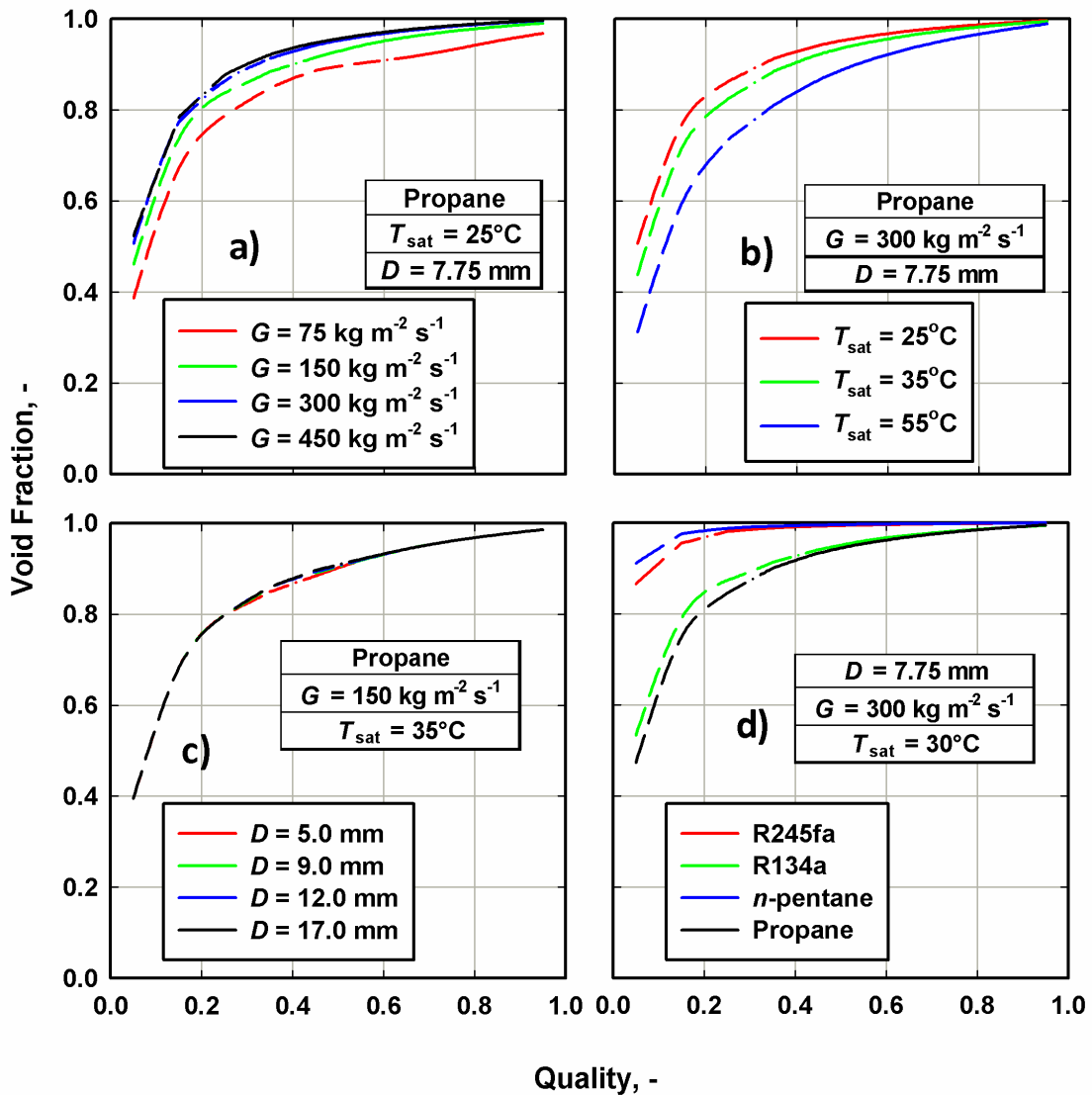
Figure 6.9. Void fraction model prediction trends with a) mass flux, b) saturation temperature, c) diameter, and d) fluid; Annular regime - solid line; wavy regime – dashed line; transition dash dot dash line

6.4 Frictional Pressure Gradient Model

The approach for modeling the frictional pressure gradient in the annular and wavy regimes is based on the model presented by Garimella *et al.* (2005). Their model assumes steady flow, uniform liquid film, equal pressure drops in the liquid film and vapor core, and no entrainment in the vapor core. Simplifying a vapor-phase momentum balance (Equation (6.23)) yields Equation (6.24).

$$-\left(\nabla P + \rho_v g\right) = \frac{\tau_i P_i}{\alpha A} \tag{6.23}$$

$$\nabla P_f = 4\tau_i / D_i \tag{6.24}$$

The interfacial shear stress can be evaluated in terms of an interfacial friction factor, f_i, the vapor phase velocity, and vapor density as shown in Equation (6.25).

$$\tau_i = 0.5 f_i \rho_v U_v^2 \tag{6.25}$$

Substituting Equation (6.25) into Equation (6.24), the frictional pressure gradient can be rewritten as shown in Equation (6.26). Rewriting the vapor phase velocity and interfacial diameter in Equation (6.26) in terms of the void fraction results in Equation (6.27).

$$\nabla P_f = 0.5 f_i \rho_v U_v^2 D_i^{-1} \tag{6.26}$$

$$\nabla P_f = \frac{1}{2} f_i \frac{\rho_v j_v^2}{\alpha^{2.5} D} = \frac{1}{2} f_i \frac{G^2 q^2}{\rho_v \alpha^{2.5} D} \tag{6.27}$$

Attempting to account for the governing phenomena for the annular and wavy regimes, the interfacial friction factor, f_i, is correlated in terms of the vapor-phase friction factor in the annular regime and liquid-phase friction factor in the wavy regime. The corresponding single-phase friction factors are calculated using the Churchill (1977b) friction factor correlation as shown in Equation (6.28).

$$f_{\mathrm{v}} = 8 \left(\left(\frac{8}{\mathrm{Re}_{\mathrm{vi}}} \right)^{12} + \left(\left[2.457 \ln \left(\frac{1}{\left(\frac{7}{\mathrm{Re}_{\mathrm{vi}}} \right)^{0.9} + 0.27 \left(\frac{\varepsilon_{\mathrm{w}}}{D_{\mathrm{i}}} \right)} \right) \right]^{16} + \left(\frac{37530}{\mathrm{Re}_{\mathrm{vi}}} \right)^{16} \right)^{-1.5} \right)^{1/12} \tag{6.28}$$

The Reynolds numbers are defined as shown in Equation (6.29).

$$\mathrm{Re}_{\mathrm{vi}} = \frac{GqD_{\mathrm{i}}}{\mu_{\mathrm{v}}}$$
$$\mathrm{Re}_{\mathrm{l}} = \frac{G(1-q)D}{\mu_{\mathrm{l}}} \tag{6.29}$$

In the above equations, the wall roughness ($e_{\mathrm{w}} = 0.000015$ mm) is used with the interfacial diameter which is calculated for the annular regime using the tube diameter and void fraction as shown in Equation (6.30). For simplicity, the interfacial diameter in the wavy regime is approximated using the same equation.

$$D_{\mathrm{i}} = D\sqrt{\alpha} \tag{6.30}$$

The interfacial friction factor increases with increasing shear between the liquid and vapor phase and with increasing vapor phase momentum. The vapor phase momentum is addressed in the vapor-phase friction factor. The annular regime interfacial friction factor is written in terms of the vapor-phase friction factor and an appropriate two-phase multiplier as shown in Equation (6.31).

$$\frac{f_{\mathrm{v,iA}}}{f_{\mathrm{v}}} = \left(1 + a_0 (1-q)^{a_1} + a_2 X_{\mathrm{tt}}^{a_3} \left(\frac{\rho_{\mathrm{l}}}{\rho_{\mathrm{v}}} \right)^{a_4} \right) \tag{6.31}$$

This form of the equation ensures that the interfacial friction factor approaches the vapor friction factor at a quality of unity. A regression analysis using on the annular flow regime pressure drop data yielded a_0, a_1, a_2, a_3, and a_4 in Equation (6.31) to be 2.54, 0.346, 0.290, 1.25, and 0.834, respectively.

$$\frac{f_{v,iA}}{f_v} = \left(1 + 2.54 \left(1 - q \right)^{0.346} + 0.290 \mathrm{X}_{tt}^{1.25} \left(\frac{\rho_l}{\rho_v} \right)^{0.834} \right) \tag{6.32}$$

Due to the larger liquid inventory in the wavy flow regime, the wavy flow regime interfacial friction factor is correlated using the liquid-phase friction factor, rather than the vapor-phase friction factor. As discussed in Section 6.2, the wavy flow regime pressure drop model is based on the sum of contributions from an upper film and the liquid pool as shown in Equation (6.33).

$$f_{v,i,W} = \frac{\theta_{Strat}}{2\pi} f_{v,i,U} + \left(1 - \frac{\theta_{Strat}}{2\pi} \right) f_l \tag{6.33}$$

The interfacial friction factor in the liquid pool is approximated using the liquid friction factor, f_l. The upper film is assumed to behave similar to annular flow and approximated using a form similar to the annular flow model. To account for the reduced liquid inventory in the upper film with changing mass flux and diameter, the fraction of liquid contained in the upper film, η_{Up}, is incorporated into the model as shown in Equations (6.34).

$$\frac{f_{v,iU}}{f_l} = \left(b_0 + b_1 \mathrm{X}_{tt}^{b_2} \left(\frac{\rho_l}{\rho_v} \right)^{b_3} \eta_{Up}^{b_4} \right) \tag{6.34}$$

A regression analysis on the wavy flow regime data, assigned based on the transitions presented in Section 6.1, using Equation (6.34) within Equation (6.33) yielded b_0, b_1, b_2, b_3, and b_4 values of 1.26, 0.335, 1.28, 0.895 and 0.339, respectively. It is interesting to note that the resulting exponents on the Lockhart-Martinelli parameter and density ratio are nearly identical to those in the annular regime, which were 1.25 and 0.834, respectively.

$$\frac{f_{v,iU}}{f_l} = \left(1.26 + 0.335 X_{tt}^{1.28} \left(\frac{\rho_l}{\rho_v} \right)^{0.895} \eta_{Up}^{0.339} \right) \tag{6.35}$$

Annular flow is expected to prevail at high qualities. Therefore, the wavy flow regime friction factor need not approach the vapor-phase friction factor at a quality of unity. Because the pressure drop formulation, Equation (6.26), is based on the vapor core, the model does not approach the liquid pressure drop at a quality of zero regardless of the friction factor used in the model. At very low qualities, an interpolation between an intermittent flow model and a single-phase friction factor could be used.

The annular and wavy flow regime interfacial friction factors are combined using Equation (6.11) as written in Equation (6.36). The resulting friction factor is substituted into Equation (6.27) to calculate the frictional pressure drop. The annular and wavy contributions in the transiton region are calculated at the local conditions and combined using a weighted average.

$$f_i = \begin{cases} f_{v,i,W} & \text{for Fr}_{so} < 10 \\ \dfrac{(\text{Fr}_{so} - 10) f_{v,i,A} + (20 - \text{Fr}_{so}) f_{v,i,W}}{10} & \text{for } 10 \leq \text{Fr}_{so} \leq 20 \\ f_{v,i,A} & \text{for Fr}_{so} > 20 \end{cases} \tag{6.36}$$

The overall agreement of the pressure drop model with the measured values is shown in Figure 6.10. The model shows good agreement over a wide range of frictional pressure drops and fluid properties. The overall AD and AAD are 1% and 10%, respectively, and 91% of the data predicted within ±25%. The regression R^2 is 0.99. The model predictions calculated at experimental conditions are overlaid on the data in Figure 6.11. The model is able to predict the trends in the data with increasing mass flux, pressure, quality, and diameter.

The 14.45 mm *n*-pentane data shows significantly lower agreement than the 7.75 mm data with 75% of the data predicted within ±25%. There are two potential causes for this low agreement. First, the measured differential pressures at these conditions are on average less than 2 kPa, while the majority of the 7.75 mm diameter tube pressure drops are significantly higher. Second, the deceleration contribution of the frictional pressure drop is significantly higher in the 14.45 mm data than the 7.75 mm tube data. The deceleration contribution in the 14.45 mm tube data contributes an average of 26% to the frictional pressure drop. In the 7.75 mm tube this contribution accounts for only 8%. The largest deviations in the 14.45 mm tube occur below 2 kPa m^{-1} (65% of the data). For these data, the average uncertainty is 15%, and the deceleration contribution accounts for 20% of the measured frictional pressure drop. The overall agreement is presented in Figure 6.10 distinguished by fluid, pressure, and tube diameter.

There are a few areas that stand out as having low agreement between the predictions and the data that merit further discussion. There are three R245fa data points that are significantly under predicted. These data were consistent outliers in the comparisons of predictions of correlations from the literature, although nothing about these data points

indicates that they should be invalid. The wavy flow model has an AAD of 16%, which is slightly larger than the AAD for the annular model. It is important to note that the number of wavy flow regime data used in the regression analysis constitute only 9% of the total data points, with very few data at some conditions. For example, less than 4% of the 7.75 mm *n*-pentane data are in wavy flow. This low number of data in the wavy regime is in part responsible for the poorer predictive capabilities for this regime.
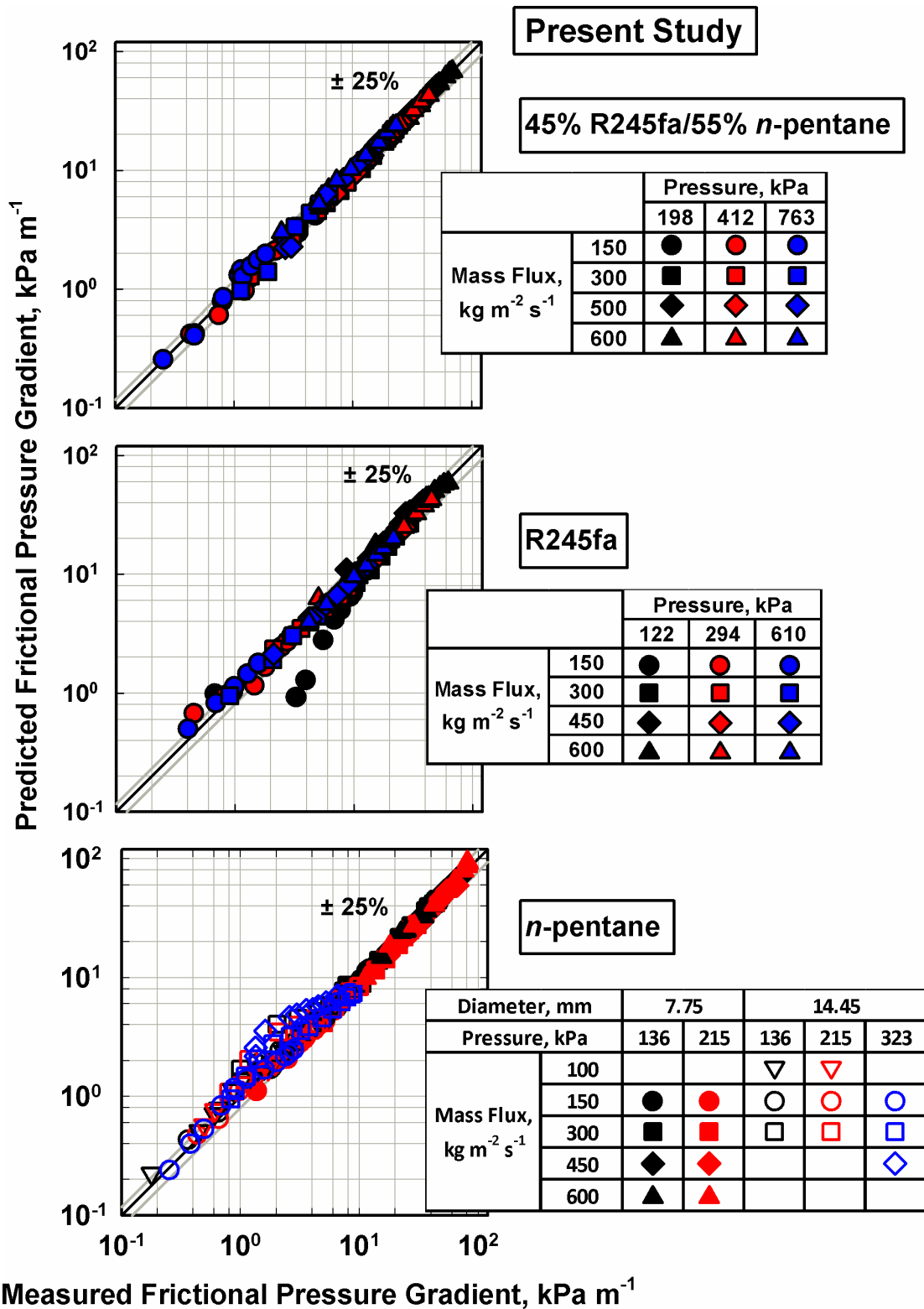
Figure 6.10. Overall pressure drop agreement
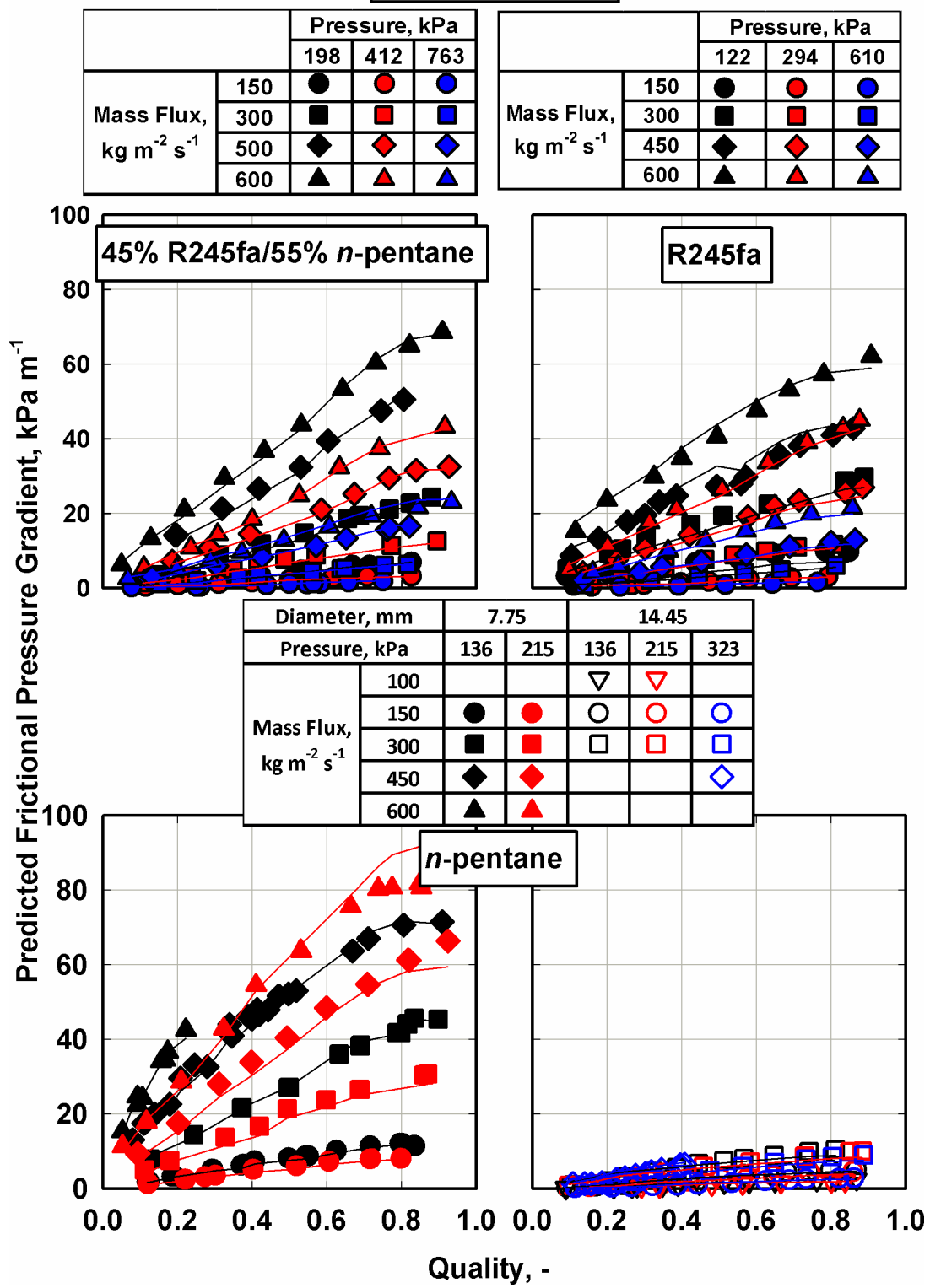
Figure 6.11. Experimental pressure drop results with model prediction overlay

Table 6.3. Frictional pressure drop model agreement with experimental results

		Pressure, kPa	# Data Points	AD	AAD	R^2	% within ±25%	Annular	Wavy
				Agreement				**AAD**	
7.75 mm	45% R245fa/ 55% *n*-pentane	198	35	-5%	6%	0.99	98%	5%	8%
		412	41	-5%	6%				
		763	37	2%	8%				
	R245fa	122	41	-7%	17%	0.99	88%	10%	25%
		294	34	-3%	9%				
		610	27	-1%	8%				
	n-pentane	136	65	2%	4%	0.99	100%	6%	12%
		215	48	-1%	9%				
14.45 mm	*n*-pentane	136	35	-1%	9%	0.94	75%	15%	21%
		215	27	14%	17%				
		323	38	24%	26%				
Total			428	1%	10%	0.99	91%	9%	16%

Trends in the pressure drop model with varying mass flux, saturation temperature, diameter, and fluid are shown in Figure 6.12. As expected, the frictional pressure drop increases with increasing mass flux and quality and decreases with increasing pressure and tube diameter. Changing the fluid under consideration leads to the expected trends in predicted frictional pressure drop; with higher pressure fluids, such as propane and R134a, a significantly lower frictional pressure drop is predicted compared to the pressure drop in low pressure fluids, such as *n*-pentane and R245fa. Using the model predictions, at otherwise identical conditions, the pressure drop scales with $D^{-1.21}$ in the annular regime and with $D^{-1.88}$ in the wavy regime. For example, for *n*-pentane at a $G =$ 300 kg m^{-2} s^{-1}, $P = 136$ kPa, and $q = 0.75$, the frictional pressure gradient decreases from 70.1 kPa m^{-1} in a 5 mm tube to 34.3 kPa m^{-1} and 24.3 kPa m^{-1} in 9 and 12 mm tubes, respectively, resulting in a 51% decrease in pressure gradient from a 5 mm tube to 9 mm tube, and a 29% decrease in pressure gradient from a 9 mm tube to a 12 mm tube. In the wavy regime, for *n*-pentane at a $G = 300$ kg m^{-2} s^{-1}, $P = 136$ kPa, and $q = 0.05$, the frictional pressure gradient decreases from 10.0 kPa m^{-1} in a 5 mm tube to 3.4 kPa m^{-1}

and 1.96 kPa m^{-1} in 9 and 12 mm tubes, respectively, resulting in a 66% decrease in pressure gradient from a 5 mm tube to 9 mm tube and a 42% decrease in pressure gradient from a 9 mm tube to a 12 mm tube.
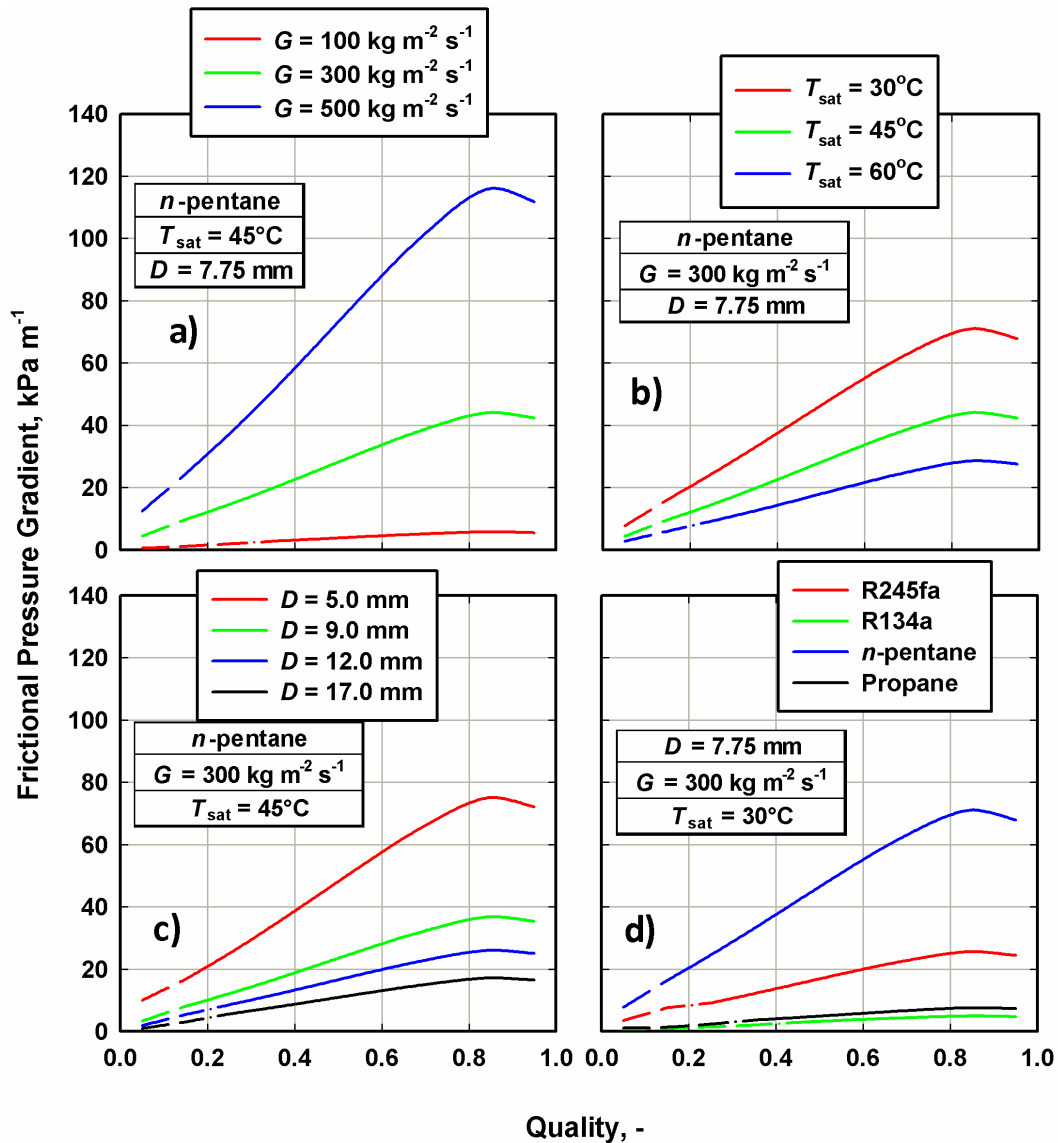
Figure 6.12. Pressure drop model prediction trends with a) mass flux, b) saturation temperature, c) diameter, and d) fluid; ; Annular regime - solid line; wavy regime – dashed line; transition dash dot dash line

6.5 Heat Transfer Coefficient Model

This section details the development of the models for condensation heat transfer coefficients based on the experiments conducted in the present study. The annular flow regime model is discussed first, followed by the wavy flow regime model.

The annular flow model follows an approach similar to that proposed by Thome *et al.* (2003), based on the liquid-film heat transfer coefficient and a term used to account for the increased heat transfer due to disturbances of the interface between the liquid and vapor regions, as shown in Equation (6.37). The interfacial roughness term was introduced in this model to account for the thinning of the liquid film through the velocity ratio and disturbances in the liquid film caused by the difference in phase velocities through the Taylor instability.

$$h_A = \frac{k_l}{\delta} a_0 \operatorname{Re}_{l,\delta}^{0.8} \operatorname{Pr}_l^{0.3} f_{l,i} \qquad (6.37)$$

$$\operatorname{Re}_{l,\delta} = \frac{4G(1-q)\delta}{\mu_l(1-\alpha)} \qquad (6.38)$$

Here the exponents on the film Reynolds number and liquid Prandtl number were set at 0.8 and 0.3, respectively, as in the Dittus and Boelter (1930) correlation for the cooling case. The interfacial roughness of the liquid film is modified from the original Thome *et al*. equation to include phase viscosities as shown in Equation (6.39). The phase viscosities tend to exaggerate or dampen the interfacial roughness. Increasing the vapor-phase viscosity could be responsible for increased agitation of the film, thus increasing the heat transfer coefficient. Conversely, increasing the liquid-phase viscosity dampens the interfacial roughness.

$$f_{l,i} = \left(\frac{\mu_v}{\mu_l}\right)^{b_1} \left(\frac{(\rho_l - \rho_v)g\delta^2}{\sigma}\right)^{b_2} \left(\frac{U_v}{U_l}\right)^{b_3} \tag{6.39}$$

A regression analysis on the annular flow data yields a_0, b_1, b_2, and b_3 values of 0.00667, 0.32, 0.16, and 0.73, respectively. Substitution of the regression results into Equations (6.37) and (6.39) results in Equations (6.40) and (6.41).

$$h_A = \frac{k_l}{\delta} 0.00667 \, \mathrm{Re}_{l,\delta}^{0.8} \, \mathrm{Pr}_l^{0.3} \, f_{l,i} \tag{6.40}$$

$$f_{l,i} = \left(\frac{\mu_v}{\mu_l}\right)^{0.32} \left(\frac{(\rho_l - \rho_v)g\delta^2}{\sigma}\right)^{0.16} \left(\frac{U_v}{U_l}\right)^{0.73} \tag{6.41}$$

The wavy flow regime heat transfer model has an upper film and lower pool contribution similar to the approach followed in the pressure drop model. However, during the visualization portion of the present study, the motion of waves in the upper film region in the direction of axial motion was observed. It is expected that this motion adds a convective component to the upper film heat transfer coefficient. The following model attempts to capture this phenomenon. Thus, the upper film is a combination of the Nusselt falling film contribution (h_{Nusselt}) and an annular convective contribution (h_A), as shown in Equation (6.42) and combined as shown in Equation (6.43).

$$h_{\mathrm{Nusselt}} = 0.728 \left[\frac{\rho_l(\rho_l - \rho_v)g\,i_{fg}k_l^3}{D\mu_l \Delta T_{\mathrm{avg}}}\right]^{1/4}$$
$$h_A = \frac{k_l}{D_i} 0.00667 \, \mathrm{Re}_{l,\delta}^{0.8} \, \mathrm{Pr}_l^{0.3} \, f_{l,i} \tag{6.42}$$

$$h_{\mathrm{Up}} = \left(h_{\mathrm{Nusselt}}^3 + h_A^3\right)^{1/3} \tag{6.43}$$

This formulation captures the convective component when sufficient liquid is present in the upper film while also tending to Nusselt condensation when the convective contribution diminishes. The upper film convective contribution is calculated using the annular regime model (Equations (6.40) and (6.41)).

The liquid pool heat transfer coefficient is calculated using the correlation of Churchill (1977a), shown in Equation (6.44). The liquid pool Reynolds number is calculated using the portion of liquid flowing in the liquid pool, shown in Equation (6.45) . The friction factor in Equation (6.44) is calculated using the liquid pool Reynolds number (Equation (6.45)), the wall roughness (ε_w) and tube diameter (D).

$$h_{lp} = \frac{k_1}{D}\left(4.364^{10} + \left(\frac{exp\left(\frac{2200 - \text{Re}_{lp}}{365}\right)}{4.364^2} + \frac{1}{\left(6.3 + 0.079\left(\frac{f_{lp}}{8}\right)^{0.5}\text{Re}_{lp}\frac{\text{Pr}}{\left(1 + \text{Pr}^{0.8}\right)^{5/6}}\right)^2}\right)^{-5}\right)^{1/10}$$ (6.44)

$$\text{Re}_{lp} = \frac{G(1-q)(1-\eta_{Up})D}{\mu_1}$$ (6.45)

The total heat transfer coefficient in the wavy regime is calculated from a surface-area-weighted contribution of the upper film heat transfer coefficient, h_{Up}, and the liquid pool heat transfer coefficient, h_{lp}, as shown in Equation (6.46). By accounting for the convective contribution to heat transfer in the wavy regime using the annular model and using the Nusselt falling film and convective pool contributions for the remaining

contribution, no new regression parameters were introduced in the wavy flow model. Therefore, no wavy flow data were used in the development of the wavy flow model.

$$h_W = \frac{\theta_{\text{Strat}}}{2\pi} h_{\text{Up}} + \left(1 - \frac{\theta_{\text{Strat}}}{2\pi}\right) h_{\text{lp}} \qquad (6.46)$$

The annular and wavy regime heat transfer coefficients are combined using Equation (6.11) as shown in Equation (6.47). The annular and wavy contributions in the transiton region are calculated at the local conditions and combined using a weighted average.

$$h = \begin{cases} h_W & \text{for Fr}_{\text{so}} < 10 \\ \dfrac{(\text{Fr}_{\text{so}} - 10) h_A + (20 - \text{Fr}_{\text{so}}) h_W}{10} & \text{for } 10 \le \text{Fr}_{\text{so}} \le 20 \\ h_A & \text{for Fr}_{\text{so}} > 20 \end{cases} \qquad (6.47)$$

Using these models to assess which region contributes most to the heat transfer in the wavy regime, it was found that the upper film accounts for an average of 91% of the total heat duty. This distribution of heat transfer is consistent with the results in the literature. In the transition region, the annular model accounts for an average of 49% of the heat duty, 48% of the heat duty is due to the upper film in the wavy model, and the remaining 3% is from the liquid pool in the wavy model. While wavy flow is not an ideal configuration for heat transfer because the liquid pool transfers considerably less heat, the present study shows the behavior of the film is also a significant aspect, because the upper film transfers the major portion of the heat in this regime. Thus, a uniformly thick film on the tube wall in annular flow may transfer appreciable heat in the lower portion also, where the wavy flow would not transfer appreciable heat. However, a thin, well agitated film on the upper portion of the tube may more than compensate for the high

thermal resistance liquid pool region at the bottom in wavy flow for the conditions investigated here. Furthermore, the relatively large film contribution suggests that a larger heat transfer coefficient in the 14.45 mm tube is possible in wavy flow due to the lack of an upper film. A transition in upper film behavior with increasing tube diameter was observed in the visualization portion of the present study for both regimes, sample images from similar conditions in both tubes are shown in Figure 6.13. In the wavy regime, the videos show that a significantly thinner upper liquid film occurs in the larger tube, decreasing the thermal resistance and resulting in an increase in the heat transfer coefficient for the larger tube. In the annular regime, the heat transfer is again dominated by the film behavior. As observed in the visualization portion of the present study, the upper film was observed to breakdown and show greater disturbances of the film in the larger tube. A breakdown of the film reduces the thermal resistance of the film in the larger tubes. Therefore, the heat transfer coefficient can be expected to increase from the 7 to the 15 mm tube. While this trend was observed over the range of tubes in the present study, it is unclear whether this trend will extrapolate to tubes with diameters larger than 15 mm or smaller than 7 mm. With the above discussion in mind, for the conditions of the present study, the larger 14.45 mm tube is preferable to the smaller 7.75 mm tube because the heat transfer performance is greater in the larger tube while incurring lower pressure drop.
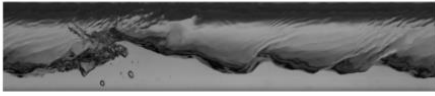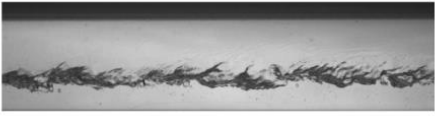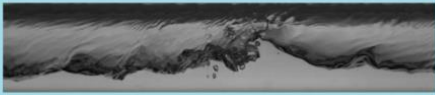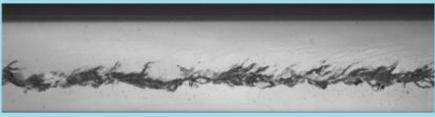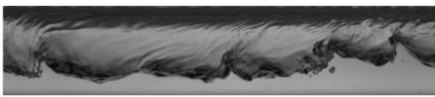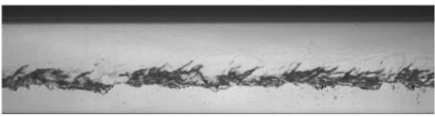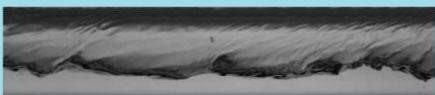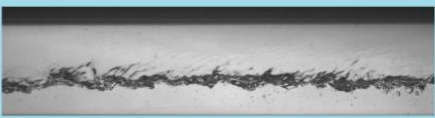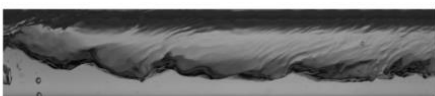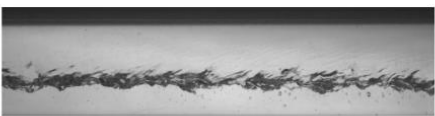
Figure 6.13. Sample propane images in 7.0 and 15.0 mm tube at $G = 150$ kg m^{-2} s^{-1}, P = 952 kPa, and $q \sim 0.2$

As described in Section 5.2, the mixture results are compared with the approximate method of Silver (1947) and Bell and Ghaly (1973) using the apparent heat transfer coefficient and the Colburn and Drew (1937) and Price and Bell (1974) method using the heat duty. The overall agreement is shown in Figure 6.14 with the mixture comparisons at the top of the figure and pure fluids at the bottom. The model predictions at experimental conditions are overlaid on the data in Figure 6.15.
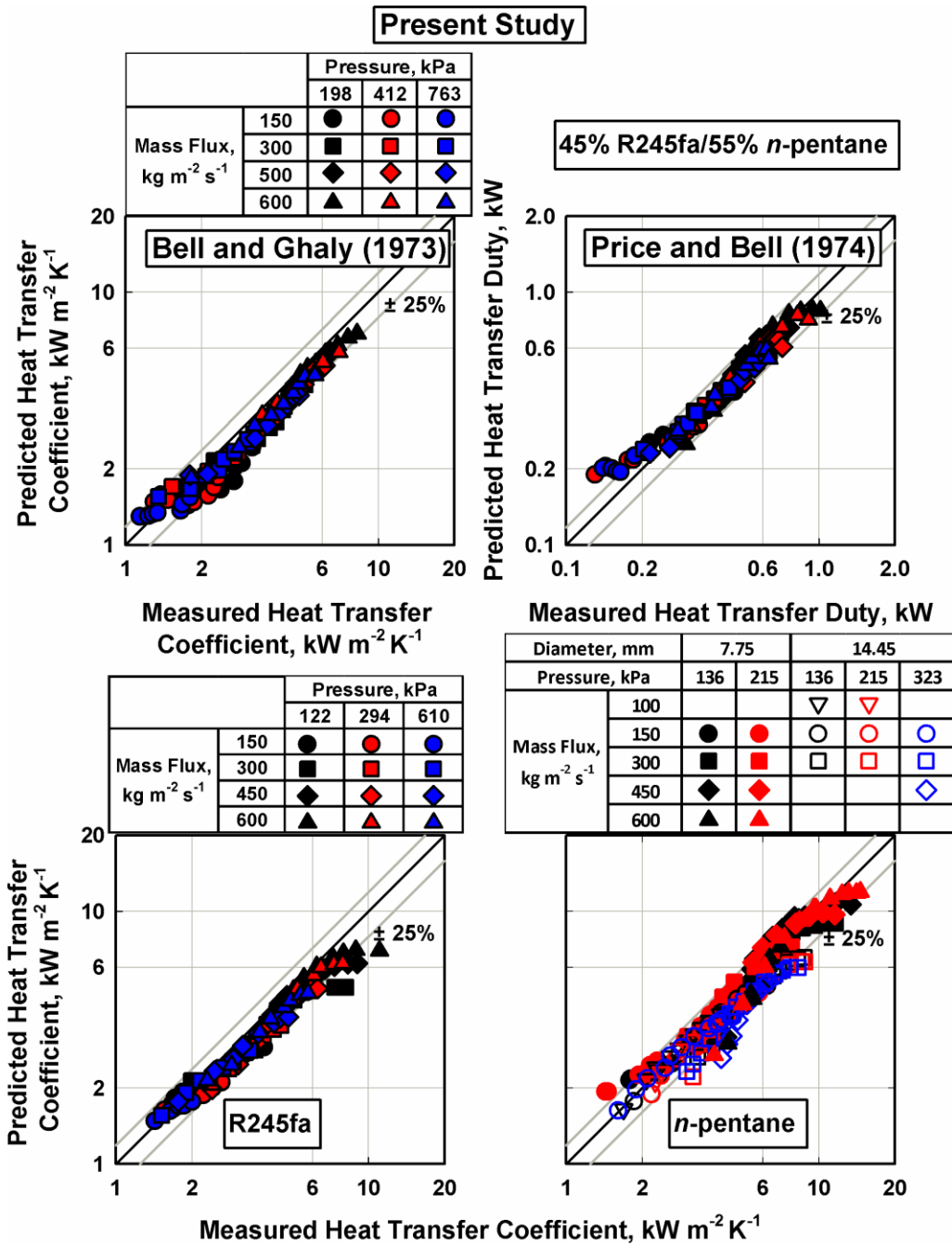
Figure 6.14. Overall heat transfer agreement
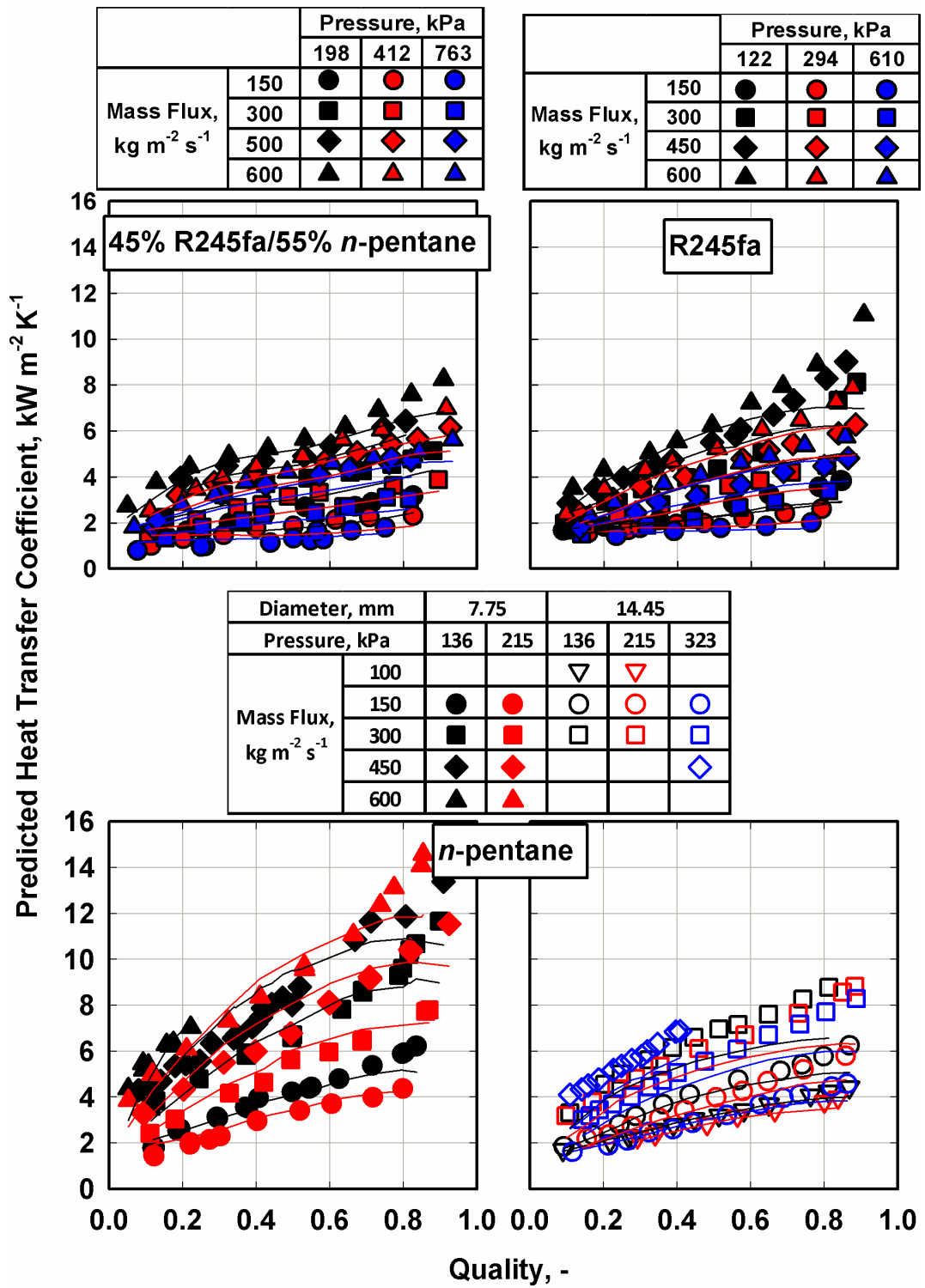
Figure 6.15. Experimental heat transfer results with model predictions overlay

The pure R245fa data are slightly under predicted with an AAD of 12%, and 95% of the data within ±25%. The pure *n*-pentane data are predicted well with an AAD of 11% and AD of -5%, with 94% of the data predicted within ±25%. The 7.75 mm diameter tube data were predicted well with an AD and AAD of 1% and 10%, respectively, while the 14.45 mm diameter tube data are slightly under predicted with an AD of -11%, indicating that the interfacial roughness term may not completely capture the diameter trend while also compensating for the diameter effect imparted by the film Nusselt number. Referring to Figure 6.15, the trends with increasing mass flux, pressure, and quality are captured well across the range of conditions.

For the mixture, both methods of accounting for the mass transfer resistance contribution to the predicted heat transfer coefficient show good agreement; the AADs for the Bell and Ghaly (1973) method and Price and Bell (1974) method are 14% and 8%, respectively. The Bell and Ghaly (1973) method predicts 93% of the data within ±25%, while the Price and Bell (1974) method predicts 96% of the data within ±25%.

In summation, for all of the measured data, the annular flow regime data are predicted better than the wavy flow regime data, with an AAD of 10% for the annular regime and 18% for the wavy regime. Because no wavy flow data were used in the development of the wavy flow heat transfer model slightly lower agreement in the wavy regime is expected. However, the agreement for the wavy regime was also reasonably good. The heat transfer model agreement is summarized in Table 6.4 for each fluid, diameter, and pressure.

Table 6.4. Heat transfer model agreement with experimental results

		Pressure, kPa	# Data Points	AD	AAD	R^2	% within ±25%	Annular	Wavy
				Agreement				**AAD**	
7.75 mm	45% R245fa/ 55% n-pentane: h Comparison	198	35	-13%	14%	0.97	93%	14%	24%
		412	41	-11%	14%				
		763	37	-6%	15%				
	45% R245fa/ 55% n-pentane: Heat Duty Comparison	198	35	-1%	7%	0.96	96%	6%	27%
		412	41	0%	7%				
		763	37	1%	9%				
	R245fa	122	41	-13%	14%	0.93	95%	14%	5%
		294	34	-12%	13%				
		610	27	-8%	9%				
	n-pentane	136	65	-2%	10%	0.92	96%	9%	27%
		215	48	3%	10%				
14.45 mm	n-pentane	136	35	-8%	10%	0.95	92%	12%	13%
		215	27	-12%	12%				
		323	38	-14%	15%				
Total (Neglects Mixture h Comparison)			428	-5%	11%	0.89	95%	10%	18%

The heat transfer coefficient model predictions with varying mass flux, saturation temperature, diameter, and fluid are shown in Figure 6.16. The heat transfer model predictions follow the observed trends with increasing quality, pressure, and mass flux. The data in the present study show a slight increase in heat transfer coefficient with increasing diameter as noted in Chapter 5. Thus, the model also predicts a small increase in heat transfer coefficient with increasing tube diameter. In the annular regime, the heat transfer coefficient scales with $\delta^{0.12}$ as a result of the regression analysis. Although a larger film thickness would ordinarily yield a lower heat transfer coefficient, in this additional agitation and the resulting mixing mechanism is considered, this result is plausible.
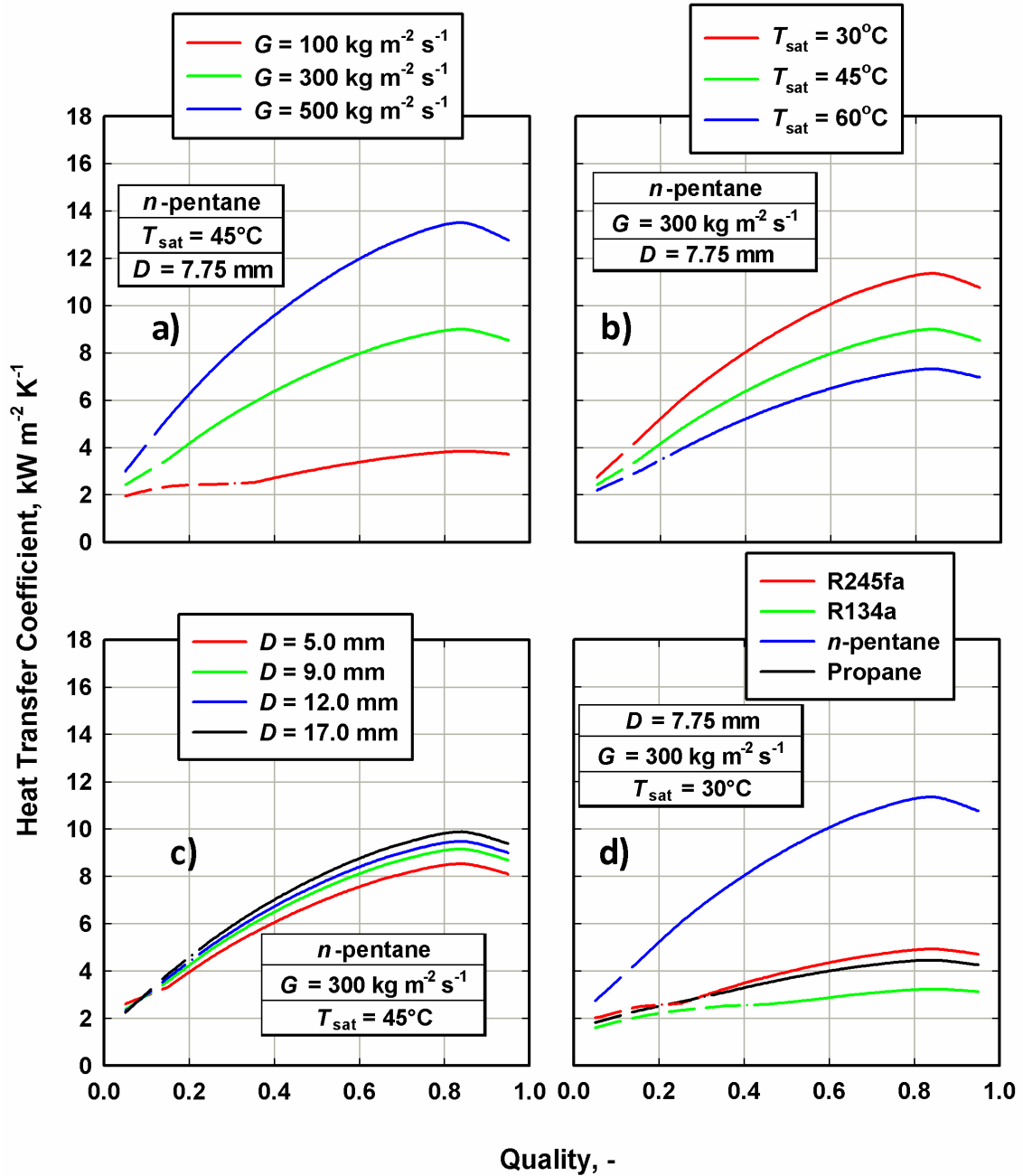
Figure 6.16. Heat transfer model prediction trends with a) mass flux, b) saturation temperature, c) diameter, and d) fluid; Annular regime - solid line; wavy regime – dashed line; transition dash dot dash line

Finally, the film heat transfer coefficient predictions for the zeotropic mixture of R245fa/n-pentane at three different concentrations are shown in Figure 6.17, where the red plots are the nominal conditions examined in the present study at a 45%/55% concentration. It should be noted that in the present study, experiments were only

conducted on one concentration of the mixture therefore use of the model at other mixture concentrations should be done with caution. The predicted heat transfer coefficients decrease with increasing R245fa concentration. R245fa has significantly higher phase densities resulting in lower phase velocities, and therefore, lower heat transfer coefficients. Additionally, in the results section, (Section 5.1) the heat transfer coefficient was shown to increase with increasing latent heat. A higher n-pentane concentration results in higher latent heats, due to the larger latent heat of n-pentane relative to R245fa, which in turn results in higher heat transfer coefficients. The 100 kg m^{-2} s^{-1} case in Figure 6.17 highlights the effect of bridging the Nusselt and convective contributions in the wavy regime. In the 100 kg m^{-2} s^{-1} case, the Nusselt contribution in the wavy regime begins to dominate the convective contributions. Thus, the three concentrations show much less variation than in the convective range.
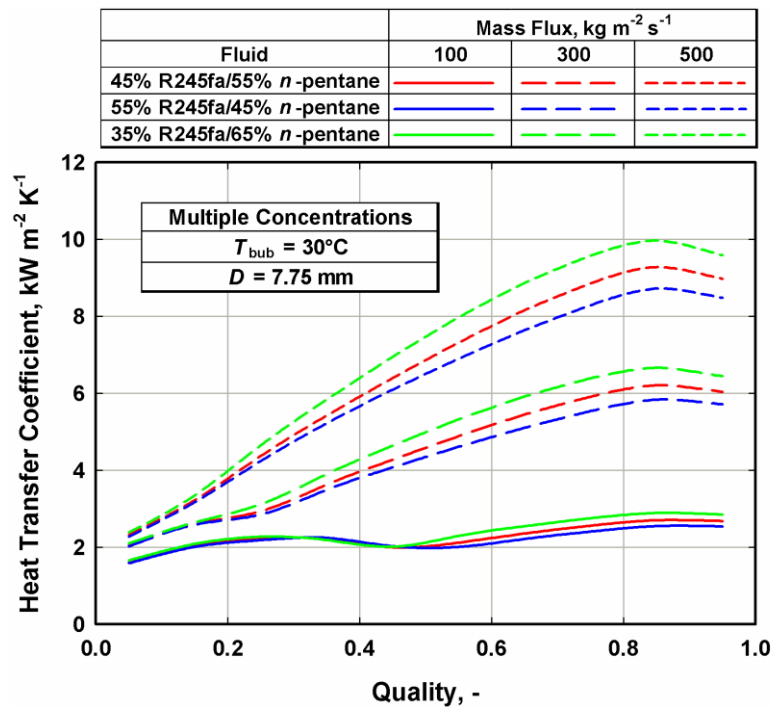
Figure 6.17. Heat transfer model predictions for zeotropic mixtures at alternate concentrations

The heat transfer coefficient model was developed using data for a zeotropic mixture at a nominal concentration of 45%55% with phase concentration shifts of less than 35%. These mixtures have temperature glides of ~15°C and liquid- and vapor- phase sensible cooling loads of less than 30% and 5% of the total heat duty, respectively. Extrapolation of these models should be done with caution for fluid pairs that exhibit temperature glides, concentration shifts, and sensible cooling loads much different from these ranges, such as ammonia and water, which exhibit significantly larger temperature glides and sensible cooling loads.

6.6 Considerations for Design Applications

The approach recommended for the design of equipment using multi-component fluids is described briefly in this section. A sample calculation is provided in Appendix F. A fixed length segmented analysis is recommended, the optimal segment length will vary depending on fluid pair and operating conditions.

First, Equation (6.10) is used to calculate the transitional Froude number and determine the flow regime based on the segment average conditions. Thus,:

- $Fr_{so} \geq 20 \rightarrow$ Annular

- $Fr_{so} \leq 10 \rightarrow$ Wavy

- $10 \leq Fr_{so} \leq 20 \rightarrow$ Annular-to-Wavy Transition

The void fraction is calculated based on the applicable flow regime using Equation (6.16). The drift flux velocity is calculated based on the flow regime as follows:

- Annular: Equation (6.20)

- Wavy: Equation (6.19)

382

- Annular-to-Wavy Transition: Equation (6.19) and Equation (6.20) combined using Equation (6.22).

The frictional pressure drop in the segment is calculated at the average segment conditions using Equation (6.27) with the interfacial friction factor calculated specific to the flow regime as follows:

- Annular: Equation (6.32)
- Wavy: Equation (6.33)
- Annular-to-Wavy Transition: Equation (6.32) and Equation (6.33) combined using Equation (6.36)

The deceleration contribution to the pressure drop should be calculated as described in Chapter 4:

$$\Delta P_{\text{Decel}} = \left[G^2 \left(\frac{q^2}{\rho_{\text{v,out}}\alpha} + \frac{(1-q)^2}{\rho_{\text{l,out}}(1-\alpha)} \right) \right]_{\substack{\alpha=\alpha_{\text{out}} \\ q=q_{\text{out}}}} - \left[G^2 \left(\frac{q^2}{\rho_{\text{v,in}}\alpha} + \frac{(1-q)^2}{\rho_{\text{l,in}}(1-\alpha)} \right) \right]_{\substack{\alpha=\alpha_{\text{in}} \\ q=q_{\text{in}}}} \qquad (6.48)$$

The total pressure change in the segment is calculated using:

$$\Delta P = \Delta P_{\text{fr}} + \Delta P_{\text{Decel}} \qquad (6.49)$$

The local heat transfer coefficient is calculated at the average segment conditions based on the applicable flow regime as follows:

- Annular: Equation (6.40)
- Wavy: Equation (6.46)

- Annular-to-Wavy Transition: Equation (6.40) and Equation (6.46) combined using Equation (6.47)

The above procedure is repeated for each segment until the desired quality change is achieved. When analyzing pure fluids, the calculated heat transfer coefficient can be used within a heat exchanger resistance network to calculate the heat transfer performance of a specific heat exchanger or to determine the required heat exchanger size in design. For zeotropic mixtures, the mixture effects should be accounted for prior to the determination of heat exchanger performance or size.

The Colburn and Drew (1937) and Price and Bell (1974) method is recommended for design applications. The local heat transfer coefficient calculated above for pure fluids is used to calculate the film heat transfer coefficient within the set of equations described in Chapter 4.2.3. A brief description of those equations is provided below. These equations must be solved iteratively; further details and a sample calculation are presented in Appendix F. In this analysis, the pressures at the inlet and outlet of the test section should be calculated using Equation (6.49).

The vapor-phase heat transfer is calculated first:

$$
\begin{aligned}
\dot{Q}_v &= h_v A_{HT} \mathrm{LMTD}_v \\
\dot{Q}_v &= \dot{m}_{v,Avg} C_{pv} (T_{v,in} - T_{v,out})
\end{aligned}
\tag{6.50}
$$

The condensing flux of each component is calculated as follows:

$$
\tilde{N}_T = \beta_v C_T \ln\left(\frac{\tilde{z} - \tilde{y}_{1,int,Avg}}{\tilde{z} - \tilde{y}_{1,Avg}} \right)
\tag{6.51}
$$

$$\tilde{N}_1 = \tilde{z}\tilde{N}_{\mathrm{T}}$$
$$\tilde{N}_2 = \left(1 - \tilde{z}\right)\tilde{N}_{\mathrm{T}}$$
(6.52)

Mass and species are balanced from the inlet to the outlet of the segment:

$$\dot{m}_{v,out} = \dot{m}_{v,in} - \left(\tilde{N}_1 MW_1 + \tilde{N}_2 MW_2\right) A_{\mathrm{HT}}$$
$$\dot{m}_{l,out} = \dot{m}_{l,in} + \left(\tilde{N}_1 MW_1 + \tilde{N}_2 MW_2\right) A_{\mathrm{HT}}$$
(6.53)

$$\tilde{y}_{1,out}\dot{m}_{v,out} = \tilde{y}_{1,in}\dot{m}_{v,in} - \tilde{N}_1 MW_1 A_{\mathrm{HT}}$$
$$\tilde{x}_{1,out}\dot{m}_{l,out} = \tilde{x}_{1,in}\dot{m}_{l,in} + \tilde{N}_1 MW_1 A_{\mathrm{HT}}$$
(6.54)

The total outlet enthalpy is calculated as follows:

$$\dot{m}_{total}i_{total,out} = \dot{m}_{v,out}i_{v,out} + \dot{m}_{l,out}i_{l,out}$$
(6.55)

The inlet enthalpy, adjusting for pressure changes across the previous segment, is calculated and used to determine the total enthalpy change in the segment. Not including the sensible cooling of the vapor- and liquid-phase can have a significant effect on the results as these were shown to account for up to 4% and 33% of the total heat duty, respectively. The liquid film and interface temperatures at the outlet are calculated using the enthalpy, pressure, concentration, and are assumed to be at saturated liquid conditions. The procedure is then closed using the heat transfer coefficients calculated as described above. The pure fluid heat transfer coefficient model described above is used to calculate the film heat transfer coefficient. This heat transfer coefficient and the LMTD between the liquid film and the coolant is used to calculate the segment heat duty:

$$\dot{Q}_{segment} = UA\, \mathrm{LMTD}_1$$
(6.56)

In the absence of other information, the inlet to the design tool can be assumed to be at thermodynamic equilibrium for the calculation in the first segment. Each subsequent section should use the calculated outlet conditions (phase temperatures/enthalpy, concentrations, and pressure) as the inlet to the next segment.

The procedure outlined above can be used to obtain the heat exchanger size for a desired heat duty, including outlet concentrations and conditions by specifying a fixed quality change (rather than a fixed length) and calculating the segment length. In this approach, the pressure drop calculation would become part of the iterative solution.

The Silver (1947) and Bell and Ghaly (1973) method showed reasonable results and does not require an iterative analysis. For a first approximation the Silver, Bell and Ghaly method can be used with reasonable results. However, the more rigorous Price and Bell approach discussed above should be used for design applications.

CHAPTER 7.CONCLUSIONS AND RECOMMENDATIONS

A comprehensive investigation of condensation of hydrocarbon/refrigerant zeotropic mixtures was conducted. Flow visualization experiments were performed on two-phase hydrocarbon propane condensing through 7.0 and 15.0 mm internal diameter tubes at saturation temperatures of 25°C and 35°C at mass fluxes ranging from 75 to 450 kg m^{-2} s^{-1}. Frictional pressure gradient and heat transfer coefficient experiments were also performed using the pure fluid constituents of the zeotropic mixture (R245fa and *n*-pentane) in 7.75 mm and 14.45 mm ID tubes at saturation temperatures ranging from 20°C to 75°C and mass fluxes ranging from 75 to 600 kg m^{-2} s^{-1}. Finally, detailed frictional pressure drop and heat transfer coefficient experiments were conducted on the 45% R245fa/55% *n*-pentane zeotropic mixture with bubble point temperatures ranging from 30°C to 80°C and mass fluxes ranging from 150 to 600 kg m^{-2} s^{-1}.

An automated video analysis program was developed to classify flow regimes and measure void fraction and film thicknesses from the high-speed videos. Annular and wavy flow regimes were observed in the conditions tested for this study and the transitions were found to agree well with the transition criteria proposed by Dobson and Chato (1998). The void fraction measurements agreed well with the models proposed by El Hajal *et al.* (2003) and Jassim *et al.* (2008), but an improved void fraction model was developed based on physical insights from the present study, resulting in improved agreement. The model agreed well with the data from the present study (AD = -1.9% and AAD = 4%) with 99% of the data predicted within ±25%. Furthermore, the model predicted the trends with mass flux, diameter, and pressure well, converges to the homogenous void fraction at the critical pressure, and converges to zero and unity at $q =$ 0 and 1, respectively.

The void fraction model and the Dobson and Chato (1998) regime transition criteria were used as the basis to develop frictional pressure drop and heat transfer coefficient models. These models have annular and wavy flow components based on the data for condensing flows of hydrocarbons, refrigerants, and hydrocarbon and refrigerant zeotropic mixtures. A linear interpolation between the annular and wavy regime models based on the transitional Froude number was used. For the wavy flow frictional pressure drop and heat transfer models, the area of the tube covered by the upper film is modeled with techniques similar to annular flow because the upper film in the wavy regime was observed in the visualization portion of the study to have an axial convective component. The fraction of liquid contained in the upper film and liquid pool was correlated from the video analysis, and the void fraction model is used to determine the liquid film thickness.

The frictional pressure drop model is based on the model of Garimella *et al.* (2005). The annular regime model is based on a vapor-phase analysis with the interfacial shear modeled using the Lockhart Martinelli parameter. The annular model approaches pure vapor phase pressure drop at a quality of unity. The wavy regime model is based on a liquid-phase analysis, but with the upper film modeled in a manner similar to the annular flow model, while the liquid pool is modeled as single-phase liquid flow. The model agreed well with the measured pressure gradient data (AD = 1% and AAD = 10%), predicting 91% of the data within ±25%.

The heat transfer model was developed based on the approach of Thome *et al.* (2003) where the liquid film heat transfer coefficient is modified by an interfacial roughness factor. The upper film component in the wavy regime is modeled as a combination of Nusselt film condensation and the annular flow model. The liquid pool is modeled as

single-phase liquid flow. The heat transfer coefficient model agreed well with the measured heat transfer coefficient data (AD = -5% and AAD = 11%), predicting 95% of the data within ±25%. The Price and Bell (1974) method with the respective heat transfer coefficients calculated using the models developed here is shown to predict the mixture data well (AD = 0% and AAD = 8%), predicting 96% of the data within ±25% and is therefore recommended to account for mass transfer effects of the zeotropic mixture. The approximate method of Bell and Ghaly (1973) was found to have satisfactory agreement, with the data (AD = -10% and AAD = 14%), predicting 93% of the data within ±25%.

The findings and correlations from the present study make an important contribution to the understanding of zeotropic mixture condensation and two phase flows of hydrocarbons over a wide range of mass fluxes and saturation temperatures. This understanding will yield more accurate condenser designs for zeotropic mixture condensation. In addition, the automated image analysis tool will allow for real time analysis of flow regime, void fraction, and film thicknesses from visualization results in future investigation.

7.1   Recommendations for Future Work

This investigation has led to an increased understanding of condensation of hydrocarbons, refrigerant, and zeotropic hydrocarbon/refrigerant mixtures. However, there are several key areas that require further investigation, which are summarized below.

- The change in flow characteristics between the 7.0 and 15.0 mm tube diameter has been noted in the literature. The present study documented the key changes in the liquid film, including the lack of a substantial upper film in the

15.0 mm tube while the 7.0 mm tube exhibits an upper film, that occur over this range. The observed increase in heat transfer coefficient with increasing pressure over this range is also not well documented. Because most studies have focused on diameters less than 8 mm or greater than 15 mm, a rigorous heat transfer investigation of condensation through tubes with diameters between 8 and 15 mm is needed for refrigerants and other hydrocarbons. Flow visualization should accompany the heat transfer measurements to document the changing flow phenomena over this range.

- The present study focused on condensation in smooth horizontal tubes. Enhanced tube geometries, including surface enhancements and inserts such as twisted tape mixers, may provide the necessary increase in condensation heat transfer, if optimal geometries that do not commensurately increase pressure drop can be designed, to compensate for the degradation in heat transfer coefficient associated with the use of zeotropic mixtures. Additional research should be conducted on condensing zeotropic mixtures in enhanced tube geometries.

- The high-speed flow visualization technique used in the present study to measure void fraction is limited in that this method is incapable of measuring liquid entrained in the vapor phase. It is clear from the videos there is a significant amount of liquid entrained in the vapor phase at some conditions. Quantification of the liquid entrainment is recommended through additional experimental techniques. Following that experimental effort, modeling of the

distribution of liquid phase between liquid entrainment and liquid film is recommended.

- The present study focused on zeotropic mixtures at low reduced pressures. Further investigation of these zeotropic mixtures at higher reduced pressures is necessary to enable the development of tailored working fluid cycles using dissimilar fluids.

- An investigation of zeotropic mixtures using different fluid types in microchannels is recommended for residential applications, where compact envelopes and minimal fluid inventories are desirable.

APPENDIX A:GAS CHROMATOGRAPH CALIBRATION AND UNCERTAINTY

In this section, the calibration of the gas chromatograph is described and the measurement uncertainty is determined. The calibration was conducted assuming a linear response of the gas chromatograph Thermal Conductivity Detector (TCD) over the range of conditions investigated in this study. The linearity of the TDC was verified by injecting vapor at several different volumes. Vapor samples of differing volumes were used due to the difficulty in changing the automated sample loop volume. The same automated valve was used to draw a sample from the loop at each mixture data point.

For the conditions described in Chapter 3, three liquid samples of each pure fluid (for a total of 6 samples) were injected using the liquid sample valve. The pressure of the liquid sample was measured while the temperature of the liquid in the sample loop was maintained at 30°C. The liquid densities at the temperatures and pressures were calculated for each point. The volume of the sample loop (1μL) and the density were used to calculate the mass of the samples injected. The response of the gas chromatograph TCD is a single peak for the fluid injected at the specific retention time. The LabSolutions software (Shimadzu, 2011) integrates the area under the peak and returns the TCD response in area units. The area response of the TCD and the retention time for each fluid is tabulated in Table A.1.

Table A.1. Pure fluid sample results

Sample Number	Fluid	Density, kg m^{-3}	Retention Time, min	Area, -
1	R245fa	1324.9	1.71	140077
2	R245fa	1324.9	1.71	140322
3	R245fa	1324.9	1.71	140534
4	*n*-Pentane	615.8	1.17	136412
5	*n*-Pentane	615.8	1.17	136527
6	*n*-Pentane	615.8	1.17	136493

The average area and uncertainty in the area measurement is determined to be 140,311 ± 323 area units for R245fa, and 136,447 ± 84 area units for n-pentane. The injected masses are calculated to be 1.325 mg and 0.616 mg for R245fa and n-pentane, respectively. A two-point calibration is done for each fluid assuming that there is no fluid present at zero area units and the measured values are the second point. The mass per area unit calibration for R245fa and n-pentane are shown in Equations (A.1) and (A.2), respectively. The associated uncertainties are a propagation of the temperature, pressure, and area uncertainties.

$$\frac{m_{\text{R-245fa}}}{Area} = \frac{1.325\,\text{mg}}{140311} = 9.44 \times 10^{-6} \pm 2.38 \times 10^{-8}\,\text{mg}\ (0.25\%) \tag{A.1}$$

$$\frac{m_{\text{n-Pentane}}}{Area} = \frac{0.616\,\text{mg}}{136477} = 4.51 \times 10^{-6} \pm 9.44 \times 10^{-9}\,\text{mg}\ (0.2\%) \tag{A.2}$$

A representative TCD response plot from the LabSolutions software is shown in Figure A.1. For the representative data point discussed in the text, the TCD responses, in area units, for the n-pentane and R245fa are approximately 95,000 and 38,000, respectively. The calibrated masses of n-pentane and R245fa are 0.432 and 0.359 mg, respectively. Therefore, the bulk concentration is calculated using Equations (A.3) and (A.4) to be 54.6% n-pentane and 45.4% R245fa. A propagation of the uncertainties in the measured concentration results in a concentration uncertainty of 0.23%.

$$x_{\text{R245fa}} = \frac{m_{\text{R245fa}}}{m_{\text{Total}}} = \frac{0.359\,\text{mg}}{0.792\,\text{mg}} = 45.4\% \tag{A.3}$$

$$x_{\text{n-Pentane}} = \frac{m_{\text{n-Pentane}}}{m_{\text{Total}}} = \frac{0.432\,\text{mg}}{0.792\,\text{mg}} = 54.6\% \tag{A.4}$$
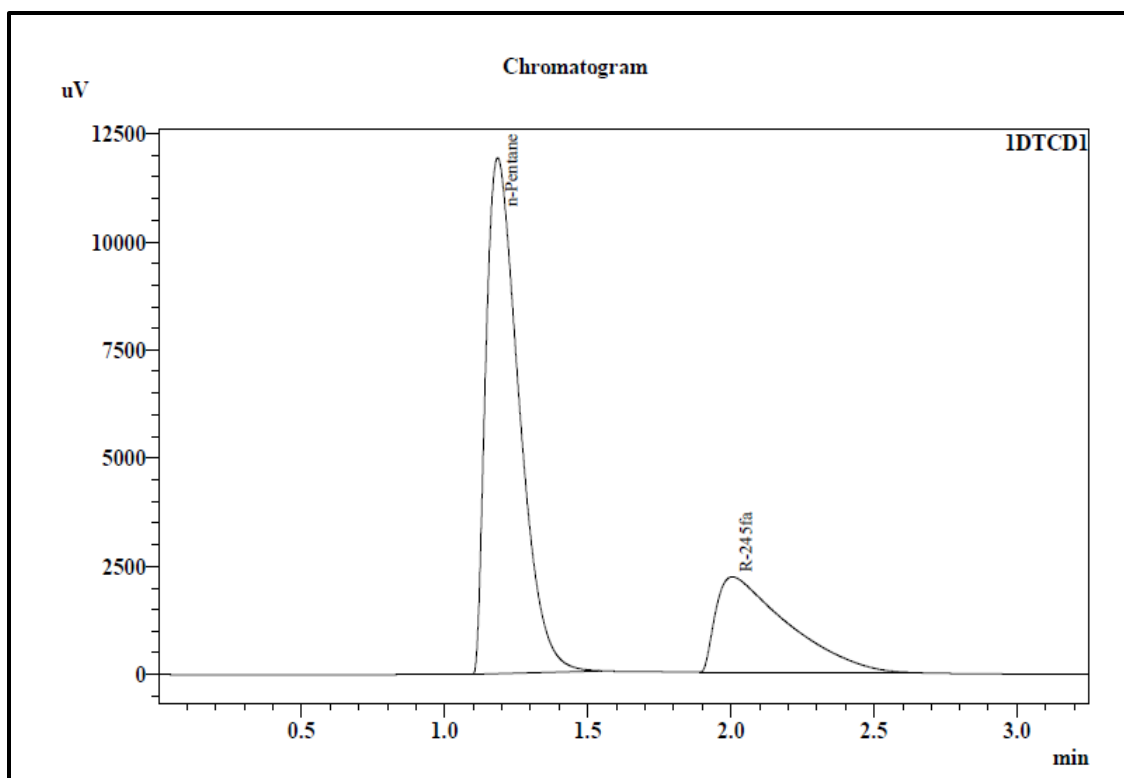
Figure A.1. Representative TDC response

Because two points were used in the calibration of the gas chromatograph, the linearity of the TCD response over the range of the calibration is critical to achieve accurate results. To validate this assumption, nine *n*-pentane vapor samples and seven R245fa vapor samples were injected at four different volumes (0.5 mL, 0.25 mL, 0.125 mL, and 0.01 mL). The mass of R245fa was determined using standard temperature and pressure of 25°C and 101 kPa; at this state, the vapor density is 5.7 kg m^{-3}. The density of *n*-pentane was determined using the saturated vapor density at 25°C, which is 2.06 kg m^{-3}. A linear fit was applied, including the zero/zero point. The vapor samples data and linear fit for *n*-pentane and R245fa are shown in Figures A.2 and A.3, respectively. The linear fit for *n*-pentane has an R^2 fit of 0.9946, while the R^2 for R245fa is 0.9996. Because the saturation pressure of *n*-pentane at 25°C is sub-atmospheric (68 kPa), the

repeatability of the vapor injections is slightly lower than that of the R245fa injections. However, in both cases a good linear fit is observed.
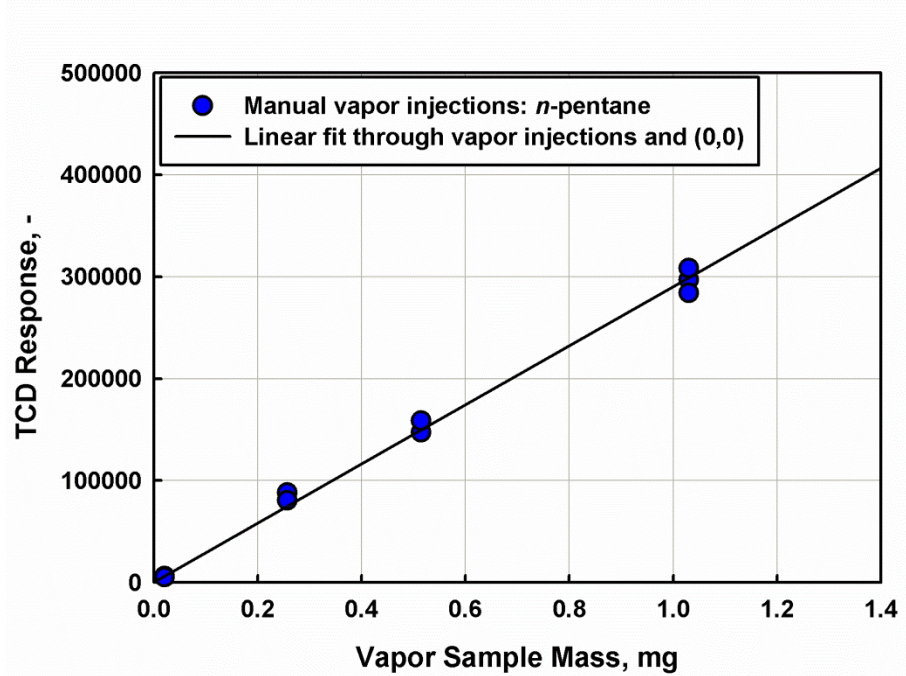
Figure A.2. Linearity of TDC response: *n*-pentane
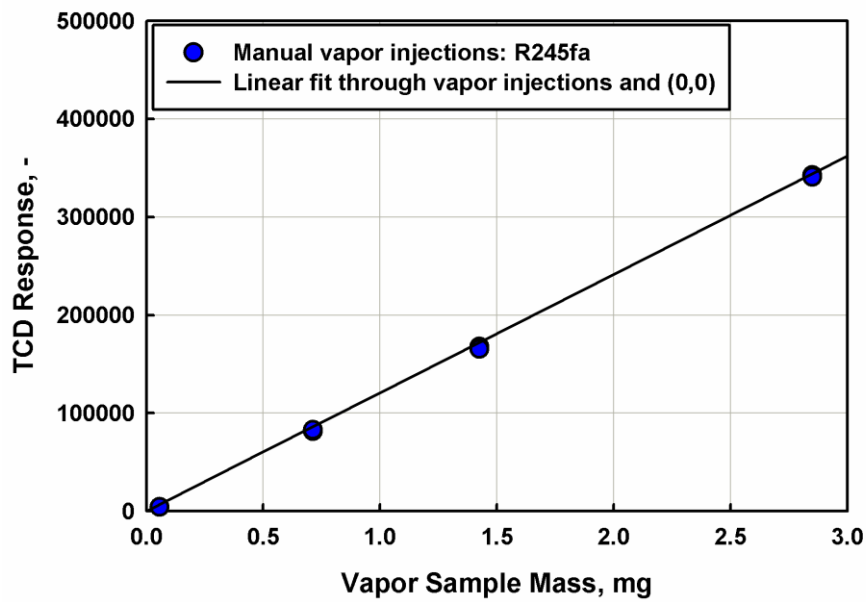
Figure A.3. Linearity of TDC response: R245fa

Based on the liquid sample repeatability, temperatures, and pressures, the uncertainty in concentration was determined to be 0.23%. To account for possible uncertainty in the linearity of the TCD, a nominal 2% uncertainty in each measured mass is assigned. This results in concentration uncertainties of 0.9% and 1.1% for R245fa and n-pentane, respectively.

APPENDIX B:VISUALIZATION TEST SECTION DISTORTION

This appendix describes the procedure used to quantify the potential distortion associated with viewing the flow through the round tube wall and the round outer chamber. It is shown that such distortion is negligible for both the 7 and 15 mm visualization test sections, and can be accounted for in the quantitative analysis of the videos. The method used for calibrating the lengths in the radial and axial direction is also described in detail.

To calibrate the test section, a 20×20 slide grid with 1×1 mm cells, shown in Figure B.1, was cut to a width equal to the internal diameter of the test sections, resulting in 7×20 mm and 15×20 mm grids, each with 1×1 mm cells for the 7 and 15 mm diameter test sections, respectively. The grid was placed on a thin clear plastic piece and inserted inside of the test section such that the grid is fit vertically along the diameter passing through the center of the cross section. The test section was mounted such that the grid was perpendicular to the camera. The test section was sealed, pressure tested, and filled with liquid propane, keeping the annulus at the conditions used for testing, i.e. pressurized nitrogen and pressurized water for the 7 mm and 15 mm test sections, respectively. The test section was backlit, similar to the data collection procedure shown in Figure 3.7, and several still images were captured for each test section, slightly changing the lighting and focus to accurately capture the grid inside the tube.
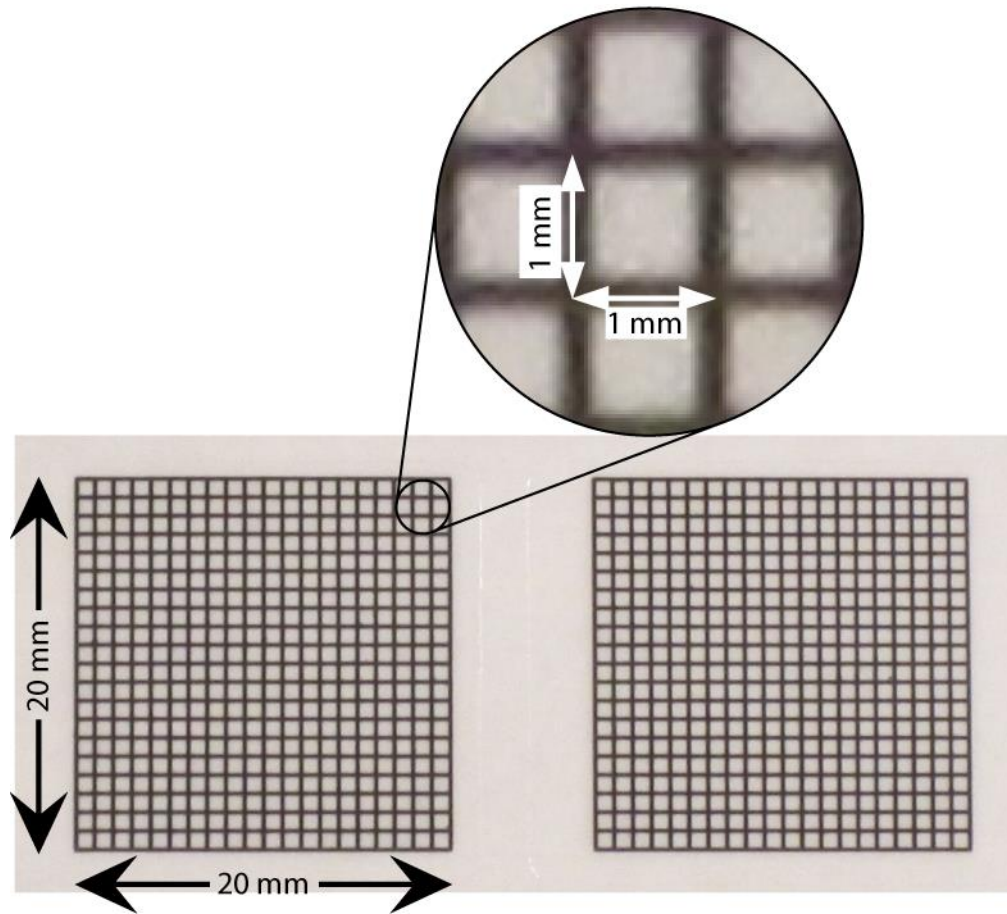
Figure B.1. Visualization calibration grid

For the 15 mm test section, the raw image is shown in (A) of Figure B.2. As shown in Figure B.2(B), the outer tube walls are highlighted in red and the inner tube walls are highlighted in orange, with the grid shown to be between the inner tube walls. Also shown in yellow in (B) are two length calibrations. The two vertical lines are stretched to fit between the inner and outer tube walls. The inner and outer diameters of the tube are 15 mm and 18 mm, respectively. The lengths of the four lines are shown in Table B.1. It can be seen that neither vertical dimension is equal to the horizontal length, meaning that neither length can be directly used for the horizontal calibration. The horizontal length corresponding to the inner diameter is 79.3% of its vertical counterpart. Similarly, the horizontal length of the outer diameter is 76.8% of its vertical counterpart. This is due to

the magnification effect of the water in the outer pressure chamber. The water was required to provide good visual separation of the apparent inner and outer tube walls. The outer diameter calibration was used to calibrate axial length measurements. This was used for consistency with the 7 mm test section, which is described here. A similar set of images is shown in Figure B.3 for the 7 mm visualization test section. However, in this case, the lengths of the two yellow bars are identical. Therefore, the difference between the outer tube walls (10.4 mm) is equal in length to the axial calibration.
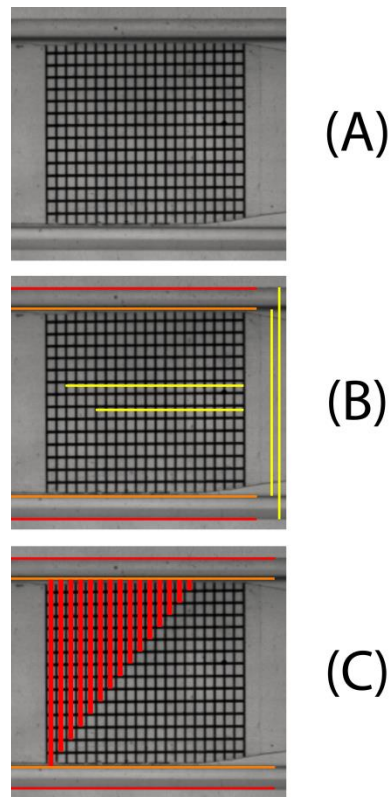
Figure B.2. 15 mm visualization calibration image analysis
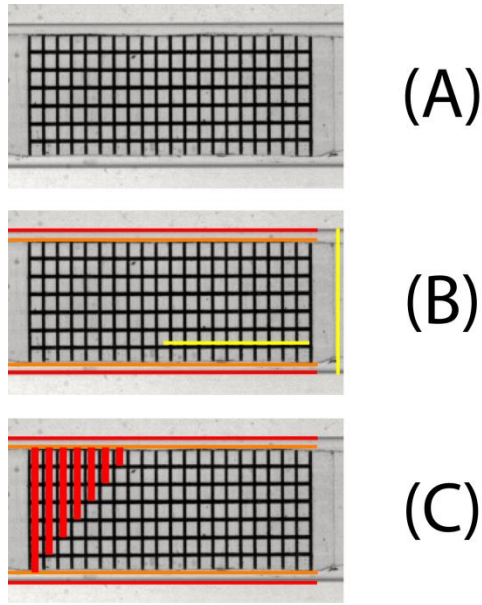
Figure B.3. 7 mm visualization calibration image analysis

Table B.1 15 mm length calibration dimensions

		Nominal Dimension, mm	
		15	**18**
Length, Pixels	**Vertical**	234.1	291.5
	Horizontal	185.7	291.5

The final step in calibrating the test section is to determine if any distortion in the vertical direction exists. Shown in (C) of both Figures B.2 and B.3 are sets of bars subtended from the upper tube wall to the center of the grid line. In the case of the 15 mm test section, there are 15 bars. Similarly the 7 mm test section image contains 7 bars. The difference between the bar lengths was calculated by measuring the length of the bars using Adobe Illustrator Software. The height of the first cell is the length from the upper wall to the first grid line, each subsequent cell is the difference between the previous segment height and the current segment height. For example, the height of cell two is

calculated using the height of the second segment (29.2 pixels) and subtracting the height of the first segment (13.5 pixels), resulting in a cell height of 15.7 pixels. Using this method, the first and last cells are expected to be slightly different than the center cells because the grid is not perfectly centered. Shown in Figures B.4 and B.5 are the cell heights of the 15 mm and 7 mm test section calibration images. Due to the grid lines' thicknesses (approximately three to four pixels) accurate determination of the center of the grid line is difficult. However, great care was taken to locate the center of the line. As shown in Figures B.4 and B.5, the cell height for both test sections is approximately 15 pixels across the entire test section. To verify that no distortion exists right at the wall, the center columns (removing the first and last cell for each set) were averaged, then the average was multiplied by the number of cells, and this height was compared with the height of the longest segment. For example, the average of the center 13 cells was calculated to be 15.6 pixels. Multiplying the average by all 15 cells, a total height of 234.4 pixels was obtained. This compared to a height of 234.3 pixels for the longest segment (segment 15), showing that there is negligible distortion in the two end cells near the tube wall. If the 1 mm region near the tube walls was significantly stretched or compressed, the average calculation would differ significantly from the height of the longest segment. Finally, observing the cell heights across the cross section, no distinguishable trend is observed, indicating that there is no non-linear distortion in the radial direction.
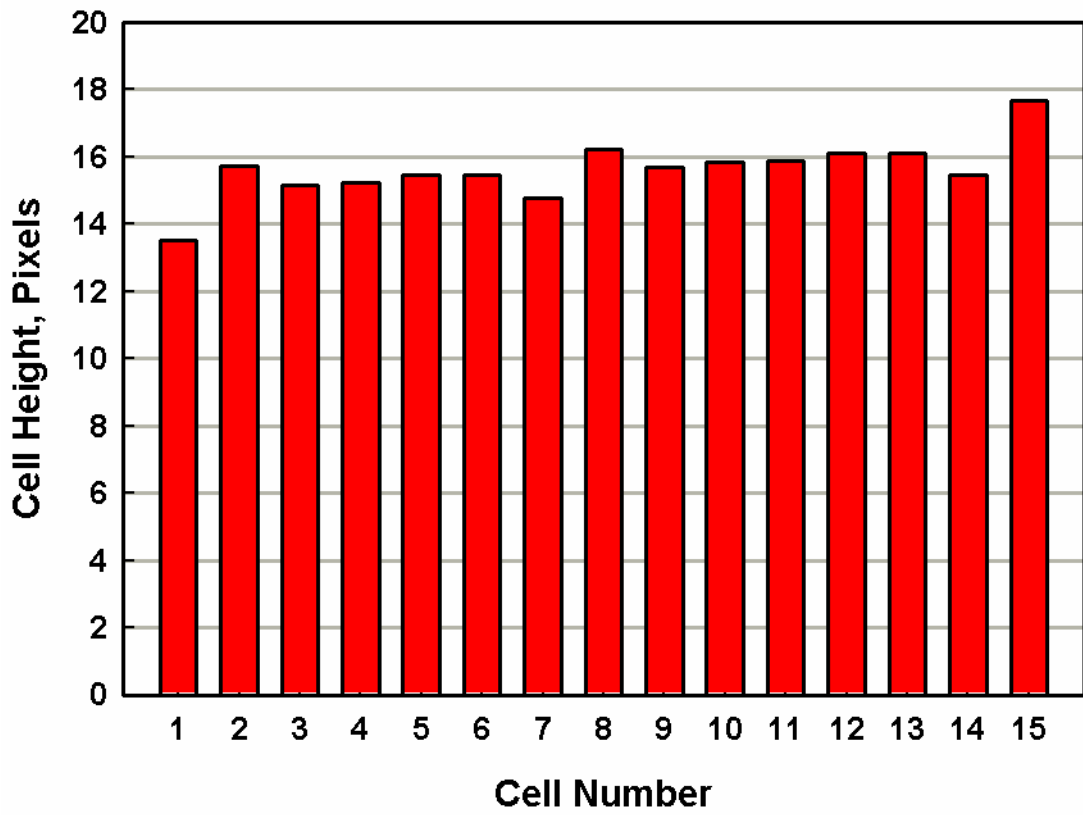
Figure B.4. Cell height in 15 mm visualization test section calibration image
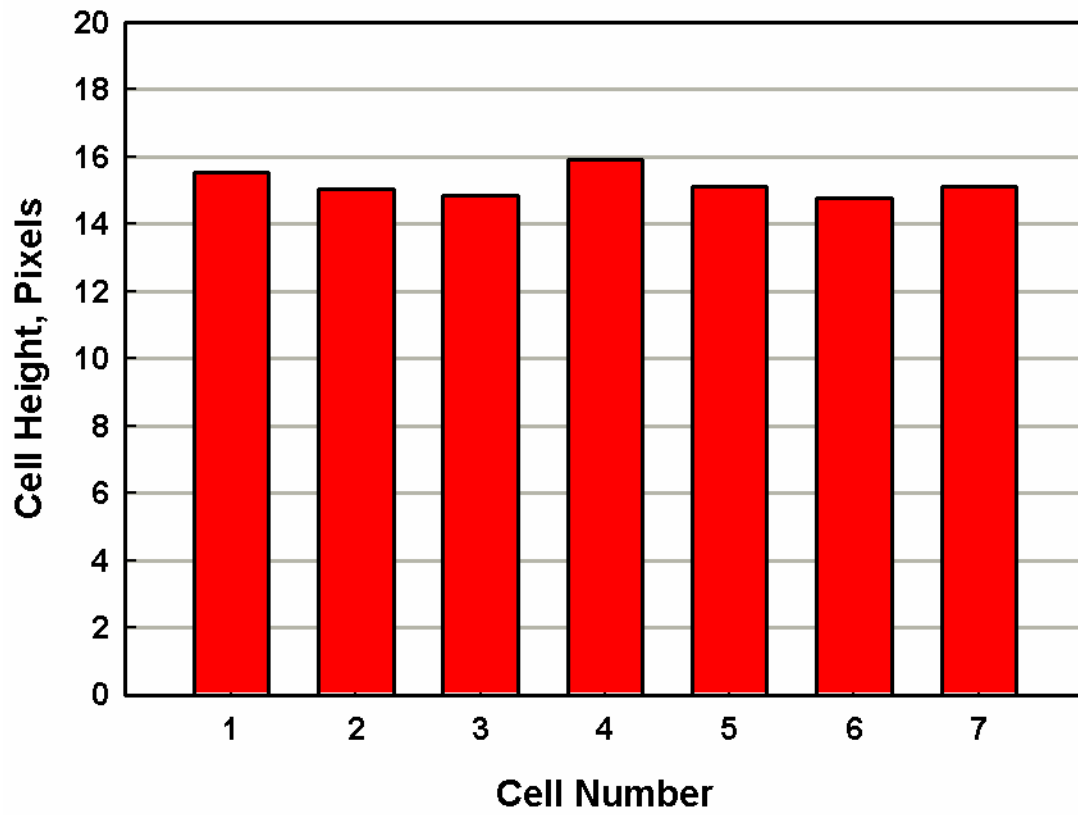
Figure B.5. Cell height in 7 mm visualization test section calibration image

APPENDIX C: PUMP HEAT ADDITION CALCULATION

The use of the thermal amplification technique requires an accurate estimate of the heat addition from the primary loop pump. A control volume analysis on the primary loop is shown in Figure C.1.
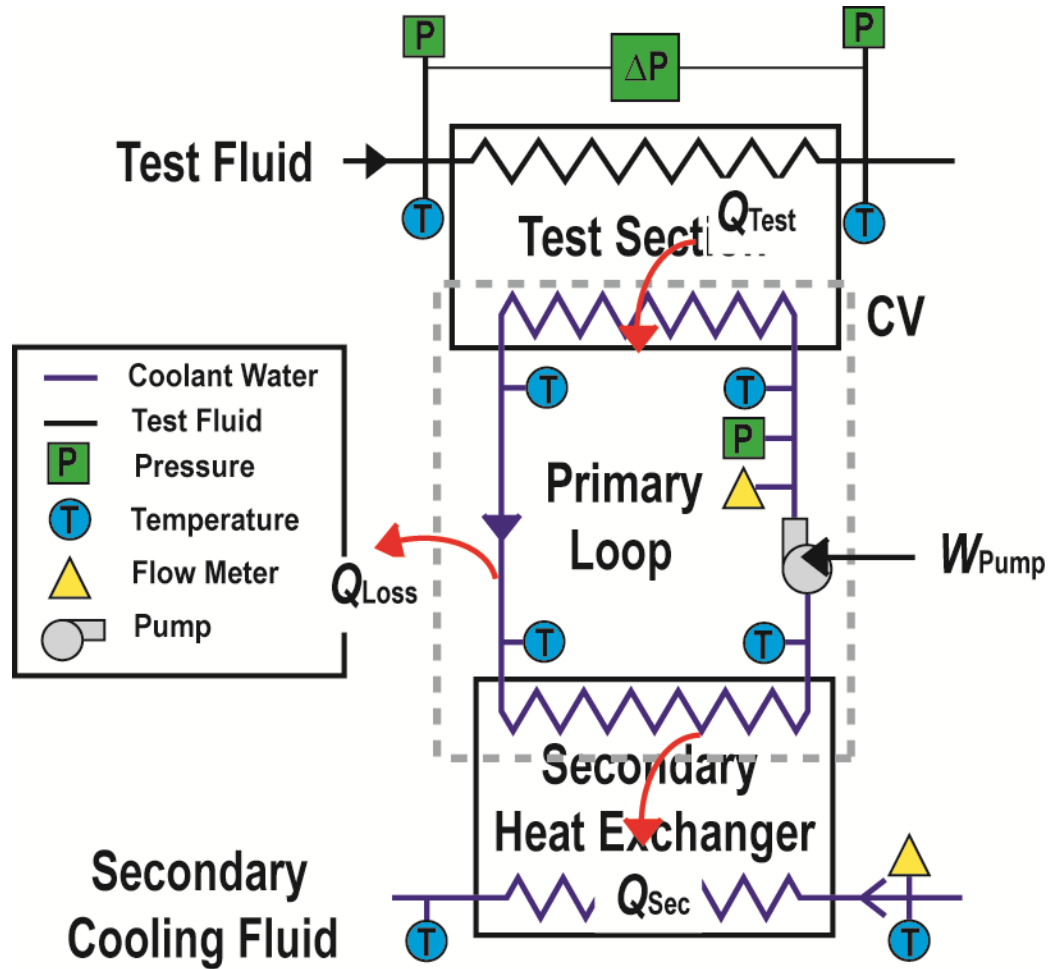
Figure C.1. Thermal amplification technique control volume

The energy balance on this control volume is given by Equation 4.79:

$$\dot{Q}_{Test} = \dot{Q}_{Sec} + \dot{Q}_{loss,Amb} - \dot{W}_{Pump}$$

Single-phase cooling experiments using the primary and secondary loops to verify the pump heat addition term were conducted by Personal Communication (2013). In this

case, rather than deducing the test section heat duty using the pump heat addition, the single-phase test section heat duty is calculated using measured temperatures and mass flowrate:

$$\dot{Q}_{\text{Test}} = \dot{m}_{\text{f}} \left(i_{\text{f,test,out}} - i_{\text{f,test,in}} \right) \tag{C.1}$$

The volumetric flowrate of the primary loop was varied across the range of conditions necessary for this study, while keeping the remainder of the system approximately constant. The primary loop flowrates used in this study varied from 2.8 to 9.6 L min^{-1}. These validation tests yielded a measured heat duty as a function of flowrate, shown in red in Figure C.2. The pump heat addition in watts was curve fit to the measured pump heat addition using a second order polynomial in terms of volumetric flowrate:

$$\dot{Q}_{\text{Pump}} = 0.1401 \dot{V}_{\text{w,Pri}}^3 + 0.9598 \dot{V}_{\text{w,Pri}}^2 + 3.025 \dot{V}_{\text{w,Pri}} \tag{C.2}$$

The resulting curve fit was found to have an R^2 value of 0.997. The curve fit is shown in black in Figure C.2. This curve fit was used to calculate the pump heat addition for the 7.75 mm experiments.
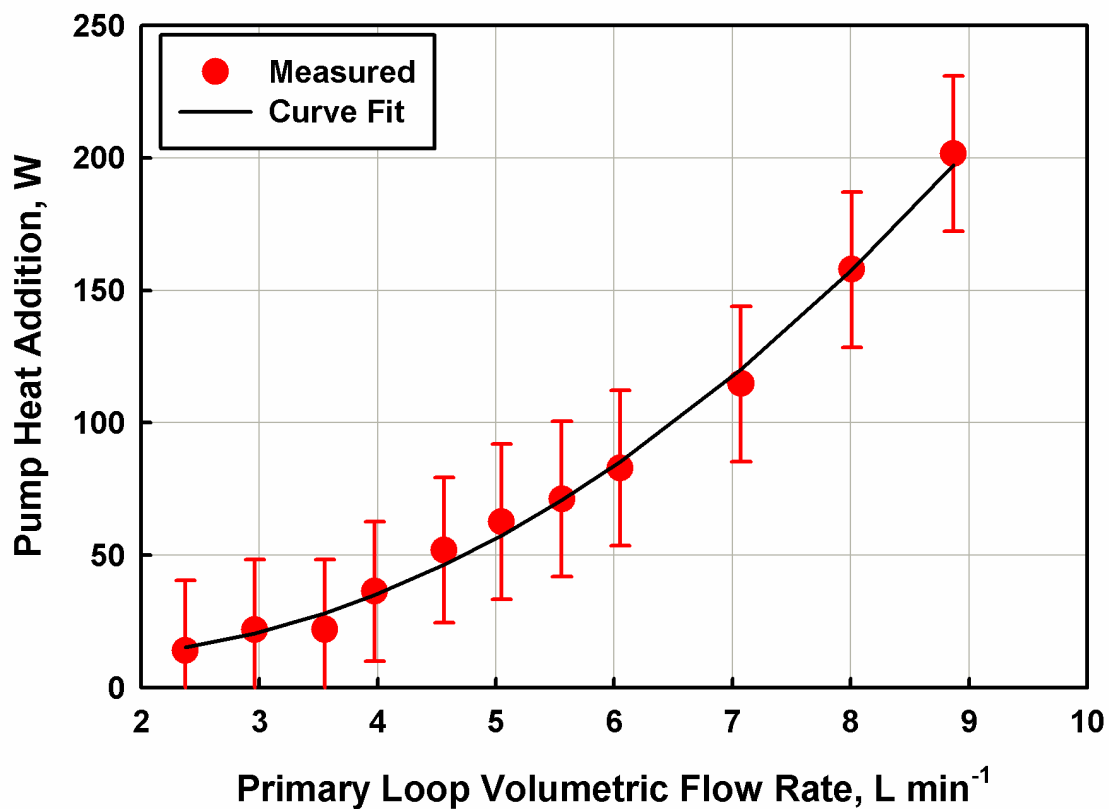
Figure C.2. Pump heat addition with increasing volumetric flowrate

The pump shaft work was approximated using the pump curve as fit for the primary

loop conditions in the 7.75 mm diameter *n*-pentane experiments. The pumping power was

approximated using the manufacturer pump curve with the measured pressure rise across

the pump and the volumetric flowrate.
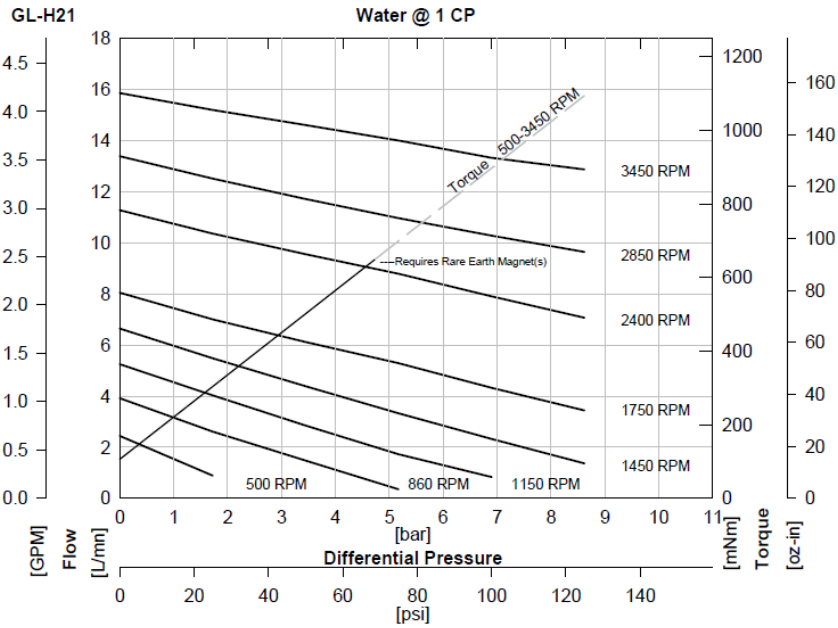
Figure C.3. Primary loop pump curve (Micropump, 2000)

A comparison between the values predicted using Equation (C.2) and the predicted

values using the pump curve yielded an efficiency of 64%. Stated another way, due to the

pump age, the pump was consuming more 36% power than the pump curve predicts. The

adjusted pump curve predictions are shown in Figure C.4 against primary loop

volumetric flowrate with the measured pump heat addition and curve fit shown in Figure

C.2.
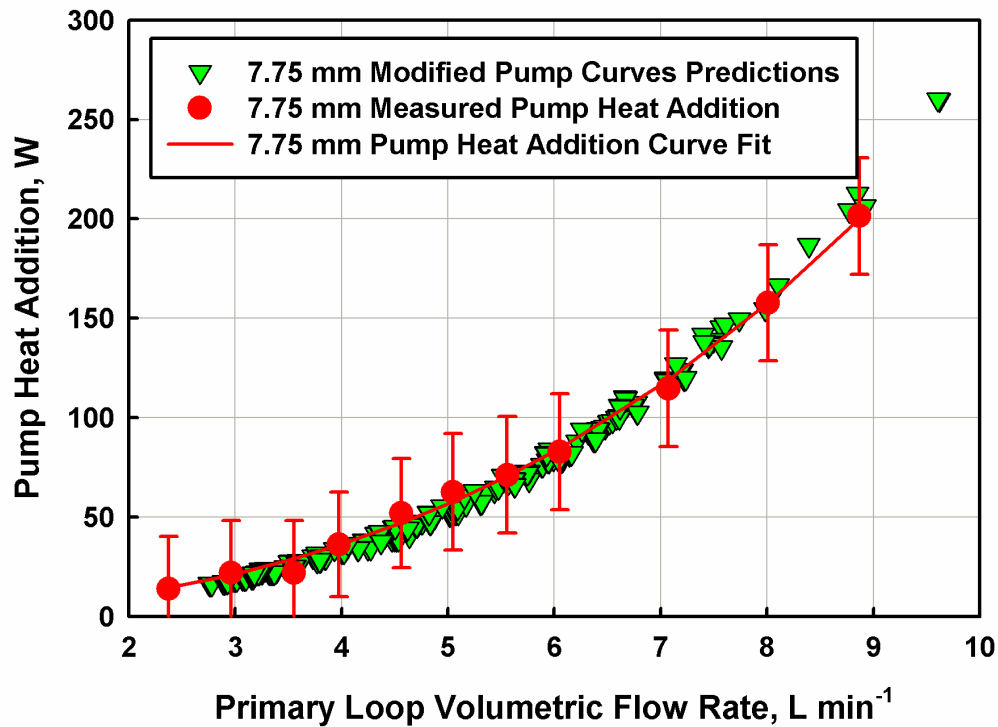
Figure C.4. Adjusted 7.75 mm pump curve predictions with measured pump heat addition overlay

To obtain a pump heat addition curve fit for the 14.45 mm tube, the primary loop pumping power was calculated using the pump curves, including the additional 36% observed in the 7.75 mm data. The results (shown in Figure C.4) were found to be approximated well by:

$$\dot{Q}_{Pump} = 0.1357\dot{V}_{w,Pri}^{3} + 0.2285\dot{V}_{w,Pri}^{2} + 3.7612\dot{V}_{w,Pri} \tag{C.3}$$

Again the R^2 value was found to be 0.997.
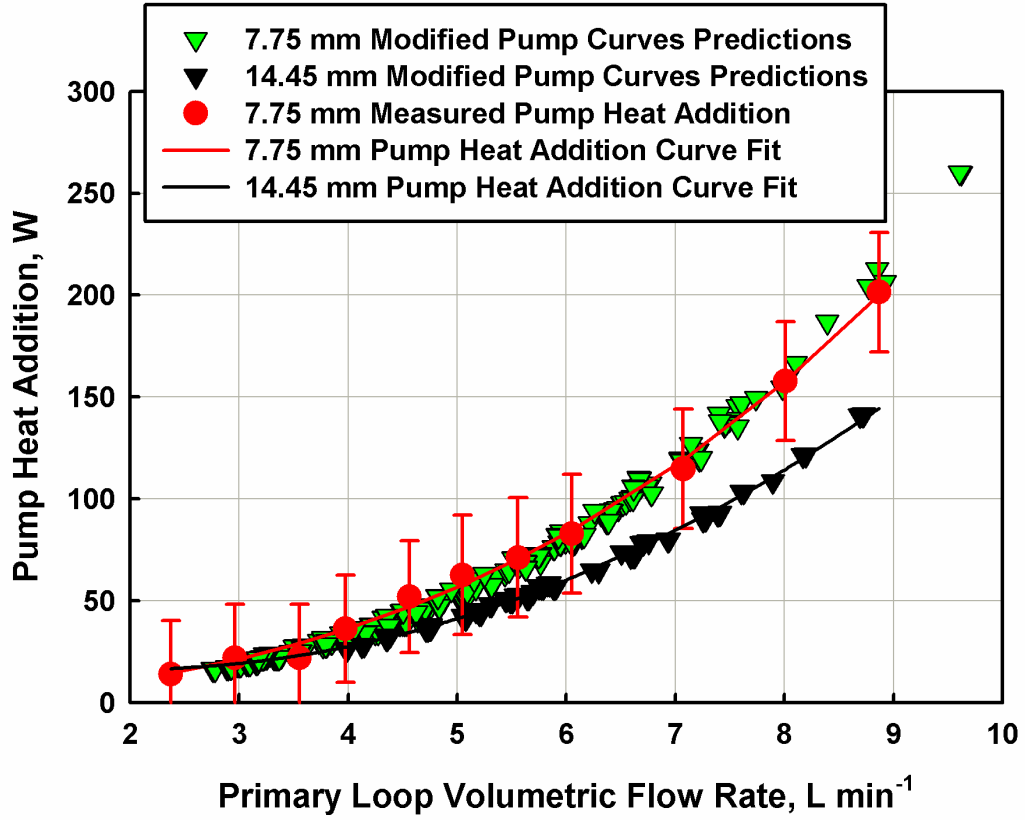
Figure C.5.Pump heat addition curve fits with modified pump curve predictions

APPENDIX D: REPRESENTATIVE DATA POINT UNCERTAINTY PROPAGATION

Uncertainty analyses were conducted using the built-in uncertainty propagation feature in the Engineering Equation Solver platform. A sample uncertainty calculation is presented here for the representative frictional pressure drop and heat transfer coefficient data point described in Chapter 4 and Appendix E. The representative data point is for the nominal case of 45% R245fa / 55% n-Pentane by mass, $G = 507$ kg m^{-2} s^{-1}, $P_{AVG} = 405.9$ kPa and $q_{AVG} = 0.39$ and was taken on January 21st, 2012.

Uncertainty in the test section heat duty

The heat duty in the test section is measured using the thermal amplification technique. Using this method, the uncertainty in the secondary loop heat duty, ambient heat losses from the primary loop, and pump heat addition all contribute to the uncertainties in the test section heat duty. The ambient heat loss from the primary loop and the pump heat addition are both assigned a conservative uncertainty of 50%. The uncertainties in the ambient loss and pump heat addition are calculated to be 9.2 and 18.4 W, respectively. The uncertainty in the secondary loop heat duty is a function of the measured secondary loop inlet and outlet temperatures and secondary loop flowrate.

$$U_{\dot{Q}_{sec}} = \sqrt{\left(\frac{\partial \dot{Q}_{sec}}{\partial \dot{m}_{sec}}\right)^2 U_{\dot{m}_{sec}}^2 + \left(\frac{\partial \dot{Q}_{sec}}{\partial i_{w,sec,in}}\right)^2 U_{i_{w,sec,in}}^2 + \left(\frac{\partial \dot{Q}_{sec}}{\partial i_{w,sec,out}}\right)^2 U_{i_{w,sec,out}}^2} \qquad (D.1)$$

The uncertainty in secondary mass flowrate is determined from the instrument uncertainty of 0.15% reading (0.0000054 kg s^{-1}). The uncertainties in inlet and outlet enthalpies are calculated as follows:

$$U_{i_{w,sec,in}}^2 = \left(\frac{\partial i_{w,sec,in}}{\partial T_{w,sec,in}}\right)^2 U_{T_{w,sec,in}}^2 = \left(C_{P_{w,sec,in}} U_{T_{w,sec,in}}\right)^2 = \left(4.20\,\text{kJ}\,\text{kg}^{-1}\,\text{K}^{-1} \cdot 0.3\,\text{K}\right)^2$$
$$= \left(1.26\,\text{kJ}\,\text{kg}^{-1}\right)^2$$

(D.2)

$$U_{i_{w,sec,out}}^2 = \left(\frac{\partial i_{w,sec,out}}{\partial T_{w,sec,out}}\right)^2 U_{T_{w,sec,out}}^2 = \left(C_{P_{w,sec,out}} U_{T_{w,sec,out}}\right)^2 = \left(4.18\,\text{kJ}\,\text{kg}^{-1}\,\text{K}^{-1} \cdot 0.3\,\text{K}\right)^2$$
$$= \left(1.25\,\text{kJ}\,\text{kg}^{-1}\right)^2$$

(D.3)

Differentiating $\dot{Q}_{sec} = \dot{m}_{sec}\left(i_{w,sec,out} - i_{w,sec,in}\right)$ with respect to the respective terms in Equation (D.1) yields:

$$U_{\dot{Q}_{sec}} = \sqrt{\left(i_{w,sec,out} - i_{w,sec,in}\right)^2 U_{\dot{m}_{sec}}^2 + \left(\dot{m}_{sec}\right)^2 U_{i_{w,sec,in}}^2 + \left(\dot{m}_{sec}\right)^2 U_{i_{w,sec,out}}^2}$$

(D.4)

Substituting the uncertainty values into Eq. (D.4) yields:

$$U_{\dot{Q}_{sec}} = \sqrt{\begin{array}{l}\left(197.1\,\text{kJ}\,\text{kg}^{-1}\,\text{K}^{-1} - 31.4\,\text{kJ}\,\text{kg}^{-1}\,\text{K}^{-1}\right)^2 \left(5.4\times10^{-6}\,\text{kg}\,\text{s}^{-1}\right)^2 \\ + \left(3.60\times10^{-3}\,\text{kg}\,\text{s}^{-1}\right)^2 \left(1.26\,\text{kJ}\,\text{kg}^{-1}\right)^2 \\ + \left(3.60\times10^{-3}\,\text{kg}\,\text{s}^{-1}\right)^2 \left(1.25\,\text{kJ}\,\text{kg}^{-1}\right)^2\end{array}}$$
$$= \sqrt{8.0\times10^{-7}\,\text{kW} + 2\left(2.1\times10^{-5}\,\text{kW}\right)} = 6.5\,\text{W}$$

(D.5)

The measured heat duty in the secondary loop is 595.5 W. Thus, this uncertainty of 6.5 W is 1.1% of the measured duty.

The uncertainty in the test section heat duty is calculated as follows:

$$U_{\dot{Q}_{\text{Test}}} = \sqrt{U_{\dot{Q}_{\text{sec}}}^2 + U_{\dot{Q}_{\text{Pump}}}^2 + U_{\dot{Q}_{\text{Amb Loss}}}^2}$$

$$= \sqrt{(6.5\,\text{W})^2 + (18.4\,\text{W})^2 + (9.2\,\text{W})^2} \qquad \text{(D.6)}$$

$$= 21.5\,\text{W}$$

The test section duty is calculated to be 577.1 W. Thus the uncertainty in the test section heat duty is 4% of the measured heat duty. In this case, the pump heat addition has the largest contribution to the uncertainty, followed by the ambient losses.

Uncertainty in the heat transfer coefficient

The uncertainty in heat transfer coefficient is a function of test section heat duty, LMTD, and thermal resistances of the wall and the annulus. The uncertainties in heat transfer area, thermal resistance of the wall, and thermal resistance of the tee fittings are not considered in this analysis but are included in the EES uncertainty analysis with no change in the calculated uncertainties. The test section tube is made of copper, which presents a low thermal resistance. Here, the tube wall presents a thermal resistance of 0.00015 K W^{-1}, while the test condensing fluid and coolant water present thermal resistances of 0.01745 K W^{-1} and 0.0031 K W^{-1}, respectively. The thermal resistance associated with the tee fittings is high (1.67 K W^{-1}), but in this case, the total heat transfer in the tee sections is small (2.1 W total). The uncertainty in *UA* is calculated first for clarity. The *UA* is calculated using Equation 4.28 and is a function of the measure heat duty and the LMTD. The uncertainty in the *UA* is calculated as follows:

$$U_{UA} = \sqrt{\left(\frac{\partial UA}{\partial \dot{Q}_{\text{Test}}}\right)^2 U_{\dot{Q}_{\text{Test}}}^2 + \left(\frac{\partial UA}{\partial \text{LMTD}}\right)^2 U_{\text{LMTD}}^2} \qquad \text{(D.7)}$$

The uncertainty in the test section duty was calculated in the previous section to be 21.5 W. The uncertainty in the LMTD is calculated as follows:

$$U_{\text{LMTD}} = \sqrt{\left(\frac{\partial \text{LMTD}}{\partial T_{\text{f,test,in}}}\right)^2 U_{T_f}^2 + \left(\frac{\partial \text{LMTD}}{\partial T_{\text{f,test,out}}}\right)^2 U_{T_f}^2 + \left(\frac{\partial \text{LMTD}}{\partial T_{\text{w,test,in}}}\right)^2 U_T^2 + \left(\frac{\partial \text{LMTD}}{\partial T_{\text{w,test,in}}}\right)^2 U_T^2} \quad (D.8)$$

Differentiating the LMTD for the respective terms using $\Delta T_1 = \left(T_{\text{f,Test,in}} - T_{\text{w,Test,out}}\right)$ and $\Delta T_2 = \left(T_{\text{f,Test,out}} - T_{\text{w,Test,in}}\right)$ to simplify Equation 4.27:

$$\frac{\partial \text{LMTD}}{\partial T_{\text{f,test,in}}} = \frac{1}{\ln\left(\frac{\Delta T_1}{\Delta T_2}\right)} - \frac{\Delta T_1 - \Delta T_2}{\ln\left(\frac{\Delta T_1}{\Delta T_2}\right)^2} \frac{1}{\Delta T_1} = 0.49$$

$$\frac{\partial \text{LMTD}}{\partial T_{\text{f,test,out}}} = \frac{-1}{\ln\left(\frac{\Delta T_1}{\Delta T_2}\right)} + \frac{\Delta T_1 - \Delta T_2}{\ln\left(\frac{\Delta T_1}{\Delta T_2}\right)^2} \frac{1}{\Delta T_2} = 0.51$$

$$\frac{\partial \text{LMTD}}{\partial T_{\text{w,pri,test,in}}} = \frac{-1}{\ln\left(\frac{\Delta T_1}{\Delta T_2}\right)} - \frac{\Delta T_1 - \Delta T_2}{\ln\left(\frac{\Delta T_1}{\Delta T_2}\right)^2} \frac{1}{\Delta T_2} = -0.51 \quad (D.9)$$

$$\frac{\partial \text{LMTD}}{\partial T_{\text{w,pri,test,out}}} = \frac{1}{\ln\left(\frac{\Delta T_1}{\Delta T_2}\right)} + \frac{\Delta T_1 - \Delta T_2}{\ln\left(\frac{\Delta T_1}{\Delta T_2}\right)^2} \frac{1}{\Delta T_1} = -0.49$$

The coolant temperatures are measured directly and have an uncertainty of 0.3 K. The uncertainty in working fluid temperatures is predominantly a function of pressure and concentration. The uncertainty in the fluid temperature is:

$$U_T(x, P) = \sqrt{\left(\frac{\partial T}{\partial P}\right)^2 U_P^2 + \left(\frac{\partial T}{\partial x}\right)^2 U_x^2} \quad (D.10)$$

The differentials are approximated as follows:

413

$$U_T(x,P) = \sqrt{\left(\frac{T[P+U_P]-T[P-U_P]}{2U_P}\right)^2 U_P^2 + \left(\frac{T[x+U_x]-T[x-U_x]}{2U_x}\right)^2 U_x^2} \quad \text{(D.11)}$$

The uncertainty in the measured pressure is 5.17 kPa, while the uncertainty in measured concentration is 0.009. Therefore the resulting uncertainty is:

$$
\begin{aligned}
U_T &= \sqrt{\left(\frac{T[P+U_P]-T[P-U_P]}{2U_P}\right)^2 U_P^2 + \left(\frac{T[x+U_x]-T[x-U_x]}{2U_x}\right)^2 U_x^2} \\
&= \sqrt{\left(\frac{60.4°C-59.5°C}{2\cdot 5.17\,\text{kPa}}\right)^2 5.17\,\text{kPa}^2 + \left(\frac{59.1°C-60.4°C}{2\cdot 0.009}\right)^2 0.009^2} \\
&= 0.7\,\text{K}
\end{aligned}
\quad \text{(D.12)}
$$

Substituting into Equation (D.8), the resulting uncertainty in LMTD is:

$$
\begin{aligned}
U_{\text{LMTD}} &= \sqrt{(0.49\cdot 0.7)^2 + (0.51\cdot 0.7)^2 + (-0.51\cdot 0.3)^2 + (-0.49\cdot 0.3)^2} \\
&= 0.6\,\text{K}
\end{aligned}
\quad \text{(D.13)}
$$

Differentiating UA in the respective terms in Equation (D.7) and substituting, the uncertainty in UA is calculated as follows:

$$
\begin{aligned}
U_{UA} &= \sqrt{\left(\frac{1}{\text{LMTD}}\right)^2 U_{\dot{Q}_{\text{Test}}}^2 + \left(\frac{-\dot{Q}_{\text{Test}}}{\text{LMTD}^2}\right)^2 U_{\text{LMTD}}^2} \\
&= \sqrt{\left(\frac{1}{11.9\,\text{K}}21.5\,\text{W}\right)^2 + \left(\frac{-577.1\,\text{W}}{(11.9\,\text{K})^2}0.5\,\text{K}\right)^2} \\
&= 2.9\,\text{W}\,\text{K}^{-1}
\end{aligned}
\quad \text{(D.14)}
$$

With a calculated UA of 48.3 W K^{-1}, the uncertainty in UA is 6%.

After calculating the UA and associated uncertainty in UA, the uncertainty in heat transfer coefficient becomes a function of UA and annulus side heat transfer coefficient:

414

$$U_{UA} = \sqrt{\left(\frac{\partial h_{\mathrm{f}}}{\partial UA}\right)^2 U_{UA}^2 + \left(\frac{\partial h_{\mathrm{f}}}{\partial h_{\mathrm{w,Annulus}}}\right)^2 U_{h_{\mathrm{w,Annulus}}}^2} \qquad \text{(D.15)}$$

The uncertainty in UA is calculated above, and a 25% uncertainty (5070 W m^{-2} K^{-1}) is applied to the annulus heat transfer coefficient, which is determined from correlations in the literature. Differentiating the respective terms yields:

$$\frac{\partial h_{\mathrm{f}}}{\partial UA} = \frac{1}{A_{\mathrm{f}}} \frac{1}{(UA)^2} \left[\frac{1}{UA} - \frac{1}{h_{\mathrm{w,annulus}} A_{\mathrm{w}}} - R_{\mathrm{wall}} \right]^{-2} = 104.5\,\mathrm{m}^{-2}$$

$$\frac{\partial h_{\mathrm{f}}}{\partial h_{\mathrm{w,Annulus}}} = -\frac{A_{\mathrm{w}}}{A_{\mathrm{f}}} \frac{1}{\left(h_{\mathrm{w,annulus}} A_{\mathrm{w}}\right)^2} \left[\frac{1}{UA} - \frac{1}{h_{\mathrm{w,annulus}} A_{\mathrm{w}}} - R_{\mathrm{wall}} \right]^{-2} = 0.038$$

$$\qquad \text{(D.16)}$$

Substituting into Equation (D.15), the uncertainty in the heat transfer coefficient is calculated as follows:

$$U_{h_{\mathrm{f}}} = \sqrt{(104.5 \cdot 2.9)^2 + (0.038 \cdot 5070)^2} = 355\,\mathrm{W\,m}^{-2}\,\mathrm{K}^{-1} \qquad \text{(D.17)}$$

With a calculated heat transfer coefficient of 4231 W m^{-2} K^{-1}, the uncertainty in the heat transfer coefficient is 8.4%.

Uncertainty in the frictional pressure gradient

The frictional pressure gradient is deduced from the measured pressure drop across the test section and deceleration of the two-phase flow due to condensation using Equations (4.45) and (4.46). A 50% uncertainty (0.5 kPa in this case) is applied to the deceleration term. The measured uncertainty for the larger range pressure transducer is 0.1 kPa. The resulting uncertainty in frictional pressure gradient is:

$$U_{\nabla P_{\mathrm{f}}} = \sqrt{\left(\frac{\partial \nabla P_{\mathrm{f}}}{\partial \Delta P_{\mathrm{measured}}}\right)^2 U_{\Delta P_{\mathrm{measured}}}^2 + \left(\frac{\partial \nabla P}{\partial \Delta P_{\mathrm{Decel}}}\right)^2 U_{\Delta P_{\mathrm{Decel}}}^2} \qquad \text{(D.18)}$$

Differentiating with respect to each term and substituting the values in yields:

$$\begin{aligned}
U_{\nabla P_{\mathrm{f}}} &= \frac{1}{L_{\Delta P}} \sqrt{U_{\Delta P_{\mathrm{measured}}}^2 + U_{\Delta P_{\mathrm{Decel}}}^2} \\
&= \frac{1}{0.75\,\mathrm{m}} \sqrt{0.1\,\mathrm{kPa}^2 + 0.5\,\mathrm{kPa}^2} \qquad \text{(D.19)} \\
&= \frac{0.55\,\mathrm{kPa}}{0.75\,\mathrm{m}} = 0.7\,\mathrm{kPa\,m^{-1}}
\end{aligned}$$

The measured frictional pressure gradient is 14.6 kPa m^{-1}. Thus, this uncertainty is 5% of the measured value. The deceleration term is 1.1 kPa or 11% of the measured value. The uncertainty in the deceleration term is the largest contributor to the uncertainty.

APPENDIX E: REPRESENTATITVE DATA POINT SAMPLE CALCULATIONS

Table E.1. Coolant loop measurements

Pre-Condenser	
$T_{w,Pre,in}$ (°C)	8.6
$T_{w,Pre,out}$ (°C)	75.5
$\dot{V}_{w,Pre}$ (L min^{-1})	1.13
Post Condenser	
$T_{w,Post,in}$ (°C)	7.3
$T_{w,Post,out}$ (°C)	40.2
$\dot{V}_{w,Post}$ (L min^{-1})	1.60
Secondary Loop	
$T_{w,Sec,in}$ (°C)	7.4
$T_{w,Sec,out}$ (°C)	47.0
$\dot{m}_{w,Sec}$ (kg s^{-1})	0.0036
Primary Loop	
$T_{w,Test,in}$ (°C)	45.6
$T_{w,Test,out}$ (°C)	47.8
$\dot{V}_{w,Pri}$ (L min^{-1})	4.02
$P_{w,Pri}$ (kPa)	405.8
$\Delta P_{w,Pri}$ (kPa)	83.0
Assumed Variables	
P_{Amb} (kPa)	101
ε_{ins}	0.85
Misc. Measurements	
$P_{w,\,pre\text{-}post}$ (kPa)	225.2
T_{Amb} (°C)	24.9

Table E.2. Mixture loop measurements

Mixture Loop	
$P_{f,Pre,in}$ (kPa)	449.4
$P_{f,Test,in}$ (kPa)	411.2
$P_{f,Test,out}$ (kPa)	400.6
$P_{f,Post,out}$ (kPa)	392.7
$\Delta P_{f,Test}$ (kPa)	9.80
$T_{f,Pre,in}$ (°C)	103.7
$T_{f,Test,in,meas}$ (°C)	59.5
$T_{f,Test,out,meas}$ (°C)	57.2
$T_{f,Post,out}$ (°C)	12.7
$\Delta T_{f,Pre,in,Sup}$ (K)	29.4
$\Delta T_{f,Test,in}$ (K)	-0.5
$\Delta T_{f,Test,out}$ (K)	-0.1
$\Delta T_{f,Post,out,Sub}$ (K)	40.4
$\dot{m}_f$ (kg s^{-1})	0.0239
Data Point	
$x_{f,R245fa}$	0.454
$x_{f,n\text{-pentane}}$	0.546
$P_{f,Test,Avg}$ (kPa)	405.9
$P_{f,crit}$ (kPa)	3713.3
P_r	0.11
G (kg m^{-2} s^{-1})	507.4
$q_{f,Test,Avg}$	0.39
Experiment Date	1/21/2012

Table E.3. R245fa / *n*-pentane data point data reduction sample calculation

Heat Transfer Sample Calculations: R245fa / *n*-pentane Mixture; 1/21/2012; Run 3		
Inputs	**Equations**	**Results**
Heat Loss in Pre-Condenser		
$P_{\text{Amb}} = 101\,\text{kPa}$ $T_{\text{Amb}} = 24.9°\text{C}$	$R_{\text{wall}} = \dfrac{\ln\left(D_{\text{Pre,o}} / D_{\text{Pre,i}}\right)}{2\pi k_{\text{wall}} L_{\text{Pre}}}$	$R_{\text{wall}} = 0.0022\,\text{K W}^{-1}$
$T_{\text{w,Pre,in}} = 8.6°\text{C}$ $T_{\text{w,Pre,out}} = 75.5°\text{C}$	$R_{\text{ins}} = \dfrac{\ln\left(D_{\text{ins,o}} / D_{\text{Pre,o}}\right)}{2\pi k_{\text{ins}} L_{\text{Pre}}}$	$R_{\text{ins}} = 7.1\,\text{K W}^{-1}$
$D_{\text{Pre,o}} = 38.1\,\text{mm}$ $D_{\text{Pre,i}} = 34.8\,\text{mm}$ $D_{\text{ins,o}} = 100\,\text{mm}$	$R_{\text{rad}} =$ $\dfrac{1}{\varepsilon_{\text{ins}} \pi D_{\text{ins,o}} L_{\text{Pre}} \sigma_{\text{SB}} \left(T_{\text{ins}}^{2} + T_{\text{amb}}^{2}\right)\left(T_{\text{ins}} + T_{\text{amb}}\right)}$	$R_{\text{rad}} = 1.2\,\text{K W}^{-1}$ $T_{\text{ins}} = 26.8°\text{C}$ $\left(\text{Solved Iteratively}\right)$
$L_{\text{Pre}} = 0.508\,\text{m}$ $k_{\text{wall}} = 13.07\,\text{W m}^{-1}\,\text{K}^{-1}$	$T_{\text{film}} = \left(T_{\text{ins}} + T_{\text{Amb}}\right)/2$	$T_{\text{film}} = 25.8°\text{C}$
$k_{\text{ins}} = 0.043\,\text{W m}^{-1}\,\text{K}^{-1}$ $\varepsilon_{\text{ins}} = 0.85$	$T_{\text{wall,i}} = \left(T_{\text{w,Pre,in}} + T_{\text{w,Pre,out}}\right)/2$	$T_{\text{wall,i}}* = 42.0°\text{C}$ *Neglecting internal fluid resistance
$\sigma_{\text{SB}} = 5.67 \times 10^{-8}$ $\text{W m}^{-2}\text{K}^{-4}$ $g = 9.81\,\text{m s}^{-2}$	Air Properties $f(P = 101\,\text{kPa}, T_{\text{film}} = 25.8°\text{C})$	$\alpha = 2.19 \times 10^{-5}\,\text{m}^{2}\,s^{-1}$ $\beta = 0.00335\,\text{K}^{-1}$ $k = 0.0259\,\text{W m}^{-1}\,\text{K}^{-1}$ $\nu = 1.58 \times 10^{-5}\,\text{m}^{2}\,s^{-1}$ $\text{Pr} = 0.72$ $\rho = 1.18\,\text{kg m}^{-3}$
	$Ra_{\text{air}} = \dfrac{g\beta\left(T_{\text{ins}} - T_{\text{Amb}}\right)\left(D_{\text{ins,o}}\right)^{3}}{\nu\alpha}$	$Ra_{\text{air}} = 173,240$
	$Nu_{\text{D}} =$ $\left(0.60 + 0.387\dfrac{Ra_{\text{air}}^{1/6}}{\left(1 + \left(0.559 / \text{Pr}\right)^{9/16}\right)^{8/27}}\right)^{2}$	$Nu_{\text{D}} = 9.0$ (Churchill and Chu, 1975)
	$h_{\text{nat,conv}} = \dfrac{k_{\text{air}}}{D_{\text{ins,o}}} Nu_{\text{D}}$	$h_{\text{nat,conv}} = 2.33\,\text{W m}^{-2}\text{K}^{-1}$
	$R_{\text{conv}} = \dfrac{1}{h_{\text{nat,conv}} \pi D_{\text{ins,o}} L_{\text{Pre}}}$	$R_{\text{conv}} = 2.7\,\text{K W}^{-1}$

Table E.3. R245fa / *n-pentane* data point data reduction sample calculation – Cont.

Heat Transfer Sample Calculations: R245fa / *n*-pentane Mixture; 1/21/2012; Run 3		
Inputs	**Equations**	**Results**
	$$\dot{Q}_{loss} = \frac{T_{wall,i} - T_{amb}}{R_{wall} + R_{ins} + \frac{R_{conv}R_{rad}}{(R_{conv} + R_{rad})}}$$	$\dot{Q}_{loss,Pre} = 2.2\,\text{W}$
Heat Loss in Line from Pre-Condenser to Test Section		
$P_{Amb} = 101\,\text{kPa}$ $T_{Amb} = 24.9°\text{C}$ $T_{f,Pre,out} = 60.8°\text{C}$ $T_{f,Test,in} = 59.5°\text{C}$ $D_{Tube,o} = 12.7\,\text{mm}$ $D_{Tube,i} = 10.92\,\text{mm}$ $D_{ins,o} = 100\,\text{mm}$ $L_{Pre\,to\,Test} = 0.615\,\text{m}$ $k_{wall} = 14.0\,\text{W m}^{-1}\,\text{K}^{-1}$ $k_{ins} = 0.043\,\text{W m}^{-1}\,\text{K}^{-1}$ $\varepsilon_{ins} = 0.85$ $\sigma_{SB} = 5.67 \times 10^{-8}$ $\quad\quad \text{W m}^{-2}\text{K}^{-4}$ $g = 9.81\,\text{m s}^{-2}$	$R_{wall} = \dfrac{\ln(D_{Tube,o}\,/\,D_{Tube,i})}{2\pi k_{wall} L_{Pre\,to\,Test}}$	$R_{wall} = 0.0028\,\text{K W}^{-1}$
	$R_{ins} = \dfrac{\ln(D_{ins,o}\,/\,D_{Tube,o})}{2\pi k_{ins} L_{Pre\,to\,Test}}$	$R_{ins} = 12.4\,\text{K W}^{-1}$
	$R_{rad} = \dfrac{1}{\begin{bmatrix} \varepsilon_{ins} \pi D_{ins,o} L_{Pre\,to\,Test} \sigma_{SB} \\ \cdot (T_{ins}^2 + T_{Amb}^2)(T_{ins} + T_{Amb}) \end{bmatrix}}$	$R_{rad} = 1.0\,\text{K W}^{-1}$ $T_{ins} = 26.8°\text{C}$ $(\text{Solved Iteratively})$
	$T_{film} = (T_{ins} + T_{Amb})/2$	$T_{film} = 25.9°\text{C}$
	$T_{wall,i} = (T_{f,Pre,out} + T_{f,Test,in})/2$	$T_{wall,i}* = 60.2°\text{C}$ *Neglecting internal fluid resistance
	Air Properties $f(P = 101\,\text{kPa}, T_{film} = 25.9°\text{C})$	$\alpha = 2.19 \times 10^{-5}\,\text{m}^2\,s^{-1}$ $\beta = 0.00334\,\text{K}^{-1}$ $k = 0.0259\,\text{W m}^{-1}\,\text{K}^{-1}$ $\nu = 1.58 \times 10^{-5}\,\text{m}^2\,\text{s}^{-1}$ $\text{Pr} = 0.72$ $\rho = 1.18\,\text{kg m}^{-3}$
	$Ra_{air} = \dfrac{g\beta(T_{ins} - T_{Amb})(D_{ins,o})^3}{\nu\alpha}$	$Ra_{air} = 176{,}547$
	$Nu_D = \left(0.60 + 0.387\,\dfrac{Ra_{air}^{1/6}}{\left(1 + (0.559/\text{Pr})^{9/16}\right)^{8/27}}\right)^2$	$Nu_D = 9.05$ (Churchill and Chu, 1975)

Table E.3. R245fa / *n-pentane* data point data reduction sample calculation – Cont.

Heat Transfer Sample Calculations: R245fa / *n*-pentane Mixture; 1/21/2012; Run 3		
Inputs	**Equations**	**Results**
	$h_{\text{nat,conv}} = \dfrac{k_{\text{air}}}{D_{\text{ins,o}}} Nu_D$	$h_{\text{nat,conv}} = 2.35\,\text{W m}^{-2}\,\text{K}^{-1}$
	$R_{\text{conv}} = \dfrac{1}{h_{\text{nat,conv}} \pi D_{\text{ins,o}} L_{\text{Pre to Test}}}$	$R_{\text{conv}} = 3.0\,\text{K W}^{-1}$
	$\dot{Q}_{\text{loss}} = \dfrac{T_{\text{wall,i}} - T_{\text{Amb}}}{R_{\text{wall}} + R_{\text{ins}} + \dfrac{R_{\text{conv}} R_{\text{rad}}}{\left(R_{\text{conv}} + R_{\text{rad}}\right)}}$	$\dot{Q}_{\text{loss,Pre to Test}} = 2.7\,\text{W}$
Heat Loss in Post-Condenser 2		
$P_{\text{Amb}} = 101\,\text{kPa}$ $T_{\text{Amb}} = 24.9°\text{C}$ $T_{\text{w,Post,2,in}} = 7.3°\text{C}$ $T_{\text{w,Post,2,out}} = 13.0°\text{C}$	$R_{\text{wall}} = \dfrac{\ln\left(D_{\text{Post,2,o}} / D_{\text{Post,2,i}}\right)}{2\pi k_{\text{wall}} L_{\text{Post,2}}}$	$R_{\text{wall}} = 0.0022\,\text{K W}^{-1}$
$D_{\text{Post,2,o}} = 38.1\,\text{mm}$ $D_{\text{Post,2,i}} = 34.8\,\text{mm}$	$R_{\text{ins}} = \dfrac{\ln\left(D_{\text{ins,o}} / D_{\text{Post,2,o}}\right)}{2\pi k_{\text{ins}} L_{\text{Post,2}}}$	$R_{\text{ins}} = 7.1\,\text{K W}^{-1}$
$D_{\text{ins,o}} = 100\,\text{mm}$ $L_{\text{Post,2}} = 0.508\,\text{m}$ $k_{\text{wall}} = 13.05\,\text{W m}^{-1}\,\text{K}^{-1}$	$R_{\text{rad}} = \dfrac{1}{\left[\begin{array}{c} \varepsilon_{\text{ins}} \pi D_{\text{ins,o}} L_{\text{Post,2}} \sigma_{\text{SB}} \\ \cdot\left(T_{\text{ins}}^{2} + T_{\text{Amb}}^{2}\right)\left(T_{\text{ins}} + T_{\text{Amb}}\right) \end{array}\right]}$	$R_{\text{rad}} = 1.2\,\text{K W}^{-1}$ $T_{\text{ins}} = 23.3°\text{C}$ (Solved Iteratively)
$k_{\text{ins}} = 0.043\,\text{W m}^{-1}\,\text{K}^{-1}$	$T_{\text{film}} = \left(T_{\text{ins}} + T_{\text{Amb}}\right)/2$	$T_{\text{film}} = 24.1°\text{C}$
$\varepsilon_{\text{ins}} = 0.85$	$T_{\text{wall,i}} = \left(T_{\text{w,Post,2,in}} + T_{\text{w,Post,2,out}}\right)/2$	$T_{\text{wall,i}}* = 10.2°\text{C}$ *Neglecting internal fluid resistance
$\sigma_{\text{SB}} = 5.67\times10^{-8}$ $\quad\quad\text{W m}^{-2}\text{K}^{-4}$ $g = 9.81\,\text{m s}^{-2}$	Air Properties $f(P = 101\,\text{kPa}, T_{\text{film}} = 24.1°\text{C})$	$\alpha = 2.17\times10^{-5}\,\text{m}^2\,s^{-1}$ $\beta = 0.00336\,\text{K}^{-1}$ $k = 0.0258\,\text{W m}^{-1}\,\text{K}^{-1}$ $\nu = 1.56\times10^{-5}\,\text{m}^2\,s^{-1}$ $\text{Pr} = 0.72$ $\rho = 1.18\,\text{kg m}^{-3}$
	$Ra_{\text{air}} = \dfrac{g\beta\left(T_{\text{ins}} - T_{\text{Amb}}\right)\left(D_{\text{ins,o}}\right)^{3}}{\nu\alpha}$	$Ra_{\text{air}} = 156,507$

Table E.3. R245fa / *n-pentane* data point data reduction sample calculation – Cont.

Heat Transfer Sample Calculations: R245fa / *n*-pentane Mixture; 1/21/2012; Run 3		
Inputs	**Equations**	**Results**
	$Nu_D = $ $$\left(0.60 + 0.387 \frac{Ra_{air}^{1/6}}{\left(1+\left(0.559/\Pr\right)^{9/16}\right)^{8/27}}\right)^2$$	$Nu_D = 8.77$ (Churchill and Chu, 1975)
	$h_{nat,conv} = \dfrac{k_{air}}{D_{ins,o}} Nu_D$	$h_{nat,conv} = 2.26\,\text{W m}^{-2}\text{K}^{-1}$
	$R_{conv} = \dfrac{1}{h_{nat,conv}\pi D_{ins,o}L_{Post,2}}$	$R_{conv} = 2.8\,\text{K W}^{-1}$
	$\dot{Q}_{loss} = \dfrac{T_{wall,i} - T_{Amb}}{R_{wall} + R_{ins} + \dfrac{R_{conv}R_{rad}}{\left(R_{conv}+R_{rad}\right)}}$	$\dot{Q}_{loss,Post,2} = -1.9\,\text{W}$ Gain from ambient Coolant T below T_{amb}
Heat Loss in Post-Condenser 1		
$P_{Amb} = 101\,\text{kPa}$ $T_{Amb} = 24.9°\text{C}$ $T_{w,Post,2,in} = 13.0°\text{C}$ $T_{w,Post,2,out} = 40.2°\text{C}$ $D_{Post,1,o} = 38.1\,\text{mm}$ $D_{Post,1,i} = 34.8\,\text{mm}$ $D_{ins,o} = 100\,\text{mm}$ $L_{Post,1} = 0.508\,\text{m}$ $k_{wall} = 13.15\,\text{W m}^{-1}\text{K}^{-1}$ $k_{ins} = 0.043\,\text{W m}^{-1}\text{K}^{-1}$ $\varepsilon_{ins} = 0.85$ $\sigma_{SB} = 5.67\times10^{-8}$ $\quad\quad\text{W m}^{-2}\text{K}^{-4}$ $g = 9.81\,\text{m s}^{-2}$	$R_{wall} = \dfrac{\ln\left(D_{Post,1,o}/D_{Post,1,i}\right)}{2\pi k_{wall}L_{Post,1}}$	$R_{wall} = 0.0022\,\text{K W}^{-1}$
	$R_{ins} = \dfrac{\ln\left(D_{ins,o}/D_{Post,1,o}\right)}{2\pi k_{ins}L_{Post,1}}$	$R_{ins} = 7.1\,\text{K W}^{-1}$
	$R_{rad} = \dfrac{1}{\left[\begin{array}{c}\varepsilon_{ins}\pi D_{ins,o}L_{Post,1}\sigma_{SB}\\ \cdot\left(\text{T}_{ins}^{\ 2}+\text{T}_{Amb}^{\ 2}\right)\left(\text{T}_{ins}+\text{T}_{Amb}\right)\end{array}\right]}$	$R_{rad} = 1.2\,\text{K W}^{-1}$ $T_{ins} = 25.1°\text{C}$ $\left(\text{Solved Iteratively}\right)$
	$T_{film} = \left(T_{ins}+T_{Amb}\right)/2$	$T_{film} = 25.0°\text{C}$
	$T_{wall,i} = \left(T_{w,Post,1,in}+T_{w,Post,1,out}\right)/2$	$T_{wall,i}{}^* = 26.6°\text{C}$ *Neglecting internal fluid resistance
	Air Properties $f\left(P = 101\,\text{kPa}, T_{film} = 25.0°\text{C}\right)$	$\alpha = 2.18\times10^{-5}\,\text{m}^2\,s^{-1}$ $\beta = 0.00335\,\text{K}^{-1}$ $k = 0.0259\,\text{W m}^{-1}\,\text{K}^{-1}$ $\nu = 1.57\times10^{-5}\,\text{m}^2\,s^{-1}$ $\Pr = 0.72$ $\rho = 1.18\,\text{kg m}^{-3}$

Table E.3. R245fa / *n-pentane* data point data reduction sample calculation – Cont.

Heat Transfer Sample Calculations: R245fa / *n*-pentane Mixture; 1/21/2012; Run 3		
Inputs	**Equations**	**Results**
	$Ra_{\text{air}} = \dfrac{g\beta\left(T_{\text{ins}} - T_{\text{amb}}\right)\left(D_{\text{ins,o}}\right)^3}{\nu\alpha}$	$Ra_{\text{air}} = 19619$
	$Nu_{\text{D}} =$ $\left(0.60 + 0.387\,\dfrac{Ra_{\text{air}}^{1/6}}{\left(1 + \left(0.559/\Pr\right)^{9/16}\right)^{8/27}}\right)^2$	$Nu_{\text{D}} = 5.15$ (Churchill and Chu, 1975)
	$h_{\text{nat,conv}} = \dfrac{k_{\text{air}}}{D_{\text{ins,o}}}Nu_{\text{D}}$	$h_{\text{nat,conv}} = 1.33\,\text{W m}^{-2}\,\text{K}^{-1}$
	$R_{\text{conv}} = \dfrac{1}{h_{\text{nat,conv}}\pi D_{\text{ins,o}}L_{\text{Post,1}}}$	$R_{\text{conv}} = 4.7\,\text{K W}^{-1}$
	$\dot{Q}_{\text{loss}} = \dfrac{T_{\text{wall,i}} - T_{\text{amb}}}{R_{\text{wall}} + R_{\text{ins}} + \dfrac{R_{\text{conv}}R_{\text{rad}}}{\left(R_{\text{conv}} + R_{\text{rad}}\right)}}$	$\dot{Q}_{\text{loss,Post,1}} = 0.2\,\text{W}$
Heat Loss in Fluid Line from Post-Condenser 1 to Post-Condenser 2		
$P_{\text{Amb}} = 101\,\text{kPa}$ $T_{\text{Amb}} = 24.9°\text{C}$ $T_{\text{f,Post,1,out}} = 26.5°\text{C}$ $T_{\text{f,Post,2,in}} = 26.5°\text{C}$ $D_{\text{Tube,o}} = 12.7\,\text{mm}$ $D_{\text{Tube,i}} = 10.92\,\text{mm}$ $D_{\text{ins,o}} = 100\,\text{mm}$ $L_{\text{Post 1 to 2}} = 0.52\,\text{m}$ $k_{\text{wall}} = 13.39\,\text{W m}^{-1}\,\text{K}^{-1}$ $k_{\text{ins}} = 0.043\,\text{W m}^{-1}\,\text{K}^{-1}$ $\varepsilon_{\text{ins}} = 0.85$ $\sigma_{\text{SB}} = 5.67\times10^{-8}$ $\quad\quad \text{W m}^{-2}\text{K}^{-4}$ $g = 9.81\,\text{m s}^{-2}$	$R_{\text{wall}} = \dfrac{\ln\left(D_{\text{Tube,o}}/D_{\text{Tube,i}}\right)}{2\pi k_{\text{wall}}L_{\text{Post 1 to 2}}}$	$R_{\text{wall}} = 0.0035\,\text{K W}^{-1}$
	$R_{\text{ins}} = \dfrac{\ln\left(D_{\text{ins,o}}/D_{\text{Tube,i}}\right)}{2\pi k_{\text{ins}}L_{\text{Post 1 to 2}}}$	$R_{\text{ins}} = 14.7\,\text{K W}^{-1}$
	$R_{\text{rad}} = \dfrac{1}{\left[\begin{array}{l}\varepsilon_{\text{ins}}\pi D_{\text{ins,o}}L_{\text{Post 1 to 2}}\sigma_{\text{SB}}\\ \cdot\left(\text{T}_{\text{ins}}^{\,2} + \text{T}_{\text{Amb}}^{\,2}\right)\left(\text{T}_{\text{ins}} + \text{T}_{\text{Amb}}\right)\end{array}\right]}$	$R_{\text{rad}} = 1.2\,\text{K W}^{-1}$ $T_{\text{ins}} = 25.0°\text{C}$ (Solved Iteratively)
	$T_{\text{film}} = \left(T_{\text{ins}} + T_{\text{Amb}}\right)/2$	$T_{\text{film}} = 25.0°\text{C}$
	$T_{\text{wall,i}} = \left(T_{\text{f,Post,1,out}} + T_{\text{f,Post,2,in}}\right)/2$	$T_{\text{wall,i}}* = 26.5°\text{C}$ *Neglecting internal fluid resistance
	Air Properties $f(P = 101\,\text{kPa}, T_{\text{film}} = 25.0°\text{C})$	$\alpha = 2.8\times10^{-5}\,\text{m}^2\,\text{s}^{-1}$ $\beta = 0.00335\,\text{K}^{-1}$ $k = 0.0259\,\text{W m}^{-1}\,\text{K}^{-1}$ $\nu = 1.57\times10^{-5}\,\text{m}^2\,\text{s}^{-1}$ $\Pr = 0.72$ $\rho = 1.18\,\text{kg m}^{-3}$

Table E.3. R245fa / *n-pentane* **data point data reduction sample calculation – Cont.**

Heat Transfer Sample Calculations: R245fa / *n*-pentane Mixture; 1/21/2012; Run 3		
Inputs	**Equations**	**Results**
	$Ra_{air} = \dfrac{g\beta(T_{ins} - T_{Amb})(D_{ins,o})^3}{\nu\alpha}$	$Ra_{air} = 9269$
	$Nu_D =$ $\left(0.60 + 0.387\dfrac{Ra_{air}^{1/6}}{\left(1 + (0.559/\mathrm{Pr})^{9/16}\right)^{8/27}}\right)^2$	$Nu_D = 4.3$ (Churchill and Chu, 1975)
	$h_{nat,conv} = \dfrac{k_{air}}{D_{ins,o}} Nu_D$	$h_{nat,conv} = 1.11\,\mathrm{W\,m^{-2}\,K^{-1}}$
	$R_{conv} = \dfrac{1}{h_{nat,conv}\pi D_{ins,o}L_{Post\,1\,to\,2}}$	$R_{conv} = 5.5\,\mathrm{K\,W^{-1}}$
	$\dot{Q}_{loss} = \dfrac{T_{wall,i} - T_{amb}}{R_{wall} + R_{ins} + \dfrac{R_{conv}R_{rad}}{(R_{conv} + R_{rad})}}$	$\dot{Q}_{loss,f,Post,12} = 0.1\,\mathrm{W}$
Heat Loss in Water Line from Post-Condenser 1 to Post-Condenser 2		
$P_{Amb} = 101\,\mathrm{kPa}$ $T_{Amb} = 24.9°\mathrm{C}$ $T_{w,Post,1,out} = 13.0°\mathrm{C}$ $T_{w,Post,2,in} = 13.0°\mathrm{C}$ $D_{Tube,o} = 15.88\,\mathrm{mm}$ $D_{Tube,i} = 12.7\,\mathrm{mm}$ $D_{ins,o} = 100\,\mathrm{mm}$ $L_{w,Post\,1\,to\,2} = 1.05\,\mathrm{m}$ $k_{wall} = 400.3\,\mathrm{W\,m^{-1}\,K^{-1}}$ $k_{ins} = 0.043\,\mathrm{W\,m^{-1}\,K^{-1}}$ $\varepsilon_{ins} = 0.85$ $\sigma_{SB} = 5.67\times10^{-8}$ $\quad\mathrm{W\,m^{-2}K^{-4}}$ $g = 9.81\,\mathrm{m\,s^{-2}}$	$R_{wall} = \dfrac{\ln(D_{Tube,o}/D_{Tube,i})}{2\pi k_{wall}L_{w,Post\,1\,to\,2}}$	$R_{wall} = 8.4\times10^{-5}\,\mathrm{K\,W^{-1}}$
	$R_{ins} = \dfrac{\ln(D_{ins,o}/D_{Tube,o})}{2\pi k_{ins}L_{w,Post\,1\,to\,2}}$	$R_{ins} = 6.5\,\mathrm{K\,W^{-1}}$
	$R_{rad} = \dfrac{1}{\left[\begin{array}{c}\varepsilon_{ins}\pi D_{ins,o}L_{w,Post\,1\,to\,2}\sigma_{SB}\\ \cdot(T_{ins}^2 + T_{Amb}^2)(T_{ins} + T_{Amb})\end{array}\right]}$	$R_{rad} = 0.6\,\mathrm{K\,W^{-1}}$ $T_{ins} = 24.2°\mathrm{C}$ (Solved Iteratively)
	$T_{film} = (T_{ins} + T_{Amb})/2$	$T_{film} = 24.6°\mathrm{C}$
	$T_{wall,i} = (T_{w,Post,1,out} + T_{w,Post,2,in})/2$	$T_{wall,i}* = 13.0°\mathrm{C}$ *Neglecting internal fluid resistance
	Air Properties $f(P = 101\,\mathrm{kPa}, T_{film} = 24.55°\mathrm{C})$	$\alpha = 2.17\times10^{-5}\,\mathrm{m^2\,s^{-1}}$ $\beta = 0.00336\,\mathrm{K^{-1}}$ $k = 0.0258\,\mathrm{W\,m^{-1}\,K^{-1}}$ $\nu = 1.56\times10^{-5}\,\mathrm{m^2\,s^{-1}}$ $\mathrm{Pr} = 0.72$ $\rho = 1.18\,\mathrm{kg\,m^{-3}}$

Table E.3. R245fa / *n-pentane* data point data reduction sample calculation – Cont.

Heat Transfer Sample Calculations: R245fa / *n*-pentane Mixture; 1/21/2012; Run 3		
Inputs	**Equations**	**Results**
	$Ra_{\text{air}} = \dfrac{g\beta(T_{\text{ins}} - T_{\text{Amb}})(D_{\text{ins,o}})^3}{\nu\alpha}$	$Ra_{\text{air}} = 72{,}987$
	$Nu_{\text{D}} =$ $\left(0.60 + 0.387\dfrac{Ra_{\text{air}}^{1/6}}{\left(1+(0.559/\Pr)^{9/16}\right)^{8/27}}\right)^2$	$Nu_{\text{D}} = 7.18$ (Churchill and Chu, 1975)
	$h_{\text{nat,conv}} = \dfrac{k_{\text{air}}}{D_{\text{ins,o}}}Nu_{\text{D}}$	$h_{\text{nat,conv}} =$ $1.85\,\text{W m}^{-2}\,\text{K}^{-1}$
	$R_{\text{conv}} = \dfrac{1}{h_{\text{nat,conv}}\pi D_{\text{ins,o}}L_{\text{w,Post 1 to 2}}}$	$R_{\text{conv}} = 1.6\,\text{K W}^{-1}$
	$\dot{Q}_{\text{loss}} = \dfrac{T_{\text{wall,i}} - T_{\text{amb}}}{R_{\text{wall}} + R_{\text{ins}} + \dfrac{R_{\text{conv}}R_{\text{rad}}}{(R_{\text{conv}} + R_{\text{rad}})}}$	$\dot{Q}_{\text{loss,w,Post,12}} = -1.7\,\text{W}$ Gain from ambient Coolant T below T_{amb}
Heat Loss in Line from Test Section to Post-Condenser 1		
$P_{\text{Amb}} = 101\,\text{kPa}$ $T_{\text{Amb}} = 24.9°\text{C}$ $T_{\text{f,Test,out}} = 56.1°\text{C}$ $T_{\text{f,Post,1,in}} = 57.2°\text{C}$ $D_{\text{Tube,o}} = 12.7\,\text{mm}$ $D_{\text{Tube,i}} = 10.92\,\text{mm}$ $D_{\text{ins,o}} = 100\,\text{mm}$ $L_{\text{Test to Post,1}} = 0.695\,\text{m}$ $k_{\text{wall}} = 13.94\,\text{W m}^{-1}\,\text{K}^{-1}$ $k_{\text{ins}} = 0.043\,\text{W m}^{-1}\,\text{K}^{-1}$ $\varepsilon_{\text{ins}} = 0.85$ $\sigma_{\text{SB}} = 5.67\times10^{-8}$ $\text{W m}^{-2}\text{K}^{-4}$ $g = 9.81\,\text{m s}^{-2}$	$R_{\text{wall}} = \dfrac{\ln(D_{\text{Tube,o}}/D_{\text{Tube,i}})}{2\pi k_{\text{wall}}L_{\text{Test to Post,1}}}$ $R_{\text{ins}} = \dfrac{\ln(D_{\text{ins,o}}/D_{\text{Tube,o}})}{2\pi k_{\text{ins}}L_{\text{Test to Post,1}}}$ $R_{\text{rad}} = \dfrac{1}{\left[\begin{array}{c}\varepsilon_{\text{ins}}\pi D_{\text{ins,o}}L_{\text{Test to Post,1}}\sigma_{\text{SB}}\\ \cdot(T_{\text{ins}}^2 + T_{\text{Amb}}^2)(T_{\text{ins}} + T_{\text{Amb}})\end{array}\right]}$ $T_{\text{film}} = (T_{\text{ins}} + T_{\text{Amb}})/2$ $T_{\text{wall,i}} = (T_{\text{f,Test,out}} + T_{\text{f,Post,1,in}})/2$ Air Properties $f(P = 101\,\text{kPa}, T_{\text{film}} = 25.8°\text{C})$	$R_{\text{wall}} = 0.0025\,\text{K W}^{-1}$ $R_{\text{ins}} = 11.0\,\text{K W}^{-1}$ $R_{\text{rad}} = 0.9\,\text{K W}^{-1}$ $T_{\text{ins}} = 26.6°\text{C}$ (Solved Iteratively) $T_{\text{film}} = 25.8°\text{C}$ $T_{\text{wall,i}}* = 56.7°\text{C}$ *Neglecting internal fluid resistance $\alpha = 2.19\times10^{-5}\,\text{m}^2\,s^{-1}$ $\beta = 0.00335\,\text{K}^{-1}$ $k = 0.0259\,\text{W m}^{-1}\,\text{K}^{-1}$ $\nu = 1.57\times10^{-5}\,\text{m}^2\,s^{-1}$ $\Pr = 0.72$ $\rho = 1.18\,\text{kg m}^{-3}$

Table E.3. R245fa / *n-pentane* data point data reduction sample calculation – Cont.

Heat Transfer Sample Calculations: R245fa / *n*-pentane Mixture; 1/21/2012; Run 3		
Inputs	**Equations**	**Results**
	$Ra_{air} = \dfrac{g\beta(T_{ins} - T_{Amb})(D_{ins,o})^3}{\nu\alpha}$	$Ra_{air} = 160{,}443$
	$Nu_D =$ $\left(0.60 + 0.387\dfrac{Ra_{air}^{1/6}}{\left(1+(0.559/\Pr)^{9/16}\right)^{8/27}}\right)^2$	$Nu_D = 8.83$ (Churchill and Chu, 1975)
	$h_{nat,conv} = \dfrac{k_{air}}{D_{ins,o}}Nu_D$	$h_{nat,conv} = 2.29\,\mathrm{W\,m^{-2}\,K^{-1}}$
	$R_{conv} = \dfrac{1}{h_{nat,conv}\pi D_{ins,o}L_{Test\ to\ Post,1}}$	$R_{conv} = 2.0\,\mathrm{K\,W^{-1}}$
	$\dot{Q}_{loss} = \dfrac{T_{wall,i} - T_{Amb}}{R_{wall} + R_{ins} + \dfrac{R_{conv}R_{rad}}{(R_{conv}+R_{rad})}}$	$\dot{Q}_{loss,f,Test\ to\ Post,1} = 2.7\,\mathrm{W}$
Heat Loss in Test Section		
$P_{Amb} = 101\,\mathrm{kPa}$ $T_{Amb} = 24.9°C$	$R_{wall} = \dfrac{\ln(D_{OT,o}/D_{OT,i})}{2\pi k_{wall}L_{Annulus}}$	$R_{wall} = 0.00010\,\mathrm{K\,W^{-1}}$
$T_{w,Pri,Test,in} = 45.6°C$ $T_{w,Pri,Test,out} = 47.8°C$	$R_{ins} = \dfrac{\ln(D_{ins,o}/D_{OT,o})}{2\pi k_{ins}L_{Annulus}}$	$R_{ins} = 14.4\,\mathrm{K\,W^{-1}}$
$D_{OT,o} = 12.7\,\mathrm{mm}$ $D_{OT,i} = 11.06\,\mathrm{mm}$ $D_{ins,o} = 100\,\mathrm{mm}$	$R_{rad} = \dfrac{1}{\left[\begin{array}{c}\varepsilon_{ins}\pi D_{ins,o}L_{Annulus}\sigma_{SB}\\ \cdot(T_{ins}^2 + T_{Amb}^2)(T_{ins}+T_{Amb})\end{array}\right]}$	$R_{rad} = 1.2\,\mathrm{K\,W^{-1}}$ $T_{ins} = 26.1°C$ (Solved Iteratively)
$L_{Annulus} = 0.53\,\mathrm{m}$	$T_{film} = (T_{ins} + T_{Amb})/2$	$T_{film} = 25.5°C$
$k_{wall} = 399.4\,\mathrm{W\,m^{-1}\,K^{-1}}$ $k_{ins} = 0.043\,\mathrm{W\,m^{-1}\,K^{-1}}$ $\varepsilon_{ins} = 0.85$	$T_{wall,i} = (T_{w,Pri,Test,in} + T_{w,Pri,Test,out})/2$	$T_{wall,i}* = 46.7°C$ *Neglecting internal fluid resistance
$\sigma_{SB} = 5.67\times10^{-8}$ $\mathrm{W\,m^{-2}\,K^{-4}}$ $g = 9.81\,\mathrm{m\,s^{-2}}$ $R_{Annulus,o} = 0.00268$ $\mathrm{K\,W^{-1}}$	Air Properties $f(P = 101\,\mathrm{kPa}, T_{film} = 25.5°C)$	$\alpha = 2.18\times10^{-5}\,\mathrm{m^2\,s^{-1}}$ $\beta = 0.00335\,\mathrm{K^{-1}}$ $k = 0.0259\,\mathrm{W\,m^{-1}\,K^{-1}}$ $\nu = 1.57\times10^{-5}\,\mathrm{m^2\,s^{-1}}$ $\Pr = 0.72$ $\rho = 1.18\,\mathrm{kg\,m^{-3}}$

Table E.3. R245fa / *n-pentane* data point data reduction sample calculation – Cont.

Heat Transfer Sample Calculations: R245fa / *n*-pentane Mixture; 1/21/2012; Run 3		
Inputs	**Equations**	**Results**
	$Ra_{\text{air}} = \dfrac{g\beta\left(T_{\text{ins}} - T_{\text{Amb}}\right)\left(D_{\text{ins,o}}\right)^3}{\nu\alpha}$	$Ra_{\text{air}} = 113{,}633$
	$Nu_{\text{D}} =$ $\left(0.60 + 0.387\dfrac{Ra_{\text{air}}^{1/6}}{\left(1 + \left(0.559/\Pr\right)^{9/16}\right)^{8/27}}\right)^2$	$Nu_{\text{D}} = 8.06$ (Churchill and Chu, 1975)
	$h_{\text{nat,conv}} = \dfrac{k_{\text{air}}}{D_{\text{ins,o}}} Nu_{\text{D}}$	$h_{\text{nat,conv}} = 2.09\,\text{W m}^{-2}\,\text{K}^{-1}$
	$R_{\text{conv}} = \dfrac{1}{h_{\text{nat,conv}}\pi D_{\text{ins,o}}L_{\text{Annulus}}}$	$R_{\text{conv}} = 2.9\,\text{K W}^{-1}$
	$\dot{Q}_{\text{loss}} = \dfrac{T_{\text{wall,i}} - T_{\text{Amb}}}{R_{\text{Annulus,o}} + R_{\text{wall}} + R_{\text{ins}} + \dfrac{R_{\text{conv}}R_{\text{rad}}}{\left(R_{\text{conv}} + R_{\text{rad}}\right)}}$	$\dot{Q}_{\text{loss,Test}} = 1.4\,\text{W}$
Heat Loss in Primary Loop		
$P_{\text{Amb}} = 101\,\text{kPa}$ $T_{\text{Amb}} = 24.9\,°\text{C}$ $T_{\text{w,Pri,Test,in}} = 45.6\,°\text{C}$ $T_{\text{w,Pri,Test,out}} = 47.8\,°\text{C}$ $D_{\text{Tube,o}} = 12.7\,\text{mm}$ $D_{\text{Tube,i}} = 10.2\,\text{mm}$ $D_{\text{ins,o}} = 100\,\text{mm}$ $L_{\text{Pri, Effective}} = 5.7\,\text{m}$ $k_{\text{wall}} = 13.76\,\text{W m}^{-1}\,\text{K}^{-1}$ $k_{\text{ins}} = 0.043\,\text{W m}^{-1}\,\text{K}^{-1}$ $\varepsilon_{\text{ins}} = 0.85$ $\sigma_{\text{SB}} = 5.67\times10^{-8}$ $\quad\text{W m}^{-2}\text{K}^{-4}$ $g = 9.81\,\text{m s}^{-2}$	$R_{\text{wall}} = \dfrac{\ln\left(D_{\text{Tube,o}} / D_{\text{Tube,i}}\right)}{2\pi k_{\text{wall}}L_{\text{Pri,Effective}}}$	$R_{\text{wall}} = 0.00045\,\text{K W}^{-1}$
	$R_{\text{ins}} = \dfrac{\ln\left(D_{\text{ins,o}} / D_{\text{Tube,o}}\right)}{2\pi k_{\text{ins}}L_{\text{Pri,Effective}}}$	$R_{\text{ins}} = 1.3\,\text{K W}^{-1}$
	$R_{\text{rad}} = \dfrac{1}{\left[\begin{array}{l}\varepsilon_{\text{ins}}\pi D_{\text{ins,o}}L_{\text{Pri,Effective}}\sigma_{\text{SB}} \\ \cdot\left(T_{\text{ins}}^2 + T_{\text{Amb}}^2\right)\left(T_{\text{ins}} + T_{\text{Amb}}\right)\end{array}\right]}$	$R_{\text{rad}} = 0.1\,\text{K W}^{-1}$ $T_{\text{ins}} = 26.1\,°\text{C}$ (Solved Iteratively)
	$T_{\text{film}} = \left(T_{\text{ins}} + T_{\text{Amb}}\right)/2$	$T_{\text{film}} = 25.5\,°\text{C}$
	$T_{\text{wall,i}} = \left(T_{\text{w,Pri,Test,in}} + T_{\text{w,Pri,Test,out}}\right)/2$	$T_{\text{wall,i}}{}^* = 46.7\,°\text{C}$ *Neglecting internal fluid resistance

Table E.3. R245fa / *n-pentane* data point data reduction sample calculation – Cont.

Heat Transfer Sample Calculations: R245fa / *n*-pentane Mixture; 1/21/2012; Run 3		
Inputs	**Equations**	**Results**
	Air Properties $f(P=101\,\text{kPa}, T_{\text{film}}=25.5°\text{C})$	$\alpha = 2.18\times10^{-5}\,\text{m}^2\,s^{-1}$ $\beta = 0.00335\,\text{K}^{-1}$ $k = 0.0259\,\text{W}\,\text{m}^{-1}\,\text{K}^{-1}$ $\nu = 1.57\times10^{-5}\,\text{m}^2\,s^{-1}$ $\text{Pr} = 0.72$ $\rho = 1.18\,\text{kg}\,\text{m}^{-3}$
	$Ra_{\text{air}} = \dfrac{g\beta\left(T_{\text{ins}}-T_{\text{amb}}\right)\left(D_{\text{ins,o}}\right)^3}{\nu\alpha}$	$Ra_{\text{air}} = 113619$
	$Nu_{\text{D}} = \left(0.60 + 0.387\dfrac{Ra_{\text{air}}^{1/6}}{\left(1+\left(0.559/\text{Pr}\right)^{9/16}\right)^{8/27}}\right)^2$	$Nu_{\text{D}} = 8.06$ (Churchill and Chu, 1975)
	$h_{\text{nat,conv}} = \dfrac{k_{\text{air}}}{D_{\text{ins,o}}}Nu_{\text{D}}$	$h_{\text{nat,conv}} = 2.086\,\text{W}\,\text{m}^{-2}\,\text{k}^{-1}$
	$R_{\text{conv}} = \dfrac{1}{h_{\text{nat,conv}}\pi D_{\text{ins,o}}L_{\text{Annulus}}}$	$R_{\text{conv}} = 0.3\,\text{K}\,\text{W}^{-1}$
	$\dot{Q}_{\text{loss}} = \dfrac{T_{\text{wall,i}}-T_{\text{Amb}}}{R_{\text{wall}}+R_{\text{ins}}+\dfrac{R_{\text{conv}}R_{\text{rad}}}{\left(R_{\text{conv}}+R_{\text{rad}}\right)}}$	$\dot{Q}_{\text{loss,Pri}} = 15.4\,\text{W}$
Heat Loss in Secondary Heat Exchanger		
$P_{\text{Amb}} = 101\,\text{kPa}$ $T_{\text{Amb}} = 24.9°\text{C}$ $T_{\text{w,Pri,Sec,in}} = 47.8°\text{C}$ $T_{\text{w,Pri,Sec,out}} = 45.6°\text{C}$ $D_{\text{Sec,o}} = 25.4\,\text{mm}$ $D_{\text{Sec,i}} = 22.9\,\text{mm}$ $D_{\text{ins,o}} = 100\,\text{mm}$ $L_{\text{sec}} = 0.376\,\text{m}$	$R_{\text{wall}} = \dfrac{\ln\left(D_{\text{Sec,o}}/D_{\text{Sec,i}}\right)}{2\pi k_{\text{wall}}L_{\text{Sec}}}$ $R_{\text{ins}} = \dfrac{\ln\left(D_{\text{ins,o}}/D_{\text{Sec,o}}\right)}{2\pi k_{\text{ins}}L_{\text{Sec}}}$ $R_{\text{rad}} = \dfrac{1}{\left[\begin{array}{c}\varepsilon_{\text{ins}}\pi D_{\text{ins,o}}L\sigma_{\text{SB}}\\ \cdot\left(T_{\text{ins}}^2+T_{\text{Amb}}^2\right)\left(T_{\text{ins}}+T_{\text{Amb}}\right)\end{array}\right]}$ $T_{\text{film}} = \left(T_{\text{ins}}+T_{\text{Amb}}\right)/2$	$R_{\text{wall}} = 0.0033\,\text{K}\,\text{W}^{-1}$ $R_{\text{ins}} = 13.5\,\text{K}\,\text{W}^{-1}$ $R_{\text{rad}} = 1.6\,\text{K}\,\text{W}^{-1}$ $T_{\text{ins}} = 26.6°\text{C}$ (Solved Iteratively) $T_{\text{film}} = 25.8°\text{C}$

Table E.3. R245fa / *n-pentane* data point data reduction sample calculation – Cont.

Heat Transfer Sample Calculations: R245fa / *n*-pentane Mixture; 1/21/2012; Run 3		
Inputs	**Equations**	**Results**
$k_{\text{wall}} = 13.4\,\text{W m}^{-1}\,\text{K}^{-1}$ $k_{\text{ins}} = 0.043\,\text{W m}^{-1}\,\text{K}^{-1}$ $\varepsilon_{\text{ins}} = 0.85$ $\sigma_{\text{SB}} = 5.67 \times 10^{-8}$ $\qquad \text{W m}^{-2}\text{K}^{-4}$ $g = 9.81\,\text{m s}^{-2}$	$T_{\text{wall,i}} = \left(T_{\text{w,Pri,Sec,in}} + T_{\text{w,Pri,Sec,out}} \right)/2$	$T_{\text{wall,i}}* = 46.7°\text{C}$ *Neglecting internal fluid resistance
	Air Properties $f(P = 101\,\text{kPa}, T_{\text{film}} = 26.5°\text{C})$	$\alpha = 2.18 \times 10^{-5}\,\text{m}^2\,s^{-1}$ $\beta = 0.00335\,\text{K}^{-1}$ $k = 0.0259\,\text{W m}^{-1}\,\text{K}^{-1}$ $\nu = 1.57 \times 10^{-5}\,\text{m}^2\,\text{s}^{-1}$ $\text{Pr} = 0.72$ $\rho = 1.18\,\text{kg m}^{-3}$
	$Ra_{\text{air}} = \dfrac{g\beta \left(T_{\text{ins}} - T_{\text{Amb}} \right) \left(D_{\text{ins,o}} \right)^3}{\nu\alpha}$	$Ra_{\text{air}} = 161,486$
	$Nu_{\text{D}} =$ $\left(0.60 + 0.387 \dfrac{Ra_{\text{air}}^{1/6}}{\left(1 + \left(0.559 / \text{Pr} \right)^{9/16} \right)^{8/27}} \right)^2$	$Nu_{\text{D}} = 8.84$ (Churchill and Chu, 1975)
	$h_{\text{nat,conv}} = \dfrac{k_{\text{air}}}{D_{\text{ins,o}}} Nu_{\text{D}}$	$h_{\text{nat,conv}} = 2.29\,\text{W m}^{-2}\text{K}^{-1}$
	$R_{\text{conv}} = \dfrac{1}{h_{\text{nat,conv}} \pi D_{\text{ins,o}} L}$	$R_{\text{conv}} = 3.7\,\text{K W}^{-1}$
	$\dot{Q}_{\text{loss}} = \dfrac{T_{\text{wall,i}} - T_{\text{Amb}}}{R_{\text{wall}} + R_{\text{ins}} + \dfrac{R_{\text{conv}} R_{\text{rad}}}{\left(R_{\text{conv}} + R_{\text{rad}} \right)}}$	$\dot{Q}_{\text{loss,Sec}} = 1.5\,\text{W}$
Average Test Section Quality		
$x_{\text{R-245fa}} = 0.454$	$i_{\text{f,Pre,in}} = f\left(P_{\text{f,Pre,in}}, T_{\text{f,Pre,in}}, x_{\text{R245fa}} \right)$	$i_{\text{f,Pre,in}} = 484.4\,\text{kJ kg}^{-1}$
$T_{\text{f,Pre,in}} = 103.7°\text{C}$	$T_{\text{f,Pre,in,Dew}} = f\left(P_{\text{f,Pre,in}}, q = 1, x_{\text{R245fa}} \right)$	$T_{\text{f,Pre,in,Dew}} = 74.3°\text{C}$
$T_{\text{f,Test,in,meas}} = 59.5°\text{C}$	$\Delta T_{\text{f,Pre,in,Sup}} = T_{\text{f,Pre,in}} - T_{\text{f,Pre,in,Dew}}$	$\Delta T_{\text{f,Pre,in,Sup}} = 29.4\,\text{K}$
$T_{\text{f,Test,out,meas}} = 57.2°\text{C}$	$i_{\text{w,Pre,in}} = f\left(P_{\text{w}}, T_{\text{w,Pre,in}} \right)$	$i_{\text{w,Pre,in}} = 36.3\,\text{kJ kg}^{-1}$
$T_{\text{f,Post,out}} = 12.7°\text{C}$	$i_{\text{w,Pre,out}} = f\left(P_{\text{w}}, T_{\text{w,Pre,out}} \right)$	$i_{\text{w,Pre,out}} = 316.2\,\text{kJ kg}^{-1}$
$T_{\text{w,Pre,in}} = 8.6°\text{C}$	$\rho_{\text{w,Pre,in}} = f\left(P_{\text{w}}, T_{\text{w,Pre,in}} \right)$	$\rho_{\text{w,Pre,in}} = 1000\,\text{kg m}^{-3}$

Table E.3. R245fa / *n*-pentane data point data reduction sample calculation – Cont.

Heat Transfer Sample Calculations: R245fa / *n*-pentane Mixture; 1/21/2012; Run 3		
Inputs	**Equations**	**Results**
$T_{w,Pre,out} = 75.5\,^{\circ}C$	$\dot{m}_{w,Pre} = \dot{V}_{w,Pre}\,\rho_{w,Pre,in}$	$\dot{m}_{w,Pre} = 0.0187\,\mathrm{kg\,s^{-1}}$
$T_{w,Post,in} = 7.3\,^{\circ}C$	$\dot{Q}_{Pre} = \dot{m}_{w,Pre}\left(i_{w,Pre,out} - i_{w,Pre,in}\right) + \dot{Q}_{loss,Pre}$	$\dot{Q}_{Pre} = 5250\,\mathrm{W}$
$T_{w,Post,out} = 40.2\,^{\circ}C$	$i_{f,Test,in} = i_{f,Pre,in} - \dfrac{\dot{Q}_{Pre}}{\dot{m}_f} - \dfrac{\dot{Q}_{loss,Pre\,to\,Test}}{\dot{m}_f}$	$i_{f,Test,in} = 265\,\mathrm{kJ\,kg^{-1}}$
$P_{f,Pre,in} = 449.4\,\mathrm{kPa}$		
$P_{f,Test,in} = 411.2\,\mathrm{kPa}$	$q_{f,Test,in} = f\left(i_{f,Test,in}, P_{f,Test,in}, x_{R245fa}\right)$	$q_{f,Test,in} = 0.442$
$P_{f,Test,out} = 400.6\,\mathrm{kPa}$	$T_{f,Test,in} = f\left(i_{f,Test,in}, P_{f,Test,in}, x_{R245fa}\right)$	$T_{f,Test,in} = 60.0\,^{\circ}C$
$P_{f,Post,out} = 392.7\,\mathrm{kPa}$	$\Delta T_{f,Test,in} = T_{f,Test,in,meas} - T_{f,Test,in}$	$\Delta T_{f,Test,in} = -0.5\,\mathrm{K}$
$P_{w,pre\text{-}post} = 225.2\,\mathrm{kPa}$	$i_{f,Post,out} = f\left(P_{f,Post,out}, T_{f,Post,out}, x_{R245fa}\right)$	$i_{f,Post,out} = 86.8\,\mathrm{kJ\,kg^{-1}}$
$\dot{V}_{w,Pre} = 1.13\,\mathrm{L\,min^{-1}}$	$i_{w,Post,in} = f\left(P_w, T_{w,Post,in}\right)$	$i_{w,Post,in} = 31.0\,\mathrm{kJ\,kg^{-1}}$
$\dot{V}_{w,Post} = 1.60\,\mathrm{L\,min^{-1}}$	$i_{w,Post,out} = f\left(P_w, T_{w,Post,out}\right)$	$i_{w,Post,out} = 168.5\,\mathrm{kJ\,kg^{-1}}$
$\dot{m}_f = 0.0239\,\mathrm{kg\,s^{-1}}$	$\rho_{w,Post,in} = f\left(P_w, T_{w,Post,in}\right)$	$\rho_{w,Post,in} = 1000\,\mathrm{kg\,m^{-3}}$
$\dot{Q}_{loss,Pre} = 2.2\,\mathrm{W}$	$\dot{m}_{w,Post} = \dot{V}_{w,Post}\,\rho_{w,Post,in}$	$\dot{m}_{w,Post} = 0.0266\,\mathrm{kg\,s^{-1}}$
$\dot{Q}_{loss,Post,1} = 0.2\,\mathrm{W}$	$\dot{Q}_{loss,Post} = \dot{Q}_{loss,Post,1} + \dot{Q}_{loss,Post,2}$ $+ \dot{Q}_{loss,w,Post,12} + \dot{Q}_{loss,f,Post,12}$	$\dot{Q}_{f,loss,Post} = -3.1\,\mathrm{W}$
$\dot{Q}_{loss,Post,2} = -1.9\,\mathrm{W}$		
$\dot{Q}_{loss,w,Post,12} = -1.7\,\mathrm{W}$	$\dot{Q}_{Post} = \dot{m}_{w,Post}\left(i_{w,Post,out} - i_{w,Post,in}\right)$ $+ \dot{Q}_{loss,Post}$	$\dot{Q}_{Post} = 3650\,\mathrm{W}$
$\dot{Q}_{loss,f,Post,12} = 0.1\,\mathrm{W}$		
$\dot{Q}_{loss,Pre\,to\,Test} = 2.7\,\mathrm{W}$	$i_{f,Test,out} = i_{f,Post,out} + \dfrac{\dot{Q}_{Post}}{\dot{m}_f} + \dfrac{\dot{Q}_{loss,Test\,to\,Post}}{\dot{m}_f}$	$i_{f,Test,out} = 239.4\,\mathrm{kJ\,kg^{-1}}$
$\dot{Q}_{loss,Test\,to\,Post,1} = 2.7\,\mathrm{W}$		
	$q_{f,Test,out} = f\left(i_{f,Test,out}, P_{f,Test,out}, x_{R245fa}\right)$	$q_{f,Test,out} = 0.346$
	$T_{f,Test,out} = f\left(i_{f,Test,out}, P_{f,Test,out}, x_{R245fa}\right)$	$T_{f,Test,out} = 57.3\,^{\circ}C$
	$\Delta T_{f,Test,out} = T_{f,Test,out,meas} - T_{f,Test,out}$	$\Delta T_{f,Test,in} = -0.5\,\mathrm{K}$
	$P_{f,Test,Avg} = \left(P_{f,Test,in} + P_{f,Test,out}\right)/2$	$P_{f,Test,Avg} = 405.9\,\mathrm{kPa}$
	$i_{f,Test,Avg} = \left(i_{f,Test,in} + i_{f,Test,out}\right)/2$	$i_{f,Test,Avg} = 251.9\,\mathrm{kJ\,kg^{-1}}$
	$q_{f,Test,Avg} = \left(q_{f,Test,in} + q_{f,Test,out}\right)/2$	$q_{f,Test,Avg} = 0.394$

Table E.3. R245fa / *n-pentane* data point data reduction sample calculation – Cont.

Heat Transfer Sample Calculations: R245fa / *n*-pentane Mixture; 1/21/2012; Run 3		
Inputs	**Equations**	**Results**
Test Section Heat Duty Calculation		
$T_{\text{w,Sec,in}} = 45.6°\text{C}$	$i_{\text{w,Sec,in}} = f\left(P_{\text{w}}, T_{\text{w,Sec,in}}\right)$	$i_{\text{w,Sec,in}} = 31.41\,\text{kJ}\,\text{kg}^{-1}$
$T_{\text{w,Sec,out}} = 47.8°\text{C}$	$i_{\text{w,Sec,out}} = f\left(P_{\text{w}}, T_{\text{w,Sec,out}}\right)$	$i_{\text{w,Sec,out}} = 197.1\,\text{kJ}\,\text{kg}^{-1}$
$P_{\text{w}} = 225.4\,\text{kPa}$	$\dot{Q}_{\text{Sec}} = \dot{m}_{\text{w,Sec}}\left(i_{\text{w,Sec,out}} - i_{\text{w,Sec,in}}\right)$	$\dot{Q}_{\text{Sec}} = 595.6\,\text{W}$
$\Delta P_{\text{w,Pri}} = 83.0\,\text{kPa}$	$\dot{Q}_{\text{Pump}} = 0.1401\dot{V}_{\text{LPM}}^{3} + 0.9598\dot{V}_{\text{LPM}}^{2}$	$\dot{Q}_{\text{Pump}} = 36.8\,\text{W}$
$\dot{V}_{\text{w,Pri}} = 4.02\,\text{L}\,\text{min}^{-1}$	$\qquad + 3.025\dot{V}_{\text{LPM}}$	
$\dot{m}_{\text{w,Sec}} = 0.0036\,\text{kg}\,\text{s}^{-1}$	$\dot{Q}_{\text{loss,Amb}} = \dot{Q}_{\text{loss,Test}} + \dot{Q}_{\text{loss,Pri}} + \dot{Q}_{\text{loss,Sec}}$	$\dot{Q}_{\text{loss,Amb}} = 18.3\,\text{W}$
$\dot{Q}_{\text{loss,Sec}} = 1.5\,\text{W}$	$\dot{Q}_{\text{Test}} = \dot{Q}_{\text{Sec}} + \dot{Q}_{\text{loss,Amb}} - \dot{Q}_{\text{Pump}}$	$\dot{Q}_{\text{Test}} = 577.1\,\text{W}$
$\dot{Q}_{\text{loss,Pri}} = 15.4\,\text{W}$		
$\dot{Q}_{\text{loss,Test}} = 1.4\,\text{W}$		
$\eta_{\text{meas}} = 0.64$		
Evaporator Energy Balance		
$T_{\text{f,Pre,in}} = 103.7°\text{C}$	$i_{\text{f,Pre,in}} = f\left(P_{\text{f,Pre,in}}, T_{\text{f,Pre,in}}, x_{\text{R245fa}}\right)$	$i_{\text{f,Pre,in}} = 484.4\,\text{kJ}\,\text{kg}^{-1}$
$T_{\text{f,Post,out}} = 12.7°\text{C}$	$i_{\text{f,Post,out}} = f\left(P_{\text{f,Post,out}}, T_{\text{f,Post,out}}, x_{\text{R245fa}}\right)$	$i_{\text{f,Post,out}} = 86.8\,\text{kJ}\,\text{kg}^{-1}$
$P_{\text{f,Pre,in}} = 449.4\,\text{kPa}$	$\dot{Q}_{\text{Evap}} = \dot{m}_{\text{f}} \cdot \left(i_{\text{f,Pre,in}} - i_{\text{f,Post,out}}\right)$	$\dot{Q}_{\text{Evap}} = 9517\,\text{W}$
$P_{\text{f,Post,out}} = 392.7\,\text{kPa}$	$\dot{Q}_{\text{Loop}} = \dot{Q}_{\text{Pre}} + \dot{Q}_{\text{loss,Pre to Test}} + \dot{Q}_{\text{Test}}$	$\dot{Q}_{\text{Loop}} = 9481\,\text{W}$
$\dot{m}_{\text{f}} = 0.02394\,\text{kg}\,\text{s}^{-1}$	$\qquad + \dot{Q}_{\text{loss,Test to Post}} + \dot{Q}_{\text{Post}}$	
$\dot{Q}_{\text{Test}} = 577.1\,\text{W}$	$\Delta\dot{Q}_{\text{Evap}} = \dot{Q}_{\text{Evap}} - \dot{Q}_{\text{Loop}}$	$\Delta\dot{Q}_{\text{Evap}} = 36.1\,\text{W}$
$\dot{Q}_{\text{Pre}} = 5250\,\text{W}$	$\%_{\text{Error}} = \dfrac{\Delta\dot{Q}_{\text{Evap}}}{\dot{Q}_{\text{Evap}}}$	$\%_{\text{Error}} = 0.4\%$
$\dot{Q}_{\text{Post}} = 3650\,\text{W}$		
$\dot{Q}_{\text{loss,Pre to Test}} = 2.7\,\text{W}$		
$\dot{Q}_{\text{loss,Test to Post}} = 2.7\,\text{W}$		
Test Section Quality Change		
$q_{\text{f,Test,in,Pri}} = 0.438$	$\Delta q_{\text{f,Test}} = q_{\text{f,Test,in,Pri}} - q_{\text{f,Test,out,Pri}}$	$\Delta q_{\text{f,Test}} = 0.09$
$q_{\text{f,Test,out,Pri}} = 0.348$		

Table E.3. R245fa / *n-pentane* data point data reduction sample calculation – Cont.

Heat Transfer Sample Calculations: R245fa / *n*-pentane Mixture; 1/21/2012; Run 3		
Inputs	**Equations**	**Results**
Test Section Annulus Heat Transfer Coefficient		
$T_{w,Pri,Test,in} = 45.6°C$	$T_{w,Pri,Avg} = \left(T_{w,Pri,Test,in} + T_{w,Pri,Test,out}\right)/4$	$T_{w,Pri,Avg} = 46.7°C$
$T_{w,Pri,Test,out} = 47.8°C$	Primary Loop Water Properties	$\mu = 1.05 \times 10^{-5}$
$P_{w,Pri} = 405.8\,kPa$	$f\left(T_{w,Pri,Avg}, P_{w,Pri}\right)$	$kg\,m^{-1}\,s^{-1}$
$D_{Test,o} = 9.525\,mm$		$\rho = 1.178\,kg\,m^{-3}$
$D_{OT,i} = 11.06\,mm$		$k = 0.640\,W\,m^{-1}\,K^{-1}$
$\dot{V}_{w,Pri} = 4.02\,L\,min^{-1}$		$Pr = 3.78$
	$A_{c,Annulus} = \pi\left(D_{OT,i}^2 - D_{Test,o}^2\right)/4$	$A_{c,Annulus} = 2.48 \times 10^{-5}\,m^2$
	$V_{Annulus} = \dot{V}_{w,Pri}/A_{c,Annulus}$	$V_{Annulus} = 2.7\,m\,s^{-1}$
	$D_{h,Annulus} = D_{OT,i} - D_{Test,o}$	$D_{h,Annulus} = 1.54\,mm$
	$Re_{Annulus} = \dfrac{\rho V_{w,Pri} D_{h,Annulus}}{\mu}$	$Re_{Annulus} = 7094$
	$r^* = D_{Test,o}/D_{OT,i}$	$r^* = 0.8612$
	$Re_{CL} = 2089.26 + 686.15\,r^*$	$Re_{CL} = 2680$
	$Re_{CU} = 2963.02 + 334.16\,r^*$	$Re_{CU} = 3251$
	$Nu_{Annulus} = 0.025\left(Re_{Annulus}^{0.78}Pr^{0.48}r^{*-0.14}\right)$	$Nu_{Annulus} = 48.7$ (Garimella and Christensen, 1995)
	$h_{w,Annulus} = \dfrac{Nu_{Annulus}k}{D_{h,Annulus}}$	$h_{w,Annulus} = 20,300\,W\,m^{-2}\,K^{-1}$

Table E.4. Heat transfer coefficient calculation assuming equilibrium conditions sample calculation

Heat Transfer Sample Calculations: R245fa / *n*-pentane Mixture; 1/21/2012; Run 3		
Inputs	**Equations**	**Results**
Test Section Heat Transfer Coefficient – Equilibrium		
$T_{\text{f,Test,in}} = 60.0°C$ $T_{\text{f,Test,out}} = 57.3°C$ $T_{\text{w,Pri,Test,in}} = 45.6°C$ $T_{\text{w,Pri,Test,out}} = 47.8°C$	LMTD = $$\dfrac{\left(T_{\text{f,Test,in}} - T_{\text{w,Test,out}}\right) - \left(T_{\text{f,Test,out}} - T_{\text{w,Test,in}}\right)}{\ln\left(\dfrac{T_{\text{f,Test,in}} - T_{\text{w,Test,out}}}{T_{\text{f,Test,out}} - T_{\text{w,Test,in}}}\right)}$$	LMTD $= 11.9\,K$
$T_{\text{w,Pri,Avg}} = 46.7°C$ $P_{\text{f,Test,Avg}} = 405.9\,kPa$	$UA_{\text{f}} = \dfrac{\dot{Q}_{\text{Test}}}{\text{LMTD}}$	$UA_{\text{f}} = 48.3\,\text{W K}^{-1}$
$P_{\text{w,Pri}} = 405.8\,kPa$ $D_{\text{Test,i}} = 7.75\,mm$	$R_{\text{Annulus,i}} = \dfrac{1}{h_{\text{w,Annulus}}\pi D_{\text{Test,o}} L_{\text{Annulus}}}$	$R_{\text{Annulus,i}} =$ $0.0031\,\text{W K}^{-1}$
$D_{\text{Test,o}} = 9.525\,mm$ $D_{\text{Tee,o}} = 10.4\,mm$	$R_{\text{Test,wall}} = \dfrac{\ln\left(D_{\text{Test,o}} / D_{\text{Test,i}}\right)}{2\pi k_{\text{Test,wall}}\left(L_{\text{Annulus}} + 2L_{\text{Tee}}\right)}$	$R_{\text{Test,wall}} =$ $0.00015\,\text{K W}^{-1}$
$L_{\text{ann}} = 0.53\,m$ $L_{\text{Tee}} = 0.0132\,m$ $\dot{Q}_{\text{Test}} = 577.1\,W$ $i_{\text{f,Test,Avg}} = 252\,\text{kJ kg}^{-1}$	Primary Loop Water Properties $f\left(T_{\text{w,Pri,Avg}}, P_{\text{w,Pri}}\right)$	$\alpha = 1.55\times10^{-7}\,\text{m}^2\,\text{s}^{-1}$ $\beta = 4.35\times10^{-4}\,\text{K}^{-1}$ $k = 0.640\,\text{W m}^{-1}\,\text{K}^{-1}$ $\text{Pr} = 3.78$ $\upsilon = 5.84\times10^{-7}\,\text{m}^2\,\text{s}^{-1}$
$\dot{m}_{\text{f}} = 0.0239\,\text{kg s}^{-1}$ $h_{\text{w,annulus}} = 20{,}300$ $\quad\quad \text{W m}^{-2}\,\text{K}^{-1}$ $k_{\text{Test,wall}} = 398.5$ $\quad\quad \text{W m}^{-1}\,\text{K}^{-1}$	$\dfrac{Ra}{L^3} = \dfrac{g\beta_{\text{w,Pri}}\left(T_{\text{Test,wall,o}} - T_{\text{w,Pri,Avg}}\right)}{\nu_{\text{w,Pri}}\alpha_{\text{w,Pri}}}$	$Ra/L^3 = 8.79\times10^{10}\,\text{m}^{-3}$ $T_{\text{Test,wall,o}} = 48.6°C$ (Solved Iteratively)
$g = 9.81\,\text{m s}^{-2}$	$Ra^{*}_{\text{Tee}} = \dfrac{Ra}{L^3}\dfrac{\left(\ln\left(D_{\text{Tee}} / D_{\text{Test,o}}\right)\right)^4}{\left(\left(D_{\text{Test,o}}\right)^{-3/5} + \left(D_{\text{Tee}}\right)^{-3/5}\right)^5}$	$Ra^{*}_{\text{Tee}} = 0.17$ (Incropera and DeWitt, 2007)
	For $Ra^{*} < 100$: $k_{\text{Tee,Effective}} = k_{\text{w,Pri}}$ For $Ra^{*} > 100$: $k_{\text{Tee,Effective}} =$ $k_{\text{w,Pri}}\,0.386\left(\dfrac{\text{Pr}_{\text{w,Pri}}}{0.861 + \text{Pr}_{\text{w,Pri}}}\right)^{0.25} Ra^{*0.25}$	$k_{\text{Tee,Effective}} =$ $0.64\,\text{W m}^{-1}\,\text{K}^{-1}$

Table E.4. Heat transfer coefficient calculation assuming equilibrium conditions sample calculation – Cont.

Heat Transfer Sample Calculations: R245fa / *n*-pentane Mixture; 1/21/2012; Run 3		
Inputs	**Equations**	**Results**
	$R_{\text{Tee}} = \dfrac{\ln\left(D_{\text{Tee}} / D_{\text{Test,o}}\right)}{2\pi k_{\text{Tee,Effective}} L_{\text{Tee}}}$	$R_{\text{Tee}} = 1.7\,\text{K W}^{-1}$ $Q_{\text{Tee}} = 1.1\,\text{W each}$
	$R_{\text{Conv,eq}} = \left(\dfrac{1}{R_{\text{Annulus,i}}} + 2\cdot\dfrac{1}{R_{\text{Tee}}}\right)^{-1}$	$R_{\text{Conv,eq}} =$ $0.0031\,\text{K W}^{-1}$ $Q_{\text{Test}} = 575.0\ \text{W}$
	$\text{UA}_{\text{f}} = \dfrac{1}{\left(R_{\text{f}} + R_{\text{Test,wall}} + R_{\text{Conv,eq}}\right)}$	$R_{\text{f}} = 0.017\,\text{K W}^{-1}$ $Q_{\text{Test}} = 577.1\ \text{W}$
	$R_{\text{Ratio}} = R_{\text{f}} / \left(R_{\text{Test,wall}} + R_{\text{Conv,eq}}\right)$	$R_{\text{Ratio}} = 5.4$
	$\dot{Q}_{\text{Test}} = \dfrac{T_{\text{f,Test,avg}} - T_{\text{Test,wall,o}}}{R_{\text{f}} + R_{\text{Test,wall}}}$	$T_{\text{Test,wall,o}} = 48.5°\text{C}$ (Solved Iteratively)
	$R_{\text{f}} = \dfrac{1}{h_{\text{f}}\pi D_{\text{Test,i}}\left(L_{\text{Annulus}} + 2L_{\text{Tee}}\right)}$	$h_{\text{f}} = 4230\,\text{W m}^{-2}\,\text{K}^{-1}$

433

Table E.5. Heat transfer coefficient calculation within Price and Bell (1974) framework sample calculation

Heat Transfer Sample Calculations: R245fa / *n*-pentane Mixture; 1/21/2012; Run 3		
Inputs	**Equations**	**Results**
Test Section Heat Transfer Coefficient –Price and Bell (1974) framework		
$x_{\text{R-245fa}} = 0.454$ $T_{\text{w,Pri,Test,in}} = 45.6°C$	$i_{\text{f,Test,in,Pri}} = i_{\text{f,Test,Avg}} + \dfrac{\dot{Q}_{\text{Test}}}{2\dot{m}_{\text{f}}}$	$i_{\text{f,Test,in,pri}} = 264.0\,\text{kJ kg}^{-1}$
$T_{\text{w,Pri,Test,out}} = 47.8°C$	$q_{\text{f,Test,in,Pri}} = f\left(i_{\text{f,Test,in,Pri}}, P_{\text{f,Test,in}}, x_{\text{R245fa}}\right)$	$q_{\text{f,Test,in,Pri}} = 0.44$
$T_{\text{w,Pri,Avg}} = 46.7°C$	$T_{\text{f,Test,in,Pri}} = f\left(i_{\text{f,Test,in,Pri}}, P_{\text{f,Test,in}}, x_{\text{R245fa}}\right)$	$T_{\text{f,Test,in,Pri}} = 59.9°C$
$\Delta T_{\text{lv,in}} = 0.001\,\text{K}$	$\tilde{x}_{\text{R245fa,in}} = f\left(i_{\text{f,Test,in,Pri}}, P_{\text{f,Test,in}}, x_{\text{R245fa}}\right)$	$\tilde{x}_{\text{R245fa,in}} = 0.177$ $\hat{x}_{\text{R245fa,in}} = 0.286$
$P_{\text{f,Test,in}} = 411.2\,\text{kPa}$ $P_{\text{f,Test,out}} = 400.6\,\text{kPa}$	$\tilde{y}_{\text{R245fa,in}} = f\left(i_{\text{f,Test,in,Pri}}, P_{\text{f,Test,in}}, x_{\text{R245fa}}\right)$	$\tilde{y}_{\text{R245fa,in}} = 0.522$
$\dot{m}_{\text{f}} = 0.02394\,\text{kg s}^{-1}$		$\hat{y}_{\text{R245fa,in}} = 0.670$
$\dot{Q}_{\text{Test}} = 577.1\,\text{W}$	Inlet Liquid Equilibrium Properties	$\rho_{\text{l,in}} = 676.0\,\text{kg m}^{-3}$
$i_{\text{f,Test,Avg}} = 252\,\text{kJ kg}^{-1}$	$f\left(i_{\text{f,Test,in,Pri}}, P_{\text{f,Test,in}}, \hat{x}_{\text{R245fa,in}}\right)$	$\mu_{\text{l,in}} = 1.63\times10^{-4}$ $\text{kg m}^{-1}\,\text{s}^{-1}$
$R_{\text{Test,wall}} = 0.00015$ K W^{-1}		$k_{\text{l,in}} = 0.09\,\text{W m}^{-1}\,\text{K}^{-1}$
$R_{\text{Conv,eq}} = 0.00309$ K W^{-1}		$\text{Pr}_{\text{l,in}} = 3.91$
$e_{\text{Test}} = 0.00015\,\text{mm}$ (Drawn tube)		$C_{\text{pl,in}} = 2.19$ $\text{kJ kg}^{-1}\,\text{K}^{-1}$
		$i_{\text{l,in}} = 134.7\,\text{kJ kg}^{-1}$
$D_{\text{Test,i}} = 7.75\,\text{mm}$	Inlet Vapor Equilibrium Properties	$\rho_{\text{v,in}} = 17.5\,\text{kg m}^{-3}$
$A_{\text{c}} = 4.72\times10^{-5}\,\text{m}^2$	$f\left(i_{\text{f,Test,in,Pri}}, P_{\text{f,Test,in}}, \hat{y}_{\text{R245fa,in}}\right)$	$\mu_{\text{v,in}} = 1.05\times10^{-5}$ $\text{kg m}^{-1}\,\text{s}^{-1}$
$L_{\text{Annulus}} = 0.53\,\text{m}$		$k_{\text{v,in}} = 0.017\,\text{W m}^{-1}\,\text{K}^{-1}$
$L_{\text{Tee}} = 0.0132\,\text{m}$		$\text{Pr}_{\text{v,in}} = 0.84$
$R_{\text{u}} = 8.314$ $\text{kJ kmol}^{-1}\,\text{K}^{-1}$		$C_{\text{pv,in}} = 1.37$ $\text{kJ kg}^{-1}\,\text{K}^{-1}$
$MW_{\text{R245fa}} = 134$ kg kmol^{-1}		$i_{\text{v,in}} = 429.8\,\text{kJ kg}^{-1}$
$MW_{n\text{-pentane}} = 72.15$ kg kmol^{-1}	$i_{\text{f,Test,out,Pri}} = i_{\text{f,Test,Avg}} - \dfrac{\dot{Q}_{\text{Test}}}{2\dot{m}_{\text{f}}}$	$i_{\text{f,Test,out,Pri}} = 239.9\,\text{kJ kg}^{-1}$

Table E.5. Heat transfer coefficient calculation within Price and Bell (1974) framework sample calculation – Cont.

Heat Transfer Sample Calculations: R245fa / *n*-pentane Mixture; 1/21/2012; Run 3		
Inputs	**Equations**	**Results**
	$q_{f,Test,Avg} = \left(q_{f,Test,in,Pri} + q_{f,Test,out,PB}\right)/2$	$q_{f,Test,Avg} = 0.39$ $q_{f,Test,out,PB} = 0.34$ $\left(\text{Solved Iteratively}\right)$
	$\dot{m}_{v,Avg} = \dot{m}_f q_{f,Test,Avg}$	$\dot{m}_{v,Avg} = 0.0093\,\mathrm{kg\,s^{-1}}$
	$G_v = \dot{m}_{v,Avg}/A_c$	$G_v = 197.6\,\mathrm{kg\,m^{-2}\,s^{-1}}$
	$\mathrm{Re}_v = \dfrac{G_v D_{Test,i}}{\mu_{v,in}}$	$\mathrm{Re}_v = 146{,}118$
	$A_{HT} = \pi D_{Test,i}\sqrt{\alpha}\left(L_{Annulus} + 2L_{Tee}\right)$	$A_{HT} = 0.0136\,\mathrm{m^2}$
	$f_v =$ $8\left[\left(\dfrac{8}{\mathrm{Re}_v}\right)^{12} + \left\{\left(2.457\ln\dfrac{1}{(\frac{7}{\mathrm{Re}_v})^{0.9} + 0.27(\frac{e_{Test}}{D_{Test,i}})}\right)^{16} + \left(\dfrac{37530}{\mathrm{Re}_v}\right)^{16}\right\}^{-3/2}\right]^{1/12}$	$f_v = 0.018$ (Churchill, 1977b)
	$Nu_v =$ $\left(4.364^{10} + \dfrac{e^{\frac{2200-\mathrm{Re}_v}{365}}}{4.364^2} + \dfrac{1}{\left(6.3 + \dfrac{0.079\left(\frac{f_v}{8}\right)^{0.5}\mathrm{Re}_v\,\mathrm{Pr}_{v,in}}{\left(1+\mathrm{Pr}_{v,in}{}^{0.8}\right)^{5/6}}\right)^2}\right)^{-5}\right)^{1/10}$	$Nu_v = 276.9$ (Churchill, 1977a)
	$h_v = \dfrac{Nu_v k_{v,in}}{D_{Test,i}}$	$h_v = 611\,\mathrm{W\,m^{-2}\,K^{-1}}$

435

Table E.5. Heat transfer coefficient calculation within Price and Bell (1974) framework sample calculation – Cont.

Heat Transfer Sample Calculations: R245fa / *n*-pentane Mixture; 1/21/2012; Run 3		
Inputs	**Equations**	**Results**
	$$LMTD_{\mathrm{v}} = \frac{\left(\Delta T_{\mathrm{lv,in}}\right) - \left(T_{\mathrm{v,out}} - T_{\mathrm{int,out}}\right)}{\ln\left(\dfrac{\Delta T_{\mathrm{lv,in}}}{T_{\mathrm{v,out}} - T_{\mathrm{int,out}}}\right)}$$	$LMTD_{\mathrm{v}} = 0.6\,\mathrm{K}$ $T_{\mathrm{v,out}} = 59.7°\mathrm{C}$ $\left(\text{Solved Iteratively}\right)$ $T_{\mathrm{int,out}} = 56.8°\mathrm{C}$ $\left(\text{Solved Iteratively}\right)$
	$\dot{Q}_{\mathrm{v}} = h_{\mathrm{v}} A_{\mathrm{HT}} LMTD_{\mathrm{v}}$	$\dot{Q}_{\mathrm{v}} = 2.8\,\mathrm{W}$
	$\dot{Q}_{\mathrm{v}} = \dot{m}_{\mathrm{v,Avg}} C_{\mathrm{pv,in}}\left(T_{\mathrm{f,Test,in,Pri}} - T_{\mathrm{v,out}}\right)$	$T_{\mathrm{v,out}} = 59.7°\mathrm{C}$
	$D_{12} =$ $f\left(\text{R245fa}, n\text{-pentane}, T_{\mathrm{f,Test,in,Pri}}, P_{\mathrm{f,Test,Avg}}\right)$	$D_{12} = 8.9 \times 10^{-7}\,\mathrm{m^2\,s^{-1}}$ Chapmann-Enskog Relation (Poling, 2001)
	$Sc_{\mathrm{v}} = \dfrac{\mu_{\mathrm{v,in}}}{D_{12}\rho_{\mathrm{v,in}}}$	$Sc_{\mathrm{v}} = 0.675$
	$Sh_{\mathrm{v}} = Nu_{\mathrm{v}}\left(\dfrac{Sc_{\mathrm{v}}}{\mathrm{Pr}_{\mathrm{v,in}}}\right)^{\!\frac{1}{3}}$	$Sh_{\mathrm{v}} = 258$
	$\beta_{\mathrm{v}} = \dfrac{Sh_{\mathrm{v}} D_{12}}{D_{\mathrm{Test,i}}}$	$\beta_{\mathrm{v}} = 0.030\,\mathrm{m\,s^{-1}}$
	$C_{\mathrm{T}} = \dfrac{P_{\mathrm{f,Test,Avg}}}{R_{\mathrm{u}} T_{\mathrm{v,Avg}}}$	$C_{\mathrm{T}} = 0.147\,\mathrm{kmol\,m^{-3}}$
	$\tilde{N}_{\mathrm{T}} = \beta_{\mathrm{v}} C_{\mathrm{T}} \ln\left(\dfrac{\tilde{z} - \tilde{y}_{\mathrm{R245fa,int,Avg}}}{\tilde{z} - \tilde{y}_{\mathrm{R245fa,Avg}}}\right)$	$\tilde{N}_{\mathrm{T}} = 0.0018$ $\qquad \mathrm{kmol\,m^{-2}\,s^{-1}}$ $\tilde{z} = 0.490$ $\tilde{y}_{\mathrm{R245fa,int,Avg}} = 0.543$ $\tilde{y}_{\mathrm{R245fa,Avg}} = 0.526$ $\left(\text{Solved Iteratively}\right)$
	$\tilde{N}_{\mathrm{R245fa}} = \tilde{z}\tilde{N}_{\mathrm{T}}$	$\tilde{N}_{\mathrm{R245fa}} = 9.0 \times 10^{-4}$ $\qquad \mathrm{kmol\,m^{-2}\,s^{-1}}$
	$\tilde{N}_{\mathrm{Pentane}} = \left(1 - \tilde{z}\right)\tilde{N}_{\mathrm{T}}$	$\tilde{N}_{\mathrm{Pentane}} = 9.2 \times 10^{-4}$ $\qquad \mathrm{kmol\,m^{-2}\,s^{-1}}$

Table E.5. Heat transfer coefficient calculation within Price and Bell (1974) framework sample calculation – Cont.

Heat Transfer Sample Calculations: R245fa / *n*-pentane Mixture; 1/21/2012; Run 3		
Inputs	**Equations**	**Results**
	$\dot{m}_{\text{v,out}} = \dot{m}_{\text{v,in}} - \begin{pmatrix} \tilde{N}_{\text{R245fa}} MW_{\text{R245fa}} \\ + \tilde{N}_{n\text{-pentane}} MW_{n\text{-pentane}} \end{pmatrix} A_{\text{HT}}$	$\dot{m}_{\text{v,out}} = 0.0081\,\text{kg s}^{-1}$
	$\dot{m}_{\text{l,out}} = \dot{m}_{\text{l,in}} + \begin{pmatrix} \tilde{N}_{\text{R245fa}} MW_{\text{R245fa}} \\ + \tilde{N}_{n\text{-pentane}} MW_{n\text{-pentane}} \end{pmatrix} A_{\text{HT}}$	$\dot{m}_{\text{l,out}} = 0.0158\,\text{kg s}^{-1}$
	$q_{\text{f,Test,out,PB}} = \dfrac{\dot{m}_{\text{v,out}}}{\dot{m}_{\text{v,out}} + \dot{m}_{\text{l,out}}}$	$q_{\text{f,Test,out,PB}} = 0.34$
	$\hat{y}_{\text{R245fa,out}} \dot{m}_{\text{v,out}} =$ $\hat{y}_{\text{R245fa,in}} \dot{m}_{\text{v,in}} - \tilde{N}_{\text{R245fa}} MW_{\text{R245fa}} A_{\text{HT}}$	$\tilde{y}_{\text{R-245fa,out}} = 0.53$ $\hat{y}_{\text{R-245fa,out}} = 0.677$
	$\hat{x}_{\text{R245fa,out}} \dot{m}_{\text{l,out}}$ $= \hat{x}_{\text{R245fa,in}} \dot{m}_{\text{l,in}} + \tilde{N}_{\text{R245fa}} MW_{\text{R245fa}} A_{\text{HT}}$	$\tilde{x}_{\text{R-245fa,out}} = 0.216$ $\hat{x}_{\text{R-245fa,out}} = 0.339$
	$i_{\text{l,out}} = f\left(P_{\text{f,Test,out}}, q = 0, \hat{x}_{\text{R245fa,out}}\right)$	$i_{\text{l,out}} = 130\,\text{kJ kg}^{-1}$
	$\dot{m}_{\text{f}} i_{\text{f,Test,out,Pri}} = \dot{m}_{\text{v,out}} i_{\text{v,out}} + \dot{m}_{\text{l,out}} i_{\text{l,out}}$	$i_{\text{v,out}} = 430.4\,\text{kJ kg}^{-1}$
	$T_{\text{l,out}} = T_{\text{int,out}} = f\left(P_{\text{f,Test,out}}, q = 0, \hat{x}_{\text{R245fa,out}}\right)$	$T_{\text{l,out}} = T_{\text{int,out}} = 56.8°\text{C}$
	$T_{\text{v,out}} = f\left(P_{\text{f,Test,out}}, i_{\text{v,out}}, y_{\text{R245fa,out}}\right)$	$T_{\text{v,out}} = 59.7°\text{C}$
	$\tilde{x}_{\text{R245fa,int,Avg}} = \left(\tilde{x}_{\text{R245fa,in}} + \tilde{x}_{\text{R245fa,out}}\right)/2$	$\tilde{x}_{\text{R245fa,int,Avg}} = 0.197$ $\hat{x}_{\text{R245fa,int,Avg}} = 0.312$
	$T_{\text{int,Avg}} = f\left(P_{\text{f,Test,Avg}}, q = 0, \hat{x}_{\text{R245fa,int,Avg}}\right)$	$T_{\text{int,Avg}} = 58.3°\text{C}$
	$\tilde{y}_{\text{R245fa,int,Avg}} = f\left(T_{\text{int,Avg}}, P_{\text{f,Test,Avg}}, q = 0\right)$	$\tilde{y}_{\text{R245fa,int,Avg}} = 0.543$ $\hat{y}_{\text{R245fa,int,Avg}} = 0.688$
	$\tilde{y}_{\text{R245fa,Avg}} = \left(\tilde{y}_{\text{R245fa,in}} + \tilde{y}_{\text{R245fa,out}}\right)/2$	$\tilde{y}_{\text{R245fa,Avg}} = 0.526$
	$T_{\text{f,Test,out,Eq}} = f\left(i_{\text{f,Test,out,Pri}}, P_{\text{f,Test,out}}, x_{\text{R245fa}}\right)$	$T_{\text{f,Test,out,Eq}} = 57.3°\text{C}$
	$\Delta T_{\text{f,Test,out,v}} = T_{\text{v,out}} - T_{\text{f,Test,out,Eq}}$	$\Delta T_{\text{f,Test,out,v}} = 2.4\,\text{K}$
	$\Delta T_{\text{f,Test,out,l}} = T_{\text{l,out}} - T_{\text{f,Test,out,Eq}}$	$\Delta T_{\text{f,Test,out,l}} = -0.5\,\text{K}$
	$\dot{Q}_{\text{Test}} = \dfrac{T_{\text{wall,i}} - T_{\text{w,Pri,Avg}}}{R_{\text{Conv,Eq}} + R_{\text{Test,wall}}}$	$T_{\text{wall,i}} = 48.6°\text{C}$

Table E.5. Heat transfer coefficient calculation within Price and Bell (1974) framework sample calculation – Cont.

Heat Transfer Sample Calculations: R245fa / *n*-pentane Mixture; 1/21/2012; Run 3		
Inputs	**Equations**	**Results**
	LMTD_1 $$= \frac{\left(T_{\text{f,Test,in,Pri}} - T_{\text{w,Pri,Test,out}}\right) - \left(T_{\text{int,out}} - T_{\text{w,Pri,Test,in}}\right)}{\ln\left(\dfrac{T_{\text{f,Test,in,Pri}} - T_{\text{w,Pri,Test,out}}}{T_{\text{int,out}} - T_{\text{w,Pri,Test,in}}}\right)}$$	$\text{LMTD}_1 = 11.7\,\text{K}$
	$\dot{Q}_{\text{Test}} = UA_{\text{f,PB}}\text{LMTD}_1$	$UA_{\text{f,PB}} = 49.5\,\text{W}\,\text{K}^{-1}$
	$UA_{\text{f,PB}} = \left(\dfrac{1}{h_{\text{f,PB}}\pi D_{\text{Test,i}}\left(L_{\text{Annulus}} + 2L_{\text{Tee}}\right)}\right)^{-1}$	$h_{\text{f,PB}} = 4350\,\text{W}\,\text{m}^{-2}\,\text{K}^{-1}$
	$\Delta h_{\text{f}} = \dfrac{h_{\text{f}} - h_{\text{f,PB}}}{h_{\text{f}}}$	$\Delta h_{\text{f}} = 2.8\%$

Table E.6. R245fa / *n*-pentane data point frictional pressure drop sample calculation

Pressure Drop Sample Calculations: R245fa / *n*-pentane Mixture; 1/21/2012; Run 3		
Inputs	**Equations**	**Results**
$x_{\text{R-245fa}} = 0.454$	Inlet Liquid Properties	$\rho_{\text{l,in}} = 676.1\,\text{kg}\,\text{m}^{-3}$
$\dot{m}_{\text{f}} = 0.02394\,\text{kg}\,\text{s}^{-1}$	$f\left(i_{\text{f,Test,in,Pri}}, P_{\text{f,Test,in}}, x_{\text{R245fa}}\right)$	$\hat{x}_{\text{R245fa,in}} = 0.285$
$P_{\text{f,Test,in}} = 411.2\,\text{kPa}$	Inlet Liquid Properties	$\mu_{\text{l,in}} = 1.63\times10^{-4}$
$P_{\text{f,Test,out}} = 400.6\,\text{kPa}$	$f\left(P_{\text{f,Test,in}}, q=0, \hat{x}_{\text{R245fa,in}}\right)$	$\text{kg}\,\text{m}^{-1}\,\text{s}^{-1}$
$\Delta P_{\text{f,Measured}} = 9.8\,\text{kPa}$	Inlet Vapor Properties	$\rho_{\text{v,in}} = 17.5\,\text{kg}\,\text{m}^{-3}$
$i_{\text{f,Test,in,Pri}} = 264.5$	$f\left(i_{\text{f,Test,in,Pri}}, P_{\text{f,Test,in}}, x_{\text{R245fa}}\right)$	$\hat{y}_{\text{R245fa,in}} = 0.669$
$\text{kJ}\,\text{kg}^{-1}$	Inlet Vapor Properties	$\mu_{\text{v,in}} = 1.05\times10^{-5}$
$i_{\text{f,Test,out,Pri}} = 239.5$	$f\left(P_{\text{f,Test,in}}, q=1, \hat{y}_{\text{R245fa,in}}\right)$	$\text{kg}\,\text{m}^{-1}\,\text{s}^{-1}$
$\text{kJ}\,\text{kg}^{-1}$	Outlet Liquid Properties	$\rho_{\text{l,out}} = 695.6\,\text{kg}\,\text{m}^{-3}$
$q_{\text{f,Test,in,Pri}} = 0.44$	$f\left(i_{\text{f,Test,out,Pri}}, P_{\text{f,Test,out}}, x_{\text{R245fa}}\right)$	$\hat{x}_{\text{R245fa,out}} = 0.326$
$q_{\text{f,Test,out,Pri}} = 0.35$	Outlet Liquid Properties	$\mu_{\text{l,out}} = 1.66\times10^{-4}$
$\dot{Q}_{\text{Test}} = 598.5\,\text{W}$	$f\left(P_{\text{f,Test,out}}, q=0, \hat{x}_{\text{R245fa,out}}\right)$	$\text{kg}\,\text{m}^{-1}\,\text{s}^{-1}$
$D_{\text{Test,i}} = 7.75\,\text{mm}$	Outlet Vapor Properties	$\rho_{\text{v,out}} = 17.5\,\text{kg}\,\text{m}^{-3}$
$L_{\Delta\text{P}} = 0.746\,\text{m}$	$f\left(i_{\text{f,Test,out,Pri}}, P_{\text{f,Test,out}}, x_{\text{R245fa}}\right)$	$\hat{y}_{\text{R245fa,out}} = 0.697$
	Outlet Vapor Properties	$\mu_{\text{v,out}} = 1.05\times10^{-5}$
	$f\left(P_{\text{f,Test,out}}, q=1, \hat{y}_{\text{R245fa,out}}\right)$	$\text{kg}\,\text{m}^{-1}\,\text{s}^{-1}$
	$\alpha_{\text{f,Test,in}} =$ $\left(1+\left(\dfrac{1-q_{\text{f,Test,in,Pri}}}{q_{\text{f,Test,in,Pri}}}\right)^{0.74}\left(\dfrac{\rho_{\text{v,in}}}{\rho_{\text{l,in}}}\right)^{0.65}\left(\dfrac{\mu_{\text{l,in}}}{\mu_{\text{v,in}}}\right)^{0.13}\right)^{-1}$	$\alpha_{\text{f,Test,in}} = 0.863$ (Baroczy, 1965)
	$\alpha_{\text{f,Test,out}} =$ $\left(1+\left(\dfrac{1-q_{\text{f,Test,out,Pri}}}{q_{\text{f,Test,out,Pri}}}\right)^{0.74}\left(\dfrac{\rho_{\text{v,out}}}{\rho_{\text{l,out}}}\right)^{0.65}\left(\dfrac{\mu_{\text{l,out}}}{\mu_{\text{v,out}}}\right)^{0.13}\right)^{-1}$	$\alpha_{\text{f,Test,out}} = 0.828$ (Baroczy, 1965)
	$\Delta P_{\text{f,Decel}} =$ $\left\{\left[G^2\left(\dfrac{q^2}{\rho_{\text{v,out}}\alpha}+\dfrac{(1-q)^2}{\rho_{\text{l,out}}(1-\alpha)}\right)\right]_{\substack{\alpha=\alpha_{\text{f,Test,out}}\\ q=q_{\text{f,Test,out,Pri}}}}-\left[G^2\left(\dfrac{q^2}{\rho_{\text{v,in}}\alpha}+\dfrac{(1-q)^2}{\rho_{\text{l,in}}(1-\alpha)}\right)\right]_{\substack{\alpha=\alpha_{\text{f,Test,in}}\\ q=q_{\text{f,Test,in,Pri}}}}\right\}$	$\Delta P_{\text{f,Decel}} = -1.1\,\text{kPa}$ $(11\%\ \text{Measured})$ (Carey, 2008)

Table E.7. R245fa / *n*-pentane data point frictional pressure drop sample calculation

Pressure Drop Sample Calculations: R245fa / *n*-pentane Mixture; 1/21/2012; Run 3		
Inputs	**Equations**	**Results**
$\Delta P_{\text{f,Measured}} = 9.8\,\text{kPa}$	$\Delta P_{\text{f,Measured}} = \Delta P_{\text{fr}} + \Delta P_{\text{f,Decel}}$	$\Delta P_{\text{fr}} = 10.9\,\text{kPa}$
$\Delta P_{\text{f,Decel}} = -1.1\,\text{kPa}$	$\nabla P_{\text{fr}} = \dfrac{\Delta P_{\text{fr}}}{L_{\Delta P}}$	$\nabla P_{\text{fr}} = 14.6\,\text{kPa}\,\text{m}^{-1}$
$L_{\Delta P} = 0.746\,\text{m}$		

APPENDIX F: MODEL DEVELOPMENT

Table F. 1. Modeling sample calculation – Flow regime

Model Sample Calculations: R245fa / *n*-pentane Mixture; 1/21/2012; Run 1		
Inputs	**Equations**	**Results**
Flow Regime Model		
$D = 7.75\,\text{mm}$	$i_{\text{in}} = f\left(q + \Delta q / 2, P_{\text{avg}}, x_{\text{R245fa}}\right)$	$i_{\text{in}} = 211.8\,\text{kJ}\,\text{kg}^{-1}$
$x_{\text{R-245fa}} = 0.45$	$i_{\text{out}} = f\left(q - \Delta q / 2, P_{\text{avg}}, x_{\text{R245fa}}\right)$	$i_{\text{out}} = 191.4\,\text{kJ}\,\text{kg}^{-1}$
$x_{n\text{-pentane}} = 0.55$	Inlet Liquid Equilibrium Properties	$\rho_{\text{l}} = 726\,\text{kg}\,\text{m}^{-3}$
$G = 505\,\text{kg}\,\text{m}^2\,\text{s}^{-1}$	$f\left(i_{\text{in}}, P_{\text{avg}}, \hat{x}_{\text{R245fa,in}}\right)$	$\mu_{\text{l}} = 1.70 \times 10^{-4}$ $\text{kg}\,\text{m}^{-1}\,\text{s}^{-1}$
$P_{\text{Avg}} = 401\,\text{kPa}$		$k_{\text{l}} = 0.09\,\text{W}\,\text{m}^{-1}\,\text{K}^{-1}$
$q = 0.19$		$\text{Pr}_{\text{l}} = 3.89$
$\Delta q = 0.095$		$C_{\text{pl}} = 2.06$ $\text{kJ}\,\text{kg}^{-1}\,\text{K}^{-1}$
		$\sigma = 0.011\,\text{N}\,\text{m}^{-1}$
	Inlet Vapor Equilibrium Properties	$\rho_{\text{v}} = 18\,\text{kg}\,\text{m}^{-3}$
	$f\left(i_{\text{in}}, P_{\text{avg}}, \hat{y}_{\text{R245fa,in}}\right)$	$\mu_{\text{v}} = 1.06 \times 10^{-5}$ $\text{kg}\,\text{m}^{-1}\,\text{s}^{-1}$
		$k_{\text{v}} = 0.017\,\text{W}\,\text{m}^{-1}\,\text{K}^{-1}$
		$\text{Pr}_{\text{v}} = 0.84$
		$C_{\text{pv}} = 1.31$ $\text{kJ}\,\text{kg}^{-1}\,\text{K}^{-1}$
	$\text{Re}_{\text{l}} = G(1-q)D / \mu_{\text{l}}$	$\text{Re}_{\text{l}} = 18{,}750$
	$X_{\text{tt}} = \left(\left(\dfrac{1-q}{q}\right)^{1.8}\left(\dfrac{\rho_{\text{v}}}{\rho_{\text{l}}}\right)\left(\dfrac{\mu_{\text{l}}}{\mu_{\text{v}}}\right)^{0.2}\right)^{0.5}$	$X_{\text{tt}} = 0.81$
	$\text{Ga} = gD^3\rho^2\mu^{-2}$	$\text{Ga} = 8.33 \times 10^7$
	$\text{Fr} = 1.26\,\text{Re}_{\text{l}}^{1.04}\left(\dfrac{1+1.09X_{\text{tt}}^{0.039}}{X_{\text{tt}}}\right)^{1.5}\dfrac{1}{\text{Ga}^{0.5}}$	$\text{Fr} = 15.77$ Transition

Table F.2. Modeling sample calculation – Void fraction

Model Sample Calculations: R245fa / *n*-pentane Mixture; 1/21/2012; Run 1		
Inputs	**Equations**	**Results**
Void Fraction Model		
	$$j = G\left[\frac{q}{\rho_v} + \frac{(1-q)}{\rho_l}\right]$$	$j = 5.78$ m s^{-1}
Wavy Contribution		
	$$\frac{\bar{V}_{vj,W}}{j} = 1.47\left(\frac{g(\rho_l - \rho_v)\sigma}{j^4\rho_l^2}\right)^{0.27}$$	$$\frac{\bar{V}_{vj,W}}{j} = 0.0205$$
Annular Contribution		
	$$\frac{\bar{V}_{vj,A}}{j} = 49.1(1-q)^{0.11}\left(\frac{g(\rho_l - \rho_v)\sigma}{j^4\rho_l^2}\right)^{0.507}$$	$$\frac{\bar{V}_{vj,A}}{j} = 0.0157$$
Transition Calculation		
	$$\frac{\bar{V}_{vj}}{j} = \frac{(\mathrm{Fr}_{so}-10)\bar{V}_{vj,A} + (20-\mathrm{Fr}_{so})\bar{V}_{vj,W}}{10}$$	$$\frac{\bar{V}_{vj}}{j} = 0.0174$$
	$$\beta = \left(1 + \frac{1-q}{q}\left(\frac{\rho_v}{\rho_l}\right)\right)^{-1}$$	$\beta = 0.90$
	$$\alpha = \frac{\beta}{1 + \bar{V}_{vj}/j}$$	$\alpha = 0.887$

Table F.3. Modeling sample calculation – Frictional pressure drop

Model Sample Calculations: R245fa / *n*-pentane Mixture; 1/21/2012; Run 1		
Inputs	**Equations**	**Results**
Frictional pressure drop model		
Annular Contribution		
	$D_i = \sqrt{\alpha} \cdot D$	$D_i = 0.0073\text{m}$
	$\text{Re}_{vi} = \dfrac{GqD_i}{\mu_v}$	$\text{Re}_{vi} = 64{,}830$
	$f_v = 8\left(\left(\dfrac{8}{\text{Re}_{vi}}\right)^{12} + \left(\left(2.457\ln\left(\dfrac{1}{\left(\dfrac{7}{\text{Re}_{vi}}\right)^{0.9}+0.27\left(\dfrac{\varepsilon}{D_i}\right)}\right)\right)^{16} + \left(\dfrac{37530}{\text{Re}_{vi}}\right)^{16}\right)^{-1.5}\right)^{1/12}$	$f_v = 0.0205$
	$\dfrac{f_{v,iA}}{f_v} = \left(1 + 2.54\left(1-q\right)^{0.346} + 0.290\text{X}_{tt}^{1.25}\left(\dfrac{\rho_l}{\rho_v}\right)^{0.834}\right)$	$f_{v,iA} = 0.165$
Wavy Contribution		
	$\eta_{Up} = 1 - \left(1 + 2.68\left(\dfrac{G}{500}\right)^{1.06}\left(\dfrac{0.007}{D}\right)^{2.08}\right)^{-1}$	$\eta_{Up} = 0.27$
	$\left(1-\alpha\right)\left(1-\eta_{Up}\right) = $ $\left(\left(1-\dfrac{\theta_{Strat}}{2\pi}\right) - \dfrac{1}{2\pi}\sin\left(2\pi - \theta_{Strat}\right)\right)$	$\theta_{Strat} = 4.77 \text{ radians}$
	$\text{Re}_l = \dfrac{G\left(1-q\right)D}{\mu_l}$	$\text{Re}_l = 18{,}750$
	$f_l = 8\left(\left(\dfrac{8}{\text{Re}_l}\right)^{12} + \left(\left(2.457\ln\left(\dfrac{1}{\left(\dfrac{7}{\text{Re}_l}\right)^{0.9}+0.27\left(\dfrac{\varepsilon}{D}\right)}\right)\right)^{16} + \left(\dfrac{37530}{\text{Re}_l}\right)^{16}\right)^{-1.5}\right)^{1/12}$	$f_l = 0.0267$

Table F.3. Modeling sample calculation – Frictional pressure drop – Cont.

Model Sample Calculations: R245fa / *n*-pentane Mixture; 1/21/2012; Run 1		
Inputs	**Equations**	**Results**
Frictional pressure drop model - Continued		
	$$\frac{f_{v,iU}}{f_l} = \left(1.26 + 0.335 X_{tt}^{1.28} \left(\frac{\rho_l}{\rho_v}\right)^{0.895} \eta_{Up}^{0.339}\right)$$	$f_{v,iU} = 0.149$
	$$f_{v,i,W} = \frac{\theta_{Strat}}{2\pi} f_{v,i,U} + \left(1 - \frac{\theta_{Strat}}{2\pi}\right) f_l$$	$f_{v,iW} = 0.120$
Transition Calculation		
	$$f_{v,i} = \frac{\left(Fr_{so} - 10\right) f_{v,i,A} + \left(20 - Fr_{so}\right) f_{v,i,W}}{10}$$	$f_{v,i} = 0.149$
	$$\nabla P_f = \frac{1}{2} f_i \frac{\rho_v j_v^2}{\alpha^{2.5} D} = \frac{1}{2} f_i \frac{G^2 q^2}{\rho_v \alpha^{2.5} D}$$	$\nabla P_f = 6.37 \, \text{kPa m}^{-1}$

Table F.4. Modeling sample calculation – Heat transfer coefficient

Model Sample Calculations: R245fa / *n*-pentane Mixture; 1/21/2012; Run 1		
Inputs	**Equations**	**Results**
Heat transfer model		
Annular Contribution		
	$\delta = D/2\left(1-\sqrt{\alpha}\right)$	$\delta = 0.00023$ m
	$\mathrm{Re}_{\mathrm{l},\delta} = \dfrac{4G(1-q)\delta}{\mu_l(1-\alpha)}$	$Re_{\mathrm{l},\delta} = 19315$
	$U_{\mathrm{v}} = \dfrac{Gq}{\rho_{\mathrm{v}}\alpha}$	$U_{\mathrm{v}} = 5.88$ m s^{-1}
	$U_{\mathrm{l}} = \dfrac{G(1-q)}{\rho_{\mathrm{l}}(1-\alpha)}$	$U_{\mathrm{l}} = 5.0$ m s^{-1}
	$f_{\mathrm{l,i}} = \left(\dfrac{\mu_{\mathrm{v}}}{\mu_{\mathrm{l}}}\right)^{0.32}\left(\dfrac{(\rho_{\mathrm{l}}-\rho_{\mathrm{v}})g\delta^2}{\sigma}\right)^{0.16}\left(\dfrac{U_{\mathrm{v}}}{U_{\mathrm{l}}}\right)^{0.73}$	$f_{\mathrm{l}} = 0.0314$
	$h_{\mathrm{A}} = \dfrac{k_{\mathrm{l}}}{\delta}0.00667\,\mathrm{Re}_{\mathrm{l},\delta}^{0.8}\,\mathrm{Pr}_{\mathrm{l}}^{0.3}\,f_{\mathrm{l,i}}$	$h_{\mathrm{A}} = 2.85$ kW m^{-2} K^{-1}
Wavy Contribution		
	$\eta_{\mathrm{Up}} = 1-\left(1+2.68\left(\dfrac{G}{500}\right)^{1.06}\left(\dfrac{0.007}{D}\right)^{2.08}\right)^{-1}$	$\eta_{\mathrm{Up}} = 0.27$
	$\delta = D/2\left(1-\sqrt{\alpha}\right)$	$\delta = 0.00023$ m
	$\mathrm{Re}_{\mathrm{l},\delta} = \dfrac{4G(1-q)\delta}{\mu_l(1-\alpha)}$	$Re_{\mathrm{l},\delta,Up} = 19{,}315$
	$U_{\mathrm{v}} = \dfrac{Gq}{\rho_{\mathrm{v}}\alpha}$	$U_{\mathrm{v}} = 5.88$ m s^{-1}
	$U_{\mathrm{l}} = \dfrac{G(1-q)}{\rho_{\mathrm{l}}(1-\alpha)}$	$U_{\mathrm{l}} = 5.0$ m s^{-1}
	$f_{\mathrm{l,i}} = \left(\dfrac{\mu_{\mathrm{v}}}{\mu_{\mathrm{l}}}\right)^{0.32}\left(\dfrac{(\rho_{\mathrm{l}}-\rho_{\mathrm{v}})g\delta^2}{\sigma}\right)^{0.16}\left(\dfrac{U_{\mathrm{v}}}{U_{\mathrm{l}}}\right)^{0.73}$	$f_{\mathrm{l,i}} = 0.0.0314$
	$h_{\mathrm{A}} = \dfrac{k_{\mathrm{l}}}{\delta}0.00667\,\mathrm{Re}_{\mathrm{l},\delta}^{0.8}\,\mathrm{Pr}_{\mathrm{l}}^{0.3}\,f_{\mathrm{l,i}}$	$h_{\mathrm{A}} = 2.85$ kW m^{-2} K^{-1}
	$h_{Nusselt} = 0.728\left(\dfrac{k_{\mathrm{l}}^{3}\rho_{\mathrm{l}}(\rho_{\mathrm{l}}-\rho_{\mathrm{v}})g i_{\mathrm{fg}}}{\mu_{\mathrm{l}}D\Delta T_{\mathrm{avg}}}\right)^{0.25}$	$h_{\mathrm{Nusselt}} = 2.05$ kW m^{-2} K^{-1}

Table F.4. Modeling sample calculation – Heat transfer coefficient – Cont.

Model Sample Calculations: R245fa / *n*-pentane Mixture; 1/21/2012; Run 1		
Inputs	**Equations**	**Results**
Heat transfer model – Continued		
	$h_{\mathrm{Up}} = \left(h_{\mathrm{Nusselt}}^3 + h_{\mathrm{A}}^3 \right)^{1/3}$	$h_{\mathrm{Up}} = 3.17$ kW m^{-2} K^{-1}
	$\mathrm{Re}_{\mathrm{lp}} = \dfrac{G(1-q)(1-\eta_{\mathrm{Up}})D}{\mu_{\mathrm{l}}}$	$\mathrm{Re}_{\mathrm{lp}} = 13{,}625$
	$f_{\mathrm{lp}} = 8 \left(\left(\dfrac{8}{\mathrm{Re}_{\mathrm{lp}}} \right)^{12} + \left(\left(2.457 \ln \left(\dfrac{1}{\left(\dfrac{7}{\mathrm{Re}_{\mathrm{lp}}} \right)^{0.9} + 0.27\left(\dfrac{\varepsilon}{D} \right)} \right) \right)^{16} + \left(\dfrac{37530}{\mathrm{Re}_{\mathrm{lp}}} \right)^{16} \right)^{-1.5} \right)^{1/12}$	$f_{\mathrm{lp}} = 0.029$
	$h_{\mathrm{lp}} = \dfrac{k_{\mathrm{l}}}{D} \left(4.364^{10} + \left(\dfrac{exp\left(\dfrac{2200 - \mathrm{Re}_{\mathrm{lp}}}{365} \right)}{4.364^2} + \dfrac{1}{\left(6.3 + 0.079\left(\dfrac{f_{\mathrm{lp}}}{8} \right)^{0.5} \mathrm{Re}_{\mathrm{lp}} \dfrac{\mathrm{Pr}}{(1+\mathrm{Pr}^{0.8})^{5/6}} \right)^2} \right)^{-5} \right)^{1/10}$	$h_{\mathrm{lp}} = 1.0$ kW m^{-2} K^{-1}
	$h_{\mathrm{W}} = \dfrac{\theta_{\mathrm{Strat}}}{2\pi} h_{\mathrm{Up}} + \left(1 - \dfrac{\theta_{\mathrm{Strat}}}{2\pi} \right) h_{\mathrm{lp}}$	$h_{\mathrm{W}} = 2.65$ kW m^{-2} K^{-1}
Transition Calculation		
	$h = \dfrac{(\mathrm{Fr}_{\mathrm{so}} - 10)h_{\mathrm{A}} + (20 - \mathrm{Fr}_{\mathrm{so}})h_{\mathrm{W}}}{10}$	$h = 2.78$ kW m^{-2} K^{-1}
Zeotropic Mixture heat transfer model – SBG Method		
	$T_{\mathrm{in,Eq}} = f\left(i_{\mathrm{in}}, P_{\mathrm{avg}}, x_{\mathrm{R245fa}} \right)$	$T_{\mathrm{in,Eq}} = 55.9°\mathrm{C}$
	$T_{\mathrm{out,Eq}} = f\left(i_{\mathrm{out}}, P_{\mathrm{avg}}, x_{\mathrm{R245fa}} \right)$	$T_{\mathrm{out,Eq}} = 54.9°\mathrm{C}$
	$\delta q_{\mathrm{vo}} = GAqCp_{\mathrm{v}}\left(T_{\mathrm{in,Eq}} - T_{\mathrm{out,Eq}} \right)$	$\delta q_{\mathrm{vo}} = 0.0056\,\mathrm{kW}$
	$\delta q_{\mathrm{seg}} = GA\left(i_{\mathrm{in}} - i_{\mathrm{out}} \right)$	$\delta q_{\mathrm{seg}} = 0.488\,\mathrm{kW}$
	$\mathrm{Re}_{\mathrm{v}} = \dfrac{GqD}{\mu_{\mathrm{v}}}$	$\mathrm{Re}_{\mathrm{v}} = 64{,}830$

Table F.4. Modeling sample calculation – Heat transfer coefficient – Cont.

Heat Transfer Sample Calculations: R245fa / *n*-pentane Mixture; 1/21/2012; Run 3		
Inputs	**Equations**	**Results**
Zeotropic Mixture heat transfer model – SBG Method - Continued		
	$$f_{\mathrm{v}} = 8 \left(\left(\frac{8}{\mathrm{Re_v}} \right)^{12} + \left(\left(2.457 \ln \left(\frac{1}{\left(\frac{7}{\mathrm{Re_v}} \right)^{0.9} + 0.27 \left(\frac{\varepsilon}{D} \right)} \right) \right)^{16} + \left(\frac{37530}{\mathrm{Re_v}} \right)^{16} \right)^{-1.5} \right)^{1/12}$$	$f_{\mathrm{v}} = 0.020$
	$$h_{\mathrm{v}} = \frac{k_{\mathrm{v}}}{D} \left(4.364^{10} + \left(\frac{exp\left(\frac{2200 - \mathrm{Re_v}}{365} \right)}{4.364^2} + \frac{1}{\left(6.3 + 0.079 \left(\frac{f_{\mathrm{v}}}{8} \right)^{0.5} \mathrm{Re_v} \frac{\mathrm{Pr}}{\left(1 + \mathrm{Pr}^{0.8} \right)^{5/6}} \right)^{2}} \right)^{-5} \right)^{1/10}$$	$h_{\mathrm{v}} = 0.30 \ \mathrm{kW \ m^{-2}}$ $\mathrm{K^{-1}}$
	$$h_{\mathrm{SBG}} = \left[\frac{1}{h} + \frac{\delta q_{\mathrm{vo}}}{\delta q_{\mathrm{seg}}} \frac{1}{h_{\mathrm{v}}} \right]^{-1}$$	$h_{\mathrm{SBG}} = 2.54 \ \mathrm{kW \ m^{-2} \ K^{-1}}$
Zeotropic Mixture heat transfer model –Price and Bell (1974) Method		
	$\tilde{x}_{\mathrm{R245fa,in}} = f\left(i_{\mathrm{in}}, P_{\mathrm{f,Avg}}, x_{\mathrm{R245fa}} \right)$	$\tilde{x}_{\mathrm{R245fa,in}} = 0.177$ $\hat{x}_{\mathrm{R245fa,in}} = 0.286$
	$\tilde{y}_{\mathrm{R245fa,in}} = f\left(i_{\mathrm{in}}, P_{\mathrm{f,Avg}}, x_{\mathrm{R245fa}} \right)$	$\tilde{y}_{\mathrm{R245fa,in}} = 0.522$ $\hat{y}_{\mathrm{R245fa,in}} = 0.670$
	$\dot{m}_{\mathrm{v,Avg}} = \dot{m}_{\mathrm{f}} q_{\mathrm{Avg}}$	$\dot{m}_{\mathrm{v,Avg}} = 0.0045 \, \mathrm{kg \, s^{-1}}$
	$G_{\mathrm{v}} = \dot{m}_{\mathrm{v,Avg}} / A_{\mathrm{c}}$	$G_{\mathrm{v}} = 97.3 \, \mathrm{kg \, m^{-2} \, s^{-1}}$
	$A_{\mathrm{HT}} = \pi D_{\mathrm{i}} \left(L_{\mathrm{Seg}} \right)$	$A_{\mathrm{VL}} = 0.0122 \, \mathrm{m^2}$
	$\mathrm{Re_v} = \dfrac{G_{\mathrm{v}} D_{\mathrm{i}}}{\mu_{\mathrm{v}}}$	$\mathrm{Re_v} = 71{,}330$

Table F.4. Modeling sample calculation – Heat transfer coefficient – Cont.

Model Sample Calculations: R245fa / *n*-pentane Mixture; 1/21/2012; Run 1		
Inputs	**Equations**	**Results**
Zeotropic Mixture heat transfer model –Price and Bell (1974) Method - Continued		
	$f_{\mathrm{v}} =$ $$8\left[\left(\frac{8}{\mathrm{Re}_{\mathrm{v}}}\right)^{12}+\left\{\left(2.457\ln\frac{1}{(\frac{7}{\mathrm{Re}_{\mathrm{v}}})^{0.9}+0.27(\frac{e_{\mathrm{Test}}}{D_{\mathrm{Test,i}}})}\right)^{16}+\left(\frac{37530}{\mathrm{Re}_{\mathrm{v}}}\right)^{16}\right\}^{-\frac{3}{2}}\right]^{1/12}$$	$f_{\mathrm{v}} = 0.020$ (Churchill, 1977b)
	$Nu_{\mathrm{v}} =$ $$\left(4.364^{10}+\left(\frac{e^{\frac{2200-\mathrm{Re}_{\mathrm{v}}}{365}}}{4.364^{2}}+\frac{1}{\left(6.3+\frac{0.079\left(\frac{f_{\mathrm{v}}}{8}\right)^{0.5}\mathrm{Re}_{\mathrm{v}}\,\mathrm{Pr}_{\mathrm{v,in}}}{\left(1+\mathrm{Pr}_{\mathrm{v,in}}{}^{0.8}\right)^{5/6}}\right)^{2}}\right)^{-5}\right)^{1/10}$$	$Nu_{\mathrm{v}} = 146$ (Churchill, 1977a)
	$h_{\mathrm{v}} = \dfrac{Nu_{\mathrm{v}}k_{\mathrm{v,in}}}{D_{\mathrm{Test,i}}}$	$h_{\mathrm{v}} = 0.314\,\mathrm{kW\,m^{-2}\,K^{-1}}$
	$LMTD_{\mathrm{v}} = \dfrac{\left(\Delta T_{\mathrm{lv,in}}\right)-\left(T_{\mathrm{v,out}}-T_{\mathrm{int,out}}\right)}{\ln\left(\dfrac{\Delta T_{\mathrm{lv,in}}}{T_{\mathrm{v,out}}-T_{\mathrm{int,out}}}\right)}$	$LMTD_{\mathrm{v}} = 0.17\,\mathrm{K}$ $T_{\mathrm{v,out}} = 56.0°\mathrm{C}$ $\left(\mathrm{Solved\ Iteratively}\right)$ $T_{\mathrm{int,out}} = 54.8°\mathrm{C}$ $\left(\mathrm{Solved\ Iteratively}\right)$
	$\dot{Q}_{\mathrm{v}} = h_{\mathrm{v}}A_{\mathrm{HT}}LMTD_{\mathrm{v}}$	$\dot{Q}_{\mathrm{v}} = 0.7\,\mathrm{W}$
	$\dot{Q}_{\mathrm{v}} = \dot{m}_{\mathrm{v,Avg}}C_{\mathrm{pv,in}}\left(T_{\mathrm{f,in}}-T_{\mathrm{v,out}}\right)$	$T_{\mathrm{v,out}} = 56.1°\mathrm{C}$
	$D_{12} =$ $f\left(\mathrm{R245fa},n\text{-pentane},T_{\mathrm{f,in}},P_{\mathrm{f,Avg}}\right)$	$D_{12} = 8.8\times10^{-7}\,\mathrm{m^{2}\,s^{-1}}$ Chapmann-Enskog Relation (Poling, 2001)

Table F.4. Modeling sample calculation – Heat transfer coefficient – Cont.

Model Sample Calculations: R245fa / *n*-pentane Mixture; 1/21/2012; Run 1		
Inputs	**Equations**	**Results**
Zeotropic Mixture heat transfer model –Price and Bell (1974) Method - Continued		
	$$Sc_v = \frac{\mu_{v,in}}{D_{12}\rho_{v,in}}$$	$Sc_v = 0.671$
	$$Sh_v = Nu_v \left(\frac{Sc_v}{Pr_{v,in}} \right)^{\frac{1}{3}}$$	$Sh_v = 136$
	$$\beta_v = \frac{Sh_v D_{12}}{D_{Test,i}}$$	$\beta_v = 0.015 \, \mathrm{m\,s^{-1}}$
	$$C_T = \frac{P_{f,Test,Avg}}{R_u T_{v,Avg}}$$	$C_T = 0.147 \, \mathrm{kmol\,m^{-3}}$
	$$\tilde{N}_T = \beta_v C_T \ln\left(\frac{\tilde{z} - \tilde{y}_{R245fa,int,Avg}}{\tilde{z} - \tilde{y}_{R245fa,Avg}} \right)$$	$\tilde{N}_T = 0.0015$ $\mathrm{kmol\,m^{-2}\,s^{-1}}$ $\tilde{z} = 0.574$ $\tilde{y}_{R245fa,int,Avg} = 0.589$ $\tilde{y}_{R245fa,Avg} = 0.581$ $(\text{Solved Iteratively})$
	$$\tilde{N}_{R245fa} = \tilde{z}\tilde{N}_T$$	$\tilde{N}_{R245fa} = 8.8 \times 10^{-4}$ $\mathrm{kmol\,m^{-2}\,s^{-1}}$
	$$\tilde{N}_{Pentane} = (1 - \tilde{z})\tilde{N}_T$$	$\tilde{N}_{Pentane} = 6.5 \times 10^{-4}$ $\mathrm{kmol\,m^{-2}\,s^{-1}}$
	$$\dot{m}_{v,out} = \dot{m}_{v,in} - \left(\begin{array}{c} \tilde{N}_{R245fa}MW_{R245fa} \\ + \tilde{N}_{n\text{-}pentane}MW_{n\text{-}pentane} \end{array} \right) A_{HT}$$	$\dot{m}_{v,out} = 0.0036 \, \mathrm{kg\,s^{-1}}$
	$$\dot{m}_{l,out} = \dot{m}_{l,in} + \left(\begin{array}{c} \tilde{N}_{R245fa}MW_{R245fa} \\ + \tilde{N}_{n\text{-}pentane}MW_{n\text{-}pentane} \end{array} \right) A_{HT}$$	$\dot{m}_{l,out} = 0.020 \, \mathrm{kg\,s^{-1}}$
	$$q_{f,Test,out,PB} = \frac{\dot{m}_{v,out}}{\dot{m}_{v,out} + \dot{m}_{l,out}}$$	$q_{f,Test,out,PB} = 0.15$
	$\hat{y}_{R245fa,out}\dot{m}_{v,out} =$ $\hat{y}_{R245fa,in}\dot{m}_{v,in} - \tilde{N}_{R245fa}MW_{R245fa}A_{HT}$	$\tilde{y}_{R\text{-}245fa,out} = 0.583$ $\hat{y}_{R\text{-}245fa,out} = 0.722$
	$\hat{x}_{R245fa,out}\dot{m}_{l,out}$ $= \hat{x}_{R245fa,in}\dot{m}_{l,in} + \tilde{N}_{R245fa}MW_{R245fa}A_{HT}$	$\tilde{x}_{R\text{-}245fa,out} = 0.268$ $\hat{x}_{R\text{-}245fa,out} = 0.404$

Table F.4. Modeling sample calculation – Heat transfer coefficient – Cont.

Model Sample Calculations: R245fa / *n*-pentane Mixture; 1/21/2012; Run 1		
Inputs	**Equations**	**Results**
	$i_{\mathrm{l,out}} = f\left(P_{\mathrm{f,Test,out}}, q=0, x_{\mathrm{R245fa,out}}\right)$	$i_{\mathrm{l,out}} = 154\,\mathrm{kJ\,kg^{-1}}$
	$\dot{m}_{\mathrm{f}} i_{\mathrm{f,Test,out,Pri}} = \dot{m}_{\mathrm{v,out}} i_{\mathrm{v,out}} + \dot{m}_{\mathrm{l,out}} i_{\mathrm{l,out}}$	$i_{\mathrm{v,out}} = 428\,\mathrm{kJ\,kg^{-1}}$
	$T_{\mathrm{l,out}} = T_{\mathrm{int,out}} = f\left(P_{\mathrm{f,Test,out}}, q=0, x_{\mathrm{R245fa,out}}\right)$	$T_{\mathrm{l,out}} = T_{\mathrm{int,out}} = 54.8^\circ\mathrm{C}$
	$T_{\mathrm{v,out}} = f\left(P_{\mathrm{f,Test,out}}, i_{\mathrm{v,out}}, y_{\mathrm{R245fa,out}}\right)$	$T_{\mathrm{v,out}} = 56.0^\circ\mathrm{C}$
	$\tilde{x}_{\mathrm{R245fa,int,Avg}} = \left(\tilde{x}_{\mathrm{R245fa,in}} + \tilde{x}_{\mathrm{R245fa,out}}\right)\big/2$	$\tilde{x}_{\mathrm{R245fa,int,Avg}} = 0.254$
		$\hat{x}_{\mathrm{R245fa,int,Avg}} = 0.388$
	$T_{\mathrm{int,Avg}} = f\left(P_{\mathrm{f,Test,Avg}}, q=0, x_{\mathrm{R245fa,int,Avg}}\right)$	$T_{\mathrm{int,Avg}} = 55.4^\circ\mathrm{C}$
	$\tilde{y}_{\mathrm{R245fa,int,Avg}} = f\left(T_{\mathrm{int,Avg}}, P_{\mathrm{f,Test,Avg}}, q=0\right)$	$\tilde{y}_{\mathrm{R245fa,int,Avg}} = 0.589$
		$\hat{y}_{\mathrm{R245fa,int,Avg}} = 0.728$
	$\tilde{y}_{\mathrm{R245fa,Avg}} = \left(\tilde{y}_{\mathrm{R245fa,in}} + \tilde{y}_{\mathrm{R245fa,out}}\right)\big/2$	$\tilde{y}_{\mathrm{R245fa,Avg}} = 0.581$
	$\mathrm{LMTD_1}$ $= \dfrac{\left(T_{\mathrm{f,in}} - T_{\mathrm{w,out}}\right) - \left(T_{\mathrm{int,out}} - T_{\mathrm{w,in}}\right)}{\ln\left(\dfrac{T_{\mathrm{f,in}} - T_{\mathrm{w,out}}}{T_{\mathrm{int,out}} - T_{\mathrm{w,in}}}\right)}$	$\mathrm{LMTD_1} = 13.8\,\mathrm{K}$
	$UA_{\mathrm{f,PB}} = \left(\dfrac{1}{h\pi D_{\mathrm{i}} L_{\mathrm{Seg}}}\right)^{-1}$	$UA_{\mathrm{f,PB}} = 32.0\,\mathrm{W\,K^{-1}}$
	$\dot{Q}_{\mathrm{Seg}} = UA_{\mathrm{f,PB}}\mathrm{LMTD_1}$	$Q_{\mathrm{Seg}} = 440\,\mathrm{W}$

REFERENCES

Akers, W. W., H. A. Deans and O. K. Crosser (1959), "Condensation Heat Transfer within Horizontal Tubes," *Chemical Engineering Progress Symposium Series* Vol. 55(29) pp. 171-176.

Akers, W. W. and H. F. Rosson (1960), "Condensation inside a Horizontal Tube," *Chemical Engineering Progress Symposium Series* Vol. 59 pp. 145-149.

Altman, M., R. H. Norris and F. W. Staub (1960), "Local and Average Heat Transfer and Pressure Drop for Refrigerants Evaporating in Horizontal Tubes," *Journal of Heat Transfer* pp. 189-198.

Ananiev, E. P., L. D. Boyko and G. N. Kruzhilin (1961), "Heat Transfer in the Presence of Steam Condensation in a Horizontal Tube," *International Heat Transfer Conference: Part II* p. 290.

Andresen, U. C. (2007). *Supercritical Gas Cooling and near-Critical-Pressure Condensation of Refrigerant Blends in Microchannels*.

Aprin, L., P. Mercier and L. Tadrist (2007), "Experimental Analysis of Local Void Fractions Measurements for Boiling Hydrocarbons in Complex Geometry," *International Journal of Multiphase Flow* Vol. 33(4) pp. 371-393.

Armand, A. A. (1946), "The Resistance During the Movement of a Two-Phase System in Horizontal Pipes," *Izv. Vses. Teplotekh. Inst.* Vol. 1 pp. 16–23 (AERE-Lib/Trans 828).

Azer, N. Z., L. V. Abis and H. M. Soliman (1972), "Local Heat Transfer Coefficients During Annular Flow Condensation," *ASHRAE Transactions* Vol. 78(2247 p 135-143 Part 2) pp. 135-143.

Baker, O. (1954), "Simultaneous Flow of Oil and Gas," *Oil and Gas Journal* Vol. 53(12) pp. 185-190.

Bandhauer, T. M., A. Agarwal and S. Garimella (2006), "Measurement and Modeling of Condensation Heat Transfer Coefficients in Circular Microchannels," *Journal of Heat Transfer* Vol. 128(10) pp. 1050-1059.

Bankoff, S. G. (1960), "Variable Density Single-Fluid Model for Two-Phase Flow with Particular Reference to Steam-Water Flow," *American Society of Mechanical Engineers -- Transactions -- Journal Heat Transfer Series C* Vol. 82(4) pp. 265-272.

Barnea, D. and N. Brauner (1985), "Holdup of the Liquid Slug in Two Phase Intermittent Flow," *International Journal of Multiphase Flow* Vol. 11(1) pp. 43-49.

Barnea, D., Y. Luninski and Y. Taitel (1983), "Flow Pattern in Horizontal and Vertical Two Phase Flow in Small Diameter Pipes," *Canadian Journal of Chemical Engineering* Vol. 61 pp. 617-620.

Barnea, D., O. Shoham and Y. Taitel (1982), "Flow Pattern Transition for Downward Inclined Two Phase Flow; Horizontal to Vertical," *Chemical Engineering Science* Vol. 37(5) pp. 735-740.

Baroczy, C. J. (1965), "Correlation of Liquid Fraction in Two-Phase Flow with Applications to Liquid Metals," *Chem. Eng. Prog. Symp. Series* Vol. 61(57) pp. 179-191.

Baroczy, C. J. (1966), "Systematic Correlation for Two-Phase Pressure Drop," *Chemical Engineering Progress Symposium Series* Vol. 62(64) pp. 232-249.

Bell, K. J. and M. A. Ghaly (1973), "An Approximate Generalized Design Method for Multicomponent/Partial Condensers," *AIChE Symposium Series* Vol. 69(131) pp. 72-79.

Bertsch, S. S., E. A. Groll and S. V. Garimella (2009), "Effects of Heat Flux, Mass Flux, Vapor Quality, and Saturation Temperature on Flow Boiling Heat Transfer in Microchannels," *International Journal of Multiphase Flow* Vol. 35(2) pp. 142-154.

Breber, G., J. W. Palen and J. Taborek (1979), "Prediction of Horizontal Tubeside Condensation of Pure Components Using Flow Regime Criteria," *American Society of Mechanical Engineers, Applied Mechanics Division, AMD*(Compendex) pp. 1-8.

Breber, G., J. W. Palen and J. Taborek (1980), "Prediction of Horizontal Tubeside Condensation of Pure Components Using Flow Regime Criteria," *Journal of Heat Transfer, Transactions ASME* Vol. 102(3) pp. 471-476.

Butterworth, D. (1975), "A Comparison of Some Void-Fraction Relationships for Co-Current Gas-Liquid Flow," *International Journal of Multiphase Flow* Vol. 1(6) pp. 845-850.

Canny, J. (1986), "A Computational Approach to Edge Detection," *IEEE Transactions on Pattern Analysis and Machine Intelligence* Vol. PAMI-8(6) pp. 679-698.

Carey, V. P. (2008). *Liquid-Vapor Phase-Change Phenomena: An Introduction to the Thermophysics of Vaporization and Condensation Processes in Heat Transfer Equipment*. Second Ed. New York, NY, Taylor and Francis.

Carpenter, F. G. and A. P. Colburn (1951), "The Effect of Vapor Velocity on Condensation inside Tubes," *ASME Proceedings of the General Discussion of Heat Transfer* pp. 20-26.

Cavallini, A., G. Censi, D. D. Col, L. Doretti, G. A. Longo and L. Rossetto (2002a), "Condensation of Halogenated Refrigerants inside Smooth Tubes," *HVAC and R Research* Vol. 8(4) pp. 429-451.

Cavallini, A., G. Censi, D. D. Col, L. Doretti, G. A. Longo and L. Rossetto (2002b), "In Tube Condensation of Halogenated Refrigerants," *ASHRAE Transactions* Vol. 108(1) pp. 146-161.

Cavallini, A., G. Censi, D. Del Col, L. Doretti, G. A. Longo and L. Rossetto (2001), "Experimental Investigation on Condensation Heat Transfer and Pressure Drop of New HFC Refrigerants (R134a, R125, R32, R410a, R236ea) in a Horizontal Smooth Tube," *International Journal of Refrigeration* Vol. 24(1) pp. 73-87.

Cavallini, A., G. Censi, D. Del Col, L. Doretti, G. A. Longo and L. Rossetto (2002c), "A Tube-in-Tube Water/Zeotropic Mixture Condenser: Design Procedure against Experimental Data," *Experimental Thermal and Fluid Science* Vol. 25(7) p. 495.

Cavallini, A., G. Censi, D. Del Col, L. Doretti, G. A. Longo, L. Rossetto and C. Zilio (2003), "Condensation inside and Outside Smooth and Enhanced Tubes -- a Review of Recent Research," *International Journal of Refrigeration* Vol. 26(4) pp. 373-392.

Cavallini, A., D. D. Col, L. Doretti, M. Matkovic, L. Rossetto, C. Zilio and G. Censi (2006), "Condensation in Horizontal Smooth Tubes: A New Heat Transfer Model for Heat Exchanger Design," *Heat Transfer Engineering* Vol. 27(8) pp. 31-38.

452

Cavallini, A. and R. Zecchin (1974), "A Dimensionless Correlation for Heat Transfer in Forced Convective Condensation," *Proceedings of the 5th International Heat transfer Conference, JSME*, pp. 309-313.

Chang, Y. S., M. S. Kim and S. T. Ro (2000), "Performance and Heat Transfer Characteristics of Hydrocarbon Refrigerants in a Heat Pump Systemperformance Et Caractéristiques De Transfert De Chaleur Des Frigorigènes Hydrocarbures Utilisés Dans Un Système De Pompe À Chaleur," *International Journal of Refrigeration* Vol. 23(3) pp. 232-242.

Chato, S. C. (1962), "Laminar Condensation inside Horizontal and Inclined Tubes," *ASHRAE Journal* Vol. 4(2) pp. 52-60.

Chen, I. Y., K.-S. Yang, Y.-J. Chang and C.-C. Wang (2001), "Two-Phase Pressure Drop of Air–Water and R-410a in Small Horizontal Tubes," *International Journal of Multiphase Flow* Vol. 27(7) pp. 1293-1299.

Chexal, B., G. Lellouche, J. Horowitz and J. Healzer (1992), "A Void Fraction Correlation for Generalized Applications," *Progress in Nuclear Energy* Vol. 27(4) pp. 255-295.

Chilton, T. H. and A. P. Colburn (1934), "Mass Transfer (Absorption) Coefficients: Prediction from Data on Heat Transfer and Fluid Friction," *Industrial Engineering Chemistry* Vol. 26(11) pp. 1183-1187.

Chisholm, D. (1967), "A Theoretical Basis for the Lockhart-Martinelli Correlation for Two-Phase Flow," *International Journal of Heat and Mass Transfer* Vol. 10(12) pp. 1767-1778.

Chisholm, D. (1970). Pressure Gradients During the Flow of Evaporating Two-Phase Mixtures. Nat. Engng. Lab., East Kilbride, Glasgow, UK. UK, 11 p.

Chisholm, D. (1973), "Pressure Gradients Due to Friction During the Flow of Evaporationg Two-Phase Mixtures in Smooth Tubes and Channels," *International Journal of Heat and Mass Transfer* Vol. 16(2) pp. 347-358.

Churchill, S. W. (1977a), "Comprehensive Correlating Equations for Heat, Mass and Momentum Transfer in Fully Developed Flow in Smooth Tubes," *Ind. Eng. Chem. Fundamentals* Vol. 16(1) pp. 109-116.

Churchill, S. W. (1977b), "Friction-Factor Equations Spans All Fluid Flow Regimes," *Chem. Eng. Prog.* Vol. 84(24) pp. 91-92.

Churchill, S. W. and H. H. S. Chu (1975), "Correlating Equations for Laminar and Turbulent Free Convection from a Horizontal Cylinder," *International Journal of Heat and Mass Transfer* Vol. 18(9) pp. 1049-1053.

Chys, M., M. van den Broek, B. Vanslambrouck and M. De Paepe (2012), "Potential of Zeotropic Mixtures as Working Fluids in Organic Rankine Cycles," *Energy* Vol. 44(1) pp. 623-632.

Cicchitti, A., C. Lombardi, M. Silvestri, G. Soldaini and R. Zavattarelli (1960), "Two-Phase Cooling Experiments: Pressure Drop, Heat Transfer and Burnout Measurements," *Energia Nucleare* Vol. 7(6) pp. 407-425.

Colburn, A. P. and T. B. Drew (1937), "The Condensation of Mixed Vapours," *AIChE Transactions* Vol. 33 pp. 197-212.

Coleman, J. W. (2000). *Flow Visualization and Pressure Drop in Small Hydraulic Diameter Geometries During Phase Change of Refrigerants*. Mechanical Engineering. Ames, Iowa State University.

Coleman, J. W. and S. Garimella (1999), "Characterization of Two-Phase Flow Patterns in Small Diameter Round and Rectangular Tubes," *International Journal of Heat and Mass Transfer* Vol. 42(15) pp. 2869-2881.

Coleman, J. W. and S. Garimella (2000a), "Two-Phase Flow Regime Transitions in Microchannel Tubes: The Effect of Hydraulic Diameter," *ASME Heat Transfer Division - 2000*, Orlando, FL, American Society of Mechanical Engineers, pp. 71-83.

Coleman, J. W. and S. Garimella (2000b), "Visualization of Two-Phase Refrigerant Flow During Phase Change.," *Proc. 34th National Heat Transfer Conference*, NHTC2000-12115 August 20-22, Pittsburgh, PA.

Coleman, J. W. and S. Garimella (2003), "Two-Phase Flow Regimes in Round, Square and Rectangular Tubes During Condensation of Refrigerant R134a," *International Journal of Refrigeration* Vol. 26(1) pp. 117-128.

Consolini, L. and J. Thome (2009), "Micro-Channel Flow Boiling Heat Transfer of R-134a, R-236fa, and R-245fa," *Microfluidics and Nanofluidics* Vol. 6(6) pp. 731-746.

Dalkilic, A. S., O. Agra, I. Teke and S. Wongwises (2010), "Comparison of Frictional Pressure Drop Models During Annular Flow Condensation of R600a in a Horizontal Tube at Low Mass Flux and of R134a in a Vertical Tube at High Mass Flux," *International Journal of Heat and Mass Transfer* Vol. 53(9-10) pp. 2052-2064.

Dalkilic, A. S. and S. Wongwises (2009), "Intensive Literature Review of Condensation inside Smooth and Enhanced Tubes," *International Journal of Heat and Mass Transfer* Vol. 52(15-16) pp. 3409-3426.

Del Col, D., A. Cavallini and J. R. Thome (2005), "Condensation of Zeotropic Mixtures in Horizontal Tubes: New Simplified Heat Transfer Model Based on Flow Regimes," *Journal of Heat Transfer* Vol. 127(3) pp. 221-230.

DiPippo, R. (2005). *Geothermal Power Plants*, Elsevier.

Dittus, W. and L. M. K. Boelter (1930), "Heat Transfer in Automobile Radiators of the Tubular Type," *University of California - Publications in Engineering* Vol. 2 p. 443.

Dobson, M. K. and J. C. Chato (1998), "Condensation in Smooth Horizontal Tubes.," *Journal of Heat Transfer* Vol. 120(1) pp. 193-213.

Dobson, M. K., J. C. Chato, J. P. Wattelet, J. A. Gaibel, M. Ponchner, P. J. Kenney, R. L. Shimon, T. C. Villaneuva, N. L. Rhines, K. A. Sweeney, D. G. Allen and T. T. Hershberger (1994). *Heat Transfer and Flow Regimes During Condensation in Horizontal Tubes*. ACRC Technical Report 57. Urbana-Champaign, University of Illinois at Urbana-Champaign.

Dukler, A. E. and M. G. Hubbard (1975), "A Model for Gas-Liquid Slug Flow in Horizontal and near Horizontal Tubes," *Industrial and Engineering Chemistry, Fundamentals* Vol. 14(4) p. 337.

El Hajal, J., J. R. Thome and A. Cavallini (2003), "Condensation in Horizontal Tubes, Part 1: Two-Phase Flow Pattern Map," *International Journal of Heat and Mass Transfer* Vol. 46(18) pp. 3349-3363.

Friedel, L. (1979), "Improved Friction Pressure Drop Correlation for Horizontal and Vertical Two Phase Flow," *3R International* Vol. 18(7) pp. 485-491.

Friedel, L. (1980), "Pressure Drop During Gas/Vapor-Liquid Flow in Pipes," *International Chemical Engineering* Vol. 20(3) pp. 352-367.

Fronk, B. M. and S. Garimella (2013), "In-Tube Condensation of Zeotropic Fluid Mixtures: A Review," *International Journal of Refrigeration* Vol. 36(2) pp. 534-561.

Fujie, H. (1964), "Relation between Steam Quality and Void Fraction in Two-Phase Flow," *AIChE Journal* Vol. 10(2) pp. 227-232.

Fukano, T. (1998), "Measurement of Time Varying Thickness of Liquid Film Flowing with High Speed Gas Flow by a Constant Electric Current Method (CECM)," *Nuclear Engineering and Design* Vol. 184(2–3) pp. 363-377.

Fuller, E. N., K. Ensley and J. C. Giddings (1969), "Diffusion of Halogenated Hydrocarbons in Helium. The Effect of Structure on Collision Cross Sections," *The Journal of Physical Chemistry* Vol. 73(11) pp. 3679-3685.

Fuller, E. N., P. D. Schettler and J. C. Giddings (1966), "New Method for Prediction of Binary Gas-Phase Diffusion Coefficients," *Industrial & Engineering Chemistry* Vol. 58(5) pp. 18-27.

Garg, P., P. Kumar, K. Srinivasan and P. Dutta (2013), "Evaluation of Isopentane, R-245fa and Their Mixtures as Working Fluids for Organic Rankine Cycles," *Applied Thermal Engineering* Vol. 51(1–2) pp. 292-300.

Garimella, S., A. Agarwal and J. W. Coleman (2003a), "Two-Phase Pressure Drops in the Annular Flow Regime in Circular Microchannels," *International Congress of Refrigeration*, Washington D.C.

Garimella, S., A. Agarwal and J. D. Killion (2005), "Condensation Pressure Drop in Circular Microchannels," *Heat Transfer Engineering* Vol. 26(3) pp. 28-35.

Garimella, S. and T. M. Bandhauer (2001), "Measurement of Condensation Heat Transfer Coefficients in Microchannel Tubes," *Proc. 2001 International Mechanical Engineering Congress and Exposition*, New York, NY, United States, American Society of Mechanical Engineers, p. 243.

Garimella, S. and R. N. Christensen (1995), "Heat Transfer and Pressure Drop Characteristics of Spirally Fluted Annuli, Part II: Heat Transfer," *ASME Journal of Heat Transfer* Vol. 117 pp. 61-68.

Garimella, S., J. D. Killion and J. W. Coleman (2002), "Experimentally Validated Model for Two-Phase Pressure Drop in the Intermittent Flow Regime for Circular Microchannels," *Journal of Fluids Engineering, Transactions of the ASME* Vol. 124(1) pp. 205-214.

Garimella, S., J. D. Killion and J. W. Coleman (2003b), "An Expermentally Validated Model for Two-Phase Pressure Drop in the Intermittent Flow Regime for Noncircular Microchannels," *Journal of Fluids Engineering, Transactions of the ASME* Vol. 125(5) p. 887.

Gilliland, E. R. (1934), "Diffusion Coefficients in Gaseous Systems," *Industrial & Engineering Chemistry* Vol. 26(6) pp. 681-685.

Gnielinski, V. (1976), "New Equations for Heat and Mass Transfer in Turbulent Pipe and Channel Flow," *International Chemical Engineering.* Vol. 16(2) pp. 359-368.

Goodykoontz, J. H. and R. G. Dorsch (1967), "Local Heat Transfer Coefficeints and Static Pressures for Condensation of Highvelocitysteam within a Tube," *NASA TN D-3953*.

Govier, G. W. and K. Aziz (1972). *Flow of Complex Mixtures in Pipes*. New York, Van Nostrand-Reinhold Co.

Graham, D. M. (1998). *Experimental Investigation of Void Fraction During Refrigerant Condensation*, University of Illinois, Urbana-Champaign, IL.

Heberle, F., M. Preißinger and D. Brüggemann (2012), "Zeotropic Mixtures as Working Fluids in Organic Rankine Cycles for Low-Enthalpy Geothermal Resources," *Renewable Energy* Vol. 37(1) pp. 364-370.

Hewitt, G. F. and A. H. Govan (1990), "Phenomenological Modelling of Non-Equilibrium Flows with Phase Change," *International Journal of Heat and Mass Transfer* Vol. 33(2) pp. 229-242.

Hewitt, G. F., S. Jayanti and C. B. Hope (1990), "Structure of Thin Liquid Films in Gas-Liquid Horizontal Flow," *International Journal of Multiphase Flow* Vol. 16(6) pp. 951-957.

Hines, A. L. (1985). *Mass Transfer: Fundamentals and Applications*. Prentice-Hall, Englewood Cliffs, N.J.

Ho, T., S. S. Mao and R. Greif (2012), "Comparison of the Organic Flash Cycle (OFC) to Other Advanced Vapor Cycles for Intermediate and High Temperature Waste Heat Reclamation and Solar Thermal Energy," *Energy* Vol. 42(1) pp. 213-223.

Hollands, K. G. T., G. D. Raithby and L. Konicek (1975), "Correlation Equations for Free Convection Heat Transfer in Horizontal Layers of Air and Water," *International Journal of Heat and Mass Transfer* Vol. 18(7-8) p. 879.

Hoogendoorn (1959), "Gas-Liquid Flow in Horizontal Pipes," *Chemical Engineering Science* Vol. 9 pp. 205-217.

Hughmark, G. A. (1962), "Holdup in Gas-Liquid Flow," *Chemical Engineering Progress* Vol. 58(4) pp. 62-65.

Hurlburt, E. T. and T. A. Newell (1996), "Optical Measurement of Liquid Film Thickness and Wave Velocity in Liquid Film Flows," *Experiments in Fluids* Vol. 21(5) pp. 357-362.

Incropera, F. P. and D. P. DeWitt (2007). *Fundamentals of Heat and Mass Transfer*. 6th Ed., John Wiley and Sons.

Isbin, H. S., H. A. Rodriguez, H. C. Larson and B. D. Pattie (1959), "Void Fractions in Two-Phase Flow," *AIChE Journal* Vol. 5(4) pp. 427-432.

Isbin, H. S., N. C. Sher and K. C. Eddy (1957), "Void Fractions in Two-Phase Steam-Water Flow," *Chemical Engineering Progress* Vol. 3(1) p. 142.

Ishii, M. (2011). *Thermo-Fluid Dynamics of Two-Phase Flow*. Springer Science+Business Media LLC, New York, NY.

Ishii, M., T. C. Chawla and N. Zuber (1976), "Constitutive Equation for Vapor Drift Velocity in Two-Phase Annular Flow," *AIChE Journal* Vol. 22(2) pp. 283-289.

Jassim, E., T. Newell and J. Chato (2007), "Probabilistic Determination of Two-Phase Flow Regimes in Horizontal Tubes Utilizing an Automated Image Recognition Technique," *Experiments in Fluids* Vol. 42(4) pp. 563-573.

Jassim, E. W. (2006). *Probabilistic Flow Regime Map Modeling of Two-Phase Flow*. United States -- Illinois, University of Illinois at Urbana-Champaign, Vol. 3242881 pp. 189-189 p.

Jassim, E. W., T. A. Newell and J. C. Chato (2008), "Prediction of Refrigerant Void Fraction in Horizontal Tubes Using Probabilistic Flow Regime Maps," *Experimental Thermal and Fluid Science* Vol. 32(5) pp. 1141-1155.

Jaster, H. and P. G. Kosky (1976), "Condensation Heat Transfer in a Mixed Flow Regime," *International Journal of Heat and Mass Transfer* Vol. 19 pp. 95-99.

Jiang, Y. (2004). *Quasi Single-Phase and Condensation Heat Transfer and Pressure Drop of Refrigerant R404a at Supercritical and near Critical Pressures*. Mechanical Engineering. Ames, Iowa State University.

Jiang, Y. and S. Garimella (2003), "Heat Transfer and Pressure Drop for Condensation of Refrigerant R-404a at near-Critical Pressures," *ASHRAE 2003 Winter Meeting CD, Technical and Symposium Papers, January 1, 2003 - January 1, 2003*, Chicago, IL, United states, Amer. Soc. Heating, Ref. Air-Conditoning Eng. Inc., pp. 667-677.

Jiang, Y., B. Mitra, S. Garimella and U. C. Andresen (2007), "Measurement of Condensation Heat Transfer Coefficients at near-Critical Pressures in Refrigerant Blends," *Journal of Heat Transfer* Vol. 129(8) pp. 958-965.

Jiang, Y. and K. S. Rezkallah (1993), "An Experimental Study of the Suitability of Using a Gamma Densitometer for Void Fraction Measurements in Gas-Liquid Flow in a Small Diameter Tube," *Measurement Science & Technology* Vol. 4(4) pp. 496-505.

Jones Jr, O. C. and N. Zuber (1975), "Interrelation between Void Fraction Fluctuations and Flow Patterns in Two-Phase Flow," Vol. 2(3) pp. 273-306.

Jung, D. S. and R. Radermacher (1989), "Prediction of Pressure Drop During Horizontal Annular Flow Boiling of Pure and Mixed Refrigerants," *International Journal of Heat and Mass Transfer* Vol. 32(12) pp. 2435-2446.

Kattan, N., J. R. Thome and D. Favrat (1998a), "Flow Boiling in Horizontal Tubes: Part 1 - Development of a Diabatic Two-Phase Flow Pattern Map," *Journal of Heat Transfer, Transactions ASME* Vol. 120(1) pp. 140-147.

Kattan, N., J. R. Thome and D. Favrat (1998b), "Flow Boiling in Horizontal Tubes: Part 3 - Development of a New Heat Transfer Model Based on Flow Pattern," *Journal of Heat Transfer, Transactions ASME* Vol. 120(1) pp. 156-165.

Kedzierski, M. A. (2006), "A Comparison of R245fa Pool Boiling Measurements to R123, and R245fa/Isopentane on a Passively Enhanced, Horizontal Surface," *International Journal of Transport Phenomena* Vol. 8(4) pp. 331-344.

Keinath, B. and S. Garimella (2010), "Bubble and Film Dynamics During Condensation of Refrigerants in Minichannels.," *14th International Heat Transfer Conference. *, Washington, DC USA

Killion, J. D. and S. Garimella (2004), "Pendant Droplet Motion for Absorption on Horizontal Tube Banks," *International Journal of Heat and Mass Transfer* Vol. 47(19-20) pp. 4403-4414.

Klein, S. A. (2011). *Engineering Equation Solver*, F-Chart Software.

Kordyban, E. (1990), "Horizontal Slug Flow: A Comparison of Existing Theories," *Transactions of the ASME. Journal of Fluids Engineering* Vol. 112(1) p. 74.

Kordyban, E. S. and T. Ranov (1970), "Mechanism of Slug Formation in Horizontal Two-Phase Flow," *Transactions of the ASME. Series D, Journal of Basic Engineering* Vol. 92(4) p. 857.

Kosky, P. G. (1971), "Thin Liquid Films under Simultaneous Shear and Gravity Forces," *International Journal of Heat and Mass Transfer* Vol. 14 pp. 1220-1224.

Kosky, P. G. and F. W. Staub (1971), "Local Condensing Heat Transfer Coefficients in the Annular Flow Regime," *AIChe Journal* Vol. 17(5) pp. 1037-1043.

Koyama, S., J. Lee and R. Yonemoto (2004), "An Investigation on Void Fraction of Vapor–Liquid Two-Phase Flow for Smooth and Microfin Tubes with R134a at Adiabatic Condition," *International Journal of Multiphase Flow* Vol. 30(3) pp. 291-310.

Lee, H. J. and S. Y. Lee (2001), "Pressure Drop Correlations for Two-Phase Flow within Horizontal Rectangular Channels with Small Heights," *International Journal of Multiphase Flow* Vol. 27(5) pp. 783-796.

Lemmon, E. W., M. L. Huber and M. O. McLinden (2013). *Reference Fluid Thermodynamic and Transport Properties - Refprop Version 9.1*. NIST Standard Reference Database 23. Gaithersburg, National Institute of Standards and Technology, Standard Reference Data Program.

Levy, S. (1960), "Steam Slip---Theoretical Prediction from Momentum Model," *Journal of Heat Transfer* Vol. 82(2) pp. 113-124.

Lockhart, R. W. and R. C. Martinelli (1949), "Proposed Correlation of Data for Isothermal Two-Phase Two-Component Flow in a Pipe," *Chem. Eng. Prog. Symp. Series* Vol. 45 p. 39.

Mandane, J. M., G. A. Gregory and K. Aziz (1974), "A Flow Pattern Map for Gas-Liquid Flow in Horizontal Pipes," *International Journal of Multiphase Flow* Vol. 1 pp. 537-553.

Martinelli, R. and D. Nelson (1948), "Prediction of Pressure Drop During Forced-Circulation Boiling of Water," *Trans. ASME* Vol. 70(6) pp. 695-702.

Mathworks, I. (2013). *Matlab R2013a (8.1.0.604) 64-Bit Windows*. Natick, MA, Mathworks, Inc.

Micropump (2000). *Micropump Series 5000 Technical Data*.

Mishima, K. and T. Hibiki (1998), "Development of High-Frame-Rate Neutron Radiography and Quantitative Measurement Method for Multiphase Flow Research," *Nuclear Engineering and Design* Vol. 184(2–3) pp. 183-201.

Mitra, B. (2005). *Supercritical Gas Cooling and Condensation of Refrigerant R410a at near-Critical Pressures*. Meachanical Enginerring. Atlanta, Georgia Institute of Technology.

Mitra, B., Y. Jiang and S. Garimella (2005), "Supercritical Gas Cooling in Refrigerant Blends," *International Institute of Refrigerantion*, Vicenza, Italy

Miyara, A. (2008), "Condensation of Hydrocarbons - A Review," *International Journal of Refrigeration* Vol. 31(4) pp. 621-632.

Moser, K., R. L. Webb and B. Na (1998), "A New Equivalent Reynolds Number Model for Condensation in Smooth Tubes," *Journal of Heat Transfer* Vol. 120 pp. 419-417.

Müller-Steinhagen, H. and K. Heck (1986), "A Simple Friction Pressure Drop Correlation for Two-Phase Flow in Pipes," *Chemical Engineering and Processing: Process Intensification* Vol. 20(6) pp. 297-308.

Nema, G., S. Garimella and B. M. Fronk (2014), "Flow Regime Transitions During Condensation in Microchannels," *International Journal of Refrigeration* Vol. 40(0) pp. 227-240.

Nusselt, W. (1916), "Die Oberflaechenkondensation Des Wasserdampfes," *Zeitschrift des Vereines Deutscher Ingenieure* Vol. 60 pp. 541-546.

Personal Communication (2013). *Primary Loop Pump Heat Addition Results*. J. Milkie, Macdonald, Malcolm

Petukhov, B. S. (1970). Heat Transfer and Friction in Turbulent Pipe Flow with Variable Physical Properties. *Advances in Heat Transfer*. T. F. Irvine, Jr. and J. P. Hartnett. New York, NY, Academic Press, Vol. 6 pp. 503-564.

Poling, B. E. (2001). *The Properties of Gases and Liquids*. 5th Ed. New York, McGraw-Hill.

Premoli, A., D. Francesco and A. Prina (1970), "An Empirical Correlation for Evaluating Two-Phase Mixture Density under Adiabatic Conditions," *European Two-Phase Flow Group Meeting, Milan*

Price, B. C. and K. J. Bell (1974), "Design of Binary Vapor Condensers Using the Colburn-Drew Equations," *AIChE Symposium Series - Heat Transfer - Research and Design* Vol. 70(138) pp. 163-171.

Reid, R. C. (1987). *The Properties of Gases and Liquids*. 4th Ed. New York, McGraw-Hill.

Revellin, R. and J. R. Thome (2007a), "Experimental Investigation of R-134a and R-245fa Two-Phase Flow in Microchannels for Different Flow Conditions," *International Journal of Heat and Fluid Flow* Vol. 28(1) pp. 63-71.

Revellin, R. and J. R. Thome (2007b), "A New Type of Diabatic Flow Pattern Map for Boiling Heat Transfer in Microchannels," *Journal of Micromechanics and Microengineering* Vol. 17(4) p. 788.

Rice, C. K. (1987), "Effect of Void Fraction Correlation and Heat Flux Assumption on Refrigerant Charge Inventory Predictions, New York, NY, USA, ASHRAE, Atlanta, GA, USA, p. 341.

Rose, J. W. (1998), "Condensation Heat Transfer Fundamentals," *Chemical Engineering Research and Design* Vol. 76(2) pp. 143-152.

Rosson, H. F. and J. A. Meyers (1965), "Point Values of Condensing Films Coefficients inside a Horizontal Tube.," *Chemical Engineering Progress Symposium Series* Vol. 61(59) pp. 190-199.

Rouhani, S. Z. and E. Axelsson (1970), "Calculation of Void Volume Fraction in the Subcooled and Quality Boiling Regions," *International Journal of Heat and Mass Transfer* Vol. 13 pp. 383-393.

Rufer, C. E. and S. P. Kezios (1966), "Analysis of Two-Phase, One-Component Stratified Flow with Condensation," *American Society of Mechanical Engineers -- Transactions -- Journal of Heat Transfer* Vol. 88(3) p. 265.

Sardesai, R. G., R. G. Owen and D. J. Pulling (1981), "Flow Regimes for Condensation of a Vapour inside a Horizontal Tube," *Chemical Engineering Science* Vol. 36(7) pp. 1173-1180.

Schubring, D., A. C. Ashwood, T. A. Shedd and E. T. Hurlburt (2010a), "Planar Laser-Induced Fluorescence (PLIF) Measurements of Liquid Film Thickness in Annular

Flow. Part I: Methods and Data," *International Journal of Multiphase Flow* Vol. 36(10) pp. 815-824.

Schubring, D., T. A. Shedd and E. T. Hurlburt (2010b), "Studying Disturbance Waves in Vertical Annular Flow with High-Speed Video," *International Journal of Multiphase Flow* Vol. 36(5) pp. 385-396.

Scott, D. S. (1964). Properties of Cocurrent Gas-Liquid Flow. *Advances in Chemical Engineering*. J. W. H. Thomas B. Drew and V. Theodore, Academic Press, Vol. Volume 4 pp. 199-277.

Sekhar, S. J., D. M. Lal and S. Renganarayanan (2004), "Improved Energy Efficiency for CFC Domestic Refrigerators Retrofitted with Ozone-Friendly HFC134a/HC Refrigerant Mixture," *International Journal of Thermal Sciences* Vol. 43(3) pp. 307-314.

Shah, M. M. (1976), "A New Correlation for Heat Transfer During Flow Boiling through Pipes," *ASHRAE Transactions* Vol. 82(2) pp. 66-86.

Shah, M. M. (1979), "A General Correlation for Heat Transfer During Film Condensation inside Pipes," *International Journal of Heat and Mass Transfer* Vol. 22 pp. 547-556.

Shao, D. W. and E. Granryd (1998), "Experimental and Theoretical Study on Flow Condensation with Non-Azeotropic Refrigerant Mixtures of R32/R134a," *International Journal of Refrigeration* Vol. 21(3) pp. 230-246.

Shimadzu (2011). *Labsolutions*.

Silver, L. (1947), "Gas Cooling with Aqueous Condensation," *Industrial Chemist and Chemical Manufacturer* Vol. 23(269) pp. 380-386.

Singal, L. C., C. P. Sharma and H. K. Varma (1983), "Pressure Drop During Forced Convection Boiling of Binary Refrigerant Mixtures," *International Journal of Multiphase Flow* Vol. 9(3) pp. 309-323.

Smith, S. L. (1969), "Void Fractions in Two-Phase Flow: A Correlation Based Upon an Equal Velocity Head Model," *Proceedings of the Institution of Mechanical Engineers* Vol. 184(1) pp. 647-664.

Soliman, H. and N. Z. Azer (1974), "Visual Studies of Flow Patterns During Condensation inside Horizontal Tubes," pp. 241-245.

Soliman, H. M. (1982), "On the Annular to Wavy Flow Pattern Transition During Condensation inside Horizontal Tubes," *Canadian Journal of Chemical Engineering* Vol. 60 pp. 475-481.

Soliman, H. M. (1983), "Correlation of Mist-to-Annular Transition During Condensation," *The Canadian Journal of Chemical Engineering* Vol. 61 pp. 178-182.

Soliman, H. M. (1986), "The Mist-Annular Transition During Condensation and Its Influence on the Heat Transfer Mechanism," *International Journal of Multiphase Flow* Vol. 12(2) pp. 277-288.

Soliman, H. M. and N. Z. Azer (1971), "Flow Patterns During Condensation inside a Horizontal Tube," *ASHRAE Transactions* Vol. 77(pt 1) pp. 210-224.

Soliman, H. M., J. R. Schuster and P. J. Berenson (1968), "A General Heat Transfer Correlation for Annular Flow Condensation," *Journal of Heat Transfer* Vol. 90 pp. 267-276.

Soliman, H. M. H. (1974). *Analytical and Experimental Studies of Flow Patterns During Condensation inside Horizontal Tubes*. United States -- Kansas, Kansas State University, Vol. Ph.D. p. 298 p.

Steiner, D. (1993). Kapitel Hbb: Strömungssieden Gesättigter Flüssigkeiten. *Vdi-Wärmeatlas*. Düsseldorf, VDI-Gesellschaft Verfahrenstechnik und Chemieingenieurwesen (GVC) pp. Hbb1-Hbb35.

Stoecker, W. F. and E. Kornota (1985), "Condensing Coefficients When Using Refrigerant Mixtures," *ASHRAE Trans.* Vol. 91(2) pp. 1351-1367.

Taitel, Y. and A. E. Dukler (1976), "A Model for Predicting Flow Regime Transitions in Horizontal and near Horizontal Gas-Liquid Flow," *AIChE Journal* Vol. 22(1) pp. 47-54.

Taitel, Y. and A. E. Dukler (1977), "A Model for Slug Frequency During Gas-Liquid Flow in Horizontal and near Horizontal Pipes," *International Journal of Multiphase Flow* Vol. 3(6) pp. 585-596.

Tandon, T. N., H. K. Varma and C. P. Gupta (1982), "A New Flow Regimes Map for Condensation inside Horizontal Tubes," *ASME Journal of Heat Transfer* Vol. 104(4) pp. 763-768.

Tandon, T. N., H. K. Varma and C. P. Gupta (1985a), "Experimental Investigation of Forced-Convection Condensation During Annular Flow inside a Horizontal Tube," *ASHRAE Transactions: Technical Papers presented at the 1985 Winter Meeting.*, Chicago, IL, USA, ASHRAE, pp. 343-355.

Tandon, T. N., H. K. Varma and C. P. Gupta (1985b), "Prediction of Flow Patterns During Condensation of Binary Mixtures in a Horizontal Tube," *Journal of Heat Transfer, Transactions ASME* Vol. 107(2) pp. 424-430.

Tandon, T. N., H. K. Varma and C. P. Gupta (1985c), "Void Fraction Model for Annular Two-Phase Flow," *International Journal of Heat and Mass Transfer* Vol. 28(1) p. 191.

Tandon, T. N., H. K. Varma and C. P. Gupta (1995), "Heat Transfer During Forced Convection Condensation inside Horizontal Tube," *International Journal of Refrigeration* Vol. 18(3) pp. 210-210.

Taylor, B. N. and C. E. Kuyatt (1994), "Guidelines for Evaluating and Expressing the Uncertainty of NIST Measurement Results," *National Institute of Standards and Technology* (SP 1297).

Thom, J. R. S. (1964), "Prediction of Pressure Drop During Forced Circulation Boiling of Water," *International Journal of Heat and Mass Transfer* Vol. 7(7) pp. 709-724.

Thome, J. R., J. El Hajal and A. Cavallini (2003), "Condensation in Horizontal Tubes, Part 2: New Heat Transfer Model Based on Flow Regimes," *International Journal of Heat and Mass Transfer* Vol. 46(18) pp. 3365-3387.

Thonon, B. (2008), "A Review of Hydrocarbon Two-Phase Heat Transfer in Compact Heat Exchangers and Enhanced Geometries," *International Journal of Refrigeration* Vol. 31(4) pp. 633-642.

Thonon, B. and A. Bontemps (2002), "Condensation of Pure and Mixture of Hydrocarbons in a Compact Heat Exchanger: Experiments and Modelling," *Heat Transfer Engineering* Vol. 23(6) pp. 3-17.

461

Toda, S. and Y. Hori (1993), "Characteristics of Two-Phase Condensing Flow by Visualization Using Computed Image Processing," *Nuclear Engineering and Design* Vol. 141(1-2) p. 35.

Traviss, D. P. and W. M. Rohsenow (1973), "Flow Regimes in Horizontal Two-Phase Flow with Condensation," *ASHRAE Trans.* Vol. 79(2) pp. 31-39.

Traviss, D. P., W. M. Rohsenow and A. B. Baron (1973), "Forced-Convection Condensation inside Tubes: A Heat Transfer Equation for Condenser Design," *ASHRAE Transactions* Vol. 79(Part 1) pp. 157-165.

Triplett, K. A., S. M. Ghiaasiaan, S. I. Abdel-Khalik, A. LeMouel and B. N. McCord (1999a), "Gas–Liquid Two-Phase Flow in Microchannels: Part II: Void Fraction and Pressure Drop," *International Journal of Multiphase Flow* Vol. 25(3) pp. 395-410.

Triplett, K. A., S. M. Ghiaasiaan, S. I. Abdel-Khalik and D. L. Sadowski (1999b), "Gas-Liquid Two-Phase Flow in Microchannels Part I: Two-Phase Flow Patterns," *International Journal of Multiphase Flow* Vol. 25(3) pp. 377-394.

Tronconi, E. (1990), "Prediction of Slug Frequency in Horizontal Two-Phase Slug Flow," *AIChE Journal* Vol. 36(5) pp. 701-709.

Ursenbacher, T., L. Wojtan and J. R. Thome (2004), "Interfacial Measurements in Stratified Types of Flow. Part I: New Optical Measurement Technique and Dry Angle Measurements," *International Journal of Multiphase Flow* Vol. 30(2) pp. 107-124.

Wallis, G. B. (1969). *One-Dimensional Two-Phase Flow*. New York, McGraw-Hill.

Wallis, G. B. and J. E. Dobson (1973), "The Onset of Slugging in Horizontal Stratified Air-Water Flow," *International Journal of Multiphase Flow* Vol. 1 pp. 173-193.

Wang, C., C. Chiang and S. Lin (1997), "Two-Phase Flow Pattern for R-134a inside a 6.5-mm (0.25-in.) Smooth Tube," *ASHRAE Transactions* Vol. 103(1) pp. 803-812.

Wang, S.-P. and J. C. Chato (1995), "Review of Recent Research on Heat Transfer with Mixtures - Part I: Condensation," *Proceedings of the 1995 ASHRAE Annual Meeting, January 29, 1995 - February 1, 1995*, Chicago, IL, USA, ASHRAE, pp. 1376-1386.

Wang, X. D. and L. Zhao (2009), "Analysis of Zeotropic Mixtures Used in Low-Temperature Solar Rankine Cycles for Power Generation," *Solar Energy* Vol. 83(5) pp. 605-613.

Webb, D. R., M. Fahrner and R. Schwaab (1996), "The Relationship between the Colburn and Silver Methods of Condenser Design," *International Journal of Heat and Mass Transfer* Vol. 39(15) pp. 3147-3156.

Weisman, J., D. Duncan, J. Gibson and T. Crawford (1979), "Effects of Fluid Properties and Pipe Diameter on Two-Phase Flow Patterns in Horizontal Lines," *International Journal of Multiphase Flow* Vol. 5(6) pp. 437-462.

Wilmarth, T. and M. Ishii (1997), "Interfacial Area Concentration and Void Fraction of Two-Phase Flow in Narrow Rectangular Vertical Channels," *Journal of Fluids Engineering, Transactions of the ASME* Vol. 119(4) pp. 916-922.

Winkler, J., J. Killion and S. Garimella (2012a), "Void Fractions for Condensing Refrigerant Flow in Small Channels. Part II: Void Fraction Measurement and Modeling," *International Journal of Refrigeration* Vol. 35(2) pp. 246-262.

Winkler, J., J. Killion, S. Garimella and B. M. Fronk (2012b), "Void Fractions for Condensing Refrigerant Flow in Small Channels: Part I Literature Review," *International Journal of Refrigeration* Vol. 35(2) pp. 219-245.

Wojtan, L., T. Ursenbacher and J. R. Thome (2004), "Interfacial Measurements in Stratified Types of Flow. Part II: Measurements for R-22 and R-410a," *International Journal of Multiphase Flow* Vol. 30(2) pp. 125-137.

Wu, C. (1985), "Non-Azeotropic Mixture Energy Conversion," *Energy Conversion and Management* Vol. 25(2) pp. 199-206.

Xu, Y. and X. Fang (2013), "A New Correlation of Two-Phase Frictional Pressure Drop for Condensing Flow in Pipes," *Nuclear Engineering and Design* Vol. 263(0) pp. 87-96.

Yashar, D. A., D. M. Graham, M. J. Wilson, J. C. Chato, H. R. Kopke and T. A. Newell (2001), "Investigation of Refrigerant Void Fraction in Horizontal, Microfin Tubes," *HVAC and R Research* Vol. 7(1) p. 67.

Zivi, S. M. (1964), "Estimation of Steady-State Steam Void-Fraction by Means of the Principle of Minimum Entropy Production," *Journal of Heat Transfer* Vol. 86(2) pp. 247-251.

Zuber, N. (1960), "On the Variable-Density Single-Fluid Model for Two-Phase Flow," *Journal of Heat Transfer* Vol. 82 pp. 255-258.

Zuber, N. and J. A. Findlay (1965), "Average Volumetric Concentration in Two-Phase Flow Systems," *Journal of Heat Transfer* Vol. 87 pp. 453-468.

Zurcher, O., D. Favrat and J. R. Thome (2002), "Development of a Diabatic Two-Phase Flow Pattern Map for Horizontal Flow Boiling," *International Journal of Heat and Mass Transfer* Vol. 45(2) p. 291.